

## The curious case of curvature

### Geometric perspectives on biomaterial design

Callens, S.J.P.

#### DOI

[10.4233/uuid:6d8f6160-5e1c-4396-a6c2-0bc67c3858b9](https://doi.org/10.4233/uuid:6d8f6160-5e1c-4396-a6c2-0bc67c3858b9)

#### Publication date

2021

#### Document Version

Final published version

#### Citation (APA)

Callens, S. J. P. (2021). *The curious case of curvature: Geometric perspectives on biomaterial design*. [Dissertation (TU Delft), Delft University of Technology]. <https://doi.org/10.4233/uuid:6d8f6160-5e1c-4396-a6c2-0bc67c3858b9>

#### Important note

To cite this publication, please use the final published version (if applicable). Please check the document version above.

#### Copyright

Other than for strictly personal use, it is not permitted to download, forward or distribute the text or part of it, without the consent of the author(s) and/or copyright holder(s), unless the work is under an open content license such as Creative Commons.

#### Takedown policy

Please contact us and provide details if you believe this document breaches copyrights. We will remove access to the work immediately and investigate your claim.

# The curious case of **curvature**

Geometric perspectives  
on biomaterial design

Sebastien Callens

The curious case of curvature



# The curious case of **CURVATURE**

Geometric perspectives on biomaterial design



# The curious case of **CURVATURE**

Geometric perspectives on biomaterial design

## PROEFSCHRIFT

ter verkrijging van de graad van doctor  
aan de Technische Universiteit Delft,  
op gezag van de Rector Magnificus Prof.dr.ir. T.H.J.J. van der Hagen,  
voorzitter van het College voor Promoties,  
in het openbaar te verdedigen op vrijdag 21 mei 2021 om 10:00 uur.

door

**Sebastien Jacob Paul CALLENS**

Ingenieur in de Luchtvaart en Ruimtevaart,  
Technische Universiteit Delft, Nederland,  
geboren te Leuven, België.



Dit proefschrift is goedgekeurd door de promotor.

Samenstelling promotiecommissie bestaat uit:

Rector Magnificus, Prof.dr. A.A. Zadpoor,	Voorzitter Technische Universiteit Delft, Nederland
--	--

*Onafhankelijke leden:*

Prof.dr.dr.h.c. P. Fratzl,	Max-Planck-Institut für Kolloid- und Grenzflächen- forschung, Duitsland
Prof.dr. G.J.V.M. van Osch,	Erasmus MC, Nederland
Prof.dr. C. Storm,	Technische Universiteit Eindhoven, Nederland
Prof.dr.ir. A. van Keulen,	Technische Universiteit Delft, Nederland

*Overig lid:*

Dr.ir. E.L. Fratila-Apachitei,	Technische Universiteit Delft, Nederland
--------------------------------	--

*Keywords:* bone tissue engineering, metabiomaterials, geometry, 4D printing.

*Cover design:* A porous material that smoothly transitions between a stochastic configuration, based on a Gaussian random field, and a periodic configuration, based on the gyroid minimal surface. Designed by the author.

*Printed by:* Gildeprint.

The research leading to these results has received funding from the European Research Council under ERC grant agreement no. [677575].

Copyright © 2021 by S.J.P. Callens

ISBN 978-94-6419-208-7

An electronic version of this dissertation is available at <http://repository.tudelft.nl/>.





# SUMMARY

The rapidly expanding field of tissue engineering presents enticing, yet demanding challenges for scientists and engineers across many different disciplines. The ultimate goal of tissue engineering is ambitious: to regenerate damaged or missing tissue in its full complexity, either *in vitro* or *in situ*, and restore organ function. In addition to cells and biochemical factors, biomaterial scaffolds form the other essential ingredient within the tissue engineering paradigm. These scaffolds support, guide, and stimulate neotissue formation and are rationally designed to meet the desired balance between mechanical, mass transport and biological properties necessary for regeneration and implantation.

Major efforts in tissue engineering have been focused on regenerating bone tissue, as bone defects and disorders impair mobility and impose large burdens on society. Bone is a complex tissue with a convoluted, hierarchical geometry that largely determines its physical properties. In bone tissue engineering, biomaterial designers have been striving to emulate this geometrical complexity in porous scaffolds, in order to obtain bone-mimicking properties and stimulate the growth of *de novo* bone tissue. Rapid advances in additive manufacturing are currently offering an increased design freedom to realize intricate scaffold morphologies, thereby rendering geometry an important aspect in the design process. Moreover, recent mechanobiological evidence has strengthened this role even further, as extracellular geometry has been found to directly influence cell and tissue behaviour. Despite clear evidence of its importance, however, the appreciation for geometry and its theoretical foundation has still been limited in scaffold design and bone tissue engineering.

Therefore, the aim of this work was to advance our understanding of the interplay between geometry and bone biology, and integrate fundamental geometric principles in the design of novel biomaterials for bone tissue engineering. We addressed this aim from three main fronts, covering both fundamental and applied research questions, and involving theoretical, computational and experimental insights.

The first part of this thesis revolves around cell-geometry interactions. Specifically, we explored the role of surface curvature, which is a fundamental local shape quantifier from differential geometry, on the spatiotemporal organization of cells and tissues. A thorough review of the existing evidence and proposed mechanisms behind curvature guidance revealed that the presence of tensile forces plays an essential role on both the cell and tissue levels (Chapter 2). Moreover, it was commonly observed that both individual cells and developing tissues preferentially patterned concave instead of convex regions. Since most prior studies relied on relatively simple substrates, often with-

out considering the mathematical basis of curvature, we designed and microfabricated substrates with controlled variations of spherical, Euclidean and hyperbolic curvatures (Chapter 3). Using quantitative image analysis, we studied the spatiotemporal organization of bone cells in these environments, and explored the role of cell contractility and extracellular matrix (ECM) development. As a general rule, we found that the cells preferred regions with negative minimum principal curvature ( $\kappa_2 < 0$ ), although they could collectively venture onto other curved regions as well, provided the distance to a region with  $\kappa_2 < 0$  was not too large. We also observed collective curvature-induced stress fibre orientation and the formation of detached cell sheets at large concavities. Finally, we observed that reducing contractility and ECM development impaired the ability of the cells to pattern unfavourably curved regions, and resulted in weaker cell bridges.

In the second part of this thesis, we zoomed out to the tissue level and established a geometric framework to quantify the morphology of trabecular bone, beyond what could be obtained with traditional morphometric indices (Chapter 4). Using a large amount of high-resolution micro-CT data, we computed the surface curvature distributions of the trabecular bone interfaces. We found that curvature probability density maps were sensitive morphological fingerprints for bone from different anatomical sites. Moreover, these maps revealed that trabecular bone does not approximate the morphology of a minimal surface, challenging a commonly made assumption. We also applied the scalar and tensorial Minkowski functionals to quantify the global geometry of the trabecular interface. The Minkowski scalars were found to unify the information of several traditional metrics within the same framework. Our work was the first to apply the relatively novel Minkowski tensors to trabecular bone morphology. Using these tensors, we were able to quantify different levels of bone anisotropy, and we found that the tensor  $W_1^{0,2}$  captures similar information as the MIL tensor, contrary to what has been assumed before. Next, we leveraged the hyperbolic geometry of triply periodic minimal surfaces (TPMS) to design architected cellular materials with independently tunable permeability and elastic mechanical properties, which could be exploited in future bone tissue scaffolds (Chapter 5). We established a parametric design strategy to decorate unit cells with hard, soft and void phases, and interpolate between strut-based and shell-based morphologies. Computational analyses confirmed that our approach substantially expanded the permeability-elasticity property space, beyond that of single-material structures. Additionally, we found that the elastic anisotropy could be tuned to a large extent by varying the spatial distribution of hard and soft materials. Furthermore, we demonstrated our approach by fabricating cellular materials with multi-material 3D printing, using a combination of hard and soft polymers.

The final part of this thesis tackles specific geometric challenges in the emerging field of 4D (bio)printing. We were particularly interested in using 4D printing to enable the 2D-to-3D fabrication of novel biomaterial scaffolds. This approach offers the advantage that the flat starting materials are accessible for planar surface functionalization techniques, which, after shape-shifting, result in a unique combination of 3D ge-

---

ometry and surface functionality. As a starting point, we sought inspiration in origami- and kirigami-based folding approaches (Chapter 6). By exploring their geometric foundations, developing physical models, and classifying different techniques, we uncovered the developability constraints that make it inherently challenging to change the intrinsic curvature of flat sheets using origami or kirigami, thereby imposing severe geometric constraints on 2D-to-3D fabrication of porous scaffolds. Building upon these insights, we developed a novel folding strategy that relies on material stretching to enable the folding of non-developable porous structures based on TPMS (Chapter 7). Through kinematical analysis, we computed foldable patches that could smoothly transition between a planar state and the final minimal surface configuration. We found that many of these patches could be connected together, by respecting the hyperbolic symmetries of TPMS, which resulted in 2D nets that could smoothly fold into large TPMS assemblies. By implementing delayed folding in certain patches, we showed that collisions during folding could be avoided. We also physically demonstrated this folding strategy by attaching pre-strained polymer sheets to 3D-printed foldable frames and exploiting the fact that the sheet pre-strain drives the folding motion and forces the sheet to adopt a configuration that approximates the minimal surface.

Taken together, this work addresses emerging concepts within biomaterials development from the fundamental perspective of geometry. Our insights further underscore the relevance of geometry, in particular surface curvature, on cell-environment interaction and scaffold design for tissue engineering. Ultimately, this work shows that geometry certainly imposes challenges to biomaterial designers, yet also offers valuable opportunities to steer biological response.



# SAMENVATTING

Het snel groeiende gebied van weefselkweek en -manipulatie, meestal “tissue engineering” genoemd, plaatst wetenschappers en ingenieurs voor interessante en multidisciplinaire uitdagingen. Het uiteindelijke doel van tissue engineering is dan ook ambitieus: het *in vitro* of *in situ* regenereren van beschadigd of ontbrekend weefsel en het herstellen van de orgaanfunctie. Naast het gebruik van cellen en biochemische factoren vormen poreuze biomaterialen, of “scaffolds” (letterlijk: steigers), een ander essentieel ingrediënt binnen tissue engineering. Deze scaffolds ondersteunen, begeleiden en stimuleren de ontwikkeling van nieuw weefsel, en worden zodanig ontworpen om de juiste balans te behalen tussen de mechanische, massatransport, en biologische eigenschappen die nodig zijn voor regeneratie en implantatie.

Binnen tissue engineering is er reeds veel aandacht besteed aan het regenereren van botweefsel, aangezien botdefecten en -aandoeningen de mobiliteit sterk kunnen verminderen en een grote last zijn voor de maatschappij. Bot is een complex weefsel met een ingewikkelde en hiërarchische structuur die voor een groot deel de fysieke eigenschappen van het weefsel bepaalt. Om botweefsel te regenereren proberen biomateriaalontwerpers poreuze scaffolds te ontwikkelen die de geometrische complexiteit van bot nabootsen, in de hoop om botachtige eigenschappen te behalen en om de groei van nieuw botweefsel te stimuleren. Dankzij de razendsnelle vooruitgang in 3D printprocessen is de ontwerpvrijheid om scaffolds met gecompliceerde vormen en structuren te maken sterk toegenomen in de afgelopen jaren. Bijgevolg is de vorm van de scaffoldstructuur op zichzelf een belangrijke ontwerpparameter geworden. Bovendien is het belang van vorm recent nog meer toegenomen, aangezien er meer en meer mechanobiologisch bewijs voorhanden is dat cellen en weefsels actief beïnvloed worden door de vorm van hun omgeving. Desalniettemin speelt meetkunde (of geometrie), de wiskundige discipline die zich bezighoudt met het bestuderen van vorm, nog al te vaak een te kleine rol in het ontwerpen van scaffolds en in tissue engineering van botweefsel.

Het doel van dit proefschrift is om het begrip van de interactie tussen geometrie en botbiologie te verbeteren, en om fundamentele meetkundige concepten in te bouwen in het ontwerp van nieuwe biomaterialen voor bot tissue engineering. We hebben dit doel vanuit drie richtingen benaderd, zowel met een fundamenteel en toegepast perspectief, en door gebruik te maken van theoretische, numerieke en experimentele inzichten.

Het eerste deel van dit proefschrift draait rond de interactie tussen cellen en vormen in hun omgeving. We hebben de rol van oppervlaktekromming, een fundamenteel concept uit de differentiaalmeetkunde om vorm te beschrijven, en de organisatie van cellen en weefsels bestudeerd. Door middel van een grondige literatuurstudie van het

beschikbare bewijs en de voorgestelde mechanismen voor het effect van oppervlaktekromming werd duidelijk dat de aanwezigheid van trekkrachten een cruciale rol speelt, zowel op het niveau van de individuele cellen als op het niveau van de weefsels (Hoofdstuk 2). Een algemene bevinding was ook dat individuele cellen en groeiende weefsels voornamelijk concave gebieden verkiezen boven convexe gebieden. Aangezien de meeste van de voorgaande studies vooral gebruik maakten van relatief eenvoudige gekromde oppervlakken, vaak zonder wiskundige basis, hebben wij specifiekere oppervlakken met gecontroleerde oppervlaktevariëaties ontworpen en gefabriceerd (Hoofdstuk 3). Onze oppervlakken bevatten zowel bolvormige, zadelvormige en Euclidische gebieden. Met behulp van kwantitatieve beeldanalyse hebben we de ruimtelijke organisatie van botcellen in deze omgevingen doorheen de tijd bestudeerd, en hebben we de rol van celcontractiliteit en de ontwikkeling van extracellulaire matrix (ECM) onderzocht. Een algemene observatie was dat cellen gebieden verkozen waar de minimale hoofdkromming negatief is ( $\kappa_2 < 0$ ), alhoewel ze collectief ook andere gekromde gebieden konden bedekken, zolang de afstand tot een regio met  $\kappa_2 < 0$  niet te groot was. We observeerden ook collectieve oriëntatie van de stressvezels en het loslaten van volledige celvellen bij grote concave vormen. Bovendien zagen we ook dat het verminderen van celcontractiliteit en ECM-ontwikkeling de capaciteit van de cellen om bepaalde krommingen te bedekken verminderde, en dat dit resulteerde in zwakkere celbruggen.

In het tweede deel van het proefschrift werd geometrie op een grotere schaal toegepast en hebben we een geometrisch raamwerk opgesteld om de morfologie van trabeculair botweefsel meer fundamenteel te bestuderen dan met traditionele morfometrische methoden (Hoofdstuk 4). We hebben gebruik gemaakt van een grote hoeveelheid hoge-resolutie micro-CT data om de oppervlaktekrommingen van menselijk trabeculair bot te bepalen. Een van onze bevindingen was dat de 2D kansverdeling van de oppervlaktekromming een gevoelige maatstaf is voor de morfologische karakteristieken van botweefsel van verschillende anatomische locaties. Bovendien lieten deze kansverdelingsdiagrammen ook zien dat trabeculair botweefsel geen benadering vormt van een minimaaloppervlak, wat eerdere aannames ontkracht. In onze nieuwe methode hebben wij ook de Minkowski scalars en tensors verwerkt om de globale geometrie van trabeculair bot te bestuderen. We observeerden dat de Minkowski scalars verschillende traditionele morfometrische concepten verenigden binnen hetzelfde raamwerk. Bovendien was ons werk het eerste dat de relatief nieuwe Minkowski tensors heeft toegepast op de analyse van trabeculair bot. Met behulp van deze tensors was het mogelijk om verschillende types van botanisotropie te kwantificeren. Een van de observaties was dat de tensor  $W_1^{0,2}$  gelijkaardige informatie bevat als de MIL tensor, in tegenstelling tot wat eerder werd aangenomen. In een volgende stap benutten we de hyperbolische meetkunde van drievoudige periodieke minimaaloppervlakken (“triply periodic minimal surfaces” of TPMS) om gestructureerde cellulaire materialen te ontwerpen waarin de permeabiliteit en de mechanische eigenschappen onafhankelijk van elkaar aangepast kunnen worden, wat interessant is voor toekomstige toepassingen.

stige botscaffolds (Hoofdstuk 5). We hebben een parametrische ontwerpstrategie opgezet waarbij we eenheidscellen konden opdelen in harde en zachte delen, en daarbij konden interpoleren tussen verschillende soorten structuren. Numerieke analyses bevestigden dat onze methode substantieel de permeabiliteit-elasticiteit ontwerpruimte kon vergroten. Bovendien werd het ook duidelijk dat de elasticiteitsanisotropie voor een groot deel aangepast kon worden door variaties in de ruimtelijke verdeling van de harde en zachte materialen. We hebben enkele van deze cellulaire materialen ook gefabriceerd met een multi-materiaal 3D-printproces, gebruikmakend van harde en zachte polymeren.

Het laatste deel van dit proefschrift behandelt specifieke geometrische vraagstukken die kaderen binnen het opkomende gebied van 4D (bio)printen. Onze interesse ligt vooral in het gebruik van 4D printen om 2D-naar-3D fabricage van nieuwe scaffolds te realiseren. Het beoogde voordeel van deze fabricagemethode is dat de vlakke startmaterialen (2D) toegankelijk zijn voor bepaalde functionaliseringstechnieken die enkel toepasbaar zijn op een vlakke ondergrond. Deze vlakke materialen kunnen, na functionalisering, dan naar de gewenste 3D structuur gevouwen worden, wat resulteert in een scaffold met een unieke combinatie van 3D structuur en oppervlaktefunctionaliteit. Als inspiratiebron hebben we eerst de eeuwenoude origami- en kirigamitechnieken bestudeerd (Hoofdstuk 6). Door de geometrische fundamenteën van deze technieken te onderzoeken, fysieke modellen te maken, en de verschillende technieken te classificeren konden we hun inherente limieten om de intrinsieke kromming van een vlak vel te veranderen blootleggen. Bijgevolg werd het duidelijk dat er significante geometrische beperkingen zijn aan het gebruik van klassieke origami of kirigami voor 2D-naar-3D fabricage van poreuze scaffolds. Daarom hebben we een nieuwe vouwstrategie bedacht die, gebruikmakend van materiaalrek, toelaat om zogeheten niet-ontwikkelbare oppervlakken gebaseerd op TPMS te vouwen (Hoofdstuk 7). Door middel van kinematische analyse hebben we vouwbare eenheden berekend die vloeiend kunnen transformeren tussen een vlakke en gekromde configuratie. Door meerdere van deze eenheden aan elkaar te bevestigen en de hyperbolische symmetrieën van TPMS te respecteren was het mogelijk om 2D patronen te creëren die vloeiend tot grotere TPMS-structuren gevouwen konden worden. Door het vouwen van sommige eenheden te vertragen ten opzichte van andere eenheden was het mogelijk om botsingen tijdens het vouwen te vermijden. We hebben deze vouwstrategie ook fysiek gerealiseerd door opgerekte polymereervellen te bevestigen aan 3D-geprinte frames. De ingebouwde spanning in de polymereervellen zorgt ervoor dat het frame zichzelf kan opvouwen, en zorgt er ook voor dat het oppervlak spontaan een zadelvormige configuratie aanneemt die dicht aanleunt bij die van het ideale minimaaloppervlak.

Dit proefschrift heeft verschillende opkomende concepten binnen de ontwikkeling van nieuwe biomaterialen behandeld vanuit een fundamenteel geometrisch perspectief. Onze inzichten hebben nog meer de relevantie van geometrie, en dan vooral oppervlaktekromming, op de interacties tussen cellen en hun omgeving bevestigd, alsook in het ontwerpproces van nieuwe scaffolds voor tissue engineering. In zijn geheel toont

dit proefschrift aan dat geometrie biomateriaalontwerpers voor belangrijke uitdagingen stelt, maar dat het ook waardevolle mogelijkheden biedt om actief biologische interacties te sturen.

# CONTENT

SUMMARY	vii
SAMENVATTING	xi

## PART I INTRODUCTION

1 INTRODUCTION	3
1.1 Shape complexity in tissues and cells	4
1.2 Geometry: the mathematical language of shape	4
1.3 Shaping biomaterial scaffolds	5
1.4 Geometric implications for 4D (bio)printing.	6
1.5 Thesis motivation, aim and objectives	7
1.6 Thesis outline	8
Bibliography	13

## PART II CELL-GEOMETRY INTERACTIONS

2 SUBSTRATE CURVATURE AS AN EXTRACELLULAR CUE	17
2.1 Introduction	18
2.2 Understanding substrate curvature	19
2.2.1 A geometrical treatment of curvature	19
2.2.2 Examples of curved biological shapes	22
2.3 Single cell response to substrate curvature	25
2.3.1 Curvature-guided cell alignment and migration	25
2.3.2 The central role of cytoskeletal mechanics.	29
2.3.3 The nucleus as a curvature sensor and regulator	33
2.4 Collective cell and tissue response to substrate curvature	36
2.4.1 Curvature-driven organization and dynamics of cell sheets	37
2.4.2 Curvature-dependent, fluidic shaping of ECM-rich tissues	41
2.5 Computational models for curvature-guidance	47
2.5.1 Cell-scale models	47
2.5.2 Tissue-scale models	50
2.6 Discussion	52
2.6.1 The implications for porous scaffold design	54
2.6.2 Opportunities for 4D printing.	56
2.6.3 Outlook	57

2.7	Conclusion . . . . .	57
2.8	Supporting information . . . . .	58
	Bibliography . . . . .	69
3	COLLECTIVE BONE CELL ORGANIZATION IN COMPLEX CURVATURE FIELDS . . . . .	71
3.1	Introduction . . . . .	72
3.2	Materials and methods . . . . .	73
3.2.1	Design of curved substrates . . . . .	73
3.2.2	Fabrication and functionalization of PDMS substrates . . . . .	73
3.2.3	Cell seeding and culture . . . . .	74
3.2.4	Immunostaining . . . . .	75
3.2.5	Confocal imaging . . . . .	75
3.2.6	Preparation of stack projections and curvature maps . . . . .	75
3.2.7	Actin frequency maps . . . . .	76
3.2.8	Intensity quantification and distance maps . . . . .	76
3.2.9	Quantification of cell sheet detachment on concave spheres and cylinders . . . . .	76
3.2.10	Quantification of stress fibre orientation . . . . .	77
3.2.11	Statistical analysis . . . . .	77
3.3	Results . . . . .	77
3.3.1	Development of cell substrates with controlled curva- tures . . . . .	77
3.3.2	Murine preosteoblasts prefer regions with negative minimum principal curvature . . . . .	79
3.3.3	Distance to $\kappa_2 < 0$ characterizes spatial cell patterning . . . . .	81
3.3.4	Cells collectively detach from large regions with $\kappa_2 < 0$ . . . . .	82
3.3.5	Curvature induces collective stress fibre orientation . . . . .	84
3.3.6	Contractility and differentiation perturbation affect cur- vature guidance . . . . .	88
3.4	Discussion . . . . .	92
3.5	Supporting information . . . . .	94
3.5.1	Surface parametrization and curvature . . . . .	94
3.5.2	FFT-based calculation of principal image orientation . . . . .	98
3.5.3	Additional figures . . . . .	100
	Bibliography . . . . .	107

## PART III A GEOMETRIC TAKE ON BONE AND SCAF- FOLDS

4	THE LOCAL AND GLOBAL GEOMETRY OF TRABECULAR BONE . . . . .	111
4.1	Introduction . . . . .	112
4.2	Materials & methods . . . . .	113
4.2.1	Trabecular bone data set . . . . .	113
4.2.2	Surface reconstruction . . . . .	113
4.2.3	Curvature estimation algorithm . . . . .	114
4.2.4	Curvature probability density distributions . . . . .	115
4.2.5	Radial distribution function of curvature . . . . .	116

4.2.6	Minkowski structure metrics . . . . .	117
4.2.7	Spatial decomposition . . . . .	118
4.2.8	Ellipsoid representation of tensors . . . . .	119
4.2.9	Standard bone morphometric analyses . . . . .	119
4.2.10	Statistical analysis . . . . .	120
4.3	Results . . . . .	120
4.3.1	Surface curvature of the trabecular bone interface . . . . .	120
4.3.2	Curvature distributions. . . . .	120
4.3.3	Radial distribution function. . . . .	123
4.3.4	Scalar Minkowski functionals . . . . .	128
4.3.5	Tensorial Minkowski functionals . . . . .	130
4.3.6	Anisotropy in spatially decomposed bone. . . . .	134
4.4	Discussion . . . . .	135
4.5	Supporting information . . . . .	137
4.5.1	Formulations of Minkowski functionals . . . . .	137
4.5.2	Additional figures. . . . .	140
	Bibliography . . . . .	146
5	TUNING METAMATERIALS USING HYPERBOLIC TILINGS . . . . .	147
5.1	Introduction . . . . .	148
5.2	Materials & Methods . . . . .	149
5.2.1	Parametric design of TPMS . . . . .	149
5.2.2	Conversion to solid structures. . . . .	150
5.2.3	Morphology . . . . .	150
5.2.4	Permeability simulations . . . . .	151
5.2.5	Effective elastic properties . . . . .	151
5.2.6	Multi-material additive manufacturing . . . . .	152
5.2.7	Mechanical compression tests . . . . .	153
5.3	Results . . . . .	153
5.3.1	Triply periodic networks from hyperbolic tilings . . . . .	153
5.3.2	Parametric design of biphasic strut-shell metamaterials. . . . .	155
5.3.3	Morphology & mass transport properties . . . . .	156
5.3.4	Elastic mechanical properties . . . . .	161
5.3.5	Balancing elasticity and permeability . . . . .	163
5.3.6	Multi-material additive manufacturing . . . . .	165
5.4	Discussion . . . . .	167
5.5	Supporting information . . . . .	171
	Bibliography . . . . .	174

## PART IV FROM FLAT SHEETS TO CURVED GEOMETRIES

6	CURVATURE IN ORIGAMI AND KIRIGAMI . . . . .	177
6.1	Introduction . . . . .	178
6.2	Geometry of surfaces and origami . . . . .	180
6.2.1	Creating intrinsic surface curvature. . . . .	180
6.2.2	Geometrical aspects of origami. . . . .	184

6.3	Origami approaches . . . . .	187
6.3.1	Origami tessellations . . . . .	187
6.3.2	Tucking molecules . . . . .	191
6.3.3	Curved-crease origami . . . . .	194
6.3.4	Concentric pleating . . . . .	196
6.4	Kirigami approaches . . . . .	199
6.4.1	Lattice kirigami . . . . .	199
6.4.2	Kirigami-engineered elasticity . . . . .	203
6.5	Discussion and conclusions . . . . .	205
6.5.1	Approximations of intrinsically curved surfaces . . . . .	205
6.5.2	Practical considerations . . . . .	207
6.5.3	Outlook . . . . .	210
	Bibliography . . . . .	218
7	HYPERBOLIC ORIGAMI OF MINIMAL SURFACES . . . . .	219
7.1	Introduction . . . . .	220
7.2	Materials and methods . . . . .	221
7.2.1	Patch kinematics . . . . .	221
7.2.2	Minimal surface generation . . . . .	221
7.2.3	Folding kinematics tool . . . . .	222
7.2.4	Design of foldable frames . . . . .	223
7.2.5	3D printing . . . . .	223
7.2.6	Micro-computed tomography and curvature estimation . . . . .	224
7.3	Results . . . . .	225
7.3.1	Hyperbolic geometry of TPMS . . . . .	225
7.3.2	Foldable minimal surface patches . . . . .	225
7.3.3	Patch connections and unit cell folding . . . . .	228
7.3.4	Multiple-unit cell assemblies . . . . .	230
7.3.5	Self-folding experiments . . . . .	232
7.4	Discussion . . . . .	234
7.5	Supporting information . . . . .	234
7.5.1	$C(P)$ bowtie patch kinematics . . . . .	234
7.5.2	Surface area change during folding . . . . .	235
7.5.3	H and Gyroid minimal surfaces . . . . .	235
7.5.4	Gauss-Bonnet theorem applied to skew polygonal patches . . . . .	235
7.5.5	Quadrilateral patches for the $P$ and $D$ surfaces . . . . .	237
7.5.6	Alternative octagonal patches for the $C(P)$ surface . . . . .	238
7.5.7	Alternative unit cell nets . . . . .	239
7.5.8	Alternative TPMS-based morphologies . . . . .	239
	Bibliography . . . . .	243

## PART V CONCLUSIONS

8	CONCLUDING REMARKS . . . . .	247
8.1	Main findings of this thesis . . . . .	248
8.2	General discussion . . . . .	250
8.3	Future research opportunities . . . . .	252

---

8.4 Parting thoughts . . . . .	255
Bibliography . . . . .	257

**PART VI EXTRA**

ACKNOWLEDGEMENTS	261
LIST OF PUBLICATIONS	265
CURRICULUM VITAE	267





# INTRODUCTION

---

1	INTRODUCTION	3
1.1	Shape complexity in tissues and cells	4
1.2	Geometry: the mathematical language of shape	4
1.3	Shaping biomaterial scaffolds	5
1.4	Geometric implications for 4D (bio)printing	6
1.5	Thesis motivation, aim and objectives	7
1.6	Thesis outline	8
	Bibliography	13

---



# 1

## INTRODUCTION

*“It is through geometry  
that one purifies the eye of the soul.”*  
- Plato

## 1.1 Shape complexity in tissues and cells

The human body is a treasure trove for material scientists, housing many functional materials across a remarkably large, multidimensional property space. For example, the stiffness spectrum of the tissues in our bodies spans nine orders of magnitude, ranging from soft intestinal mucus, to stiff cortical bone<sup>1</sup>. Such exciting properties do not merely emerge from the tissues' chemical composition, but are also due to their architectural complexity. A prototypical example is bone tissue, which is a hierarchical multiphysics material that endows our body with its load-carrying ability and locomotion, but also serves as an ion reservoir<sup>2</sup>. From a structural perspective, bone contains several structural motifs across multiple scales, such as trabeculae (Latin for “small beams”), osteons, or mineralized collagen fibrils, all contributing to its heterogeneous and anisotropic properties<sup>3</sup>.

Function-specific tissue architectures are not the unique privilege of the human body, but are found in all corners of the animal and plant kingdoms. For example, wood achieves high specific properties due to its hierarchical tubular structure<sup>4</sup>, cork is temperature-resistant due to its closed-cell foam structure<sup>5</sup>, the diabolical ironclad beetle demonstrates extreme toughness due to interdigitated sutures in its exoskeleton<sup>6</sup>, and many butterflies exhibit bright colours due to bicontinuous morphologies in their wing scales<sup>7</sup>. The remarkable properties of those natural architected materials have ushered in an era of bioinspired materials and structures, where natural design principles are borrowed to develop multifunctional (composite) materials from synthetic constituents<sup>8;9</sup>.

While material shape is, thus, a key factor in the properties of natural materials, it also directly affects biology. *In vivo*, cells dynamically and bidirectionally interact with the extracellular matrix (ECM) in which they reside, for example by exchanging biochemical signals<sup>10</sup>. However, cells also react to biophysical signals in their environment, such as forces and shapes, which has given rise to the field of mechanobiology<sup>11</sup>. In recent decades, it has become clear that such physical signals control cell function, dynamics, and fate, yet many of the underlying (mechanotransduction) mechanisms remain elusive, especially concerning the role of extracellular shape<sup>12</sup>. The dynamic nature of these cell-ECM interactions also translates to the tissue level, resulting in constantly evolving tissue architectures. In bone, for example, this modelling/remodelling process is orchestrated through the targeted action of osteoblasts and osteoclasts, and disruptions in this delicate balance are associated with bone disorders, such as osteoporosis<sup>13</sup>. Hence, the shape of tissues is also of clinical and pathological relevance. Combined, these insights are spurring the need for a deeper understanding and appreciation for shape among scientists and engineers in the bio-related fields.

## 1.2 Geometry: the mathematical language of shape

Humankind has always been fascinated by the shape of space and matter around us. As such, it is no surprise that geometry, the study of shape, is one of the oldest branches of mathematics<sup>14</sup>. Just like the other disciplines in mathematics, geometry

comes in many flavors. Here, we are primarily concerned with the differential geometry of surfaces, which provides tools to characterize the shape of three-dimensional (3D) objects, by quantifying the properties of their bounding surfaces. A quintessential concept within differential geometry is that of surface curvature, which is a measure for how much a surface locally deviates from a flat plane. Quantifying curvature at different points along the surface of a smooth object provides information on its convexity or concavity, and on the local spherical, saddle-shaped (hyperbolic), or planar (Euclidean) nature. The definition of surface curvature also extends towards discrete objects, consisting of planar faces joined by edges and vertices, which are often encountered in engineering and computational design (*e.g.* triangle meshes). For these discrete geometries, all the surface curvature is concentrated in the edges and vertices, instead of being distributed along the surface of a smooth object<sup>15</sup>.

Differential geometry, in particular surface curvature, has become an essential ingredient in contemporary materials science. Indeed, many materials, such as liquid interfaces, foams, cellular membranes, or biological tissues have convoluted morphologies that can be quantified using surface curvature, providing insight into their physical properties and formation processes<sup>16</sup>. Additionally, it is often relevant to also consider the topology of these complex materials. Topology is a related mathematical field, quantifying “connectedness”, *i.e.* the number of holes and handles in an object, thereby providing a more global perspective of shape<sup>16</sup>. Combined, surface geometry and topology provide robust tools to quantify the shape of complex natural systems, and to develop synthetic, biomimetic analogues.

“*Ubi materia, ibi geometria*”

“Where there is matter, there is geometry”

- Johannes Kepler

### 1.3 Shaping biomaterial scaffolds

Tissue engineering has emerged as a promising paradigm in regenerative medicine to replace or repair damaged tissue and restore organ function. Major efforts in tissue engineering have long been directed at regenerating bone tissue, for example, for the treatment of segmental bone defects. The classical treatment of such large defects relies on sourcing bone grafts and implanting those in the defect site, a strategy which is hindered by graft shortages, donor site morbidity, high costs, and risks of disease transfer<sup>17–19</sup>. As an alternative, the combination of bone-substituting materials and tissue engineering has attracted widespread attention. Generally, *in vitro* and *in situ* tissue engineering approaches rely on biomaterial scaffolds to act as templates that support and stimulate tissue regeneration<sup>20</sup>. Developing such functional biomaterial scaffolds presents enticing challenges for materials science. For example, the chemistry of such biomaterials should be optimized to afford biocompatibility, bioactivity and preferably controlled biodegradation<sup>21</sup>. However, it is also necessary to incorporate an intercon-

nected pore structure in the scaffolds, to enable bone ingrowth, vascularization, and the supply of nutrients and oxygen, while ensuring an appropriate and bone-mimicking set of mechanical properties<sup>18;22</sup>.

Following rapid progress in recent years, biomaterial designers have started to embrace additive biomanufacturing techniques and computational design tools to rationally design complex, porous scaffolds for bone tissue regeneration (Figure 1.1). The underlying goal is to optimize the scaffold geometries to achieve a desirable set of mechanical, mass transport and biological properties. Therefore, these architected scaffolds have earned the term “metabiomaterials”, after analogy with mechanical, acoustic or optical metamaterials that rely on material architecture to achieve unique properties<sup>23</sup>. Supported by growing mechanobiological insights, it is becoming clear that geometry is playing an important and active role in controlling cell behaviour and stimulating tissue regeneration, and thus deserves sufficient attention in biomaterial design<sup>22;24</sup>.

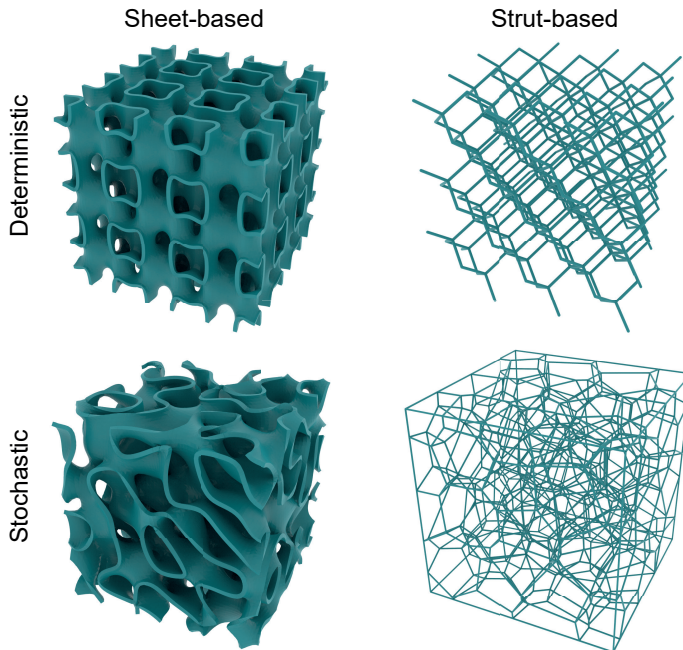


**Figure 1.1:** Examples of architected, porous scaffolds. The designs are classified in four quadrants, depending on their stochastic or deterministic nature, and their strut-based or sheet-based nature.

## 1.4 Geometric implications for 4D (bio)printing

While traditional additive manufacturing techniques (often collectively referred to as 3D printing) are still colonizing the biomedical research field and have only recently entered translational applications, researchers are already exploring more advanced fabrication routes. Recent years have witnessed a surge of interest in 4D printing, where

the fourth dimension refers to time. Specifically, 4D printing encompasses techniques where structures are 3D-printed and change shape over time, upon external triggering. Such techniques afford interesting design, fabrication, and functionalization opportunities. For example, shape-changing materials could form the basis for remotely-actuated soft robots, minimally invasive implantation, controlled drug release, or cell encapsulation<sup>25–27</sup>. A particularly interesting application of 4D printing is 2D-to-3D fabrication, where 3D structures are shape-shifted from planar (2D) configurations. This fabrication route offers the advantage that the flat starting materials are accessible for planar surface functionalization techniques, such as nanolithography, prior to shape-shifting. Hence, 2D-to-3D fabrication could offer a unique combination of 3D geometry (micro-to-macroscale) and surface topography (nanoscale), which could drastically enhance the overall biomaterial functionality.

4D printing presents unique challenges from the perspectives of materials science and geometry. From a materials point of view, challenges are related to establishing triggering mechanisms, *e.g.* by using thermo-responsive shape-memory polymers, or to the generation of sufficiently high and localized forces to enable shape-shifting. Yet, the largest hurdles to overcome lie with the geometric challenges. In general, it is not trivial to define the starting configuration and spatial planning that is required to end up at a desired final shape, especially not for topologically and geometrically complex shapes (such as porous biomaterial scaffolds). Moreover, there are mathematical restrictions to the attainable shapes, particularly in the case of 2D-to-3D fabrication. Inspiration to overcome such challenges and establish geometric “rules” for 2D-to-3D shape-shifting may come from two areas. The first is the concept of differential growth, a ubiquitous principle in nature whereby certain regions in a material grow faster than others, resulting in spontaneous buckling and shape emergence (*e.g.* in plant leaves)<sup>28</sup>. A second inspiration source is the traditional Japanese art of paper-folding: origami. Origami-inspired folding benefits from its deterministic nature, which is why it has attracted many mathematicians to uncover fundamental axioms and develop inverse-design algorithms<sup>29</sup>. Irrespective of the inspiration source, however, it is clear that geometry holds the key to unlock 4D printing as a fabrication route for next-generation biomaterials.

## 1.5 Thesis motivation, aim and objectives

The descriptions above undeniably underscore the importance of geometry as a regulator of cell and tissue behaviour, and as a design parameter in biomaterials development. Fuelled by insights in mechanobiology and advances in free-form fabrication, it is anticipated that geometric considerations will become even more important in the future. However, while robust and quantitative shape descriptions have long been established in mathematics, the appreciation for geometry and its theoretical foundation is still very limited across the biological and biomedical research spectra. Therefore, we set out to bridge the field of geometry with biology and biomaterial design.

The aim of this thesis is *to advance the understanding of the interactions between*

*geometry and bone biology, and integrate fundamental geometry in the design of next-generation biomaterials for bone tissue engineering.* As explained before, surface curvature is a key concept in this endeavour and, therefore, adopts a prominent role in this thesis. Through our theoretical, computational and experimental explorations, we aim to demonstrate that geometry imposes critical challenges, but also offers exciting opportunities for pushing the boundaries of biomaterial design and tissue engineering. To work towards this overall aim, we identified the following three major research objectives:

1. To study the role of surface curvature on the spatiotemporal organization of cells and *de novo* tissue formation.
2. To develop geometry-based tools for studying bone morphology and for designing architected materials that could serve as bone scaffolds.
3. To uncover geometric rules and develop folding algorithms for the 2D-to-3D fabrication of architected porous biomaterials.

## 1.6 Thesis outline

This thesis is structured in three major parts, corresponding to the three main research objectives outlined above. The content of this thesis touches upon a broad spectrum of topics, yet they are all connected to the overarching aim of providing a geometric perspective on bone biology and biomaterial design. The first half of the thesis covers more fundamental research, while the second half deals with more applied research questions (See also the overview figure on pages 10 and 11). Below, we provide a brief overview and structure of the chapters in this thesis.

**Part II** of the thesis covers the first research objective, and deals with the role of surface curvature on cell and tissue behaviour. In **Chapter 2**, the current insights and proposed mechanisms behind curvature-guidance are reviewed, at the scales of individual cells, cell collectives, and developing tissues. Moreover, computational approaches to model these behaviours are outlined, and the implications for scaffold design are discussed. Since most of the previous work has focussed on relatively simple geometries of constant curvature, we set out to investigate the spatiotemporal organization of bone precursor cells in microengineered, complex landscapes that span a broad and varying curvature spectrum, which is reported in **Chapter 3**. We study curvature-guided spatial patterning and orientation of the cells using quantitative imaging analysis, and we explore the role of cell contractility and extracellular matrix development on these phenomena.

In **Part III**, we zoom out and explore geometry at the scale of trabecular bone tissue and architected meta(bio)materials, corresponding to the second research objective. In **Chapter 4**, we establish a fundamental geometrical framework for the morphological characterization of trabecular bone, and apply the analysis to hundreds of microcomputed tomography scans of human bone biopsies. Specifically, we characterize the local geometry of trabecular bone using surface curvature distributions, and quantify the

---

global geometry using the scalar and tensorial Minkowski functionals that have recently been established as fundamental shape descriptors. Next, we shift focus from naturally to artificially architected materials in **Chapter 5**, and we leverage geometry to design meta(bio)materials with independently tunable properties. Specifically, we develop a parametric strategy, relying on hyperbolic geometry, to design multi-material structures based on triply periodic minimal surfaces (TPMS), which have attracted great interest as templates for bone-substituting tissue scaffolds. Using computational homogenization, we explore the elasticity-permeability property space of a broad spectrum of metamaterial designs.

**Part IV** addresses some of the above-mentioned geometric challenges in 2D-to-3D fabrication, which hinder its adoption as a viable fabrication route for architected biomaterials (research objective 3). In **Chapter 6**, the ancient arts of origami and kirigami are discussed in light of their ability to generate 3D curved structures. We describe the inherent developability constraints of these techniques but also show how apparent curvature could be generated with specific origami and kirigami designs. Based on these insights, we develop a novel origami-inspired strategy to fold complex TPMS structures from planar starting configurations in **Chapter 7**, which is theoretically challenging due to their intrinsically curved nature. However, by leveraging several geometric properties of TPMS, including their hyperbolic symmetries, we are able to compute and physically demonstrate the folding motion of several TPMS assemblies, paving the way towards 2D-to-3D fabrication of complex, porous architectures.

Finally, **Part V** concludes this thesis by providing a brief summary and discussion of our findings, as well as a reflection on the overall aim and research objectives. Moreover, we present an outlook towards future research directions.

What are the local and global geometrical properties of trabecular bone?

4

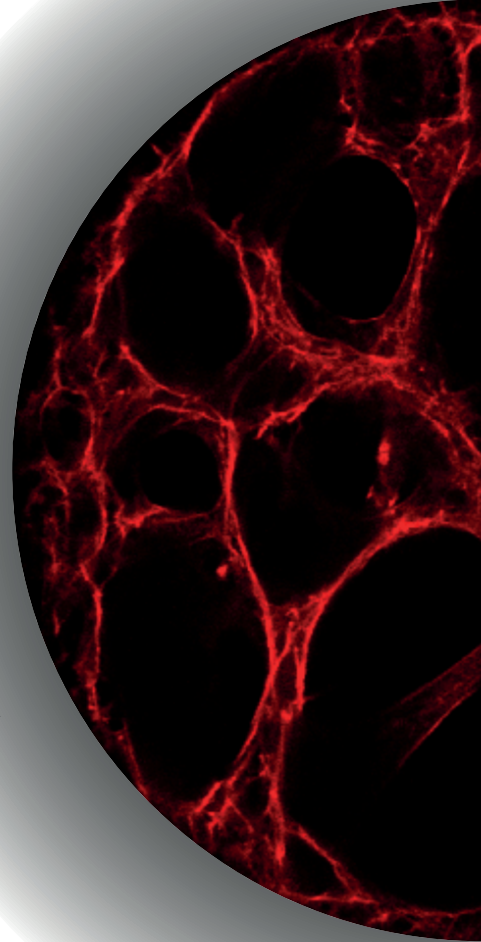
How do cells collectively pattern complex curved landscapes?

3

How is curvature guidance manifested at the cell and tissue levels ?

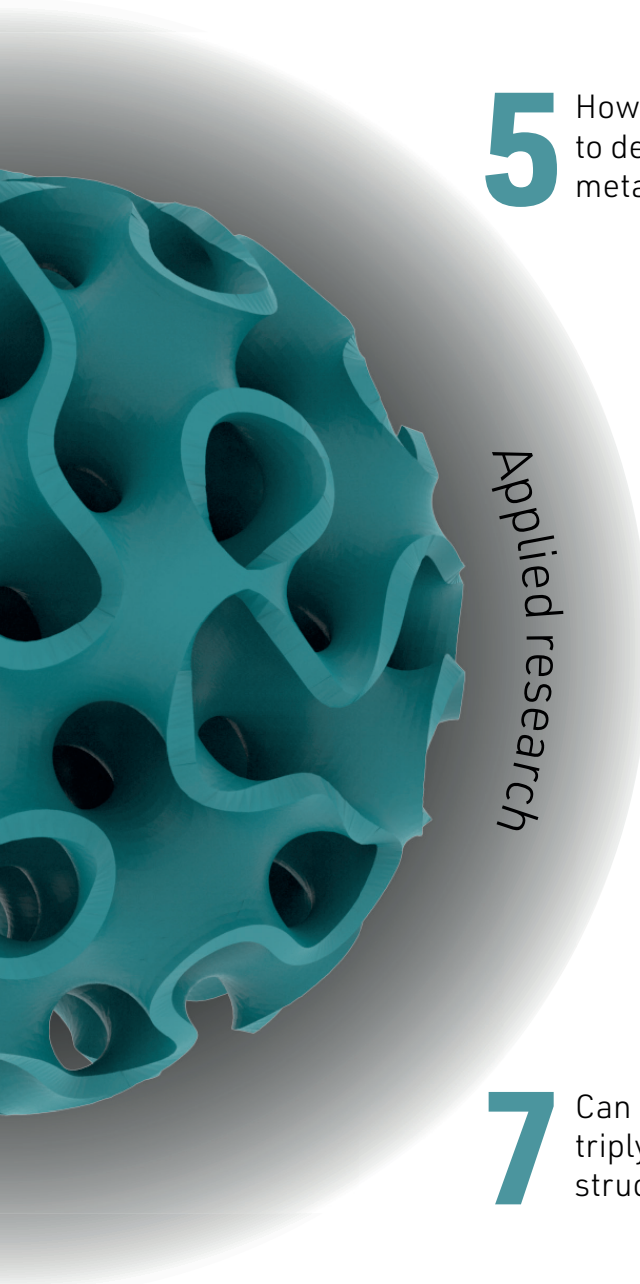
2

Fundamental research



## THE CURIOUS CASE OF CURVATURE

### Geometric perspectives on biomaterial design



**5** How can geometry be leveraged to design tunable, multifunctional meta(bio)materials?

*Applied research*

**6** How can origami and kirigami give rise to 3D curved shapes from flat sheets?

**7** Can origami inspire the folding of triply periodic minimal surface structures?

## Bibliography

- [1] C. F. Guimarães, L. Gasperini, A. P. Marques, and R. L. Reis. The stiffness of living tissues and its implications for tissue engineering. *Nature Reviews Materials*, pages 1–20, 2020.
- [2] P. Fratzl and R. Weinkamer. Nature’s hierarchical materials. *Progress in materials Science*, 52(8):1263–1334, 2007.
- [3] S. Weiner and H. D. Wagner. The material bone: structure-mechanical function relations. *Annual review of materials science*, 28(1):271–298, 1998.
- [4] C. Chen, Y. Kuang, S. Zhu, I. Burgert, T. Keplinger, A. Gong, T. Li, L. Berglund, S. J. Eichhorn, and L. Hu. Structure–property–function relationships of natural and engineered wood. *Nature Reviews Materials*, pages 1–25, 2020.
- [5] L. J. Gibson, M. F. Ashby, and B. A. Harley. *Cellular materials in nature and medicine*. Cambridge University Press, 2010.
- [6] J. Rivera, M. S. Hosseini, D. Restrepo, S. Murata, D. Vasile, D. Y. Parkinson, H. S. Barnard, A. Arakaki, P. Zavattieri, and D. Kisailus. Toughening mechanisms of the elytra of the diabolical ironclad beetle. *Nature*, 586(7830):543–548, 2020.
- [7] K. Michielsen and D. G. Stavenga. Gyroid cuticular structures in butterfly wing scales: biological photonic crystals. *Journal of the Royal Society Interface*, 5(18):85–94, 2008.
- [8] U. G. Wegst, H. Bai, E. Saiz, A. P. Tomsia, and R. O. Ritchie. Bioinspired structural materials. *Nature materials*, 14(1):23–36, 2015.
- [9] M. C. Fernandes, J. Aizenberg, J. C. Weaver, and K. Bertoldi. Mechanically robust lattices inspired by deep-sea glass sponges. *Nature Materials*, pages 1–5, 2020.
- [10] M. J. Bissell, H. G. Hall, and G. Parry. How does the extracellular matrix direct gene expression? *Journal of theoretical biology*, 99(1):31–68, 1982.
- [11] T. Iskratsch, H. Wolfenson, and M. P. Sheetz. Appreciating force and shape—the rise of mechanotransduction in cell biology. *Nature Reviews Molecular Cell Biology*, 15(12):825, 2014.
- [12] V. Vogel and M. Sheetz. Local force and geometry regulate cell functions. *Nature reviews Molecular cell biology*, 7(4):265, 2006.
- [13] X. Feng and J. M. McDonald. Disorders of bone remodeling. *Annual Review of Pathology: Mechanisms of Disease*, 6:121–145, 2011.
- [14] D. M. Burton and D. M. Burton. *The history of mathematics: An introduction*. Allyn and Bacon Boston, 1985.
- [15] K. Crane and M. Wardetzky. A glimpse into discrete differential geometry. *Notices of the AMS*, 64(10).
- [16] S. Hyde, Z. Blum, T. Landh, S. Lidin, B. Ninham, S. Andersson, and K. Larsson. *The Language of Shape: The Role of Curvature in Condensed Matter: Physics, Chemistry and Biology*. Elsevier Science, Amsterdam, The Netherlands, 1996.
- [17] R. Dimitriou, E. Jones, D. McGonagle, and P. V. Giannoudis. Bone regeneration: current concepts and future directions. *BMC medicine*, 9(1):1–10, 2011.
- [18] M. M. Stevens. Biomaterials for bone tissue engineering. *Materials today*, 11(5):18–25, 2008.
- [19] F. J. O’Brien. Biomaterials & scaffolds for tissue engineering. *Materials Today*, 14(3):88–95, 2011.
- [20] N. A. Kurniawan. The ins and outs of engineering functional tissues and organs: evaluating the in-vitro and in-situ processes. *Current opinion in organ transplantation*, 24(5):590, 2019.
- [21] G. L. Koons, M. Diba, and A. G. Mikos. Materials design for bone-tissue engineering. *Nature Reviews Materials*, pages 1–20, 2020.
- [22] A. A. Zadpoor. Bone tissue regeneration: the role of scaffold geometry. *Biomaterials Science*, 3(2):231–45, 2015.
- [23] A. A. Zadpoor. Meta-biomaterials. *Biomaterials science*, 8(1):18–38, 2020.
- [24] M. Werner, N. A. Kurniawan, and C. V. Bouten. Cellular geometry sensing at different length scales and its implications for scaffold design. *Materials*, 13(4):963, 2020.
- [25] S. Felton, M. Tolley, E. Demaine, D. Rus, and R. Wood. A method for building self-folding machines. *Science*, 345(6197):644–646, 2014.
- [26] S. Babae, S. Pajovic, A. R. Kirtane, J. Shi, E. Caffarel-Salvador, K. Hess, J. E. Collins, S. Tamang,

- 
- A. V. Wahane, and A. M. Hayward. Temperature-responsive biometamaterials for gastrointestinal applications. *Science translational medicine*, 11(488), 2019.
- [27] B. Gao, Q. Yang, X. Zhao, G. Jin, Y. Ma, and F. Xu. 4D bioprinting for biomedical applications. *Trends in biotechnology*, 34(9):746–756, 2016.
- [28] A. S. Gladman, E. A. Matsumoto, R. G. Nuzzo, L. Mahadevan, and J. A. Lewis. Biomimetic 4D printing. *Nat Mater*, 15(4):413–8, 2016.
- [29] T. Tachi. Origamizing polyhedral surfaces. *IEEE Transactions on Visualization and Computer Graphics*, 16(2):298–311, 2010.





# CELL-GEOMETRY INTERACTIONS

---

2	SUBSTRATE CURVATURE AS AN EXTRACELLULAR CUE	17
2.1	Introduction	18
2.2	Understanding substrate curvature	19
2.3	Single cell response to substrate curvature	25
2.4	Collective cell and tissue response to substrate curvature	36
2.5	Computational models for curvature-guidance	47
2.6	Discussion	52
2.7	Conclusion	57
2.8	Supporting information	58
	Bibliography	69
3	COLLECTIVE BONE CELL ORGANIZATION IN COMPLEX CURVATURE FIELDS	71
3.1	Introduction	72
3.2	Materials and methods	73
3.3	Results	77
3.4	Discussion	92
3.5	Supporting information	94
	Bibliography	107

---



# 2

## SUBSTRATE CURVATURE AS AN EXTRACELLULAR CUE

Recent evidence clearly shows that cells respond to various physical cues in their environments, guiding many cellular processes and tissue morphogenesis, pathology, and repair. One aspect that is gaining significant traction is the role of local geometry as an extracellular cue. Elucidating how geometry affects cell and tissue behavior is, indeed, crucial to design artificial scaffolds and understand tissue growth and remodeling. Perhaps the most fundamental descriptor of local geometry is surface curvature, and a growing body of evidence confirms that surface curvature affects the spatiotemporal organization of cells and tissues. While well-defined in differential geometry, curvature remains somewhat ambiguously treated in biological studies. Here, we provide a more formal curvature framework, based on the notions of mean and Gaussian curvature, and summarize the available evidence on curvature guidance at the cell and tissue levels. We discuss the involved mechanisms, highlighting the interplay between tensile forces and substrate curvature that forms the foundation of curvature guidance. Moreover, we show that relatively simple computational models, based on some application of curvature flow, are able to capture experimental tissue growth remarkably well. Since curvature guidance principles could be leveraged for tissue regeneration, the implications for geometrical scaffold design are also discussed. Finally, perspectives on future research opportunities are provided.

S. J. P. Callens, R. J. C. Uyttendaele, L. E. Fratila-Apachitei, A. A. Zadpoor, Substrate curvature as a cue to guide spatiotemporal cell and tissue organization, *Biomaterials*, 232, 229739, 2020.

## 2.1 Introduction

Complex shapes are omnipresent in our physical world and are found at all length scales, ranging from nanostructured materials<sup>1</sup> to the abstract shape of the universe<sup>2</sup>. Such shape complexity is also observed in biology, and the intriguing way it could emerge from a single zygote forms a central topic in embryogenesis. It has long been understood that biological form and function are intimately connected, and that mechanical forces are at play in the growth of complex biological shapes<sup>3</sup>. The appreciation for this interplay between force and shape on one hand, and biology on the other, has laid the foundation for mechanobiology as an important discipline explaining cell behavior<sup>4</sup>. Indeed, it is now well established that the physical aspects of a cell's surroundings deserve as much attention as the chemical nature of the environment. For example, cell shape, motility, and fate could all be affected by physical cues in the environment such as stiffness<sup>5;6</sup>, viscoelasticity<sup>7</sup>, or the applied mechanical stretch<sup>8;9</sup>. These physical cues are sensed by cells through integrin-mediated force-feedback between the cell and the extracellular matrix (ECM) or through cell-cell interactions, and elicit a cell-level response that contributes to the emergent organization of tissue and organism shapes<sup>10-12</sup>. The transduction of physical signals into biochemical responses is enabled through mechanotransduction pathways, which are not limited to conformation-dependent molecular processes at the cell surface but also involve the nucleus, being mechanically linked to the ECM through the cytoskeleton.<sup>10;13</sup>

In addition to material-dependent physical cues<sup>14</sup>, purely shape-dependent signals can also affect cell response. For example, it has long been known that small-scale topographies in the environment (*e.g.*, grooves or pillars) could affect cell fate and motility<sup>15-18</sup>. In addition to such sub-cellular-scale features, however, it is now understood that the three-dimensional (3D) shape of the environment at a larger scale ( $\geq$  cell size) can also guide cell and tissue behavior<sup>19</sup>. As such, it is of crucial importance to be able to quantitatively describe the (3D) shape of the cell environment. This may be best achieved using the notion of surface curvature. Surface curvature is a fundamental concept within the mathematical field of differential geometry, capable of describing the local geometry of a 3D object (*i.e.*, the geometry of the bounding surface of that object). Indeed, a rapidly growing body of experimental evidence, supported by computational insights, shows that the organization, dynamics, and fate of individual cells can be influenced by substrate curvature, on a scale larger than the individual cell size. Furthermore, the impact of substrate curvature extends to the tissue level, and affects both the temporal and spatial organization of tissue growth.

Here, we review the recent evidence demonstrating the role of substrate curvature on cell organization and motility, as well as on *de novo* tissue growth. We first introduce the “language of shape”<sup>20</sup> in terms of the formal descriptions of surface curvature, aiming to provide a bridge between the fields of differential geometry and biology. Then, we discuss the response of individual cells to mesoscale substrate curvature and address the specific roles of intracellular components, such as the cytoskeleton and the nucleus. Next, we move on to the collective behavior of cells, starting with cell monolayers and

continuing with more advanced (often bone-like) tissue constructs. We also show how cell and tissue-level computational models can reproduce many of the experimental observations on curvature guidance. Understanding the response of cells and tissues to substrate curvature is important, not only to elucidate the mechanisms involved in tissue morphogenesis, pathology, and repair, but also to advance the development of novel biomaterial strategies for tissue engineering and regenerative medicine. Therefore, we also briefly address the implications of the reviewed curvature guidance principles for scaffold design. We conclude with an outlook on future research directions.

## 2.2 Understanding substrate curvature

### 2.2.1 A geometrical treatment of curvature

The concept of curvature is unavoidable to everyone attempting to describe shape. Whether dealing with lines, surfaces, or higher-dimensional objects, curvature is a fundamental geometrical property that provides local information about the shape of the object. Though intuitive to some extent, curvature is often informally treated in applied contexts using ambiguous terms such as “concavity” and “convexity” that do not capture its full complexity. However, the field of differential geometry provides formal curvature definitions, enabling precise and unambiguous descriptions of the local shape of objects. Here, we aim to introduce these definitions and equip the reader with a more formal understanding of surface curvature, in order to better discuss its relevance within mechanobiology.

Perhaps the most intuitive notion of curvature is that of a curved line drawn on a two-dimensional plane. In this case, the curvature can be calculated at any point along the line as the reciprocal of the radius of the osculating circle at that point (Figure 2.1a). The curvature of this one-dimensional (1D) line embedded in a two-dimensional (2D) plane provides a measure for how much the line deviates from a straight line at any particular point. Increasing the dimension by one order, it is possible to consider the curvature of a two-dimensional (2D) surface that is embedded in three-dimensional (3D) space. Analogous to the previous case, the surface curvature is again evaluated at a single point, and it describes how the surface deviates from the tangent plane at that point<sup>21</sup>. This means that curvature is a local property of a surface. It is, therefore, not possible to assign a single value of curvature to a surface, unless that surface has constant curvature. Within the context of this chapter, we are concerned with this concept of surface curvature. That is, we are interested in the curvature of the outer surface of the substrates that cells are situated on. Surface curvature is an inherently more complex concept than the curvature of a line in a 2D plane, since surface curvature depends on the direction that is being considered. For example, a surface might be curved in one direction while remaining flat in the orthogonal direction (*e.g.*, the curvature of a cylinder). To quantitatively describe surface curvature, two important measures have been established, namely the mean curvature,  $H$ , and the Gaussian curvature,  $K$ , both of which are useful and provide complementary perspectives on curvature.

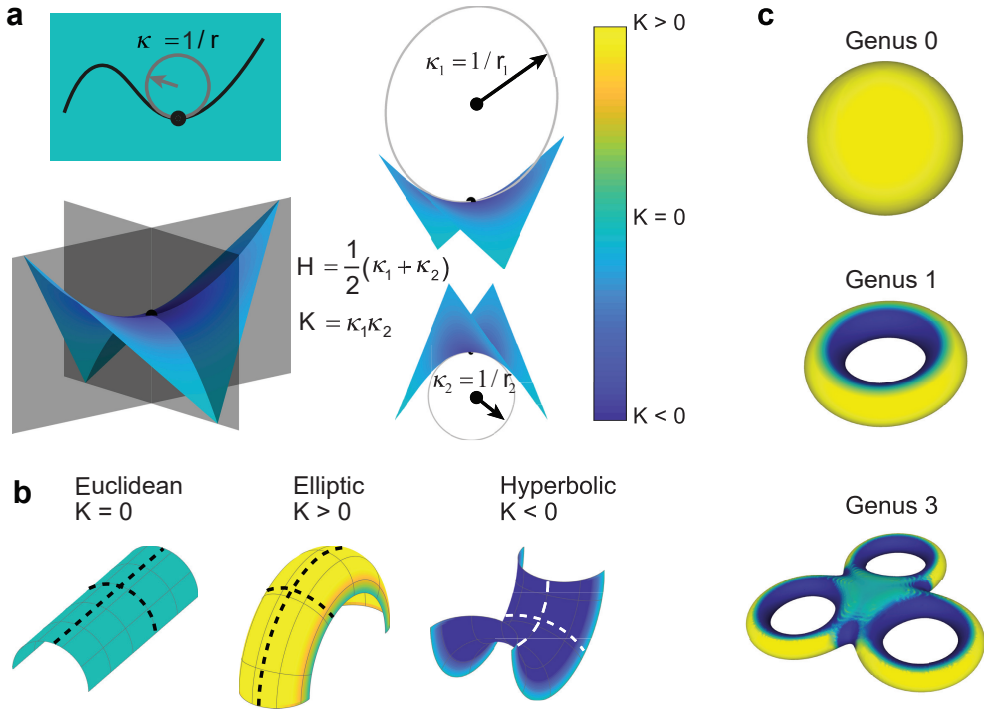


**Figure 2.1:** The definition of surface curvature. a) Top left inset displays curvature of a 1D line embedded in a 2D plane. Remainder of the panel displays mean ( $H$ ) and Gaussian ( $K$ ) surface curvatures as functions of the principal curvatures, demonstrated on a saddle shape. b) Some examples of intrinsically flat and intrinsically curved geometries: a cylinder (left), an elliptic surface (middle), and a hyperbolic surface (right). c) The relation between the genus of a surface (topology) and the Gaussian curvature of that surface.

To define both mean and Gaussian curvatures, it is useful to first introduce the principal curvatures at a point on the surface. Imagine intersecting a curved surface at a given point with a normal plane, *i.e.* a plane that contains the normal to the surface at that point. The plane and the surface intersect along a curved line, with normal curvature  $\kappa_n$  (determined as the inverse of the radius of the osculating circle,  $\kappa_n = 1/r_n$ ). Rotating through all possible normal planes at this particular point yields a maximum and minimum value for the normal curvature, which are the principal curvatures,  $\kappa_1$  and  $\kappa_2$ , of the surface at that point. The principal curvatures can then be used to define both the mean ( $H$ ) and Gaussian ( $K$ ) curvatures as:

$$H = \frac{1}{2}(\kappa_1 + \kappa_2) \quad (2.1)$$

$$K = \kappa_1 \cdot \kappa_2 \quad (2.2)$$

For every point on a curved surface, it is possible to calculate a single real-valued mean and Gaussian curvature using the above definitions. Note that both measures

are dimensional, with the mean curvature having the dimension  $[1/l]$  and the Gaussian curvature having the dimension  $[1/l^2]$ , where  $l$  is the length dimension. A flat plane, not surprisingly, has mean and Gaussian curvatures of zero, since  $\kappa_1 = \kappa_2 = 0$ . Rolling a flat plane into a cylinder produces nonzero mean curvature, but leaves the Gaussian curvature unaffected since one of the two principal curvatures remains zero for a cylinder. To achieve non-zero Gaussian curvature, both principal curvatures have to be nonzero. This is, for example, the case on a sphere, where the principal curvatures are equal and positive, or on a saddle, where the principal curvatures have opposite sign (Figure 2.1a). As a consequence, the Gaussian curvature is always positive on sphere-like or “elliptic” geometries ( $K > 0$ ) while it is negative for saddle-like or “hyperbolic” geometries ( $K < 0$ ). It is important to realize that the sign of the Gaussian curvature is an important indicator of the type of surface that is dealt with, since it remains unchanged regardless of the side of the surface being considered. For example, the Gaussian curvature of a point on a sphere is always positive, no matter when looking at the outside (“convex” part) or inside (“concave” part) of the sphere. This is different for the sign of the mean curvature, which depends on the chosen convention for the positive and negative principal curvatures, *i.e.* it depends on the chosen direction of the surface normal. This fact hints at a deeper difference between the mean and Gaussian curvatures: the mean curvature is an extrinsic measure, meaning that it can be defined from outside the surface, while the Gaussian curvature is an intrinsic measure, which can be defined from within the surface itself<sup>20–22</sup>. Otherwise stated, a resident living on a curved surface would be able to measure the Gaussian (or the intrinsic) curvature of that surface. This could, for example, be achieved by calculating the sum of the interior angles of a triangle drawn on the surface. On an intrinsically flat surface, such as a plane or a cylinder, the sum of the interior angles would equal  $\pi$ . On a spherical surface, however, the sum of the interior angles would exceed  $\pi$ , while the sum would be less than  $\pi$  on a saddle-shaped surface. It would, therefore, be possible to extract information about the intrinsic curvature of the surface merely by measuring the angles within a surface. This is, however, not true for the mean or extrinsic curvature, as this type of curvature depends on the way the surface is embedded in the reference 3D space. That is, the resident living on the surface would not be able to distinguish between, say, a cylinder and a flat plane<sup>21</sup>.

While surface curvature remains a local property, an intimate relationship between the curvature of a surface and its global topology, or “connectedness”, exists. The Gauss-Bonnet theorem dictates that the area-integrated Gaussian curvature, or the total curvature of a surface is proportional to the genus ( $g$ ) of that surface, which is a topological invariant describing the number of “handles” of the surface<sup>20</sup>:

$$\int_A K da = 4\pi(1 - g) \quad (2.3)$$

The Gauss-Bonnet theorem, therefore, shows that any surface with given genus,  $g$ , has the same integral Gaussian curvature. Moreover, the genus provides information on

the sign of the integral Gaussian curvature. A surface with  $g=0$  (e.g., a sphere), should have a positive integral Gaussian curvature. A surface with  $g = 1$  (e.g., a torus), has zero integral Gaussian curvature. Indeed, the region with positive Gaussian curvature on the outside of the torus is balanced by the negative Gaussian curvature on the inside. Any surface with a higher genus, has negative integral Gaussian curvature (Figure 2.1c). In other words, surfaces with  $g > 1$  are, in an integral sense, hyperbolic<sup>20</sup>.

Equipped with these definitions of the mean and Gaussian curvatures, it is possible to more formally describe the surface curvature and link it to the mechanobiological response of cells. It should be clear that surface curvature should primarily be discussed using these formal descriptors, and not solely using ambiguous terms such as “convex” and “concave” surfaces. For example, the inner surface of a cylinder and a spherical cap could both be considered as concave, but they are very different from a more formal curvature perspective (i.e., a cylinder has  $K = 0$  everywhere whereas a sphere has  $K > 0$  everywhere). Moreover, the inner and outer sides of a sphere surface are often distinguished from each other using convexity and concavity, but could more formally be described using mean and Gaussian curvatures: the Gaussian curvature is the same for both cases (and it is positive), but the mean curvatures are opposite in sign. The usefulness of convexity and concavity fades further away when discussing saddle surfaces ( $K < 0$ ), which are convex in one direction and concave in another. Hence, the usage of the terms “convex” and “concave” should be accompanied by the more formal descriptions of the mean and Gaussian curvatures.

### 2.2.2 Examples of curved biological shapes

While *in vitro* biological experiments often deal with cells that are constrained to 2D flat surfaces, the natural environment that cells inhabit *in vivo* is 3D, and can be highly complex. The extracellular environment is not only complex due to its hierarchical and composite nature, but is also structured in such a way that gives rise to spatially varying Gaussian and mean curvature distributions, resulting in a myriad of shapes that are geometrically and topologically more complex than planar surfaces. Curvature appears on various scales in biological matter, ranging from the sub-cellular (radius of curvature  $\approx 10^1 - 10^3 \mu m$ ), and plays an important role in both morphogenesis and pathology<sup>23;24</sup>. On the smallest scale, lipid bilayer membranes can take on complex curved shapes, a consequence of the interplay between the biochemistry of the membrane formation, membrane mechanics, and geometrical frustration<sup>25-27</sup>. Examples of intrinsically curved membrane structures are membrane-bound spherical vesicles (positive Gaussian curvature), cleavage furrows during cytokinesis (negative Gaussian curvature)<sup>26</sup>, or the intracellular structures of the endoplasmic reticulum and the Golgi apparatus<sup>25</sup> that exhibit high degrees of curvature variation. More convoluted membrane organizations have also been observed, whereby the membrane adopts a 3D minimal surface morphology with cubic periodicity, for example, in the mitochondria of giant amoebae *Chaos carolinensis*<sup>28;29</sup>. It is, however, the curvature that appears on a larger scale in the extracellular environment that we are primarily concerned with in this

chapter. A high level of shape complexity is observed throughout many organs, which are lined by epithelial tissue. One type of recurring geometry that is, to some extent, representative for many epithelial tissue constructs are cylindrical structures. Examples are tubular vessels, ranging from small capillaries to large arteries, tubular glands, and ducts<sup>30</sup>. Despite their tubular nature, the geometry of these biological structures quickly deviates from mathematically defined cylinders (with zero Gaussian curvature everywhere) once the tubular structures are bent or branched, as this introduces curvature in the second principal direction, hence resulting in regions with positive or negative Gaussian curvatures (Figure 2.2). The intricate epithelial geometries of complex organs, such as the kidney, lung or intestine, all emerge from a simple planar cell sheet during embryonic development<sup>31</sup>. Interestingly, this morphogenetic sculpting from a planar to a complex, curved geometry is not solely driven by genetic factors, but also relies heavily on thin-sheet mechanics. It has been found that mechanical instabilities in cell sheets, in the form of buckling and wrinkling, could drive the morphogenesis of the cerebral cortex<sup>32</sup>, intestinal villi<sup>33</sup>, airway branching<sup>34</sup>, or tooth development<sup>31;35</sup>. Such mechanical instabilities arise as a consequence of a faster growth of the epithelial sheet with respect to the constraining mesenchyme that surrounds it, causing the sheet to buckle within the mesenchyme (in engineering mechanics, this problem is known as the buckling of a plate on an elastic foundation<sup>36</sup>). The mechanical forces applied to flat epithelia could, therefore, explain much of the spontaneous formation of complex curvature distributions during morphogenesis. The convoluted geometries that arise from these instabilities could, in turn, control further morphogenesis, for example, by regulating the spatial patterns of cell proliferation<sup>37;38</sup> or by controlling the spatial distribution of morphogens<sup>23</sup>. In addition to epithelial morphogenesis, complex curvatures could also emerge during disease, for example, in colonic diverticulosis<sup>39</sup> or polycystic kidney disease<sup>40</sup>. In both cases, outwards-bulging spherical pouches are formed on the colon (Figure 2.2) or kidney respectively, characterized by a primarily positive Gaussian curvature, with negative Gaussian curvature in the neck region. Some similar types of curvature distributions could be observed in the presence of tumors. In fact, tumorigenesis has been found to be partly controlled by geometrical cues, such as curvature<sup>24;41</sup>. In mice pancreatic ducts subject to oncogenic transformation, for example, the direction of tumor growth was found to depend on the radius of curvature of the duct: tumors expanded outwards on narrow ducts (exophytic), while they grew inwards on larger ducts (endophytic)<sup>24</sup>.

Among the other types of tissue, osseous tissue is also well known to exhibit complex curvature fields. At a small scale, osteoclasts generate small pits and trenches in the surface of the mineralized matrix during bone resorption, resulting in local curvature variations sensible by osteocytes and osteoblasts. On a slightly larger scale, however, bone tissue is also characterized by complex curvature distributions, particularly trabecular bone. The network-like structure of trabecular bone has been shown to be characterized by an average negative Gaussian surface curvature, rendering trabecular bone on average “hyperbolic” or saddle-shaped<sup>42;43</sup>. Moreover, the average mean

surface curvature of trabecular bone was found to be close to zero ( $H \approx 0$ )<sup>42</sup>.

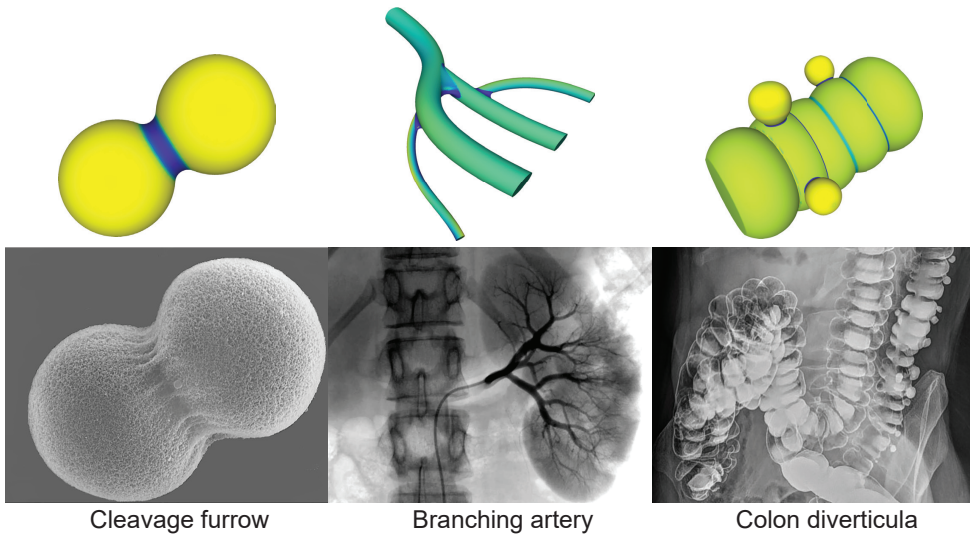


**Figure 2.2:** Some examples of Gaussian curvature in biological structures. Left: a cleavage furrow during cytokinesis<sup>44</sup>. Middle: Branching in an arterial network<sup>45</sup>. Right: Diverticula on the colon<sup>46</sup>.

It should be clear that a plethora of curved biological structures exists, and that truly flat structures are rather the exception than the rule in native tissues. However, the question of scale should not be neglected when discussing curvature, as this only makes sense when doing so relative to the cell size. For example, very low values of curvature, with very large radii of curvature, might not be “noticed” by the cells at all. On the other hand, very high values of curvature, with radii much smaller than the characteristic cell length, should be considered more as a topographical feature (*i.e.* micro- or nanotopographies<sup>15;17;47;48</sup>) rather than a truly curved substrate. At such small scales, curvature is manifested in the form of local, curved deformations in the cell membrane<sup>10</sup>. In this case, BAR (Bin/Amphiphysin/Rvs) domain proteins have been known to be involved, both as curvature generators and as curvature sensors<sup>49</sup>. Due to the inherent curved nature of these BAR domains, they could impose curvature in initially flat membranes when binding to the membrane through electrostatic interactions<sup>50</sup>. Alternatively, the BAR domain structures could act as sensors of already curved membranes (*e.g.*, curved due to an external geometrical feature) by preferentially binding to these curved portions of the membrane and recruiting small *G* proteins<sup>10;51</sup>. Because the cell membrane is a bilayer, curving it will induce differences in stress distributions between both sides of the membrane, which could lead to ion channel opening in the membrane<sup>52</sup>. It has been suggested that this selective channel opening could constitute another curvature sensing mechanism<sup>10</sup>. While membrane curvature is important for various cell processes, such as endocytosis<sup>53</sup> and membrane fusion<sup>54</sup>, we are dealing with curvature at much larger length scales in this chapter, and we refer the interested

reader to other reviews on the physics behind membrane curving<sup>49;50;54</sup>. For the remainder of this review, we will focus on substrate curvature on length scales equal to or higher than that of typical (mammalian) cell sizes, *i.e.* the radii of curvature in the approximate range of  $10^1 - 10^3 \mu\text{m}$ .

## 2.3 Single cell response to substrate curvature

The appreciation for substrate curvature as a mechanism to guide cellular behavior (*i.e.*, “curvotaxis”<sup>55</sup>) is much more recent than that for other environmental cues such as chemical gradients (“chemotaxis”) or substrate stiffness (“durotaxis”). Nevertheless, there is a growing body of experimental evidence demonstrating that individual cells can respond to substrate curvature in various ways, ranging from initial migratory patterns to the differentiation behavior. While substrate curvature originally seemed to be considered within the perspective of contact guidance, *i.e.* the guiding principle where cells align along (small) ECM fibers<sup>56;57</sup>, it is now typically being considered as separate guiding mechanism, *i.e.* “curvotaxis”<sup>55</sup> or “curvature guidance”, rather than a subset of contact guidance<sup>58</sup>. This is primarily due to the larger curvature radii in the context of curvature guidance ( $\geq$  cell size) as opposed to the subcellular-scale features in the case of contact guidance.

Despite a rapidly growing interest in single-cell experiments on curved substrates, only a few types of curved geometries have been considered so far, in part due to the challenge of fabricating precisely-defined microscale substrates with controllable curvatures (Figure 2.3)<sup>59</sup>. In many studies, cylindrical substrates have been employed, either by seeding cells on thick (compared to cell size) fibers<sup>57;60–63</sup>, or on hemi-cylindrical patterned substrates<sup>64–66</sup>. In addition to these discrete cylindrical geometries, smoothly-varying sinusoidal or “wavy” patterns have also been used<sup>67–69</sup>. From a formal curvature perspective, all these geometries are examples of developable surfaces, which have non-zero mean curvatures ( $H > 0$  on the convex parts and  $H < 0$  on the concave parts), but zero Gaussian curvature ( $K = 0$ ) everywhere. In addition to cylindrical geometries, substrates patterned with hemispherical convex caps ( $H > 0, K > 0$ ) or concave pits ( $H < 0, K > 0$ ) have also been employed in several studies<sup>64;70–73</sup>, as well as smoothly-varying, wavy patterns of alternating caps and pits<sup>55</sup>. Surprisingly, little research has been performed on the response of cells to substrates with negative Gaussian curvatures ( $K < 0$ ), which are saddle-shaped substrates<sup>30;66</sup>. In this section, we outline recent results on the behavior of individual cells on curved substrates, first by describing how curvature affects cell alignment and migration, and later by addressing the specific roles of cytoskeletal tension and the cell nucleus in sensing and responding to curvature.

### 2.3.1 Curvature-guided cell alignment and migration

Cell alignment and migration are the most commonly investigated phenomena in single-cell experiments on curved substrates. Throughout the lifetime of multicellular organisms, cell migration plays a fundamental role in the development, maintenance,

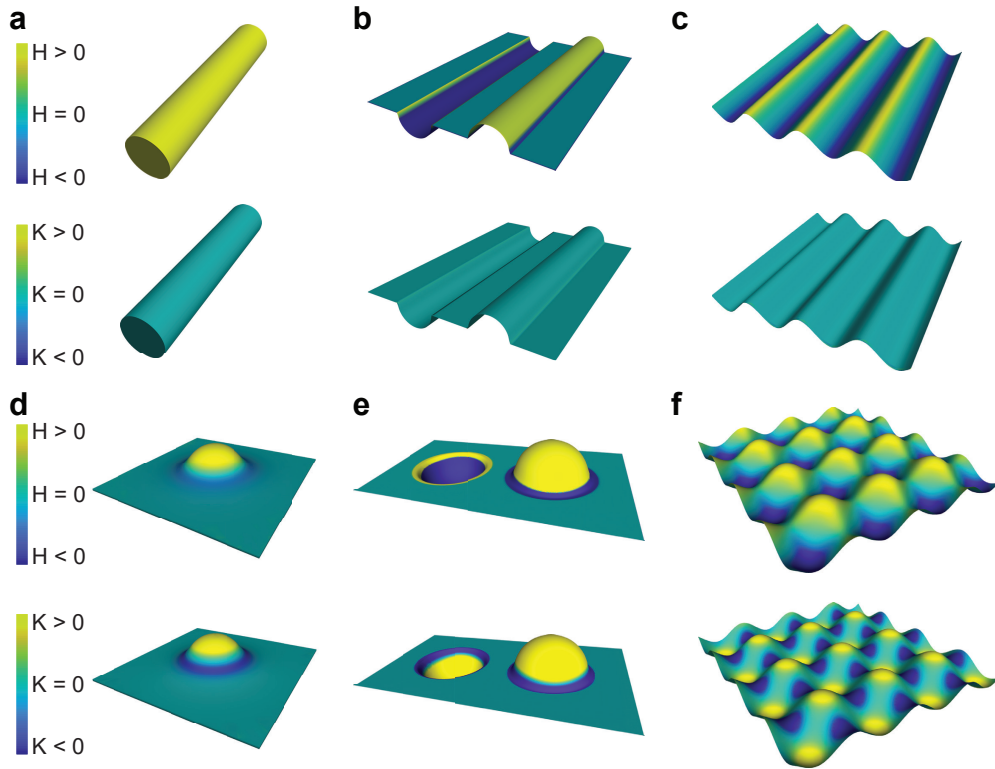


**Figure 2.3:** Some examples of the curved substrates used in single-cell experiments. The mean (top) and Gaussian (bottom) curvature distributions of cylinders (a), hemicylindrical substrates (b), sinusoid wavy substrates (c), sphere-with-skirt substrate (d), hemispherical substrates (e), and double-sinusoid wavy substrate (f). While a-c are examples of developable (intrinsically flat) surfaces, d-f showcase non-developable (intrinsically curved) surfaces.

pathology, and repair of tissue. Although it is a complicated multi-step process involving bi-directional cell-ECM interactions<sup>74</sup> and variations among different cell types, some basic principles of the cell migration cycle are conserved<sup>75</sup>. An adherent cell migrating on flat surfaces first establishes polarity, developing distinct leading (front) and trailing (rear) edges in the direction of migration. This polarity is characterized by a polarized cytoskeletal structure and different molecular processes at the front and rear of the cell, regulated in part by Rho GTPases<sup>75-77</sup>. Upon polarization, the leading edge of the cell develops protrusions in the form of broad lamellipodia and “spiky” filopodia, enabled by actin polymerization<sup>75;78</sup>. Subsequently, the protrusions bind to the ECM, forming anchoring points for the cytoskeletal network to exert traction and pull the cell forward over these adhesion sites<sup>76;79</sup>. Finally, detachment at the rear of the cell and the retraction of the trailing edge occurs in order for the cell to translocate across the substrate.

Associated with migration is the tendency of cells to align (and elongate) in response to curvature. Fibroblasts, smooth muscle cells, and mesenchymal stromal cells seeded

on cylindrical substrates (convex side, *i.e.*,  $H > 0$  and  $K = 0$ ) have been shown to preferentially align their elongated bodies and cytoskeletal structure along the cylinder axis<sup>57;60;64;66–68;80–82</sup>. As such, the cells tend to avoid curvature by aligning along the (principal) direction of zero curvature. Epithelial cells on the other hand, have been found to orient their cytoskeletal structure in circumferential direction and “wrap” the cylindrical substrate<sup>61–63;83</sup>, thereby aligning in the (principal) direction of maximum curvature. In experiments with fibroblasts on cylindrical substrates, the degree of longitudinal alignment was found to increase with curvature (*i.e.*, a decreasing radius of curvature)<sup>60;64;66</sup>. Indeed, the scale of the substrate curvature is important, since too large curvature radii (*i.e.*,  $\kappa \gg$  cell size) cannot be detected by individual cells. Interestingly, sufficiently large curvature cues could overrule a competing cue in the form of nanoscale contact guidance in determining cell alignment<sup>64</sup>. While cylinders could induce preferential cell alignment, this is not observed on spherical substrates ( $K > 0$ ), because the curvature is constant in all directions (both the mean and Gaussian curvatures are constant and positive on a sphere). As opposed to cylinders, there is no option for cells on spheres to find an orientation that either minimizes or maximizes curvature. In this regard, it would be interesting to observe cellular alignment on ellipsoidal substrates ( $K > 0$  and varying), where the principal curvature in one direction is higher than in the other. It might be expected that cells with pronounced stress fibers would then align preferentially along the direction with the lowest curvature. Furthermore, cell alignment on saddle surfaces ( $K < 0$ ) is still largely unexplored<sup>30;66</sup>.

In addition to static cell body alignment, time-lapse microscopy has revealed that substrate curvature also impacts directional cell migration. Human bone-marrow derived stromal cells (hBMSCs) cultured on convex cylindrical substrates ( $K = 0$ ,  $H > 0$ ) were shown to migrate increasingly along the cylinder axis for increasing curvatures (decreasing radii)<sup>64;66</sup>. However, hBMSCs on concave cylindrical substrates ( $K = 0$ ,  $H < 0$ ) were shown to exhibit a non-aligned and non-persistent migration mode without angular preference<sup>66</sup>. In the case of T-cells seeded on sinusoidal wavy surfaces ( $K = 0$ ,  $H$  is varying), a zigzagging migration mode in the concave grooves of the waves ( $H < 0$ ) was observed<sup>69</sup>. On (hemi-)spherical substrates, a different migration behavior has been observed on the convex ( $K > 0$ ,  $H > 0$ ) sides as opposed to the concave ( $K > 0$ ,  $H < 0$ ) sides of the spheres<sup>72;73</sup>. Fibroblasts and mesenchymal stromal cells (MSCs) migrate significantly faster inside concave pits as compared to convex caps and flat surfaces, with no significant difference between the latter two<sup>72;73</sup>. Moreover, two distinct migration modes have been observed: a typical 2D migration response on the convex caps, but a faster, spider-like “extend-and-pull” movement in the concave pits, whereby the cells first form long body extensions that span over the pits, and consequently retract their cell body towards the attachment sites of the extension<sup>72</sup>. On a smoothly varying double-sinusoid landscape (Figure 2.3f), exhibiting varying mean and Gaussian curvatures, MSCs and fibroblasts consistently migrate into the valleys ( $K > 0$ ,  $H < 0$ ) and avoid the hills ( $K > 0$ ,  $H > 0$ ) along their trajectory, a response that increases with increasing curvature values (Figure 2.4)<sup>55</sup>. During the

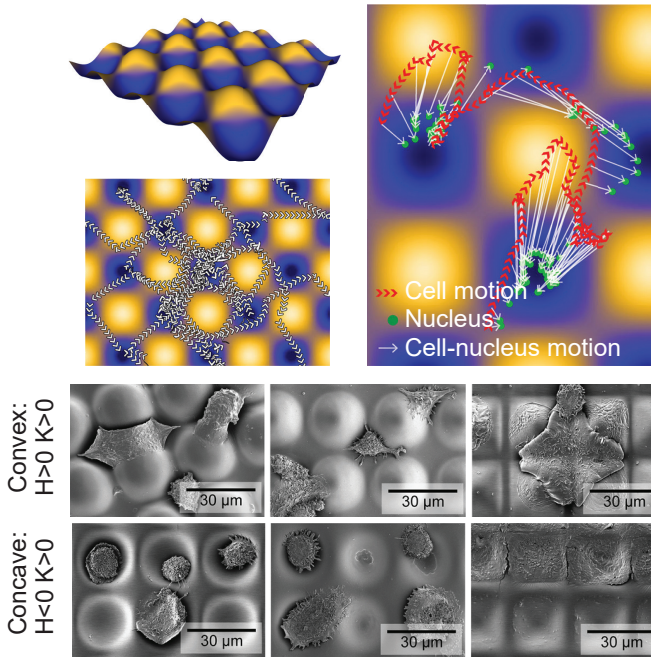


**Figure 2.4:** Top: the migration trajectories of MSCs (obtained with time-lapse microscopy) on double-sinusoid wavy substrates. Obtained with permission from Ref.<sup>55</sup>. Bottom: the positioning of macrophages on substrates with various types of convex hills and concave valleys. Obtained with permission from Ref.<sup>71</sup>.

migration phase, the nuclei of the cells are first located near the deepest point of the valleys, while the cell protrusions probe the environment. During a translocation step, the nuclei quickly locate from one valley to the next, reaching high velocities on the hills. This increased velocity on the convex parts is conflicting with some of the earlier results<sup>72;73</sup>, but is likely a consequence of the dynamic exploration behavior of the cells in this smoothly varying, hilly landscape, as opposed to the more discrete, separated hemispheres in other studies. The observation that cells avoid convex spherical caps ( $K > 0$ ,  $H > 0$ ) is common<sup>30;70;71</sup>, provided that the curvature values are sufficiently large (*e.g.*, spheres with  $r < 500\mu\text{m}$  for fibroblasts<sup>70</sup>). In addition to fibroblasts or stromal cells, this observation is also made with macrophages (Figure 2.4 bottom): cells avoid the regions with positive values of mean and Gaussian curvatures (*i.e.*, convex caps) and actively migrate into regions of negative mean and positive Gaussian curvatures (*i.e.*, concave pits)<sup>71</sup>. In curvature landscapes with larger feature sizes, however, macrophages do not exhibit this curvature-driven behavior, potentially due to relatively lower curvature values as compared to the macrophage cell size<sup>55</sup>. Despite the general avoidance of convex caps, however, active cell migration on shallow convex caps has been observed in some studies<sup>73;84</sup>. These shallow caps are spherical sections with an aspect ratio below 0.5, which would correspond to a hemispherical section. Such shallow convex caps may pose less of an obstruction to the cells migrating from the flat

surroundings, as compared to truly hemispherical caps.

While cell migration on developable ( $K = 0$ ) and spherical ( $K > 0$ ) surfaces has been the subject of several studies, cell behavior on hyperbolic ( $K < 0$ ) surfaces is largely unexplored. In one study, axisymmetric sphere-with-skirt substrates have been used for culturing fibroblasts<sup>30</sup>. The substrates consisted of convex caps ( $K > 0$ ) that smoothly transitioned towards the flat surroundings ( $K = 0$ ) through a saddle-shaped region ( $K < 0$ ) (Figure 2.3d). Cells on such substrates avoided the convex spherical part of the substrate, but occasionally probed it using short-lived lamellipodia<sup>30</sup>. Instead, the cells showed an azimuthal cell polarity and migrated around the cap on the saddle-shaped region. In another recent study, mesenchymal stromal cells were cultured on a saddle-shaped section of a torus, and preferential migration along the concave direction of the saddle was observed<sup>66</sup>. While deliberate investigations into the response of cells to saddle shapes are still uncommon, it is important to understand that many other substrates also contain saddle-shaped regions. For example, the transition region from a hemispherical cap to the flat surroundings must have a negative Gaussian curvature, though this region could be very narrow and is typically not considered in curvature-guided cell culture studies (Figure 2.3e). Nonetheless, the relevance of hyperbolic geometry in biological tissue necessitates more dedicated investigations to elucidate the role of saddle shapes on cell migration.

### 2.3.2 The central role of cytoskeletal mechanics

A recurring theme in the discussions of cell response to curved substrates is the central role that cytoskeletal arrangement and tension seem to play. The contractile stresses that arise in the filamentous cytoskeletal network endow cells with both a sensory function, enabling them to sense the physical properties of their environment<sup>5</sup>, and a force generation function<sup>19</sup>, not only facilitating cell migration and cytokinesis<sup>85</sup> but also enabling the wrinkling of soft substrates<sup>86</sup> and even cell-scale origami folding<sup>87</sup>. The contraction of the cytoskeleton, which consists of a network of actin microfilaments, intermediate filaments, and microtubules, is governed by the actomyosin machinery, consisting of filamentous actin (F-actin) in conjunction with myosin II motors that sit in between<sup>85</sup>. A crucial ingredient for the contractility-induced sensory and force generating functions is the adhesion of the cells to the substrate that they are situated on and the ability to transmit force<sup>88</sup>. Cells use transmembrane proteins, called integrins, to bind to ligands in the extracellular matrix (*e.g.*, fibronectin). Upon activation by force, several proteins are recruited, such as talin<sup>89</sup> and vinculin<sup>90</sup>, through which a mechanical link between the ECM and the actin filaments of the cytoskeleton can be established<sup>91</sup>. Moreover, the exertion of force on the integrins also activates the RhoA signaling pathway, which, through the activation of Rho kinases (ROCK) and myosin light chain (MLC), ultimately triggers the assembly of myosin II filaments<sup>91</sup>. Those myosin II filaments interact with actin to enable contraction and cross-linking<sup>92</sup>, and have also been implicated in actin polymerization<sup>93</sup>, thereby contributing to the force-induced remodeling of the cytoskeleton, as well as the establishment of mature focal

adhesions<sup>91</sup>. In other words, this mechanical interaction between the extracellular environment and the intracellular cytoskeleton results in a force-feedback mechanism that triggers the cell to remodel its cytoskeleton. This force-feedback mechanism will be affected when a cell is situated on a 3D, curved geometry instead of an isotropic planar substrate, which is why cytoskeletal arrangement and contractility are important aspects to consider in any discussion of curvature guidance.

As mentioned before, fibroblasts and MSCs seeded on convex cylindrical substrates ( $H > 0$ ,  $K = 0$ ) typically align longitudinally along the cylinder axis, an effect that increases with curvature. Typically, this global cell alignment is accompanied by an arrangement of stress fibers (*i.e.*, bundles of actin microfilaments)<sup>94</sup> in the longitudinal direction (*i.e.*, in the direction of zero principal curvature)<sup>57;60;64;66;81;81</sup>. In a seminal work, Dunn and Heath hypothesized that this cytoskeletal arrangement (and cell body alignment) occurs because the stress fibers cannot assemble or operate in a bent condition (*i.e.*, there is a bending energy penalty), which is why the cells avoid the substrate curvature and align longitudinally<sup>57</sup>. While plausible, this theory does not explain the different behavior exhibited by epithelial cells where stress fibers align circumferentially<sup>61–63</sup>. It has, therefore, been suggested that the cell and cytoskeletal orientation on convex cylindrical substrates ( $K = 0$ ,  $H > 0$ ) is driven by a competition between the bending resistance of the stress fibers and a shear deformation that develops as a consequence of cell contractility<sup>95</sup> (Figure 2.14(a) and Subsection 2.5.1). When adhering to a flat substrate, the top surface of the cell is free to contract in the direction of the stress fibers, while the attached (bottom) surface is constrained, resulting in a shear deformation throughout the cell thickness. When the cell is bent along a convex cylindrical substrate, an additional deformation ensues: the top surface is subject to extension while the bottom surface contracts. In this case, it is energetically favorable for the cell to align its stress fibers perpendicularly to the cylinder axis, since the actomyosin-induced contraction could partly compensate for the bending-induced extension. However, this imposes an energetic penalty due to stress fiber bending, which prefer to alignment along the zero-curvature direction<sup>95</sup>. The stress fiber orientation is, therefore, determined by an energy trade-off: longitudinal alignment is predicted when the bending energy dominates (*e.g.*, in the case of thick stress fibers in fibroblasts), while circumferential alignment is predicted when the contractility-term dominates (*e.g.*, for the relatively thin stress fibers in epithelial cells)<sup>95</sup>. Indeed, cells with pronounced straight stress fibers (*e.g.*, polarized fibroblasts) have been found to orient longitudinally on cylinders, while cells with circular actin bundles (*e.g.*, epithelial cells) or cells with insufficient or no stress fibers (*e.g.*, transformed *L* fibroblasts) bend around the cylinder with much lower elongation and longitudinal orientation (Figure 2.5a)<sup>62</sup>. While this theoretical explanation provides an interesting mechanistic perspective, it cannot elucidate all the aspects at play in stress fiber orientation. For example, in experiments on convex cylinders ( $K = 0$ ,  $H > 0$ ) with fibroblasts and smooth muscle cells, two distinct stress fiber populations have been observed that are not predicted by this theory: a set of long, apical stress fibers located above the nucleus and a set of shorter, basal stress fibers situated

beneath the nucleus<sup>60</sup>. The apical and basal stress fibers increasingly align in axial and circumferential directions respectively with increasing curvature<sup>60</sup>. Interestingly, the circumferentially aligned stress fibers lie underneath the nucleus, while it might be expected from the theoretical explanation that they should lie close to the upper side of the cell to maximally compensate for the extension caused by cell bending. It, therefore, seems likely that predicting the energetically optimal orientation of cells encompasses more aspects than cell contractility and stress fiber bending.

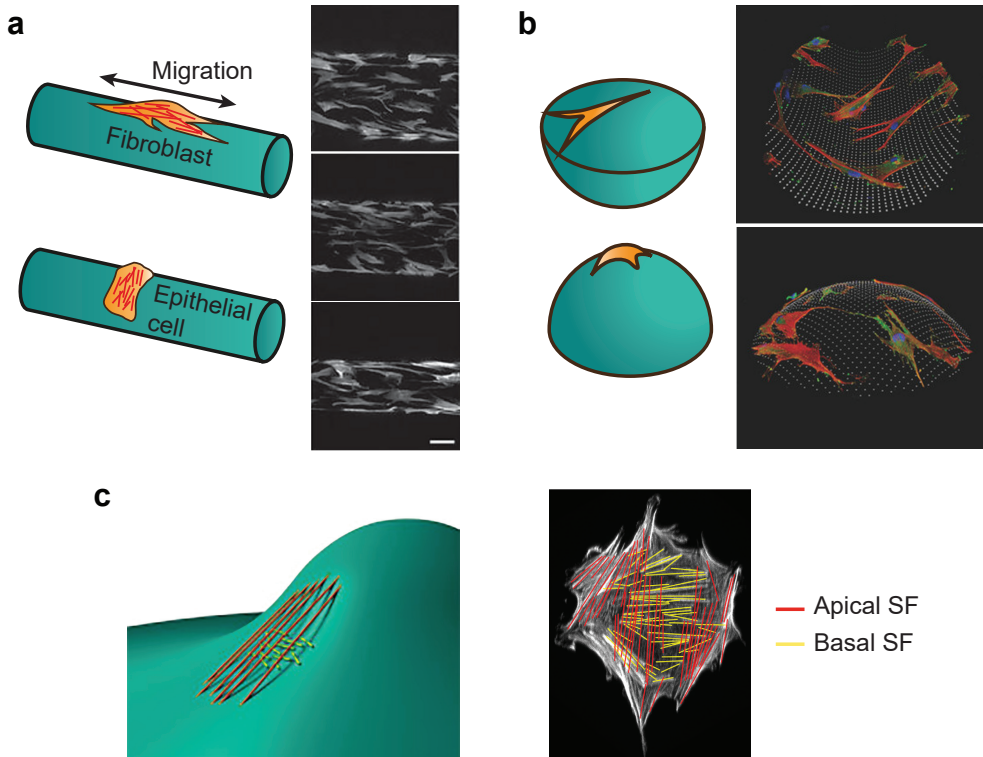


**Figure 2.5:** Single-cell response on curved substrates. a) Fibroblastic-like cells align longitudinally on cylindrical substrates, while epithelial cells wrap the substrates. Insets show increasing hBMSC alignment for increasing curvature on convex cylindrical substrates<sup>64</sup>, reproduced with permission from The Royal Society. b) MSCs on concave and convex hemispherical substrates. Insets obtained with permission from Ref.<sup>72</sup> c) Fibroblasts on sphere-with-skirt substrates, exhibiting apical and basal stress fiber alignment, reproduced with permission from Elsevier<sup>30</sup>.

Cells have no way to avoid curvature on convex spherical caps ( $H > 0, K > 0$ ). In other words, the stress fibers in cells adhering to such spherical substrates must bend regardless of their orientation. Bone marrow stromal cells seeded on convex spherical caps were found to exhibit lower F-actin levels (*i.e.*, less pronounced stress fibers), yet higher phosphorylated myosin levels, indicative of higher myosin II filament activity as compared to the cells residing on convex cylindrical substrates of the same diameter<sup>64</sup>. It has been suggested that these increased phosphorylated myosin levels are necessary to

compensate for the lower number of stress fibers whose formation seems to be impeded on convex curved substrates, such that an adequate cytoskeletal tension and cell motility could still be maintained<sup>64</sup>. This observation has been confirmed in other studies, where less pronounced, shorter stress fibers or lower F-actin levels were observed on the convex spherical caps as compared to other geometries in the surroundings<sup>70;72;96</sup>. From a curvature perspective, one expects a concave spherical pit ( $K > 0$ ,  $H < 0$ ) to elicit the same response, since there is also no direction of zero principal curvature ( $K > 0$  on the concave and convex sides). However, there is a way in which cells could still avoid stress fiber bending: by spanning the pit with strong actin bundles, attached to a few anchoring points on the side walls, that contract and lift the cell body away from the substrate. Indeed, mesenchymal stromal cells cultured on spherical pits or inside spherical confinements form large extensions to bridge the concavity underneath and adopt a spider-like morphology, with most focal adhesions being located at the anchoring sites on the periphery of the cells (Figure 2.5b)<sup>72;97</sup>. A similar lift-off behavior has recently been observed for stromal cells on concave cylindrical substrates ( $K = 0$ ,  $H < 0$ ), and this has been linked to the non-aligned, non-persistent migration behavior that these cells exhibit<sup>66</sup>. The spider-like morphology is reminiscent of the shape of cells on micropatterned adhesive substrates, exhibiting arc-like boundaries that form naturally due to cellular contractility (Figure 2.12a)<sup>98;99</sup>. Cells on smooth, double-sinusoid substrates (varying  $K$  and  $H$ ) seem to exhibit a somewhat similar behavior: the nucleus is typically positioned in a valley ( $K > 0$ ,  $H < 0$ ), and most focal adhesions are situated on the surrounding hills ( $K > 0$ ,  $H > 0$ ), though some more stable, higher tensioned FA could be present in the valleys<sup>55</sup>. Lower nuclear compression has been observed in the valleys, yet it is unclear if the cells were fully lifted away from the double-sinusoid substrate.

Based on these results for convex and concave spherical geometries ( $K > 0$ ), a natural question to ask is what happens to the actin organization when cells are subjected to both convex and concave curvatures simultaneously (*i.e.*, saddle surfaces,  $K < 0$ )? On the saddle-shaped region of sphere-with-skirt substrates, two distinct subpopulations of stress fibers have been observed in fibroblasts: apical stress fibers (above the nucleus) that align in the radial direction, and basal stress fibers (below the nucleus) that align in the circumferential direction. Interestingly, the apical stress fibers do not follow the local concave curvature of the substrate but bridge this concavity instead, much like the previously described spanning behavior on concave pits (Figure 2.5c)<sup>30</sup>. Therefore, by aligning along the concave principal direction ( $\kappa_1 < 0$ ) and consequently spanning the substrate, the apical stress fibers can avoid bending. The basal stress fibers, however, do not avoid bending and are oriented in the other principal (convex,  $\kappa_2 > 0$ ) direction, showing a similar behavior as on cylindrical substrates in a previous study<sup>60</sup>. Therefore, while the argument of bending avoidance seems to hold for the apical stress fibers, it does not explain the orientation of the basal stress fibers: why do the basal fibers align in the most curved direction instead of trying to avoid curvature altogether? Elucidating the underlying mechanisms requires further investigation, but it is noteworthy

that the cells cultured on the saddle region migrate in the direction of the basal stress fibers, while they typically migrate in the direction of the apical stress fibers on planar substrates<sup>30</sup>. Migration and basal stress fiber orientation may, therefore, be linked on those regions of negative Gaussian curvature.

The effects of cytoskeletal mechanics can be studied more in-depth by using drugs to inhibit or enhance specific cell components. Activation of Rho GTPases (*i.e.*, regulators of stress fiber formation<sup>100</sup>) in fibroblasts and vascular smooth muscle cells on the outside of cylinders ( $K = 0, H > 0$ ) results in a strong reduction of apical, longitudinally aligned stress fibers, while basal stress fibers become more pronounced and align circumferentially<sup>60</sup>. While the opposite was expected (following the stress fiber bending argument), it has been hypothesized that this observation is due to a shift in the balance between the bending energy of stress fibers and cell contractility<sup>60</sup>. Rho inhibition, on the other hand, results in the loss of the curvature sensing ability of mesenchymal stromal cells cultured on double-sinusoid substrates (with varying  $K$  and  $H$ )<sup>55</sup>. A similar effect is obtained by drug-induced actin depolymerisation and myosin II blocking, both of which are among the components of the actomyosin contractile apparatus<sup>55</sup>. These results underpin the intimate connection between the formation of a contractile cytoskeletal structure and the ability of the cells to sense and respond to substrate curvature. While the full set of the mechanisms behind curvotaxis are not yet fully uncovered, the experimental observations seem to support at least some aspects of the hypothesis that cytoskeletal (and cellular) alignment is driven by an energetic balance between contractility and stress fiber bending on curved substrates.

### 2.3.3 The nucleus as a curvature sensor and regulator

Located in between the cytoskeletal network of eukaryotes is the cell nucleus, the largest organelle that contains the cell's genetic material. Mechanically, the nucleus is a membrane-bound structure that is internally supported by a fibrous network-like nucleoskeleton, built up of lamins, actin, and other proteins<sup>101;102</sup>. The nucleus behaves like a viscoelastic solid<sup>103</sup>, and is considerably stiffer than the cytoskeleton<sup>102;104</sup>. Nevertheless, it is still a deformable structure, and nuclear shape and deformability have been shown to play a role in various cell processes, including the regulation of gene expression, and have been associated with various diseases (*e.g.*, laminopathies)<sup>104–106</sup>. The deformation of the nucleus is enabled through intimate connections between the nuclear envelope and the cytoskeleton in the form of the LINC (linkers of nucleus and cytoskeleton) complex<sup>107</sup>. On the outer side of the nuclear envelope, nesprin proteins bind to the various components of the cytoskeleton: nesprins 1/2 bind to actin, nesprin 3 binds to intermediate filaments, and nesprin 4 to microtubules. At their other ends, nesprins bind to SUN proteins, which pass through the nuclear envelope and bind to nuclear lamins (proteins that form a reinforcing layer on the inner side of the nuclear membrane). These lamins are, in turn, connected to the chromatin cargo inside the nucleus<sup>106;108</sup>. Hence, there is a mechanical connection between the cytoskeleton and the nucleus, enabling force transmission of intracellularly and extracellularly gener-

ated forces<sup>106</sup>. This force transmission results in dynamic deformations of the nucleus, which have been linked to different mechanotransduction mechanisms. For example, nuclear deformation could result in conformational changes of proteins at the nuclear lamina, affecting their interaction with enzymes<sup>109</sup>. Additionally, nuclear deformation could rearrange the spatial distribution of chromatin (into loose and compact regions), affecting gene expression<sup>105;108–110</sup>. For these reasons, the cell nucleus could actually be considered a “sensor” that plays an important role in mechanotransduction<sup>13;108</sup>.

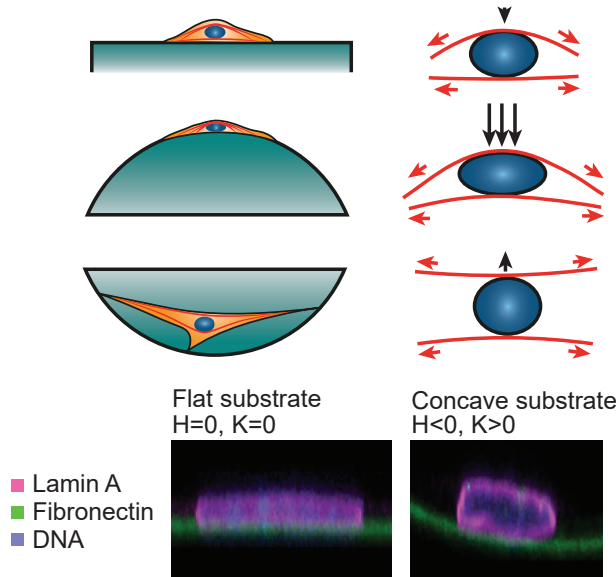


**Figure 2.6:** Curvature-induced compression of the nucleus on flat, concave spherical and convex spherical substrates. The schematic drawing is adapted from Ref.<sup>72</sup>. Bottom insets show the shape of the nucleus on concave and flat substrates, obtained with permission from Ref.<sup>55</sup>.

The nuclei of certain cells (*e.g.*, fibroblasts) adhering to flat surfaces are naturally flattened due to the presence of a perinuclear actin cap, which is a dome-like arrangement of apical stress fibers that lie on top of the nucleus and that exert a compressive force on the nucleus due to actomyosin contraction<sup>111</sup> (Figure 2.6, top row). Alterations in the shape of the nucleus are, therefore, expected to arise in the cells residing on curved substrates as compared to those cultured on planar substrates, due to the curvature-induced cytoskeletal rearrangement and the cell morphology that we described previously. Indeed, the nuclei of mesenchymal stromal cells seeded on planar ( $K = 0$ ,  $H = 0$ ), convex spherical ( $K > 0$ ,  $H > 0$ ), or concave spherical ( $K > 0$ ,  $H < 0$ ) substrates exhibit distinctly different shapes: a flattened morphology on flat and convex spherical substrates and a more spherical morphology on concave spherical substrates<sup>72</sup>. For a cell on a planar substrate, the perinuclear actin cap generates a relatively small compressive force, flattening the nucleus. On a convex spherical cap ( $K > 0$ ,  $H > 0$ ), however, this vertical force component increases due to the increased vertical arrangement of the stress fibers, leading to a more flattened shape. On a concave

spherical pit ( $K > 0$ ,  $H < 0$ ), on the other hand, the nuclear compression is relieved because the cell is lifted off the surface, leading to a more spherical shape of the nucleus (Figure 2.6)<sup>55;72</sup>.

One of the primary components governing nuclear deformability is lamin A. This is a type V intermediate filament that is a key constituent of the nuclear lamina, a reinforcing meshwork at the nuclear envelope<sup>106;112</sup>. Increased lamin A intensity levels have been measured in cells on convex spherical substrates, as opposed to concave spherical and flat substrates, suggesting a nuclear stress-protection response induced by curvature<sup>72</sup>. On the other hand, active lamin A silencing using small interfering RNAs has been shown to significantly reduce the curvature-sensing ability of cells<sup>55</sup>. In addition to nuclear deformation due to curvature-induced forces, the nucleus has also been found to dynamically change its intracellular position in response to curvature, essentially positioning itself in the locations of low deformation (*i.e.*, valleys instead of hills) and potentially playing an important role in guiding cell migration<sup>55;71</sup>.

Curvature-induced deformation of the nucleus has also been linked to gene expression and differentiation. On substrates with a zero Gaussian curvature (*i.e.*, cylindrically-shaped hydroxyapatite substrates), no curvature-induced changes in the differentiation and mineralization rates of pre-osteoblast cells have been observed (using RUNX2, ALP, DMP1 and Osteopontin markers)<sup>67</sup>. However, curvature-dependent differentiation behavior has been observed on substrates with non-zero (positive) Gaussian curvatures<sup>72</sup>. Higher osteocalcin levels, a marker for osteogenic differentiation, were observed in MSCs seeded on hemispherical caps as opposed to flat and hemispherical pits (both in expansion and osteogenic medium)<sup>72</sup>. Remarkably, these higher osteocalcin levels were associated with lower F-actin levels and vice versa, while previous results on planar substrates indicated that higher cytoskeletal forces enhance osteogenic commitment<sup>113</sup>. This difference could indicate that surface curvature plays an equally important role in governing nuclear deformation, next to the magnitude of cytoskeletal tension. Nuclear deformation might also explain the lack of increased differentiation activity on cylinders as opposed to hemispherical caps: on the cylindrical substrates ( $K = 0$ ), the stress fibers orient in the longitudinal direction and, therefore, might not compress the nucleus as much as on hemispherical caps ( $K > 0$ ), and, thus, may not trigger the osteogenic pathways. The transcriptome of MSCs cultured on double-sinusoid substrates (varying  $K$  and  $H$ ) has also been compared to that of the cells cultured on planar substrates ( $K = H = 0$ ), showing several downregulated genes in cells on the sinusoid substrates, including factors involved in differentiation and cytoskeletal remodeling<sup>55</sup>.

In conclusion, it should be clear that individual cells could sense and respond to various types of substrate curvatures (see Table 2.1 for an overview of studies on cell-scale curvature guidance). While generating and sensing curvature at membrane scale involves dedicated biochemical pathways and proteins at the membrane<sup>10;49;50;54</sup>, the interaction with curvature at larger scales requires a more holistic, mechanical explanation<sup>52</sup>. In general, the mechanisms driving spatiotemporal organization of individ-

ual cells on curved substrates seem to be governed by the interplay between the cell's contractile apparatus and the relatively stiff, yet deformable nucleus<sup>19;55;72</sup>. By means of protrusions at their periphery<sup>30</sup>, cells dynamically explore the 3D curved substrate and establish discrete focal adhesion sites, enabling them to anchor to the substrate, remodel their cytoskeleton, and build up cellular tension. This cytoskeletal contraction, in conjunction with the specific geometry that the cell is constrained to (*e.g.*, convex or concave spherical pits), results in different net forces on the nucleus as opposed to cells adhering to isotropic flat substrates. As a first consequence, these anisotropic force distributions could result in intracellular nuclear sliding, potentially driving whole-cell migration in a particular direction<sup>55</sup>. Additionally, the specific substrate that cells adhere to could result in varying degrees of nuclear compression, affecting chromatin distribution and potentially triggering other nuclear pathways<sup>64;72</sup>. The preferred orientation and migration trajectory that the cells then commit to, is typically discussed from an energy minimization perspective. Although it is still unclear to what extent different cell components contribute to the energy balance, it has been argued several times that stress fiber bending plays a major role<sup>60;95</sup>. Indeed, cells with pronounced stress fibers seem to favor orientations that minimize bending, such as a longitudinal alignment on convex cylinders or a "spanning" configuration over local concavities (*e.g.*, on concave pits, concave cylinders or saddles)<sup>63;66</sup>. While the full set of the involved mechanisms remains elusive, it should be clear that cell-scale curvature guidance is not purely a biochemical process that is restricted to specific regions inside the cell, but instead requires a whole-cell approach involving the interplay between the cell as a dynamic mechanical system and the constraining extracellular geometry.

## 2.4 Collective cell and tissue response to substrate curvature

While single-cell experiments offer useful insights into the mechanisms behind curvature sensing and response, cells are generally not solitary agents *in vivo*, but are, instead, linked together in a multicellular network<sup>11</sup>. This could be a direct link through intercellular connections such as tight junctions, gap junctions, desmosomes, and adherens junctions<sup>11</sup>, or an indirect connection via cell-ECM adhesion<sup>91;114</sup>. These cell-cell and cell-ECM interactions establish a mechanical linkage that enables force transmission between different cells. As mentioned before, cell-ECM force transmission involves transmembrane integrins that bind to extracellular matrix ligands and link back to the cell cytoskeleton<sup>115</sup>. In the case of cell-cell interactions, a similar force transmission mechanism exists, this time mediated by transmembrane cadherins<sup>91</sup>. The extracellular domains of the cadherins of different cells form adhesive bonds that link the cells together. At the cytoplasmic domain of the cadherins, different proteins are recruited, such as  $\alpha$ -catenin,  $\beta$ -catenin, or vinculin, that enable direct or indirect binding to actin<sup>91;116</sup>. As such, a mechanical connection between the cytoskeleton of different cells is constructed. Through these cell-cell and cell-ECM connections, a multicellular force-feedback network is established that increases the range within which cells could

sense and respond to their environment, enabling them to act cooperatively<sup>19</sup>. For example, collective cell contraction on patterned adhesive islands or confinements could result in stress gradients in the multicellular constructs that drive spatial cell proliferation patterns<sup>37</sup> and the spatial distribution of biochemical signals<sup>23</sup>. Hence, the collective force-generation of multicellular systems coupled with constraining extracellular geometries could initiate heterogeneous cell patterning and guide the structural organization of the extracellular matrix<sup>19</sup>. In the current section, we approach this coupling between collective cell action and extracellular geometry from the perspective of substrate curvature, first by discussing the response of single-layer cell sheets and later by considering the shaping of more convoluted ECM-rich tissues.

### 2.4.1 Curvature-driven organization and dynamics of cell sheets

Upon reaching confluence, cells link up to form a cohesive cell sheet, or monolayer, that covers the substrate they are situated on. At this moment, cells can operate collectively, for example, to generate forces across the entire sheet<sup>114</sup>. While various cell types could form monolayers, most studies of monolayer mechanics and structure are focused on epithelial cell sheets, which have a high physiological relevance, since they line the surfaces of many 3D curved structures *in vivo*, such as organs, cysts, and vessels<sup>117;118</sup>. In addition to inducing, for example, spatial proliferation patterns, the collective organization can enable cells in monolayers to sense and respond to weaker curvature fields than individual cells. Indeed, confluent monolayers of fibroblasts and vascular smooth muscle cells residing on cylindrical substrates ( $K = 0, H > 0$ ) align along the cylinder axis more strongly than individual cells on cylinders with low curvature (Figure 2.7a)<sup>60</sup>. As a potential explanation, it was suggested that these monolayers have a larger “effective length scale” due to the cell-cell connections that link stress fibers together, thereby creating a stress fiber network that has a higher bending energy penalty than in individual cells<sup>60</sup>. Cylindrical geometries also play an important role in the organization and dynamics of epithelial and endothelial sheets (*e.g.*, during tubular morphogenesis)<sup>119</sup>. Indeed, cells in such monolayers plated on cylindrical substrates align and elongate in response to curvature, although the orientation and curvature sensitivity depends on the cell type. Longitudinal alignment is observed for umbilical vein endothelial cells cultured on convex cylinders ( $H > 0$ ) and renal epithelial cells in concave cylinders ( $H < 0$ ), while renal epithelial cells align perpendicularly to the cylinder axis on convex cylinders (Figure 2.7b)<sup>83;120–122</sup>. The curvature sensitivity seems to be reduced in cell sheets with stronger cell-cell junctions and/or higher cell stiffness, which has been linked to an organ-dependent requirement to minimize paracellular transport (*e.g.*, in the blood-brain barrier)<sup>120;121</sup>. On double-sinusoid substrates with varying, non-zero Gaussian curvatures, an expanding epithelial monolayer showed curvature-dependent organization at the leading edges of the front, where cells are positioned in the concave areas, but not in the central part<sup>55</sup>. As a potential explanation, it was suggested that the cells at the edges of the expanding colony have a higher freedom to reposition themselves in response to curvature, while the cells in the center part do not have such

freedom due to cell-cell interactions which provide constraints on the position of the cell within the epithelium<sup>55</sup>.

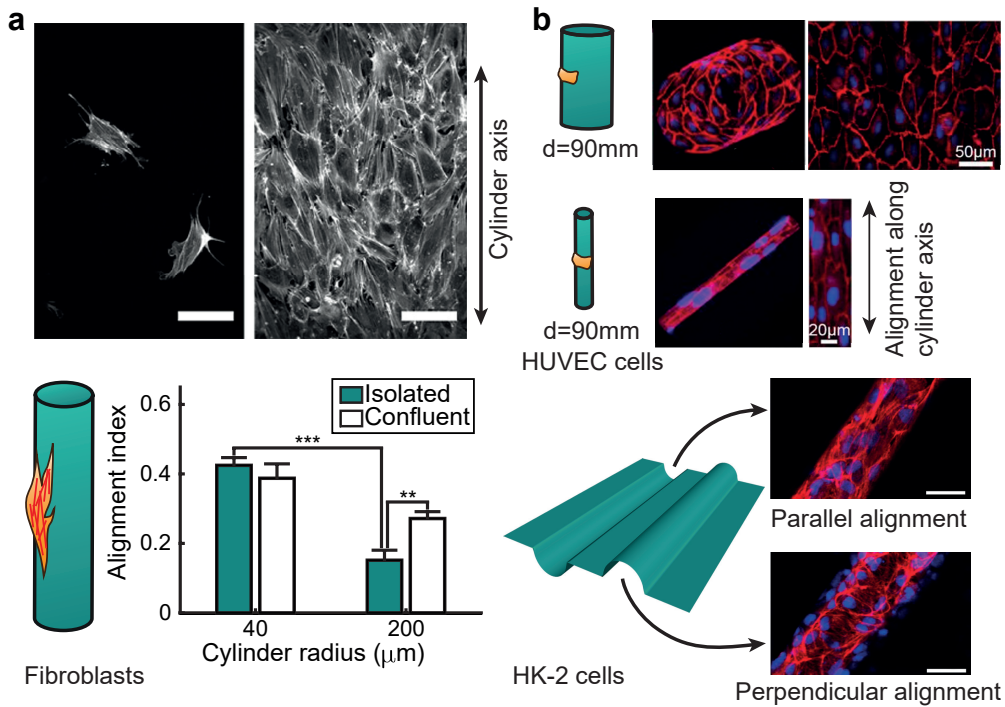


**Figure 2.7:** The response of cell sheets to substrate curvature. a) A confluent layer of fibroblasts senses substrate curvature better than individual cells, obtained with permission from Ref.<sup>60</sup>. b) Top: human umbilical vein endothelial cells (HUVEC) show increasing alignment in the longitudinal direction on cylindrical substrates, obtained with permission from Ref.<sup>120</sup>. Bottom: human kidney (HK-2) epithelial cells showing different alignments on concave and convex hemicylindrical substrates, obtained with permission from<sup>121</sup>.

When organized in monolayers, cells also exhibit a collective migration behavior that plays a crucial role during morphogenesis, wound healing, and cancer progression, and has been found to depend on substrate curvature<sup>76;123;124</sup>. Epithelial cell sheets on the outside of cylindrical wires ( $H > 0$ ) migrate collectively in the longitudinal direction, and the migration speed increases with curvature<sup>83</sup>. On the inside of hollow cylindrical substrates ( $H < 0$ ), however, the migration speed of an advancing epithelium decreases with increasing curvature, potentially due to cell jamming (Figure 2.8)<sup>118;122</sup>. Moreover, cells can detach from the front edge of the monolayer on cylindrical substrates at high curvatures, and switch to an individual migration mode, a phenomenon that is reminiscent of epithelial-to-mesenchymal transition<sup>83;125</sup>. Despite ample evidence showing that curved substrates guide cell sheet organization and migration, this does not mean that the sheet maintains this geometry for extended periods of time<sup>126</sup>. Instead, cell sheets can detach from concave cylindrical substrates ( $H < 0$ ), a phenomenon that is more profound for increased curvatures and increased

cell contractility and can be explained by the existence of a net normal stress pointing away from the surface (Figure 2.9)<sup>126;127</sup>.

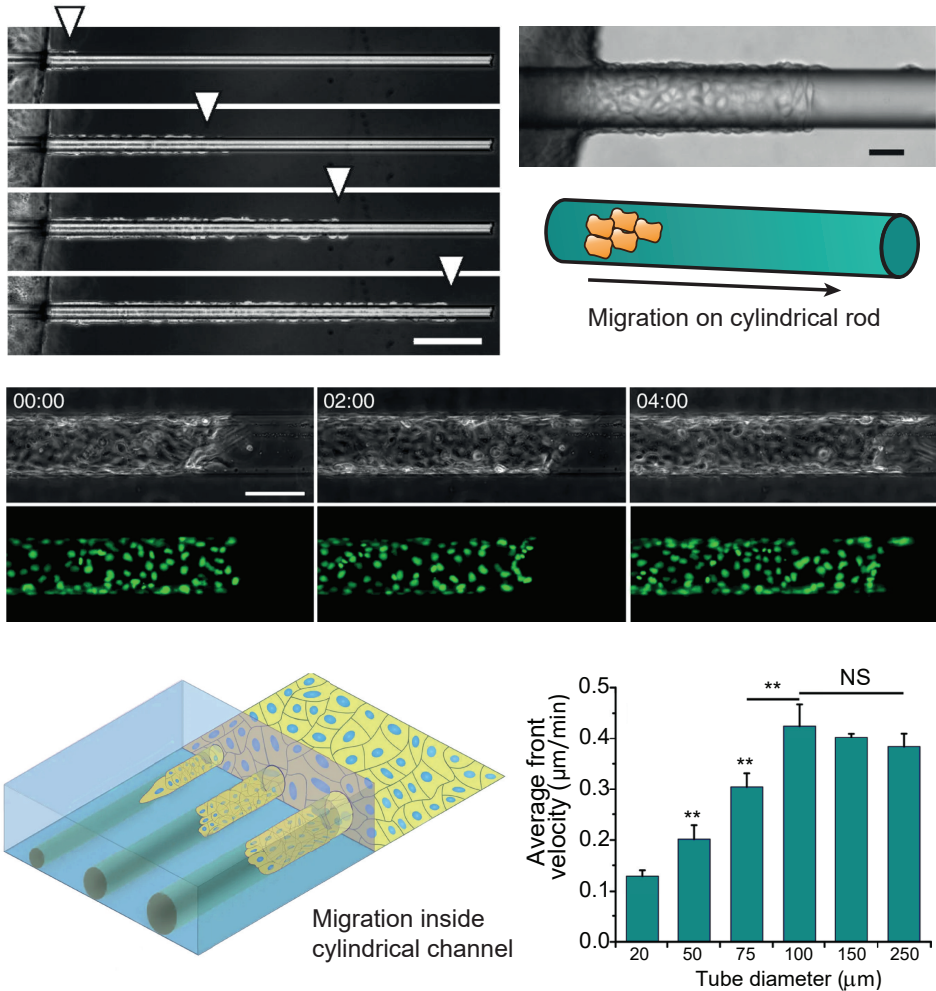


**Figure 2.8:** Top: the collective migration of an epithelium on the outside of a cylindrical wire, obtained with permission from Ref.<sup>83</sup>. Bottom: the collective migration of an epithelium inside cylindrical channels, with decreasing speeds for increasing curvatures, obtained with permission from Ref.<sup>122</sup>.

Cell sheet detachment is not limited to cylindrical geometries, but can also occur on substrates with non-zero Gaussian curvatures. For example, epithelial cell sheets grown in bent cylindrical tubes, effectively representing a portion of a torus with  $K < 0$  at the inside and  $K > 0$  at the outside of the bend, consistently detach from the outer side of the bend as a consequence of cell sheet contraction (Figure 2.10a)<sup>127</sup>. Moreover, cell sheet contraction can cause initially planar substrates to buckle into spherical-like microlenses ( $K > 0$ ), hence giving rise to spontaneous curvature formation<sup>128</sup>.

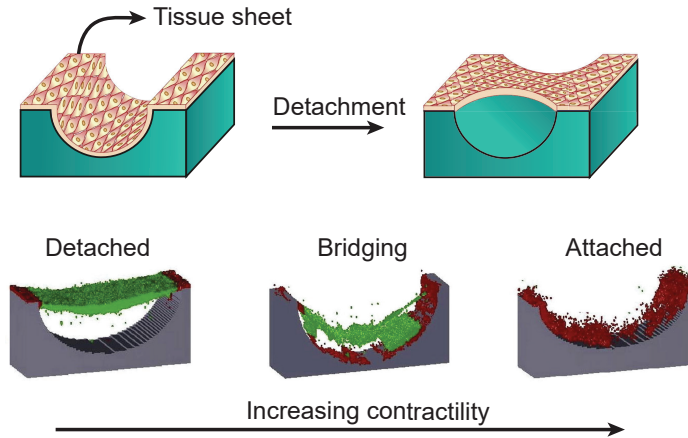


**Figure 2.9:** A schematic drawing of cell sheet detachment in response to substrate curvature, reproduced with permission from Elsevier<sup>126</sup>.

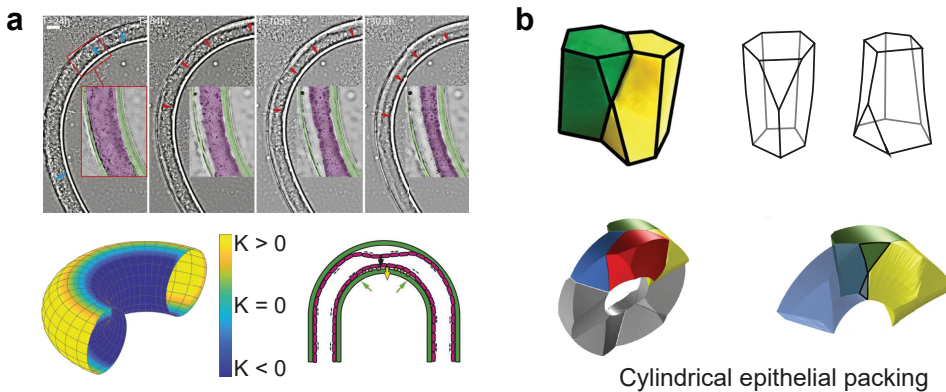


**Figure 2.10:** a) An epithelium cultured inside a bent cylindrical tube, detaching from the outer side (positive Gaussian curvature). Experimental images and inset on the right were reproduced with permission from Ref.<sup>127</sup>. b) The scutoid cell shapes emerging in a cylindrical epithelial packing, obtained with permission from Ref.<sup>129</sup>.

Substrate curvature not only influences the organization, migration, and detachment of entire cell sheets, but can also affect individual cells within the sheet. More specifically, recent evidence has shown that some cells in a curved epithelium must adopt a previously unknown mathematical shape, termed a scutoid, in order to geometrically enable the packing of cells in such a curved morphology (Figure 2.10b)<sup>129</sup>. Similar to a prism and a frustum, a scutoid is a polyhedron connecting two parallel polygonal faces. In contrast to the prism and frustum, however, a scutoid connects different polygons at the top and bottom (*e.g.*, a hexagon on top and a pentagon on the bottom, Figure 2.10b). Previously, it was assumed that epithelial cells adopt a prism or frustum shape in a closely-packed epithelial sheet<sup>130;131</sup>. Mathematical models, however, revealed that certain cells in a curved epithelium have different neighboring cells at the apical and basal sides, necessitating scutoid shapes in the epithelial packing rather

than only prisms and frusta<sup>129</sup>.

### 2.4.2 Curvature-dependent, fluidic shaping of ECM-rich tissues

Cell sheets could, thus, exhibit complex shape formation and adaptation in response to geometrical cues in their environment. Moreover, spatial force patterns or mechanical instabilities arising from differential growth further contribute to shape formation in cell sheets, as was already mentioned in Subsection 2.2.2 in connection to morphogenesis and pathology<sup>24;31;32;37</sup>. Such complex shape formation is, however, not restricted to cell sheets but could also be observed in 3D bulk tissue constructs in which extracellular matrix is gradually deposited as 3D tissue grows. This matrix reinforces the cell collective and enhances the load-bearing capacity of the developing tissue<sup>132</sup>. Despite the fact that a dense cell-ECM network is formed, these tissue constructs still exhibit geometry-dependent, fluid-like shape formation<sup>133</sup>. The effects of geometry in general and curvature in particular on the shape and kinetics of tissue growth has been studied primarily using osteoid-like tissues as model systems<sup>133–135</sup>. This is likely driven by the clinical demand for geometrically optimized porous biomaterials that facilitate bone tissue regeneration. Typically, curvature-guided tissue growth has been studied *in vitro* and has involved non-mineralized (osteoid-like) tissue, although *in vivo* curvature guidance of mineralized tissue has been also recently reported<sup>136</sup>. In the current section, the general observations regarding curvature-guided tissue growth will first be outlined, after which the physical basis for this behavior will be discussed by comparing it to surface tension-driven shape formation in inanimate materials.

Following the seminal work of Rumpler et al.<sup>134</sup>, several *in vitro* studies involving pre-osteoblasts or mesenchymal stromal cells seeded inside straight channels with pre-defined pore shapes have consistently revealed that the curvature of the pores affects the shape and kinetics of tissue growth (Figure 2.11a)<sup>134;135;137–142</sup>. More specifically, after an initial stage that is dependent on cell-material interactions, pore curvature becomes the dominant factor for tissue growth<sup>139</sup>. In channels with circular pores, non-mineralized tissue has been found to grow uniformly inwards, with larger tissue thickness for higher curvatures (*i.e.*, narrower pores)<sup>134;137;138</sup>, and similar results have been obtained for mineralized tissue under static and perfused conditions<sup>140</sup>. In non-circular channels (*e.g.*, with triangular or square cross sections), preferential tissue growth starts in the pore corners (*i.e.*, the regions of high curvature), while no tissue is formed on the flat sides initially<sup>134;135;139;142</sup>. As tissue is progressively deposited in the corners, effectively rounding the pore, the local geometry of the flat sides is altered and tissue starts to grow on those locations too. With time, this leads to a circular tissue front that grows uniformly inwards. In channels with convex polygonal pores, the tissue growth rate in the corners increases with corner curvature, meaning that it is higher in the corners of triangular than in square or hexagonal pores<sup>134</sup>. Nevertheless, the average growth rate of convex pores with the same perimeter is independent of their shape, which has been attributed to the fact that, in convex polygons, the average curvature and, thus, average growth rate is inversely proportional to the perimeter<sup>134;135</sup>. How-

ever, in channels with concave polygonal cross sections such as cross shapes, the initial overall growth rate can be significantly higher than in square (convex) shapes, due to the higher number of “growth-inducing” corners in the cross (8 concave corners) as compared to the square (4 concave corners) shape<sup>135</sup>. This implies that the pore geometry of artificial tissue scaffolds should be optimized not only for mass transport and mechanical properties, but also for the desired tissue growth rate<sup>135</sup>.

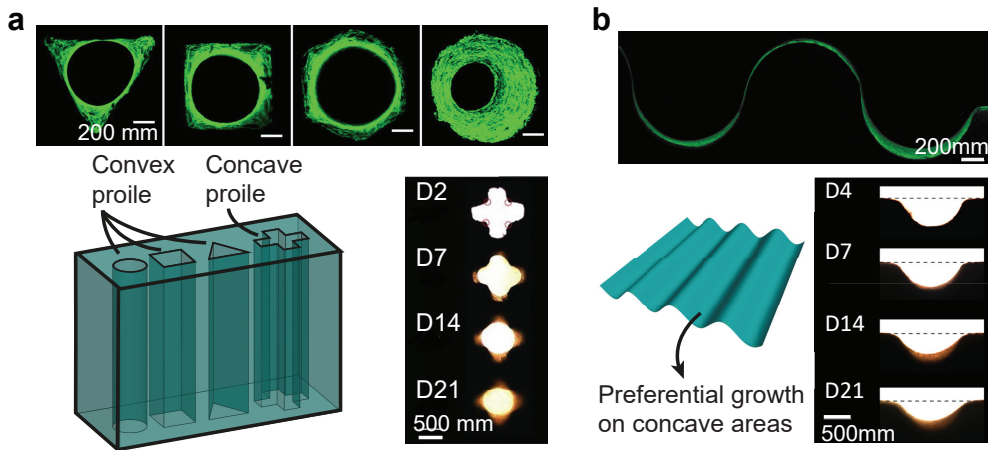


**Figure 2.11:** Curvature-driven tissue growth. a) Bone-like tissue growth front evolving towards a circular geometry in pore channels with various cross-sectional shapes. The experimental images on top and on the right are obtained with permission from Ref.<sup>134</sup> and Ref.<sup>135</sup>, respectively. b) The differences in the bone-like tissue growth on concave cylindrical *versus* convex cylindrical regions. The experimental images on top and on the right are obtained with permission from Ref.<sup>143</sup> and Ref.<sup>138</sup>, respectively.

These straight pore channels, whether with convex or non-convex cross-sectional shapes, all classify as “generalized cylinders” (*i.e.*, developable geometries,  $K = 0$ ) with parallel ruling lines that are curved in one direction but remain flat in the other. Other examples are hemi-cylindrical, open channels, or wavy substrates that only curve in one direction. A general and important observation regarding such geometries is that the tissue is predominantly formed on concave regions ( $H < 0$ ), with virtually no (initial) tissue deposition on the convex regions ( $H > 0$ , Figure 2.11b). In hemicylindrical channels, for example, tissue progressively grows in the concave part of the substrate, effectively “flattening” the cylindrical cavity, and the tissue front is pinned at the convex edges<sup>135</sup>. Moreover, the tissue grows at a significantly lower rate than in full cylindrical channels of the same radius, which is attributed to the presence of the convex boundaries on which no tissue is formed until the local geometry becomes concave due to the advancing tissue front<sup>135</sup>. On wavy substrates, exhibiting alternating patterns of convex and concave regions (*i.e.*, positive and negative mean curvatures), tissue is also almost exclusively generated inside the concave regions<sup>138;143</sup>. Similar results are seen inside prismatic channels with non-convex pores, such as a cross shape, where tissue starts growing from the concave corners and only forms on the convex corners once

they become immersed in the advancing tissue front<sup>135</sup>.

In most curvature-guided tissue growth studies, channel-like (*i.e.*, intrinsically flat,  $K = 0$ ) substrates have been employed, and tissue growth has been typically quantified from a 2D perspective by using the projected tissue area perpendicular to the channel length<sup>134;135;138;139;141</sup>. However, the projected tissue area as seen from the top (or bottom) of the channel would only be an accurate measure of the total tissue formation, if the tissue growth is uniform along the depth of the channel, which might not be the case due to the non-uniform initial cell density or the disturbing presence of the convex boundaries<sup>138</sup>. Indeed, it has been suggested that the tissue growing in a cylindrical channel should exhibit curvature in both principal directions (*i.e.*, intrinsic curvature) and adopt a catenoid-like saddle shape ( $K < 0$ )<sup>135</sup>, although the 3D reconstructions of *in vitro* grown mineralized tissue under static and perfused conditions could not confirm this hypothesis<sup>140</sup>. Nevertheless, it seems plausible that tissue could develop into more complex architectures than developable geometries ( $K = 0$ ) and instead adopt intrinsically curved shapes ( $K \neq 0$ ). It would, thus, be relevant to also study tissue growth on such intrinsically curved (sphere-like or saddle-like) geometries, yet surprisingly little research has been conducted in this direction. A recent study involving human corneal stromal cells seeded on shallow dome-like substrates ( $K > 0$ ) shows that substrate curvature enables the formation of highly aligned extracellular matrix in the radial direction, giving rise to tissue equivalents that resemble many of the characteristics of natural corneal tissue<sup>84</sup>. In another recent study, osteoid-like tissue was grown from pre-osteoblasts on saddle-shapes with controlled curvature<sup>133</sup>. More specifically, the tissue was formed on rotationally symmetric capillary bridges of constant mean curvature and non-constant negative Gaussian curvature. The saddle-shaped tissue front is pinned by the convex edges of the substrates and progressively extends outwards, effectively flattening the initial geometry. Accordingly, the final tissue thickness is higher on substrates with narrow neck regions (*i.e.*, higher concave principal curvature and higher Gaussian curvature)<sup>133</sup>. These intriguing initial results call for more detailed investigations into tissue growth on intrinsically curved geometries, both spherical and hyperbolic, as these bear significant physiological relevance.

It should, thus, be clear that the shape of newly formed, ECM-rich tissue depends on the geometry, more specifically curvature, of the underlying substrates. But why does tissue adopt these particular shapes? A consistent observation that could elucidate this matter is that the tissue shapes are reminiscent of the shapes that viscous fluids would adopt, as dictated by the laws of physics<sup>19</sup>. In other words, the emergent shape of biological materials is somewhat similar to observations made in physics-driven inanimate materials, such as wetting droplets, soap bubbles, or other systems involving liquid interfaces. For example, the pattern formation of cone cells in the developing *Drosophila* retina exhibits a striking similarity to soap bubble clustering (Figure 2.12a)<sup>144</sup>. The underlying physical mechanism driving shape formation of these inanimate materials is the minimization of surface or interfacial tension, resulting in a tendency to minimize the surface area<sup>20</sup>. Due to the apparent similarity between the liquid and biological

shape formations, on long enough timescales, tissues are said to behave like viscous liquids with a certain surface tension<sup>145–147</sup>. As such, the emergent organization of tissue on curved substrates is often attributed to surface tension minimization, although other factors are at play as well<sup>19;148</sup>. The relation between the shape and surface tension is governed by the Young-Laplace equation<sup>149</sup>, which states that the pressure difference ( $\Delta p$ ) sustained across a fluid interface is proportional to the surface tension ( $\sigma$ ) and the mean curvature ( $H$ ):

$$\Delta p = 2\sigma H \quad (2.4)$$

Indeed, the Young-Laplace equation, or a slightly modified version thereof, has been employed to describe the shape of cells and tissues pinned at discrete sites on a flat substrate<sup>150;152</sup>, but also that of the osteoid-like tissue grown on intrinsically curved substrates<sup>133</sup>. While tension in a liquid results from various intermolecular cohesive interactions (*e.g.*, van der Waals forces), the origin of tissue tension has been explained using different theories, such as the “differential adhesion hypothesis”, but seems to involve both intercellular adhesion and cortical contractility<sup>145;146</sup>. Indications of interfacial tension in the *in vitro* curvature-driven growth of connective tissue are provided in the form of strong actin fibers that are highly aligned with the tissue-medium interface<sup>134;135;137–139</sup>. Moreover, the actin density is higher close to the tissue-medium interface, despite uniform cell density throughout the tissue bulk (Figure 2.12b)<sup>135;138</sup>. It has been hypothesized that the collective alignment of actin at the tissue front could result in a net normal force pointing away from the surface, thereby driving further advancement of the tissue front<sup>137</sup>. Additionally, the high tension that exists at the growth front can induce cell transitions, such as a reversible transition between fibroblasts and myofibroblasts that is essential in wound healing<sup>151</sup>. In addition to cell-scale actin orientation, the collagen fibers in the synthesized extracellular matrix follow the same alignment, indicating also tissue-level organization<sup>135</sup>. In fact, the tensile forces generated by cytoskeletal contractions are gradually transferred to the collagen fibers as tissue progresses, resulting in a permanently stressed matrix that can partly take over some of the cell-generated tension<sup>142</sup>. On saddle-shaped substrates ( $K < 0$ ), actin fibers have been shown to exhibit chirality and align roughly in the direction of local zero curvature<sup>133</sup>. This could potentially indicate an energetically favorable orientational order in line with the recent hypotheses that tissues can behave like active nematic liquid crystals, with cells being the nematic agents, although more evidence is required to confirm this hypothesis<sup>133;153</sup>.

Most curvature-driven tissue growth studies have been performed *in vitro*, yet some *in vivo* results also indicate that curvature plays a role in the organization and kinetics of tissue formation. In strut-based scaffolds used for the treatment of large bone defects *in vivo*, fibrous tissue formation has been found to be guided by the scaffold geometry with fibers aligning and spanning between cylindrical struts<sup>154</sup>. Furthermore, newly formed blood vessels were found to be primarily situated in the concave regions

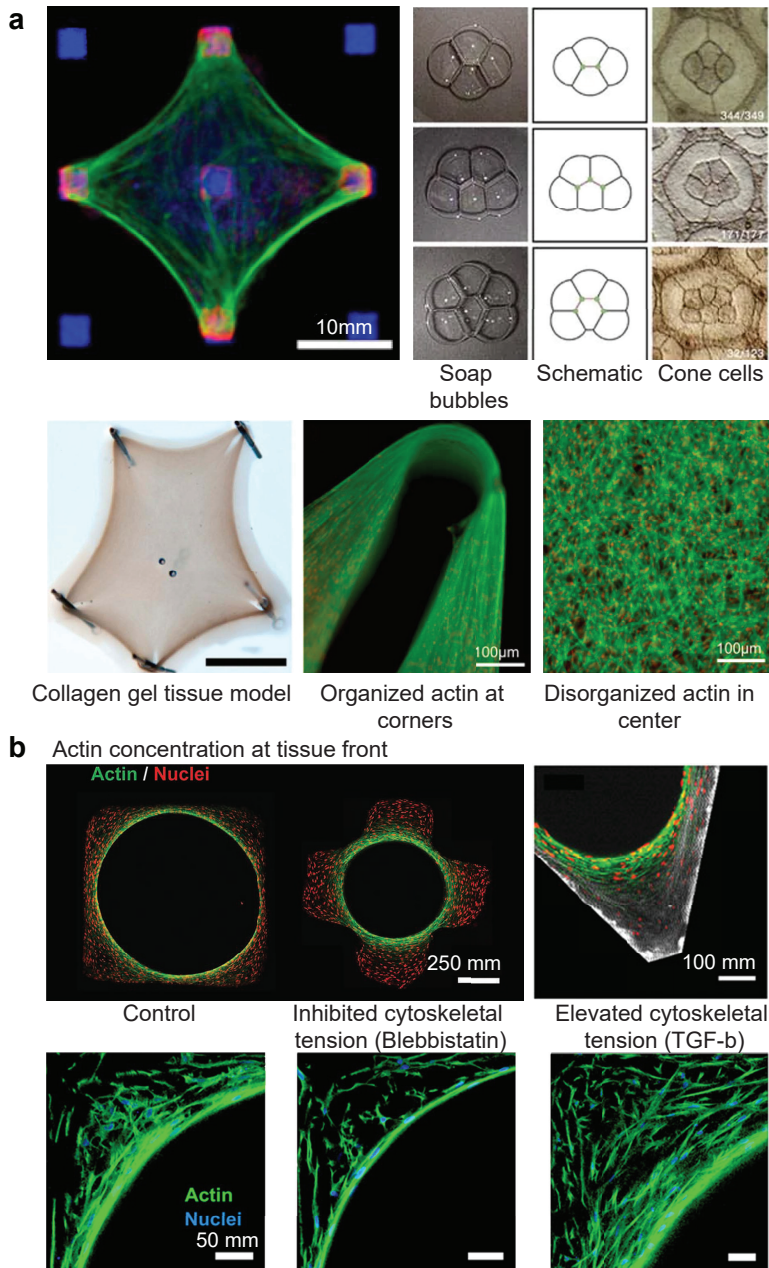


**Figure 2.12:** a) Surface tension determines confined cell and tissue shapes. Top left: A buffalo rat liver cell on a micropatterned adhesive substrate, obtained with permission from Elsevier.<sup>150</sup> Top right: similarity between clustering soap bubbles and cone cells in the developing *Drosophila* retina, obtained with permission from Springer-Nature<sup>144</sup>. Bottom: Tension-driven shape adaption of a collagen gel tissue model pinned at discrete locations, obtained with permission from Elsevier<sup>150</sup>. b) Actin alignment and increased concentration at the tissue front. Experimental images obtained with permission from Ref.<sup>135</sup> (top left), Ref.<sup>142</sup> (top right) and Ref.<sup>151</sup> (bottom).

( $H < 0$ ) of a bone implant in the initial stages after implantation, potentially indicating curvature-guided angiogenesis during bone regeneration<sup>155</sup>. Using a scaffold with horizontal struts in a  $0/90^\circ$  pattern, it was recently shown that scaffold curvature drives soft tissue formation *in vivo*, and a novel matrix mineralization process was observed (Figure 2.13)<sup>136</sup>. More specifically, tissue growth was initiated at the scaffold regions of high mean curvature, and could be predicted effectively using a curvature-driven tissue growth model (Figure 2.15 c)<sup>136</sup>.

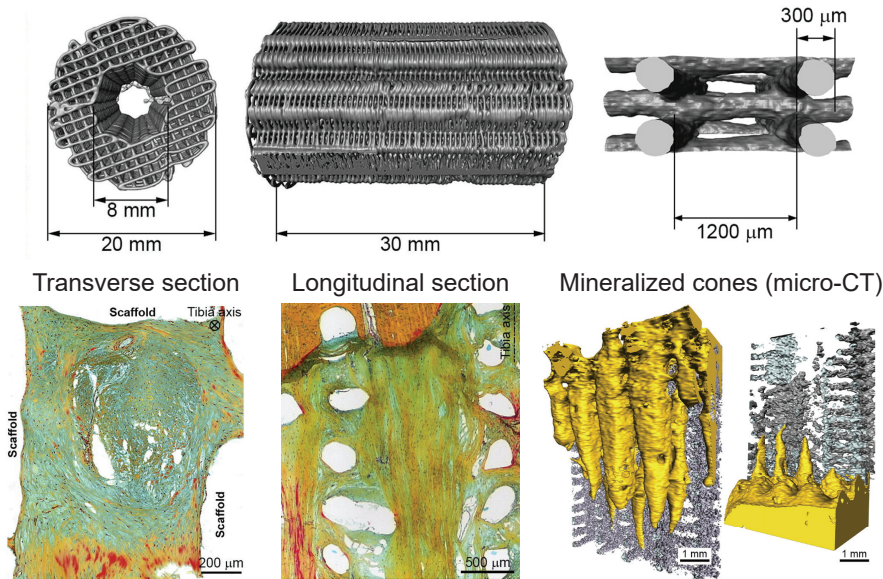


**Figure 2.13:** Top: additively manufactured scaffold implanted in a critical-sized defect in an ovine animal model. Bottom: Soft tissue growth towards cylindrical pores (left and middle), and mineralized cones as obtained with microcomputed tomography (right). Images are obtained with permission from Elsevier<sup>136</sup>.

In conclusion, it should be clear that the interplay between mechanics and geometry extends beyond the level of individual cells, and also plays an important role in shaping more complex, multicellular tissue constructs. In the case of single-layer cell sheets, such as epithelial monolayers, the balance between substrate curvature, cell-cell adhesion, and collective sheet contraction could affect collective migration<sup>83;122</sup>, sheet detachment<sup>126;127</sup>, or even the shape of individual cells<sup>129</sup>. Additionally, these thin cell sheets could buckle, wrinkle, or fold from a flat state into complex, curved shapes in response to externally applied loads (potentially balanced by internal pre-stress<sup>156</sup>). In the case of ECM-rich tissues, such as osteoid-like tissues, an apparent liquid-like behavior is observed as the tissue grows in a 3D (curved) environment. In general, such tissues grow preferentially on concave areas (*e.g.*, in the corner regions of straight-sided pores) causing a gradual smoothing in the extracellular geometry that is sensed by new cells<sup>134;138</sup>. These growing tissues exhibit cells with aligned actin fibers (primarily at the tissue front)<sup>157</sup>. Similar alignments are also observed in the ECM fibers that

are deposited<sup>142</sup>. The liquid-like shape-formation observed in these ECM-rich tissues has, consequently, been linked to the concept of surface tension<sup>133</sup>. Mechanical principles, therefore, seem to govern much of the shape formation at the tissue level in a manner similar to the spatiotemporal organization of single cells on curved substrates. While force-transmission and long-range cytoskeletal remodeling through cell-cell or cell-ECM interactions undoubtedly plays a key role in this emergent organization, more insights are required to uncover how cell-level organization translates to tissue-level organization.

## 2.5 Computational models for curvature-guidance

In addition to *in vivo* and *in vitro* experiments, the role of substrate curvature on the cell and tissue response could be elucidated further using *in silico* models. Computational approaches are particularly relevant for the design and optimization of artificial tissue scaffolds, and their importance is expected to increase significantly in the future<sup>158</sup>. Many phenomenological and mechanistic theoretical models capable of predicting experimentally observed behavior have been developed on various scales. Here, we aim to highlight those models that have been specifically directed at modelling the behavior of cells and tissues on curved geometries, and we refer to other reviews for a broader perspective on the *in silico* models of cells and tissues<sup>19;159;160</sup>.

### 2.5.1 Cell-scale models

Mathematical models of the cell, either discrete or continuum, have been developed to describe and predict a variety of cell-scale processes, including cell contractility<sup>161</sup>, focal adhesion formation<sup>162</sup>, or migration<sup>163</sup>. Given the relatively recent interest in cell-scale curvature guidance, however, theoretical models that specifically address the effects of substrate curvature on single-cell response are not yet widespread. In one of the earliest models (briefly mentioned in Subsection 2.3.2, Figure 2.14a), the cell body and stress fibers are respectively modelled as elastic plates and rods, and the stress fiber orientation is predicted by minimizing the total elastic energy of the system. Essentially, the orientation is determined by a competition between the bending energy of the stress fibers and the energy arising from cell contractility, the balance of which can be captured using a dimensionless parameter<sup>95</sup>. Consequently, the model is able to predict that fibroblasts, with a high stress fiber bending modulus, should align along the cylinder axis, while epithelial cells, with thin stress fibers, should align perpendicularly, in accordance with experimental results<sup>62</sup>.

Another study implemented a phenomenological constitutive model based on a theoretical description of actomyosin contractility homogenized to the macroscale cell level in commercial finite element software to investigate the cytoskeletal stress distributions in the cells adhering to curved substrates<sup>166</sup>. According to this model, the substrate curvature can inhibit actomyosin contractility in two independent ways: through stress fiber bending, causing the contractile apparatus to perform sub-optimally, and through a pre-stress that arises when a flat cell should conform to a curved substrate.

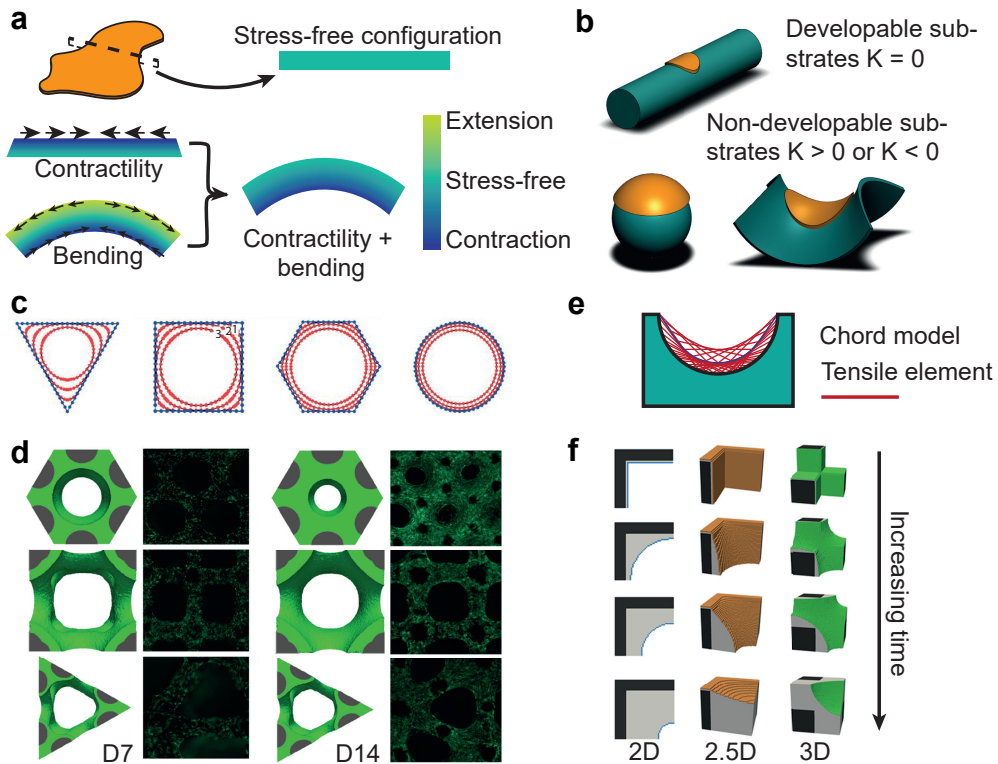


**Figure 2.14:** Cell and tissue-scale computational models. a) A schematic overview of the through-thickness strain variation of a cell adhering to a convex cylindrical substrate, showing the combined effects of active contractility and cell bending. Adapted from Ref.<sup>95</sup>. b) A schematic illustration of a cell (orange) adhering to developable (top) and non-developable (bottom) substrates. The conformation of an initially flat cell to a non-developable substrate requires cell stretching or shrinking. c) Three consecutive evolutions of the tissue front as predicted by the curvature-driven growth model of Rumpler et al. Obtained with permission from Ref.<sup>134</sup>. d) 3D tissue growth predictions of a level-set curvature-driven growth model, with experimental images from *in vitro* grown bone tissue on day 7 (left) and day 14 (right), obtained with permission from Springer-Nature<sup>164</sup>. e) The geometrical chord model<sup>138</sup>, representing tissue front evolution as an assembly of tensile elements. f) The predictions of a curvature-driven growth model (using a scanning mask) on different types of geometries, obtained with permission from Springer-Nature<sup>165</sup>.

This last aspect is particularly interesting, as it allows delineating between intrinsically curved substrates (*i.e.*, spheres or saddles) and intrinsically flat substrates such as cylinders (Figure 2.14b). On cylinders, the pre-stress is not present since an isometric transformation (*i.e.*, a transformation that does not require stretching) between a flat cell and the cylindrical substrate is possible. On spheres and saddles, however, the cell should locally stretch or shrink in order to conform to the substrate, a consequence of Gauss’ “remarkable theorem”<sup>21</sup>, giving rise to a pre-stress in the cell. The model, thus, dictates that contractility in cells on cylinders (or other developable substrates) is only impeded

by the bending of stress fibers, while cell contractility on intrinsically curved substrates is affected by both the bending of stress fibers and a cellular pre-stress.

In a more recent numerical model, a discrete approach was employed where the cell is modelled as a tensegrity system (*i.e.*, a network-like structure containing isolated compression elements stabilized by tension elements)<sup>167</sup>, using non-smooth contact dynamics<sup>168</sup>. Several intracellular components that are important in cell mechanics were explicitly implemented in the model, such as the cell membrane, focal adhesions, and the different types of cytoskeletal filaments. The non-smooth contact dynamics method treats the intracellular components as collections of rigid elements that interact with each other through contact, cable, or spring interactions<sup>168;169</sup>. The ensemble of all these components and their interactions then constitutes a model that, after calibration and verification using experimental data, enables the estimation of the forces and strains acting on all considered intracellular components in response to curved, perfectly rigid substrates. For example, the model predicts a more stable and rounder nucleus on concave ( $K > 0$ ,  $H < 0$ ) than on convex ( $K > 0$ ,  $H > 0$ ) hemispherical substrates, in accordance with some single-cell experimental results<sup>55;72;168</sup>. Furthermore, the discrete nature of the model enables the investigation of the relative importance of certain cellular components (*e.g.*, microtubules) on the overall mechanics, reminiscent of drug targeting that has been used experimentally to inhibit certain cell components<sup>168</sup>.

Another recent discrete approach models cells on convex and concave cylindrical substrates as a collective of a deformable cell membrane, a solid spherical nucleus, and a string-like cytoskeletal structure<sup>170</sup>. By modelling temporary integrin-ligand bonds to account for the cell-substrate adhesion, and by calculating the protrusion forces created at the adhesion sites, the model aims to simulate the migration of the cells residing on curved substrates. The purely mechanics-based model indicates that the curvature of the substrate provides a geometrical constraint on the protrusion force direction, meaning that it promotes protrusion in the longitudinal direction and consequent migration in that direction<sup>170</sup>.

Despite capturing various experimental observations, these continuum and discrete models have, thus far, primarily provided qualitative insights on cell response to curvature. To a large extent, this is the consequence of the major assumptions that are necessary in the model development stage, either because the biophysical mechanisms are not yet fully understood, or to keep the model tractable. For example, most models assume that cells fully conform to the curved substrates, while experimental evidence seems to indicate that cells might lift off from some substrates<sup>72</sup>. Additionally, most models employ a purely mechanics-based approach, neglecting various biochemical processes, and typically consider a quasi-static situation, despite the dynamic behavior observed in the experiments<sup>168</sup>. Nevertheless, *in silico* attempts at understanding curvature-guided cell response are valuable for elucidating the importance of intracellular components, and their value will only increase when more of the underlying physical principles are understood and implemented.

### 2.5.2 Tissue-scale models

While single-cell models could eventually lead to a deeper understanding of the cell-scale mechanisms behind curvature-sensing, most theoretical efforts on this matter have been directed at the tissue level, often by means of phenomenological tissue growth models that consider a continuum or interfacial evolution perspective<sup>19</sup>. In most cases, these models are specifically used to predict bone tissue growth, although the components of the tissue (*e.g.*, collagen fibrils) are generally not explicitly modelled.

The simplest (and first) curvature-driven tissue growth model considers a 2D case, simulating tissue growing progressively inwards in pores with pre-defined cross-sectional shapes (Figure 2.14c)<sup>134</sup>. In this type of phenomenological models, tissue is deposited only in concave regions ( $\kappa \leq 0$ ), at a rate ( $ds/dt$ ) proportional to the curvature ( $\lambda$  is a growth rate constant):

$$\kappa \leq 0 : ds/dt = -\lambda\kappa \quad (2.5)$$

$$\kappa > 0 : ds/dt = 0 \quad (2.6)$$

Despite its simplicity, this 2D growth law is able to replicate experimentally observed tissue growth (in terms of the projected tissue area) in various pore types remarkably well, showing the typical corner smoothing and the development of a circular growth front<sup>134;137</sup>. To a first approximation, the local curvature at discrete points along the pore can be estimated from the radius of the circumcircle that passes through each point and its two immediate neighbors<sup>134</sup>. In a more general version of the model, the local curvature is estimated using the Frette's algorithm<sup>171</sup>, by sliding a circular mask across the scaffold-medium interface on binarized images and calculating the curvature as a function of the ratio of the pixels present on both sides of the interface<sup>138;171</sup>. This enables the simulation of tissue growth on the digital images of as-manufactured pore geometries, and facilitates consequent comparison with the corresponding experimental results<sup>135;138</sup>. The radius of the circular mask, defined in terms of the number of pixels, should be chosen appropriately (*e.g.*, in the order of the cell size), as it directly affects the curvature estimation. Furthermore, this growth law has no intrinsic time dependency. A time scaling is, therefore, necessary in order to match the experimentally observed tissue growth rates with the simulations<sup>135;138</sup>. Considering the evolution of the (projected) tissue-medium interface, this 2D curvature-driven growth law is in fact equivalent to the mathematical concept of curve-shortening flow, during which points on a smooth, closed curve move inwards perpendicularly, at a speed proportional to the curvature, thereby shortening the curve and decreasing the enclosed area<sup>172</sup>. Eventually, this causes convex and non-convex shapes to smoothen into a circle that uniformly shrinks towards a single point, reminiscent of the tissue front evolution observed experimentally<sup>134;135;138;139</sup>.

The same type of growth law can be extended to 3D, by employing a spherical, voxelized scanning mask for curvature estimation rather than a circular mask (Figure 2.14f)<sup>173</sup>. In this case, the tissue growth rate is taken to be proportional to the mean

curvature,  $H$ , of the substrate and tissue is only deposited in concavities, with  $H < 0$  (or  $H > 0$  depending on the normal definition). Similar to the 2D case, the 3D implementation requires some fine-tuning of the mask diameter and time scale parameter, to achieve a realistic growth behavior that matches the experimental results. Additionally, in order to accurately model growth in the third dimension (*e.g.*, in a 3D pore channel), the volume scanned by the mask should progressively increase downwards, effectively simulating the migration of cells down the pore channel<sup>173</sup>. Instead of using a scanning mask for curvature estimation, a similar growth law could be implemented in a model that is based on the level set method<sup>164</sup>. This is a numerical approach to track the interface evolution between two domains,  $\Omega_a$  and  $\Omega_b$ , that has applications in diverse fields<sup>174;175</sup>. The level set function,  $\Phi$ , is defined to be zero on the interface between both domains, and non-zero inside the domains. By numerically solving an advection equation of the level set function, with an advection velocity that is proportional to the mean curvature, the evolution of tissue growth can realistically be simulated, albeit some time scaling is required to match the growth rate to the experiments. An important advantage of the level set method is its intrinsic curvature evaluation, eliminating the need for a scanning mask and the associated fine-tuning<sup>164</sup>. 3D growth models like these can be readily applied for the *in silico* investigations of tissue growth on various types of artificial scaffolds, thereby facilitating the optimization of scaffold geometries in terms of the predicted tissue growth behavior (Figure 2.14d)<sup>164;165</sup>. Essentially, the tissue evolution predicted by these 3D growth models is intimately connected to the mathematical concept of mean curvature flow, which is a more general, higher-dimensional form of the curve shortening flow that could describe the 2D growth models<sup>176</sup>. The fact that mean curvature-driven growth models can capture experimental observations so well once more supports the idea that (apparent) surface tension plays a role in tissue front evolution, because the evolution of systems governed by surface tension, such as soap films, has been described using mean curvature flow. Moreover, such soap-film-like systems evolve towards energy-minimizing configurations in the form of minimal surfaces (*i.e.*, surfaces of zero mean curvature)<sup>20;173</sup>. Indeed, the natural structure of trabecular bone has been found to exhibit a mean surface curvature close to zero<sup>42;43</sup>, which is why minimal surfaces have seen a surge of interest for the design of bone-substituting biomaterials<sup>177</sup>. While more research is needed to confirm that tissue, indeed, evolves towards a surface with  $H = 0$  (recent results suggest it might evolve towards a constant, non-zero mean curvature configuration<sup>178</sup>), it is clear that surface tension plays an important role, and that models describing the interface evolution based on some applications of the mean curvature flow can yield realistic predictions.

In addition to the phenomenological models describing the interface evolution, attempts have been made at developing more mechanistic theories to describe tissue growth. For example, a thermodynamically admissible growth law for volumetric tissue growth can be constructed in terms of an eigenstrain that arises as new tissue is added to the bulk<sup>179</sup>. This continuum model, thus, predicts tissue growth as a function of the stress state that would be felt by the cells in the tissue. While still requiring

some phenomenological input, the model can replicate the experimentally observed tissue deposition in circular pores, and predicts higher circumferential stress close to the tissue-medium interface, in line with the observations of strong actin signals at the interface<sup>134;179</sup>. By extending the growth law to incorporate the surface stress in addition to the eigenstress, the model is capable of replicating the inhibition of tissue growth on convex as opposed to concave cylindrical substrates<sup>143</sup>. Alternatively, experimentally observed smoothing of the substrate and tissue growth slowdown could be simulated by modelling the changes in cell density and spreading due to curvature (volumetric crowding), and also accounting for cell diffusion and depletion<sup>180;181</sup>.

Another mechanistic explanation builds upon a remarkably simple geometrical analysis in 2D, yet captures experimental results surprisingly well<sup>138</sup>. By considering the tissue as a set of stretched cells represented by straight lines with a fixed length that span a curved substrate, the evolution of the tissue front can be visualized in a layer-by-layer fashion (Figure 2.14e). This geometrical interpretation, while not explicitly modelling the formation of new tissue, is supported by the frequent observations of aligned actin filaments in pore channels and cells spanning concave spherical ( $K > 0$ ,  $H < 0$ ) substrates<sup>72;134;138</sup>.

One aspect that is often not explicitly considered in these tissue growth models is the change in fluid flow properties that occurs as tissue progresses and fills the scaffold structure, potentially lowering the permeability and inhibiting the transport of oxygen and nutrients. Some models, however, consider the flow-induced shear stress in addition to the effects of substrate curvature<sup>182;183</sup>. This could be useful to quantitatively match the tissue growth predictions to *in vitro* experiments performed in a perfusion bioreactor<sup>182</sup>. Moreover, such models could assist in determining how to optimize scaffolds for tissue regeneration that balance curvature cues with a sufficient level of permeability<sup>183</sup>. In conclusion, it should be clear that relatively simple tissue growth laws, often based on some phenomenological applications of the curvature flow, perform remarkably well in predicting the shape and kinetics of tissue growth observed *in vitro*, and even *in vivo*<sup>136</sup>. It is, therefore, expected that such models will play ever more prominent roles in the scaffold design, especially when more of the underlying curvature guidance mechanisms are elucidated.

## 2.6 Discussion

We have reviewed the experimental evidence demonstrating that both individual cells and multicellular tissue constructs respond to the curvature of the underlying substrate, and have highlighted the dedicated theoretical models that aim to simulate this phenomenon. By emphasizing the notions of mean and Gaussian curvature, which are well-defined concepts from differential geometry, we hope to provide a more formal framework to describe cell- and tissue-level curvature guidance, with the ultimate aim of better understanding geometry-driven tissue regeneration. While many of the underlying mechanisms are still not understood, it is clear that mesoscale substrate curvature should be considered as an important cue for directing the organization and kinet-

ics of cells and tissues. The experimental and theoretical results that we have reviewed provide some general insights into curvature guidance at the cell and tissue levels, the most important of which are summarized below.

First, cells with pronounced stress fibers (*e.g.*, fibroblasts) seem to avoid curvature whenever possible. On cylindrical substrates, such cells align in the longitudinal direction (*i.e.*, the direction of zero curvature). On the concave side of spherical substrates, where curvature is omnipresent, cells have the option to span the substrate to avoid being curved. Even on saddle shapes, which are convex in one direction and concave in the other, cells could span the concave part to avoid curvature as much as possible. As such, one might use the term curvature-avoidance rather than curvature guidance<sup>64</sup>.

Second, both individually operating cells and multicellular ECM-rich tissue seem to favor concavities ( $H < 0$ ) over convexities ( $H > 0$ ). This observation holds for cylindrical-like ( $K = 0$ ) as well as spherical-like ( $K > 0$ ) substrates. Individual cells seem to favor migration towards concavities and avoid convex spherical caps, unless they are shallow. Osteoid-like tissue grows faster in concavities with higher curvature, and hardly shows any growth on convex regions, until the moment when the local curvature becomes concave due to tissue progression.

Third, tensile forces form the foundation of curvature guidance at both the single-cell and tissue-level scales. At the cell level, actomyosin contractility in conjunction with substrate geometry gives rise to a net normal force that either relieves or compresses the nucleus, thereby enabling individual cells to sense and respond to mesoscale curvature. The collective organization of cells in osteoid-like tissue results in a surface tension, causing the developing tissue to exhibit a viscous fluid-like behavior that evolves towards seemingly energy-minimizing configurations.

Finally, surfaces with negative Gaussian curvature (*i.e.*, saddle shapes) are largely unexplored in the current cell-response and tissue-growth studies, despite bearing high physiological relevance. Most research has been performed using either developable or spherical geometries, and the focus has been on either line curvature (*i.e.*, the curvature of pore cross sections), or on the mean curvature. The geometries that cells encounter *in vivo* are generally more complex, exhibiting wide variations of both mean and Gaussian curvatures, rendering purely spherical and intrinsically flat shapes rather the exception than the rule. For example, saddle shapes will emerge wherever branching and bending of tubular structures occurs, such as in blood vessels or the respiratory system. Additionally, every outwards-bulging spherical pouch, cyst, or vessel-like structure attached to a relatively flat tissue layer will exhibit negative Gaussian curvature at the neck region (the transition between the flat substrate and the spherical bulge). Moreover, complex network topologies, such as those found in trabecular bone, are known to be hyperbolic (saddle-shaped) on average. As such, it is essential to include substrates with negative Gaussian curvature within the spectrum of future curvature guidance studies.

Despite such general observations, it is important to emphasize that different cell types could be expected to behave differently to substrate curvature. For example, epithelial cells and fibroblasts align differently on cylindrical substrates, attributed to a

change in the elastic energy balance<sup>62;95</sup>. Moreover, the curvature magnitudes that can be sensed by cells depend on the cell size. For example, MSCs might respond to certain curvature magnitudes while macrophages do not, possibly because of the smaller sizes of the latter<sup>55</sup>. Nonetheless, it is safe to state that substrate curvatures with the appropriate magnitude present an important cue to various types of adherent cells, and that the response of those cells can be understood from a mechanics-based perspective. Regarding tissue growth, most research has focused on osteoid-like tissue, with the ultimate aim of understanding scaffold geometry-guided tissue regeneration. Despite consistent experimental observations and promising predictions with theoretical models, a more mechanistic understanding of tissue evolution in response to curvature would be desirable. In this respect, it would be of interest to better link the insights made at the level of individual cells to the tissue scale, to understand how the response of single cells eventually gives rise to emergent tissue organization.

### 2.6.1 The implications for porous scaffold design

Within the field of tissue engineering, porous scaffolds are increasingly being considered for the active guidance and stimulation of the tissue regeneration process<sup>159</sup>. The rapid advances in additive manufacturing have resulted in an unprecedented freedom and control in the design of 3D porous scaffolds<sup>184</sup>. As such, the curvature of these scaffolds could be optimized to meet the various criteria that are relevant for tissue engineering applications including the mechanical, mass transfer, and biological properties. For example, scaffold curvatures could be optimized to provide a high initial tissue growth rate, yet maintain a desirable level of permeability<sup>135;165</sup>, an endeavor that significantly benefits from efficient *in silico* models that consider both criteria<sup>182</sup>. The majority of the research into geometrical scaffold design and the effects of scaffold geometry on cell and tissue response has been directed at bone scaffolds, used in the treatment of segmental bone defects<sup>185</sup>. This is partly because bone itself is characterized by a highly complex, porous geometry, making it only natural that geometrical cues are considered in the design of synthetic bone substitutes<sup>159</sup>. Moreover, the developments in additively manufactured bone scaffolds build upon several decades of research into orthopedic implants, making this type of tissue scaffolds one of the most widely studied. As such, we will focus on bone scaffolds in this section, but we emphasize that the same principle of involving curvature in the design process could be applied to the other types of tissue scaffolds as well.

Although a myriad of 3D scaffold designs could be generated, such designs can roughly be classified in two major categories: 1. strut-based, network-like scaffolds and 2. sheet-based, foam-like scaffolds, both of which could be periodic or irregular<sup>186</sup>. The former has been widely considered for bone tissue applications, and could, for example, be derived from space-filling tessellations of polyhedra or well-known crystallographic arrangements (Figure 2.15a). Sheet-based scaffolds exhibit more complex, smooth morphologies that could, for example, be designed using numerically simulated spinodal decomposition (Figure 2.15b)<sup>187;188</sup>. From a curvature perspective, the

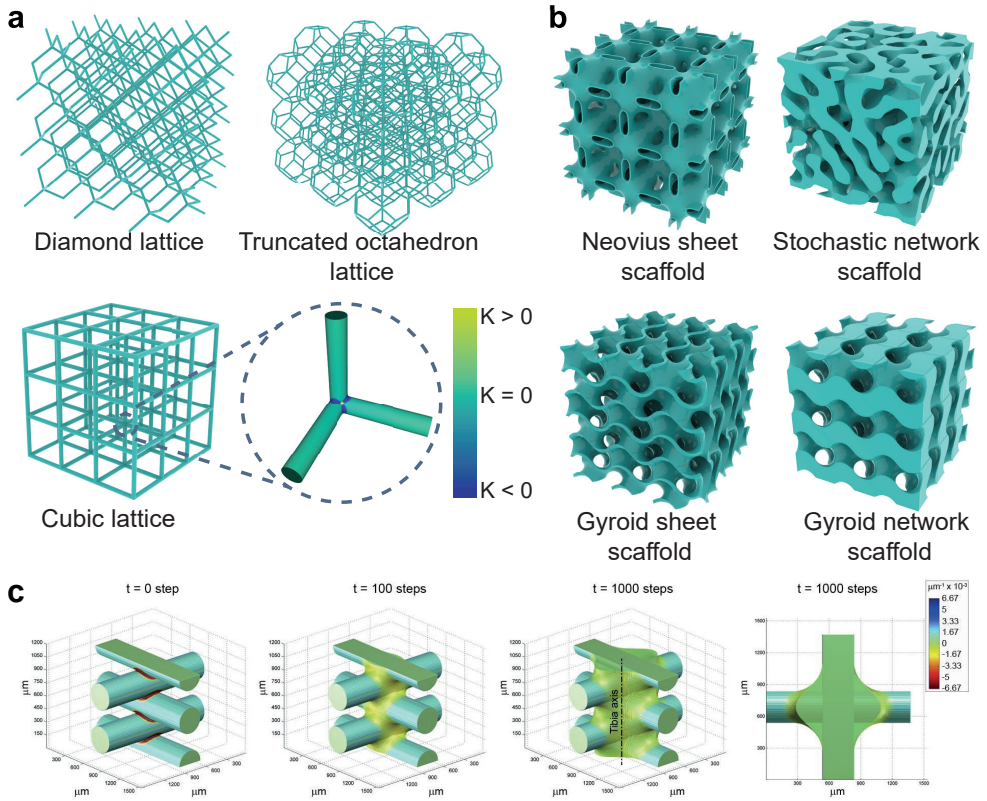


**Figure 2.15:** 3D porous scaffolds for bone tissue regeneration. a) Some examples of strut-based scaffolds: the diamond lattice (top left), the truncated octahedron lattice (top right), and the cubic lattice (bottom left). Lattice structures with cylindrical struts exhibit non-zero Gaussian curvatures at the locations of the strut connections. b) Some examples of sheet-based scaffold designs: a Neovius sheet-scaffold (top left), a stochastic network-scaffold obtained with Gaussian random fields (top right), a Gyroid sheet-scaffold (bottom left), and a Gyroid network-scaffold (bottom right). The Neovius and Gyroid scaffolds are examples of scaffolds based on TPMS. c) Curvature-driven tissue growth predictions on the 0/90° scaffold used *in vivo* by Paris et al.<sup>136</sup>. Tissue starts growing from the strut intersections. Obtained with permission from Elsevier.

sheet-based morphologies offer a richer design space, whereby large variations in both mean and Gaussian curvatures throughout the scaffold are possible. The strut-based scaffolds, however, offer a much smaller and more discrete curvature spectrum. For example, typical scaffolds with cylindrical struts exhibit zero Gaussian curvature and constant (positive) mean curvature on the strut surface, and only show concave regions with higher mean curvatures and non-zero Gaussian curvatures at the strut intersections (Figure 2.15a). Given the experimental evidence showing very limited tissue growth on convex regions, it could be argued that cylindrical-strut based scaffolds are not very efficient from a curvature-guided tissue growth perspective. Indeed, *in vivo* and *in silico* results have confirmed that tissue growth initiates from the strut intersec-

tions in a simple strut-based scaffold (Figure 2.15c)<sup>136</sup>. It, therefore, seems desirable to tune the mean and Gaussian curvatures of a scaffold in such a way to favor fast tissue regeneration. However, there are geometrical restrictions to the possible combinations of the mean and Gaussian curvatures, making it impossible to tune them independently or to fully decouple them from the global scaffold topology. For example, constant positive Gaussian curvature can only be achieved on the surface of a sphere, while a surface with constant negative Gaussian curvature can even not be realized in 3D Euclidean space according to Hilbert's theorem<sup>21</sup>. Moreover, curvature is scale-dependent, which means that a change in the curvature must be accompanied by a change in size. However, it is primarily the connection between surface curvature and global topology that places constraints on the ability to tune curvature distributions throughout a scaffold. As mentioned in Subsection 2.2.1, the Gauss-Bonnet theorem dictates that the area-integrated Gaussian curvature of a surface is proportional to the genus (number of "handles") of that surface. More specifically, surfaces with  $g > 1$  will be, in an integral sense, saddle-shaped or hyperbolic. The intricate network- or foam-like topologies of strut- and sheet-based scaffolds have  $g \gg 1$ , which means that they must contain regions with  $K < 0$  to satisfy the Gauss-Bonnet theorem. Even the strut-based scaffolds, in which most of the area has  $K = 0$  (on the strut surfaces), must contain saddle-shaped regions to balance the integral Gaussian curvature. Indeed, saddle-shaped regions are found at the intersections. The inherent hyperbolic nature of 3D porous scaffolds calls for a deeper investigation into the effects of negative Gaussian curvature on cells and tissues, yet very few studies have employed saddle-shaped substrates in single cell and tissue growth studies so far. Nonetheless, a particular class of saddle-shaped sheet-like morphologies, namely triply periodic minimal surfaces (TPMS), has recently started to receive widespread attention, in part due to the curvature arguments. TPMS are periodic, bicontinuous morphologies that locally minimize area and have  $H = 0$  and  $K \leq 0$  everywhere (Figure 2.15b). It has been hypothesized that TPMS-based scaffolds could present "biomimetic" curvature cues, due to the similar mean curvature profile that has been observed in trabecular bone<sup>177;189;190</sup>. However, it remains unclear whether regular TPMS or their variations could, indeed, constitute optimal "curvature-guiding" scaffolds. In this regard, it could be questioned whether designing scaffolds based on the structure of healthy bone (*i.e.*, the homeostatic "end-state"), is an effective strategy towards fast regeneration of new tissue<sup>191</sup>.

### 2.6.2 Opportunities for 4D printing

While 3D printing enables the fabrication of a wealth of complex porous geometries, emerging 4D printing technologies have recently started to receive considerable interest too. 4D printing adds time as another dimension to conventional 3D printing, resulting in structures that can change shape over time, typically by employing stimuli-responsive materials<sup>192–194</sup>. Since inception, 4D printing (or shape-shifting in general) has been considered as a novel platform for biomedical applications<sup>195–197</sup>, opening new avenues towards encapsulation<sup>87;198</sup>, biomedical devices<sup>199;200</sup>, shape-changing scaffolds<sup>201;202</sup>,

or 2D-to-3D fabrication of cellular solids<sup>203;204</sup>. In the light of the curvature guidance principles discussed here, shape-shifting could enable temporal control over the geometrical environment of cells and tissues, in order to guide their evolution. For example, stimuli-responsive materials can be used to develop shape-changing substrates that allow for dynamic spatio-temporal control over the single-cell environment<sup>205</sup>. This might, for example, be useful to endow stem cells with a history of curvature cues that could affect their fate, as the lineage commitment of stem cells has been shown to be influenced by their past physical environments<sup>206;207</sup>. Furthermore, precisely patterning mesenchymal stromal cells in a collagenous ECM gel enables spontaneous *in vitro* tissue shape-shifting, reminiscent of the complex shape formation observed during *in vivo* development<sup>208</sup>. While 4D printing for tissue engineering is still in its infancy, it is expected that the ability to change the local geometry (*i.e.*, curvature) of the cellular environment with time could offer novel pathways to enhance the guiding and stimulating functions of tissue scaffolds.

### 2.6.3 Outlook

We already mentioned that a limited number of different substrate geometries has been employed in many single cell studies, often involving cylindrical or spherical shapes. This could, in part, be explained by the challenges associated with the microfabrication of cell-scale substrates. For example, most early studies resorted to cylindrical wires<sup>57;61-63</sup> to present the cells with a curved environment. However, rapid advances in microfabrication techniques, including micromachining<sup>55;209</sup>, soft lithography<sup>210;211</sup>, and two-photon polymerization<sup>212;213</sup> are enabling the robust fabrication of curved cellular environments with unprecedented design freedom<sup>214</sup>. Consequently, these technologies are expected to facilitate more in-depth studies of cell response to the various types of substrate curvatures. For example, they could allow for the investigation of cell response to developable surfaces other than cylinders (*e.g.*, cones or tangent developables), which also have zero Gaussian and non-zero mean curvature. Given the observed behavior on cylinders, it is expected that cells align in the zero-curvature direction on all types of developable surfaces. In addition to those specific types of substrates, curvature guidance studies could in general benefit from a broader spectrum of curved substrates, such as symmetric and non-symmetric saddles, ellipsoidal shapes, and other curvature landscapes with variations in mean and Gaussian curvatures. The same rationale at a larger scale applies to the tissue level, where additively manufactured scaffolds with precise curvature fields would be useful tools for investigating the curvature-guided tissue growth. In this regard, sheet-based scaffolds with controllable curvature profiles (*e.g.*, structures based on triply periodic constant mean curvature surfaces<sup>215</sup>), hold the most promise.

## 2.7 Conclusion

In conclusion, we reviewed the recent evidence that demonstrates the role of mesoscale substrate curvature on cell and tissue responses. By invoking the formal

curvature descriptions provided by differential geometry (*i.e.*, mean and Gaussian surface curvatures), we hope to equip the reader with a more univocal framework to describe cell and tissue-level curvature guidance. We highlighted that much of the emergent organization and dynamics in response to substrate curvature could be explained from a mechanics perspective, involving actomyosin contractility on the cell level and surface tension on the tissue level. Moreover, experimental observations of tissue growth on 3D scaffolds can be replicated surprisingly well using phenomenological growth models that are reminiscent of the mathematical concept of curvature flow. While the underlying mechanisms are not yet fully uncovered and experimental evidence involving a broader curvature spectrum is necessary, the experimental and computational insights that we have reviewed show that substrate curvature should, indeed, be considered as an important cue in regulating cell response and guiding tissue growth. These curvature guidance principles could have far-reaching implications not only in understanding morphogenesis, defect healing, and bone remodeling, but also in the design of tissue engineering scaffolds and regenerative medicine therapies.

## 2.8 Supporting information

**Table 2.1:** General overview of cell-level curvature guidance studies, showing substrate type, curvature classification, scale, materials, cell types and key observations. Radius of curvature is denoted as  $r_c$ , wavelength and amplitude of sinusoidal substrates are denoted as  $\lambda$  and  $A$  respectively. Material abbreviations are as follows: PDMS = polydimethylsiloxane, PTMC = poly(trimethylene carbonate), PLGA = poly(lactic-co-glycolic acid), gelMA = gelatin methacryloyl.

Substrate type	K	H	Curvature scale ( $\mu\text{m}$ )	Materials	Cell type	Key observations
Convex cylinders	$K = 0$	$H > 0$	$r_c = 5-15$ <sup>57</sup>	Glass <sup>57,60-63,80</sup> PDMS <sup>64,66</sup> PLGA <sup>81</sup>	Fibroblasts <sup>57,60-62,80,81</sup> VSMC <sup>60</sup> Epithelial cells <sup>61-63</sup> MSC <sup>64,66</sup>	Longitudinal alignment <sup>57,60-64,66,80,81</sup> Transverse alignment <sup>61-63</sup>
			$r_c = 18$ <sup>61,63</sup>			
			$r_c = 12-25$ <sup>62</sup>			
			$r_c = 5-121$ <sup>81</sup>			
			$r_c = 150$ <sup>64</sup>			
Concave cylinders	$K = 0$	$H < 0$	$r_c = 40-200$ <sup>60</sup>	PDMS <sup>66</sup> Hydroxyapatite <sup>67</sup>	MSC <sup>66</sup> Osteoblasts <sup>67</sup>	Substrate spanning <sup>66</sup> Individual random alignment, collective longitudinal alignment <sup>67</sup>
			$r_c = 125-500$ <sup>66</sup>			
			$r_c = 220$ <sup>80</sup>			
			$r_c = 50-250$ <sup>67</sup>			
			$r_c = 125-500$ <sup>66</sup>			
Convex hemispheres	$K > 0$	$H > 0$	$r_c = 10$ <sup>71</sup>	Glass <sup>70</sup> PDMS <sup>71,73</sup> PTMC <sup>72</sup>	MSC <sup>70,72,73</sup> Macrophages <sup>71</sup> Fibroblasts <sup>73</sup>	Increased nuclear deformation, osteogenic differentiation <sup>72</sup>
			$r_c = 50-150$ <sup>73</sup>			
			$r_c = 125-375$ <sup>72</sup>			
			$r_c = 250-2000$ <sup>70</sup>			
			$r_c = 10$ <sup>71</sup>			
Concave hemispheres	$K > 0$	$H < 0$	$r_c = 50-150$ <sup>73</sup>	PDMS <sup>71,73</sup> PTMC <sup>72</sup>	Macrophages <sup>71</sup> MSC <sup>72,73</sup>	Substrate spanning <sup>72</sup> Escape from concave wells <sup>73</sup>
			$r_c = 125-375$ <sup>72</sup>			
			$r_c = 125-375$ <sup>72</sup>			
			$r_c = 125-375$ <sup>72</sup>			
			$r_c = 375$ <sup>66</sup>			
Saddle	$K < 0$	$H \neq 0$	$r_c = 375$ <sup>66</sup>	PDMS <sup>66</sup>	MSC <sup>66</sup>	Substrate spanning and migration in concave direction <sup>66</sup>
			$r_c = 80-500$ <sup>30</sup>			
			$r_c = 80-500$ <sup>30</sup>			
			$r_c = 80-500$ <sup>30</sup>			
			$r_c = 80-500$ <sup>30</sup>			
Sphere-with-skirt	$K_{min} < 0 < K_{max}$	$H_{min} < H < H_{max}$	$r_c = 80-500$ <sup>30</sup>	PDMS <sup>30</sup>	Fibroblasts <sup>30</sup>	Avoidance of spherical cap, perpendicular alignment of SF subpopulations on saddle-shaped region <sup>30</sup>
			$r_c = 80-500$ <sup>30</sup>			
			$r_c = 80-500$ <sup>30</sup>			
			$r_c = 80-500$ <sup>30</sup>			
			$r_c = 80-500$ <sup>30</sup>			
Single sinusoidal sheet	$K = 0$	$H_{min} < 0 < H_{max}$	$\lambda = 200, A = 40$ <sup>68</sup>	GelMA <sup>68</sup> PUA <sup>69</sup>	Myoblasts <sup>68</sup> T cells <sup>69</sup>	Longitudinal alignment <sup>68</sup> Longitudinal, zigzagging migration <sup>69</sup>
			$\lambda = 20-160, A = 10$ <sup>69</sup>			
			$\lambda = 20-160, A = 10$ <sup>69</sup>			
			$\lambda = 20-160, A = 10$ <sup>69</sup>			
			$\lambda = 20-160, A = 10$ <sup>69</sup>			
Double sinusoidal sheet	$K_{min} < 0 < K_{max}$	$H_{min} < 0 < H_{max}$	$\lambda = 30-300, A = 1-30$ <sup>55</sup>	PDMS <sup>55</sup>	MSC <sup>55</sup>	Migration to concave valleys, avoidance of convex hills <sup>55</sup>
			$\lambda = 30-300, A = 1-30$ <sup>55</sup>			
			$\lambda = 30-300, A = 1-30$ <sup>55</sup>			
			$\lambda = 30-300, A = 1-30$ <sup>55</sup>			
			$\lambda = 30-300, A = 1-30$ <sup>55</sup>			

## Bibliography

- [1] B. D. Wilts, P. L. Clode, N. H. Patel, and G. E. Schröder-Turk. Nature's functional nanomaterials: Growth or self-assembly? *MRS Bulletin*, 44(2):106–112, 2019.
- [2] J. R. Weeks. *The shape of space*. CRC press, Boca Raton, FL, USA, 2001.
- [3] D. W. Thompson. *On Growth and Form*. Canto. Cambridge University Press, Cambridge, 1992.
- [4] T. Iskratsch, H. Wolfenson, and M. P. Sheetz. Appreciating force and shape—the rise of mechanotransduction in cell biology. *Nature Reviews Molecular Cell Biology*, 15(12):825, 2014.
- [5] D. E. Discher, P. Janmey, and Y.-I. Wang. Tissue cells feel and respond to the stiffness of their substrate. *Science*, 310(5751):1139–1143, 2005.
- [6] A. J. Engler, S. Sen, H. L. Sweeney, and D. E. Discher. Matrix elasticity directs stem cell lineage specification. *Cell*, 126(4):677–689, 2006.
- [7] O. Chaudhuri, L. Gu, D. Klumpers, M. Darnell, S. A. Bencherif, J. C. Weaver, N. Huebsch, H.-p. Lee, E. Lippens, and G. N. Duda. Hydrogels with tunable stress relaxation regulate stem cell fate and activity. *Nature materials*, 15(3):326, 2016.
- [8] X. Trepats, L. Deng, S. S. An, D. Navajas, D. J. Tschumperlin, W. T. Gerthoffer, J. P. Butler, and J. J. Fredberg. Universal physical responses to stretch in the living cell. *Nature*, 447(7144):592, 2007.
- [9] A. Livne, E. Bouchbinder, and B. Geiger. Cell reorientation under cyclic stretching. *Nature communications*, 5:3938, 2014.
- [10] V. Vogel and M. Sheetz. Local force and geometry sensing regulate cell functions. *Nature reviews Molecular cell biology*, 7(4):265, 2006.
- [11] J. Eyckmans, T. Boudou, X. Yu, and C. S. Chen. A hitchhiker's guide to mechanobiology. *Developmental cell*, 21(1):35–47, 2011.
- [12] K. A. Jansen, D. M. Donato, H. E. Balcioglu, T. Schmidt, E. H. Danen, and G. H. Koenderink. A guide to mechanobiology: where biology and physics meet. *Biochimica et Biophysica Acta (BBA)-Molecular Cell Research*, 1853(11):3043–3052, 2015.
- [13] N. Wang, J. D. Tytell, and D. E. Ingber. Mechanotransduction at a distance: mechanically coupling the extracellular matrix with the nucleus. *Nature reviews Molecular cell biology*, 10(1):75, 2009.
- [14] Y. Li, Y. Xiao, and C. Liu. The horizon of materiobiology: a perspective on material-guided cell behaviors and tissue engineering. *Chemical reviews*, 117(5):4376–4421, 2017.
- [15] M. J. Dalby, N. Gadegaard, and R. O. Oreffo. Harnessing nanotopography and integrin–matrix interactions to influence stem cell fate. *Nature materials*, 13(6):558, 2014.
- [16] L. E. McNamara, R. J. McMurray, M. J. Biggs, F. Kantawong, R. O. Oreffo, and M. J. Dalby. Nanotopographical control of stem cell differentiation. *J Tissue Eng*, 2010:120623, 2010.
- [17] S. Dobbenga, L. E. Fratila-Apachitei, and A. A. Zadpoor. Nanopattern-induced osteogenic differentiation of stem cells - a systematic review. *Acta Biomater*, 46:3–14, 2016.
- [18] K. Modaresifar, S. Azizian, M. Ganjian, L. E. Fratila-Apachitei, and A. A. Zadpoor. Bactericidal effects of nanopatterns: A systematic review. *Acta biomaterialia*, 2018.
- [19] P. Kollmannsberger, C. M. Bidan, J. W. C. Dunlop, and P. Fratzl. The physics of tissue patterning and extracellular matrix organisation: how cells join forces. *Soft Matter*, 7(20), 2011.
- [20] S. Hyde, Z. Blum, T. Landh, S. Lidin, B. Ninham, S. Andersson, and K. Larsson. *The Language of Shape: The Role of Curvature in Condensed Matter: Physics, Chemistry and Biology*. Elsevier Science, Amsterdam, The Netherlands, 1996.
- [21] D. Hilbert and S. Cohn-Vossen. *Geometry and The Imagination*. Chelsea Publishing Company, New York, USA, 1990.
- [22] S. J. P. Callens and A. A. Zadpoor. From flat sheets to curved geometries: Origami and kirigami approaches. *Materials Today*, 21(3):241–264, 2018.
- [23] C. M. Nelson, M. M. VanDuijn, J. L. Inman, D. A. Fletcher, and M. J. Bissell. Tissue geometry determines sites of mammary branching morphogenesis in organotypic cultures. *Science*, 314(5797):298–300, 2006.
- [24] H. A. Messal, S. Alt, R. M. Ferreira, C. Gribben, V. M.-Y. Wang, C. G. Cotoi, G. Salbreux, and A. Behrens. Tissue curvature and apicobasal mechanical tension imbalance instruct cancer morphogenesis. *Nature*, 566(7742):126, 2019.

- [25] J. Zimmerberg and M. M. Kozlov. How proteins produce cellular membrane curvature. *Nature reviews Molecular cell biology*, 7(1):9, 2006.
- [26] R. Parthasarathy and J. T. Groves. Curvature and spatial organization in biological membranes. *Soft Matter*, 3(1):24–33, 2006.
- [27] M. E. Evans and G. E. Schröder-Turk. In a material world hyperbolic geometry in biological materials. *Asia Pacific Mathematics Newsletter*, 5(2):21–30, 2015.
- [28] Z. A. Almsherqi, T. Landh, S. D. Kohlwein, and Y. Deng. Cubic membranes: the missing dimension of cell membrane organization. *International Review of Cell and Molecular Biology*, 274:275–342, 2009.
- [29] Y. Deng and M. Mieczkowski. Three-dimensional periodic cubic membrane structure in the mitochondria of amoeba *chaos carolinensis*. *Protoplasma*, 203(1-2):16–25, 1998.
- [30] N. D. Bade, T. Xu, R. D. Kamien, R. K. Assoian, and K. J. Stebe. Gaussian curvature directs stress fiber orientation and cell migration. *Biophys J*, 114(6):1467–1476, 2018.
- [31] C. M. Nelson. On buckling morphogenesis. *Journal of biomechanical engineering*, 138(2):021005, 2016.
- [32] D. P. Richman, R. M. Stewart, J. W. Hutchinson, and V. S. Caviness. Mechanical model of brain convolutional development. *Science*, 189(4196):18–21, 1975.
- [33] A. E. Shter, T. Tallinen, N. L. Nerurkar, Z. Wei, E. S. Gil, D. L. Kaplan, C. J. Tabin, and L. Mahadevan. Villification: how the gut gets its villi. *Science*, 342(6155):212–218, 2013.
- [34] H. Y. Kim, M.-F. Pang, V. D. Varner, L. Kojima, E. Miller, D. C. Radisky, and C. M. Nelson. Localized smooth muscle differentiation is essential for epithelial bifurcation during branching morphogenesis of the mammalian lung. *Developmental cell*, 34(6):719–726, 2015.
- [35] H. Takigawa-Imamura, R. Morita, T. Iwaki, T. Tsuji, and K. Yoshikawa. Tooth germ invagination from cell–cell interaction: Working hypothesis on mechanical instability. *Journal of theoretical biology*, 382:284–291, 2015.
- [36] S. P. Timoshenko and S. Woinowsky-Krieger. *Theory of plates and shells*. McGraw-hill, 1959.
- [37] C. M. Nelson, R. P. Jean, J. L. Tan, W. F. Liu, N. J. Sniadecki, A. A. Spector, and C. S. Chen. Emergent patterns of growth controlled by multicellular form and mechanics. *Proceedings of the National Academy of Sciences*, 102(33):11594–11599, 2005.
- [38] D. E. Ingber. Mechanical control of tissue growth: function follows form. *Proceedings of the National Academy of Sciences*, 102(33):11571–11572, 2005.
- [39] N. Stollman and J. B. Raskin. Diverticular disease of the colon. *The Lancet*, 363(9409):631–639, 2004.
- [40] P. D. Wilson. Polycystic kidney disease. *New England Journal of Medicine*, 350(2):151–164, 2004.
- [41] J. Lee, A. A. Abdeen, K. L. Wycislo, T. M. Fan, and K. A. Kilian. Interfacial geometry dictates cancer cell tumorigenicity. *Nature materials*, 15(8):856, 2016.
- [42] H. Jinnai, H. Watashiba, T. Kajihara, Y. Nishikawa, M. Takahashi, and M. Ito. Surface curvatures of trabecular bone microarchitecture. *Bone*, 30(1):191–194, 2002.
- [43] H. Jinnai, Y. Nishikawa, M. Ito, S. D. Smith, D. A. Agard, and R. J. Spontak. Topological similarity of sponge-like bicontinuous morphologies differing in length scale. *Advanced Materials*, 14(22):1615–1618, 2002.
- [44] E. Spiegel and L. Howard. *Lytechinus pictus*, embryonic cell, CIL:39782, 2012. CIL Dataset.
- [45] O. Bashir. Renal artery, in r. 17109 (ed.). <https://radiopaedia.org/cases/renal-angiogram-arterial-anatomy?lang=us>.
- [46] A. Puerta. Colonic diverticulosis: Double contrast barium enema, in: r. 59378 (ed.). <https://radiopaedia.org/cases/colonic-diverticulosis-3?lang=us>.
- [47] T. L. Downing, J. Soto, C. Morez, T. Houssin, A. Fritz, F. Yuan, J. Chu, S. Patel, D. V. Schaffer, and S. Li. Biophysical regulation of epigenetic state and cell reprogramming. *Nature materials*, 12(12):1154, 2013.
- [48] A. Mathur, S. W. Moore, M. P. Sheetz, and J. Hone. The role of feature curvature in contact guidance. *Acta biomaterialia*, 8(7):2595–2601, 2012.
- [49] M. Simunovic, G. A. Voth, A. Callan-Jones, and P. Bassereau. When physics takes over: Bar proteins

- and membrane curvature. *Trends in cell biology*, 25(12):780–792, 2015.
- [50] C. Mim and V. M. Unger. Membrane curvature and its generation by bar proteins. *Trends in biochemical sciences*, 37(12):526–533, 2012.
- [51] B. J. Peter, H. M. Kent, I. G. Mills, Y. Vallis, P. J. G. Butler, P. R. Evans, and H. T. McMahon. Bar domains as sensors of membrane curvature: the amphiphysin bar structure. *Science*, 303(5657):495–499, 2004.
- [52] A. J. Patel, M. Lazdunski, and E. Honoré. Lipid and mechano-gated 2p domain k<sup>+</sup> channels. *Current opinion in cell biology*, 13(4):422–428, 2001.
- [53] W. Zhao, L. Hanson, H.-Y. Lou, M. Akamatsu, P. D. Chowdary, F. Santoro, J. R. Marks, A. Grassart, D. G. Drubin, and Y. Cui. Nanoscale manipulation of membrane curvature for probing endocytosis in live cells. *Nature nanotechnology*, 12(8):750, 2017.
- [54] H. T. McMahon and J. L. Gallop. Membrane curvature and mechanisms of dynamic cell membrane remodelling. *Nature*, 438(7068):590, 2005.
- [55] L. Pieuchot, J. Marteau, A. Guignandon, T. Dos Santos, I. Brigaud, P.-F. Chauvy, T. Cloatre, A. Ponche, T. Petithory, P. Rougerie, M. Vassaux, J.-L. Milan, N. T. Wakhloo, A. Spangenberg, M. Bigerelle, and K. Anselme. Curvotaxis directs cell migration through cell-scale curvature landscapes. *Nature communications*, 9(1):3995, 2018.
- [56] P. Weiss. Experiments on cell and axon orientation in vitro: the role of colloidal exudates in tissue organization. *Journal of Experimental Zoology*, 100(3):353–386, 1945.
- [57] G. Dunn and J. Heath. A new hypothesis of contact guidance in tissue cells. *Experimental cell research*, 101(1):1–14, 1976.
- [58] U. S. Schwarz and I. B. Bischofs. Physical determinants of cell organization in soft media. *Medical engineering & physics*, 27(9):763–772, 2005.
- [59] D. Baptista, L. Teixeira, C. van Blitterswijk, S. Giselbrecht, and R. Truckenmüller. Overlooked? underestimated? effects of substrate curvature on cell behavior. *Trends in biotechnology*, 2019.
- [60] N. D. Bade, R. D. Kamien, R. K. Assoian, and K. J. Stebe. Curvature and rho activation differentially control the alignment of cells and stress fibers. *Science advances*, 3(9):e1700150, 2017.
- [61] T. M. Svitkina, Y. A. Rovensky, A. D. Bershadsky, and J. M. Vasiliev. Transverse pattern of microfilament bundles induced in epitheliocytes by cylindrical substrata. *Journal of Cell Science*, 108(2):735–745, 1995.
- [62] Y. Rovensky and V. Samoilov. Morphogenetic response of cultured normal and transformed fibroblasts, and epitheliocytes, to a cylindrical substratum surface. possible role for the actin filament bundle pattern. *Journal of cell science*, 107(5):1255–1263, 1994.
- [63] E. M. Levina, L. V. Domnina, Y. A. Rovensky, and J. M. Vasiliev. Cylindrical substratum induces different patterns of actin microfilament bundles in nontransformed and in ras-transformed epitheliocytes. *Experimental cell research*, 229(1):159–165, 1996.
- [64] M. Werner, N. A. Kurniawan, G. Korus, C. V. Bouten, and A. Petersen. Mesoscale substrate curvature overrules nanoscale contact guidance to direct bone marrow stromal cell migration. *Journal of The Royal Society Interface*, 15(145):20180162, 2018.
- [65] A. K. Yip, P. Huang, and K. H. Chiam. Cell-cell adhesion and cortical actin bending govern cell elongation on negatively curved substrates. *Biophys J*, 114(7):1707–1717, 2018.
- [66] M. Werner, A. Petersen, N. A. Kurniawan, and C. V. Bouten. Cell-perceived substrate curvature dynamically coordinates the direction, speed, and persistence of stromal cell migration. *Advanced Biosystems*, page 1900080, 2019.
- [67] M. Pilia, T. Guda, S. M. Shiels, and M. R. Appleford. Influence of substrate curvature on osteoblast orientation and extracellular matrix deposition. *Journal of biological engineering*, 7(1):23, 2013.
- [68] V. Hosseini, P. Kollmannsberger, S. Ahadian, S. Ostrovidov, H. Kaji, V. Vogel, and A. Khademhosseini. Fiber-assisted molding (fam) of surfaces with tunable curvature to guide cell alignment and complex tissue architecture. *Small*, 10(23):4851–4857, 2014.
- [69] K. H. Song, S. J. Park, D. S. Kim, and J. Doh. Sinusoidal wavy surfaces for curvature-guided migration of t lymphocytes. *Biomaterials*, 51:151–160, 2015.
- [70] S. J. Lee and S. Yang. Substrate curvature restricts spreading and induces differentiation of human

- mesenchymal stem cells. *Biotechnology journal*, 12(9):1700360, 2017.
- [71] V. Malheiro, F. Lehner, V. Dinca, P. Hoffmann, and K. Maniura-Weber. Convex and concave microstructured silicone controls the shape, but not the polarization state of human macrophages. *Bio-materials science*, 4(11):1562–1573, 2016.
- [72] M. Werner, S. B. Blanquer, S. P. Haimi, G. Korus, J. W. Dunlop, G. N. Duda, D. W. Grijpma, and A. Petersen. Surface curvature differentially regulates stem cell migration and differentiation via altered attachment morphology and nuclear deformation. *Adv Sci*, 4(2):1600347, 2017.
- [73] J. Y. Park, D. H. Lee, E. J. Lee, and S.-H. Lee. Study of cellular behaviors on concave and convex microstructures fabricated from elastic pdms membranes. *Lab on a Chip*, 9(14):2043–2049, 2009.
- [74] S. Van Helvert, C. Storm, and P. Friedl. Mechanoreciprocity in cell migration. *Nature cell biology*, 20(1):8, 2018.
- [75] A. J. Ridley, M. A. Schwartz, K. Burridge, R. A. Firtel, M. H. Ginsberg, G. Borisy, J. T. Parsons, and A. R. Horwitz. Cell migration: integrating signals from front to back. *Science*, 302(5651):1704–1709, 2003.
- [76] R. Mayor and S. Etienne-Manneville. The front and rear of collective cell migration. *Nature reviews Molecular cell biology*, 17(2):97, 2016.
- [77] S. Etienne-Manneville and A. Hall. Rho gtpases in cell biology. *Nature*, 420(6916):629, 2002.
- [78] M. D. Welch and R. D. Mullins. Cellular control of actin nucleation. *Annual review of cell and developmental biology*, 18(1):247–288, 2002.
- [79] D. A. Lauffenburger and A. F. Horwitz. Cell migration: a physically integrated molecular process. *Cell*, 84(3):359–369, 1996.
- [80] S. J. Lee and S. Yang. Micro glass ball embedded gels to study cell mechanobiological responses to substrate curvatures. *Review of Scientific Instruments*, 83(9):094302, 2012.
- [81] C. Hwang, Y. Park, J. Park, K. Lee, K. Sun, A. Khademhosseini, and S. H. Lee. Controlled cellular orientation on plga microfibers with defined diameters. *Biomedical microdevices*, 11(4):739–746, 2009.
- [82] J. R. Soiné, N. Hersch, G. Dreissen, N. Hampe, B. Hoffmann, R. Merkel, and U. S. Schwarz. Measuring cellular traction forces on non-planar substrates. *Interface focus*, 6(5):20160024, 2016.
- [83] H. G. Yevick, G. Duclos, I. Bonnet, and P. Silberzan. Architecture and migration of an epithelium on a cylindrical wire. *Proceedings of the National Academy of Sciences*, 112(19):5944–5949, 2015.
- [84] R. M. Gouveia, E. Koudouna, J. Jester, F. Figueiredo, and C. J. Connon. Template curvature influences cell alignment to create improved human corneal tissue equivalents. *Advanced Biosystems*, 2017.
- [85] M. Murrell, P. W. Oakes, M. Lenz, and M. L. Gardel. Forcing cells into shape: the mechanics of actomyosin contractility. *Nature reviews Molecular cell biology*, 16(8):486, 2015.
- [86] A. K. Harris, P. Wild, and D. Stopak. Silicone rubber substrata: a new wrinkle in the study of cell locomotion. *Science*, 208(4440):177–179, 1980.
- [87] K. Kuribayashi-Shigetomi, H. Onoe, and S. Takeuchi. Cell origami: self-folding of three-dimensional cell-laden microstructures driven by cell traction force. *PLoS One*, 7(12):e51085, 2012.
- [88] N. Q. Balaban, U. S. Schwarz, D. Riveline, P. Gochberg, G. Tzur, I. Sabanay, D. Mahalu, S. Safran, A. Bershadsky, and L. Addadi. Force and focal adhesion assembly: a close relationship studied using elastic micropatterned substrates. *Nature cell biology*, 3(5):466, 2001.
- [89] S. Tadokoro, S. J. Shattil, K. Eto, V. Tai, R. C. Liddington, J. M. de Pereda, M. H. Ginsberg, and D. A. Calderwood. Talin binding to integrin  $\beta$  tails: a final common step in integrin activation. *Science*, 302(5642):103–106, 2003.
- [90] J. D. Humphries, P. Wang, C. Streuli, B. Geiger, M. J. Humphries, and C. Ballestrem. Vinculin controls focal adhesion formation by direct interactions with talin and actin. *The Journal of cell biology*, 179(5):1043–1057, 2007.
- [91] K. A. DeMali, X. Sun, and G. A. Bui. Force transmission at cell–cell and cell–matrix adhesions. *Biochemistry*, 53(49):7706–7717, 2014.
- [92] M. Vicente-Manzanares, X. Ma, R. S. Adelstein, and A. R. Horwitz. Non-muscle myosin ii takes centre stage in cell adhesion and migration. *Nature reviews Molecular cell biology*, 10(11):778, 2009.

- [93] C. S. Rex, C. F. Gavin, M. D. Rubio, E. A. Kramar, L. Y. Chen, Y. Jia, R. L. Haganir, N. Muzyczka, C. M. Gall, and C. A. Miller. Myosin iib regulates actin dynamics during synaptic plasticity and memory formation. *Neuron*, 67(4):603–617, 2010.
- [94] S. Tojkander, G. Gateva, and P. Lappalainen. Actin stress fibers—assembly, dynamics and biological roles. *J Cell Sci*, 125(8):1855–1864, 2012.
- [95] Y. Biton and S. Safran. The cellular response to curvature-induced stress. *Physical biology*, 6(4):046010, 2009.
- [96] H. Jinnai, T. Kajihara, H. Watashiba, Y. Nishikawa, and R. J. Spontak. Interfacial and topological measurements of bicontinuous polymer morphologies. *Phys Rev E Stat Nonlin Soft Matter Phys*, 64(1 Pt 1):010803, 2001.
- [97] Y.-P. Lo, Y.-S. Liu, M. G. Rimando, J. H.-C. Ho, K.-h. Lin, and O. K. Lee. Three-dimensional spherical spatial boundary conditions differentially regulate osteogenic differentiation of mesenchymal stromal cells. *Scientific reports*, 6:21253, 2016.
- [98] M. Théry, A. Pépin, E. Dressaire, Y. Chen, and M. Bornens. Cell distribution of stress fibres in response to the geometry of the adhesive environment. *Cell motility and the cytoskeleton*, 63(6):341–355, 2006.
- [99] A. Pathak, V. S. Deshpande, R. M. McMeeking, and A. G. Evans. The simulation of stress fibre and focal adhesion development in cells on patterned substrates. *Journal of The Royal Society Interface*, 5(22):507–524, 2007.
- [100] A. J. Ridley and A. Hall. The small gtp-binding protein rho regulates the assembly of focal adhesions and actin stress fibers in response to growth factors. *Cell*, 70(3):389–399, 1992.
- [101] K. N. Dahl and A. Kalinowski. Nucleoskeleton mechanics at a glance. *J Cell Sci*, 124(5):675–678, 2011.
- [102] D. N. Simon and K. L. Wilson. The nucleoskeleton as a genome-associated dynamic ‘network of networks’. *Nature reviews Molecular cell biology*, 12(11):695, 2011.
- [103] F. Guilak, J. R. Tedrow, and R. Burgkart. Viscoelastic properties of the cell nucleus. *Biochemical and biophysical research communications*, 269(3):781–786, 2000.
- [104] J. Lammerding. Mechanics of the nucleus. *Comprehensive Physiology*, 1(2):783–807, 2011.
- [105] C. H. Thomas, J. H. Collier, C. S. Sfeir, and K. E. Healy. Engineering gene expression and protein synthesis by modulation of nuclear shape. *Proceedings of the National Academy of Sciences*, 99(4):1972–1977, 2002.
- [106] K. N. Dahl, A. J. Ribeiro, and J. Lammerding. Nuclear shape, mechanics, and mechanotransduction. *Circulation research*, 102(11):1307–1318, 2008.
- [107] M. Crisp, Q. Liu, K. Roux, J. Rattner, C. Shanahan, B. Burke, P. D. Stahl, and D. Hodzic. Coupling of the nucleus and cytoplasm: role of the linc complex. *J Cell Biol*, 172(1):41–53, 2006.
- [108] K. Anselme, N. T. Wakhloo, P. Rougerie, and L. Pieuchot. Role of the nucleus as a sensor of cell environment topography. *Advanced healthcare materials*, 7(8):1701154, 2018.
- [109] S. Cho, J. Irianto, and D. E. Discher. Mechanosensing by the nucleus: From pathways to scaling relationships. *J Cell Biol*, 216(2):305–315, 2017.
- [110] S. E. Szczeny and R. L. Mauck. The nuclear option: evidence implicating the cell nucleus in mechanotransduction. *Journal of biomechanical engineering*, 139(2):021006, 2017.
- [111] S. B. Khatau, C. M. Hale, P. Stewart-Hutchinson, M. S. Patel, C. L. Stewart, P. C. Searson, D. Hodzic, and D. Wirtz. A perinuclear actin cap regulates nuclear shape. *Proceedings of the National Academy of Sciences*, 106(45):19017–19022, 2009.
- [112] J. Lammerding, L. G. Fong, J. Y. Ji, K. Reue, C. L. Stewart, S. G. Young, and R. T. Lee. Lamins a and c but not lamin b1 regulate nuclear mechanics. *Journal of Biological Chemistry*, 281(35):25768–25780, 2006.
- [113] R. McBeath, D. M. Pirone, C. M. Nelson, K. Bhadriraju, and C. S. Chen. Cell shape, cytoskeletal tension, and rhoa regulate stem cell lineage commitment. *Developmental cell*, 6(4):483–495, 2004.
- [114] J. Foolen, T. Yamashita, and P. Kollmannsberger. Shaping tissues by balancing active forces and geometric constraints. *Journal of Physics D: Applied Physics*, 49(5), 2016.
- [115] A. Katsumi, A. W. Orr, E. Tzima, and M. A. Schwartz. Integrins in mechanotransduction. *Journal*

- of Biological Chemistry*, 279(13):12001–12004, 2004.
- [116] D. E. Leckband and J. De Rooij. Cadherin adhesion and mechanotransduction. *Annual review of cell and developmental biology*, 30:291–315, 2014.
- [117] A. R. Harris, L. Peter, J. Bellis, B. Baum, A. J. Kabla, and G. T. Charras. Characterizing the mechanics of cultured cell monolayers. *Proceedings of the National Academy of Sciences*, 109(41):16449–16454, 2012.
- [118] W. Xi, T. B. Saw, D. Delacour, C. T. Lim, and B. Ladoux. Material approaches to active tissue mechanics. *Nature Reviews Materials*, page 1, 2018.
- [119] B. Lubarsky and M. A. Krasnow. Tube morphogenesis: making and shaping biological tubes. *Cell*, 112(1):19–28, 2003.
- [120] M. Ye, H. M. Sanchez, M. Hultz, Z. Yang, M. Bogorad, A. D. Wong, and P. C. Searson. Brain microvascular endothelial cells resist elongation due to curvature and shear stress. *Scientific reports*, 4:4681, 2014.
- [121] S.-M. Yu, J. M. Oh, J. Lee, W. Lee-Kwon, W. Jung, F. Amblard, S. Granick, and Y.-K. Cho. Substrate curvature affects the shape, orientation, and polarization of renal epithelial cells. *Acta biomaterialia*, 77:311–321, 2018.
- [122] W. Xi, S. Sonam, T. B. Saw, B. Ladoux, and C. T. Lim. Emergent patterns of collective cell migration under tubular confinement. *Nature communications*, 8(1):1517, 2017.
- [123] M. Poujade, E. Grasland-Mongrain, A. Hertzog, J. Jouanneau, P. Chavrier, B. Ladoux, A. Buguin, and P. Silberzan. Collective migration of an epithelial monolayer in response to a model wound. *Proceedings of the National Academy of Sciences*, 104(41):15988–15993, 2007.
- [124] B. Ladoux and R.-M. Mège. Mechanobiology of collective cell behaviours. *Nature Reviews Molecular Cell Biology*, 18(12):743, 2017.
- [125] J. P. Thiery, H. Acloque, R. Y. Huang, and M. A. Nieto. Epithelial-mesenchymal transitions in development and disease. *Cell*, 139(5):871–90, 2009.
- [126] T. Yamashita, P. Kollmannsberger, K. Mawatari, T. Kitamori, and V. Vogel. Cell sheet mechanics: How geometrical constraints induce the detachment of cell sheets from concave surfaces. *Acta biomaterialia*, 45:85–97, 2016.
- [127] F. A. Maechler, C. Allier, A. Roux, and C. Tomba. Curvature dependent constraints drive remodeling of epithelia. *Journal of Cell Science*, page jcs.222372, 2018.
- [128] G. Miquelard-Garnier, J. A. Zimmerlin, C. B. Sikora, P. Wadsworth, and A. Crosby. Polymer microlenses for quantifying cell sheet mechanics. *Soft matter*, 6(2):398–403, 2010.
- [129] P. Gómez-Gálvez, P. Vicente-Munuera, A. Tagua, C. Forja, A. M. Castro, M. Letrán, A. Valencia-Expósito, C. Grima, M. Bermúdez-Gallardo, and s. Serrano-Pérez-Higueras. Scutoids are a geometrical solution to three-dimensional packing of epithelia. *Nature communications*, 9(1):2960, 2018.
- [130] C. M. Nelson. Epithelial packing: Even the best of friends must part. *Current Biology*, 28(20):R1197–R1200, 2018.
- [131] E. Hannezo, J. Prost, and J.-F. Joanny. Theory of epithelial sheet morphology in three dimensions. *Proceedings of the National Academy of Sciences*, 111(1):27–32, 2014.
- [132] J. K. Mouw, G. Ou, and V. M. Weaver. Extracellular matrix assembly: a multiscale deconstruction. *Nature reviews Molecular cell biology*, 15(12):771, 2014.
- [133] S. Ehrig, B. Schamberg, C. Bidan, A. West, C. Jacobi, K. Lam, P. Kollmannsberger, A. Petersen, P. Tomancak, and K. Kommareddy. Surface tension determines tissue shape and growth kinetics. *Science Advances*, 5(9):eaav9394, 2019.
- [134] M. Rumpler, A. Woesz, J. W. Dunlop, J. T. van Dongen, and P. Fratzl. The effect of geometry on three-dimensional tissue growth. *J R Soc Interface*, 5(27):1173–80, 2008.
- [135] C. M. Bidan, K. P. Kommareddy, M. Rumpler, P. Kollmannsberger, P. Fratzl, and J. W. Dunlop. Geometry as a factor for tissue growth: towards shape optimization of tissue engineering scaffolds. *Advanced Healthcare Materials*, 2(1):186–94, 2013.
- [136] M. Paris, A. Gotz, I. Hettrich, C. M. Bidan, J. W. C. Dunlop, H. Razi, I. Zizak, D. W. Hutmacher, P. Fratzl, G. N. Duda, W. Wagermaier, and A. Cipitria. Scaffold curvature-mediated novel biominer-

- alization process originates a continuous soft tissue-to-bone interface. *Acta Biomaterialia*, 60:64–80, 2017.
- [137] J. Knychala, N. Bouropoulos, C. Catt, O. Katsamenis, C. Please, and B. Sengers. Pore geometry regulates early stage human bone marrow cell tissue formation and organisation. *Annals of biomedical engineering*, 41(5):917–930, 2013.
- [138] C. M. Bidan, K. P. Kommareddy, M. Rumpler, P. Kollmannsberger, Y. J. Brechet, P. Fratzl, and J. W. Dunlop. How linear tension converts to curvature: geometric control of bone tissue growth. *PLoS One*, 7(5):e36336, 2012.
- [139] K. P. Kommareddy, C. Lange, M. Rumpler, J. W. Dunlop, I. Manjubala, J. Cui, K. Kratz, A. Lendlein, and P. Fratzl. Two stages in three-dimensional in vitro growth of tissue generated by osteoblastlike cells. *Biointerphases*, 5(2):45–52, 2010.
- [140] J. R. Vetsch, R. Muller, and S. Hofmann. The influence of curvature on three-dimensional mineralized matrix formation under static and perfused conditions: an in vitro bioreactor model. *J R Soc Interface*, 13(123), 2016.
- [141] E. Tamjid, A. Simchi, J. W. Dunlop, P. Fratzl, R. Bagheri, and M. Vossoughi. Tissue growth into three-dimensional composite scaffolds with controlled micro-features and nanotopographical surfaces. *Journal of Biomedical Materials Research Part A*, 101(10):2796–2807, 2013.
- [142] C. M. Bidan, P. Kollmannsberger, V. Gering, S. Ehrig, P. Joly, A. Petersen, V. Vogel, P. Fratzl, and J. W. Dunlop. Gradual conversion of cellular stress patterns into pre-stressed matrix architecture during in vitro tissue growth. *Journal of The Royal Society Interface*, 13(118):20160136, 2016.
- [143] E. Gamsjager, C. M. Bidan, F. D. Fischer, P. Fratzl, and J. W. Dunlop. Modelling the role of surface stress on the kinetics of tissue growth in confined geometries. *Acta Biomater*, 9(3):5531–43, 2013.
- [144] T. Hayashi and R. W. Carthew. Surface mechanics mediate pattern formation in the developing retina. *Nature*, 431(7009):647, 2004.
- [145] M. L. Manning, R. A. Foty, M. S. Steinberg, and E.-M. Schoetz. Coaction of intercellular adhesion and cortical tension specifies tissue surface tension. *Proceedings of the National Academy of Sciences*, 107(28):12517–12522, 2010.
- [146] T. Lecuit and P.-F. Lenne. Cell surface mechanics and the control of cell shape, tissue patterns and morphogenesis. *Nature reviews Molecular cell biology*, 8(8):633, 2007.
- [147] R. A. Foty, G. Forgacs, C. M. Pfleger, and M. S. Steinberg. Liquid properties of embryonic tissues: Measurement of interfacial tensions. *Physical review letters*, 72(14):2298, 1994.
- [148] J. Käfer, T. Hayashi, A. F. Marée, R. W. Carthew, and F. Graner. Cell adhesion and cortex contractility determine cell patterning in the drosophilaretina. *Proceedings of the National Academy of Sciences*, 104(47):18549–18554, 2007.
- [149] P. S. Laplace. *Traité de mécanique céleste*, volume 1. de l’Imprimerie de Crapelet, 1799.
- [150] I. B. Bischofs, F. Klein, D. Lehnert, M. Bastmeyer, and U. S. Schwarz. Filamentous network mechanics and active contractility determine cell and tissue shape. *Biophysical journal*, 95(7):3488–3496, 2008.
- [151] P. Kollmannsberger, C. M. Bidan, J. W. Dunlop, P. Fratzl, and V. Vogel. Tensile forces drive a reversible fibroblast-to-myofibroblast transition during tissue growth in engineered clefts. *Science advances*, 4(1):eaao4881, 2018.
- [152] I. B. Bischofs, S. S. Schmidt, and U. S. Schwarz. Effect of adhesion geometry and rigidity on cellular force distributions. *Physical review letters*, 103(4):048101, 2009.
- [153] T. B. Saw, W. Xi, B. Ladoux, and C. T. Lim. Biological tissues as active nematic liquid crystals. *Advanced materials*, 30(47):1802579, 2018.
- [154] A. Cipitria, C. Lange, H. Schell, W. Wagermaier, J. C. Reichert, D. W. Hutmacher, P. Fratzl, and G. N. Duda. Porous scaffold architecture guides tissue formation. *Journal of Bone and Mineral Research*, 27(6):1275–1288, 2012.
- [155] A. Scarano, V. Perrotti, L. Artese, M. Degidi, D. Degidi, A. Piattelli, and G. Iezzi. Blood vessels are concentrated within the implant surface concavities: A histologic study in rabbit tibia. *Odontology*, 102(2):259–266, 2014.
- [156] T. P. Wyatt, J. Fouchard, A. Lisica, N. Khalilgharibi, B. Baum, P. Recho, A. J. Kabla, and G. T. Char-

- ras. Actomyosin controls planarity and folding of epithelia in response to compression. *Nature materials*, pages 1–9, 2019.
- [157] V. Robins, S. J. Ramsden, and S. T. Hyde. 2D hyperbolic groups induce three-periodic euclidean reticulations. *The European Physical Journal B*, 39(3):365–375, 2004.
- [158] L. Geris, T. Lambrechts, A. Carlier, and I. Papantoniou. The future is digital: in silico tissue engineering. *Current Opinion in Biomedical Engineering*, 6:92–98, 2018.
- [159] A. A. Zadpoor. Bone tissue regeneration: the role of scaffold geometry. *Biomaterials Science*, 3(2):231–45, 2015.
- [160] D. Ambrosi, G. A. Ateshian, E. M. Arruda, S. Cowin, J. Dumais, A. Goriely, G. A. Holzapfel, J. D. Humphrey, R. Kemkemer, and E. Kuhl. Perspectives on biological growth and remodeling. *Journal of the Mechanics and Physics of Solids*, 59(4):863–883, 2011.
- [161] V. S. Deshpande, R. M. McMeeking, and A. G. Evans. A bio-chemo-mechanical model for cell contractility. *Proceedings of the National Academy of Sciences*, 103(38):14015–14020, 2006.
- [162] I. L. Novak, B. M. Slepchenko, A. Mogilner, and L. M. Loew. Cooperativity between cell contractility and adhesion. *Physical review letters*, 93(26):268109, 2004.
- [163] G. Danuser, J. Allard, and A. Mogilner. Mathematical modeling of eukaryotic cell migration: insights beyond experiments. *Annual review of cell and developmental biology*, 29:501–528, 2013.
- [164] Y. Guyot, I. Papantoniou, Y. C. Chai, S. Van Bael, J. Schrooten, and L. Geris. A computational model for cell/ECM growth on 3D surfaces using the level set method: a bone tissue engineering case study. *Biomech Model Mechanobiol*, 13(6):1361–71, 2014.
- [165] P. F. Egan, K. A. Shea, and S. J. Ferguson. Simulated tissue growth for 3D printed scaffolds. *Biomech Model Mechanobiol*, 2018.
- [166] J. A. Sanz-Herrera, P. Moreo, J. M. Garcia-Aznar, and M. Doblaré. On the effect of substrate curvature on cell mechanics. *Biomaterials*, 30(34):6674–6686, 2009.
- [167] D. E. Ingber. Tensegrity: the architectural basis of cellular mechanotransduction. *Annual review of physiology*, 59(1):575–599, 1997.
- [168] M. Vassaux and J. Milan. Stem cell mechanical behaviour modelling: substrate’s curvature influence during adhesion. *Biomechanics and modeling in mechanobiology*, 16(4):1295–1308, 2017.
- [169] M. Jean. The non-smooth contact dynamics method. *Computer methods in applied mechanics and engineering*, 177(3-4):235–257, 1999.
- [170] X. He and Y. Jiang. Substrate curvature regulates cell migration. *Physical biology*, 14(3):035006, 2017.
- [171] O. I. Frette, G. Virnovsky, and D. Silin. Estimation of the curvature of an interface from a digital 2D image. *Computational Materials Science*, 44(3):867–875, 2009.
- [172] C. Epstein and M. Gage. *The curve shortening flow*, pages 15–59. Springer, 1987.
- [173] C. M. Bidan, F. M. Wang, and J. W. Dunlop. A three-dimensional model for tissue deposition on complex surfaces. *Computer methods in biomechanics and biomedical engineering*, 16(10):1056–1070, 2013.
- [174] J. A. Sethian and P. Smereka. Level set methods for fluid interfaces. *Annual review of fluid mechanics*, 35(1):341–372, 2003.
- [175] J. A. Sethian. *Level set methods and fast marching methods: evolving interfaces in computational geometry, fluid mechanics, computer vision, and materials science*, volume 3. Cambridge university press, 1999.
- [176] K. A. Brakke. *The Motion of a Surface by Its Mean Curvature*. Princeton University Press, 2015.
- [177] S. C. Kapfer, S. T. Hyde, K. Mecke, C. H. Arns, and G. E. Schröder-Turk. Minimal surface scaffold designs for tissue engineering. *Biomaterials*, 32(29):6875–82, 2011.
- [178] S. Ehrig, C. M. Bidan, A. West, C. Jacobi, K. Lam, P. Kollmannsberger, A. Petersen, P. Tomancak, K. Kommareddy, F. D. Fischer, P. Fratzl, and J. W. C. Dunlop. Surface tension determines tissue shape and growth kinetics. *bioRxiv*, page 456228, 2018.
- [179] J. W. C. Dunlop, F. D. Fischer, E. Gamsjäger, and P. Fratzl. A theoretical model for tissue growth in confined geometries. *Journal of the Mechanics and Physics of Solids*, 58(8):1073–1087, 2010.
- [180] M. A. Alias and P. R. Buenzli. Modeling the effect of curvature on the collective behavior of cells

- growing new tissue. *Biophysical journal*, 112(1):193–204, 2017.
- [181] M. A. Alias and P. R. Buenzli. Osteoblasts infill irregular pores under curvature and porosity controls: a hypothesis-testing analysis of cell behaviours. *Biomechanics and modeling in mechanobiology*, 17(5):1357–1371, 2018.
- [182] Y. Guyot, I. Papantoniou, F. P. Luyten, and L. Geris. Coupling curvature-dependent and shear stress-stimulated neotissue growth in dynamic bioreactor cultures: a 3D computational model of a complete scaffold. *Biomech Model Mechanobiol*, 15(1):169–80, 2016.
- [183] P. Sanaei, L. Cummings, S. Waters, and I. Griffiths. Curvature-and fluid-stress-driven tissue growth in a tissue-engineering scaffold pore. *Biomechanics and modeling in mechanobiology*, pages 1–17, 2018.
- [184] A. A. Zadpoor and J. Malda. Additive manufacturing of biomaterials, tissues, and organs. *Ann Biomed Eng*, 45(1):1–11, 2017.
- [185] F. J. O’Brien. Biomaterials & scaffolds for tissue engineering. *Materials Today*, 14(3):88–95, 2011.
- [186] A. A. Zadpoor. Additively manufactured porous metallic biomaterials. *Journal of Materials Chemistry B*, 2019.
- [187] C. Soyarslan, S. Bargmann, M. Pradas, and J. Weissmüller. 3D stochastic bicontinuous microstructures: Generation, topology and elasticity. *Acta Materialia*, 149:326–340, 2018.
- [188] A. Vidyasagar, S. Krödel, and D. Kochmann. Microstructural patterns with tunable mechanical anisotropy obtained by simulating anisotropic spinodal decomposition. *Proc. R. Soc. A*, 474(2218):20180535, 2018.
- [189] F. S. L. Bobbert, K. Lietaert, A. A. Eftekhari, B. Pouran, S. M. Ahmadi, H. Weinans, and A. A. Zadpoor. Additively manufactured metallic porous biomaterials based on minimal surfaces: A unique combination of topological, mechanical, and mass transport properties. *Acta Biomater*, 53:572–584, 2017.
- [190] S. B. Blanquer, M. Werner, M. Hannula, S. Sharifi, G. P. Lajoinie, D. Eglin, J. Hyttinen, A. A. Poot, and D. W. Grijpma. Surface curvature in triply-periodic minimal surface architectures as a distinct design parameter in preparing advanced tissue engineering scaffolds. *Biofabrication*, 9(2):025001, 2017.
- [191] B. M. Willie, A. Petersen, K. Schmidt-Bleek, A. Cipitria, M. Mehta, P. Strube, J. Lienau, B. Wildemann, P. Fratzl, and G. Duda. Designing biomimetic scaffolds for bone regeneration: why aim for a copy of mature tissue properties if nature uses a different approach? *Soft Matter*, 6(20), 2010.
- [192] S. Tibbitts. 4D printing: multi-material shape change. *Architectural Design*, 84(1):116–121, 2014.
- [193] T. van Manen, S. Janbaz, and A. A. Zadpoor. Programming 2D/3D shape-shifting with hobbyist 3D printers. *Materials Horizons*, 4(6), 2017.
- [194] Y. Liu, J. K. Boyles, J. Genzer, and M. D. Dickey. Self-folding of polymer sheets using local light absorption. *Soft Matter*, 8(6):1764–1769, 2012.
- [195] S. Miao, N. Castro, M. Nowicki, L. Xia, H. Cui, X. Zhou, W. Zhu, S.-j. Lee, K. Sarkar, G. Vozzi, Y. Tabata, J. Fisher, and L. G. Zhang. 4D printing of polymeric materials for tissue and organ regeneration. *Materials Today*, 2017.
- [196] A. S. Gladman, E. A. Matsumoto, R. G. Nuzzo, L. Mahadevan, and J. A. Lewis. Biomimetic 4D printing. *Nat Mater*, 15(4):413–8, 2016.
- [197] V. A. Bolaños Quiñones, H. Zhu, A. A. Solovev, Y. Mei, and D. H. Gracias. Origami biosystems: 3D assembly methods for biomedical applications. *Advanced Biosystems*, page 1800230, 2018.
- [198] T. G. Leong, C. L. Randall, B. R. Benson, N. Bassik, G. M. Stern, and D. H. Gracias. Tetherless thermobiochemically actuated microgrippers. *Proceedings of the National Academy of Sciences of the United States of America*, 106(3):703–708, 2009.
- [199] K. Kuribayashi, K. Tsuchiya, Z. You, D. Tomus, M. Umemoto, T. Ito, and M. Sasaki. Self-deployable origami stent grafts as a biomedical application of ni-rich tini shape memory alloy foil. *Materials Science and Engineering A*, 419(1-2):131–137, 2006.
- [200] W. Hu, G. Z. Lum, M. Mastrangeli, and M. Sitti. Small-scale soft-bodied robot with multimodal locomotion. *Nature*, 554(7690):81, 2018.
- [201] S. Miao, W. Zhu, N. J. Castro, M. Nowicki, X. Zhou, H. Cui, J. P. Fisher, and L. G. Zhang. 4D printing

- smart biomedical scaffolds with novel soybean oil epoxidized acrylate. *Scientific reports*, 6:27226, 2016.
- [202] R. J. Morrison, S. J. Hollister, M. F. Niedner, M. G. Mahani, A. H. Park, D. K. Mehta, R. G. Ohye, and G. E. Green. Mitigation of tracheobronchomalacia with 3D-printed personalized medical devices in pediatric patients. *Science translational medicine*, 7(285):285ra64–285ra64, 2015.
- [203] S. Janbaz, N. Noordzij, D. S. Widyaratih, C. W. Hagen, L. E. Fratila-Apachitei, and A. A. Zadpoor. Origami lattices with free-form surface ornaments. *Science Advances*, 3(11), 2017.
- [204] S. J. Callens, N. Tümer, and A. A. Zadpoor. Hyperbolic origami-inspired folding of triply periodic minimal surface structures. *Applied Materials Today*, 15:453–461, 2019.
- [205] C. M. Bidan, M. Fratzl, A. Coullomb, P. Moreau, A. H. Lombard, I. Wang, M. Balland, T. Boudou, N. M. Dempsey, and T. Devillers. Magneto-active substrates for local mechanical stimulation of living cells. *Scientific reports*, 8(1):1464, 2018.
- [206] J. Eyckmans and C. S. Chen. Stem cell differentiation: Sticky mechanical memory. *Nature materials*, 13(6):542, 2014.
- [207] C. Yang, M. W. Tibbitt, L. Basta, and K. S. Anseth. Mechanical memory and dosing influence stem cell fate. *Nature materials*, 13(6):645, 2014.
- [208] A. J. Hughes, H. Miyazaki, M. C. Coyle, J. Zhang, M. T. Laurie, D. Chu, Z. Vavrušová, R. A. Schneider, O. D. Klein, and Z. J. Gartner. Engineered tissue folding by mechanical compaction of the mesenchyme. *Developmental cell*, 44(2):165–178. e6, 2018.
- [209] S. Kaihara, J. Borenstein, R. Koka, S. Lalan, E. R. Ochoa, M. Ravens, H. Pien, B. Cunningham, and J. P. Vacanti. Silicon micromachining to tissue engineer branched vascular channels for liver fabrication. *Tissue engineering*, 6(2):105–117, 2000.
- [210] G. Vozzi, C. Flaim, A. Ahluwalia, and S. Bhatia. Fabrication of plga scaffolds using soft lithography and microsyringe deposition. *Biomaterials*, 24(14):2533–2540, 2003.
- [211] G. M. Whitesides, E. Ostuni, S. Takayama, X. Jiang, and D. E. Ingber. Soft lithography in biology and biochemistry. *Annual review of biomedical engineering*, 3(1):335–373, 2001.
- [212] T. Weiß, G. Hildebrand, R. Schade, and K. Liefelth. Two-photon polymerization for microfabrication of three-dimensional scaffolds for tissue engineering application. *Engineering in Life Sciences*, 9(5):384–390, 2009.
- [213] A. Marino, C. Filippeschi, G. G. Genchi, V. Mattoli, B. Mazzolai, and G. Ciofani. The osteoprint: a bioinspired two-photon polymerized 3-d structure for the enhancement of bone-like cell differentiation. *Acta biomaterialia*, 10(10):4304–4313, 2014.
- [214] A. Khademhosseini, R. Langer, J. Borenstein, and J. P. Vacanti. Microscale technologies for tissue engineering and biology. *Proceedings of the National Academy of Sciences*, 103(8):2480–2487, 2006.
- [215] K. Grosse-Brauckmann. Triply periodic minimal and constant mean curvature surfaces. *Interface focus*, 2(5):582–588, 2012.



# 3

## COLLECTIVE BONE CELL ORGANIZATION IN COMPLEX CURVATURE FIELDS

Individual cells and multicellular systems have been shown to respond to cell-scale curvatures in their environments, guiding migration, orientation, and tissue formation. However, it remains unclear how cells collectively explore and pattern complex landscapes with curvature gradients across the Euclidean and non-Euclidean spectra, partly owing to fabrication limitations and the lack of formal geometric considerations. Here, we show that micro-engineered substrates with controlled curvature variations induce the collective spatiotemporal organization of preosteoblasts. By leveraging mathematical surface design and a high-resolution free-form fabrication process, we exposed cells to a broad yet controlled, heterogeneous spectrum of curvature fields. We quantified curvature-induced spatial patterning at different time points and found that cells generally prefer regions with at least one negative principal curvature. We also show that multicellular cooperation enables cells to venture into unfavourably-curved territories, bridging large portions of the substrates, and collectively aligning their stress fibres. We demonstrate that this behaviour is partly regulated by cellular contractility and extracellular matrix development, underscoring the mechanical nature of curvature guidance. Our findings offer unifying perspectives on cell-geometry interactions that could be harnessed in the design of micro-engineered biomaterials, for example, for tissue engineering applications.

S. J. P. Callens, D. Fan, I. J. van Hengel, M. Minneboo, L. E. Fratila-Apachitei, A. A. Zadpoor, Emergent collective organization of bone cells in complex curvature fields, *bioRxiv*, 2020. (in revision)

### 3.1 Introduction

The dynamic, bidirectional interactions between cells and their intricate environment orchestrate tissue morphogenesis, homeostasis, and repair, and are implicated in numerous diseases<sup>1-3</sup>. The complexity of the extracellular environment is not only due to its diverse and heterogeneous composition but is also caused by its hierarchical spatial structure that imposes geometrical constraints on the force-generating cells<sup>4:5</sup>. Cells have long been known to sense such geometrical cues at subcellular scales<sup>6:7</sup>, yet recent evidence shows that geometrical features at much larger scales also affect cell migration, differentiation, and fate, as well as tissue shape and growth kinetics<sup>8</sup>. Unravelling this interplay between cells and the shape of their surroundings is key to advance the design of artificial scaffolds and biomaterials, where geometry can be harnessed as a micro-engineered cell cue<sup>9-11</sup>.

From a mathematical viewpoint, the local geometry of the extracellular environment can be fundamentally characterized using the concept of surface curvature<sup>12</sup>. In recent years, numerous studies have begun to address the role of cell-scale curvature on the dynamics and organisation of cells and tissues. Indeed, curvature guidance has been observed in the directional migration and preferential orientation of a variety of individual cells and multicellular monolayers<sup>13-17</sup>. Moreover, various cell types have expressed an overall preference for local concavities as opposed to convexities<sup>18:19</sup>. Biophysical models have suggested key roles for cytoskeletal contractility and nuclear deformation in this large-scale curvature sensation, generally implying that cells with pronounced stress fibres avoid bending and search for relaxed configurations<sup>20-23</sup>. Despite the availability of such pioneering findings, it remains elusive how cells behave in more complex curvature landscapes. Early studies typically resorted to substrates with limited architectural complexity, involving cylindrical wires<sup>13;24:25</sup> or patterned hemispherical substrates<sup>26:27</sup>, precluding many physiologically-relevant geometries, including saddle shapes or sharp curvature transitions. Moreover, the mathematical descriptions of the surface curvature have not received much attention, hampering the development of a unified, unambiguous theory of cell-scale curvature guidance. Indeed, many studies have considered only a single class of curved substrates<sup>24:25</sup>, or have relied exclusively on the concepts of convexity and concavity instead of the fundamental definitions of curvature as described by differential geometry<sup>19:26</sup>.

Here, we adopt a geometry-centred perspective and demonstrate collective spatiotemporal cell organization in precise environments with varying curvature distributions. To this end, we designed several substrates, derived from mathematically-defined surface families, covering a wide range of cell-scale types of curvature variation. Using high-resolution multiphoton lithography (*i.e.*, a 3D printing technique with submicron resolution) and replica moulding, we fabricated chips on which we cultured murine preosteoblasts for several days. Our focus on bone-like cells was motivated by the ongoing quest for geometrically-optimized biomaterials that enhance bone tissue regeneration. While previous studies have either focused on individual cell behaviour at short time scales<sup>14:19</sup> or on tissue-level performance in larger-scale environments<sup>28-30</sup>, we studied

curvature guidance at the intermediate time points where cells collectively pattern their environment and establish a template for bone-like tissue formation. By mapping 3D confocal microscopy data to the underlying curvature distributions, we explored the rules for emergent collective cell patterning. Specifically, we found that the curved-to-planar transitions, often ignored in earlier studies, are highly attractive to cell collectives and that cell sheets spontaneously detach from certain curved regions, thereby altering the extracellular geometry sensed by new cells. Moreover, we studied curvature-guided stress fibre orientation and investigated the important role of contractility in collective curvature guidance. Our results provide unifying perspectives on curvature-driven collective cell organization, paving the way towards the geometric optimization of micro-engineered environments.

## 3.2 Materials and methods

### 3.2.1 Design of curved substrates

Curved substrates were designed in MATLAB (MATLAB 2018b, Mathworks, Natick, MA, USA) and SolidWorks (Dassault Systèmes, Vélizy-Villacoublay, France). In the case of axisymmetric substrates, the generatrix curves were generated in MATLAB using the parametrizations provided in Subsection 3.5.1. The curves were then imported into SolidWorks and  $\pi$ -revolutions around the central axis were generated, resulting in convex half-surfaces of revolution. Next, end-caps and a rectangular bottom layer (with 20  $\mu\text{m}$  thickness) were added to convert the surfaces to printable solids. Additionally, a sinusoidal cylinder substrate was directly designed in SolidWorks, by sweeping a hemi-circular cross-section along a sinusoidal guiding curve. The corresponding substrate designs were exported in the STL format, to prepare them for the printing process.

### 3.2.2 Fabrication and functionalization of PDMS substrates

Mould masters were fabricated using a two-photon lithography 3D printer (Nanoscribe GT2, Nanoscribe GmbH, Karlsruhe, Germany). A silicon substrate was cleaned with isopropanol (IPA, Merck KGaA, Darmstadt, Germany) and was treated with oxygen plasma (Femto, Diener electronic GmbH + Co. KG, Ebhausen, Germany) to improve its adhesion. A droplet of IP-S acrylate-based resin (Nanoscribe GmbH) was drop cast onto the substrate. Four sets of six convex master substrates were 3D printed on the silicon substrate using a 25X objective ( $NA = 0.8$ ), 0.5  $\mu\text{m}$  hatching, 0.5  $\mu\text{m}$  slicing, 50 mW nominal laser power, and 50 mm/s scanning speed. To save time, an internal support scaffold was written instead of a solid block. The structures were developed in propylene glycol methyl ether acetate (PGMEA, Merck KGaA, Darmstadt, Germany) for 25 minutes followed by 5 minutes of treatment with isopropyl alcohol (IPA) and blow drying using a filtered air gun.

To perform the moulding, the master was first placed in a vacuum desiccator beside a glass petri dish containing a droplet of trichloro(1H,1H,2H,2H-perfluorooctyl)-silane (Merck KGaA, Darmstadt, Germany), which subsequently coated the surface of the master with a hydrophobic layer allowing easy future peeling of the polydimethyl-

siloxane (PDMS) copy. PDMS (Sylgard 184, Dow Inc., Midland, MI, U.S.A.) mixed with the curing agent at a weight ratio of 10:1 was mixed thoroughly, drop-cast on the master, desiccated in vacuum for 30 minutes to remove any air bubbles, and cured in an oven at a temperature of 40 °C for 16 hours. The resulting copy was cut out by scalpel and gently peeled off the master. Typically, 7-10 PDMS copies were made with a single master without loss of fidelity. This single-step moulding process resulted in specimens with concave curved substrates (imprints in the PDMS). To obtain the convex counterparts (protrusions), a double moulding step was performed. To this end, a PDMS copy originating from the single-moulding operation was thermally aged in an oven at 100 °C for 48 hours<sup>31</sup>. This PDMS substrate was consequently used as a new mould for the second moulding stage, which was performed in the same way as before. After curing, the second PDMS could easily be peeled off the PDMS mould, without loss of fidelity. The quality of the single-step and two-step PDMS moulding processes was verified using a scanning electron microscope (SEM, JSM-IT100LA, JEOL, Tokyo, Japan) with a beam energy of 10 kV and a working distance of 12 mm. Prior to SEM imaging, the PDMS substrates were gold sputtered (layer thickness of  $5 \pm 2$  nm) to enhance conductivity. Additionally, the quality of the replica moulding procedures was confirmed through laser confocal scanning (Keyence VK-X 3D scanner, Keyence, Osaka, Japan) using a 20x magnification lens.

In preparation for cell seeding, circular specimens of 8 mm diameter were punched from the PDMS copies. Next, the specimens were sterilized inside an oven at 110 °C for 1 hour. To reduce the inherent hydrophobicity of PDMS and facilitate substrate wetting, the specimens were subsequently treated with oxygen plasma (Femto, Diener electronic GmbH + Co. KG, Ebhausen, Germany) for 3 minutes. Then, the PDMS specimens were transferred to a 48-well plate, washed twice with  $10 \times$  PBS, submerged in a solution of 50 µg/ml bovine fibronectin (Sigma-Aldrich, St. Louis, MO, USA), and incubated at 37 °C and 5%  $CO_2$  for 30 minutes to functionalize the PDMS surface and promote cell adhesion. After the removal of the fibronectin solution, the specimens were thoroughly washed with  $10 \times$  PBS.

### 3.2.3 Cell seeding and culture

Prior to cell seeding, murine preosteoblasts (MC3T3-E1, Sigma-Aldrich, St. Louis, MO, USA) were cultured for 7 days in minimum essential medium ( $\alpha$ -MEM, Sigma-Aldrich) with the addition of 10% fetal bovine serum and 1% penicillin-streptomycin (both from Thermo Fischer Scientific, Waltham, MA, USA). The medium was refreshed every 2 to 3 days. In all the experiments, approximately  $5 \times 10^3$  cells were seeded on the fibronectin-coated PDMS specimens in 250 µl culture medium, which were then cultured for up to 8 days at 37 °C and 5%  $CO_2$  with the medium being refreshed every 2 to 3 days. To induce osteogenic differentiation, the culture medium was supplemented with 4 mM  $\beta$ -glycerophosphate and 50 µg/ml ascorbic acid (both from Sigma-Aldrich), starting from day 3. In the experiments where differentiation was inhibited, the cells were cultured in the standard culture medium throughout the entire duration of the

experiments (*i.e.*, without the addition of ascorbic acid or  $\beta$ -glycerophosphate). In the experiments with enhanced cell contractility, 1 ng/ml of TGF- $\beta$ 3 (Sigma-Aldrich) was added to the culture medium on day 3 and this concentration was maintained throughout the remainder of the experiments. To inhibit cell contractility, the culture medium was supplemented with 10  $\mu$ M of blebbistatin (Sigma-Aldrich), which was also maintained throughout the remainder of the experiments.

### 3.2.4 Immunostaining

Immunostaining was performed at different time points (days 3, 5, and 8). The specimens were washed twice in  $10 \times$  PBS and fixated in 4% formaldehyde/PBS for 15 minutes at room temperature. Next, the specimens were washed with  $1 \times$  PBS and the cells were permeabilized in 0.5% Triton/PBS at 4 °C for 5 minutes, followed by incubation in 1% BSA/PBS at 37 °C for 5 minutes. To stain for F-actin, the specimens were incubated in 1% BSA/PBS with rhodamine phalloidin (1 : 1000, Thermo Fischer Scientific). Afterwards, the specimens were washed 3 times for 5 minutes with 0.5% Tween/PBS at room temperature, followed by washing for 5 minutes with  $1 \times$  PBS at room temperature. The specimens were subsequently mounted in a glass-bottom dish using a droplet of ProLong Gold antifade reagent with 4',6-diamidino-2-phenylindole (DAPI, Thermo Fischer Scientific) to stain the chromatin cargo in the nuclei. The specimens that were also stained for RUNX2 followed a similar protocol, involving a first incubation step with anti-RUNX2 primary antibody (Abcam, Cambridge, UK) followed by Tween/PBS washing and a second incubation step with Alexa Fluor 488 conjugated secondary antibody (Thermo Fischer Scientific).

### 3.2.5 Confocal imaging

Fluorescence confocal laser scanning microscopy (CLSM) was performed using a Nikon Eclipse Ti inverted confocal microscope (Nikon, Tokyo, Japan) with a Nikon Plan Apochromat  $\lambda$  10x objective (0.45 NA). The images were acquired using 2 or 3 laser lines with excitation wavelengths of 405 nm (DAPI), 488 nm (Alexa Fluor 488), and 561 nm (Rhodamine-phalloidin) with the detection windows set accordingly. Z-stacks were obtained at an xy-resolution of  $0.60 \times 0.60 \mu\text{m}$  and a z-spacing of 1  $\mu\text{m}$  (for specific cases) to 5  $\mu\text{m}$  (nominal cases). The acquisition in the different channels was performed sequentially to minimize inter-channel cross-talk.

### 3.2.6 Preparation of stack projections and curvature maps

Maximum intensity projections were obtained from the image stacks using Fiji<sup>32</sup>. A custom image registration script in MATLAB was used to select a rectangular region of interest (ROI), defined by the bottom layer of the curved substrates, and crop the image to the ROI. The resulting image was subsequently rotated to align the rectangular ROI in the vertical direction. To assess the relationship between the confocal image data and the curvature of the underlying substrate, curvature maps were created in MATLAB using the parametrizations provided in Subsection 3.5.1. The transition re-

gion between the curved substrates and the flat surroundings was assigned a radius of curvature of  $15 \mu\text{m}$  to account for the local concavity that this narrow region presents. The curvature maps were defined as pixelated images, matching the resolution of the corresponding confocal images, enabling a pixel-by-pixel comparison of the confocal data and the curvature. The principal curvatures were non-dimensionalised by multiplying with the radius of the spherical substrate (leading to  $\kappa_1 = \kappa_2 = 1$  for the convex spherical substrates).

### 3.2.7 Actin frequency maps

To create actin frequency maps, several images belonging to the same experimental group were split into periodic units and superimposed in MATLAB. First, the intensity was normalized with respect to the mean intensity of the image. All the images within the same group were then summed. Finally, the images were split into periodic units and summed again to create the final frequency map.

### 3.2.8 Intensity quantification and distance maps

The actin maximum intensity projections were normalized with respect to the mean intensity and were converted to grayscale. Using custom MATLAB scripts, every image was rasterized (downsampled) into a set of “superpixels”, where the intensity of each superpixel is the average of all the pixels it is composed of. Through this rasterized approach, the intensity variations are considered for local neighbourhoods (better corresponding to the scale of the cells), rather than at the individual pixel level. The size of the superpixels is mentioned in figure captions. Distance maps were created by binarizing the curvature maps of the minimum principal curvature ( $\kappa_2$ ). These binarized curvature maps were used to compute the Euclidean distance transform for which every pixel was assigned a value depending on its distance from the nearest point with a negative minimum principal curvature. To assign a higher weight to the regions with  $\kappa_2 > 0$  than regions with  $\kappa_2 = 0$  (corresponding to the observed relative preference of the cells for the latter as opposed to the former regions), the final distance map was defined as the average of two distance maps: a map representing the distance to points with  $\kappa_2 \leq 0$  and a map with the distance to points with  $\kappa_2 < 0$ .

### 3.2.9 Quantification of cell sheet detachment on concave spheres and cylinders

To quantify the amount of cell sheet displacement and anchor density, the actin z-stacks were first cropped to a square ROI and then resliced from the top with  $5 \mu\text{m}$  spacing in Fiji. Using custom scripts in MATLAB, the middle image of the resliced stack was selected, the detached cell sheet was traced, and the maximum displacement of the sheet with respect to the endpoints of the sheet was quantified. The anchor density was quantified by masking and binarizing the region below the detached sheet in the resliced stacks. Consequently, the density of the actin voxels in the binarized image stack was determined. 3D reconstructions of the confocal stacks were generated using

the open-source Fiji plugin 3Dscript<sup>33</sup>.

### 3.2.10 Quantification of stress fibre orientation

To determine the dominant stress fibre orientation in an ROI, a custom script based on the Fast Fourier Transform (FFT) was implemented, similar to a previously reported method<sup>34</sup>. Details of the implementation are provided in Subsection 3.5.2 and Figure 3.16. Briefly, the approach involved computing the power spectrum of the FFT applied to a grayscale ROI and detecting the orientation of the dominant band of the elevated power values in the spectrum. This orientation was then converted to the dominant orientation in the grayscale image. The orientation analysis was applied to every sub-image in the rasterized images. For all the structures, the maps of both principal directions were created (similar to the curvature maps described before). The DA between the SF and the first principal direction (pd, corresponding to  $\kappa_2$ ) was defined as:

$$DA = 1 - \frac{\angle(sf, pd)}{90} \quad (3.1)$$

where  $\angle(sf, pd) \in (0, 90)$  indicates the angular difference between the SF and the principal direction.

### 3.2.11 Statistical analysis

All statistical analyses were performed using GraphPad Prism 8 (GraphPad Software, CA, USA). For all the relevant figures, the type of the data presented, the choice of the statistical tests, and the significance levels are all indicated in the corresponding figure captions.

## 3.3 Results

### 3.3.1 Development of cell substrates with controlled curvatures

We first set out to design substrates that would expose cells to a broad, yet controlled spectrum of curvatures. A complete description of surface curvature requires two independent curvature measures. The most common choices are either the two principal curvatures (*i.e.*, the maximum and minimum curvatures,  $\kappa_1$  and  $\kappa_2$ , respectively), or the pair of the mean ( $H = 1/2(\kappa_1 + \kappa_2)$ ) and Gaussian ( $K = \kappa_1\kappa_2$ ) curvatures (Figure 3.1a). We explored different surface families based on their mean and Gaussian curvature profiles, and focused on axisymmetric surfaces, as these could readily be converted to printable substrates. The first geometry that we selected was the unduloid, which is a simply-periodic surface family with constant, non-zero mean curvature. An unduloid interpolates between a cylinder and a string of connected spheres, depending on its specific parametrization (Supplementary Movie 1<sup>35</sup>)<sup>36</sup>. This interpolative nature enabled us to select a cylinder, a set of spheres, and an intermediate unduloid all of which with the same (constant) mean, yet different Gaussian curvatures

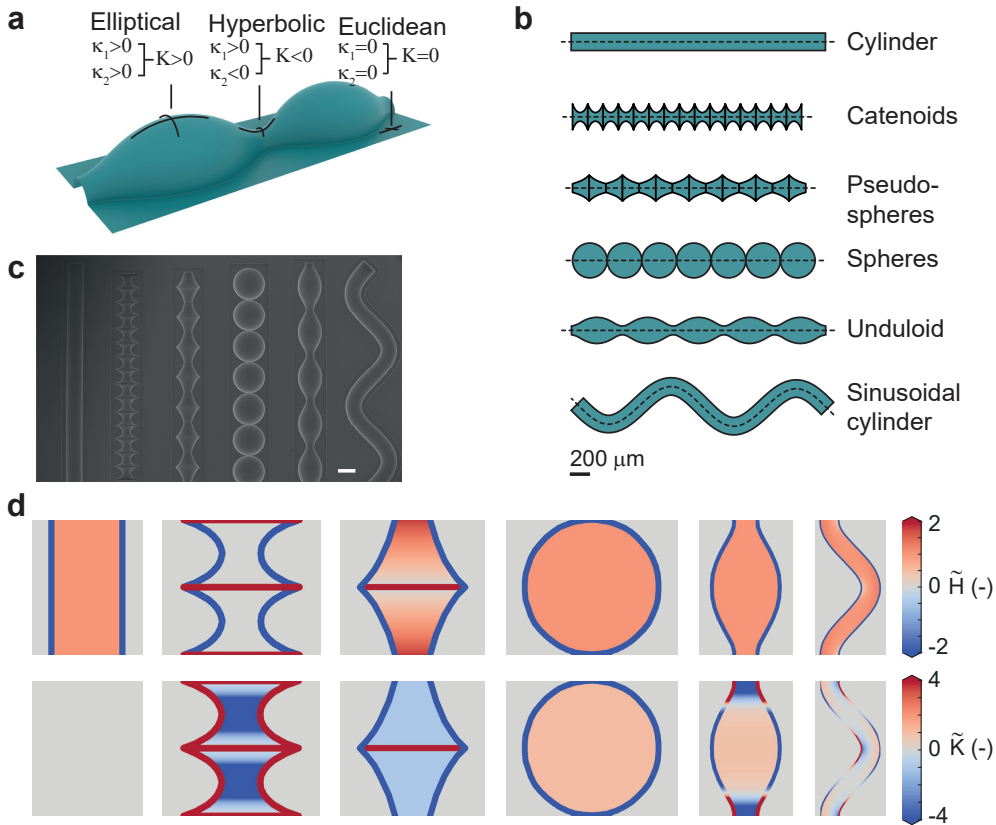


**Figure 3.1:** Design and microfabrication of curved cell substrates. a) Local surface geometry defined in terms of the principal curvatures,  $\kappa_1$  and  $\kappa_2$ , and the Gaussian curvature,  $K$ . b) The surface profiles (top view) used to design curved cell substrates. The first five surfaces are surfaces of revolution (the dotted line is the rotation axis), while the last surface is obtained by sweeping a circle along a sinusoidal path (dotted line). c) SEM image of a PDMS sample with imprinted (concave) substrates. Scale bar represents  $200 \mu\text{m}$ . d) Projected curvature maps for the six types of substrates, displaying repetitive unit cells. The top and bottom rows represent the normalized mean and Gaussian curvatures, respectively. From left to right: cylinder, catenoids, pseudospheres, spheres, unduloid, and sinusoidal cylinder. The curvatures are visualized for the convex substrate variants. For the concave substrates, the mean curvatures are equal in magnitude but opposite in sign. The Gaussian curvatures remain the same.

(Figure 3.1b, Figure 3.1d). Next, we selected two saddle surfaces (*i.e.*,  $K < 0$ ): the pseudosphere, having constant negative Gaussian curvature (as opposed to a sphere with constant positive Gaussian curvature), and the catenoid, having constant zero mean curvature (*i.e.*, a minimal surface). Since these surfaces are not simply-periodic by nature, we designed strings of repeating pseudospheres and catenoids, in accordance with the other surfaces (Figure 3.1b). Finally, we included a sinusoidally-deformed cylinder. In contrast to a normal cylinder ( $K = \kappa_2 = 0$ ), this deformed variant is enriched with alternating regions of positive and negative Gaussian curvatures (Figure 3.1d).

We sized the surfaces to appropriate cell-scale dimensions, based on previous studies<sup>14;19</sup>, and used them as templates for half-revolution master moulds that were 3D printed using two-photon polymerization (2PP). Single- and two-step replica moulding with poly(dimethylsiloxane) (PDMS) provided us with precisely curved cell culture environments, consisting of both concave imprints ( $H < 0$ ) and convex protrusions ( $H > 0$ ) of the same surfaces (Figure 3.1c and Figure 3.2). By using both the concave and convex variants, we could significantly expand our total curvature spectrum, as these substrates feature the same Gaussian curvatures, yet opposite mean curvatures.

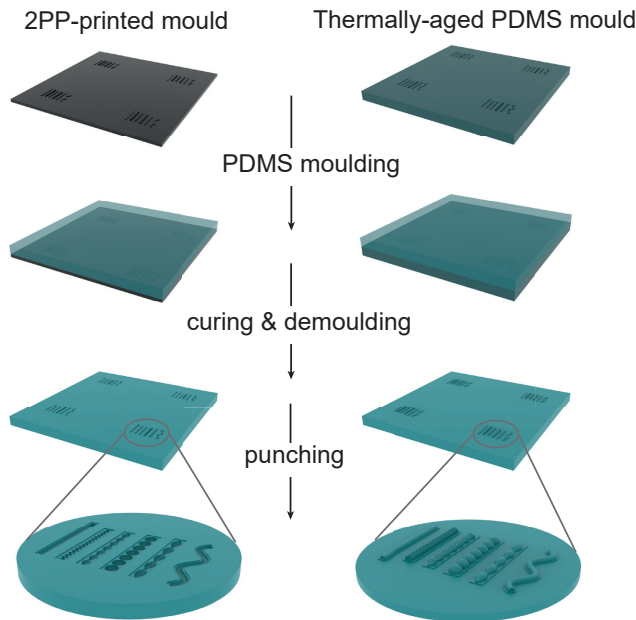


**Figure 3.2:** Fabrication of the PDMS substrates with curved imprints (concave, left column) or protrusions (convex, right column). Left: A master-mould containing four sets of curved substrates (protruding halves of the surfaces of revolution) was fabricated using 2PP. Next, PDMS counter-moulding was performed and circular specimens were stamped and prepared for cell culture. Right: A PDMS mould with imprinted substrates was thermally aged and used as a master-mould for moulding specimens with protruded (convex) substrates. The illustration is not shown to scale.

### 3.3.2 Murine preosteoblasts prefer regions with negative minimum principal curvature

To investigate curvature-guided spatiotemporal cell patterning, we cultured murine preosteoblasts (MC3T3-E1) on the curved substrates for several days. This cell line has been used before in the context of curvature-driven tissue growth<sup>30;37</sup>. After 5 days, we observed confluent layers on the planar regions and curvature-dependent patterning on the non-planar regions (Figure 3.3a). After 8 days, this trend continued and large cell collectives were found to differentially cover the substrates. The frequency maps of the spatial actin distribution, created by superimposing confocal image projections, re-

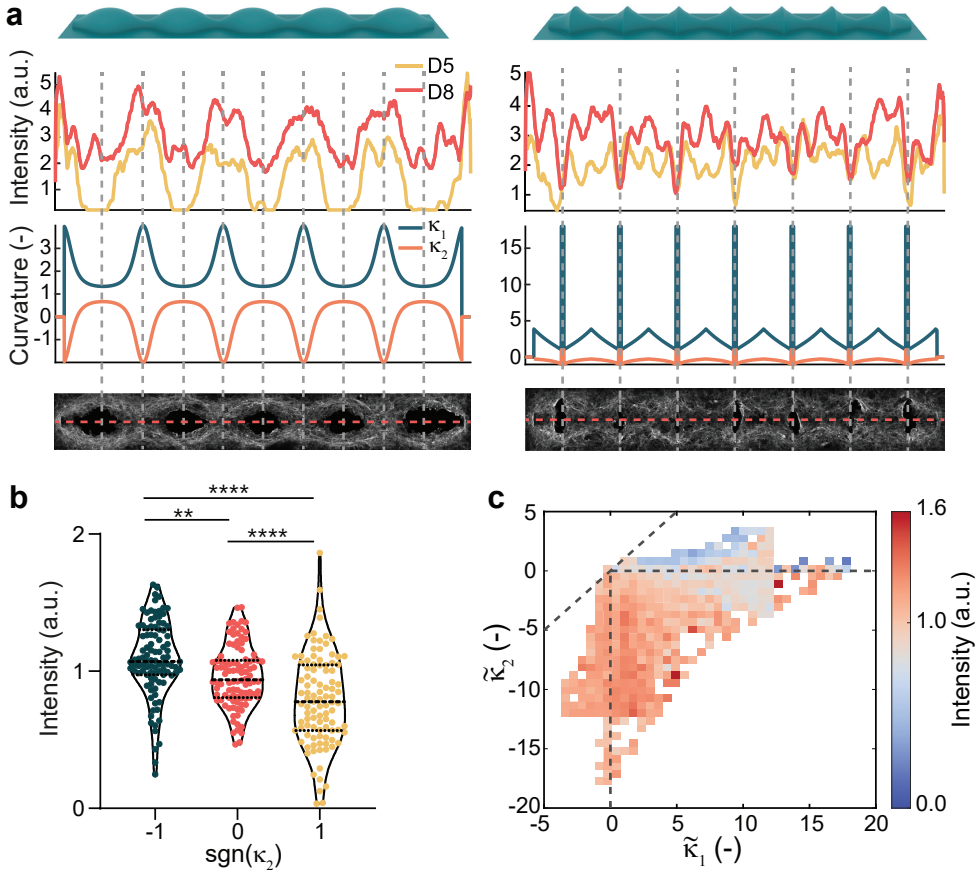


**Figure 3.3:** Collective spatiotemporal cell patterning on curved substrates. a) Normalized actin intensity, measured along the centreline, varies as a function of the principal curvatures  $\kappa_1$  and  $\kappa_2$ . The intensity profiles are obtained from multiple specimens ( $n > 3$ ) for the convex unduloid (left) and convex pseudosphere (right) substrates (see also Figure 3.17). b) Normalized actin intensity *versus* the sign of  $\kappa_2$  for convex substrates on day 8. 100 random data points for each category were sampled from all the available data (superpixels of  $80 \times 80$  pixels). The data are shown as violin plots with median and interquartile range. Welch's ANOVA with Games-Howell's multiple comparisons test: \*\*  $p < 0.01$ , \*\*\*\*  $p < 0.0001$ . c) Heat map of the median normalized actin intensity *vs.* the two normalized principal substrate curvatures  $\tilde{\kappa}_1$  and  $\tilde{\kappa}_2$  for all substrates on day 8. The data points are obtained by rasterizing the projected confocal images in elements of 20 by 20 pixels.

vealed strong differences in the patterning on the concave ( $H < 0$ ) and convex ( $H > 0$ ) variants of the substrates (Figure 3.4, Figure 3.18 and Figure 3.19). Uniform cell coverage was observed in the concave substrates, while the convex variants exhibited distinct regions with high and low actin intensities. On these convex substrates, we found more coverage on the hyperbolic regions (saddle-shaped,  $K < 0$ ) than on the elliptical regions (sphere-like,  $K > 0$ ), as exemplified on the unduloid substrate with a constant mean and varying Gaussian curvatures (Figure 3.3a and Figure 3.4). On the convex

catenoids and pseudospheres ( $K < 0$ ), we observed full cell coverage along the entire substrate, except for the sharp (locally elliptic) transition regions between the saddles. Moreover, we consistently found high cell densities at the transition regions between the convex structures and their planar surroundings, while the reverse was observed at the concave-to-planar transitions. Taken together, these observations demonstrate the collective preference of the cells to pattern regions where the minimum principal curvature is negative (*i.e.*,  $\kappa_2 < 0$ ), which includes all regions with at least one concave direction (Figure 3.3b). This translates to regions with either  $K < 0$  (saddle shapes), or  $K \geq 0$  combined with  $H < 0$  (*e.g.*, concave spheres). Indeed, the convex-to-planar transitions, that feature strong cell attraction, are also characterized by  $\kappa_2 < 0$ . This general preference for  $\kappa_2 < 0$  was confirmed when considering the mean actin intensity across the full curvature spectrum presented to the cells, showing higher intensities for regions with a negative minimum principal curvature (Figure 3.3c). Nevertheless, the frequency maps and the intensity plots also show that cells do not entirely avoid unfavourably-curved regions. For example, substantial regions of the spherical substrates were covered with cells, despite the constant positive  $\kappa_2$ , suggesting a collective ability to conquer such less favourable curvatures.

### 3.3.3 Distance to $\kappa_2 < 0$ characterizes spatial cell patterning

We hypothesized that the presence of cells on the convex regions with  $\kappa_2 \geq 0$ , which was more apparent on day 8 than on day 5, was caused by a collective crowding effect, whereby cells expand from preferentially curved regions into less favourable territory. To investigate this, we created distance maps, quantifying the shortest distance to a region with  $\kappa_2 < 0$  for every point on the substrate.

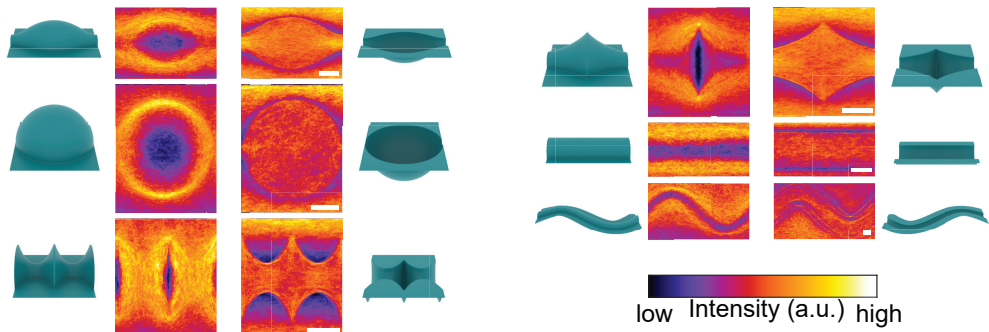


**Figure 3.4:** Frequency maps displaying spatial actin patterning on day 8. The data is obtained by stacking periodic units from multiple images ( $n > 15$ ) for both the convex (left column) and concave (right column) variants of the six substrates (see also Figure 3.18 and Figure 3.19). The scale bars represent  $100 \mu\text{m}$ .

For the convex cylinder, unduloid, and spherical substrates, which all contain substantial regions with  $\kappa_2 \geq 0$ , we observed that the distance maps closely resemble the spatial distribution of cells (Figure 3.4, Figure 3.5). This observation was quantified by plotting the normalized intensity *versus* the distance value (termed  $\delta_{\kappa_2 < 0}$ ), clearly

demonstrating a reduction in intensity for increasing distance (Figure 3.5). The effect is particularly clear on day 5, where the intensity rapidly drops off to zero in all three cases. On day 8, the rate of intensity reduction is lower, as cells have collectively ventured onto all regions of the substrate, albeit at a lower density for higher  $\delta\kappa_2 < 0$ . We, therefore, found that, at long enough time scales, the cells can collectively conquer curvatures that are not initially attractive. In this regard, it is not the instantaneous curvature that governs cell patterning, but rather the presence of a region with  $\kappa_2 < 0$  in the vicinity.

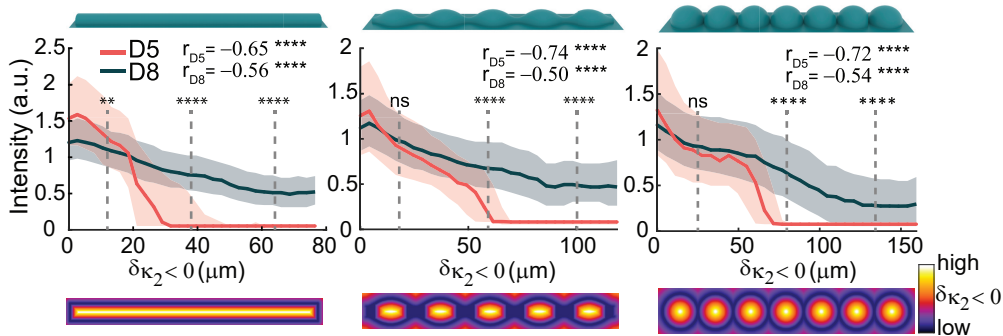


**Figure 3.5:** Normalized actin intensity reduces with increasing distance to the closest region with  $\kappa_2 < 0$  ( $\delta\kappa_2 < 0$ ). The data are shown for three convex substrates ( $n > 3$ ) and two time points (day 5 and day 8). The solid line represents the median value, while the shaded areas correspond to the interquartile range. The  $r$ -values represent the Spearman's correlation coefficients. Mann-Whitney U tests: \*\*  $p < 0.01$ , \*\*\*\*  $p < 0.0001$ . The bottom row depicts the Euclidean distance maps for the three considered (convex) substrates.

### 3.3.4 Cells collectively detach from large regions with $\kappa_2 < 0$

Closer inspection of the image stacks on the concave substrates revealed that cells do not uniformly fill the concavities, but form suspended cell sheets that span the entire curved region while remaining anchored to the substrate through cell bridges (Figure 3.6 and Supplementary Movie 2<sup>35</sup>). As demonstrated on a spherical substrate (Figure 3.6b), the establishment of a detached sheet begins with the individual exploration and spreading of cells in the spherical well. After 5 days, the cell density is high enough for the cells to link up and exert tensile forces to each other, enabling them to lift off the substrate and form bridges. After 8 days, the bridging cells have coalesced into sheets that span the entire concavity, while cell bridges underneath the sheet form anchors to the substrate. These phenomena were not exclusive to the spherical substrates but were observed in all concave substrates after 8 days, across the entire substrate length (Figure 3.6c). Curvature-induced cell bridging has also been observed in individual mesenchymal stromal cells (MSCs)<sup>8;38</sup>, and cell sheet detachment has been reported in smooth muscle cells<sup>39</sup> and cardiomyocytes<sup>40</sup> seeded in microgrooves, though along shorter lengths than we have observed.

When evaluating cell sheet detachment across specimens, we observed a variation in the vertical sheet displacement ( $\Delta h$  in Figure 3.7). To discern whether this was re-

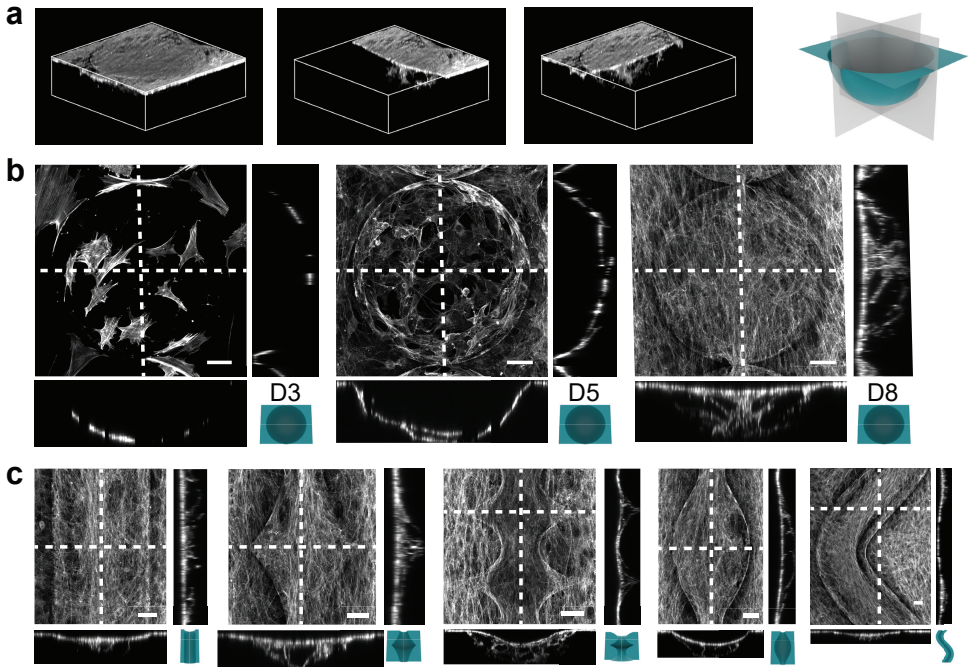


**Figure 3.6:** Curvature-induced cell bridging and cell sheet detachment. a) Cell sheet bridging over a concave spherical substrate ( $K > 0$ ,  $H < 0$ ). The 3D reconstruction in the top left panel displays the full coverage of the spherical well, while the cut-away views demonstrate the anchoring cell bridges that connect the sheet to the substrate (see also Supplementary Movie 2<sup>35</sup>). b) Maximum intensity projections and cross-sectional views on spherical wells at days 3, 5, and 8, showing the temporal evolution of bridge formation and sheet detachment. On day 3 (left panel), the cells spread and individually explore the spherical substrate. On day 5 (middle panel), the cells start to link up and form bridges, thereby detaching their body from the substrate. On day 8 (right panel), the cells form detached sheets that completely cover the concave well and are anchored to the substrate through clear cell bridges. c) Maximum intensity projections and cross-sectional views, showing the formation of cell sheets on the other concave substrates. From left to right: cylinder, pseudospheres, catenoids, unduloid, and sinusoidal cylinder.

lated to the presence of anchors, we calculated  $\Delta h$  and the anchor density below the sheet for standard experiments on spheres and cylinders, as well as for the experiments with up- or downregulated contractility (see Subsection 3.3.6). As expected, we observed a positive correlation between  $\Delta h$  and the anchor density (Spearman's  $r = 0.77$  for the cylinders and Spearman's  $r = 0.72$  for the spheres). We also looked for evidence of cell sheet detachment on the convexly curved substrates. We observed cell sheet detachment at the convex-to-planar transition ( $\kappa_2 < 0$ ) on all convex structures, though most notably on the sinusoidal cylinder (Figure 3.8). Interestingly, we found that sheet detachment is much more pronounced at the concave side of a substrate bend, exhibiting a detached sheet that departs from the top of the substrate and is suspended over a distance that is 4 times longer than at the convex side of the bend (Figure 3.8 and

Supplementary Movie 5<sup>35</sup>). At the concave side, the cells collectively sense the concavity of the transition region ( $\kappa_2 < 0$ ) as well as the overall concavity of the substrate ( $\kappa_1 < 0$ ). The combination of these curvatures ( $K > 0, H < 0$ ) appears to stimulate the formation of a substantial detached cell sheet, suspended over a large region of the planar surroundings.

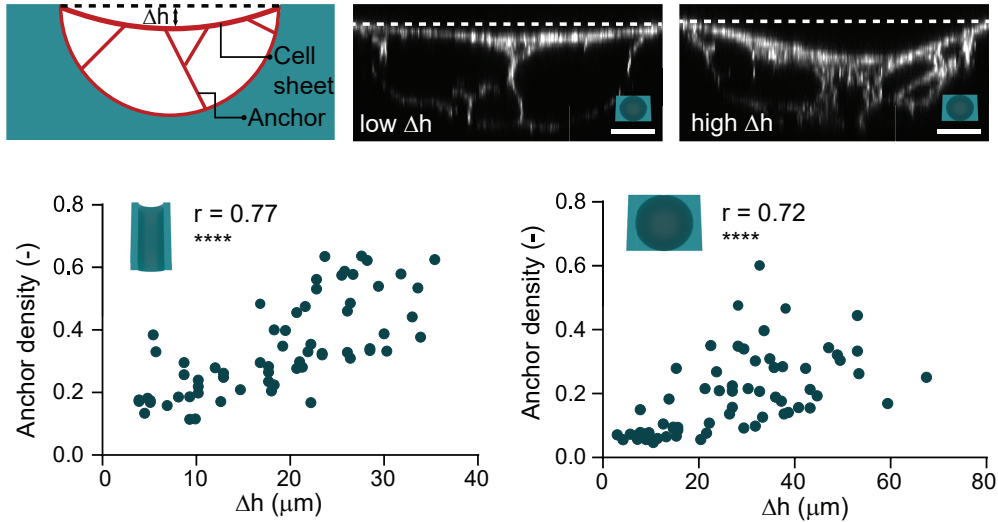


**Figure 3.7:** Quantification of cell sheet displacement ( $\Delta h$ ) in relation to the anchor density for concave cylindrical substrates (left graph) and concave spherical substrates (right graph). The  $r$ -value indicates the Spearman's correlation coefficient; \*\*\*\*  $p < 0.0001$ . The data from the cells treated with TGF- $\beta$  and blebbistatin are also included in these graphs.

### 3.3.5 Curvature induces collective stress fibre orientation

We next asked how curvature affects the collective orientation of stress fibres (SF) on our substrates. While curvature-induced orientation has been observed in individual cells<sup>13;41</sup>, cells in monolayers and in developing tissues have shown to cooperatively sense weaker curvature fields<sup>15;30</sup>. From a differential geometric perspective, it is interesting to compare the orientation of SF to the principal directions of the curved substrates, which are the directions along which  $\kappa_1$  and  $\kappa_2$  occur (Figure 3.9b and Figure 3.20). The cells with pronounced SF have been previously found to align along the direction of minimum principal curvature ( $P_{\kappa_2}$ ), which is often attributed to the tendency to minimize the bending energy of SF<sup>13;20</sup>. We calculated the degree of alignment (DA, see Materials and Methods) between the SF and  $P_{\kappa_2}$  on the convex substrates. The spherical substrates were excluded, since the principal directions are not defined for spheres ( $\kappa_1 = \kappa_2$ ). The strongest DA was observed on the cylinders, showing the collective orientation of SF along the zero-curvature direction ( $\kappa_2 = 0$ ) (Figure 3.10a). While the cells were also found to align well with  $P_{\kappa_2}$  on the unduloid, this was not found to be the case for the pseudospheres and catenoids. On those saddle-shaped substrates, the DA distributions indicate a lower overall alignment with  $P_{\kappa_2}$ , yet the peaks

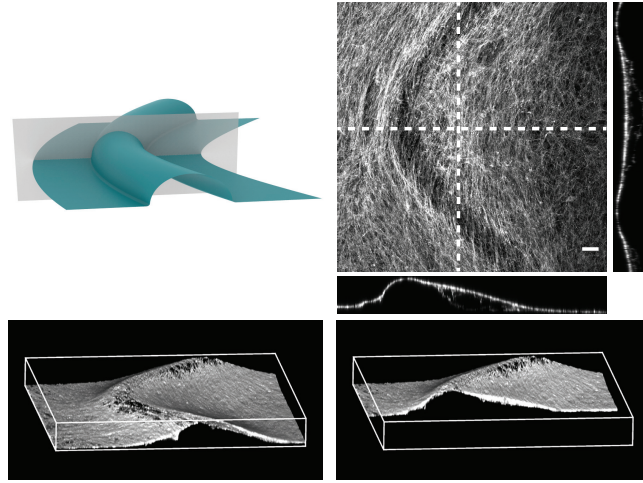


**Figure 3.8:** Cell sheet detachment also occurs at local concavities on predominantly convex substrates, as demonstrated for the convex sinusoidal cylinder. The top right panel displays a maximum intensity projection and cross-sectional views, while the bottom panels display 3D reconstructions (full view on the left, cut-away view on the right). All scale bars represent 50  $\mu\text{m}$ .

at  $DA = 0$  suggest some alignment with  $P_{\kappa_1}$  ( $P_{\kappa_1}$  and  $P_{\kappa_2}$  are orthogonal). Interestingly, the cells on the sinusoidal-cylinder were found to collectively align, yet with some deviation from the principal direction  $P_{\kappa_2}$  ( $DA \approx 0.7$ ). We attribute this deviation to a bypassing effect, whereby SF follow the sinusoidal orientation of the substrate to some extent, but exhibit a collective resistance to change their orientation in response to the alternating curvatures.

On the concave substrates, where the cells coalesced in detached sheets, we also observed the collective alignment of SF. In the channel-like substrates (*i.e.*, cylinder, unduloid, catenoids, and pseudospheres), we found a strong longitudinal preference, typically exemplified by the presence of a central SF bundle (Figure 3.9c, Figure 3.10b). This longitudinal preference was attributed to a confinement effect<sup>42</sup>, where cell crowding in the detached sheet induces collective alignment after 8 days. Indeed, we did not observe longitudinal alignment in the concavities after 5 days, when cells were forming randomly-oriented local bridges (Figure 3.21b). Considering the concave sinusoidal cylinder, we observed SF bundles that trace a lower-amplitude sinusoidal path than the original substrate (Figure 3.9d). This path is reminiscent of the shape that a tensioned string confined to a sinusoidal channel would adopt, implying a role for actomyosin contractility in the collective orientation of SF.

Finally, we investigated the SF orientation in the regions where the superimposed layers of cells were observed, such as on the saddle-shaped region of the convex unduloid or at the saddle-shaped transition between convex spheres. Interestingly, we found distinct SF subpopulations with orthogonal orientations on both substrates (Figure 3.11). In the lower focal planes, horizontally-oriented SF were observed, while

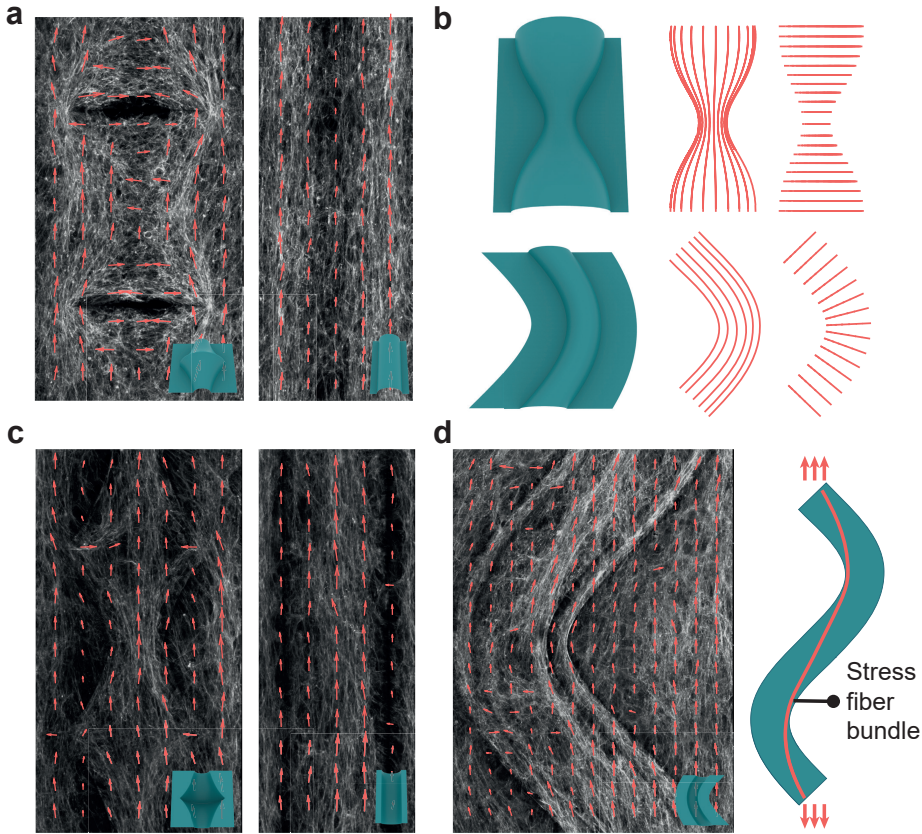


**Figure 3.9:** Collective stress fibre orientation on curved substrates. a) Local dominant stress fibre orientations at day 8 on the convex pseudospheres (left) and convex cylinder (right), computed for superpixels containing  $80 \times 80$  pixels. b) Illustrations of the principal directions on some portions of the convex unduloid (top) and convex sinusoidal cylinder (bottom). The left and right set of lines represent the principal directions corresponding to the minimum ( $\kappa_2$ ) and maximum ( $\kappa_1$ ) principal curvatures, respectively. c) Orientation of SF at day 8 on the concave pseudospheres (left) and concave cylinder (right), computed for superpixels of  $80 \times 80$  pixels. d) Orientation of SF at day 8 on the concave sinusoidal cylinder. The right panel schematically illustrates the presence of the central SF bundles that display a lower-amplitude wave, effectively smoothing the geometry of the original sinusoidal substrate.

the top focal planes displayed vertically-oriented SF. In a different study, orthogonally-oriented SF have been observed within individual cells on saddle shapes<sup>18</sup>. It was postulated that SF above the nucleus preferentially align in the concave direction to minimize bending, while SF below the nucleus align in the convex direction to support cell migration. Based on these observations, we hypothesize that lower SFs align in the convex direction when cells migrate onto the substrate from both sides and form mechanical connections. Once these regions have been conquered, new cells can align in the concave direction to minimize bending.

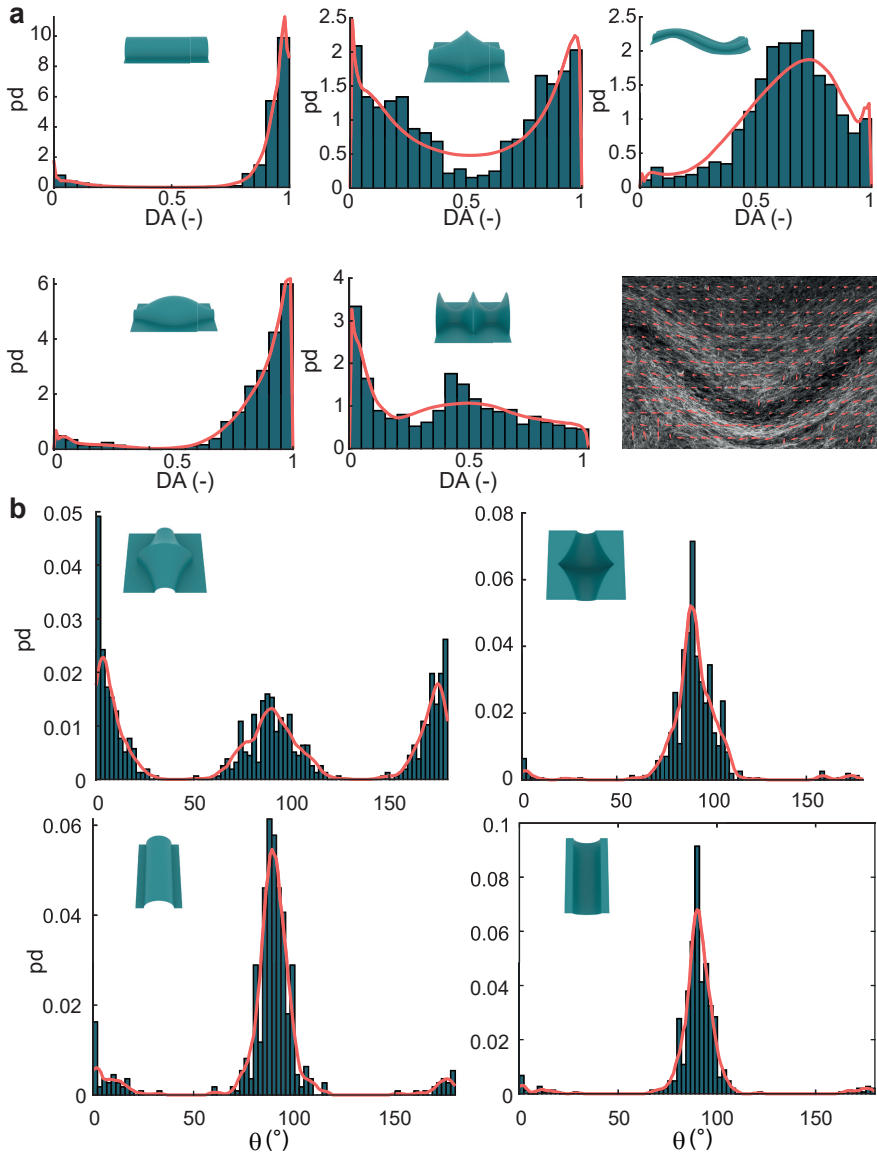


**Figure 3.10:** a) Probability density distributions (PD) of the degree of alignment (DA) of the SF with respect to the first principal direction (corresponding to  $\kappa_2$ ) on the convex substrates. When  $DA = 1$ , the stress fibres are perfectly aligned with the first principal direction. Data are obtained from all the specimens at day 8 ( $n > 3$ ), using superpixels of  $80 \times 80$  pixels. The red lines represent the Epanechnikov kernel density estimates. The inset figure on the bottom right displays the local orientation of SF on the convex sinusoidal cylinder at day 8, displaying collective deviation from the first principal direction. b) PD distributions of the local orientation of SF (with respect to the horizontal axis) on the convex and concave pseudospheres (top left and top right, respectively), and on the convex and concave cylinders (bottom left and bottom right, respectively). The data were obtained from all the specimens at day 8, using superpixels of  $80 \times 80$  pixels. The red lines represent the Epanechnikov kernel density estimates.

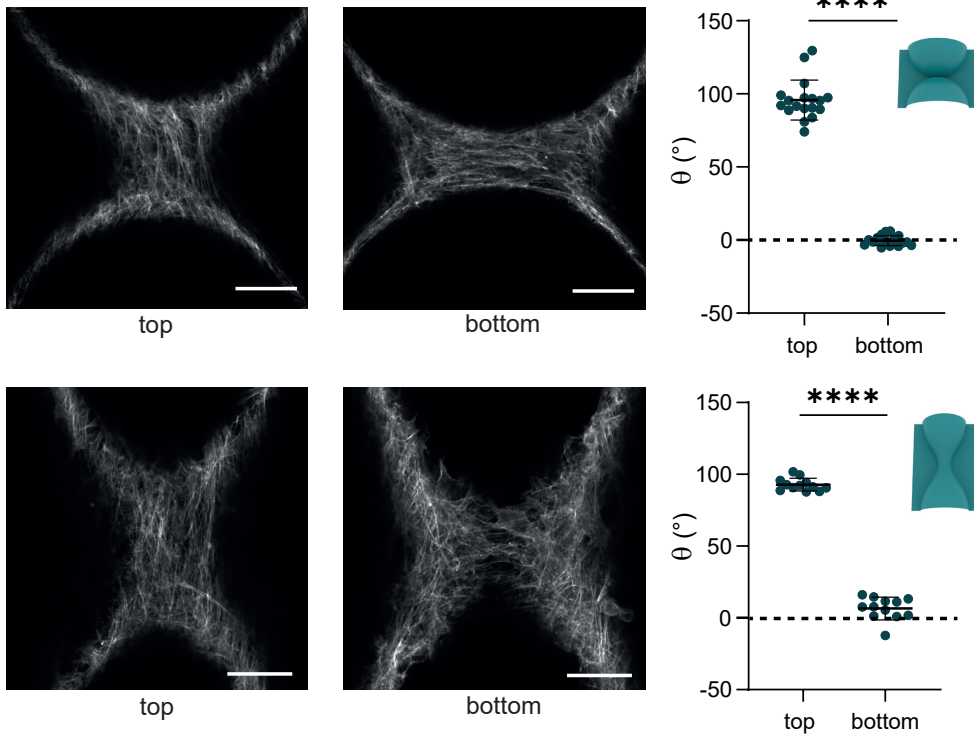


**Figure 3.11:** SF subpopulations on the convex spheres (top row) and convex unduloids (bottom row), displaying orthogonal orientations. The top layer of SF (left) orients along the longitudinal direction ( $90^\circ$ ), while the bottom layer (right) adopts a horizontal orientation ( $0^\circ$ ). The graphs on the right display the computed orientations of SF. The data were obtained from three specimens in each case, at multiple locations along the periodic substrates. Paired two-tailed t-tests: \*\*\*\*  $p < 0.0001$ . Scale bars represent  $50 \mu\text{m}$ .

### 3.3.6 Contractility and differentiation perturbation affect curvature guidance

We explored the role of contractility on the collective organization in our complex, curved landscapes. We enhanced cell contractility with transforming growth factor- $\beta$  (TGF- $\beta$ ) and downregulated contractility using myosin-II-inhibiting blebbistatin. In general, the cells with perturbed contractility patterned the curved substrates similarly to the unperturbed cases, yet exhibited more- or less-pronounced SF in response to TGF- $\beta$  and blebbistatin, respectively (Figure 3.12a and Figure 3.22). However, we found that the cells treated with blebbistatin did not cover the unfavourably curved regions ( $\kappa_2 > 0$ ) as well as unperturbed cells (Figure 3.13a).

Cell contractility is the driving force behind the formation of individual or multicellular bridges. Indeed, we found that perturbing contractility affects the morphology of the detached cell sheets and anchoring bridges on the concave substrates (Figure 3.12b and Supplementary Movies 3-4<sup>35</sup>). Enhancing contractility results in lower sheet displacement and fewer bridges as compared to the cases where contractility is inhibited

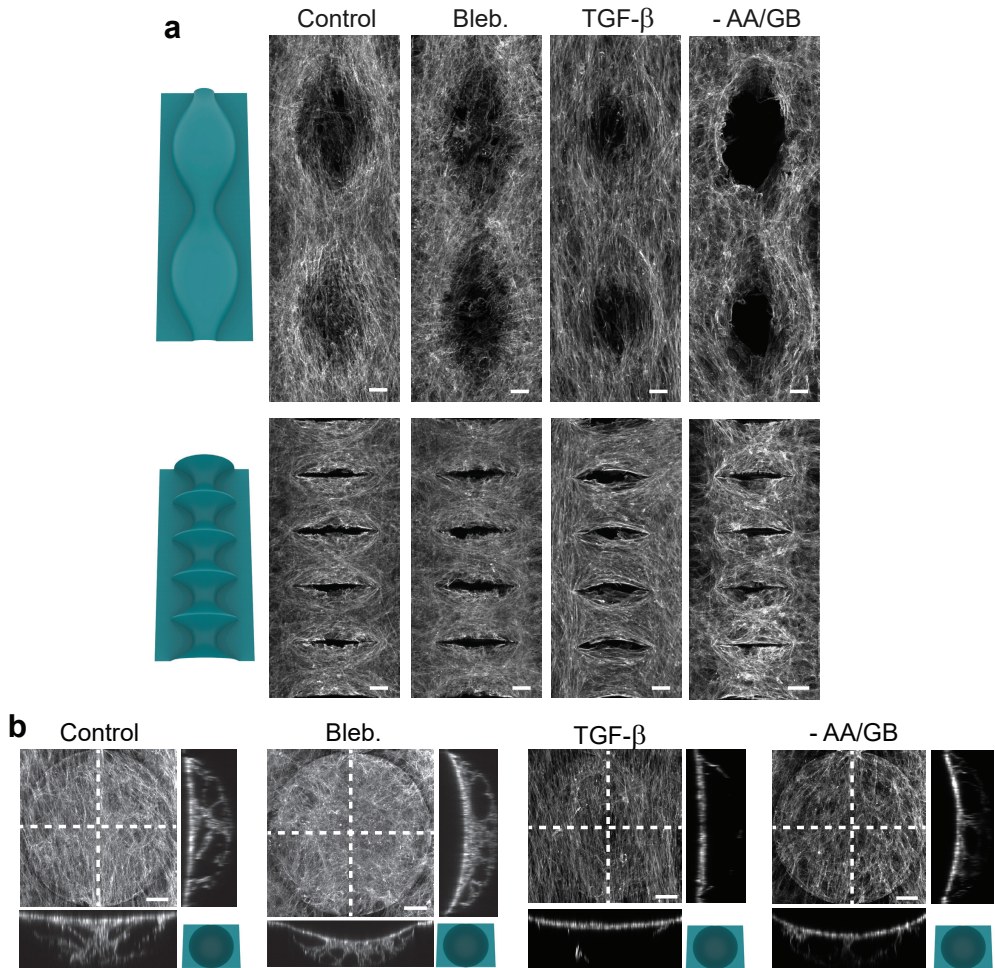


**Figure 3.12:** Effect of contractility perturbation and differentiation inhibition on the curvature-induced organization. a) Representative maximum intensity projections (actin) on the convex unduloids (top) and catenoids (bottom), displaying the effects of contractility inhibition (Bleb.), contractility enhancement (TGF- $\beta$ ), and differentiation inhibition (-AA/GB). b) Effect of contractility perturbation and differentiation inhibition on cell sheet detachment over concave hemispheres at day 8.

(Figure 3.13b), implying that higher cell contractility translates to a higher overall tension in the suspended sheets. When considering specific focal planes within the cell sheets of the different cases, we also observed different SF morphologies and orientations. As compared to the unperturbed case, the cells treated with blebbistatin are more dendritic-like and form many small anchoring bridges that adopt circular configurations, while TGF- $\beta$  induces strong SF with a more pronounced longitudinal alignment (Figure 3.14). The effects of collectively enhanced contractility were also apparent on the convex substrates, where strong cell sheets were observed that bridge the underlying curved structures. On the spherical substrates, for example, the cells cultured under

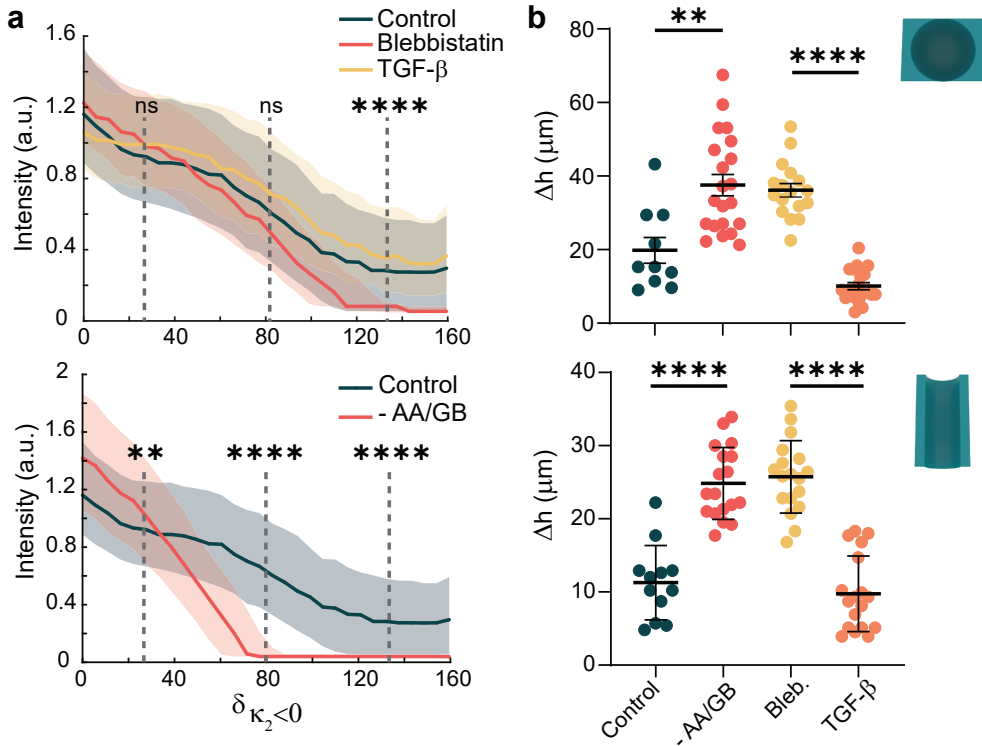


**Figure 3.13:** a) Intensity reduction as a function of  $\delta \kappa_2 < 0$ . The top chart demonstrates the effects of contractility perturbation. The Kruskal-Wallis test: \*\*\*\*  $p < 0.0001$ . The bottom chart demonstrates the effects of differentiation inhibition. The Mann-Whitney test: \*\*  $p < 0.014$ , \*\*\*\*  $p < 0.0001$ . The solid lines represent the median values while the shaded areas represent the interquartile range. b) Quantification of cell sheet displacement ( $\Delta h$ ) due to contractility perturbation or differentiation inhibition.

normal conditions form modest bridges in between the spheres, while contractility-enhanced cells form much stronger cell sheets that remain almost planar and seem to avoid the underlying curvature (Figure 3.15a). These results are in line with previous studies at the cell and tissue scales<sup>19;30</sup>, and underpin the important role of individual cell contractility as a driving force for the collective organization in varying curvature fields.

We also stained cells for runt-related transcription factor 2 (RUNX2), a marker for osteoblast differentiation. We observed that RUNX2 was clearly expressed in the cells in the control group, but also in specimens with up- or downregulated contractility. When considering RUNX2 expression on the spherical and saddle-shaped regions of the convex unduloid (constant mean curvature), we consistently observed significantly higher RUNX2 intensities on the saddle-shaped ( $\kappa_2 < 0$ ) regions as opposed to the spherical ( $\kappa_2 > 0$ ) regions (Figure 3.23). This points towards a role for curvature in the regulation of cell differentiation, which has been reported by others in MSCs<sup>19;38</sup>.

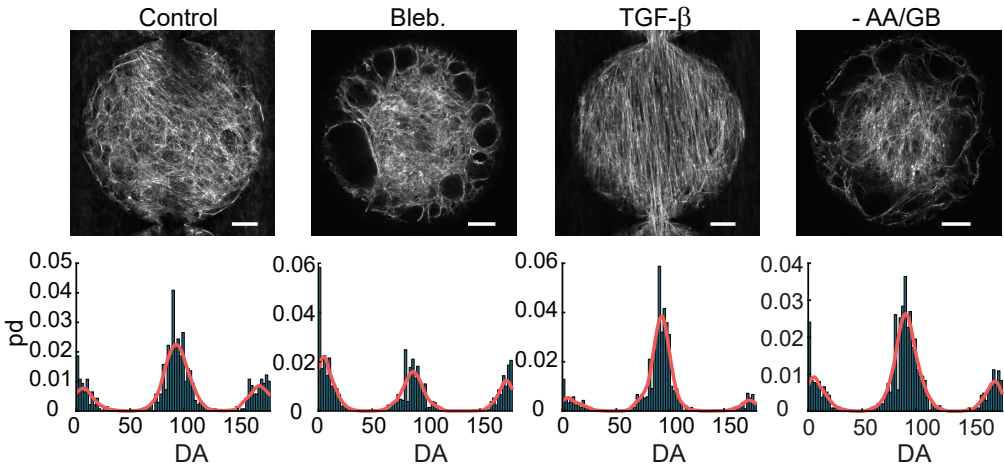


**Figure 3.14:** Effects of contractility perturbation and differentiation inhibition on the morphology and orientation of SF. The top row displays representative slices through the confocal z-stacks, while the bottom row displays the PD of the SF for all the specimens in each category.

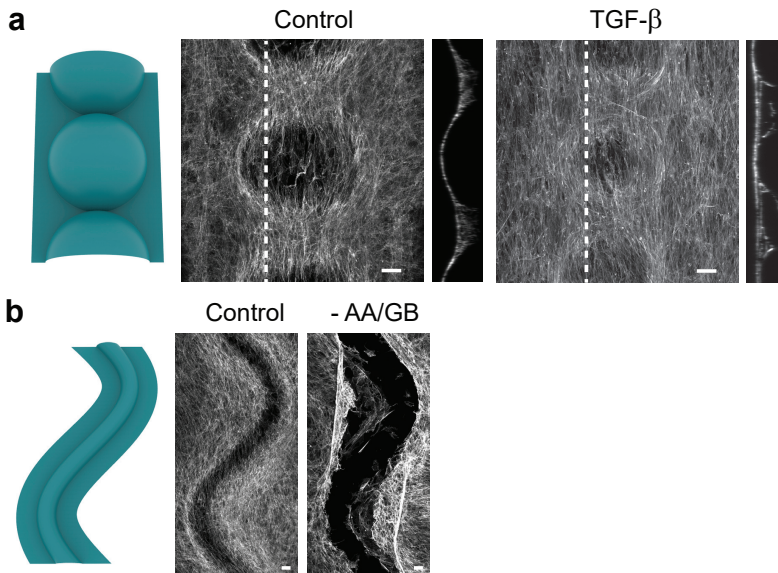


**Figure 3.15:** a) Contractility enhancement affects bridge formation on the convex spherical substrates. A stronger cell sheet is observed in the specimens treated with TGF- $\beta$ . b) Differentiation inhibition causes cell sheet detachment on the convex sinusoidal cylinders in some specimens. The cells collectively pull away from the concave bend of the substrate. All scale bars represent 50  $\mu\text{m}$ .

The osteogenic culture medium that was used during our experiments contained ascorbic acid (AA) and  $\beta$ -glycerophosphate (GB), which support the development of mineralized extracellular matrix (ECM) and promote osteoblast differentiation<sup>43</sup>. AA induces the secretion of type I collagen (Col1) in the ECM, while GB works syner-

gistically with AA and acts as a phosphate source for mineralization<sup>43–45</sup>. To study how collective curvature-guidance is affected by the inhibition of ECM development, we performed experiments with a culture medium deprived of AA and GB<sup>34</sup>. While the cells cultured in this medium generally exhibited similar curvature-induced organization, we observed significantly lower degrees of cell coverage on unfavourably-curved regions ( $\kappa_2 > 0$ ) (Figure 3.12a, Figure 3.13a). On the concave structures, we found that AA/GB deprivation resulted in weaker cell sheets, displaying similar SF morphologies and  $\Delta h$  as compared to the cells treated with blebbistatin (Figure 3.12b, Figure 3.13b, Figure 3.14). Interestingly, we observed that the cells cultured in non-osteogenic medium in some cases collectively pulled away from the concave bends of the convex sinusoidal cylinders, a phenomenon that was never observed in the cells cultured in osteogenic medium (Figure 3.15). These results indicate that the development of ECM, induced by osteogenic medium, provides a reinforcing scaffold that enables the cells to collectively conquer unfavourable curvatures within our complex landscapes.

### 3.4 Discussion

We have demonstrated the collective organization of preosteoblasts in cell-scale, varying-curvature landscapes. By designing mathematically-defined surface families with controlled curvature variations and by leveraging high-resolution free-form fabrication, we micro-engineered substrates that cover a wide range of Euclidean, hyperbolic, and elliptical geometries. This broad curvature spectrum enabled us to systematically study collective curvature-guidance and unify recent findings within a geometry-centred framework. We found that cells preferentially pattern regions with at least one concave direction (*i.e.*, regions where the minimum principal curvature is negative,  $\kappa_2 < 0$ ), while curved regions with  $\kappa_2 \geq 0$  are generally avoided. Previous studies have also reported preferences for local concavities, which has been attributed to a more relaxed stress configuration in the concavities<sup>19;29;38</sup>. However, those observations were typically made from a 2D perspective or without addressing the formal mathematical framework of surface curvature. Specifically, curvature guidance has often been studied by considering cell behaviour on convex or concave substrates, typically spheres or cylinders, without addressing the specific mean or Gaussian curvatures. Moreover, hyperbolic substrates, containing both concave and convex directions, have received little attention until recently<sup>14;30</sup>, despite their high physiological relevance<sup>8</sup>. Our results show that one concave direction in a specific region is sufficient for cells to preferentially cover that region. This includes not only all hyperbolic geometries ( $K < 0$ ) but also elliptical ( $K > 0$ ) and Euclidean ( $K = 0$ ) regions where the mean curvature is negative, such as the convex-to-planar transitions that have been typically ignored in previous studies. In this regard, there is no single mean or Gaussian curvature that could be pinpointed as ideal for cell patterning, but rather a spectrum of shapes where  $\kappa_2 < 0$ . Despite a general preference for  $\kappa_2 < 0$ , we found that cells can eventually conquer unfavourably-curved regions through cooperative action, provided that the distance to favourably-curved regions is not too large. However, this ability to venture onto curved

regions with  $\kappa_2 \geq 0$  reduces when cell contractility or ECM production is impaired.

Our widespread observations of cell bridging and cell sheet detachment, including observations with blebbistatin and TGF- $\beta$ , further illustrate the crucial role of cell contractility and the ability of the cells to collectively override the geometrical cues imposed by the substrate. However, an important parameter governing these phenomena is the cell adhesion to the substrate. Our substrates were functionalized by fibronectin (FN) adsorption, facilitating integrin-mediated adhesion. However, different results might be obtained when the FN is covalently bonded to the substrate<sup>30</sup>. In such cases, cell sheet detachment may be reduced or avoided<sup>39</sup>.

Our results on the curvature-induced collective orientation of SF are in line with the biophysical arguments that SF-dominated cells align in directions that minimize SF bending<sup>13;20</sup>. Indeed, we find that cells on convex cylinders or unduloids align well with the direction of minimum principal curvature. On the convex hyperbolic substrates (where  $H > 0$ ), however, we found that cells show less uniform alignment, and that a substantial portion of SF align along a locally convex direction. Moreover, we observed orthogonally-oriented SF subpopulations on some local saddles and confinement-induced longitudinal orientation of SF in detached cell sheets. In general, we concluded that substrate curvature, indeed, affects SF orientation, but that cell interactions, mediated by contractility and ECM production, result in a collective resistance to local variations in the underlying curvature.

Taken together, our results underpin the importance of local, cell-scale geometrical cues on the emergent organization of bone-like cells. In particular, these findings emphasize the role of multicellular cooperation, enabling cells to collectively conquer unfavourably-curved regions or alter their local environment through collective detachment. However, cells are typically exposed to several other biophysical cues *in vivo*, such as stiffness gradients<sup>46</sup> or nanotopographies<sup>6</sup>. In this regard, it would be interesting to explore the collective cell organization in a tailored multi-cue environment to unravel the dominant cues and potential crosstalk<sup>14</sup>. Our results could ultimately inspire the design of tissue engineering scaffolds<sup>10</sup>. Based on our findings, one could argue that scaffolds with substantial regions with  $\kappa_2 < 0$  are preferred. In scaffolds based on cylindrical strut networks, which have often been proposed<sup>47–50</sup>, such regions occur at the intersections of struts. Indeed, tissue formation has been found to initiate from those locations *in vivo*<sup>51</sup>. Alternatively, one could consider hyperbolic sheet-based scaffolds, such as those based on triply periodic minimal surfaces (TPMS), which have  $\kappa_2 \leq 0$  at every point. However, developing geometrically-optimized scaffold designs requires further investigation into the intricacies of cell-geometry interaction, likely involving computational studies that take geometry explicitly into consideration<sup>52</sup>. Nevertheless, fuelled by rapid advances in high-resolution free-form fabrication, we anticipate exciting avenues for geometric control of cells and tissues, relying on surface curvature as the language of shape.

## 3.5 Supporting information

### 3.5.1 Surface parametrization and curvature

The curvatures of the substrates can be calculated analytically using the expressions provided below. For completeness, we first provide the relationship between the principal curvatures ( $\kappa_1$  and  $\kappa_2$ ) and the mean ( $H$ ) and Gaussian ( $K$ ) curvature:

$$H = \frac{1}{2} (\kappa_1 + \kappa_2) \quad (3.2)$$

$$K = \kappa_1 \kappa_2 \quad (3.3)$$

The inverse relationships are given as:

$$\kappa_1 = H + \sqrt{H^2 - K} \quad (3.4)$$

$$\kappa_2 = H - \sqrt{H^2 - K} \quad (3.5)$$

#### Cylinder

The constant principal curvatures of the cylindrical substrate are given by:

$$\kappa_1 = \frac{1}{r_{\text{cylinder}}} \quad (3.6)$$

$$\kappa_2 = 0 \quad (3.7)$$

where  $r_{\text{cylinder}}$  is the radius of the cylinder. In our case,  $r_{\text{cylinder}} = 90\mu\text{m}$ .

#### Unduloid

The unduloid surface is parametrized as<sup>53</sup>:

$$x(u, v) = (x(u), z(u)\cos(v), z(u)\sin(v)) \quad (3.8)$$

with  $u \in \mathbb{R}$  and  $0 \leq v \leq 2\pi$ . In this parametrization,  $x(u)$  and  $z(u)$  are given by:

$$x(u) = r_1 F\left(\frac{u}{r_1 + r_2} - \frac{\pi}{4}, \frac{r_2^2 - r_1^2}{r_2^2}\right) + r_2 E\left(\frac{u}{r_1 + r_2} - \frac{\pi}{4}, \frac{r_2^2 - r_1^2}{r_2^2}\right) \quad (3.9)$$

$$z(u) = \sqrt{\frac{r_2^2 - r_1^2}{2}} \sin\left(\frac{2u}{r_1 + r_2}\right) + \frac{r_2^2 + r_1^2}{2} \quad (3.10)$$

where  $r_1$  and  $r_2$  are the smallest and largest radii of the unduloid, respectively. In our experiments,  $r_1 = 45\mu\text{m}$  and  $r_2 = 135\mu\text{m}$ . In these expressions,  $F$  and  $E$  respectively represent the incomplete elliptic integrals of the first and second kind, provided by:

$$F(\Phi, k) = \int_0^\Phi \frac{d\theta}{\sqrt{(1 - k^2 \sin^2(\theta))}} \quad (3.11)$$

$$E(\Phi, k) = \int_0^\Phi \sqrt{(1 - k^2 \sin^2(\theta))} d\theta \quad (3.12)$$

The unduloid is characterized by a constant mean curvature, which is defined as:

$$H = \frac{1}{r_1 + r_2} \quad (3.13)$$

The Gaussian curvature of the unduloid varies as a function of  $z(u)$ :

$$K = \frac{1 - \left(\frac{r_1 r_2}{z(u)^2}\right)^2}{(r_1 + r_2)^2} \quad (3.14)$$

### Spheres

The principal curvatures on the surface of the spheres are constant and equal:

$$\kappa_1 = \kappa_2 = \frac{1}{r_{\text{sphere}}} \quad (3.15)$$

where  $r_{\text{sphere}}$  is the radius of a single sphere. For our experiments,  $r = 180\mu\text{m}$ .

### Catenoids

The catenoids in the catenoid-substrate are parametrized by:

$$x(u, v) = (x(u, v), y(u, v), z(v)) \quad (3.16)$$

where  $u \in [0, 2\pi)$ ,  $v \in \mathbb{R}$ , and:

$$x(u, v) = r \cdot \cosh\left(\frac{v}{r}\right) \cos(u) \quad (3.17)$$

$$y(u, v) = r \cdot \cosh\left(\frac{v}{r}\right) \sin(u) \quad (3.18)$$

$$z(v) = v \quad (3.19)$$

In these expressions,  $r$  is a non-zero, real parameter describing the catenoid neck radius. In our case,  $r = 45\mu\text{m}$  and  $-79.32\mu\text{m} < v < 79.32\mu\text{m}$ . The principal curvatures of the catenoid are given by:

$$k_1 = \frac{1}{r} \operatorname{sech}^2(v) \quad (3.20)$$

$$\kappa_2 = -\frac{1}{r} \operatorname{sech}^2(v) \quad (3.21)$$

which, indeed, leads to the defining characteristic of the catenoid as a minimal surface (*i.e.*,  $H = 0$ ).

### Pseudospheres

The pseudospheres (or tractricoids) in the corresponding substrate are parametrized by:

$$x(u, v) = (x(u, v), y(u, v), z(u)) \quad (3.22)$$

where  $u \in (-\infty, \infty)$ ,  $v \in [0, 2\pi)$ , and:

$$x(u, v) = r \cdot \operatorname{sech}(u) \cos(v) \quad (3.23)$$

$$y(u, v) = r \cdot \operatorname{sech}(u) \sin(v) \quad (3.24)$$

$$z(u) = r \cdot (u - \tanh(u)) \quad (3.25)$$

Here,  $r$  defines the mean pseudosphere radius. For our substrates, a section of the infinitely extending pseudosphere was defined by  $r = 180\mu\text{m}$  and  $u \in [0.795, 2.0635]$ . The principal curvatures of the pseudosphere are defined as:

$$\kappa_1 = \frac{\operatorname{sech}(u)}{r \cdot \tanh(u)} \quad (3.26)$$

$$\kappa_2 = -\frac{\tanh(u)}{r \cdot \operatorname{sech}(u)} \quad (3.27)$$

Multiplying these expressions for the principal curvatures, indeed, results in the constant Gaussian curvature of  $K = -\frac{1}{r^2}$ , which is the defining characteristic of the pseudosphere.

### Sinusoidal cylinder

The sinusoidal cylinder is defined by creating a sinusoidal wave and “extruding” a cylinder along the sinusoidal path. The footprint of the sinusoidal hemi-cylinder is defined by the parallel waves to a standard sine wave. A sine wave can be parametrized as:

$$x(t) = t \quad (3.28)$$

$$y(t) = a \sin(\omega t) \quad (3.29)$$

where  $t \in \mathbb{R}$ , and  $a$  and  $\omega$  are the constants that define the amplitude and frequency of the wave. In our case,  $t \in [0, 2600]$ ,  $a = 200$ , and  $\omega = \pi/650$ . A parallel sine wave, at a signed distance  $l$  ( $l \in [-90, 90]$ ) from the original wave, is parametrized by:

$$x(t, l) = t + \frac{l a \omega \cos(\omega t)}{\sqrt{1 + a^2 \omega^2 \cos^2(\omega t)}} \quad (3.30)$$

$$y(t, l) = a \sin(\omega t) - \frac{l}{\sqrt{(1 + a^2 \omega^2 \cos^2(\omega t))}} \quad (3.31)$$

One of the principal curvatures of the sinusoidal cylinder is equal to the reciprocal of the cylinder radius (in our case  $r_{\text{cylinder}} = 90$ ):

$$\kappa_1 = \frac{1}{r_{\text{cylinder}}} \quad (3.32)$$

The other principal curvature is the reciprocal of the radius of curvature of the parallel sine wave at a particular point. For example, for the points on the centreline of the sinusoidal cylinder, the principal curvature  $\kappa_2$  is equal to the reciprocal of the radius of curvature of the original sine wave (with  $l = 0$ ). The radius of curvature for a (parallel) curve  $(x(t, l), y(t, l))$  is given by:

$$R(t, l) = \frac{\left( \left( \frac{dx}{dt} \right)^2 + \left( \frac{dy}{dt} \right)^2 \right)^{\frac{3}{2}}}{\frac{dx}{dt} \frac{d^2y}{dt^2} - \frac{dy}{dt} \frac{d^2x}{dt^2}} \quad (3.33)$$

For the specific case of our experiments, the components of this expression are given as:

$$\frac{dx}{dt} = 1 + d \cdot \left( \frac{32\pi^4 \sin\left(\frac{\pi t}{650}\right) \cos^2\left(\frac{\pi t}{650}\right)}{714025 \left(\frac{16}{169} \pi^2 \cos^2\left(\frac{\pi t}{650}\right) + 1\right)^{\frac{3}{2}}} - \frac{2\pi^2 \sin\left(\frac{\pi t}{650}\right)}{4225 \sqrt{\frac{16}{169} \pi^2 \cos^2\left(\frac{\pi t}{650}\right) + 1}} \right) \quad (3.34)$$

$$\frac{dy}{dt} = \frac{4\pi}{13} \cos\left(\frac{\pi t}{650}\right) - d \cdot \frac{8\pi^3 \sin\left(\frac{\pi t}{650}\right) \cos\left(\frac{\pi t}{650}\right)}{25 \left(16\pi^2 \cos^2\left(\frac{\pi t}{650}\right) + 169\right)^{\frac{3}{2}}} \quad (3.35)$$

$$\begin{aligned}
\frac{d^2x}{dt^2} = \frac{4\pi d}{13} & \left[ -\frac{\pi^2 \cos\left(\frac{\pi t}{650}\right)}{422500 \sqrt{\frac{16}{169} \pi^2 \cos^2\left(\frac{\pi t}{650}\right) + 1}} \right. \\
& - \frac{8\pi^4 \sin^2\left(\frac{\pi t}{650}\right) \cos\left(\frac{\pi t}{650}\right)}{17850625 \left(\frac{16}{169} \pi^2 \cos^2\left(\frac{\pi t}{650}\right) + 1\right)^{\frac{3}{2}}} \\
& + \cos\left(\frac{\pi t}{650}\right) \left[ \frac{4\pi^4 \cos^2\left(\frac{\pi t}{650}\right)}{17850625 \left(\frac{16}{169} \pi^2 \cos^2\left(\frac{\pi t}{650}\right) + 1\right)^{3/2}} \right. \\
& + \frac{192\pi^6 \sin^2\left(\frac{\pi t}{650}\right) \cos^2\left(\frac{\pi t}{650}\right)}{3016755625 \left(\frac{16}{169} \pi^2 \cos^2\left(\frac{\pi t}{650}\right) + 1\right)^{\frac{5}{2}}} \\
& \left. \left. - \frac{4\pi^4 \sin^2\left(\frac{\pi t}{650}\right)}{17850625 \left(\frac{16}{169} \pi^2 \cos^2\left(\frac{\pi t}{650}\right) + 1\right)^{\frac{3}{2}}} \right] \right]
\end{aligned} \tag{3.36}$$

$$\begin{aligned}
\frac{d^2y}{dt^2} = \frac{-2\pi^2}{4225 \sin\left(\frac{\pi t}{650}\right)} & \\
& - d \left[ \frac{4\pi^4 \cos^2\left(\frac{\pi t}{650}\right)}{17850625 \left(\frac{16}{169} \pi^2 \cos^2\left(\frac{\pi t}{650}\right) + 1\right)^{\frac{3}{2}}} \right. \\
& + \frac{192\pi^6 \sin^2\left(\frac{\pi t}{650}\right) \cos^2\left(\frac{\pi t}{650}\right)}{3016755625 \left(\frac{16}{169} \pi^2 \cos^2\left(\frac{\pi t}{650}\right) + 1\right)^{\frac{5}{2}}} \\
& \left. - \frac{4\pi^4 \sin^2\left(\frac{\pi t}{650}\right)}{17850625 \left(\frac{16}{169} \pi^2 \cos^2\left(\frac{\pi t}{650}\right) + 1\right)^{\frac{3}{2}}} \right]
\end{aligned} \tag{3.37}$$

Using these components, the radius of curvature  $R(t, l)$  can be determined, which is then used to calculate the second principal curvature on the surface of the sinusoidal cylinder:

$$\kappa_2 = \frac{1}{R(t, l)} \tag{3.38}$$

### 3.5.2 FFT-based calculation of principal image orientation

The principal orientations in the stack projections were determined using an image processing approach based on the discrete Fourier transform (DFT). First, the image,

or image section in case of a domain-wise analysis, was multiplied by a cosine-shaped windowing function (Figure 3.16a-b) to avoid artefacts in the power spectrum of the DFT that would otherwise appear due to the image boundaries (the DFT assumes periodicity at the image boundaries, which is not the case in general). Next, the fast Fourier transform (FFT) was applied and the power spectrum  $P$  was calculated as:

$$P = \log(|Y| + 1) \quad (3.39)$$

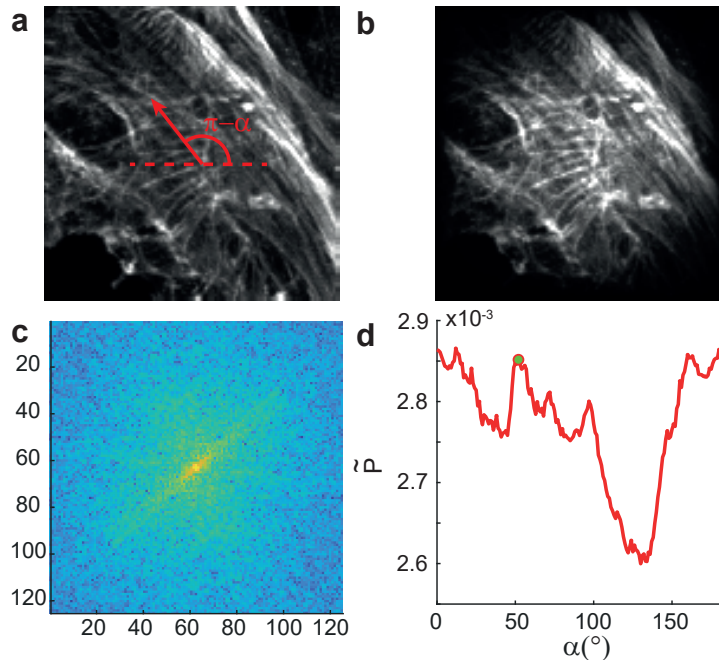


**Figure 3.16:** FFT-based approach to quantify image orientation. a) Original image section with principal orientation highlighted by the red arrow. b) Image after windowing operation. c) Power spectrum obtained after FFT on the image shown in b). d)  $\sum P_c(\alpha)$  vs.  $\alpha$  curve with peaks highlighted by red markers. The green marker corresponds to the peak with maximum prominence. The corresponding angle  $\alpha$  determines the principal orientation in the power spectrum.

where  $Y$  is the complex result of the FFT, shifted such that the low frequencies are situated in the centre of the spectrum (Figure 3.16c). The oriented components in the original image appear as oriented lines or ellipses in the power spectrum (albeit rotated by  $\pi/2$ ). The power spectrum was rotated in the range  $[0, \pi]$  and the sum of the power in the central columns was calculated for every instance of the rotated spectrum ( $\sum P_c(\alpha)$ ). This operation resulted in a  $\sum P_c(\alpha)$  vs.  $\alpha$  curve, in which several peaks could be detected (Figure 3.16d). The principal orientation in the power spectrum was found at the peak with the maximum prominence. To determine the strength of the orientation, the maximum prominence of the curve was divided by the sum of the prominences

of all the peaks in the  $\sum P_c(\alpha)$  vs.  $\alpha$  curve. To visualize the orientation distribution in the domain-wise analyses, the vectors were scaled by the orientation strength and mean intensity for that domain.

### 3.5.3 Additional figures

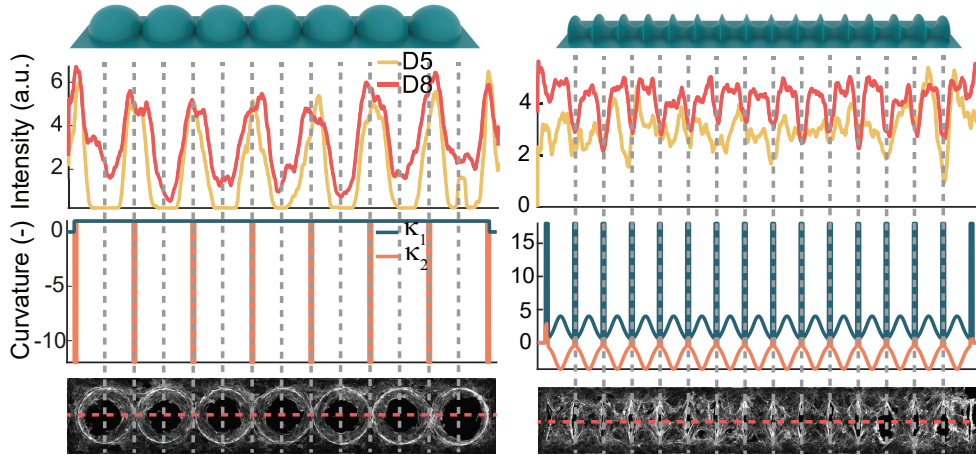


**Figure 3.17:** Spatial cell patterning on curved substrates. Normalized actin intensity at the midline of the convex spherical (left) and convex catenoidal (right) substrates. The normalized principal curvatures are indicated in the centre row plots.

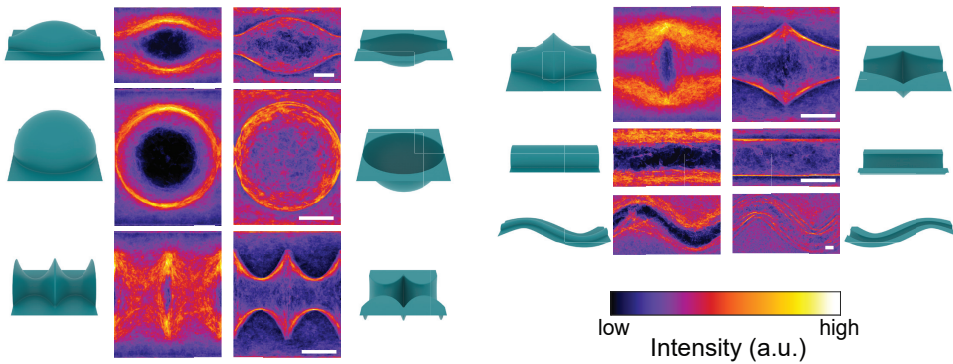


**Figure 3.18:** Normalized actin frequency maps for the convex (left) and concave (right) substrates on day 5. The scale bars represent  $100 \mu\text{m}$ .

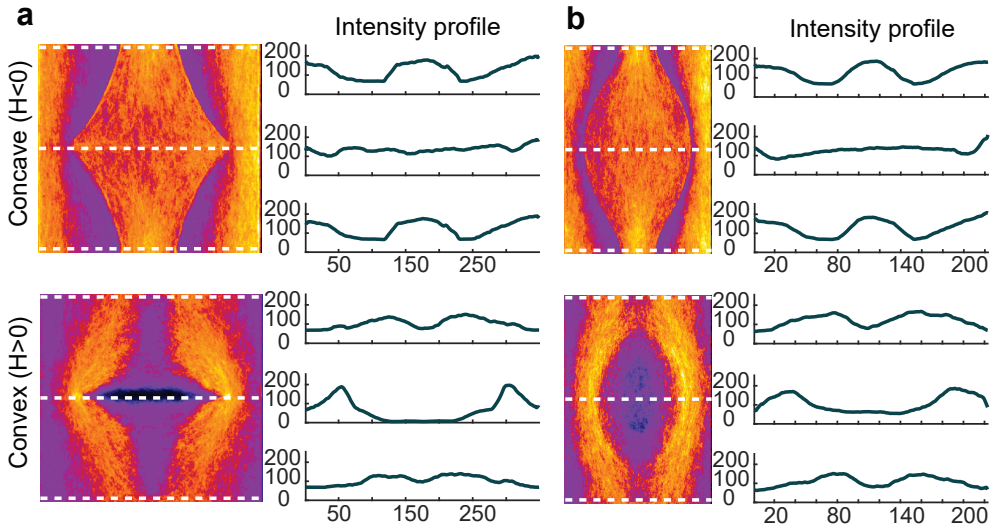


**Figure 3.19:** a) Actin intensity profiles at different locations obtained from the frequency map of the pseudospherical substrates at day 8 for the concave (top) and convex (bottom) variants. b) Similar representation as in a) but for the concave (top) and convex (bottom) unduloid substrates.

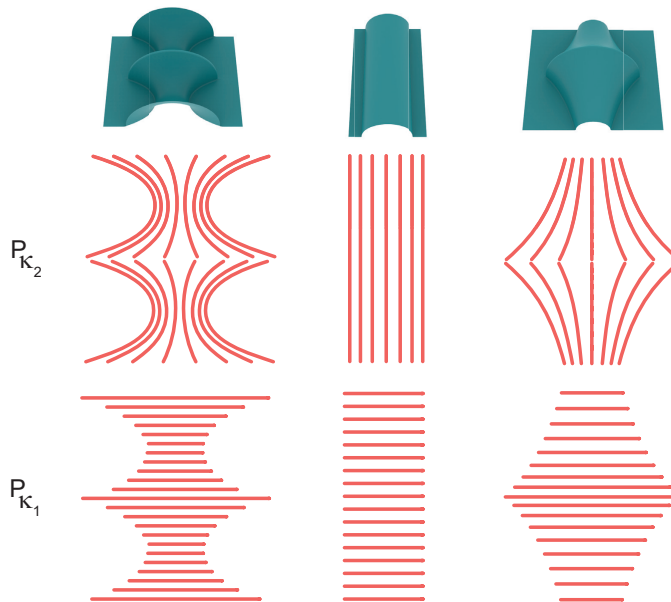


**Figure 3.20:** Principal directions for curved substrates. The two principal directions  $P_{\kappa_2}$  and  $P_{\kappa_1}$  corresponding to the minimum ( $\kappa_2$ ) and maximum ( $\kappa_1$ ) principal curvatures, respectively. From left to right: catenoids, cylinder, and pseudospheres.

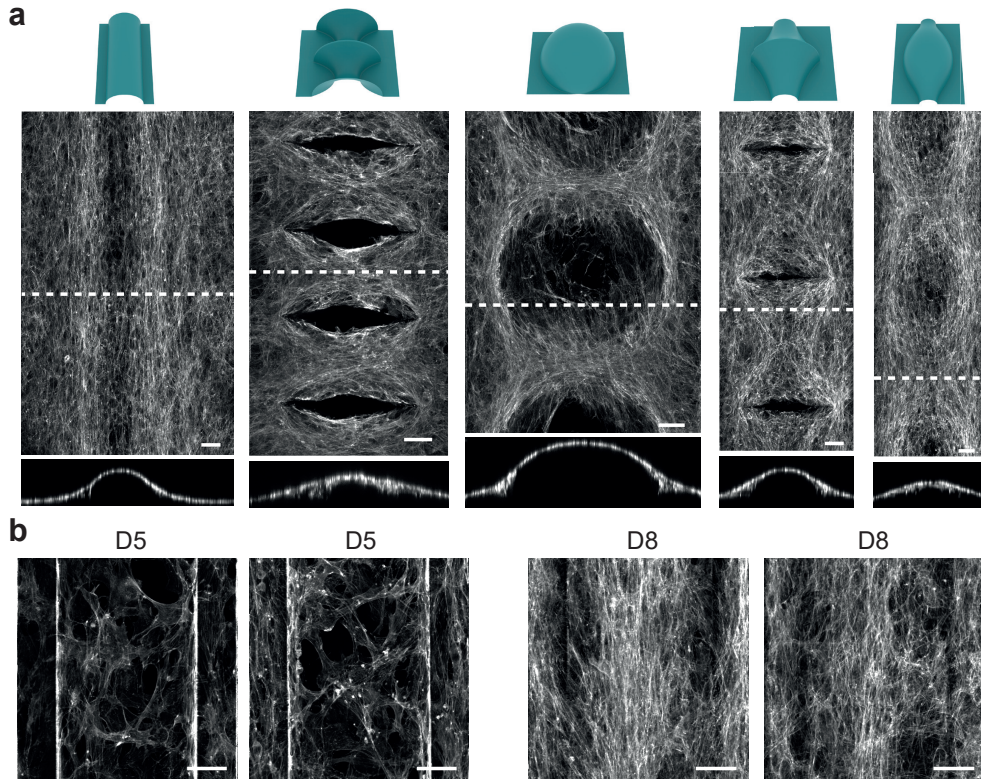


**Figure 3.21:** Cell sheet bridging on the convex and concave substrates. a) The convex-to-planar transition is a local concavity, which is collectively bridged by the cells. Images depict the maximum intensity projections and orthogonal views of the actin channel for the representative cases on day 8. From left to right: cylinder, catenoids, spheres, pseudospheres, and unduloid. b) Cell bridging on the concave cylindrical substrates. On day 5, the bridges are randomly oriented. On day 8, a longitudinal, collective SF alignment is observed.

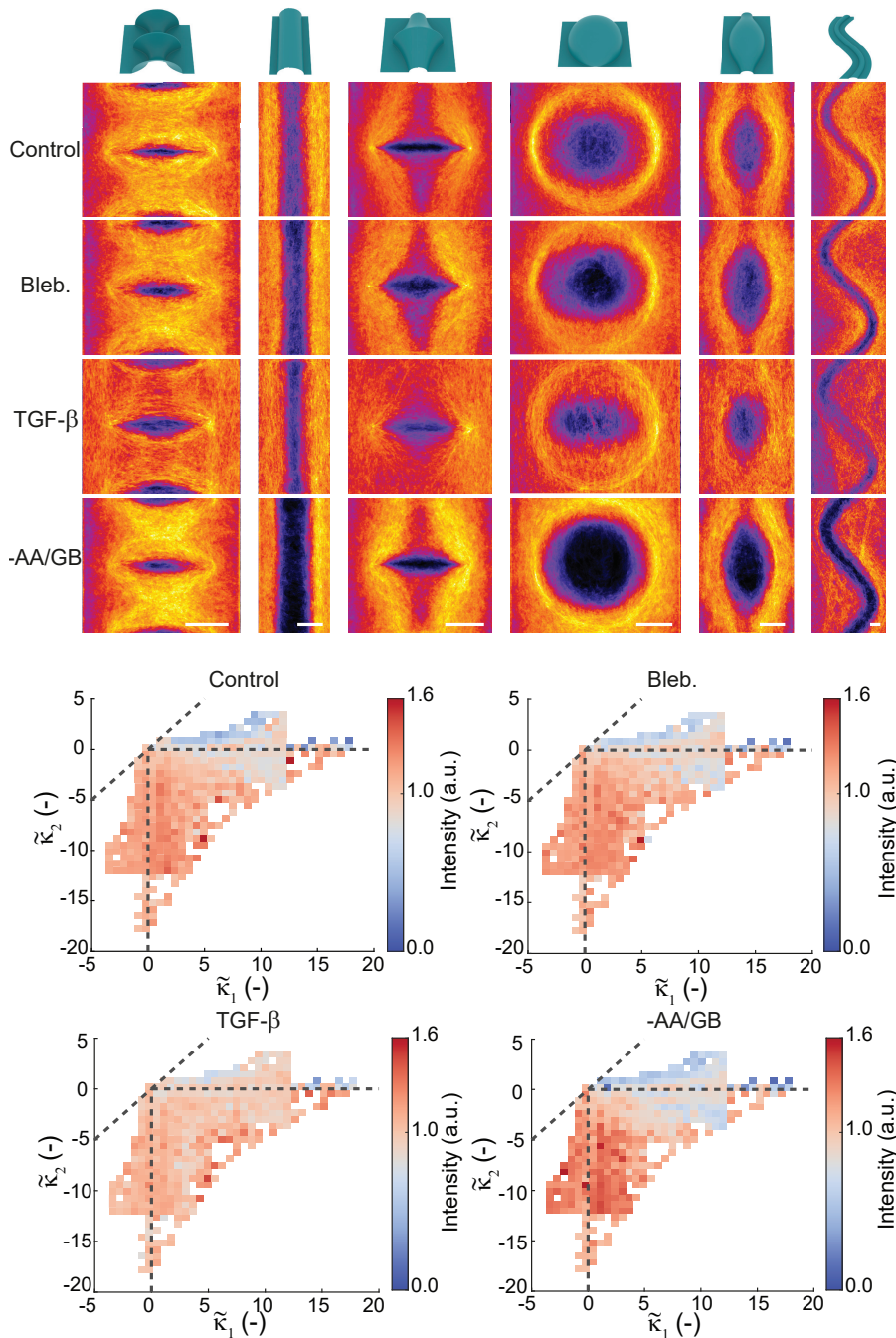


**Figure 3.22:** Frequency maps and intensity *versus* curvature. Frequency maps depicting the normalized actin signal for all the six convex substrates on day 8. Comparison between the control cells, cells treated with blebbistatin, cells treated with TGF- $\beta$ , and cells deprived of ascorbic acid (AA) and  $\beta$ -glycerophosphate (GB). The bottom row shows the heatmaps of the intensity *vs.* the two principal curvatures.

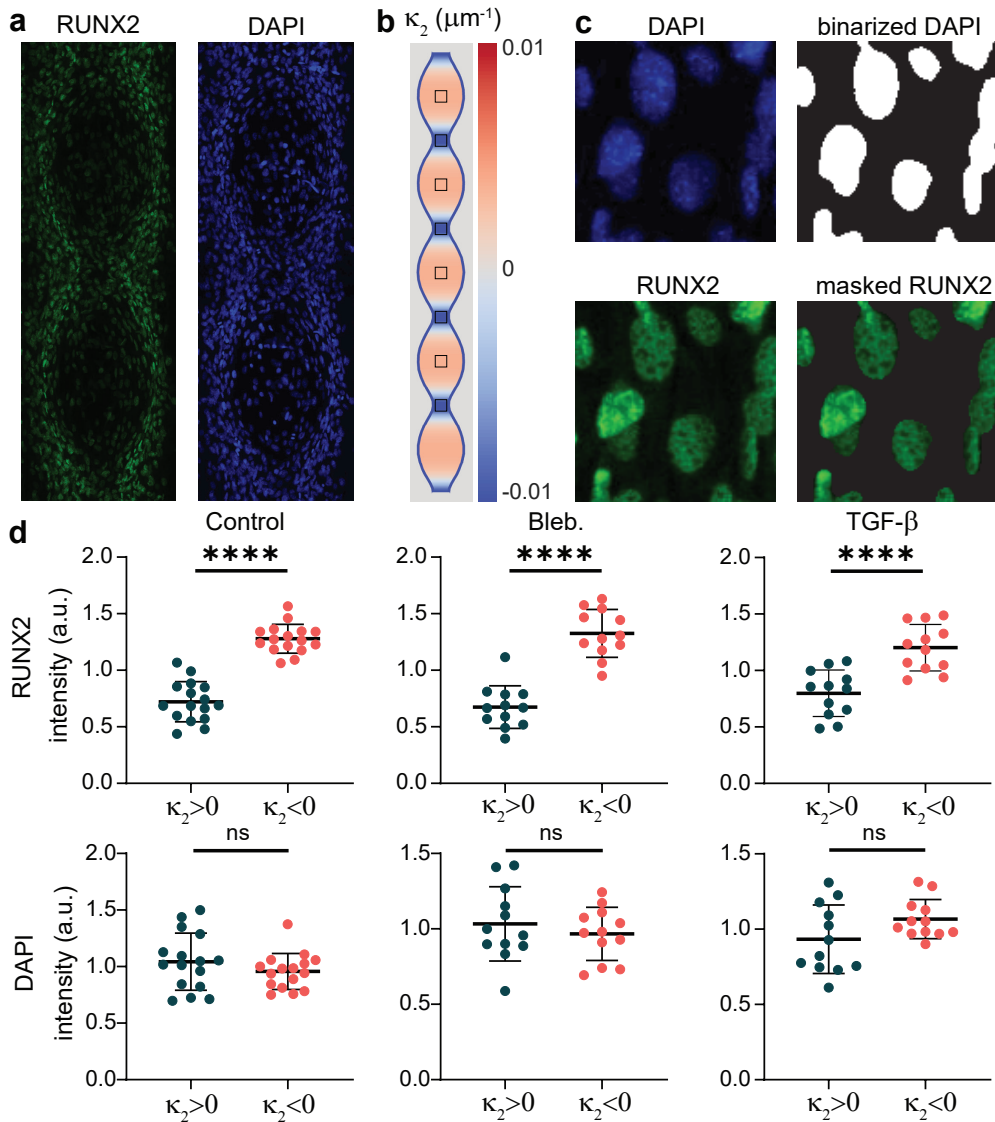


**Figure 3.23:** RUNX2 and DAPI intensity analysis on the convex unduloid. a) Representative images of RUNX2 and DAPI staining on a convex unduloid. Scale bar represents  $100 \mu\text{m}$ . b) Curvature map of the minimum principal curvature ( $\kappa_2$ ) of the convex unduloid. Squares ( $110 \times 110$  pixels) indicate the regions of interest (ROI) used in the subsequent analysis. c) Workflow to quantify DAPI and RUNX2 intensity. The ROI of the DAPI channel was binarized and used as a mask. Then, the mean intensity of the masked RUNX2 and DAPI images was calculated. d) RUNX2 (top row) and DAPI (bottom row) intensity *versus* the sign of the minimum principal curvature ( $\kappa_2$ ). The mean intensity of ROI was normalized with respect to the mean intensity of all ROIs within the same image. The plots indicate higher relative RUNX2 intensities for  $\kappa_2 < 0$  as opposed to  $\kappa_2 > 0$ , yet no significant difference in DAPI intensity between both cases. Unpaired two-tailed t-test, \*\*\*\*:  $p < 0.0001$ , ns: not significant.

## Bibliography

- [1] M. J. Bissell, H. G. Hall, and G. Parry. How does the extracellular matrix direct gene expression? *Journal of theoretical biology*, 99(1):31–68, 1982.
- [2] S. Van Helvert, C. Storm, and P. Friedl. Mechanoreciprocity in cell migration. *Nature cell biology*, 20(1):8, 2018.
- [3] R. V. Iozzo and M. A. Gubbiotti. Extracellular matrix: the driving force of mammalian diseases. *Matrix Biology*, 71:1–9, 2018.
- [4] C. Frantz, K. M. Stewart, and V. M. Weaver. The extracellular matrix at a glance. *Journal of cell science*, 123(24):4195–4200, 2010.
- [5] J. K. Mouw, G. Ou, and V. M. Weaver. Extracellular matrix assembly: a multiscale deconstruction. *Nature reviews Molecular cell biology*, 15(12):771, 2014.
- [6] M. J. Dalby, N. Gadegaard, and R. O. Oreffo. Harnessing nanotopography and integrin–matrix interactions to influence stem cell fate. *Nature materials*, 13(6):558, 2014.
- [7] V. Vogel and M. Sheetz. Local force and geometry sensing regulate cell functions. *Nature reviews Molecular cell biology*, 7(4):265, 2006.
- [8] S. J. Callens, R. J. Uyttendaele, L. E. Fratila-Apachitei, and A. A. Zadpoor. Substrate curvature as a cue to guide spatiotemporal cell and tissue organization. *Biomaterials*, 232:119739, 2020.
- [9] M. Werner, N. A. Kurniawan, and C. V. Bouten. Cellular geometry sensing at different length scales and its implications for scaffold design. *Materials*, 13(4):963, 2020.
- [10] A. A. Zadpoor. Bone tissue regeneration: the role of scaffold geometry. *Biomaterials Science*, 3(2):231–45, 2015.
- [11] W. Xi, T. B. Saw, D. Delacour, C. T. Lim, and B. Ladoux. Material approaches to active tissue mechanics. *Nature Reviews Materials*, page 1, 2018.
- [12] D. Hilbert and S. Cohn-Vossen. *Geometry and The Imagination*. Chelsea Publishing Company, New York, USA, 1990.
- [13] G. Dunn and J. Heath. A new hypothesis of contact guidance in tissue cells. *Experimental cell research*, 101(1):1–14, 1976.
- [14] M. Werner, A. Petersen, N. A. Kurniawan, and C. V. Bouten. Cell-perceived substrate curvature dynamically coordinates the direction, speed, and persistence of stromal cell migration. *Advanced Biosystems*, page 1900080, 2019.
- [15] N. D. Bade, R. D. Kamien, R. K. Assoian, and K. J. Stebe. Curvature and rho activation differentially control the alignment of cells and stress fibers. *Science advances*, 3(9):e1700150, 2017.
- [16] W. Xi, S. Sonam, T. B. Saw, B. Ladoux, and C. T. Lim. Emergent patterns of collective cell migration under tubular confinement. *Nature communications*, 8(1):1517, 2017.
- [17] H. G. Yevick, G. Duclos, I. Bonnet, and P. Silberzan. Architecture and migration of an epithelium on a cylindrical wire. *Proceedings of the National Academy of Sciences*, 112(19):5944–5949, 2015.
- [18] N. D. Bade, T. Xu, R. D. Kamien, R. K. Assoian, and K. J. Stebe. Gaussian curvature directs stress fiber orientation and cell migration. *Biophys J*, 114(6):1467–1476, 2018.
- [19] L. Pieuchot, J. Marteau, A. Guignandon, T. Dos Santos, I. Brigaud, P.-F. Chauvy, T. Cloatre, A. Ponche, T. Petithory, P. Rougerie, M. Vassaux, J.-L. Milan, N. T. Wakhloo, A. Spangenberg, M. Bigerelle, and K. Anselme. Curvotaxis directs cell migration through cell-scale curvature landscapes. *Nature communications*, 9(1):3995, 2018.
- [20] Y. Biton and S. Safran. The cellular response to curvature-induced stress. *Physical biology*, 6(4):046010, 2009.
- [21] M. Vassaux, L. Pieuchot, K. Anselme, M. Bigerelle, and J.-L. Milan. A biophysical model for curvature-guided cell migration. *Biophysical journal*, 117(6):1136–1144, 2019.
- [22] J. A. Sanz-Herrera, P. Moreo, J. M. García-Aznar, and M. Doblaré. On the effect of substrate curvature on cell mechanics. *Biomaterials*, 30(34):6674–6686, 2009.
- [23] M. A. Alias and P. R. Buenzli. Modeling the effect of curvature on the collective behavior of cells growing new tissue. *Biophysical journal*, 112(1):193–204, 2017.
- [24] E. M. Levina, L. V. Domnina, Y. A. Rovensky, and J. M. Vasiliev. Cylindrical substratum induces different patterns of actin microfilament bundles in nontransformed and in ras-transformed epithe-

- liocytes. *Experimental cell research*, 229(1):159–165, 1996.
- [25] Y. Rovinsky and V. Samoilov. Morphogenetic response of cultured normal and transformed fibroblasts, and epitheliocytes, to a cylindrical substratum surface. possible role for the actin filament bundle pattern. *Journal of cell science*, 107(5):1255–1263, 1994.
- [26] J. Y. Park, D. H. Lee, E. J. Lee, and S.-H. Lee. Study of cellular behaviors on concave and convex microstructures fabricated from elastic pdms membranes. *Lab on a Chip*, 9(14):2043–2049, 2009.
- [27] V. Malheiro, F. Lehner, V. Dinca, P. Hoffmann, and K. Maniura-Weber. Convex and concave microstructured silicone controls the shape, but not the polarization state of human macrophages. *Biomaterials science*, 4(11):1562–1573, 2016.
- [28] M. Rumpler, A. Woesz, J. W. Dunlop, J. T. van Dongen, and P. Fratzl. The effect of geometry on three-dimensional tissue growth. *J R Soc Interface*, 5(27):1173–80, 2008.
- [29] C. M. Bidan, K. P. Kommareddy, M. Rumpler, P. Kollmannsberger, Y. J. Brechet, P. Fratzl, and J. W. Dunlop. How linear tension converts to curvature: geometric control of bone tissue growth. *PLoS One*, 7(5):e36336, 2012.
- [30] S. Ehrig, B. Schamberger, C. Bidan, A. West, C. Jacobi, K. Lam, P. Kollmannsberger, A. Petersen, P. Tomancak, and K. Kommareddy. Surface tension determines tissue shape and growth kinetics. *Science Advances*, 5(9):eaav9394, 2019.
- [31] K. Kwapiszewska, K. Żukowski, R. Kwapiszewski, and Z. Brzózka. Double casting prototyping with a thermal aging step for fabrication of 3D microstructures in poly (dimethylsiloxane). *AIMS Biophys*, 3(4):553–562, 2016.
- [32] J. Schindelin, I. Arganda-Carreras, E. Frise, V. Kaynig, M. Longair, T. Pietzsch, S. Preibisch, C. Rueden, S. Saalfeld, and B. Schmid. Fiji: an open-source platform for biological-image analysis. *Nature methods*, 9(7):676–682, 2012.
- [33] B. Schmid, P. Tripal, T. Fraaß, C. Kersten, B. Ruder, A. Grüneboom, J. Huisken, and R. Palmisano. 3Dscript: animating 3D/4D microscopy data using a natural-language-based syntax. *Nature methods*, 16(4):278–280, 2019.
- [34] C. M. Bidan, P. Kollmannsberger, V. Gering, S. Ehrig, P. Joly, A. Petersen, V. Vogel, P. Fratzl, and J. W. Dunlop. Gradual conversion of cellular stress patterns into pre-stressed matrix architecture during in vitro tissue growth. *Journal of The Royal Society Interface*, 13(118):20160136, 2016.
- [35] S. Callens. Chapter 3 - si movies. 4tu.researchdata online resource. <https://figshare.com/s/36c76d489b92f4265275>, 2021.
- [36] K. Grosse-Brauckmann. Triply periodic minimal and constant mean curvature surfaces. *Interface focus*, 2(5):582–588, 2012.
- [37] C. M. Bidan, K. P. Kommareddy, M. Rumpler, P. Kollmannsberger, P. Fratzl, and J. W. Dunlop. Geometry as a factor for tissue growth: towards shape optimization of tissue engineering scaffolds. *Advanced Healthcare Materials*, 2(1):186–94, 2013.
- [38] M. Werner, S. B. Blanquer, S. P. Haimi, G. Korus, J. W. Dunlop, G. N. Duda, D. W. Grijpma, and A. Petersen. Surface curvature differentially regulates stem cell migration and differentiation via altered attachment morphology and nuclear deformation. *Adv Sci*, 4(2):1600347, 2017.
- [39] T. Yamashita, P. Kollmannsberger, K. Mawatari, T. Kitamori, and V. Vogel. Cell sheet mechanics: How geometrical constraints induce the detachment of cell sheets from concave surfaces. *Acta biomaterialia*, 45:85–97, 2016.
- [40] N. Tanaka, T. Yamashita, Y. Yalikus, S. Amaya, A. Sato, V. Vogel, and Y. Tanaka. An ultra-small fluid oscillation unit for pumping driven by self-organized three-dimensional bridging of pulsatile cardiomyocytes on elastic micro-piers. *Sensors and Actuators B: Chemical*, 293:256–264, 2019.
- [41] M. Werner, N. A. Kurniawan, G. Korus, C. V. Bouten, and A. Petersen. Mesoscale substrate curvature overrules nanoscale contact guidance to direct bone marrow stromal cell migration. *Journal of The Royal Society Interface*, 15(145):20180162, 2018.
- [42] S. R. K. Vedula, M. C. Leong, T. L. Lai, P. Hersen, A. J. Kabla, C. T. Lim, and B. Ladoux. Emerging modes of collective cell migration induced by geometrical constraints. *Proceedings of the National Academy of Sciences*, 109(32):12974–12979, 2012.
- [43] L. D. Quarles, D. A. Yohay, L. W. Lever, R. Caton, and R. J. Wenstrup. Distinct proliferative and dif-

- ferentiated stages of murine mc3t3-e1 cells in culture: An in vitro model of osteoblast development. *Journal of Bone and Mineral Research*, 7(6):683–692, 1992.
- [44] F. Langenbach and J. Handschel. Effects of dexamethasone, ascorbic acid and  $\beta$ -glycerophosphate on the osteogenic differentiation of stem cells in vitro. *Stem cell research & therapy*, 4(5):1–7, 2013.
- [45] J.-B. Park. The effects of dexamethasone, ascorbic acid, and  $\beta$ -glycerophosphate on osteoblastic differentiation by regulating estrogen receptor and osteopontin expression. *Journal of Surgical Research*, 173(1):99–104, 2012.
- [46] D. E. Discher, P. Janmey, and Y.-I. Wang. Tissue cells feel and respond to the stiffness of their substrate. *Science*, 310(5751):1139–1143, 2005.
- [47] S. Van Bael, Y. C. Chai, S. Truscetto, M. Moesen, G. Kerckhofs, H. Van Oosterwyck, J.-P. Kruth, and J. Schrooten. The effect of pore geometry on the in vitro biological behavior of human periosteum-derived cells seeded on selective laser-melted ti6al4v bone scaffolds. *Acta biomaterialia*, 8(7):2824–2834, 2012.
- [48] X. Wang, S. Xu, S. Zhou, W. Xu, M. Leary, P. Choong, M. Qian, M. Brandt, and Y. M. Xie. Topological design and additive manufacturing of porous metals for bone scaffolds and orthopaedic implants: A review. *Biomaterials*, 83:127–141, 2016.
- [49] S. A. Yavari, J. van der Stok, Y. C. Chai, R. Wauthle, Z. T. Birgani, P. Habibovic, M. Mulier, J. Schrooten, H. Weinans, and A. A. Zadpoor. Bone regeneration performance of surface-treated porous titanium. *Biomaterials*, 35(24):6172–6181, 2014.
- [50] S. J. Hollister. Porous scaffold design for tissue engineering. *Nat Mater*, 4(7):518–524, 2005.
- [51] M. Paris, A. Gotz, I. Hettrich, C. M. Bidan, J. W. C. Dunlop, H. Razi, I. Zizak, D. W. Hutmacher, P. Fratzl, G. N. Duda, W. Wagermaier, and A. Cipitria. Scaffold curvature-mediated novel biomineralization process originates a continuous soft tissue-to-bone interface. *Acta Biomaterialia*, 60:64–80, 2017.
- [52] J. Dunlop, G. Zickler, R. Weinkamer, F. Fischer, and P. Fratzl. The emergence of complexity from a simple model for tissue growth. *Journal of Statistical Physics*, pages 1–15, 2019.
- [53] M. Hadzhilazova, I. M. Mladenov, and J. Oprea. Unduloids and their geometry. *Archivum mathematicum*, 43(5):417–429, 2007.





# A GEOMETRIC TAKE ON BONE AND SCAFFOLDS

---

4	THE LOCAL AND GLOBAL GEOMETRY OF TRABECULAR BONE	111
4.1	Introduction	112
4.2	Materials & methods	113
4.3	Results	120
4.4	Discussion	135
4.5	Supporting information	137
	Bibliography	146
5	TUNING METAMATERIALS USING HYPERBOLIC TILINGS	147
5.1	Introduction	148
5.2	Materials & Methods	149
5.3	Results	153
5.4	Discussion	167
5.5	Supporting information	171
	Bibliography	174

---



# 4

## THE LOCAL AND GLOBAL GEOMETRY OF TRABECULAR BONE

The organization and shape of the microstructural elements of trabecular bone govern its physical properties, are implicated in bone disease, and serve as blueprints for biomaterial design. To devise fundamental structure-property relationships and design bone-mimicking biomaterials, it is essential to characterize trabecular bone structure from the perspective of geometry, the mathematical study of shape. Using microcomputed tomography images from 70 donors at five different sites, we analyze the local and global geometry of human trabecular bone in detail, respectively by quantifying surface curvatures and Minkowski functionals. We find that curvature density maps provide distinct and sensitive shape fingerprints for bone from different sites. Contrary to a common assumption, these curvature maps also show that bone morphology does not approximate a minimal surface but exhibits a much more intricate curvature landscape. At the global (or integral) perspective, our Minkowski analysis illustrates that trabecular bone exhibits other types of anisotropy/ellipticity beyond interfacial orientation, and that anisotropy varies substantially within the trabecular structure. Moreover, we show that the Minkowski functionals unify several traditional morphometric indices. Our geometric approach to trabecular morphometry provides a fundamental language of shape that could be useful for bone failure prediction, understanding geometry-driven tissue growth, and the design of geometrically complex tissue scaffolds.

S. J. P. Callens, D. C. B. Tourolle, R. Müller, A. A. Zadpoor, The local and global geometry of trabecular bone, *bioRxiv*, 2020. (in revision)

## 4.1 Introduction

Many natural and man-made materials are characterized by a complex and often hierarchical spatial architecture. A well-known biological example of such a spatially structured material is trabecular bone, exhibiting a characteristic sponge-like morphology<sup>1</sup>. The quantitative morphological characterization of trabecular bone and other structured materials is essential in the study of these systems, for two primary reasons<sup>2</sup>. First, the morphology or architecture of many materials is often the outcome of a biological or physical process. The study of such morphologies, therefore, provides insight into the mechanisms governing their formation. In trabecular bone, for example, the organization of the microstructure is driven by external loading, and changes in the morphology can be indicative of bone diseases, such as osteoporosis<sup>3–5</sup>. Second, the morphology of spatially complex materials can strongly affect their physical properties, making morphological characterization indispensable for establishing structure-property relationships. For example, this intimate structure-property connection is what enables foams and metamaterials to attain their unique properties<sup>6</sup>. Moreover, material morphology can also directly elicit biological responses in biomaterials, affecting aspects such as cell migration, cell fate and spatial tissue organization<sup>7–10</sup>.

In the context of trabecular bone, the importance of the microarchitecture has long been recognized, and many morphometric indices have been proposed<sup>11</sup>. However, such indices typically only quantify a particular morphological aspect, such as density, thickness, or interfacial anisotropy, and often lack a fundamental geometric foundation or interpretation<sup>12</sup>. For example, the well-known structure model index (SMI), which classifies trabecular bone by its rod-like or plate-like nature<sup>13;14</sup>, is known to be conceptually flawed by its inability to capture all types of naturally-occurring shapes within the trabecular structure<sup>13;14</sup>. Moreover, calculating the same metric using different software tools often provides significantly different results, owing to substantial variations in the algorithm implementations<sup>15;16</sup>. Hence, there is a need for a unifying, robust approach to quantitatively characterize the shape of complex materials, including trabecular bone. Such a well-defined, mathematical framework is established in the realms of differential and integral geometry, providing fundamental descriptors of local and global shape. Local shape can be accurately captured using the concept of surface curvature. For any small neighborhood on a surface, the mean and Gaussian curvatures, defined in terms of the principal curvatures, capture the most fundamental shape information. The magnitudes and signs of these measures characterize the local convexity/concavity or the sphere-like *vs.* saddle-like character of the surface. Global shape, on the other hand, can be characterized by the so-called Minkowski functionals (MF). MF are versatile shape indices with strong roots in integral geometry, capable of robustly quantifying different aspects of spatial structure<sup>2;17;18</sup>. These shape indices, which can be of scalar or tensorial nature, are fundamental in the sense that they form a basis for any other additive functional that describes the shape of a 3D body (Hadwiger-Alesker theorems)<sup>19–21</sup>.

These mathematically defined shape metrics have been used to quantify the struc-

ture of complex, inanimate materials, such as blends undergoing spinodal decomposition<sup>22</sup> or granular packings<sup>17</sup>, but have not yet been used to characterize trabecular bone. Here, we applied these local and global shape measures to hundreds of micro-computed tomography ( $\mu$ CT) scans obtained from bone biopsies of 70 donors at five anatomical sites<sup>5</sup>. At the local level, we computed the mean, Gaussian and net curvatures of the trabecular bone interfaces. We observed that the spatial curvature distributions are sensitive to differences in bone microarchitecture from different sites. At the global level, we computed the scalar and tensorial MF, and compared them with traditional morphometric indices. We focused on the more potent tensorial MF that can sensitively quantify the various types of intrinsic anisotropy, which is highly relevant in the study of trabecular bone<sup>23;24</sup>. By using these fundamental shape descriptors, and reconciling them with previous metrics, we provide a novel geometric perspective on trabecular morphometry, that is also compatible with virtually every other type of complex microstructure, including tissue engineering scaffolds and architected biomaterials. As such, our approach does not only offer new insights into trabecular morphology, but also provides a more unified “language of shape” that is useful in the design of bone-mimicking biomaterials<sup>25</sup>.

## 4.2 Materials & methods

### 4.2.1 Trabecular bone data set

All analyses were performed using previously-published, high-resolution  $\mu$ CT data from the European Union BIOMED I Concerted Action “Assessment of Bone Quality in Osteoporosis”. The details of the database composition and data acquisition protocols can be found elsewhere<sup>5;26</sup>. Briefly, the data set comprised trabecular bone biopsies harvested from 70 donors (38 male, 32 female, age between 23 and 92 years) at five anatomical sites: the femoral head (FH), the iliac crest (IC), the calcaneus (CA), the second lumbar vertebra (L2), and the fourth lumbar vertebra (L4). The specimens were scanned using a high-resolution  $\mu$ CT system ( $\mu$ CT 20, Scanco Medical AG, Switzerland) with a spatial resolution of 28  $\mu$ m and cubic voxels with 14  $\mu$ m length (for the CA samples, cubic voxels with an edge length of 28  $\mu$ m were used). A 4 mm<sup>3</sup> cubic volume of interest (VOI) was selected from the resulting scanned data, and 3D binary images of the mineralized bone phase were obtained after Gaussian filtering and thresholding. These binary images served as the basis for all consecutive analyses.

### 4.2.2 Surface reconstruction

The binary volume data was processed using custom Python codes and Python-based mesh processing libraries<sup>27;28</sup>. First, a triangle mesh of the trabecular bone surface was reconstructed from the volume data using a marching cubes algorithm with a spacing equal to the voxel size (Figure 4.1a)<sup>29</sup>. No padding was applied to the volume data prior to the marching cubes algorithm, ensuring that only the trabecular interface was meshed and resulting in a mesh that was a 2-manifold with boundary (Figure 4.1c). Next, degenerate (zero-area) faces and small disconnected components were removed

from the mesh. To account for the roughness inherent in marching cubes meshes, the triangle meshes were smoothed using implicit fairing. This is an efficient smoothing approach that is based on the implicit integration of a diffusion process, and guarantees volume preservation during smoothing<sup>30</sup>. The algorithm solves the linear system:

$$(I - \lambda dt L)M^{n+1} = M^n \quad (4.1)$$

where  $M^n$  represents the set of mesh vertices at iteration  $n$ ,  $L$  represents the Laplacian, and  $\lambda dt$  is a user-defined smoothing constant. The trabecular bone meshes were all smoothed using a single iteration and  $\lambda dt = 5$ , enabling the smoothing of the marching cubes artefacts while maintaining small curved features on the trabecular bone surfaces.

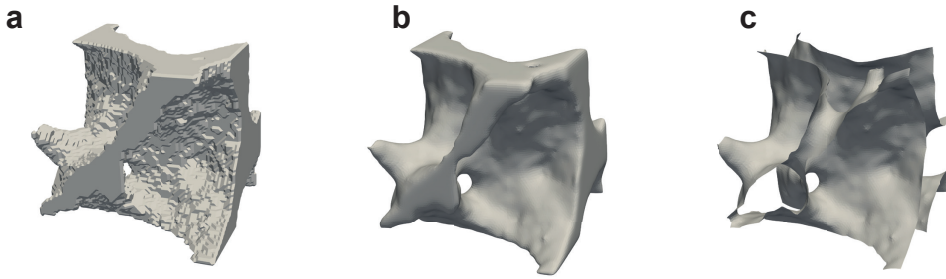


**Figure 4.1:** Trabecular bone surface reconstruction. a) Triangle mesh obtained by applying the marching cubes algorithm to padded binary image data, for a small section of an FH trabecular sample. b) Triangle mesh after smoothing using implicit fairing. c) Smoothed triangle mesh without padding, representing the trabecular interface that is considered in this study.

### 4.2.3 Curvature estimation algorithm

The principal curvatures of the trabecular bone surface were estimated at every vertex of the discrete triangle mesh using an efficient multiscale fitting algorithm<sup>27;31</sup>. The applied algorithm was an adaption of the Osculating Jets method<sup>32</sup>, and fitted a second-order polynomial to a local neighborhood around every vertex for the curvature estimation. The local neighborhood was defined as a ball with a user-defined radius, which was centered at the vertex of interest. For the FH, IC, L2, and L4 trabecular bone meshes, the radius was defined as:

$$r = 10\langle e \rangle \quad (4.2)$$

where  $\langle e \rangle$  represents the average mesh edge length for a particular bone specimen ( $\langle e \rangle \approx 20\mu m$ ). In the case of the CA meshes, which were scanned with a larger voxel size, the radius was set to  $r = 5\langle e \rangle$ , corresponding to a similarly-sized neighborhood as compared to the other bone specimens. The sensitivity of the curvature estimation algorithm to the neighborhood size ( $r$ ) and smoothing parameter ( $\lambda dt$ ) was assessed by

calculating the interface shape distributions (ISD) for a representative sample at different combinations of  $r$  and  $\lambda dt$ , and by visualizing color-coded curvature distributions on the triangle meshes (Figure 4.2 and Figure 4.3).

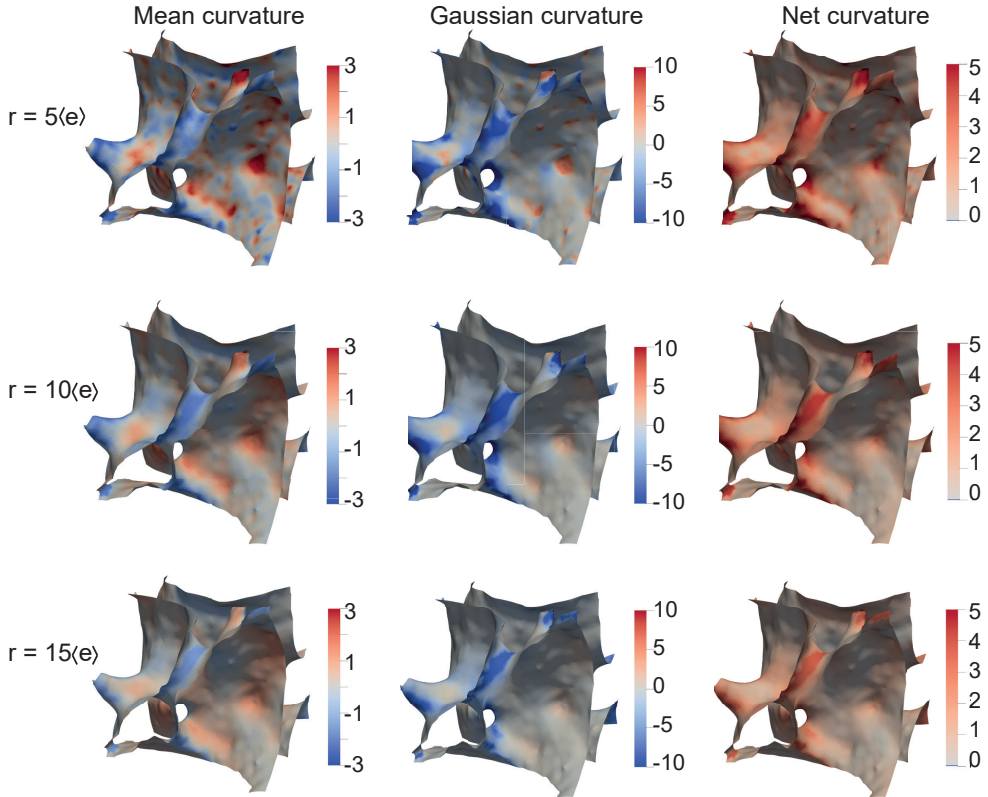


**Figure 4.2:** Effect of local neighborhood on curvature estimation. Visualization of mean (left), Gaussian (middle) and net (right) curvature on a small section of an FH trabecular bone sample, showing the effect of different local neighborhoods (defined as a factor multiplied with average edge length). Top row:  $r = 5\langle e \rangle$ , middle row:  $r = 10\langle e \rangle$ , bottom row:  $r = 15\langle e \rangle$ . In this study  $r = 10\langle e \rangle$  for the curvature computations (except for the CA samples, where  $r = 5\langle e \rangle$  due to the larger edge length).

#### 4.2.4 Curvature probability density distributions

All reported curvatures were non-dimensionalized using a characteristic length parameter<sup>33</sup>:

$$S_v = \frac{S}{V} \quad (4.3)$$

where  $S$  is the total mesh area and  $V=4^3 \text{ mm}^3$  is the volume of the cubic specimen. Face curvature values were calculated by averaging the curvatures of the three vertices

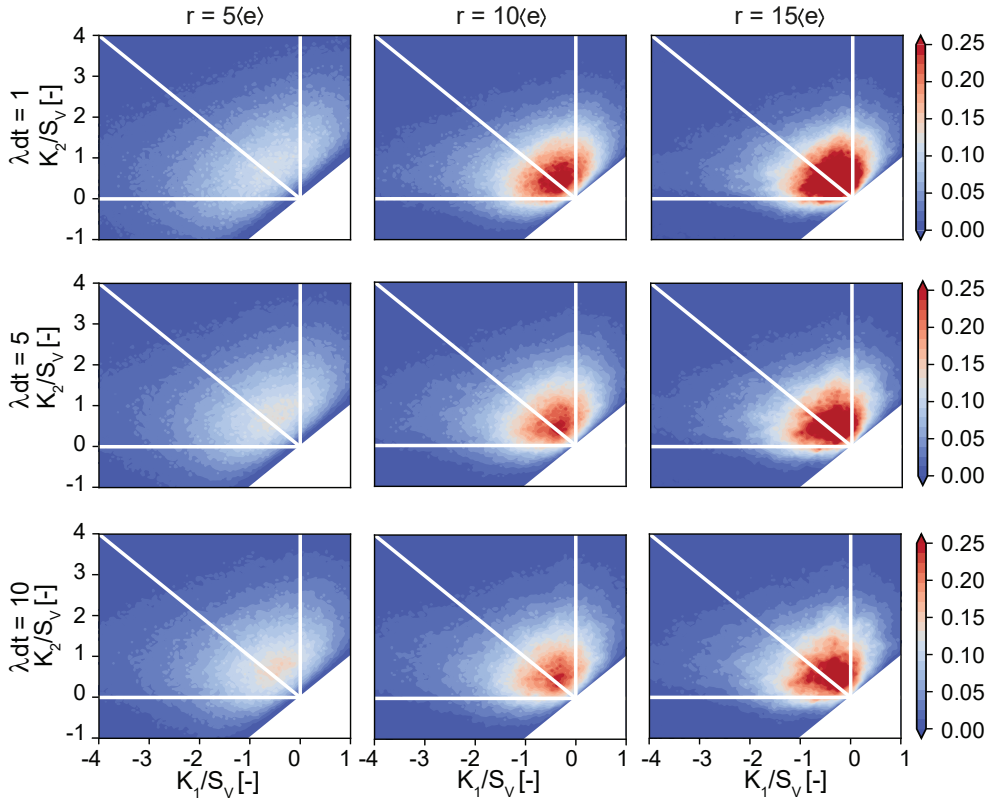


**Figure 4.3:** Sensitivity of the ISD to curvature neighborhood and mesh smoothness. Principal curvature ISD for a representative IC sample at different values of curvature neighborhood ( $r = 5(e), 10(e), 15(e)$ ) and smoothing parameter ( $\lambda dt = 1, 5, 10$ ).

associated with every face. In constructing the probability density distributions of curvature, the face curvatures were weighted by their face area. In case of the interface shape distributions (ISD), this implied that the ratio of the face areas with a certain combination of curvature to the total mesh area was considered. For example, in case of the ISD of the principal curvature, this means<sup>34</sup>:

$$P_{ISD}(\kappa_1, \kappa_2) = \frac{A(\kappa_1, \kappa_2)}{A_{Total}} \quad (4.4)$$

#### 4.2.5 Radial distribution function of curvature

The radial distribution functions (RDF) of the mean and Gaussian curvatures were computed, by considering the curvature values in the range of the 0.5 percentile and the 99.5 percentile. These curvature values were binned in 100 bins of equal width and were weighted by their face areas. Since the RDF considers the curvatures of face pairs separated by a given distance, a characteristic distance was defined in function of the previously described characteristic length scale  $S_v$ :

$$r = \tilde{r}S_v^{-1} \quad (4.5)$$

where  $\tilde{r}$  is a user-defined length parameter. In order to find face pairs, a spherical shell of nominal radius  $r$  and thickness  $\Delta r$  was centered around the barycenter of every sample face of interest, where:

$$\Delta r = \frac{1}{10}S_v^{-1} \quad (4.6)$$

All faces with barycenters inside the spherical shell were considered as paired faces to the sampled face. For every bin, 1000 unique random faces were selected and the curvatures of the corresponding paired faces were computed and stored in area-weighted histograms with 100 bins of equal width. If the bin contained less than 1000 faces, which could occur at the extreme values of the curvature range, all available faces were used as sample points in the RDF. By sampling every bin, and combining the corresponding area-weighted curvature histograms of the paired faces, the RDF was constructed as a  $100 \times 100$  matrix with probability values.

#### 4.2.6 Minkowski structure metrics

The Minkowski functionals (scalars  $W_v$ , tensors  $W_v^{r,s}$ ) and the rotational invariants of the irreducible Minkowski tensors (IMT) ( $q_s$  and  $w_s$ ) were computed on the trabecular triangle meshes using a C++ code (<https://github.com/morphometry/karambola>) that iterates over all faces, edges, or vertices to compute the relevant Minkowski metrics, in accordance with Table 2 of reference<sup>20</sup>. In order to prepare the trabecular bone meshes for the Minkowski metric computation, the non-manifold edges and vertices that could result after the marching cubes reconstruction had to be removed. The non-manifold edges were removed by constructing the face adjacency matrix of the mesh and removing those faces with edges shared by more than two faces. Non-manifold vertices that remained after the deletion of non-manifold edges were removed using Meshlab<sup>35</sup>. Of the six relevant Minkowski tensors, only the tensors  $W_1^{0,2}$  and  $W_2^{0,2}$  are translation-invariant tensors, which means that:

$$W_v^{r,s}(B \cup t) = W_v^{r,s}(B) \quad (4.7)$$

where  $B \cup t$  signifies the translation of body  $B$  along vector  $t^{20}$ . The other Minkowski tensors are translation-covariant, and do not satisfy this relationship. For those translation-covariant tensors, a consistent definition of the mesh origin is required to enable a fair comparison between the different meshes. For all the trabecular bone meshes, the origin was defined to be in the center of the cubic bounding box.

In order to deal with the open trabecular bone meshes, a domain-wise analysis of the Minkowski metrics was performed. To this end, the faces at the boundaries of the

mesh were assigned a different label than the faces inside the trabecular surface, and the Minkowski metrics were computed for each labeled domain separately. In this way, the faces not on the boundary are effectively considered to be part of a “closed” surface, and all the relevant Minkowski metrics could be calculated, which is not the case for the “open” boundary faces<sup>20</sup>. Representing a mesh as a doubly-connected edge list (DCEL), the boundary faces are those faces with at least one half-edge that appears only once in list (*i.e.*, it is not shared with another face). A visual representation of the boundary face labeling is provided in Figure 4.4a.

#### 4.2.7 Spatial decomposition

A domain-wise Minkowski analysis was performed on spatially decomposed meshes. The mesh was subdivided into a  $3 \times 3 \times 3$  cubic grid, and all faces were assigned a label based on the location in the grid, resulting in a total of 28 different labels (27 labels for the grid domains and one label for the boundary, see Figure 4.4b). The relative difference between the local and global DA was defined as:

$$\tilde{\lambda}_v^{r,s} = \frac{\frac{|\lambda_v^{r,s}|_{min}}{|\lambda_v^{r,s}|_{max}} - \frac{|\lambda_v^{r,s}|_{min}}{|\lambda_v^{r,s}|_{max}}}{\frac{|\lambda_v^{r,s}|_{min}}{|\lambda_v^{r,s}|_{max}}} \quad (4.8)$$

Here,  $\frac{|\lambda_v^{r,s}|_{min}}{|\lambda_v^{r,s}|_{max}}$  defines the ratio of the minimal to the maximal eigenvalue of the tensor  $W_v^{r,s}$ , while  $\langle \cdot \rangle$  refers to the average value.

For the calculation of the quadratic and cubic invariants of the irreducible Minkowski tensors (IMT), the rank  $s$  was in the range of  $[0, 8]$ .

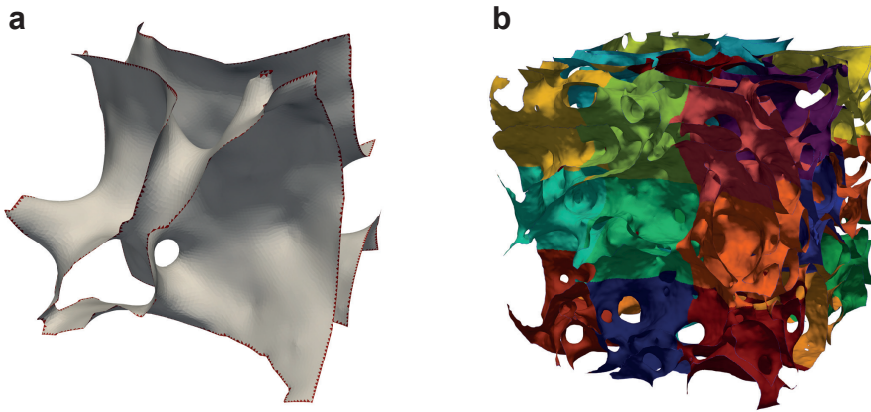


**Figure 4.4:** Mesh labeling for Minkowski analysis. a) boundary detection in a small example mesh. Red faces are detected as being on the boundary, and are labeled differently than the white faces within the surface. b) Spatial subdivision of a trabecular sample (FH) into 27 equal-size subdomains. Each domain is given a different label for the Minkowski analysis.

### 4.2.8 Ellipsoid representation of tensors

The rank-2 Minkowski and MIL tensors were visualized by ellipsoid surfaces, with radii and directions that were defined by the eigenvalues and eigenvectors of the tensors, respectively<sup>36;37</sup>. The surface of an arbitrarily oriented ellipsoid, centered at the origin is obtained by solving the following expression for  $\mathbf{x}$ :

$$\mathbf{x}^T \mathbf{M} \mathbf{x} = 1 \quad (4.9)$$

where  $\mathbf{M}$  is a positive-definite matrix. The eigenvalues  $\lambda_s$  of  $\mathbf{M}$  are related to the semi-axes  $c_s$  of the ellipsoid by:

$$\lambda_s = \frac{1}{c_s^2} \quad (4.10)$$

The corresponding eigenvectors then represent the principal orientations of the ellipsoid. By exploiting this relationship, the eigenvalues and eigenvectors of the rank-2 tensors used in this work could be represented as ellipsoid surfaces. In visualizing the ellipsoids of the spatially decomposed samples, the ellipsoids were uniformly scaled to the same volume, which is given by:

$$V = \frac{4}{3} \pi c_1 c_2 c_3 \quad (4.11)$$

### 4.2.9 Standard bone morphometric analyses

Mean intercept length (MIL) analysis was performed by applying the algorithms implemented in BoneJ (version BoneJ2), which is an ImageJ plug-in, to the binary image stacks of the trabecular specimens<sup>38</sup>. While the earlier implementations of the MIL could suffer from significant deviations in the predicted anisotropy due to sampling bias<sup>37;39</sup>, the current implementation draws test lines through the entire image stack, offering a more uniform sampling. A convergence analysis was performed to assess the influence of the number of the parallel test lines and the number of different test line directions. For the final analyses, 2000 directions and 10000 lines per direction were used. Moreover, the MIL results for every sample were taken as the average of three runs of the MIL algorithm. The Euler characteristic (*chi*) was also estimated using BoneJ, on the same binary image data as was used for the MIL analysis. Since the estimation of the Euler characteristic assumes a single connected component, the images were purified (using the Purify command in BoneJ) prior to the connectivity computation. The other reported morphometric indices (*i.e.*, BS and  $\partial S / \partial r$ ) were obtained from the Scanco micro-CT scanner software (Scanco Medical AG, Switzerland).

### 4.2.10 Statistical analysis

The Kruskal-Wallis H test was used to detect significant differences between the means of the different groups of data. Post hoc comparisons of the means were performed using the two-sided Mann-Whitney U tests. The two-sample Kolmogorov-Smirnov test was used to assess the differences between the probability distributions of the  $q_s$  and  $w_s$  metrics, and the age-related curvature probability distributions. The obtained results were considered to be statistically significant when  $p < 0.01$ . All statistical analyses were performed using the python library Scipy.

## 4.3 Results

### 4.3.1 Surface curvature of the trabecular bone interface

We started our geometric analysis at the most local scale, by estimating the mean ( $H$ ), Gaussian ( $K$ ), and net ( $D$ ) curvatures of the trabecular bone interfaces from their triangulated mesh representations. The mean curvature describes how much a surface is locally convex or concave. The Gaussian curvature quantifies the type of the surface:  $K < 0$  signifies a saddle-shaped region (hyperbolic),  $K = 0$  implies an intrinsically flat region (such as a plane, cylinder or cone), and  $K > 0$  describes a sphere-shaped region (Figure 4.5). The net curvature is less common and describes how much a surface locally deviates from a planar region (Figure 4.5).

Figure 4.6 depicts the mesh representations of three representative trabecular bone specimens from the femoral head (FH), iliac crest (IC), and second lumbar vertebra (L2), color-coded by their curvature (representative visualizations of the calcaneus (CA) and fourth lumbar vertebra (L4) are provided in Figure 4.15). The FH samples typically exhibited an apparently uniform dispersion of regions with positive and negative values of the mean curvature. Comparing this to the L2 specimen, we observed that the latter showed much more regions of highly negative mean curvature. This is the consequence of the many rod-like elements that are typically present in specimens from the lumbar spine, as opposed to the primarily plate-like architecture in FH specimens<sup>5</sup>. The Gaussian curvature distributions clearly showed that the geometry of trabecular bone is, on average, hyperbolic in nature ( $K < 0$ ). This has been reported before for a few bone biopsies<sup>40</sup>. This prevalence of negative Gaussian curvature is consistent with the high topological complexity (*i.e.*, high genus) of trabecular bone, according to the Gauss-Bonnet theorem<sup>41</sup>. The net curvature captures regions where the trabecular surface is strongly bent, without distinguishing between the saddle- or sphere-like nature of these bends. In FH specimens, such regions corresponded primarily to arc-like transitions between plate-like elements, while high net curvature in IC or L2 specimens was concentrated in the cylindrically-shaped rod-like elements.

### 4.3.2 Curvature distributions

Due to the inherently local nature of surface curvature, the average values of curvature are not of much descriptive use. In fact, the average mean and Gaussian curvatures are already captured in the structure model index ( $SMI \sim \langle H \rangle$ ) and Euler-Poincaré

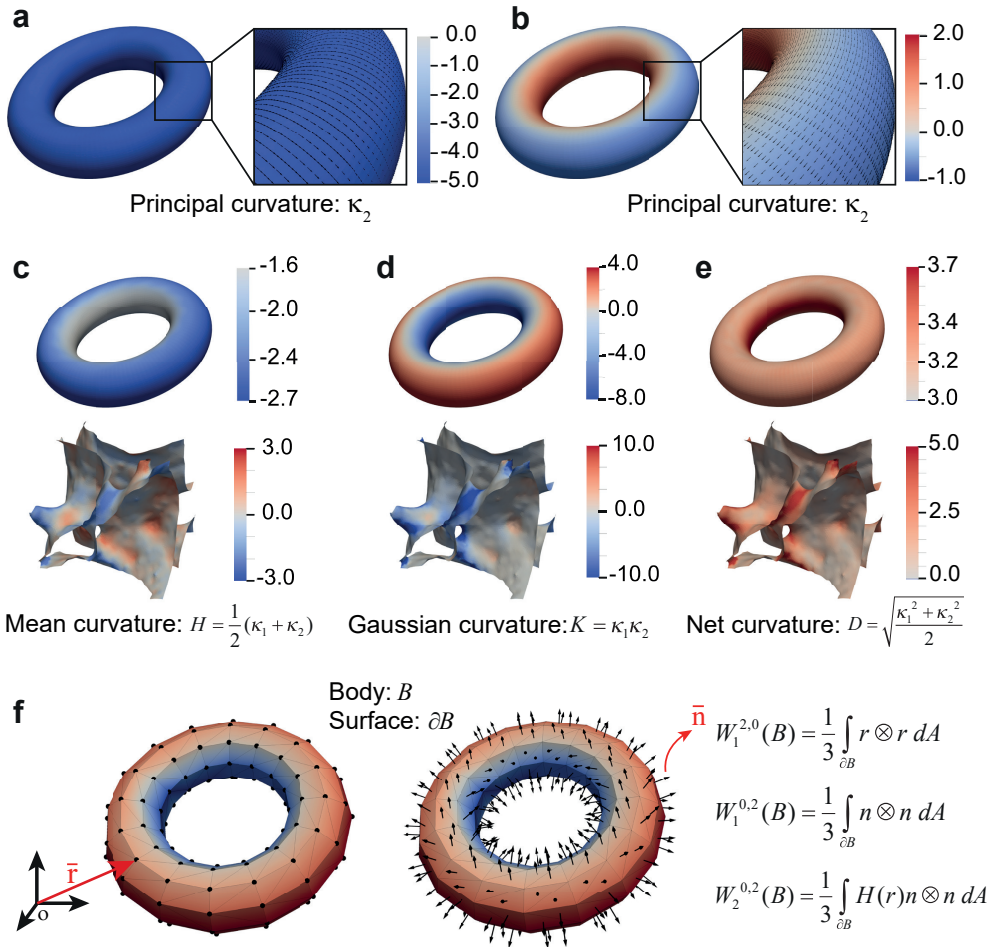


**Figure 4.5:** Surface curvature and Minkowski tensors. a-b) The minimum ( $\kappa_1$ ) and maximum ( $\kappa_2$ ) principal curvatures and associated principal directions on a torus model. c-e) The definitions of the mean ( $H$ ), Gaussian ( $K$ ), and net ( $D$ ) curvatures as functions of the principal curvatures. The top row visualizes the curvatures of the torus, while the bottom row depicts some small sections of a trabecular bone interface. f) A visualization of the components used in the computation of the Minkowski tensors of a coarse torus model, showing the position vectors ( $\vec{r}$ ) and normal vectors ( $\vec{n}$ ), as well as the expressions for the tensors considered in this study.

characteristic ( $\chi \sim \langle H \rangle$ ), respectively<sup>40</sup>. Instead, it is important to consider the distribution of curvature throughout the trabecular specimens. Therefore, we computed the 1D and 2D probability distributions of the different curvature measures, obtained from more than 60 subjects at every anatomical location. The 1D probability densities of the mean curvature (Figure 4.7) confirmed the above-mentioned observation that plate-like specimens (*i.e.*, FH) exhibit a more uniform distribution of the normalized mean curvature, with a peak close to  $H/S_v \approx 0$ , than rod-like specimens (*i.e.*, L2 and L4). The latter displayed a flattened and more negatively skewed distribution, centered around  $H/S_v \approx -0.5$ . The mean curvature density also reflected the intermediate na-

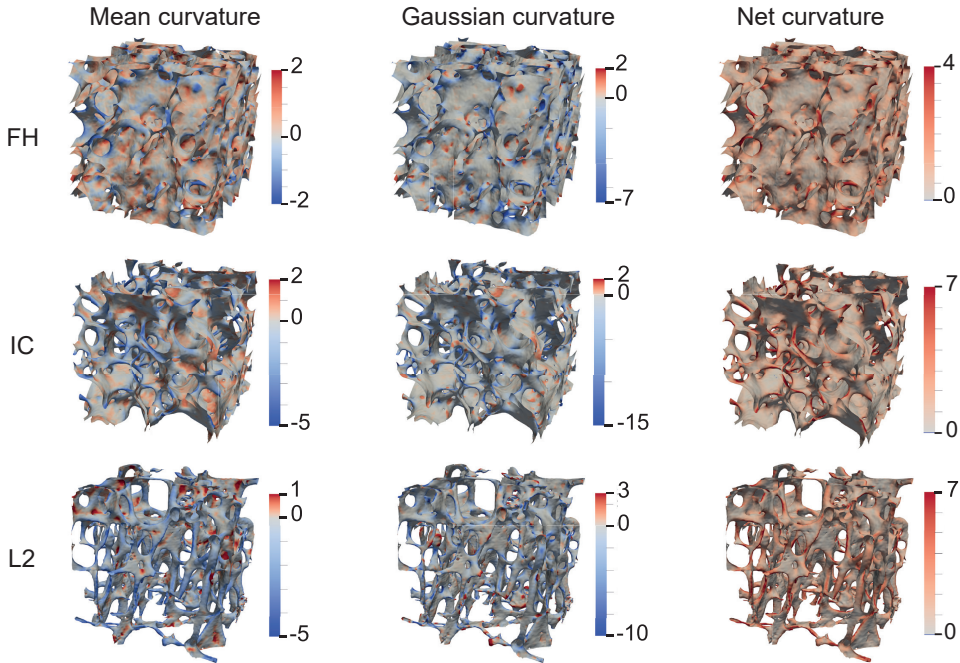


**Figure 4.6:** Curvature estimation on triangle meshes. The normalized mean, Gaussian, and net curvature visualizations of some representative (regarding morphology) trabecular samples from the femoral head (FH), iliac crest (IC), and second lumbar vertebra (L2).

ture of the iliac crest (IC) and calcaneus (CA) specimens, containing both plate-like and rod-like elements. As expected, the Gaussian curvature density functions were negatively skewed, with a sharp peak around  $K/S_v^2 \approx 0$ . To assess the potential impact of age on curvature, we compared the curvature distributions of the specimens harvested from donors younger than 60 and those older than 80 for each anatomical site (Figure 4.16). In the case of the mean curvature, significant differences in the probability distributions of both age groups were only observed for the L4 samples (two-sample Kolmogorov-Smirnov,  $p < 0.01$ ). Indeed, the curve belonging to the donors older than 80 was more flattened and exhibited a lower peak value than the curve corresponding to donors younger than 60. These differences could be attributed to the progressive thinning and disappearance of thin rod-like elements, which is known to be more prevalent in the lumbar spine<sup>42</sup>. The Gaussian and net curvature profiles, however, did not show significant differences between age groups.

Since a full description of surface curvature is typically built on two variables, such as the pair of principal curvatures, we quantified the interface shape distributions (ISD) for different curvature measures. These types of 2D probability density maps have been used to characterize the morphological evolution of spinodal decomposition systems during coarsening<sup>34;43</sup>. The ISD of the principal curvatures is subdivided into different regions (Figure 4.8), providing an intuitive overview of the types of geometries that are encountered in the trabecular bone specimens. Saddle shapes appear in regions II and

III, spherical shapes are situated in regions I and IV, and cylindrical shapes are found on the boundaries between the saddle-shaped and spherical regions (horizontal and vertical lines). For example, the principal curvature ISD of the FH specimens showed that most of the interface corresponds to saddle-shaped regions, and that sphere-like indentations (region I), and not protrusions (region IV), were the primary source of positive Gaussian curvature.

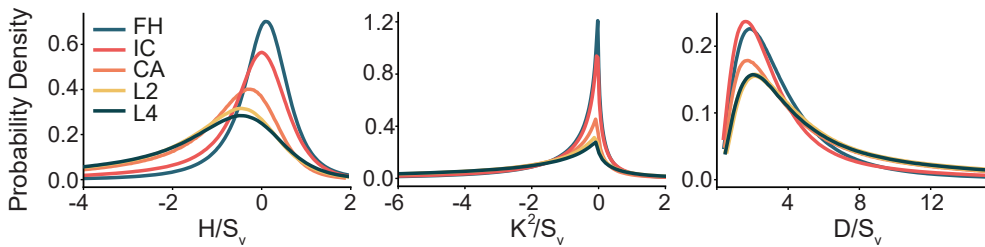


**Figure 4.7:** 1D and 2D curvature distributions. Probability density distribution of the normalized mean (left), Gaussian (middle) and net (right) curvature per bone type. Each curve contains data from several samples ( $n_{CA} = 66$ ,  $n_{FH} = 62$ ,  $n_{IC} = 68$ ,  $n_{L2} = 65$ ,  $n_{L4} = 68$ ).

The ISD of the principal curvatures captured the progressive transition from primarily plate-like to primarily rod-like bone specimens (Figure 4.8). While the plate-like FH specimens exhibited a relatively concentrated, circular distribution of curvatures, the rod-like specimens of L2 and L4 were characterized by a much broader distribution with a horizontal orientation. This horizontal preference is due to the presence of rod-like elements in those specimens. These rod-like elements were not perfect cylinders, however, but were slightly saddle-shaped. The IC samples exhibited a principal curvature distribution that was similar to that of the FH, indicating primarily plate-like elements. For the CA samples, a horizontal orientation of the distribution was apparent, indicating a higher proportion of rod-like elements in the structures. The morphological differences between bone types were also observed in the joint probability distributions of the normalized net ( $D/S_v$ ) and mean curvature ( $H/S_v$ ), and the transition from plate-like to rod-like specimens was clearly visible (Figure 4.8). Moreover, these distributions again showed that the mean curvature of trabecular bone is, in general, not uniformly centered around zero. For our FH specimens, the peak of the mean curvature was situated slightly above  $H=0$ , indicating shapes that were more concave than they were convex. This peak transitioned towards negative values for rod-like specimens, due to the convex nature of the rods. The ISD of the mean and Gaussian curvatures also captured this distinction between the different bone types, again showing a broader distribution for more rod-like specimens.

### 4.3.3 Radial distribution function

The ISD characterizes the local shape of trabecular bone by providing insight into the range and frequencies of the different types of curvature. However, it does not provide information about the way these curvatures are distributed in space and how the

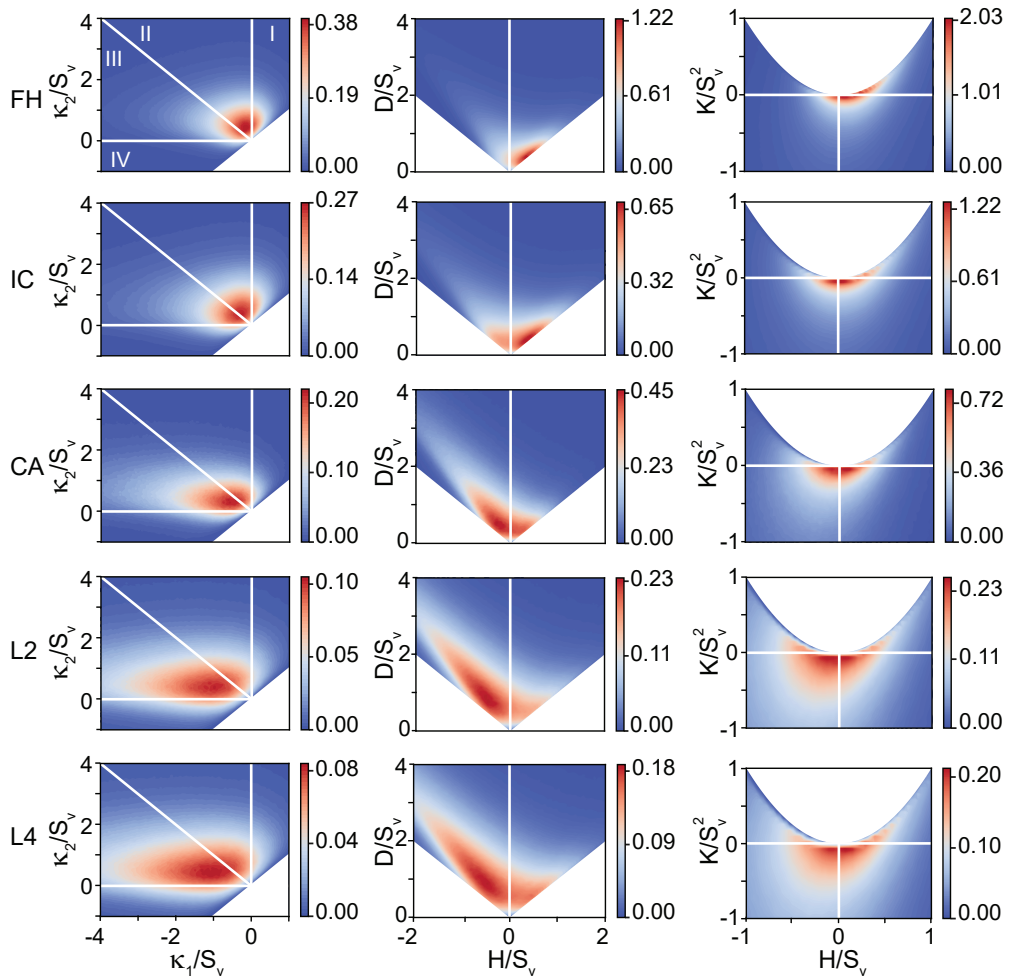


**Figure 4.8:** The interface shape distributions (ISD) for specimens from every anatomical site, showing the normalized curvature probability densities. Left column displays the ISD of the principal curvatures ( $\kappa_1$  and  $\kappa_2$ ). Middle column displays the ISD of the net ( $D$ ) and mean ( $H$ ) curvatures. Right column displays the ISD of the Gaussian ( $K$ ) and mean ( $H$ ) curvatures. Each plot contains data from several specimens ( $n_{CA} = 66$ ,  $n_{FH} = 62$ ,  $n_{IC} = 68$ ,  $n_{L2} = 65$ ,  $n_{L4} = 68$ ).

curvatures at different locations in the structure are related. Knowledge of this spatial correlation is relevant, since two structures could (theoretically) exhibit the same ISD, while having their curvatures distributed differently throughout space<sup>22</sup>. Therefore, we quantified the spatial correlation of the mean and Gaussian curvatures, using a curvature-based radial distribution function (RDF). Traditionally, the RDF has been employed in the analysis of granular systems, where it quantifies the likelihood of finding particles at a certain distance from a reference particle, relative to what would be expected based on the overall density of the system<sup>44</sup>. Depending on the type of the particle system and the associated interactions, the (excess) probability of finding

neighboring particles will vary as a function of distance. The RDF has also gained popularity to quantify the spatial correlation in non-particulate systems<sup>2</sup>. When defined on the basis of the mean curvature, the RDF has been used to complement the ISD in characterizing the coarsening dynamics of spinodal decomposition systems<sup>22,33</sup>. In this sense, the RDF provides a slightly more global interpretation of curvature than the ISD. Here, we used a similar approach to compute the RDF of the mean and Gaussian curvature for the trabecular bone specimens from the different anatomical sites. In case of the mean curvature, we define the RDF as:

$$G(H_2 | r, H_1) = \frac{A_{H_2,S}(r)/A_S(r)}{A_{H_2,T}/A_T} \quad (4.12)$$

Here,  $A_{H_2,S}(r)$  is the total area of faces with a mean curvature of  $H_2$  within a spherical shell of radius  $r$ , centered around a reference point with a mean curvature of  $H_1$ .  $A_S(r)$  represents the total area of all faces inside the spherical shell,  $A_{H_2,T}$  is the total area of faces with the mean curvature  $H_2$  in the entire specimen, and  $A_T$  is the total face area of the entire specimen. Hence,  $G(H_2 | r, H_1)$  describes the area-density of the faces with  $H_2$  at a distance  $r$  from a face with  $H_1$ , relative to the overall area-density of the faces with  $H_2$ . As such, the RDF captures how much more ( $G > 1$ ) or less ( $G < 1$ ) likely it is to find pairs of faces with a certain combination of mean curvature at a given distance from each other as compared to a random distribution throughout the specimen<sup>33</sup>.

We plotted the RDF of the normalized mean (Figure 4.9) and Gaussian (Figure 4.10) curvature at several characteristic distances. Taking the mean curvature RDF as the running example, the plots should be symmetric about the line  $H_1/S_v = H_2/S_v$ , since  $G(H_2 | r, H_1) = G(H_1 | r, H_2)$ <sup>22</sup>. Considering the RDF plots for  $\tilde{r} = 0.06$  (left column in Figure 4.9), several observations could be made. For example, distinct positive correlations ( $G > 1$ ) and anti-correlations ( $G < 1$ ) were observed in all specimens. The positive correlations increased for the more extreme values of curvature, indicating that those strongly curved regions are highly concentrated in the structure. In other words, points with high mean curvature values are likely to have neighbors with high mean curvature as well. On the other hand, it is less likely to encounter neighbors with curvatures on the opposite sides of the spectrum (anti-correlation). For the FH, IC, and CA samples, a relatively stronger positive correlation was observed along the entire line  $H_1 = H_2$  than for the L2 and L4 samples. Additionally, stronger anti-correlations were observed in the FH, IC and CA specimens. It is also noteworthy that the range of curvatures is substantially larger for the rod-like samples (L2 and L4) than for the plate-like samples (FH), indicating that the positive correlations in the rod-like samples occur at more extreme locations (relatively speaking) than for the plate-like samples. At the larger values of  $r$  the correlations and anti-correlations gradually dissipated, and the RDF became more uniform and approached  $G=1$ . The most extreme values of curvature maintained some positive correlation at  $\tilde{r} = 0.14$ , for all specimens. However, the correlation dissipation occurred faster in the L2 and L4 specimens, showing a more

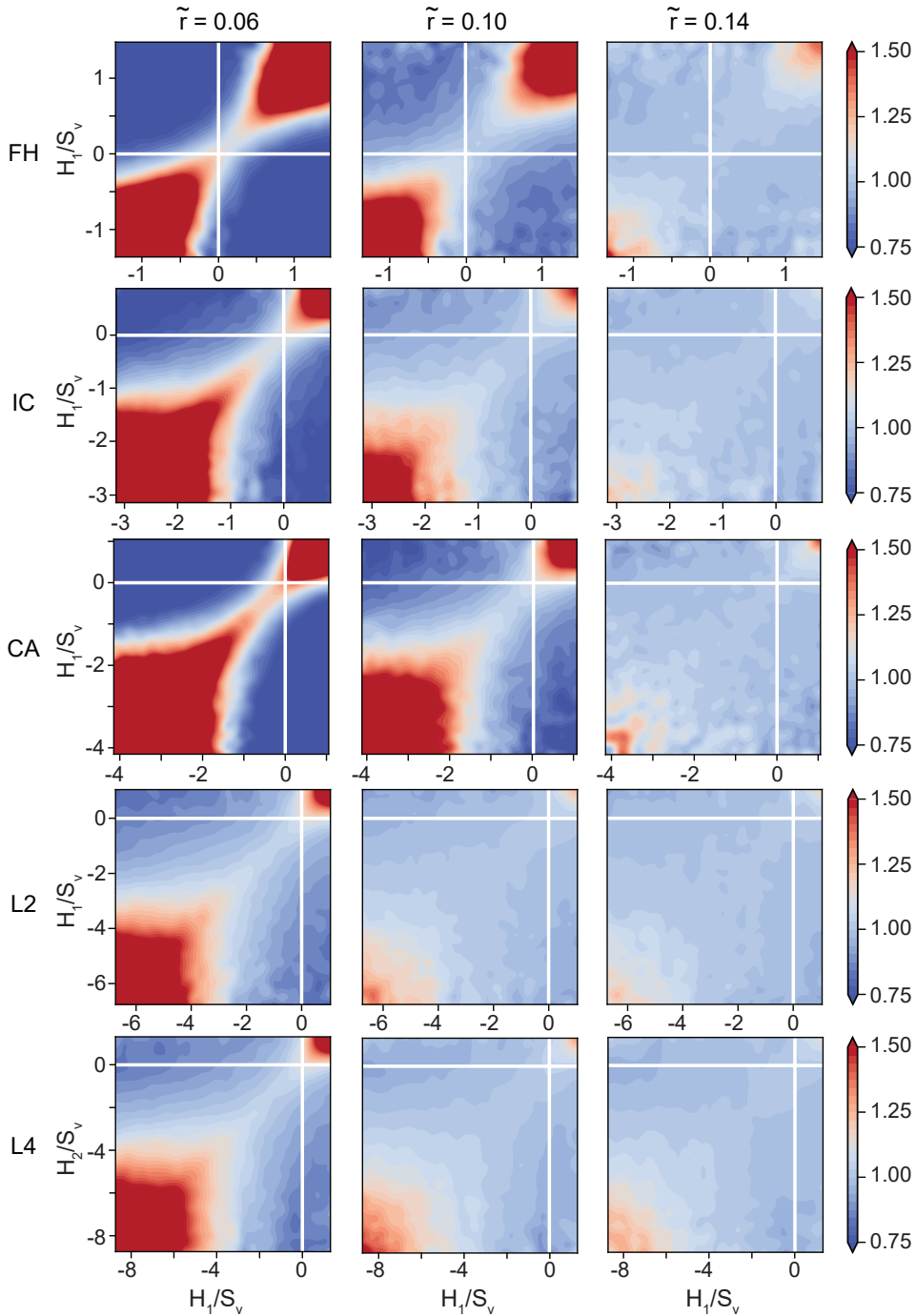


**Figure 4.9:** Radial distribution function of the mean curvature. Plots showing the radial distribution function of normalized mean curvature ( $G$ ) for representative (regarding morphology) specimens from the five anatomical sites, at different values of the characteristic distance  $\tilde{r}$ . Color bar indicates enhanced ( $G > 1$ ) or reduced ( $G < 1$ ) probability of finding mean curvature pairs ( $H_1 - H_2$ ) at a given distance ( $\tilde{r}$ ) from each other, with respect to randomly distributed curvatures. Left column:  $\tilde{r} = 0.06$ , middle column:  $\tilde{r} = 0.1$ , right column:  $\tilde{r} = 0.14$ .

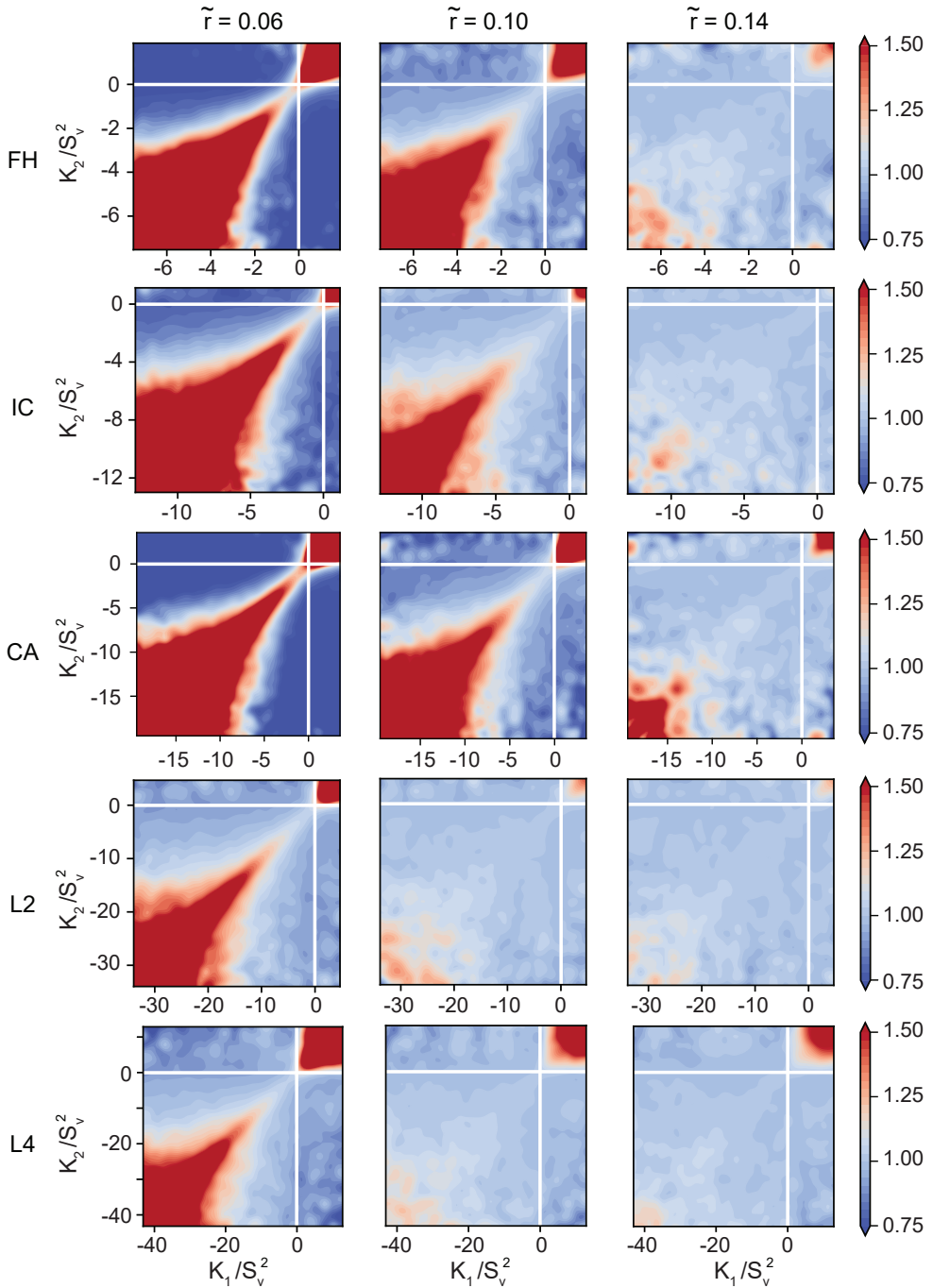


**Figure 4.10:** Radial distribution function of the Gaussian curvature. Plots showing the radial distribution function of normalized Gaussian curvature ( $G$ ) for representative samples from the five anatomical sites, at different values of the characteristic distance  $\tilde{r}$ . Color bar indicates enhanced ( $G > 1$ ) or reduced ( $G < 1$ ) probability of finding mean curvature pairs  $(K_1 - K_2)$  at a given distance ( $\tilde{r}$ ) from each other, with respect to randomly distributed curvatures. Left column:  $\tilde{r} = 0.06$ , middle column:  $\tilde{r} = 0.1$ , right column:  $\tilde{r} = 0.14$ .

uniform distribution of  $G$  around unity than the FH, IC, and CA samples. The RDF of the Gaussian curvature (Figure 4.10) exhibited a similar effect, although the positively correlated region had a more triangular shape. Moreover, at small and intermediate distances, high positive correlations were observed for the entire range of the positive Gaussian curvatures, indicating that locally spherical features are highly concentrated in trabecular bone.

#### 4.3.4 Scalar Minkowski functionals

The ISD presents the most local measure of trabecular shape, by characterizing the curvatures at individual points along the interface. Two-point correlation functions, such as the RDF presented above, provide a slightly more global picture by considering pairs of points throughout the structure. Nevertheless, it is useful to complement these approaches with truly global, or integral, metrics that describe the shape as a whole. From an integral geometric viewpoint, the most fundamental indices to characterize the global shape are the Minkowski functionals. Their fundamental nature for shape description is described in Hadwiger's theorem (generalized to tensors by Alesker), stating that any other motion-covariant, conditionally continuous, additive functional on a body is a linear combination of the Minkowski functionals<sup>19–21</sup>. In addition to their fundamental nature, Minkowski shape indices are also highly versatile, meaning that they can be applied to a broad spectrum of complex structures, and are robust against noise<sup>2,20</sup>.

The simplest types of Minkowski functionals are of a scalar nature and are further referred to as the Minkowski scalars (see Subsection 4.5.1 for the mathematical formulations and background). For a 3D body  $B$  (Figure 4.5), four scalar MF can be defined, which are proportional to the volume ( $W_0(B)$ ), the total area of the bounding surface ( $W_1(B)$ ), the area-integrated mean curvature ( $W_2(B)$ ), and the area-integrated Gaussian curvature ( $W_3(B)$ ). The latter is proportional to the Euler-Poincaré index, a topological invariant describing connectivity. The Minkowski scalars have been applied in the analysis of various spatial architectures, including voxelized representations of trabecular bone<sup>45</sup>. Here, we computed the Minkowski scalars  $W_1$ ,  $W_2$ , and  $W_3$  on the smoothed triangle meshes of the trabecular bone interface, and compared them to traditional bone morphometric indices that characterize the global trabecular shape (Figure 4.11)<sup>5,12</sup>. The scalar  $W_0$  was omitted, since it is not defined for open surfaces. The scalar  $W_1$  and the bone surface area (BS) were relatively well correlated (Figure 4.11a). The strongest correlation was observed for the L4 specimens ( $\rho = 0.91$ ), while the weakest correlation was attained in the CA specimens ( $\rho = 0.66$ ). The deviations between the computed  $W_1$  and BS could potentially be attributed to different underlying meshes (BS was directly calculated on a marching cubes mesh<sup>5</sup>). The scalar  $W_2$ , which captures the area-integrated mean curvature, is plotted against the morphometric parameter  $\partial S/\partial r$ , showing strong correlations for all bone types ( $\rho > 0.87$ , Figure 4.11b). The parameter  $\partial S/\partial r$  represents a surface area derivative, and is estimated as the change in surface area ( $dS$ ) when the surface is dilated by a small amount, divided by the length

of that dilation ( $dr$ ). The area of such a dilated parallel surface ( $S_r$ ) is related to the area of the original surface ( $S_0$ ) and its curvature by<sup>40</sup>:

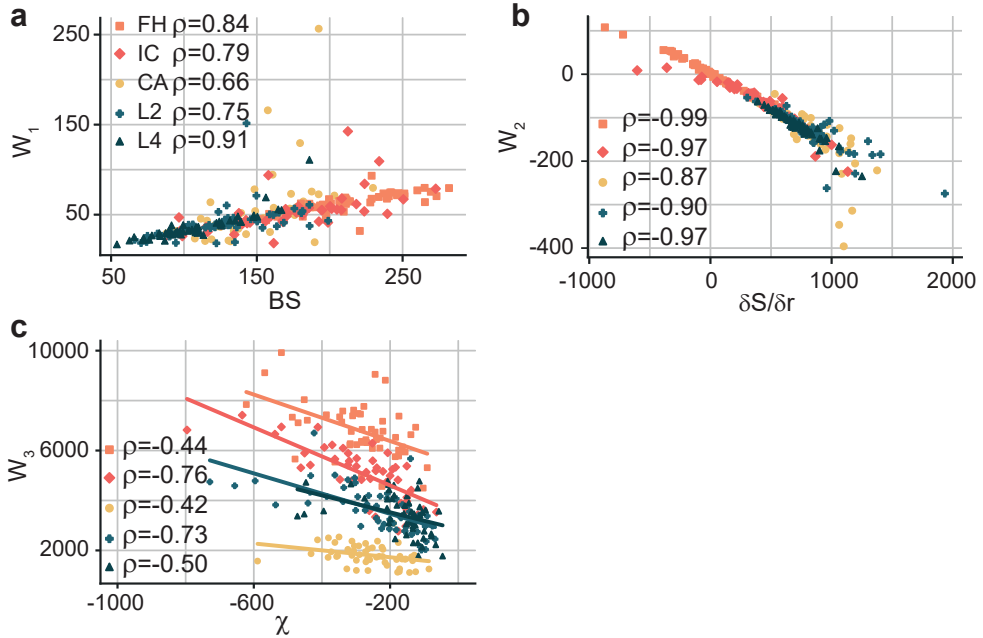


**Figure 4.11:** Scalar and tensorial Minkowski functionals applied to trabecular bone. Results for the three Minkowski scalars, plotted *versus* their equivalent standard morphometric index: a)  $W_1$  *versus* bone surface (BS), b)  $W_2$  *versus* surface area derivative ( $\partial S/\partial r$ ), c)  $W_3$  *versus* Euler-Poincaré characteristic ( $\chi$ ).

$$S_r = S_0(1 + \langle H \rangle r + \langle K \rangle r^2) \quad (4.13)$$

where  $r$  is the signed distance from the original surface,  $\langle H \rangle$  is the average mean curvature, and  $\langle K \rangle$  is the average Gaussian curvature. The dilation-based parameter  $\partial S/\partial r$  appears in two well-known bone morphometric indices: the SMI and the 3D trabecular bone pattern factor (TBPf)<sup>13;46;47</sup>:

$$SMI = 6 \frac{BV \cdot \frac{\partial S}{\partial r}}{BS^2} \quad (4.14)$$

$$TBPf = \frac{\frac{\partial S}{\partial r}}{BS} \quad (4.15)$$

In that sense, both SMI and TBPf are proportional to the average mean curvature ( $\langle H \rangle$ ) of the surface (for small dilations ( $r^2 \approx 0$ ), the second-order Gaussian curvature contribution can be neglected), essentially meaning that the  $\langle H \rangle$  is a global morphometric index<sup>40;42</sup>. Overall, the correlation between  $W_3$  and the Euler-Poincaré index ( $\chi$ ) is

lower ( $0.42 < \rho < 0.76$ ) than the correlations between the previous Minkowski scalars and their corresponding morphometric indices (Figure 4.11c). This could again be attributed to the different calculation approaches:  $W_3$  is based on the integral Gaussian curvature of the triangle meshes, while  $\chi$  is computed on 3D binary images. Finally, an important observation is that  $W_3$  captures the differences between the specimens from different anatomical sites, while these are not reflected in the  $\chi$  values (Figure 4.11c). This implies that  $W_3$  could potentially be more sensitive to subtle changes in connectivity than  $\chi$ , *e.g.* in case of disease.

### 4.3.5 Tensorial Minkowski functionals

A relatively novel extension of the Minkowski scalars for global shape quantification is provided by the so-called Minkowski tensors (MT). Due to their tensorial nature, these MT capture the orientation-dependent aspects of morphology, a feature that is highly relevant for the study of heterogeneous materials such as trabecular bone<sup>23;24</sup>. While the MT have been employed to characterize granular packings, galaxies, or foams<sup>17;48;49</sup>, we are the first to apply these tensors to the study of trabecular bone. As a natural consequence of their mathematical foundation, many different MT can be defined, each characterizing a different aspect of morphology. In principle, the MT can be defined for any arbitrary rank, but we primarily focused on rank-two tensors, due to their intuitive physical interpretation<sup>2</sup>. Higher rank MT are briefly considered in Subsection 4.3.6. For a 3D body, six relevant rank-two MT are defined (Figure 4.5 and Subsection 4.5.1). As an example, the tensor  $W_0^{2,0}(B)$  is a measure of the spatial distribution of mass for a solid body B, in some sense analogous to the moment of inertia tensor. The tensor  $W_1^{2,0}(B)$ , on the other hand, measures the mass distribution when the entire mass of B is homogeneously distributed on the surface (*i.e.*, a “hollow” body). Here, we considered the aforementioned (translation-covariant) tensor  $W_1^{2,0}$  as well as two other (translation-invariant) Minkowski tensors, namely  $W_1^{0,2}$  and  $W_2^{0,2}$ . The tensor  $W_1^{0,2}$  describes the distribution of the surface normal vectors, while  $W_2^{0,2}$  describes the distribution of the mean curvature (surface normals weighted by curvature).

Every MT can be used to quantify anisotropy with respect to that particular tensor. We define the degree of anisotropy (DA) for a tensor  $W_v^{r,s}$  as:

$$DA_v^{r,s} = 1 - \frac{|\lambda_v^{r,s}|_{\min}}{|\lambda_v^{r,s}|_{\max}} \quad (4.16)$$

Here,  $|\lambda_v^{r,s}|_{\min}$  and  $|\lambda_v^{r,s}|_{\max}$  are the absolute values of the minimum and maximum eigenvalues of the tensor  $W_v^{r,s}$ . As such, we were able to quantify the different types of anisotropy of the trabecular bone samples, including the anisotropy of the interface orientation ( $DA_1^{0,2}$ ) or the anisotropy of the mean curvature ( $DA_2^{0,2}$ ). For trabecular bone, a classical and popular approach to quantify anisotropy has been based on the mean intercept length (MIL) method<sup>12;37;50</sup>. However, the MIL is limited to in-

terfacial anisotropy (by definition) and is known to suffer from some conceptual shortcomings, such as noise sensitivity, sampling bias, and poor data fitting in specific cases, that could invalidate the anisotropy results<sup>51</sup>. Instead, Minkowski tensors are robust alternatives, showing higher sensitivity to anisotropy in 2D boolean model systems<sup>36</sup>. To assess the potential of Minkowski tensors as alternatives to the MIL tensor for bone anisotropy quantification, we computed the DA of both approaches on 259 trabecular bone specimens. The relevant Minkowski tensor for this comparison is  $W_1^{0,2}$ , as it describes the interfacial orientation. We found that, with the most recent algorithm for the calculation of  $DA_{MIL}$  (in BoneJ<sup>38</sup>), all the data for  $DA_{MIL}$  and  $DA_1^{0,2}$  were strongly correlated (Spearman's  $\rho = 0.957$ , Pearson's  $\rho = 0.963$ ) and centered around the identity line (Figure 4.12). Both methods also predicted similar principal directions with most angle differences below  $10^\circ$  (Figure 4.12b). In contrast to theoretical predictions on 2D model systems, our analysis indicates that both approaches yield similar results on high-resolution trabecular bone scans<sup>36</sup>. Despite these similar results, it must be emphasized that  $DA_{MIL}$  is highly dependent on the specific MIL implementation, which has been shown to be a potential source of significant variation in classical MIL algorithms<sup>15;39;52</sup>. Moreover, the MT approach is inherently less sensitive to noise and more computationally efficient than the MIL approach, since it does not rely on counting lines and intersections<sup>36</sup>, and also offers the ability to quantify the other types of anisotropy.

Comparing the  $DA_1^{0,2}$  distributions (Figure 4.13a), we observed that all bone types exhibit a distinct level of interfacial anisotropy, with significant differences between the means of the different bone types (Table 4.1). Higher mean values were obtained in the CA ( $\langle DA_1^{0,2} \rangle = 0.59$ ) and FH ( $\langle DA_1^{0,2} \rangle = 0.58$ ) specimens, as opposed to the IC ( $\langle DA_1^{0,2} \rangle = 0.49$ ), the L2 ( $\langle DA_1^{0,2} \rangle = 0.45$ ), and L4 ( $\langle DA_1^{0,2} \rangle = 0.48$ ) samples. Moreover, a wider spread in the anisotropy values was observed in the L2 and L4 specimens. In all cases, the degree of anisotropy with respect to the tensor  $W_1^{2,0}$ , which characterizes the mass distribution of the “hollow” trabecular bone, was much lower (Figure 4.13b). Significant differences between the different bone types were detected, and higher mean values were attained for the IC ( $\langle DA_1^{2,0} \rangle = 0.20$ ), the L2 ( $\langle DA_1^{2,0} \rangle = 0.20$ ) and the L4 ( $\langle DA_1^{2,0} \rangle = 0.21$ ) samples as opposed to the CA ( $\langle DA_1^{2,0} \rangle = 0.13$ ) and the FH ( $\langle DA_1^{2,0} \rangle = 0.09$ ) samples. Finally,  $DA_2^{0,2}$  quantifies the anisotropy of the curvature-weighted surface normals (Figure 4.13c), again displaying significant differences in the means between the bone types. The CA ( $\langle DA_1^{0,2} \rangle = 0.25$ ), L2 ( $\langle DA_1^{0,2} \rangle = 0.21$ ), and L4 ( $\langle DA_1^{0,2} \rangle = 0.18$ ) specimens exhibited narrower distributions than the FH ( $\langle DA_1^{0,2} \rangle = 0.61$ ) and IC ( $\langle DA_1^{0,2} \rangle = 0.33$ ) specimens. Interestingly, there were statistically significant differences between the mean  $DA_2^{0,2}$  values calculated for the specimens harvested from male and female donors in the case of the CA ( $n_1 = 25, n_2 = 27$ , Mann-Whitney  $U = 179, p = 0.004$ ) and L2 ( $n_1 = 25, n_2 = 30$ , Mann-Whitney  $U = 179, p = 0.001$ ) bone types.

In reporting DA, only the extremal tensor eigenvalues were considered. To extend our characterization of the Minkowski tensors, we also plotted the ratio of the median to the maximum eigenvalue against the ratio of the minimum to the maximum eigenvalue.

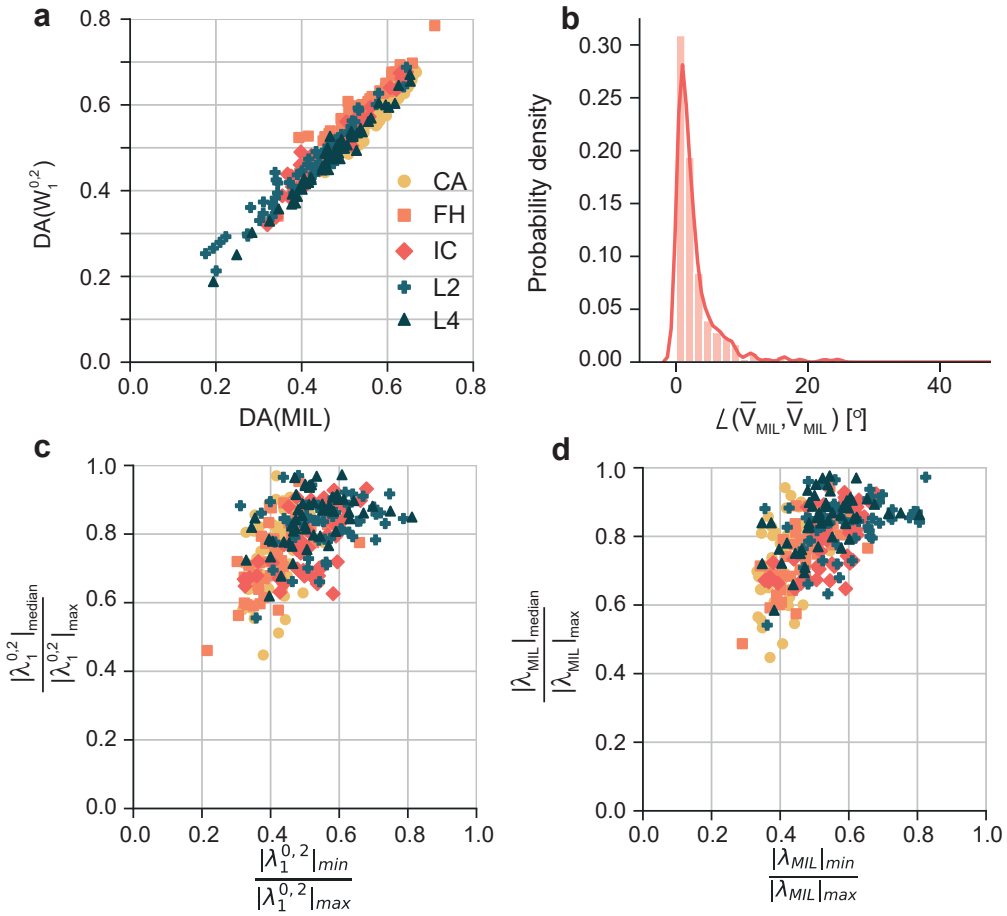


**Figure 4.12:** Comparisons between the MIL and  $W_1^{0,2}$  tensors. a) Degree of anisotropy (DA) with respect to the tensor  $W_1^{0,2}$  versus DA with respect to the MIL tensor, for samples from each anatomical group. b) Probability density distribution of the angle difference between the principal directions obtained from the MIL and  $W_1^{0,2}$  tensors. c) Ellipticity of the  $W_1^{0,2}$  tensor, with every marker indicating a different trabecular sample (also shown in Figure 4.13). d) Ellipticity of the MIL tensor, showing good agreement with the plot in c).

Since rank-2 tensors can be represented by the surface of an ellipsoid (Subsection 4.2.7), these plots provide insight into the “ellipticity” of the bone specimens with respect to a particular tensor (Figure 4.13d). Data for which  $\lambda_{median}/\lambda_{max} = 1$  are represented by prolate spheroids, while data on  $\lambda_{min}/\lambda_{max} = \lambda_{median}/\lambda_{max}$  are represented by oblate spheroids. When  $\lambda_{min}/\lambda_{max} = \lambda_{median}/\lambda_{max} = 1$ , a perfect sphere is obtained and the data is considered fully isotropic with respect to that particular tensor. For the tensor  $W_1^{0,2}$ , the data was clustered between the oblate and prolate shapes on the ellipsoid spectrum (Figure 4.13e). Moreover, the ellipticity of the  $W_1^{0,2}$  data was in good agreement with the ellipticity of the MIL data (Figure 4.12d). In the case of the  $W_1^{2,0}$  tensor, most of the specimens were highly concentrated in the nearly isotropic re-

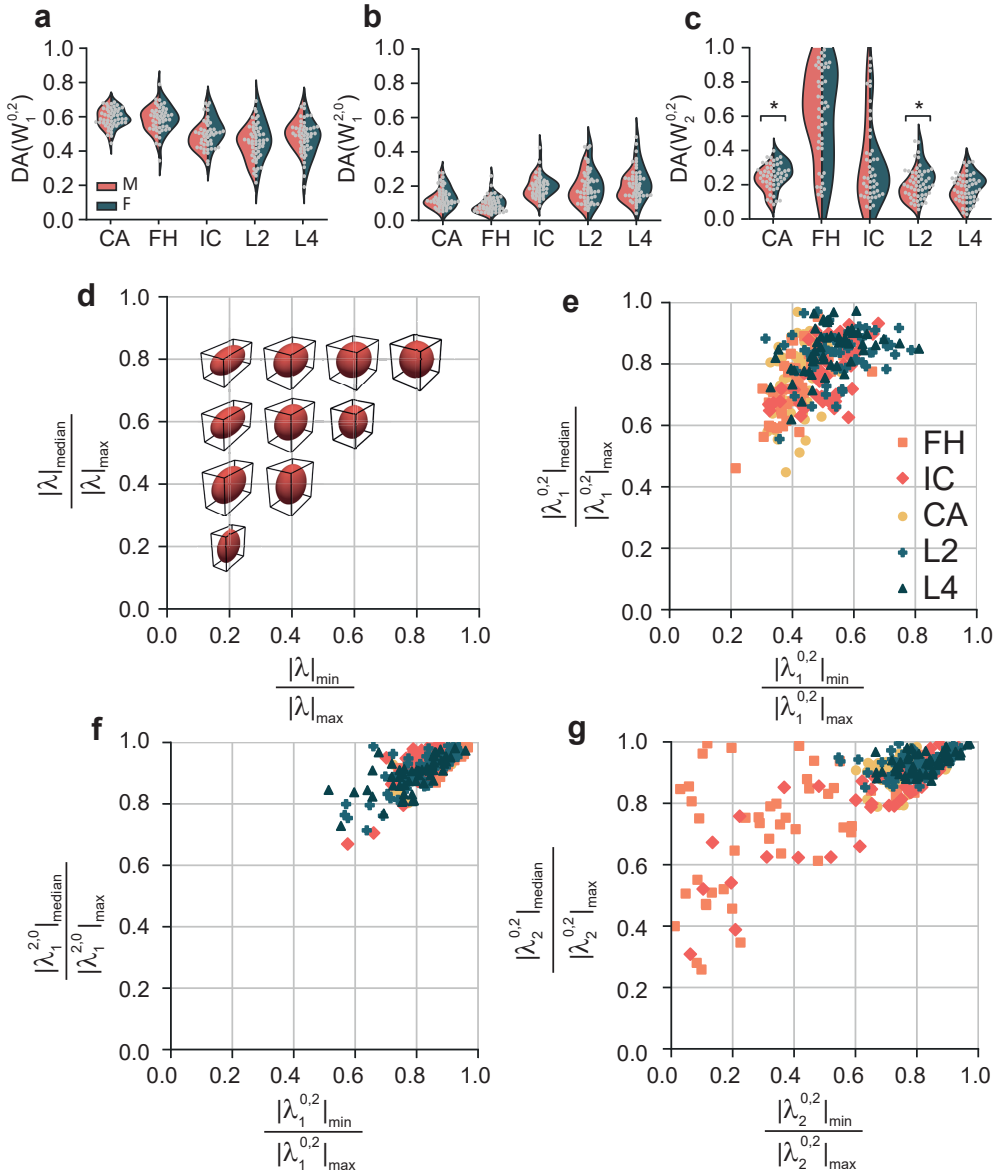


**Figure 4.13:** The distribution plots for the degree of anisotropy (DA) with respect to the different Minkowski tensors, plotted per anatomical site and split between the specimens from male (M) and female (F) donors: a) DA for tensor  $W_1^{0,2}$ , b) DA for tensor  $W_1^{2,0}$ , and c) DA for tensor  $W_2^{0,2}$ .  $*p < 0.01$ . d-g) Ellipticity with respect to the different Minkowski tensors, shown as the ratio of the median to the maximum eigenvalue *versus* the ratio of the minimum to the maximum eigenvalue: d) an illustration of the various degrees of ellipticity, e) ellipticity with respect to  $W_1^{0,2}$ , f) ellipticity with respect to  $W_1^{2,0}$ , and g) ellipticity with respect to  $W_2^{0,2}$ .

gion, with some data points (IC, L2, and L4) exhibiting higher ellipticity (Figure 4.13f). For the  $W_2^{0,2}$  tensor, the data for the CA, L2 and L4 specimens was again concentrated

in the nearly isotropic region, but the data for the FH and IC specimens were scattered over the entire ellipsoid spectrum. For example, the FH specimens covered both highly oblate and prolate ellipticity, with various degrees of anisotropy (Figure 4.13g). Taken together, these plots underscore that interfacial orientation is only one of several sources of bone anisotropy and ellipticity, and that other sources can be quantified by considering a different Minkowski tensor (e.g.  $W_1^{2,0}$  or  $W_2^{0,2}$ ).

#### 4.3.6 Anisotropy in spatially decomposed bone

The Minkowski functionals provide a global (integral) interpretation of trabecular shape, by assigning either a scalar or a tensor to the entire region of interest. However, the shape and size of this region could be chosen arbitrarily within the cubic specimen volume. Hence, it is possible to apply the Minkowski analysis to several smaller substructures, in order to create a Minkowski map that quantifies the intra-specimen variations of the integral shape indices<sup>2</sup>. In that sense, such a spatially decomposed analysis of the Minkowski functionals occupies an intermediate position between the highly localized analysis of curvature distributions and the whole-specimen shape characterization presented in Subsection 4.3.3 and Subsection 4.3.4.

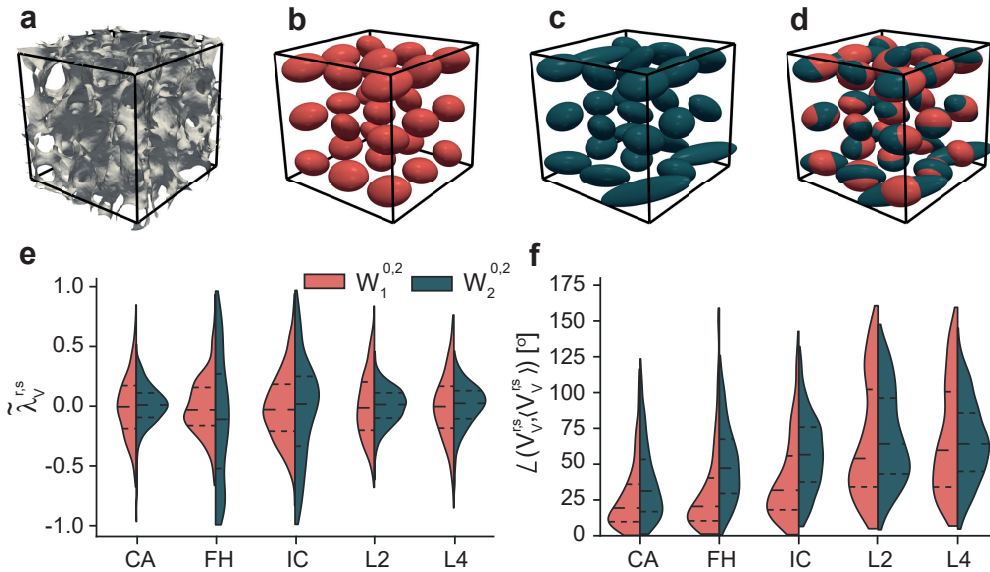


**Figure 4.14:** Minkowski tensor analysis on spatially decomposed samples. a) A visualization of a full FH trabecular bone specimen. b) Ellipticity with respect to the normal density tensor ( $W_1^{0,2}$ ) of the sample in 27 subdomains. The ellipsoids are oriented in their principal direction. c) Ellipticity with respect to the curvature density tensor ( $W_2^{0,2}$ ) of the sample in 27 subdomains. d) An overlay of the ellipticities of b) and c). e) The relative differences in the local and global anisotropy for  $W_1^{0,2}$  and  $W_2^{0,2}$ , plotted for each anatomical site. f) The differences in the local and global principal orientations for  $W_1^{0,2}$  and  $W_2^{0,2}$ , plotted for each anatomical site.

To quantify the intra-specimen anisotropy changes, we decomposed 100 trabecu-

lar specimens into a set of smaller components. In order to maintain representative trabecular substructures, we used a  $3 \times 3 \times 3$  cubic grid for this spatial subdivision (Figure 4.4b). We computed the two translation-invariant Minkowski tensors  $W_1^{0,2}$  and  $W_2^{0,2}$  on the resulting 2700 substructures, enabling a local characterization of the ellipticity with respect to those tensors. We found that, in general, the ellipticity varies throughout the specimens and is different for both tensors (Figure 4.14a-d). To quantify the spatial variation, we calculated the relative difference between the anisotropy of a substructure and that of the entire specimen ( $\tilde{\lambda}_v^{r,s}$ , Subsection 4.2.8), as well as the angle difference between the local and global principal orientations ( $\tilde{V}_v^{r,s}$ ). For both tensors, the local DA varied substantially with respect to the whole-sample value and led to different distributions for both tensors (Figure 4.14e). Distinct angle differences in the local and global principal directions were also observed for both tensors, and wider variations were detected in the L2 and L4 specimens (Figure 4.14f).

Finally, we asked whether higher-rank Minkowski tensors (beyond rank two) could provide additional insight into the structural and anisotropy differences between the different bone types. To this end, we calculated the quadratic ( $q_s$ ) and cubic ( $w_s$ ) rotational invariants of the so-called irreducible Minkowski tensors (Subsection 4.5.1) for the spatially decomposed specimens. This analysis was motivated by the recent results in particulate matter, where these scalar invariants have been used as efficient structure metrics to detect local crystalline states in disordered packings of convex shapes<sup>53;54</sup>. Due to their higher-rank nature, however, the physical significance of these structure metrics is less easily understood than for the rank-2 Minkowski tensors. Plotting the probability distributions of  $q_s$  and  $w_s$  for the FH and L4 specimens (540 data points each, Figure 4.17 and Figure 4.18), we observed globally smooth distributions for  $q_s$  and  $w_s$  that are qualitatively similar to those obtained for hyperuniform amorphous cellular solids<sup>54</sup>. Sharp peaks in the distribution would indicate the presence of a locally crystalline region with a certain structural symmetry. Significant differences between the structure metric distributions of the FH and L4 specimens were detected (two-sample Kolmogorov-Smirnov,  $p < 0.01$ ), except for  $q_5$ , indicating that these higher-order structure metrics are sensitive to the structural differences between the plate-like and rod-like specimens.

## 4.4 Discussion

The aim of this study was to provide a more fundamental geometric viewpoint on the quantification of trabecular bone shape. Such a geometry-centered approach not only offers a more mathematical foundation to the long-standing field of trabecular bone morphometry, but also provides a framework to study other spatially complex materials, including bone-mimicking architected scaffolds and biomaterials (*e.g.* metabiomaterials<sup>55</sup>). At the local perspective, this geometric characterization could be accomplished by quantifying the surface curvature of the trabecular interface. In fact, curvature is the defining characteristic when it comes to distinguishing between local structural features, such as rods ( $K = 0, H < 0$ ), plates ( $K = 0, H = 0$ ), and saddle-

shaped arcs ( $K < 0$ ), or to identify primarily convex ( $H < 0$ ) or concave ( $H > 0$ ) regions. We quantified the complex curved landscapes of trabecular bone using the ISD, finding that these density maps serve as effective shape fingerprints for trabecular bone from different anatomical sites. Indeed, the ISD captured the morphological differences between plate-like (FH) and rod-like (L2 and L4) specimens, but were also sensitive to intermediate morphologies along the plate-rod spectrum (IC and CA). Interestingly, the ISD also revealed that trabecular bone is not approximating a minimal surface, opposing a claim often made in the literature to support the use of minimal surface-based scaffolds. Minimal surfaces, for which  $H = 0$  everywhere, arise in systems where surface energy is minimized (*e.g.*, soap films). It is often assumed that a similar phenomenon takes place in the formation and remodeling of trabecular bone, leading to an overall minimal surface morphology. However, we find that the principal curvature ISD of trabecular bone is distinctly different from the minimal surface ISD, where all data points lie on the boundary between regions II and III ( $\kappa_1 = -\kappa_2$ , Figure 4.8).

We also performed a global shape analysis of the trabecular bone interface. To this end, we employed the scalar and tensorial Minkowski functionals, since these are fundamental, highly versatile, and robust indices for integral shape quantification. We found that the Minkowski scalars, which were computed directly on the triangulated bone meshes, correlated with traditional bone morphometric indices, such as BS,  $\partial S/\partial r$ , or  $\chi$ . Moreover, we found that  $W_3$  was more sensitive to differences in bone microarchitecture than the corresponding traditional metric  $\chi$ . Our work was the first to apply the Minkowski tensors to the quantification of trabecular bone shape. This analysis revealed different degrees of anisotropy and ellipticity, depending on the morphological aspect that is being considered. Moreover, anisotropy differences between bone specimens harvested from different anatomical sites could be detected. An important aspect of this Minkowski functional approach is that it unifies several traditional morphometric indices within the same geometrical theory. For example, interfacial and volume anisotropy are traditionally characterized using different methods (*e.g.*, the MIL and SVD methods), while both can be described within the Minkowski tensor framework by using a different tensor. We also applied higher-rank Minkowski metrics to the shape quantification of spatially-decomposed bone specimens, showing that they are also sensitive to morphological differences in bone from different anatomical sites. However, we note that these higher-rank metrics are usually applied to disordered assemblies of discrete convex bodies, such as the Voronoi diagram of a granular packing<sup>53;54</sup>. Such materials are naturally well-suited for this type of domain-wise analysis, since the basic definition of these structure metrics is centered around decomposing the normal density of convex bodies into spherical harmonics. As such, analyses using these metrics might be more compatible with convex particle systems than with non-convex, smooth trabecular bone structures. In this regard, it would be interesting to apply this analysis to specimens that are decomposed into (almost) convex units, for example by volumetric decomposition

into rods and plates<sup>46</sup>, or by approximate convex decomposition<sup>56</sup>. Additionally, the use of clustering algorithms (*e.g.* k-means or DBSCAN) could shed light on the classification sensitivity of such higher-order metrics.

The key characteristic of our metrics is their fundamental geometric nature, which offers a unifying view and geometrical foundation for traditional bone morphometric indices. This geometric perspective could advance the understanding of morphological changes in aging and disease, such as the elusive plate-to-rod transition in osteoporosis<sup>57</sup>. Our approaches could also provide a framework for shape description within the context of bone healing, for example, to characterize the structure of the developing callus *in vivo*<sup>58;59</sup>. Since these metrics are not bound by scale, they could also readily be applied to high-resolution images of much smaller structures within bone, such as the lacuno-canalicular network<sup>60</sup>. Moreover, our insights into trabecular bone curvature are relevant for recent investigations into the role of substrate curvature as a mechanobiological cue at the cell and tissue levels<sup>7;61</sup>, which could be leveraged in tissue engineering applications. Additionally, our geometric framework could also offer a quantitative basis for assessing the extent to which various bone tissue scaffold morphologies are actually mimicking the trabecular bone architecture.

In summary, we have provided a geometric approach to trabecular bone morphometry, quantifying both the local and global shape of trabecular bone, and unifying several traditional morphometric indices within the mathematical language of geometry. Our analyses were centered around surface curvature and Minkowski functionals, which proved to be sensitive fingerprints to site-specific differences in bone morphology. These approaches could facilitate the geometrical characterization of a broad spectrum of spatially-complex materials beyond bone, ultimately advancing the development of accurate structure-property relationships for such materials.

## 4.5 Supporting information

### 4.5.1 Formulations of Minkowski functionals

The concepts of scalar and tensorial Minkowski functionals (MF) have strong roots in integral and convex geometry. Here, we provide a brief overview of their mathematical formulations and notations. Comprehensive accounts of the underlying mathematics and computational implementations can be found elsewhere<sup>2;20;62;63</sup>. The four Minkowski scalars ( $W_\nu$ ) in 3D are defined for a body  $B$  with sufficiently smooth bounding surface  $\partial B$  as:

$$W_0(B) = \int_B dV \quad (4.17)$$

$$W_1(B) = \frac{1}{3} \int_{\partial B} dA \quad (4.18)$$

$$W_2(B) = \frac{1}{3} \int_{\partial B} H dA \quad (4.19)$$

$$W_3(B) = \frac{1}{3} \int_{\partial B} K dA \quad (4.20)$$

Where  $H$  is the mean curvature,  $K$  is the Gaussian curvature,  $dV$  is the infinitesimal volume element and  $dA$  is the infinitesimal area element. The label  $v$  corresponds to the type of integral used in the calculation:  $v = 0$  corresponds to a volume integral,  $v = 1$  to a surface integral,  $v = 2$  to a mean curvature-weighted surface integral, and  $v = 3$  to a Gaussian curvature-weighted integral.

In 3D, the six rank-2 Minkowski tensors of interest ( $W_v^{r,s}$ ) are obtained by volume and surface integrals of tensor products of position vectors ( $\mathbf{r}$ ) and surface normal vectors ( $\mathbf{n}$ ):

$$W_0^{2,0}(B) = \int_B \mathbf{r} \otimes \mathbf{r} dV \quad (4.21)$$

$$W_1^{2,0}(B) = 1/3 \int_{\partial B} \mathbf{r} \otimes \mathbf{r} dA \quad (4.22)$$

$$W_2^{2,0}(B) = 1/3 \int_{\partial B} H(\mathbf{r}) \mathbf{r} \otimes \mathbf{r} dA \quad (4.23)$$

$$W_3^{2,0}(B) = 1/3 \int_{\partial B} K(\mathbf{r}) \mathbf{r} \otimes \mathbf{r} dA \quad (4.24)$$

$$W_1^{0,2}(B) = 1/3 \int_{\partial B} \mathbf{n} \otimes \mathbf{n} dA \quad (4.25)$$

$$W_2^{0,2}(B) = 1/3 \int_{\partial B} H(\mathbf{r}) \mathbf{n} \otimes \mathbf{n} dA \quad (4.26)$$

Here, the additional labels  $r$  and  $s$  respectively represent the powers of the position and normal vectors in the integrals. The symbol  $\otimes$  represents the tensor product, defined as  $(a \otimes b)_{ij} = a_i b_j$ . The tensor  $W_3^{0,2}$  is not defined here, as it would reduce to the unit tensor multiplied with the Euler-Poincaré characteristic<sup>64</sup>. The four first tensors  $W_v^{2,0}$  for  $v = 0, 1, 2, 3$  are translation-covariant, meaning that they are dependent upon the choice of origin. The tensors  $W_1^{0,2}$  and  $W_2^{0,2}$ , on the other hand, are translation-invariant.

The starting point in the definition of MF are smooth convex bodies, *i.e.* convex bodies with a continuous normal field on the bounding surface. However, the trabecular bone structures that we investigate are non-convex and are represented by a discrete triangle mesh, which presents singularities in the curvatures and the normal definitions at the edges and vertices of the triangles. Two defining properties of the MF are employed to address these challenges. First, the construction of a parallel body  $B_\varepsilon$  by an infinitesimally small dilation ( $\varepsilon \rightarrow 0$ ) enables the continuous definition of surface normals, since discrete vertices and edges are mapped to smooth spherical and cylindrical segments in the dilated body. While useful for convex bodies, this approach does not hold for concave bodies. However, the additivity property of the MF provides an elegant solution. For two convex bodies  $B_1$  and  $B_2$ , the additivity property states that:

$$W_v^{r,s}(B_1 \cup B_2) = W_v^{r,s}(B_1) + W_v^{r,s}(B_2) - W_v^{r,s}(B_1 \cap B_2) \quad (4.27)$$

That is, the MF of the union of two convex bodies is equal to the sum of the MF of the separate bodies, minus the MF of the intersection of those bodies. While,  $(B_1 \cup B_2)$  is, in general, not convex,  $(B_1 \cap B_2)$  is convex. Thus, a non-convex body can be decomposed into convex bodies, enabling a continuous definition of the MF<sup>20</sup>. It is because of these continuity and additivity properties that the MF are robust and versatile indices for the characterization of complex spatial structure. There is also a mathematical argument that supports the fundamental nature of the MF, that is, their completeness to describe complex spatial structure. Alesker's theorem states that any motion-covariant, conditionally continuous, and additive tensorial functional of a 2D or 3D body can be expressed as a linear combination of the MF<sup>19;20</sup>. Thus, Minkowski functionals form a fundamental basis for structure characterization using other additive functionals.

While we have focused on rank-2 Minkowski tensors, higher-rank generalizations can be defined as well. Specifically, one can consider the so-called irreducible Minkowski tensors (IMT), which generalize the  $W_1^{0,s}$  tensors to higher rank  $s$ . These tensors decompose the surface normal density of the body  $B$  into spherical harmonics<sup>53</sup>:

$$\Psi_{s,m} = \sqrt{\frac{4\pi}{2s+1}} \frac{\sum_b A_b Y_s^m(\mathbf{n}_b)}{\sum_b A_b} \quad (4.28)$$

Where  $\Psi_{s,m}$  are the tensor components,  $A_b$  is the area of face  $b$  with outward normal  $\mathbf{n}_b$ , and  $Y_s^m$  represent the spherical harmonics. Based on these higher-rank IMTs, quadratic ( $q_s$ ) and cubic ( $w_s$ ) structure metrics that are invariant under rotation, scaling and translation can be defined as:

$$q_s = \sum_{m=-s}^s |\Psi_{s,m}|^2 \quad (4.29)$$

$$w_s = \sum_{m_1=-s}^s \sum_{m_2=-s}^s \sum_{m_3=-s}^s \begin{pmatrix} s & s & s \\ m_1 & m_2 & m_3 \end{pmatrix} \Psi_{s,m_1} \Psi_{s,m_2} \Psi_{s,m_3} \quad (4.30)$$

Where the array in parentheses represents Wigner's  $3j$  symbols. These structure metrics are related to the classical bond-orientational order parameters, and have, for example, been applied to detect local crystalline states in disordered particle systems<sup>17;53;54;65</sup>.

## 4.5.2 Additional figures

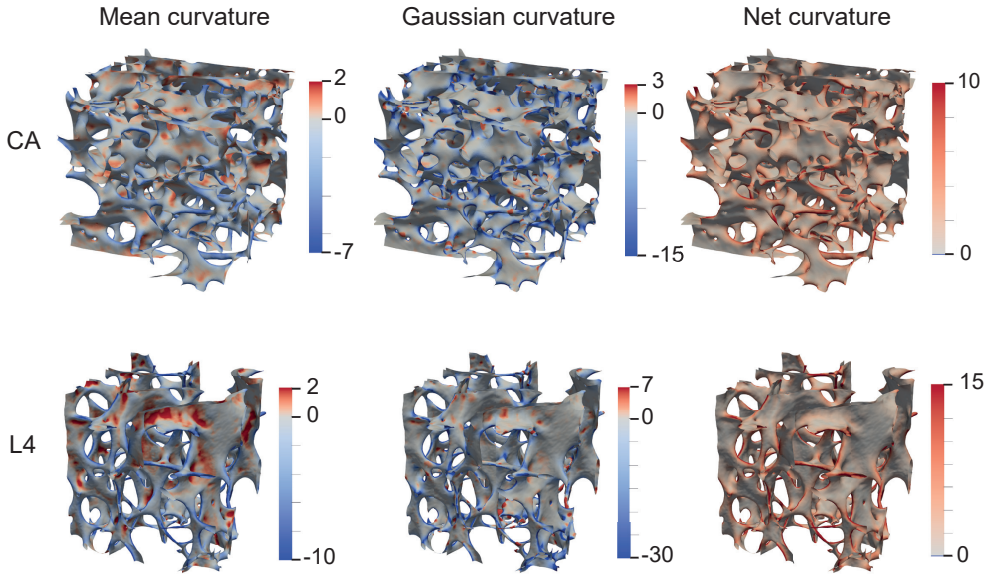


**Figure 4.15:** Visualizations of normalized curvature of the trabecular interface. Left: mean curvature, middle: Gaussian curvature, right: net curvature. Top row: representative sample from the calcaneus (CA), bottom row: representative sample from the fourth lumbar vertebra (L4).

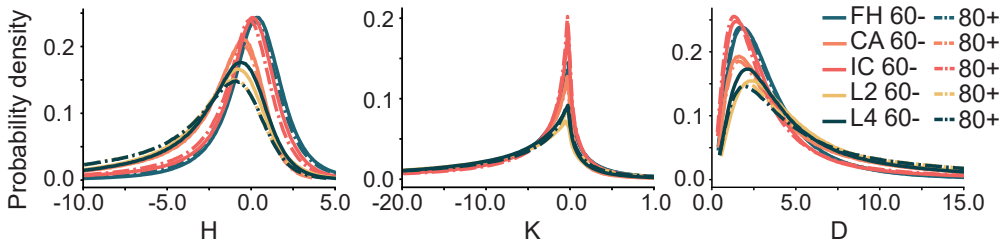


**Figure 4.16:** Age-dependent effects on curvature probability distributions. Probability density distribution of non-normalized mean (left), Gaussian (middle) and net (right) curvature, split between bone type and age group (younger than 60 years and older than 80 years). Data was not normalized to exclude the effect of changing BS/BV with age. Each curve contains data from several samples (age < 60 years:  $n_{CA} = 14$ ,  $n_{FH} = 15$ ,  $n_{IC} = 13$ ,  $n_{L2} = 16$ ,  $n_{L4} = 16$ . Age > 80 years:  $n_{CA} = 18$ ,  $n_{FH} = 17$ ,  $n_{IC} = 17$ ,  $n_{L2} = 18$ ,  $n_{L4} = 19$ ).

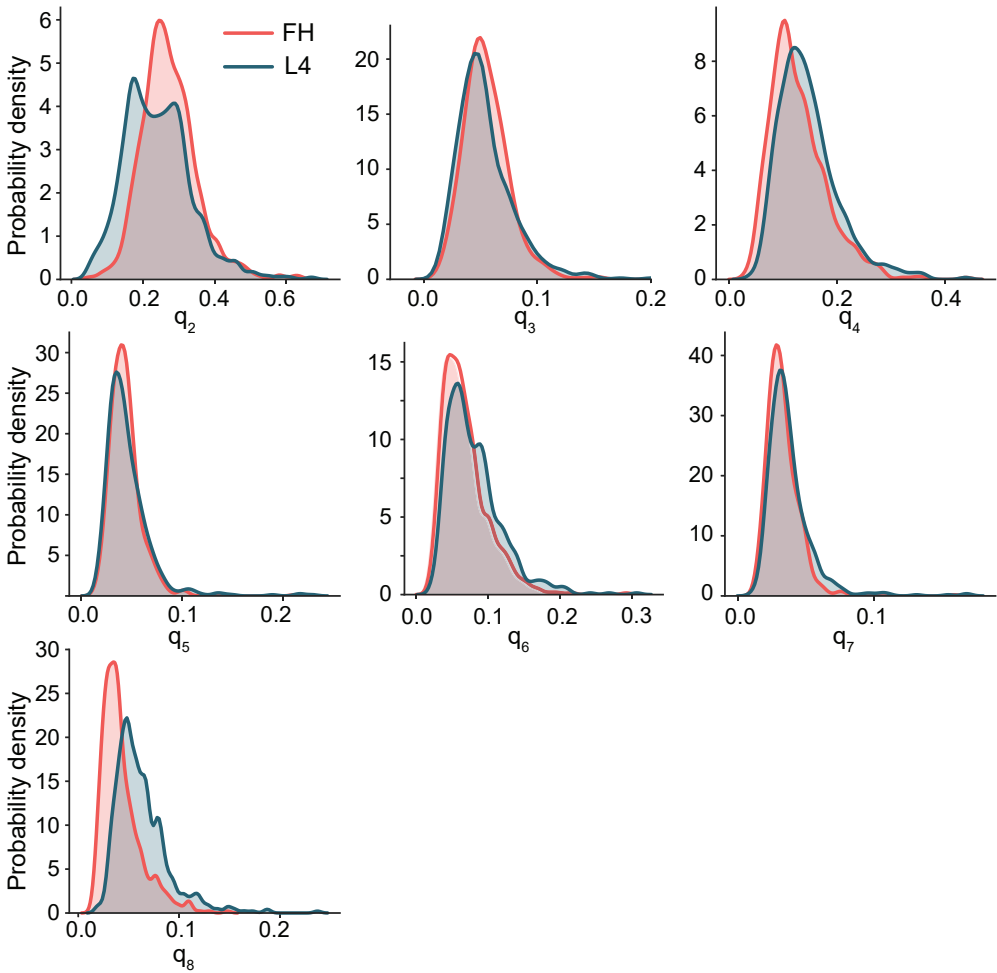
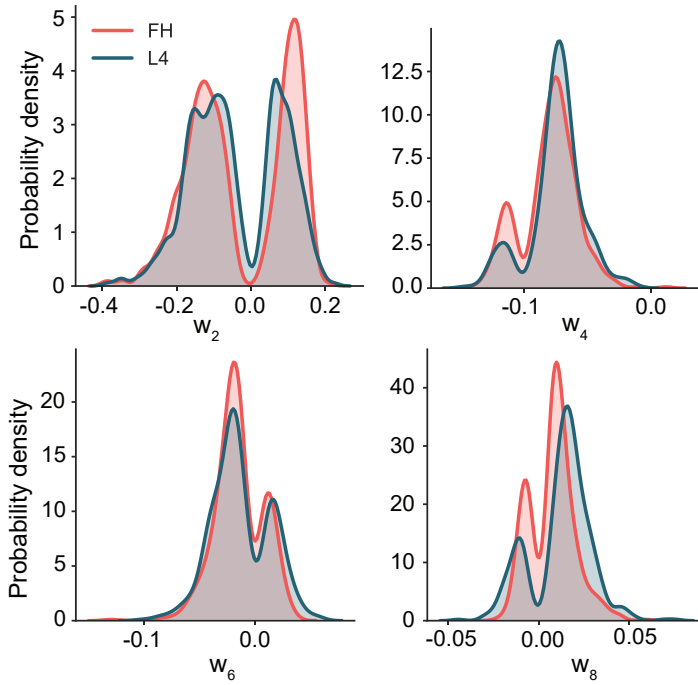


Figure 4.17: Quadratic invariants of the irreducible Minkowski tensors. Probability density distributions of the quadratic invariants of the IMT ( $q_s$ ), for rank  $s \in [2, 8]$ . Only the curves of the FH and L4 samples are shown, which were created using kernel density estimates on 540 data points each (20 trabecular samples, each split into 27 subdomains).



**Figure 4.18:** Cubic invariants of the irreducible Minkowski tensors. Probability density distributions of the cubic invariants of the IMT ( $w_s$ ), for rank  $s \in [2, 4, 6, 8]$  ( $w_s = 0$  for odd  $s$ ). Only the curves of the FH and L4 samples are shown, which were created using kernel density estimates on 540 data points each (20 trabecular samples, each split into 27 subdomains).

**Table 4.1:** Statistics for the DA. P-values for the two-sided Mann-Whitney-U tests between all sample groups for the three Minkowski tensors that were being considered. Differences in the means were considered statistically significant for  $p < 0.01$ .

	Type	CA	FH	IC	L2	L4
$DA_1^{0,2}$	CA					
	FH	0.5716				
	IC	7.59E-09	2.70E-07			
	L2	3.42E-12	4.04E-10	0.039		
	L4	3.60E-10	5.57E-08	0.745	0.088	
$DA_1^{2,0}$	CA					
	FH	3.65E-04				
	IC	2.86E-07	2.85E-13			
	L2	1.65E-04	4.39E-10	0.573		
	L4	8.45E-07	3.13E-12	0.636	0.323	
$DA_2^{0,2}$	CA					
	FH	8.16E-10				
	IC	0.708	2.00E-06			
	L2	0.006	5.67E-12	0.032		
	L4	2.56E-05	4.50E-13	0.001	0.137	

## Bibliography

- [1] U. G. Wegst, H. Bai, E. Saiz, A. P. Tomsia, and R. O. Ritchie. Bioinspired structural materials. *Nature materials*, 14(1):23–36, 2015.
- [2] G. E. Schröder-Turk, W. Mickel, S. C. Kapfer, M. A. Klatt, F. M. Schaller, M. J. F. Hoffmann, N. Kleppmann, P. Armstrong, A. Inayat, D. Hug, M. Reichelsdorfer, W. Peukert, W. Schwieger, and K. Mecke. Minkowski tensor shape analysis of cellular, granular and porous structures. *Advanced Materials*, 23(22-23):2535–2553, 2011.
- [3] R. Huiskes, R. Ruimerman, G. H. Van Lenthe, and J. D. Janssen. Effects of mechanical forces on maintenance and adaptation of form in trabecular bone. *Nature*, 405(6787):704–706, 2000.
- [4] A. Parfitt, C. Mathews, A. Villanueva, M. Kleerekoper, B. Frame, and D. Rao. Relationships between surface, volume, and thickness of iliac trabecular bone in aging and in osteoporosis. implications for the microanatomic and cellular mechanisms of bone loss. *The Journal of clinical investigation*, 72(4):1396–1409, 1983.
- [5] T. Hildebrand, A. Laib, R. Müller, J. Dequeker, and P. Rüeggsegger. Direct three-dimensional morphometric analysis of human cancellous bone: microstructural data from spine, femur, iliac crest, and calcaneus. *Journal of bone and mineral research*, 14(7):1167–1174, 1999.
- [6] A. A. Zadpoor. Mechanical meta-materials. *Mater. Horiz.*, 3(5):371–381, 2016.
- [7] S. J. Callens, R. J. Uyttendaele, L. E. Fratila-Apachitei, and A. A. Zadpoor. Substrate curvature as a cue to guide spatiotemporal cell and tissue organization. *Biomaterials*, 232:119739, 2020.
- [8] M. Rumpfer, A. Woesz, J. W. Dunlop, J. T. van Dongen, and P. Fratzl. The effect of geometry on three-dimensional tissue growth. *J R Soc Interface*, 5(27):1173–80, 2008.
- [9] L. Pieuchot, J. Marteau, A. Guignandon, T. Dos Santos, I. Brigaud, P.-F. Chauvy, T. Cloatre, A. Ponche, T. Petithory, P. Rougerie, M. Vassaux, J.-L. Milan, N. T. Wakhloo, A. Spangenberg, M. Bigerelle, and K. Anselme. Curvotaxis directs cell migration through cell-scale curvature landscapes. *Nature communications*, 9(1):3995, 2018.
- [10] S. Ehrig, B. Schamberger, C. Bidan, A. West, C. Jacobi, K. Lam, P. Kollmannsberger, A. Petersen, P. Tomancak, and K. Kommareddy. Surface tension determines tissue shape and growth kinetics.

- Science Advances*, 5(9):eaav9394, 2019.
- [11] M. L. Bouxsein, S. K. Boyd, B. A. Christiansen, R. E. Guldberg, K. J. Jepsen, and R. Müller. Guidelines for assessment of bone microstructure in rodents using micro-computed tomography. *Journal of bone and mineral research*, 25(7):1468–1486, 2010.
- [12] A. Odgaard. Three-dimensional methods for quantification of cancellous bone architecture. *Bone*, 20(4):315–328, 1997.
- [13] T. Hildebrand and P. Rüeggsegger. Quantification of bone microarchitecture with the structure model index. *Computer Methods in Biomechanics and Bio Medical Engineering*, 1(1):15–23, 1997.
- [14] P. L. Salmon, C. Ohlsson, S. J. Shefelbine, and M. Doube. Structure model index does not measure rods and plates in trabecular bone. *Frontiers in endocrinology*, 6:162, 2015.
- [15] L. Steiner, A. Synek, and D. H. Pahr. Comparison of different microct-based morphology assessment tools using human trabecular bone. *Bone Reports*, page 100261, 2020.
- [16] K. Verdelis, L. Lukashova, E. Atti, P. Mayer-Kuckuk, M. Peterson, S. Tetradis, A. Boskey, and M. van der Meulen. Microct morphometry analysis of mouse cancellous bone: intra-and inter-system reproducibility. *Bone*, 49(3):580–587, 2011.
- [17] S. C. Kapfer, W. Mickel, K. Mecke, and G. E. Schröder-Turk. Jammed spheres: Minkowski tensors reveal onset of local crystallinity. *Physical Review E*, 85(3):030301, 2012.
- [18] F. M. Schaller, S. C. Kapfer, J. E. Hilton, P. W. Cleary, K. Mecke, C. De Michele, T. Schilling, M. Saadatfar, M. Schröter, and G. W. Delaney. Non-universal voronoi cell shapes in amorphous ellipsoid packs. *EPL (Europhysics Letters)*, 111(2):24002, 2015.
- [19] S. Alesker. Description of continuous isometry covariant valuations on convex sets. *Geometriae dedicata*, 74(3):241–248, 1999.
- [20] G. E. Schröder-Turk, W. Mickel, S. C. Kapfer, F. M. Schaller, B. Breidenbach, D. Hug, and K. Mecke. Minkowski tensors of anisotropic spatial structure. *New Journal of Physics*, 15(8):083028, 2013.
- [21] H. Hadwiger. *Vorlesungen über inhalt, Oberfläche und isoperimetrie*, volume 93. Springer-Verlag, 2013.
- [22] A. Genau, P. Voorhees, and K. Thornton. The morphology of topologically complex interfaces. *Scripta Materialia*, 60(5):301–304, 2009.
- [23] S. C. Cowin. The relationship between the elasticity tensor and the fabric tensor. *Mechanics of materials*, 4(2):137–147, 1985.
- [24] A. Odgaard, J. Kabel, B. van Rietbergen, M. Dalstra, and R. Huiskes. Fabric and elastic principal directions of cancellous bone are closely related. *Journal of biomechanics*, 30(5):487–495, 1997.
- [25] S. Hyde, Z. Blum, T. Landh, S. Lidin, B. Ninham, S. Andersson, and K. Larsson. *The Language of Shape: The Role of Curvature in Condensed Matter: Physics, Chemistry and Biology*. Elsevier Science, Amsterdam, The Netherlands, 1996.
- [26] J. Dequeker. Assessment of quality of bone in osteoporosis—biomed i: fundamental study of relevant bone. *Clinical rheumatology*, 13:7–12, 1994.
- [27] A. Jacobson, D. Panozzo, C. Schüller, O. Diamanti, Q. Zhou, and N. Pietroni. libigl: A simple C++ geometry processing library. <http://libigl.github.io/libigl>, 2016.
- [28] M. Dawson-Haggerty. Trimesh 3.2.0. <https://trimesh.org>, 2019.
- [29] T. Lewiner, H. Lopes, A. W. Vieira, and G. Tavares. Efficient implementation of marching cubes’ cases with topological guarantees. *Journal of graphics tools*, 8(2):1–15, 2003.
- [30] M. Desbrun, M. Meyer, P. Schröder, and A. H. Barr. Implicit fairing of irregular meshes using diffusion and curvature flow. In *Proceedings of the 26th annual conference on Computer graphics and interactive techniques*, pages 317–324.
- [31] D. Panozzo, E. Puppo, and L. Rocca. Efficient multi-scale curvature and crease estimation. *Proceedings of Computer Graphics, Computer Vision and Mathematics (Brno, Czech Republic)*, 1(6), 2010.
- [32] F. Cazals and M. Pouget. Estimating differential quantities using polynomial fitting of osculating jets. *Computer Aided Geometric Design*, 22(2):121–146, 2005.
- [33] A. Genau and P. W. Voorhees. Spatial correlations in symmetric and asymmetric bicontinuous structures. *Acta materialia*, 57(20):6226–6233, 2009.
- [34] C.-L. Park, J. Gibbs, P. W. Voorhees, and K. Thornton. Coarsening of complex microstructures fol-

- lowing spinodal decomposition. *Acta Materialia*, 132:13–24, 2017.
- [35] P. Cignoni, M. Callieri, M. Corsini, M. Dellepiane, F. Ganovelli, and G. Ranzuglia. Meshlab: an open-source mesh processing tool. In *Eurographics Italian chapter conference*, volume 2008, pages 129–136.
- [36] M. A. Klatt, G. E. Schröder-Turk, and K. Mecke. Mean-intercept anisotropy analysis of porous media. ii. conceptual shortcomings of the mil tensor definition and minkowski tensors as an alternative. *Medical physics*, 44(7):3663–3675, 2017.
- [37] T. Harrigan and R. Mann. Characterization of microstructural anisotropy in orthotropic materials using a second rank tensor. *Journal of Materials Science*, 19(3):761–767, 1984.
- [38] M. Doube, M. M. Klosowski, I. Arganda-Carreras, F. P. Cordelières, R. P. Dougherty, J. S. Jackson, B. Schmid, J. R. Hutchinson, and S. J. Shefelbine. Bonej: free and extensible bone image analysis in imagej. *Bone*, 47(6):1076–1079, 2010.
- [39] C. A. Simmons and J. A. Hipp. Method-based differences in the automated analysis of the three-dimensional morphology of trabecular bone. *Journal of Bone and Mineral Research*, 12(6):942–947, 1997.
- [40] H. Jinnai, H. Watashiba, T. Kajihara, Y. Nishikawa, M. Takahashi, and M. Ito. Surface curvatures of trabecular bone microarchitecture. *Bone*, 30(1):191–194, 2002.
- [41] D. Hilbert and S. Cohn-Vossen. *Geometry and The Imagination*. Chelsea Publishing Company, New York, USA, 1990.
- [42] M. Stauber and R. Muller. Age-related changes in trabecular bone microstructures: global and local morphometry. *Osteoporos Int*, 17(4):616–26, 2006.
- [43] R. Mendoza, I. Savin, K. Thornton, and P. W. Voorhees. Topological complexity and the dynamics of coarsening. *Nature materials*, 3(6):385–388, 2004.
- [44] N. Akaiwa and P. W. Voorhees. Late-stage phase separation: dynamics, spatial correlations, and structure functions. *Physical Review E*, 49(5):3860, 1994.
- [45] C. R ath, R. Monetti, J. Bauer, I. Sidorenko, D. M uller, M. Matsuura, E. Lochm uller, P. Zysset, and F. Eckstein. Strength through structure: visualization and local assessment of the trabecular bone structure. *New Journal of Physics*, 10(12):125010, 2008.
- [46] M. Stauber and R. M uller. Volumetric spatial decomposition of trabecular bone into rods and plates—a new method for local bone morphometry. *Bone*, 38(4):475–484, 2006.
- [47] M. Hahn, M. Vogel, M. Pompesius-Kempa, and G. Delling. Trabecular bone pattern factor—a new parameter for simple quantification of bone microarchitecture. *Bone*, 13(4):327–330, 1992.
- [48] M. Saadatfar, M. Mukherjee, M. Madadi, G. Schröder-Turk, F. Garcia-Moreno, F. Schaller, S. Hutzler, A. Sheppard, J. Banhart, and U. Ramamurty. Structure and deformation correlation of closed-cell aluminium foam subject to uniaxial compression. *Acta materialia*, 60(8):3604–3615, 2012.
- [49] C. Beisbart, R. Dahlke, K. Mecke, and H. Wagner. *Vector-and tensor-valued descriptors for spatial patterns*, pages 238–260. Springer, 2002.
- [50] W. Whitehouse. The quantitative morphology of anisotropic trabecular bone. *Journal of microscopy*, 101(2):153–168, 1974.
- [51] M. A. Klatt, G. E. Schröder-Turk, and K. Mecke. Mean-intercept anisotropy analysis of porous media. i. analytic formulae for anisotropic boolean models. *Medical physics*, 44(7):3650–3662, 2017.
- [52] R. Ketcham and T. M. Ryan. Quantification and visualization of anisotropy in trabecular bone. *Journal of microscopy*, 213(2):158–171, 2004.
- [53] W. Mickel, S. C. Kapfer, G. E. Schröder-Turk, and K. Mecke. Shortcomings of the bond orientational order parameters for the analysis of disordered particulate matter. *The Journal of Chemical Physics*, 138(4):044501, 2013.
- [54] M. A. Klatt, J. Lovrić, D. Chen, S. C. Kapfer, F. M. Schaller, P. W. Schönhöfer, B. S. Gardiner, A.-S. Smith, G. E. Schröder-Turk, and S. Torquato. Universal hidden order in amorphous cellular geometries. *Nature communications*, 10(1):1–9, 2019.
- [55] A. A. Zadpoor. Meta-biomaterials. *Biomaterials science*, 8(1):18–38, 2020.
- [56] J.-M. Lien and N. M. Amato. Approximate convex decomposition of polyhedra. In *Proceedings of the 2007 ACM symposium on Solid and physical modeling*, pages 121–131.

- 
- [57] A. Felder, S. Monzem, R. De Souza, D. Mills, A. Boyde, and M. Doube. The plate-to-rod transition in trabecular bone loss is elusive. *BioRxiv*, 2020.
- [58] E. Wehrle, D. C. T. né Betts, G. A. Kuhn, A. C. Scheuren, S. Hofmann, and R. Müller. Evaluation of longitudinal time-lapsed in vivo micro-ct for monitoring fracture healing in mouse femur defect models. *Scientific reports*, 9(1):1–12, 2019.
- [59] D. C. T. né Betts, E. Wehrle, G. R. Paul, G. A. Kuhn, P. Christen, S. Hofmann, and R. Müller. The association between mineralised tissue formation and the mechanical local in vivo environment: Time-lapsed quantification of a mouse defect healing model. *Scientific Reports*, 10(1):1–10, 2020.
- [60] P. Goggin, K. Zygalkis, R. Oreffo, and P. Schneider. High-resolution 3D imaging of osteocytes and computational modelling in mechanobiology: insights on bone development, ageing, health and disease. *Eur Cell Mater*, 31:264–295, 2016.
- [61] M. Werner, N. A. Kurniawan, and C. V. Bouten. Cellular geometry sensing at different length scales and its implications for scaffold design. *Materials*, 13(4):963, 2020.
- [62] G. E. Schröder-Turk, S. Kapfer, B. Breidenbach, C. Beisbart, and K. Mecke. Tensorial minkowski functionals and anisotropy measures for planar patterns. *Journal of microscopy*, 238(1):57–74, 2010.
- [63] K. R. Mecke. Integral geometry in statistical physics. *International Journal of Modern Physics B*, 12(09):861–899, 1998.
- [64] W. Mickel, G. E. Schröder-Turk, and K. Mecke. Tensorial minkowski functionals of triply periodic minimal surfaces. *Interface focus*, 2:623–633, 2012.
- [65] P. J. Steinhardt, D. R. Nelson, and M. Ronchetti. Bond-orientational order in liquids and glasses. *Physical Review B*, 28(2):784, 1983.

# 5

## TUNING METAMATERIALS USING HYPERBOLIC TILINGS

Rapid advances in additive manufacturing over the past decade have kindled widespread interest in the rational design of metamaterials with unique properties. However, many applications require multi-physics metamaterials, where multiple properties are simultaneously optimized. This is challenging, since different properties, such as mechanical and mass transport properties, typically impose competing requirements on the nano-/micro-/meso-architecture of metamaterials. Here, we propose a parametric metamaterial design strategy that enables independent tuning of the effective permeability and elastic properties. We apply hyperbolic tiling theory to devise simple templates based on which triply periodic minimal surfaces (TPMS) are partitioned into hard and soft regions. Through computational analyses, we demonstrate how the decoration of hard, soft, and void phases within the TPMS substantially enhances their permeability-elasticity property space and offers high tunability in the elastic properties and anisotropy, at constant permeability. We also show that this permeability-elasticity balance is well captured using simple scaling laws. We then proceed to demonstrate the proposed concept through multi-material additive manufacturing of representative specimens. Our approach, which is generalizable to other designs, offers a route towards multi-physics metamaterials that need to simultaneously carry a load and enable mass transport, such as architected tissue-substituting metabiomaterials.

S. J. P. Callens, C. Arns, A. Kuliesh, A. A. Zadpoor, Decoupling minimal surface metamaterial properties through multi-material hyperbolic tilings, *Advanced Functional Materials*, 2021. (accepted)

## 5.1 Introduction

The fundamental paradigm of metamaterials is that their macroscale properties are largely driven by their nano-, micro- or mesoscale architecture. This intimate structure-property connection has been leveraged to develop metamaterials with unique, unusual, and extreme acoustic<sup>1</sup>, photonic<sup>2</sup>, or mechanical properties<sup>3</sup>. Historically, most types of metamaterial architectures have been based on periodic arrangements of struts, often inspired by crystallographic lattices<sup>4–7</sup>. In search for higher mass-specific mechanical properties, periodic plate-lattices have been proposed, capable of storing strain energy more efficiently<sup>8;9</sup>. More recently, smooth shell-based lattices have also attracted great interest, since these architectures are devoid of the stress concentrations that are inherent at the intersections of strut- or plate-lattices, and since their intrinsically curved morphology endows them with high specific stiffness and attractive energy absorption behavior<sup>10–13</sup>. Among the shell-based metamaterials, those derived from triply periodic minimal surfaces (TPMS) have most widely been studied<sup>14–18</sup>. These are bicontinuous, infinitely-extending, saddle-shaped surfaces that locally minimize area and have the defining characteristic of zero mean curvature ( $H = 0$ ) at every point along the surface<sup>19</sup>. The widespread interest in TPMS-based structures has partly been fueled by their intriguing mathematical foundation and their widespread observations in spontaneously-assembled natural systems<sup>20;21</sup>, but is also due to their attractive and extremal physical properties<sup>22</sup>.

Irrespective of the architecture type, the central challenge in metamaterial design is to optimize the material geometry to attain the desired macroscale physical properties. In the case of multi-physics metamaterials, however, several properties are targeted simultaneously. It turns out that optimizing the geometry for one property often leads to a decrease in the performance with respect to the others. This is exemplified in architected tissue scaffolds, or “metabiomaterials”<sup>23</sup>, where the material geometry has conflicting effects on the mechanical and mass transport functionality<sup>24–27</sup>: increasing the mechanical properties, by increasing the relative density of the metamaterial<sup>28</sup>, generally results in a decreased fluid permeability. A notable example where the decoupling of these properties is somewhat possible is a pentamode metamaterial, consisting of spindle-shaped struts that meet at relatively weak nodes<sup>29</sup>. The mechanical properties of these materials mainly depend on the node geometry and not on the overall relative density, offering the ability to partially tune the permeability independently of the mechanical properties<sup>30</sup>. However, this ability is limited, because the upper bound on permeability is constrained by the desired mechanical properties, and because pentamode metamaterials inherently rely on highly-specific strut-based architectures.

An attractive and more potent, strategy to unlock a larger metamaterial design space is to spatially distribute multiple materials with widely different properties, instead of architecting only a single material. This approach has only recently become possible, owing to advances in multi-material additive manufacturing, and has enabled the design of mechanical metamaterials with exotic deformation modes and tunable Poisson’s ratios<sup>31–34</sup>. Here, we leverage the multi-material strategy to develop periodic meta-

materials with independently tunable properties. Specifically, we propose a strategy to parametrically design biphasic, TPMS-based architectures that interpolate between strut- and shell-lattices. Our design strategy builds upon the inherent hyperbolic symmetries of TPMS, offering a robust approach to tailor unit cell geometry and the spatial distribution of the different materials. This enables us to decouple the mechanical and mass transport properties to an extent that is not possible in uniphase metamaterials. Using computational homogenization, we determine the effective elastic properties and anisotropy of a wide range of structures as a function of the unit cell geometry and material choice. Moreover, we quantify the intrinsic permeability of the metamaterials using computational fluid dynamics (CFD). Our results confirm that our parametric design strategy and the combination of two different materials significantly expands the achievable space of multi-physics properties and greatly enhances the ability to independently tune the permeability and elastic properties. Additionally, we demonstrate the proposed concept by additively manufacturing and mechanically testing metamaterials that combine hard and soft polymers. While we focus here on two types of TPMS, this concept is directly extendable to other types of TPMS and could also be generalized to other types of shell-lattices, even those of a stochastic nature. Ultimately, this approach of spatially decorating shell-based metamaterials with multiple materials could be useful in many applications where mechanical and mass transport properties are both important, such as load-bearing heat exchangers, noise-abating permeable airfoils, or architected tissue scaffolds.

## 5.2 Materials & Methods

### 5.2.1 Parametric design of TPMS

3D mesh representations of the labelled P and G surfaces were computed using the Enneper-Weierstrass parametrization, which maps the points in an integration domain in the complex plane to the curved fundamental patch in  $\mathbb{E}^3$  that is used to build the TPMS. Specifically, the Cartesian coordinates of the points on the fundamental patch are obtained by:

$$\begin{pmatrix} x \\ y \\ z \end{pmatrix} = \text{Re} \left[ e^{i\theta} \int_{\omega_0}^{\omega} \begin{pmatrix} 1 - \tilde{\omega}^2 \\ i(1 + \tilde{\omega}^2) \\ 2\tilde{\omega} \end{pmatrix} R(\tilde{\omega}) d\tilde{\omega} \right] + p_0 \quad (5.1)$$

Here,  $R(\tilde{\omega})$  is the Weierstrass function,  $\theta$  is the Bonnet angle,  $p_0$  is an arbitrary translation to define the origin (here,  $p_0 = [0, 0, 0]$ ),  $\omega_0$  is a fixed point in the integration domain (here,  $\omega_0 = 0$ ), and  $\omega$  is any other point in the integration domain. For the PDG surface family, the Weierstrass function is defined as:

$$R(\tilde{\omega}) = [\tilde{\omega}^8 - 14\tilde{\omega}^4 + 1]^{-\frac{1}{2}} \quad (5.2)$$

For the P surface,  $\theta = \pi/2$ . For the G surface,  $\theta = \arccot\left(\frac{E_k \frac{3}{4}}{E_k \frac{1}{4}}\right)$ , where  $E_k(k)$  is the complete elliptic integral of the first kind with parameter  $k$ . Thus, any point  $\omega$  in the complex domain is mapped to a point in the 3D fundamental patch through this parametrization. The points  $\omega$  were uniformly sampled from the complex domain, depending on the patch type and the desired density. Next, the Delaunay triangulation of the set of discrete points  $\omega$  was computed to obtain a triangular (2D) mesh of the complex domain. The faces of the 2D mesh were labelled as hard, soft, or void phase. The Enneper-Weierstrass equations were then used to map the points  $\omega$  to their Cartesian coordinates in  $\mathbb{E}^3$ . The mesh topology and face labelling that was computed on the 2D complex domain was applied to the 3D set of points to obtain a meshed representation of the fundamental patch. Finally, the patch was patterned in 3D according to the P and G symmetry operations to obtain the translational unit cells<sup>35;36</sup>.

All computations and consequent mesh processing steps were performed in MATLAB (MATLAB 2018b, Mathworks, Natick, MA, USA) using custom code, as well as by using several of the functions of the GIBBON toolbox<sup>37</sup>.

### 5.2.2 Conversion to solid structures

The zero-thickness meshes were converted to solid, 3D-printable structures by a surface thickening approach. To this end, all vertices were offset in the positive and negative normal directions by a distance  $d/2$ , where  $d$  is a user-defined fraction of the unit cell bounding box length  $L$  (*i.e.*,  $d = \frac{t}{20}L$ ). This offsetting operation resulted in two parallel meshes, one at each side of the original minimal surface mesh. Triangular bounding faces were added at the edges of the two parallel meshes to create a watertight mesh that represents the solid structure. This thickening approach was applied for every labeled region of the mesh separately, resulting in a solid triangle mesh for both the hard and soft phases. The surface area and relative densities were then computed on the basis of these triangle meshes, and the meshes were exported in the STL format for 3D printing and visualization in Keyshot (Keyshot 5, Luxion, Tustin, CA, USA). The voxelized representations of the unit cells were created from the triangle meshes using the function `patch2Im` in the GIBBON toolbox<sup>37</sup>.

### 5.2.3 Morphology

The Gaussian curvature ( $K$ ) of the TPMS mesh vertices was computed from the complex domain as<sup>38</sup>:

$$K(\omega) = -4(1 + |\omega|^2)^{-4} |R(\omega)|^{-2} \quad (5.3)$$

The area element ( $dS$ ) or surface metric for a point  $\omega = u + iv$  is defined as<sup>39</sup>:

$$dS = dudv(1 + |\omega|^2)^2 |R(\omega)|^2 \quad (5.4)$$

A shell factor  $\xi$ , capturing the local shell-like nature of the structures, was computed on the voxelized mesh representations ( $100 \times 100 \times 100$  voxels) of the entire unit cell. First, the soft phase of the unit cells was thresholded, resulting in a binary  $100 \times 100 \times 100$  array with label 1 for all the voxels in the soft phase, and label 0 for all other voxels. Then, the Euclidean distance map (EDM) was computed on this 3D array, specifying the distance from every voxel to the nearest voxel in the soft phase. The hard phase was then used as a mask to extract the distance of every voxel in the hard phase to the nearest voxel in the soft phase. The distance value was then divided by the local shell thickness to compute the shell factor at every point  $p$  in the hard phase (the factor 2 is to obtain the diameter of the largest circular shell that fits inside the hard phase at every point):

$$\xi(p) = 2 \cdot \frac{EDM(p)}{t(p)} \quad (5.5)$$

### 5.2.4 Permeability simulations

The effective fluid permeability for the different uniphase designs was computed using a lattice-Boltzmann (LB) scheme that has previously been used for determining permeabilities of standard TPMS microstructures<sup>26</sup>. Briefly, the LB method models the temporal evolution of a particle velocity distribution function at discrete lattice positions under collision and streaming steps, and subject to a small pressure gradient<sup>40</sup>. Here, the LB simulations were performed with standard D3Q19 elements (*i.e.*, 3D elements with 19 possible momentum components)<sup>41</sup> and a lattice discretization of  $256^3$  voxels was used. The intrinsic permeability was extracted using the Darcy's law, and were normalized to the cross-sectional area of the unit cell $L^2$ .

### 5.2.5 Effective elastic properties

The effective elastic mechanical properties of the different unit cell designs were computed using a computational homogenization scheme based on the finite element method (FEM) in MATLAB<sup>42</sup>. Briefly, the effective (homogenized) elasticity tensor  $C^*$  ( $6 \times 6$ , using Voigt notation) was extracted from six independent, linear elastic FEM simulations on voxelized representations of the unit cells with periodic boundary conditions. In the simulations, the Poisson's ratio was set to 0.3, and the stiffness of the hard phase was set to 2 GPa. Following a convergence study on the basis of the effective elastic modulus (considered converged when the variation was below 1%), a discretization of the unit cells into  $128^3$  voxels was found to be sufficient to compute the effective elastic properties. The linear force-displacement equations in the FEM simulations were solved using the preconditioned conjugate gradient (pcg) scheme in MATLAB, with a tolerance set to  $10^{-8}$ . Due to the cubic symmetry of the metamaterial designs,  $C^*$  contains only three independent components (*i.e.*,  $C_{11}$ ,  $C_{12}$  and  $C_{44}$ ). From those components, the effective uniaxial Young's modulus ( $E_{11}^*$  in  $\langle 100 \rangle$  direction), effective bulk modulus ( $K^*$ ), effective shear modulus ( $G^*$ , *e.g.* applied on the  $(100)$  plane in the

[010] direction), and the effective Poisson's ratio ( $\nu^*$ , for loading in the (100) direction) could be determined<sup>17</sup> as:

$$E_{11}^* = \frac{1}{S_{11}^*} \quad (5.6)$$

$$K^* = \frac{C_{11} + 2C_{12}}{3} \quad (5.7)$$

$$G^* = C_{44} \quad (5.8)$$

$$\nu^* = \frac{C_{12}}{C_{11} + C_{12}} \quad (5.9)$$

Here,  $S_{11}^*$  is the (1, 1) component of the homogenized compliance tensor  $S^*$ . The Zener anisotropy index for cubic crystals ( $\alpha_Z$ ) was determined as<sup>17</sup>:

$$\alpha_Z = \frac{2C_{44}}{C_{11} - C_{12}} \quad (5.10)$$

To plot the elastic modulus surfaces, the effective Young's modulus in different directions was calculated by transforming the effective stiffness tensor using the appropriate rotation matrix for every direction<sup>42</sup>.

The Hashin-Shtrikman (HS) upper bounds for the effective bulk ( $K_{HSU}$ ) and shear ( $G_{HSU}$ ) moduli of a nearly isotropic material were computed as<sup>9</sup>:

$$K_{HSU} = \frac{4G_S K_S \rho}{4G_S + 3K_S(1 - \rho)} \quad (5.11)$$

$$G_{HSU} = \frac{(9K_S + 8G_S)\rho G_S}{20G_S + 15K_S - 6(K_S + 2G_S)\rho} \quad (5.12)$$

The corresponding HS bound for the Young's modulus (assuming isotropic linear elasticity) was then determined as a function of  $K_{HSU}$  and  $G_{HSU}$  is given by:

$$E_{HSU} = \frac{9K_{HSU}G_{HSU}}{3K_{HSU} + G_{HSU}} \quad (5.13)$$

### 5.2.6 Multi-material additive manufacturing

Four different designs were additively manufactured through a material jetting process, using a combination of hard and soft photocurable polymer resins. The length of the unit cell bounding box was set to  $L = 20$  mm, the shell thickness was  $t = 2$  mm, and the lattices consisted of 27 unit cells in a  $3 \times 3 \times 3$  arrangement. The fabrication was performed using a Connex3 Objet 350 printer (Stratasys, Minnesota, USA). Both the hard and soft phases were made with commercial polymer resins designed for this

printing system: the hard phase was printed using the VeroMagenta polymer (Stratasys,  $E = 2 - 3$  GPa according to the manufacturer), while the soft phase was printed using the translucent, rubber-like Agilus30 polymer (Stratasys, Shore A hardness: 30-35 according to the manufacturer, which corresponds to  $E \approx 1.2 - 1.4$  MPa using Gent's relation<sup>43</sup>). This combination of materials has previously been used to print 2D metamaterials with  $E_h/E_s \approx 10^3$ <sup>33</sup>. The lattices were printed with soluble support material (SUP706, Stratasys), which was carefully removed after printing using chemical washing (according to the manufacturer's protocol), water rinsing, and compressed air blowing.

### 5.2.7 Mechanical compression tests

The specimens were mechanically tested in a displacement-controlled uniaxial compression test, using a Lloyd universal test bench (LR5K, Ametek STC, Bognor Regis, UK), equipped with a 5kN load cell. The test was performed under ambient temperatures (22 °C) at a strain rate of  $10^{-3} \text{ s}^{-1}$ . A preload of 5 N was used and the test was halted at 2% macroscopic strain. Every specimen was tested five times, allowing ample time between consecutive tests for the material to recover its original shape. Throughout the low-strain testing, the specimens maintained their integrity and the force-displacement curves did not show signs of failure. The effective Young's modulus was obtained from the linear-elastic gradient of the linear portion of the stress-strain curve.

## 5.3 Results

### 5.3.1 Triply periodic networks from hyperbolic tilings

The foundation of our design approach is the intimate connection between TPMS and the hyperbolic geometry: the geometry of saddle shapes (with negative Gaussian curvature). Every TPMS can be constructed from a single, fundamental patch that is symmetrically patterned throughout 3D space. This repeating pattern corresponds to a triangular tiling on the hyperbolic plane  $\mathbb{H}^2$ . Essentially, this implies that a portion of 2D hyperbolic space ( $\mathbb{H}^2$ ) can be projected onto a TPMS (with minor distortions) in 3D Euclidean space ( $\mathbb{E}^3$ ), in a manner similar to how a portion of the 2D Euclidean plane ( $\mathbb{E}^2$ ) can be embedded in  $\mathbb{E}^3$  by wrapping it on a cylinder<sup>44</sup>. Here, we focus on two well-known TPMS of cubic symmetry, namely the P (primitive) and G (gyroid) surfaces. Both of these surfaces belong to the same TPMS family – they are related through the so-called Bonnet transformation – and they can both be derived from the same hyperbolic tiling. This hyperbolic tiling is called the \*246 tiling (using orbifold notation), and consists of a repeating triangular patch with angles  $\pi/2$ ,  $\pi/4$ , and  $\pi/6$  (Figure 5.1a).

The remarkable connection between the hyperbolic plane and the TPMS enables the creation of a vast set of convoluted 3D networks, six of which are used as a template in this study. By decorating  $\mathbb{H}^2$  with a periodic line pattern, *i.e.* a tiling that is a subgroup of the \*246 tiling, and by wrapping that line pattern onto the P or G minimal surface, a

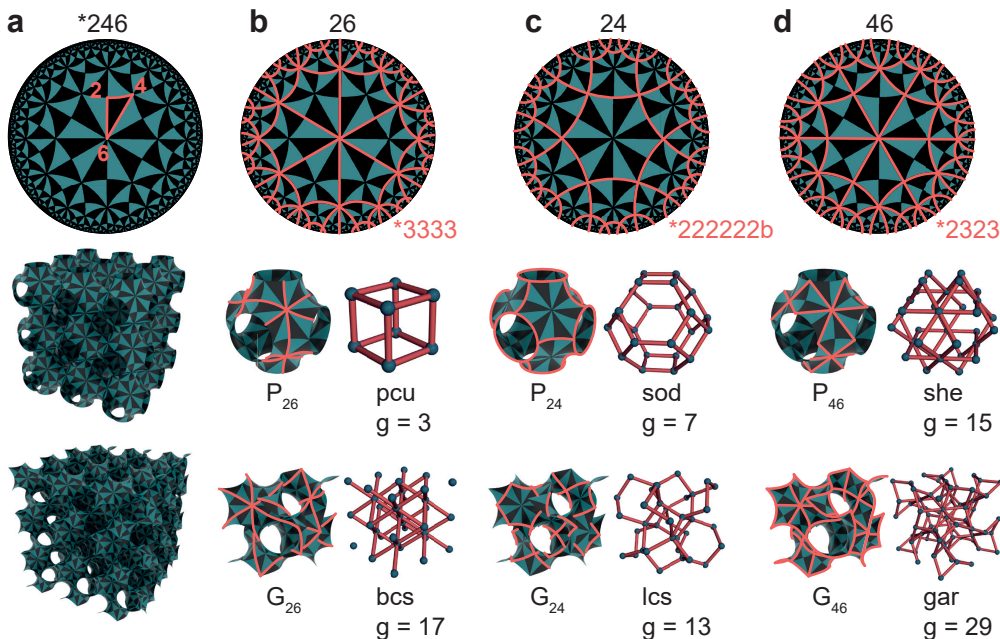


**Figure 5.1:** Hyperbolic tilings projected onto TPMS. a) The  $*246$  hyperbolic tiling shown in the Poincaré disk model, with the fundamental triangular patch highlighted in red (top). The same hyperbolic tiling projected onto 27 translational unit cells of the P (middle) and G (bottom) surfaces. b) The “26” tiling in the Poincaré disk model (top) that results in two distinct networks on the P (middle) and G (bottom) surfaces. The orbifold naming of the tiling is indicated with red digits ( $*3333$ ) and the RCSR naming<sup>45</sup> of the 3D net topology is indicated with three letters (pcu and bcs). We show both the network by its embedding in the TPMS (left) as well as its canonical form (right)<sup>46</sup>, which are topologically equivalent. The genus of the network (per unit cell) is indicated by  $g$ . c-d) Analogous to b), but now for the “24” and “46” hyperbolic tilings.

periodic three-dimensional network, or surface reticulation, is obtained<sup>44;46–48</sup>. Here, we consider three different hyperbolic tilings that give rise to six periodic networks, though many other tilings are available to generate different networks<sup>46</sup> (Figure 5.1b-d). The three hyperbolic tilings are obtained by drawing lines along one of the three edges of the fundamental patch. For example, the “26” tiling (Figure 5.1b) is obtained by connecting the edges between the  $\pi/2$  and  $\pi/6$  angles of all triangular patches. All of the six surface reticulations that we design are topologically equivalent to 3D networks that are known in reticular chemistry<sup>45</sup>. For example, the  $P_{24}$  and  $G_{46}$  surface reticulations correspond to the crystal network structures of the minerals sodalite and garnet, respectively. Notably, the same hyperbolic tiling wrapped onto the P or G surface results in substantially different networks from a topological perspective. For example, the “26” tiling (Figure 5.1b) on the P surface generates a network with a primitive cubic topology of genus 3 (per unit cell), while the same tiling on the G surface generates a much more complex network with genus 17, even though the P and G surfaces themselves

are both of genus 3. It is interesting to note that the  $P_{46}$  network consists entirely out of (Euclidean) straight lines, which is not the case for the other networks (Figure 5.1d). In fact, only a specific subset of TPMS, the so-called spanning minimal surfaces<sup>49</sup>, have embedded straight lines, a property that is not shared by the G surface.

### 5.3.2 Parametric design of biphasic strut-shell metamaterials

The realization of 3D networks embedded in the P and G surfaces is the starting point of our strategy to parametrically design biphasic metamaterials. Essentially, our approach consists of “widening” these embedded networks to a desired degree, in order to form skeleton-like decorations on the TPMS that are templates to rationally distribute hard and soft phases (Figure 5.2 and Figure 5.3). To construct the decorated translational unit cells of the P and G surfaces, we used the formal Enneper-Weierstrass parametrization<sup>35;36</sup>. This parametrization maps an integration domain in the complex plane  $\mathbb{C}^2$  to the fundamental patch in  $\mathbb{E}^3$ , which is then symmetrically patterned to form the translational unit cell (Subsection 5.2.1). The simplicity of the integration domain enabled us to easily label portions of it with either a hard or a soft phase. This labeling is transferred to the unit cell through the Enneper-Weierstrass mapping. We based the labeling of the integration domain on the previously described hyperbolic tilings: the domain is subdivided into different regions through lines that are parallel to one of the three domain edges (Figure 5.2a). This subdivision is parametrized by two offset parameters  $\phi_h \in [0, 1]$  and  $\phi_s \in [0, 1]$ , which respectively control the amount of hard and soft phases and are defined such that  $\phi_h + \phi_s \leq 1$ . The default scenario is to set  $\phi_s = 1 - \phi_h$  and vary the offset parameter of the hard phase. When  $\phi_h = 0$  or  $\phi_h = 1$ , the unit cell entirely consists of a soft or a hard phase, respectively. Any intermediate value of  $\phi_h$  results in a biphasic partitioning of the unit cell, whereby the hard phase interpolates between predominantly strut-like or shell-like architectures (Figure 5.2a). It is also possible to decrease the offset parameter of the soft phase such that  $\phi_h + \phi_s < 1$ . In this case, not all points in the integration domain are utilized in the Enneper-Weierstrass mapping, and an incomplete fundamental patch is obtained. This results in a unit cell with additional openings as opposed to the traditional P or G morphology (Figure 5.2b).

We converted the zero-thickness surfaces into solid metamaterial unit cells by bidirectionally thickening the surface in the normal direction by a fraction of the bounding box length (Figure 5.2b). Using the three hyperbolic tilings shown in Figure 5.1, six distinct biphasic metamaterial morphologies could be generated with tunable amounts of hard and soft materials (by varying  $\phi_s$  and  $\phi_h$ ). We termed the designs with  $\phi_s + \phi_h = 1$  “full” structures, and the designs with  $\phi_s + \phi_h < 1$  “skeleton” structures (Figure 5.2b). The full biphasic designs with  $\phi_s = 1 - \phi_h$  shown in Figure 5.3 all have the same overall morphology, *i.e.* that of the standard P or G surface, yet exhibit widely different material decorations. It is important to observe that the hard phase always forms a triply connected structure, while the soft phase consists of isolated inclusions. For sufficiently small values of  $\phi_h$ , the hard phase essentially forms a strut-like skeleton that

reinforces the predominantly soft-phased unit cell. For the larger values of  $\phi_h$ , the area of the soft inclusions diminishes and the hard-phased skeleton approaches the shell-like morphology of the original unit cell.

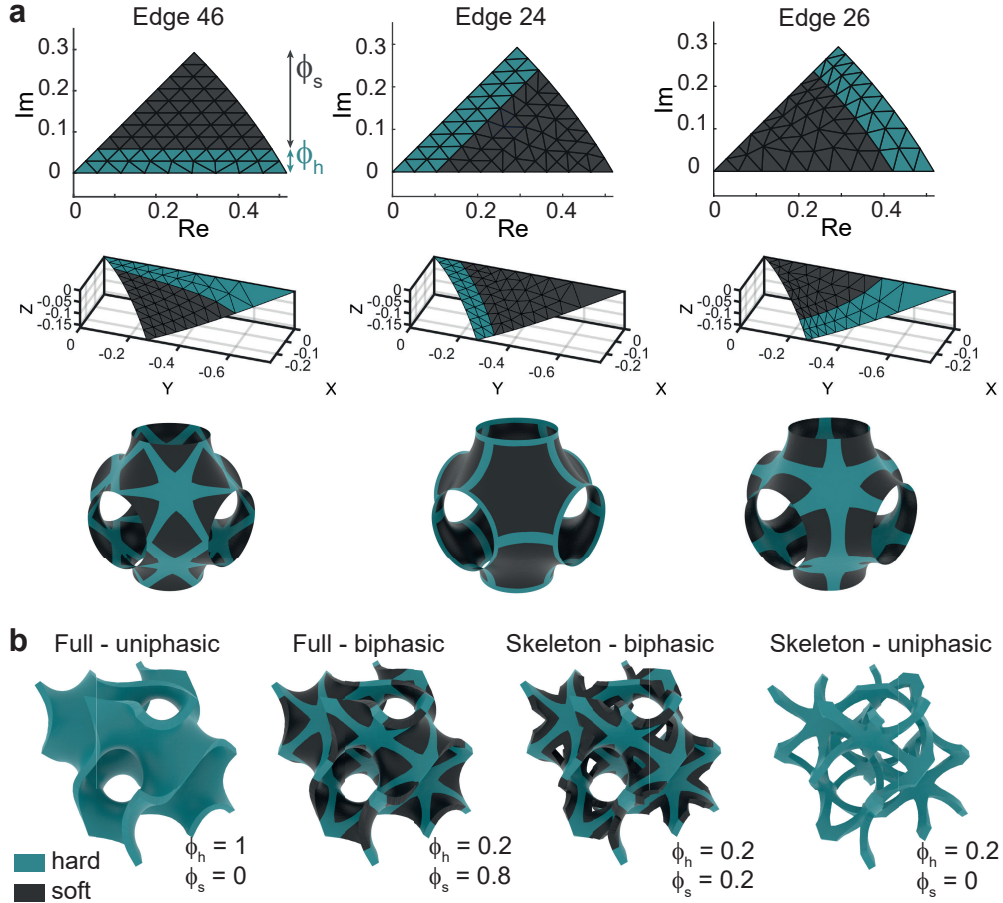


**Figure 5.2:** Parametric design approach for biphasic TPMS. a) Top row: the integration domain in the complex plane  $\mathbb{C}^2$  that is parametrically partitioned into hard and soft regions for the “46”, “24”, and “26” designs. Middle row: the integration domain is mapped to  $\mathbb{E}^3$  through the Enneper-Weierstrass parametrization, resulting in saddle-shaped fundamental patch with a biphasic partition. Bottom row: The translational unit cell of the P surface obtained through symmetry operations on the fundamental patches of the middle row. b) The different types of uni- and biphasic unit cell designs derived from the G surface.

### 5.3.3 Morphology & mass transport properties

The defining characteristic of TPMS is their specific curvature profile: they are defined as surfaces with zero mean curvature ( $H = 0$ ) and negative or vanishing Gaussian curvature ( $K \leq 0$ ). Hence, TPMS are saddle-shaped everywhere, except at some isolated points where the surface is locally flat ( $K = 0$ ). The specific curvature characteristic is part of the reason why TPMS have attracted interest as templates for tis-

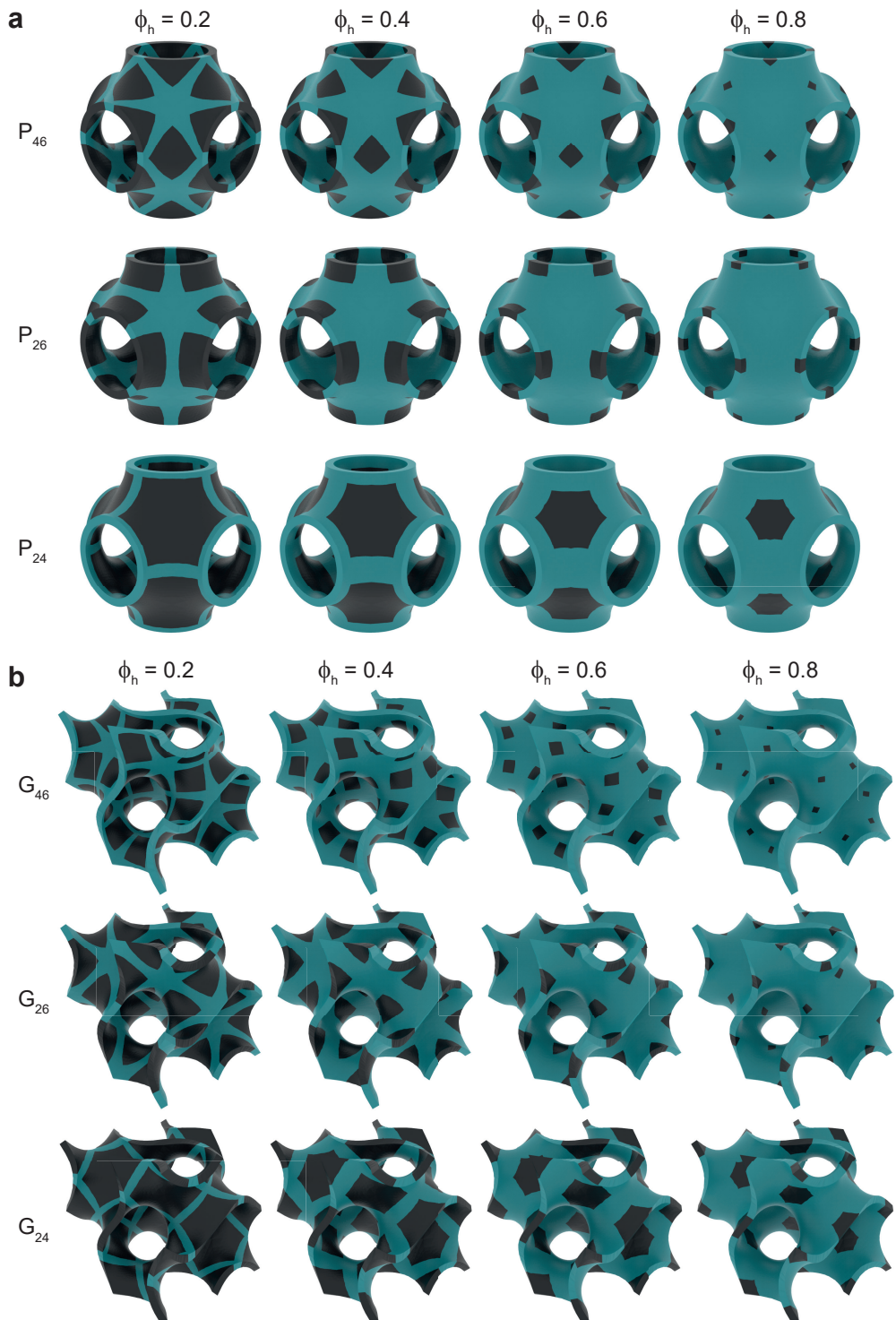


**Figure 5.3:** Metamaterial unit cells for the three P and G designs, respectively. In all cases,  $\phi_s = 1$  and  $\phi_h$  is varied between 0.2 and 0.8.

sue engineering scaffolds, since surface curvature is known to control the organization and dynamics of tissues and cells<sup>50–52</sup>. We quantified the curvature distributions of the P and G unit cells, as well as that of their skeletonized variants that are obtained at  $\phi_h = 0.2$  and  $\phi_s = 0$  (Figure 5.4a). We found that the “46” and “26” skeletonized designs of the P and G surfaces are, on average, less intrinsically curved than the “24” designs. Indeed, the  $P_{46}$ ,  $P_{26}$ ,  $G_{46}$ , and  $G_{26}$  designs all maintain the locally flat regions in the skeletonized representations. These flat regions are connected through weakly or strongly curved ribbons in the “26” and “46” designs, respectively. In the  $P_{24}$  and  $G_{24}$  designs, however, the flat regions are absent and the skeletonized representation consists entirely out of highly curved ribbons (Figure 5.4a).

As mentioned before, the surfaces are converted to sheet-solids by offsetting the surface in both normal directions by a desired amount. This thickening operation, combined with variations in  $\phi_s$  and  $\phi_h$ , enabled us to achieve a wide range of meta-material volume fractions  $\rho$ . Here,  $\rho = V_{solid}/L^3$ , where  $V_{solid}$  is the volume of the solid material and  $L$  is the length of the cubic bounding box. We quantified the scaling of  $\rho_h$ , *i.e.* the volume fraction of the hard phase, with respect to the offset parameter  $\phi_h$ , finding that the “26” and “46” designs follow the same nonlinear scaling law in both the P (Figure 5.4b) and G (Figure 5.4e) surfaces. In the “24” designs, an almost linear relation between  $\phi_h$  and  $\rho_h$  is observed, with lower values of  $\rho_h$  than in the “26” and “46” designs for  $\phi_h < 1$ . Indeed, the soft phases in the  $P_{24}$  and  $G_{24}$  designs are always larger for a given value of  $\phi_h$  (provided  $\phi_h < 1$ ) than in the other designs of the same family (Figure 5.3). Since these plots were made at constant shell thickness ( $t$ ), these relations also approximate the scaling of the surface area with  $\phi_h$  ( $S_{solid} \approx V_{solid}/t$ ). Hence, for a fixed value of  $\phi_h$ , these plots indicate that the total surface area is lower in the “24” designs. This is because the “24” skeleton designs do not contain the locally flat mesh regions (Figure 5.4a), which are the largest contributors to the overall unit cell area. Specifically, if the Enneper-Weierstrass map is applied to a uniformly meshed integration domain with equal-area triangles, then the corresponding fundamental patch triangles in the regions with small Gaussian curvature will have larger area than the triangles in regions with strongly negative Gaussian curvature (Figure 5.2a). Indeed, the area element of the P and G minimal surfaces at a local point is inversely related to the Gaussian curvature at that point (Subsection 5.2.3).

In order to study the local shell-like or strut-like nature of the hard phase, which forms the reinforcing backbone of the entire unit cell, we introduced the shell factor  $\xi$ . We defined  $\xi$  for any point in the hard phase as the shortest distance to the soft phase, divided by the shell thickness of the unit cell (Subsection 5.2.3). As such,  $\xi$  is a measure of the largest circular shell that locally fits inside the hard phase at every point, with larger  $\xi$  representing a locally more shell-like morphology. We quantified  $\xi_{max}$  for the P (Figure 5.4c-d) and G (Figure 5.4f-g) designs as a function of the offset factor  $\phi_h$ . All the three P designs exhibited a different scaling of  $\xi_{max}$  with  $\phi_h$ , while the  $G_{26}$  and  $G_{46}$  showed the same scaling behavior. Moreover, the  $P_{24}$  and  $G_{24}$  designs achieved the lowest values for  $\xi_{max}$ , indicating a more strut-like morphology across the range

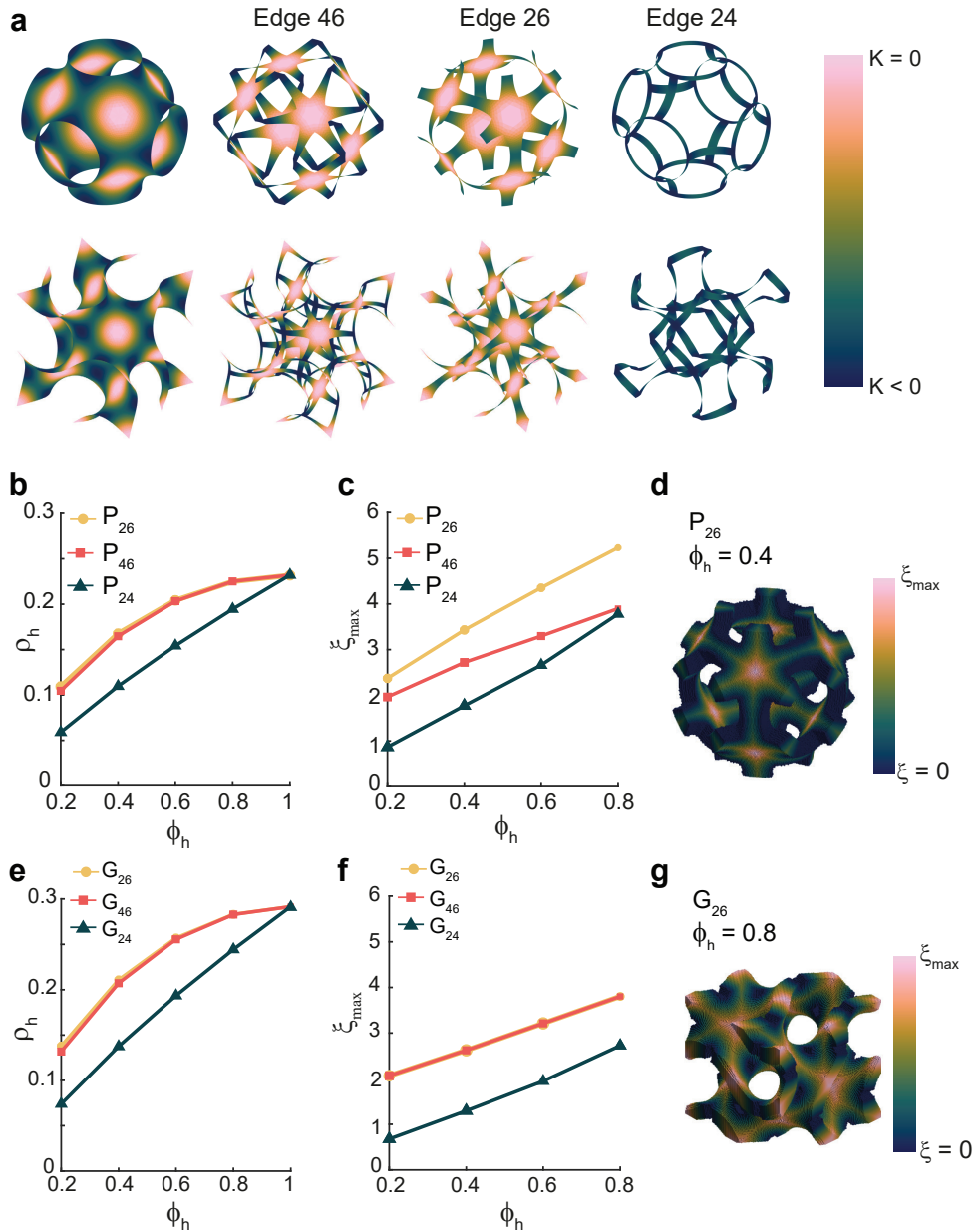


**Figure 5.4:** Morphology of TPMS-based metamaterials. a) The Gaussian curvature distribution of the P and G surfaces, as well as their different skeletonized representations. b) The hard-phase volume fraction ( $\rho_h$ ) versus the offset parameter ( $\phi_h$ ) for the different P surface designs with a shell thickness of  $t = L/10$ . c) The maximum shell factor ( $\xi_{max}$ ) versus the offset parameter ( $\phi_h$ ) for the different P surface designs with a shell thickness of  $t = L/10$ . d) The visualization of the shell factor  $\xi$  for the  $P_{26}$  design with  $\phi_h = 0.4$  and  $t = L/10$ . e-f) Analogous to the plots shown in b-c) but for the G surface designs. g) The visualization of  $\xi$  for the  $G_{26}$  design with  $\phi_h = 0.8$  and  $t = L/10$ .

of  $\phi_h$ . This is the consequence of the selective removal of flat regions in these designs (Figure 5.4a).

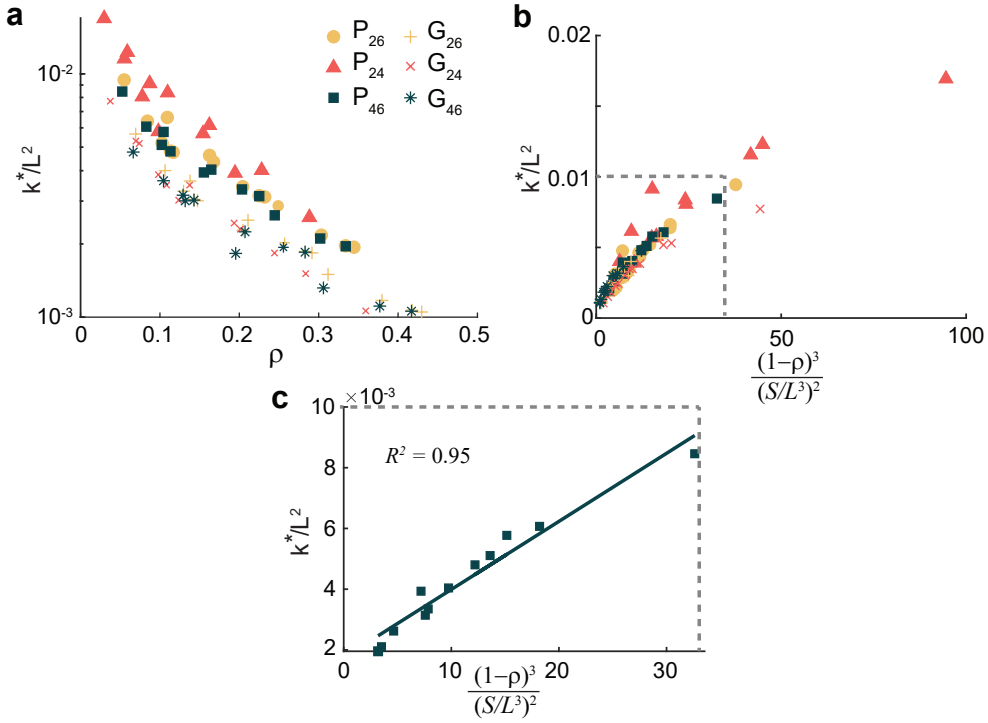


**Figure 5.5:** a) The normalized effective permeability ( $k^*/L^2$ ) versus volume fraction ( $\rho$ ) for full and skeleton P and G designs. b)  $k^*/L^2$  versus the geometric factor  $(1 - \rho)^3/(S/L^3)^2$  for all the designs in a). c) A magnified view of the data for the  $P_{46}$  designs in b).

We were interested in the fluid permeability of the different metamaterial designs, as this is an important property in various applications. In metabiomaterials, for example, permeability affects the supply of oxygen and nutrients to cells, the ingrowth of regenerated tissue, and the potential biodegradation behavior of the scaffolds<sup>53</sup>. Therefore, we estimated the effective intrinsic permeability using a lattice-Boltzmann simulation scheme (Subsection 5.2.4). The permeability is entirely determined by the unit cell geometry, and is independent of the shape and size of the partitioned domains. For example, all P designs in Figure 5.3a would exhibit the same permeability as their overall geometry is that of the standard P surface. Therefore, the only parameters affecting permeability are the design type, the shell thickness, and the total offset parameter  $\phi = \phi_h + \phi_s$ . As expected, the normalized effective permeability  $k^*/L^2$  decreases with the volume fraction  $\rho$  (Figure 5.5a), following a similar trend for all designs. Moreover, the permeabilities of the designs based on the G surface are consistently lower than those of the P surface designs. This has previously been observed for full P and G designs, and was attributed to the lower specific surface area of the P surface<sup>54</sup>. While permeability clearly scales inversely (and nonlinearly) with the volume fraction, it is not

the only geometric parameter of relevance. We find that the permeability values scale almost linearly with  $(1 - \rho)^3 / (S/L^3)^2$ , where  $S$  is the surface area of the unit cell and  $L$  is the bounding box length (Figure 5.5b-c). This factor also appears in the so-called Kozeny equation for predicting the permeability of porous materials, and indicates that the specific surface area ( $S/L^3$ ) also plays a role in dictating the metamaterial permeability<sup>53;54</sup>.

### 5.3.4 Elastic mechanical properties

The other set of key properties of interest in this study are the elastic mechanical properties, which depend not only on the unit cell geometry (*i.e.*,  $\rho$ ,  $\phi$ , and  $t$ ) but also on the bulk properties of both materials. We computed the effective elastic properties of our designs using a computational homogenization scheme (Subsection 5.2.5). Through this finite element-based approach, we calculated the effective stiffness tensor  $C^*$  for every design, from which properties, such as the effective elastic modulus ( $E^*$ ), bulk modulus ( $K^*$ ), shear modulus ( $G^*$ ) and Poisson's ratio ( $\nu$ ) could be obtained (Subsection 5.2.5).

The effective elastic modulus  $E_{11}^*$ , *i.e.* the stiffness under uniaxial loading in the  $\langle 100 \rangle$  direction, of the uniphase skeleton and full structures scaled according to a power law of  $\rho$  (Figure 5.6a), as expected from the well-known Gibson-Ashby relationships<sup>55</sup>. The weakest structures corresponded to the strut-like  $P_{24}$  and  $G_{24}$  designs with an offset parameter of  $\phi = 0.2$  and a shell thickness of  $t = L/20$ . All of our strut-like designs (*i.e.*, those with low  $\phi$ ), correspond to bending-dominated architectures according to the Maxwell-Calladine criterion, indicating sub-optimal stiffness<sup>56</sup>. The stiffest structures, corresponding to G-based shell-like architectures ( $\phi \geq 0.8$ ), achieved specific stiffness values close to the Hashin-Shtrikman upper bound (HSU) for nearly isotropic structures, which was also the case for the bulk and shear moduli (Figure 5.6b-c)<sup>9</sup>. It is, however, important to realize that the priority in (and the novelty of) this study is achieving high tunability in mechanical and mass transport properties, rather than presenting new geometries that achieve extreme (specific) properties. Finally, we also observed positive effective Poisson's ratios for all designs (Figure 5.6d).

The central concept of our design approach is the ability to parametrically partition the unit cells into two distinct domains. As such, we are able to tune the mechanical properties using a combination of geometry and material distribution. To study the effects of material choice, we plotted the effective stiffness against the ratio of the Young's moduli of the hard and soft materials ( $E_h/E_s$ ) for all six design types, with  $\phi_h \in [0.2, 0.8]$  and  $\phi_s = 1 - \phi_h$  (Figure 5.7). When  $E_h/E_s = 1$ , the behavior of the standard uniphase P or G unit cell is obtained. For increasing values of  $E_h/E_s$ , the stiffness reduces for all six design types. As expected, this stiffness reduction is much stronger for the lower values of  $\phi_h$ , where the proportion of the hard phase is low. For example, the stiffness of the  $P_{26}$  design with  $\phi_h = 0.8$  and  $E_h/E_s = 10^3$  is 15% lower than at  $E_h/E_s = 1$ , while it is 92% lower when  $\phi_h = 0.2$  (Figure 5.7). Moreover, in all designs, the stiffness reduction curves flatten out when  $E_h/E_s \approx 100$ . Beyond this

point, the soft phase hardly contributes to the overall stiffness, and the load is primarily carried by the hard phase, which forms a reinforcing skeleton for the overall unit cell. Additionally, the stiffness reduction behavior varies among the different designs. For the same values of  $\phi_h$ , the  $P_{24}$  and  $P_{46}$  designs exhibit the highest and lowest reduction behavior, respectively. This could be attributed to the overall geometry of the hard phase in both cases: the  $P_{24}$  skeleton consists entirely out of highly-curved, slender struts, while the  $P_{46}$  skeleton contains a higher number of struts, which are approximately straight and, hence, more efficiently carry load (Figure 5.4a).

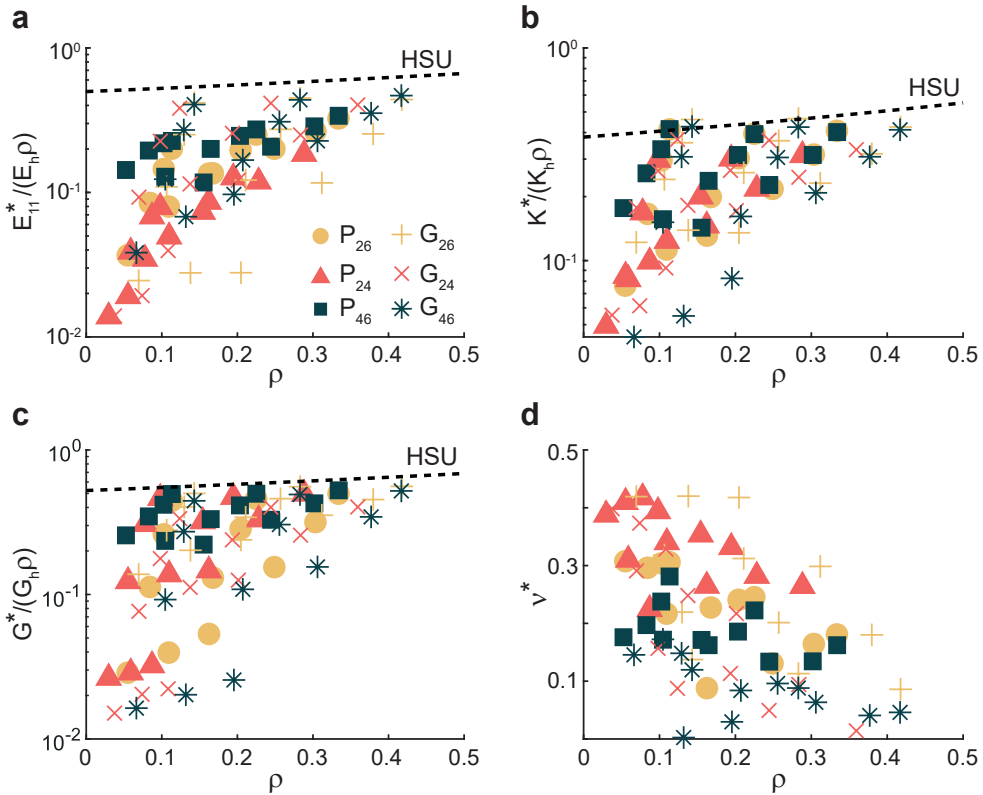


**Figure 5.6:** Effective elastic properties. a) The normalized effective elastic modulus for uniphase full and skeleton designs ( $\phi_s = 0$ ). b-d) The effective bulk modulus, shear modulus, and Poisson's ratio for the uniphase full and skeleton designs, respectively. The black dashed line indicates the Hashin-Shtrikman upper bound for nearly isotropic structures.

The elastic properties of metamaterial architectures are, in general, anisotropic, though isotropic variants have been proposed<sup>8</sup>. We quantified the elastic anisotropy of the different designs as function of  $E_h/E_s$  using the Zener anisotropy index  $\alpha_Z$  (Subsection 5.2.5). When  $\alpha_Z = 1$ , the structure is elastically isotropic, meaning that the effective stiffness is equal in all directions. We found that  $\alpha_Z$  varies with  $E_h/E_s$  and shell thickness  $t$  for all the designs, although the extent to which it varies depends on the design type (Figure 5.8, Figure 5.9 and Figure 5.15). For example, the standard,

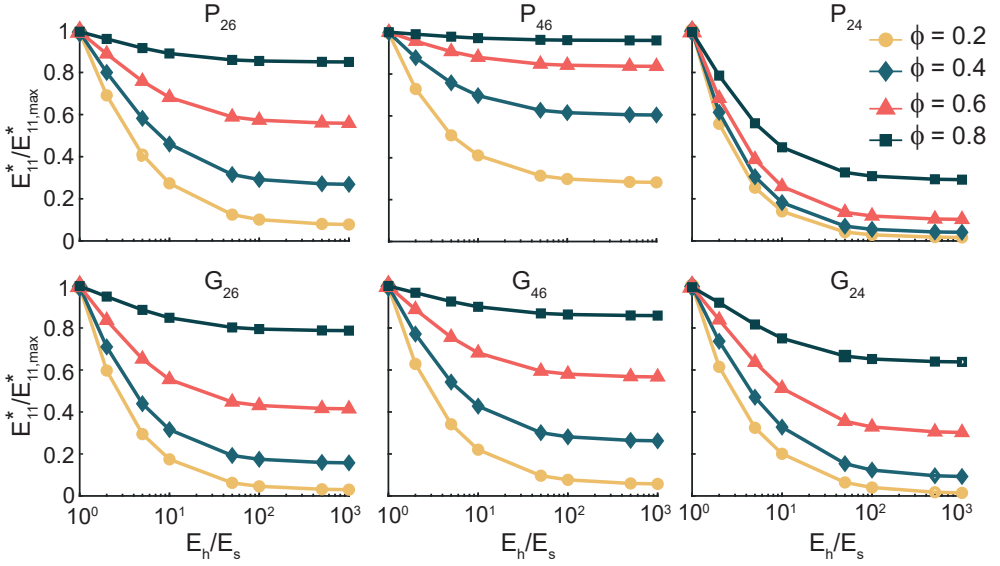


**Figure 5.7:** The effective stiffness *versus* the ratio of the Young's moduli of both phases ( $E_h/E_s$ ) for the six biphasic design types with  $t = L/20$  and  $\phi_s = 1 - \phi_h$ .

uniphase unit cell of the P designs (obtained at  $E_h/E_s = 1$ ) is anisotropic, with  $\alpha_Z > 1$ . However, the anisotropy index changes with  $E_h/E_s$  for biphasic designs, as exemplified in the  $P_{26}$  design (Figure 5.9). For  $\phi_h = 0.8$ ,  $\alpha_Z$  remains almost constant throughout the range of material ratios. In this case, the effective elastic surface, representing the effective stiffness in all directions (Figure 5.9), indicates a higher stiffness in the  $\langle 111 \rangle$  direction as opposed to the  $\langle 100 \rangle$  direction. However, for  $\phi_h = 0.2$ ,  $\alpha_Z$  rapidly reduces with increasing  $E_h/E_s$ , achieving an isotropic design when  $E_h/E_s \approx 10^2$ . The G designs, on the other hand, start off as quasi-isotropic structures for  $E_h/E_s = 1$ . For the  $G_{26}$  design specifically, an increase in  $\alpha_Z$  was observed as  $E_h/E_s$  increased, in particular when  $\phi_h = 0.2$  (Figure 5.9b). To summarize the elastic property space, we plotted the normalized effective modulus *versus* the Zener anisotropy index (Figure 5.8b). We found that most anisotropic designs have  $\alpha_Z > 1$ , although some designs (*e.g.*, for  $G_{46}$  and  $P_{26}$ ) exhibited  $\alpha_Z < 1$ . The largest spread in anisotropies were found in the  $G_{26}$  and  $P_{24}$  designs, the latter reaching a maximum of  $\alpha_Z \approx 10$ . Moreover, we observed a relatively large number of designs in the quasi-isotropic range ( $\alpha_Z \approx 1$ ), which cover approximately two orders of magnitude in the effective stiffness. Overall, these results confirm that our metamaterial design strategy not only enables the effective tuning of the uniaxial stiffness, but also of the elastic anisotropy.

### 5.3.5 Balancing elasticity and permeability

Our parametric design approach substantially enhanced the ability to independently tailor the mass transport and mechanical properties of TPMS-based metamaterials. This is visualized in the elasticity-permeability property space, where

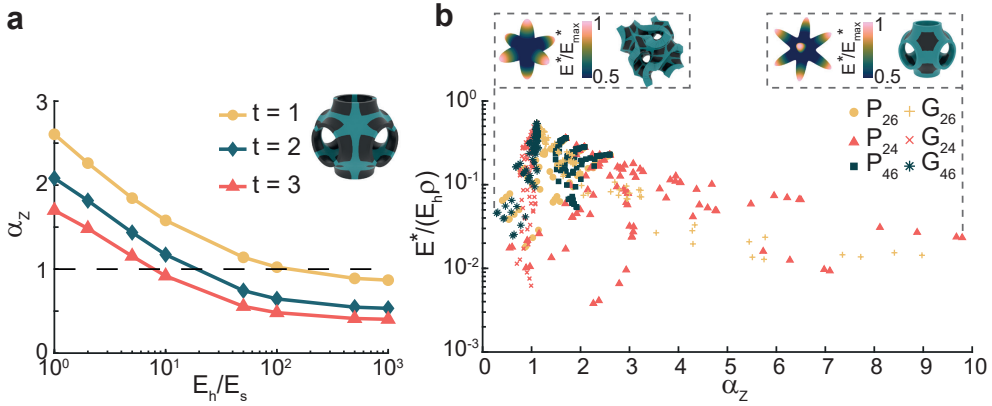


**Figure 5.8:** a) The Zener anisotropy index ( $\alpha_Z$ ) versus  $E_h/E_s$  for the  $P_{24}$  design with different thicknesses. b) The normalized effective stiffness versus Zener anisotropy index. The inset figures show the elastic surfaces and unit cells for both extremal designs regarding  $\alpha_Z$ .

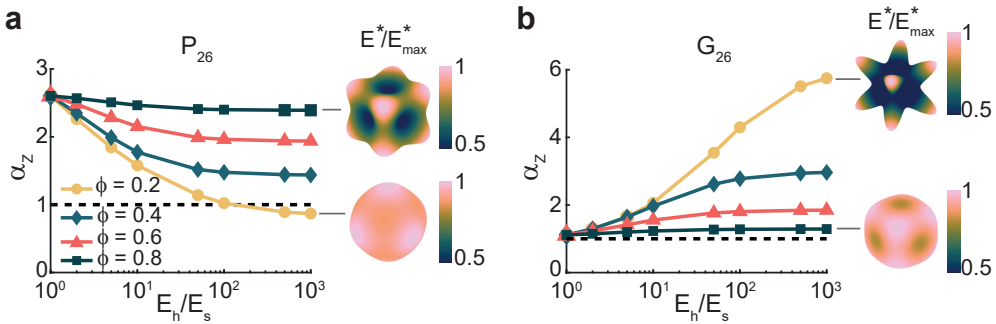


**Figure 5.9:** Some examples of the scaling of  $\alpha_Z$  with  $E_h/E_s$  for the different amounts of the hard phase ( $\phi_h$ ) in the  $P_{26}$  (top) and  $G_{26}$  (bottom) designs. The inset figures on the right represent the effective elastic surface (effective modulus in all directions).

the effective elastic modulus normalized by the hard-phase elastic modulus ( $E^*/E_h$ ) is plotted against the intrinsic (area-normalized) effective permeability ( $k^*/L^2$ ) for all uni- and biphasic designs (Figure 5.10a). In the case of the “full” unit cells (*i.e.*, the unit cells with the standard P or G morphology,  $\phi_s = 1 - \phi_h$ ), the biphasic partitioning unlocks a wide range of attainable stiffness values for a constant value of permeability (the data points in the yellow bands in Figure 5.10a). Indeed, for those designs, the permeability is only determined by the overall unit cell type (P or G) and shell thickness ( $t$ ), while the stiffness is also driven by the material distributions. The maximum stiffness for the full designs is, not surprisingly, obtained for  $\phi_h = 1$  (*i.e.*, unit cells that consist entirely out of the hard phase).

While biphasic partitioning enables continuous stiffness tuning in standard TPMS unit cells, their intrinsic permeability range is still limited and is only a function of the shell thickness ( $t$ ). However, the range of intrinsic permeability values is extended by the skeleton TPMS structures ( $\phi_h + \phi_s < 1$ ), which have more holes in their surfaces, thereby altering the fluid flow through the unit cell. Indeed, all data points outside

of the yellow bands in Figure 5.10a correspond to uni- or biphasic skeleton designs. Similar to the case of full designs, using two different materials in the skeleton designs enables the tuning of the elastic properties independently from permeability. Alternatively, one could fix the effective normalized stiffness and tune the permeability by choosing a different design at the same level of stiffness. We note that we have visualized the elasticity-permeability design space using discrete values of  $t$ ,  $\phi_h$ ,  $\phi_s$  and  $E_h/E_s$  in Figure 5.10, and that intermediate data points could be obtained at intermediate values of the design parameters.

Our design approach enables this level of mechanical and mass transport tunability by leveraging the fact that permeability solely depends on geometry, while the elastic properties depend on geometry and material choice. To further demonstrate this, we plotted  $\rho_h + E_s/E_h \cdot \rho_s$  against  $(1-\rho)^3/(S/L^3)^2$  (Figure 5.10b), which captures the same trend as in the elasticity-permeability map. The former quantity captures the combined effect of the geometry and the material properties on the effective stiffness: the stiffness is primarily controlled by the volume fraction of the hard phase, while the soft phase has a weighted contribution, depending on its stiffness relative to the hard phase. The second quantity  $((1-\rho)^3/(S/L^3)^2)$  is the purely geometry-dependent metric that was introduced before (Figure 5.5b-c) and that correlates with the permeability. Taken together, these results summarize our enhanced ability to tune elasticity and permeability independently, by combining spatial distribution of multiple materials with geometric control over the unit cell architecture.

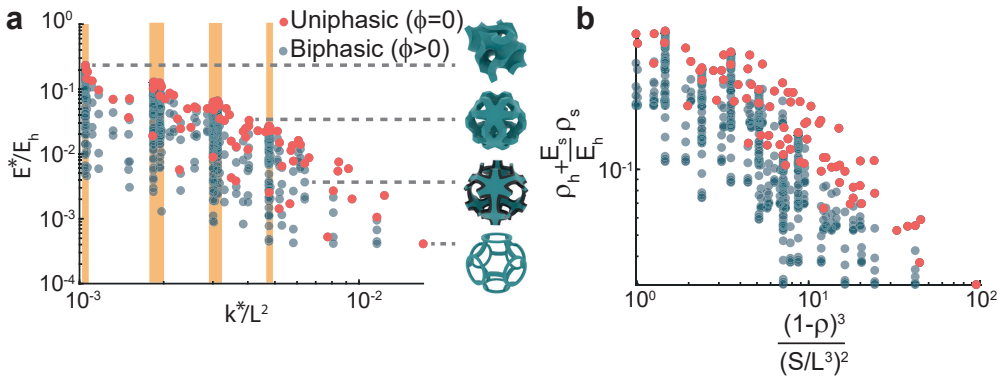


**Figure 5.10:** Effective stiffness *versus* effective permeability. a) The normalized effective elastic modulus *versus* the normalized effective permeability for uni- and biphasic designs. The yellow bands indicate the “full” designs (*i.e.*,  $\phi_s + \phi_h = 1$ ). The unit cell structures belonging to four data points are visualized in the inset figures. b) Simple scaling laws that capture the behavior from a). The elastic properties are determined by the geometry and materials choice, captured by  $\rho_h + E_s/E_h \cdot \rho_s$  while the permeability depends on the geometry alone, as described by  $(1-\rho)^3/(S/L^3)^2$ .

### 5.3.6 Multi-material additive manufacturing

We physically realized metamaterial lattices based on the P surface, using multi-material additive manufacturing (Subsection 5.2.6). The lattices consisted of 27 unit

cells, in a  $3 \times 3 \times 3$  arrangement (Figure 5.11a). We printed two uniphase full designs in a hard (top left in Figure 5.11a) and soft (bottom right in Figure 5.11a) polymer, as well as a uniphase  $P_{46}$  skeleton design ( $\phi_h = 0.2$ ,  $\phi_s = 0$ , top right in Figure 5.11a), and a biphasic  $P_{46}$  design ( $\phi_h = 0.2$ ,  $\phi_s = 0.8$ , bottom left in Figure 5.11a). All structures were successfully printed, and showed no signs of defects. In the case of the biphasic design, the soft phase was well integrated with the hard-phased skeleton.

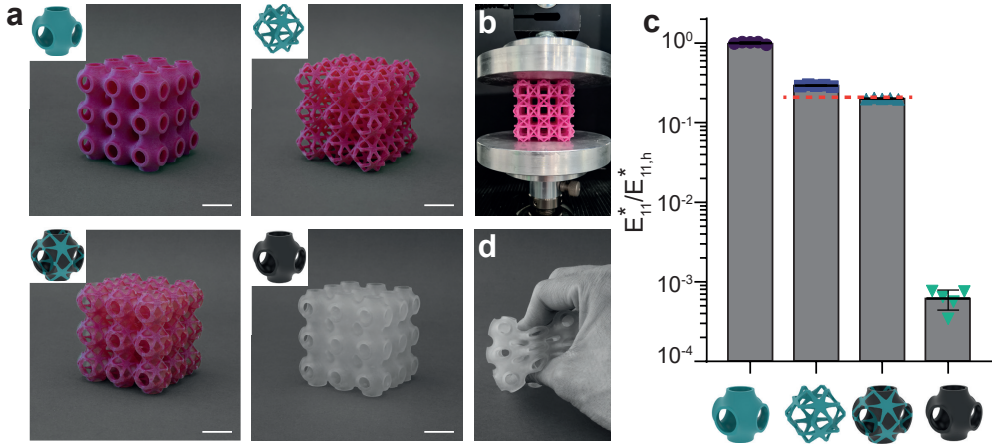


**Figure 5.11:** Additively manufactured structures and mechanical testing. a) Lattices consisting of 27 unit cells fabricated using multi-material polymer printing. The pink material is a stiff polymer (VeroMagenta), while the white transparent material is soft (Agilus30) and easily deformable. b) A 3D-printed structure in the displacement-controlled compression test setup. c) Normalized compression testing results for the four printed specimens, showing the uniaxial effective modulus. Each test was repeated five times. The markers show the individual test results, while the bar graph represents the mean and standard deviations. The red dashed line corresponds to the predicted stiffness for the uni- and biphasic skeletons. d) The structure that consists entirely out of the soft phase is highly deformable and has a negligible stiffness as compared to the other designs. All scale bars represent 20 mm.

We mechanically tested the specimens by imposing a small macroscale compressive strain (Figure 5.11b and Subsection 5.2.7), in order to examine the effective elastic modulus. Compared to the fully hard structure, the stiffness of the skeletonized structures (uni- and biphasic) was 70–80% lower, while the stiffness of the fully soft structures was three orders of magnitude lower (Figure 5.11c-d). We observed that the stiffness reduction in the biphasic design corresponded well with the computationally predicted stiffness reduction (dotted line in Figure 5.11c). However, the stiffness of the uniphase skeleton was higher than that of the corresponding biphasic design, while their predicted stiffness values are equal. While this difference warrants further investigation, we believe that is the consequence of differences in hard-phase thickness due the presence or lack of the soft phase. For example, the transition region of the hard and soft phase in the biphasic design might locally have different material properties than in the uniphase skeleton design, due to the localized mixing of the polymer droplets in

the material jetting process. Nevertheless, these lattices demonstrate that the biphasic TPMS-based metamaterials can be successfully manufactured using commercially available printing processes.

## 5.4 Discussion

We have presented an approach to parametrically design multifunctional metamaterials in which the mechanical and mass transport properties can be decoupled to a large extent. The ability to independently tailor such properties is relevant in many applications, yet is challenging to achieve in uniphase metamaterials due to the competing dependence of both properties on the metamaterial geometry<sup>27</sup>. Our design approach relies on partitioning the P and G TPMS unit cells into hard, soft, or void domains, according to templates that are based on hyperbolic tilings, effectively resulting in hybrid strut-shell-based metamaterials. The permeability of the structures is purely geometry-driven and can be tailored by changing the shell thickness or through the controlled introduction of additional openings in unit cells. The elastic properties, on the other hand, also depend on the choice of the materials and their spatial distribution. We showed that these biphasic decorations enabled us to achieve a wide range of effective stiffness values at fixed permeability, but also offered a route to tailor the elastic anisotropy (maintaining cubic symmetry). While we have focused on elastic properties here, it is likely that the combination of hard and soft phases would also affect the other mechanical properties of TPMS-based architectures, such as the energy absorption at high strains, crack growth (the soft inclusions might act as crack inhibitors), or fatigue response. In any case, our results confirm that the ability to control the material architecture of multiple materials instead of a single one can significantly expand the overall property space of the resulting<sup>32,33</sup> and enabling the multi-objective design of multi-physics metamaterials.

Our approaches could be generalized and extended in various ways. First, it would be possible to vary the unit cell type throughout the metamaterial lattice, for example, to spatially vary the permeability without affecting the local elastic properties. This could be achieved by fixing the geometry of the hard phase in all the unit cells, but varying the amount of the soft phase (Figure 5.12a). Alternatively, the overall unit cell geometry could be preserved, hence fixing permeability, but the elasticity could be spatially tuned by varying the amount of the load-carrying hard phase (Figure 5.12b). Our approach could also be extended to enable other types of shell-based biphasic metamaterials. For example, the same hyperbolic tilings that we have used here could be projected onto the D (diamond) minimal surface, which belongs to the same family as the P and G surfaces (Figure 5.13). We did not include the D designs in this study, as these unit cells contain non-manifold regions where different patches meet along single edges, rendering them unattractive from a mechanical viewpoint. Moreover, many other biphasic P and G designs could be created, beyond the ones we have presented here. For example, the tilings that we have used could be combined together to form hybrid structures (Figure 5.14). Alternatively, many other tilings exist that could be

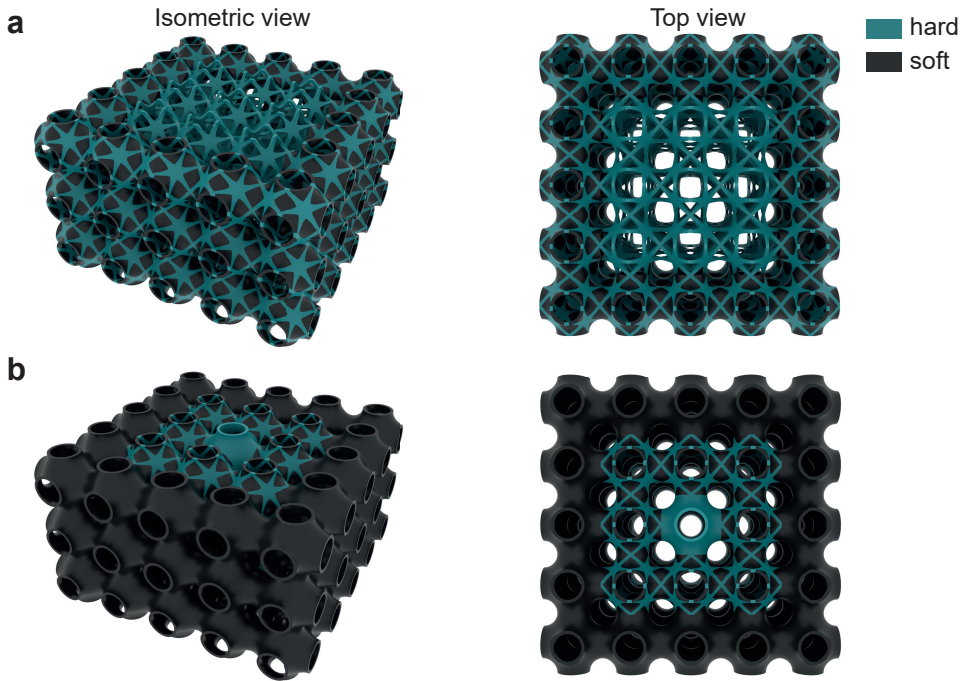


**Figure 5.12:** Decoupled gradients in permeability and elasticity. a) A  $5 \times 5 \times 5$  lattice based on the P surface. The outermost unit cells are full biphasic  $P_{46}$  designs, while the innermost unit cells are uniphase skeletons of the  $P_{46}$  design. At sufficiently high values of  $E_h/E_s$ , all the unit cells have the same elastic properties (determined by the hard phase), but the permeability of the innermost unit cells is substantially higher than that of the outermost unit cells (due to the absence of the soft phase in the innermost unit cells). b) Analogous to a), but this time with varying elasticity and constant permeability throughout the unit cells. The innermost unit cells are stiffer (fully hard phase, or biphasic full designs) than the outermost unit cells (fully soft phase). Due to the constant overall unit cell morphology, the fluid permeability of all unit cells is the same.

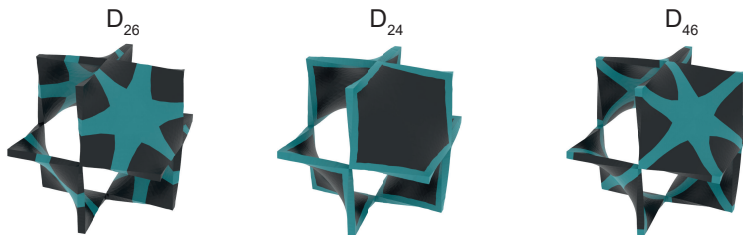


**Figure 5.13:** Full biphasic designs of the D minimal surface. The same design approach as for the P and G surfaces was used to decorate the D surface unit cells. For those cases,  $\phi_h = 0.2$  and  $\phi_s = 0.8$ .

projected onto these cubic TPMS to make different admissible biphasic designs<sup>46,47</sup>. In addition to the PDG surface family of minimal surfaces, our design approach could be extended to other TPMS families, provided their Enneper-Weierstrass parametriza-

tion is known. The Weierstrass function has already been determined for several other TPMS families, but can also be uncovered for newer types of TPMS on the basis of the local flat points, which could be determined numerically<sup>57;58</sup>. Finally, the central concept of decorating a lattice with two (or more) different materials could also be applied to stochastic microstructures. Recently, such stochastic shell-based architectures have emerged as attractive metamaterial geometries, due to their high tunability, large design space, and robustness against deteriorating symmetry-breaking defects<sup>13;59</sup>. However, applying the multi-material methodology to such stochastic geometries would require a different strategy to rationally distribute the different phases, for example, by parametrically applying a skeletonization algorithm to obtain the medial graph (or an inflated version) of the shell-based structure<sup>60</sup>, and assigning different material properties to this region than to the remainder of the geometry.

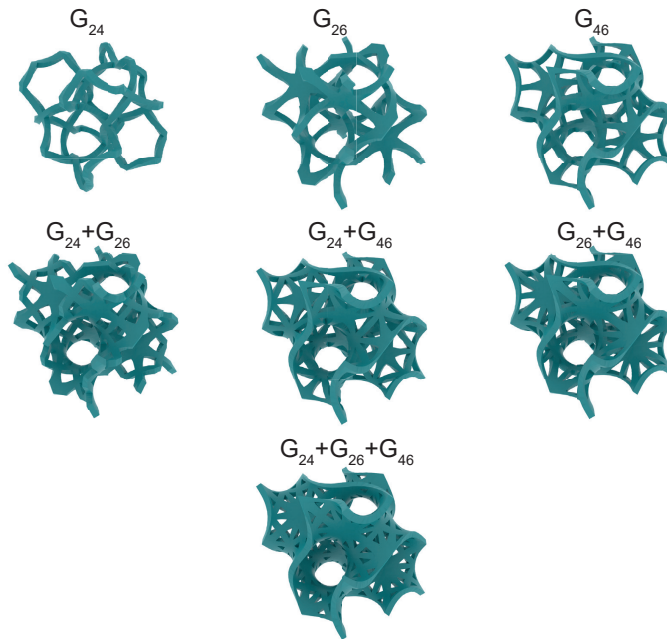


**Figure 5.14:** Hybrid G surface uniphase skeletons. By taking the union of two or three of the uniphase skeleton designs presented in the main text (top row), additional designs can be generated. For those visualizations,  $\phi_s = 0$  and  $\phi_h = 0.2$ .

It is important to note that the mechanical and mass transport properties of metamaterials scale differently with the unit cell size, which has consequences for any design strategy where both types of properties are simultaneously tailored. A uniform scaling of the unit cell length by a factor  $l$  does not affect the elastic properties of the lattice. The permeability, on the other hand, scales with  $l^2$ , which is why we have reported area-normalized (intrinsic) permeability here ( $k^*/L^2$ ). This implies that one could tune both properties somewhat independently, merely by scaling the structure<sup>26</sup>. However, in many applications of multifunctional metamaterials, the unit cell size is

not a parameter that could freely be altered, at least not without affecting other relevant properties or violating the requirements of the applied manufacturing processes. In metabiomaterials, for example, the pore size should remain within experimentally-determined bounds to promote tissue regeneration<sup>61</sup>. Moreover, scaling of the unit cell size would also affect properties, such as overall cell attachment or biodegradation behavior, which are dependent on the specific surface area and scale with  $l^{-1}$ <sup>26</sup>. Furthermore, the resolution of the additive manufacturing process or the desired number of unit cells to obtain sufficiently homogenized behavior could impose additional constraints on unit cell scaling. Our design approach, which does not rely on unit cell scaling, could therefore offer more freedom for the independent tuning of elasticity and permeability at different scales.

From a broader perspective, this study also underscores the relevance of reticular (or structural) chemistry as a source of inspiration for metamaterial design. In addition to the hyperbolic networks described here, there are vast databases of complex topologies that could be used as metamaterial templates<sup>45</sup>. For example, the wealth of zeolitic networks and metal-organic frameworks (MOFs) could inspire complex designs that go beyond the traditional lattice choices (*e.g.* cubic or diamond lattices), resulting in so-called “meta-MOFs”<sup>62</sup>. Moreover, metamaterial properties could be enhanced even further by incorporating the same hardening mechanisms that are found at the atomic scale in crystalline materials<sup>63</sup>.

Taken together, we demonstrated a new strategy for the multi-objective design of multi-physics metamaterials and a route to decouple properties that are conflicting in uniphase metamaterials. By leveraging the hyperbolic symmetries of TPMS, our design approach maintains a surprising tractability, yet produces complex 3D, biphasic architectures. Together with advances in multi-material additive manufacturing, this design approach could unlock exciting routes towards multi-physics metamaterials in a variety of applications. In this regard, we believe that decoupling elasticity and permeability is only one example of the potential for enhanced tunability in biphasic metamaterials.

## 5.5 Supporting information

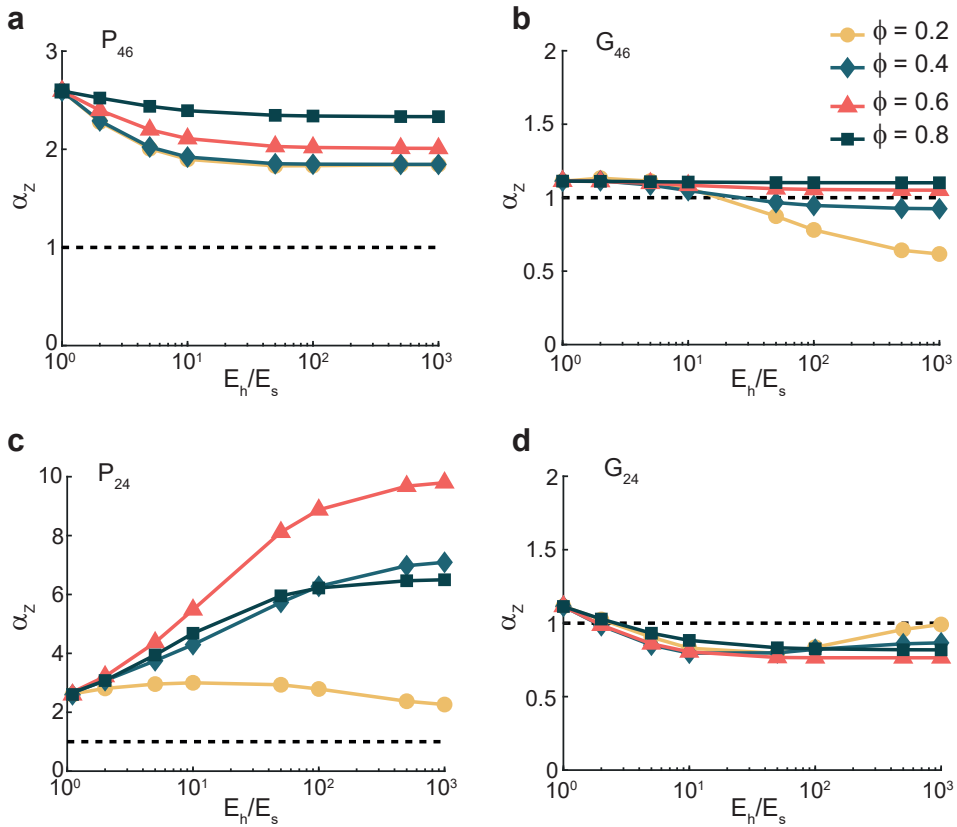


Figure 5.15: The Zener anisotropy index ( $\alpha_Z$ ) versus ratio of the Young's moduli of the bulk materials ( $E_h/E_s$ ) for the  $P_{46}$ ,  $G_{46}$ ,  $P_{24}$ , and  $G_{24}$  designs with a thickness of  $t = L/20$ .

## Bibliography

- [1] T. Brunet, A. Merlin, B. Mascaro, K. Zimny, J. Leng, O. Poncelet, C. Aristégui, and O. Mondain-Monval. Soft 3D acoustic metamaterial with negative index. *Nature materials*, 14(4):384, 2015.
- [2] J. Pendry. A chiral route to negative refraction. *Science*, 306(5700):1353–1355, 2004.
- [3] X. Zheng, H. Lee, T. H. Weisgraber, M. Shusteff, J. DeOtte, E. B. Duoss, J. D. Kuntz, M. M. Biener, Q. Ge, J. A. Jackson, S. O. Kucheyev, N. X. Fang, and C. M. Spadaccini. Ultralight, ultrastiff mechanical metamaterials. *Science*, 344(6190):1373–1377, 2014.
- [4] V. S. Deshpande, N. A. Fleck, and M. F. Ashby. Effective properties of the octet-truss lattice material. *Journal of the Mechanics and Physics of Solids*, 49(8):1747–1769, 2001.
- [5] L. R. Meza, S. Das, and J. R. Greer. Strong, lightweight, and recoverable three-dimensional ceramic nanolattices. *Science*, 345(6202):1322–1326, 2014.
- [6] J. Bauer, A. Schroer, R. Schwaiger, and O. Kraft. Approaching theoretical strength in glassy carbon nanolattices. *Nature materials*, 15(4):438–443, 2016.
- [7] C. M. Portela, J. R. Greer, and D. M. Kochmann. Impact of node geometry on the effective stiffness of non-slender three-dimensional truss lattice architectures. *Extreme Mechanics Letters*, 22:138–148, 2018.
- [8] T. Tancogne-Dejean, M. Diamantopoulou, M. B. Gorji, C. Bonatti, and D. Mohr. 3D plate-lattices:

- An emerging class of low-density metamaterial exhibiting optimal isotropic stiffness. *Advanced Materials*, 30(45):1803334, 2018.
- [9] J. Berger, H. Wadley, and R. McMeeking. Mechanical metamaterials at the theoretical limit of isotropic elastic stiffness. *Nature*, 543(7646):533–537, 2017.
- [10] S. C. Han, J. W. Lee, and K. Kang. A new type of low density material: Shellular. *Advanced Materials*, 27(37):5506–5511, 2015.
- [11] C. Bonatti and D. Mohr. Mechanical performance of additively-manufactured anisotropic and isotropic smooth shell-lattice materials: Simulations & experiments. *Journal of the Mechanics and Physics of Solids*, 122:1–26, 2019.
- [12] C. Bonatti and D. Mohr. Smooth-shell metamaterials of cubic symmetry: anisotropic elasticity, yield strength and specific energy absorption. *Acta Materialia*, 164:301–321, 2019.
- [13] C. M. Portela, A. Vidyasagar, S. Krödel, T. Weissenbach, D. W. Yee, J. R. Greer, and D. M. Kochmann. Extreme mechanical resilience of self-assembled nanolabyrinthine materials. *Proceedings of the National Academy of Sciences*, 117(11):5686–5693, 2020.
- [14] O. Al-Ketan and R. K. Abu Al-Rub. Multifunctional mechanical metamaterials based on triply periodic minimal surface lattices. *Advanced Engineering Materials*, 21(10):1900524, 2019.
- [15] O. Al-Ketan, R. Rezgui, R. Rowshan, H. Du, N. X. Fang, and R. K. Abu Al-Rub. Microarchitected stretching-dominated mechanical metamaterials with minimal surface topologies. *Advanced Engineering Materials*, 20(9):1800029, 2018.
- [16] D. Li, N. Dai, Y. Tang, G. Dong, and Y. F. Zhao. Design and optimization of graded cellular structures with triply periodic level surface-based topological shapes. *Journal of Mechanical Design*, 141(7), 2019.
- [17] C. Soyarslan, V. Blümer, and S. Bargmann. Tunable auxeticity and elastomechanical symmetry in a class of very low density core-shell cubic crystals. *Acta Materialia*, 177:280–292, 2019.
- [18] S. J. Callens, N. Tümer, and A. A. Zadpoor. Hyperbolic origami-inspired folding of triply periodic minimal surface structures. *Applied Materials Today*, 15:453–461, 2019.
- [19] S. Hyde, Z. Blum, T. Landh, S. Lidin, B. Ninham, S. Andersson, and K. Larsson. *The Language of Shape: The Role of Curvature in Condensed Matter: Physics, Chemistry and Biology*. Elsevier Science, Amsterdam, The Netherlands, 1996.
- [20] S. T. Hyde and G. E. Schröder-Turk. Geometry of interfaces: topological complexity in biology and materials. *Interface Focus*, 2:529–538, 2012.
- [21] G. E. Schröder-Turk, A. Fogden, and S. T. Hyde. Bicontinuous geometries and molecular self-assembly: comparison of local curvature and global packing variations in genus-three cubic, tetragonal and rhombohedral surfaces. *The European Physical Journal B-Condensed Matter and Complex Systems*, 54(4):509–524, 2006.
- [22] S. Torquato, S. Hyun, and A. Donev. Multifunctional composites: optimizing microstructures for simultaneous transport of heat and electricity. *Physical review letters*, 89(26):266601, 2002.
- [23] A. A. Zadpoor. Meta-biomaterials. *Biomaterials science*, 8(1):18–38, 2020.
- [24] H. Montazerian, E. Davoodi, M. Asadi-Eydivand, J. Kadkhodapour, and M. Solati-Hashjin. Porous scaffold internal architecture design based on minimal surfaces: A compromise between permeability and elastic properties. *Materials & Design*, 126:98–114, 2017.
- [25] F. S. L. Bobbert, K. Lietaert, A. A. Eftekhari, B. Pouran, S. M. Ahmadi, H. Weinans, and A. A. Zadpoor. Additively manufactured metallic porous biomaterials based on minimal surfaces: A unique combination of topological, mechanical, and mass transport properties. *Acta Biomater*, 53:572–584, 2017.
- [26] S. C. Kapfer, S. T. Hyde, K. Mecke, C. H. Arns, and G. E. Schröder-Turk. Minimal surface scaffold designs for tissue engineering. *Biomaterials*, 32(29):6875–82, 2011.
- [27] J. K. Guest and J. H. Prévost. Optimizing multifunctional materials: design of microstructures for maximized stiffness and fluid permeability. *International Journal of Solids and Structures*, 43(22-23):7028–7047, 2006.
- [28] M. F. Ashby. The properties of foams and lattices. *Philosophical Transactions of the Royal Society A: Mathematical, Physical and Engineering Sciences*, 364(1838):15–30, 2006.

- [29] M. Kadic, T. Bückmann, N. Stenger, M. Thiel, and M. Wegener. On the practicability of pentamode mechanical metamaterials. *Applied Physics Letters*, 100(19):191901, 2012.
- [30] R. Hedayati, A. M. Leeflang, and A. A. Zadpoor. Additively manufactured metallic pentamode metamaterials. *Applied Physics Letters*, 110(9):091905, 2017.
- [31] S. Janbaz, M. McGuinness, and A. A. Zadpoor. Multimaterial control of instability in soft mechanical metamaterials. *Physical Review Applied*, 9(6):064013, 2018.
- [32] S. Janbaz, F. Bobbert, M. Mirzaali, and A. Zadpoor. Ultra-programmable buckling-driven soft cellular mechanisms. *Materials Horizons*, 6(6):1138–1147, 2019.
- [33] M. Mirzaali, A. Caracciolo, H. Pahlavani, S. Janbaz, L. Vergani, and A. Zadpoor. Multi-material 3D printed mechanical metamaterials: Rational design of elastic properties through spatial distribution of hard and soft phases. *Applied Physics Letters*, 113(24):241903, 2018.
- [34] D. Chen and X. Zheng. Multi-material additive manufacturing of metamaterials with giant, tailorable negative poisson's ratios. *Scientific reports*, 8(1):1–8, 2018.
- [35] P. J. Gandy and J. Klinowski. Exact computation of the triply periodic schwarz p minimal surface. *Chemical Physics Letters*, 322(6):579–586, 2000.
- [36] P. J. Gandy and J. Klinowski. Exact computation of the triply periodic g (gyroid') minimal surface. *Chemical Physics Letters*, 321(5-6):363–371, 2000.
- [37] K. M. Moerman. Gibbon: the geometry and image-based bioengineering add-on. *Journal of Open Source Software*, 3(22):506, 2018.
- [38] W. Mickel, G. E. Schröder-Turk, and K. Mecke. Tensorial minkowski functionals of triply periodic minimal surfaces. *Interface focus*, 2:623–633, 2012.
- [39] A. Fogden and S. T. Hyde. Continuous transformations of cubic minimal surfaces. *The European Physical Journal B-Condensed Matter and Complex Systems*, 7(1):91–104, 1999.
- [40] N. S. Martys and J. G. Hagedorn. Multiscale modeling of fluid transport in heterogeneous materials using discrete boltzmann methods. *Materials and structures*, 35(10):650–658, 2002.
- [41] C. H. Arns, M. A. Knackstedt, W. V. Pinczewski, and N. S. Martys. Virtual permeametry on microtomographic images. *Journal of Petroleum Science and Engineering*, 45(1-2):41–46, 2004.
- [42] G. Dong, Y. Tang, and Y. F. Zhao. A 149 line homogenization code for three-dimensional cellular materials written in matlab. *Journal of Engineering Materials and Technology*, 141(1), 2019.
- [43] A. N. Gent. On the relation between indentation hardness and young's modulus. *Rubber Chemistry and Technology*, 31(4):896–906, 1958.
- [44] T. Castle, M. E. Evans, S. T. Hyde, S. Ramsden, and V. Robins. Trading spaces: building three-dimensional nets from two-dimensional tilings. *Interface Focus*, 2(5):555–66, 2012.
- [45] M. O'Keeffe, M. A. Peskov, S. J. Ramsden, and O. M. Yaghi. The reticular chemistry structure resource (rcsr) database of, and symbols for, crystal nets. *Accounts of chemical research*, 41(12):1782–1789, 2008.
- [46] S. . Ramsden, V. Robins, and S. Hyde. Three-dimensional euclidean nets from two-dimensional hyperbolic tilings: kaleidoscopic examples. *Acta Crystallographica Section A: Foundations of Crystallography*, 65(2):81–108, 2009.
- [47] V. Robins, S. J. Ramsden, and S. T. Hyde. 2D hyperbolic groups induce three-periodic euclidean reticulations. *The European Physical Journal B*, 39(3):365–375, 2004.
- [48] M. E. Evans, V. Robins, and S. T. Hyde. Periodic entanglement i: networks from hyperbolic reticulations. *Acta Crystallographica Section A: Foundations of Crystallography*, 69(3):241–261, 2013.
- [49] W. Fischer and E. Koch. Spanning minimal surfaces. *Philosophical Transactions of the Royal Society of London A: Mathematical, Physical and Engineering Sciences*, 354(1715):2105–2142, 1996.
- [50] S. J. Callens, R. J. Uyttendaele, L. E. Fratila-Apachitei, and A. A. Zadpoor. Substrate curvature as a cue to guide spatiotemporal cell and tissue organization. *Biomaterials*, 232:119739, 2020.
- [51] C. M. Bidan, K. P. Kommareddy, M. Rumpfer, P. Kollmannsberger, Y. J. Brechet, P. Fratzl, and J. W. Dunlop. How linear tension converts to curvature: geometric control of bone tissue growth. *PLoS One*, 7(5):e36336, 2012.
- [52] L. Pieuchot, J. Marteau, A. Guignandon, T. Dos Santos, I. Brigaud, P.-F. Chauvy, T. Cloatre, A. Ponche, T. Petithory, P. Rougerie, M. Vassaux, J.-L. Milan, N. T. Wakhloo, A. Spangenberg, M. Bigerelle,

- and K. Anselme. Curvotaxis directs cell migration through cell-scale curvature landscapes. *Nature communications*, 9(1):3995, 2018.
- [53] S. Truscello, G. Kerckhofs, S. Van Bael, G. Pyka, J. Schrooten, and H. Van Oosterwyck. Prediction of permeability of regular scaffolds for skeletal tissue engineering: a combined computational and experimental study. *Acta biomaterialia*, 8(4):1648–1658, 2012.
- [54] Y. Jung and S. Torquato. Fluid permeabilities of triply periodic minimal surfaces. *Physical Review E*, 72(5):056319, 2005.
- [55] L. J. Gibson and M. F. Ashby. *Cellular solids: structure and properties*. Cambridge university press, 1999.
- [56] V. Deshpande, M. Ashby, and N. Fleck. Foam topology: bending versus stretching dominated architectures. *Acta materialia*, 49(6):1035–1040, 2001.
- [57] A. Fogden and S. Hyde. Parametrization of triply periodic minimal surfaces. i. mathematical basis of the construction algorithm for the regular class. *Acta Crystallographica Section A: Foundations of Crystallography*, 48(4):442–451, 1992.
- [58] S. G. Markande, M. Saba, G. Schroeder-Turk, and E. A. Matsumoto. A chiral family of triply-periodic minimal surfaces derived from the quartz network. *arXiv preprint arXiv:1805.07034*, 2018.
- [59] S. Kumar, S. Tan, L. Zheng, and D. M. Kochmann. Inverse-designed spinodoid metamaterials. *npj Computational Materials*, 6(1):1–10, 2020.
- [60] C. Soyarslan, H. Argeso, and S. Bargmann. Skeletonization-based beam finite element models for stochastic bicontinuous materials: Application to simulations of nanoporous gold. *Journal of Materials Research*, 33(20):3371–3382, 2018.
- [61] A. A. Zadpoor. Bone tissue regeneration: the role of scaffold geometry. *Biomaterials Science*, 3(2):231–45, 2015.
- [62] E. Jin, I. S. Lee, D. Kim, H. Lee, W.-D. Jang, M. S. Lah, S. K. Min, and W. Choe. Metal-organic framework based on hinged cube tessellation as transformable mechanical metamaterial. *Science advances*, 5(5):eaav4119, 2019.
- [63] M.-S. Pham, C. Liu, I. Todd, and J. Lertthanasarn. Damage-tolerant architected materials inspired by crystal microstructure. *Nature*, 565(7739):305–311, 2019.

# IV

## FROM FLAT SHEETS TO CURVED GEOMETRIES

---

6	CURVATURE IN ORIGAMI AND KIRIGAMI	177
6.1	Introduction	178
6.2	Geometry of surfaces and origami	180
6.3	Origami approaches	187
6.4	Kirigami approaches	199
6.5	Discussion and conclusions	205
	Bibliography	218
7	HYPERBOLIC ORIGAMI OF MINIMAL SURFACES	219
7.1	Introduction	220
7.2	Materials and methods	221
7.3	Results	225
7.4	Discussion	234
7.5	Supporting information	234
	Bibliography	243

---



# 6

## CURVATURE IN ORIGAMI AND KIRIGAMI

Transforming flat sheets into three-dimensional structures has emerged as an exciting manufacturing paradigm on a broad range of length scales. Among other advantages, this technique permits the use of functionality-inducing planar processes on flat starting materials, which after shape-shifting, result in a unique combination of macro-scale geometry and surface topography. Fabricating arbitrarily complex three-dimensional geometries requires the ability to change the intrinsic curvature of initially flat structures, while simultaneously limiting material distortion to not disturb the surface features. The centuries-old art forms of origami and kirigami could offer elegant solutions, involving only folding and cutting to transform flat papers into complex geometries. Although such techniques are limited by an inherent developability constraint, the rational design of the crease and cut patterns enables the shape-shifting of (nearly) inextensible sheets into geometries with apparent intrinsic curvature. Here, we review recent origami and kirigami techniques that can be used for this purpose, discuss their underlying mechanisms and create physical models to demonstrate and compare their feasibility. Moreover, we highlight practical aspects that are relevant in the development of advanced materials with these techniques. Finally, we provide an outlook on future applications that could benefit from origami and kirigami to create intrinsically curved surfaces.

S. J. P. Callens, A. A. Zadpoor, From flat sheets to curved geometries: origami and kirigami approaches, *Materials Today*, 21, 241-264, 2018.

## 6.1 Introduction

The many developments in additive manufacturing (AM) over the last decades have significantly increased the attractiveness of this manufacturing technique to fabricate arbitrarily complex three-dimensional (3D) geometries at the nano-, micro- and macro-scales. Examples include bone-substituting biomaterials<sup>1</sup>, penta-mode mechanical metamaterials<sup>2;3</sup>, triply periodic minimal surfaces<sup>4</sup>, and energy-absorbing cellular architectures<sup>5</sup>. Despite many advantages of AM, one major limitation is the incompatibility with planar surface patterning and imprinting processes, which are crucial for imbuing surfaces with specific functionalities such as hydro- or oleophobicity<sup>6</sup>, integration of electronic circuits<sup>7</sup>, or control over cell interaction in the case of biomaterials<sup>8</sup>. The ability to combine arbitrarily complex surface features with arbitrarily complex geometries could enable development of advanced materials with an unprecedented set of functionalities.

A potential solution to this deadlock is provided by another manufacturing paradigm, which has been of growing interest to the scientific community during recent years: the shape-shifting of thin, planar sheets (which we consider 2D) into 3D structures<sup>9–12</sup>. The planar sheets could first be decorated using planar patterning processes, after which they are transformed into complex 3D geometries. Additional advantages are the fast and inexpensive production methods of the 2D sheets and their efficient packing for storage and transportation<sup>11;13</sup>. Moreover, the 2D-to-3D paradigm is particularly interesting for the development of micro- or nanoscale 3D constructs (*e.g.* micro- and nanoelectromechanical devices<sup>14</sup>), since conventional macroscale techniques cannot easily be scaled down to allow fabrication of such small structures<sup>15;16</sup>. As such, the out-of-plane transformation of 2D sheets opens up new opportunities for the development of complex 3D structures with functionalized surfaces, especially at small length scales.

An important parameter governing the complexity of 3D structures is the surface curvature and the variation thereof throughout the structure. In order to create arbitrarily complex 3D structures from 2D sheets, the curvature of the initially flat sheets should be altered in a controllable manner. The simplest curved shapes could be obtained through bending or rolling of flat sheets. However, more complex target shapes are characterized by “double curvature” and exhibit spherical (dome-shaped) or hyperbolic (saddle-shaped) geometries, which cannot be realized with inextensional deformations of a flat sheet (this is readily understood when attempting to wrap a sphere or saddle with paper). Instead, the flat sheet would need to be subjected to in-plane distortions in order to achieve double-curved parts. At the macro-scale, for example, flat sheet-metal is plastically stretched to create double-curved shells (*e.g.* using (multi-point) stretch-forming<sup>17</sup>), and fiber-reinforced composite laminates are subjected to in-plane shearing deformations<sup>18</sup>. At smaller scales, researchers have recently used stimuli-responsive materials that exhibit in-plane distortions in the form of differential shrinkage<sup>13;19</sup> or swelling<sup>20;21</sup> to achieve complex curved shapes from initially flat sheets, which is closely related to non-uniform growth processes in initially planar shapes observed in nature,

resulting in wavy patterns at the edges of plant leaves<sup>22;23</sup> and enabling the blooming of the lily flower<sup>24</sup>.

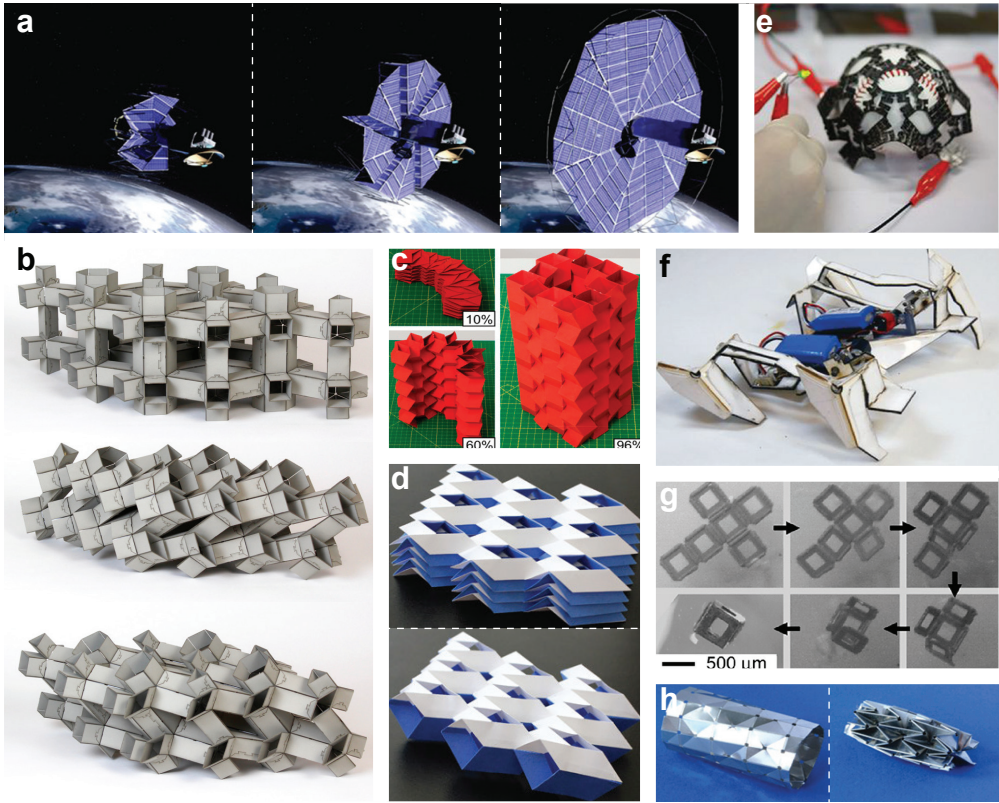


**Figure 6.1:** Various examples of scientific and engineering applications of origami and kirigami. a) An artist impression of an origami-based deployable solar array for space satellites (adapted from reference<sup>25</sup>). b) A cardboard prototype of a reconfigurable origami-based metamaterial (top), which has two degrees of freedom (middle and bottom). Adapted by permission from Macmillan Publishers Ltd: Nature<sup>26</sup>, copyright 2017. c) A deployable paper structure based on origami zipper tubes. Reproduced from reference<sup>27</sup>. d) Paper versions of cellular metamaterials combining aspects from origami and kirigami. Reproduced from Fig. 3G and Fig. 3H of reference<sup>28</sup>. e) A stretchable electrode based on a fractal kirigami cut-pattern, capable of wrapping around a spherical object while lighting an LED. Reproduced from reference<sup>29</sup>. f) A centimeter-scale, crawling robot that is self-folded from shape-memory composites. Reproduced with permission from AAAS from reference<sup>30</sup>. g) A biomedical application of origami: a self-folding microscale container that could be used for controlled drug delivery. Reproduced from reference<sup>31</sup> with permission from Elsevier. h) Another biomedical application: a self-deployable origami stent graft based on the waterbomb pattern, developed by *K. Kuribayashi et al.*<sup>32</sup> (Reproduced with permission from reference<sup>33</sup>).

Subjecting 2D sheets to in-plane distortions is therefore a feasible strategy to achieve complex curvature in 3D. Significant downsides are that the strategy is primarily applicable to soft elastic materials (such as gel sheets) and requires complicated programming of the shape-shifting or complex external stimuli to achieve the target

shapes. Moreover, the in-plane distortions are likely to disturb any of the surface features that were imprinted on the 2D sheets, hence partially eliminating one of the major advantages that the 2D-to-3D shape-shifting offers. Fortunately, an alternative strategy that is more compatible with rigid materials and delicate surface features exists at the intersection of art and science: the use of origami (traditional Japanese paper folding) and kirigami (extended version of origami, also allowing cuts) to create, or at least approximate, complex curved shapes. Simply by imposing specific fold patterns, extended with cuts in the case of kirigami, initially flat sheets could be transformed into 2D or 3D geometries. Owing to their predictability, controllability, and scalability, origami and kirigami techniques have gained traction among scientists and engineers to develop deployable structures<sup>25;34;35</sup>, reconfigurable metamaterials<sup>26–28;36;37</sup>, self-folding robots<sup>9;30</sup>, biomedical devices<sup>31–33;38</sup>, and stretchable electronics<sup>29;39;40</sup>. Figure 6.1 presents some examples of the potential applications of origami and kirigami across a range of length scales. By folding or cutting along the right patterns, origami and kirigami could transform planar sheets to approximate complex curved geometries, without the need for in-plane distortions.

Here, the different origami and kirigami approaches to approximate surfaces with “double” (or “intrinsic”) curvature are discussed. We begin by providing a closer look at differential geometry and its links to origami, providing a more formal definition of the concepts “surface curvature” and “flat sheets”. The several origami techniques proposed to approximate curved surfaces are discussed in the following section, followed by a section on recent advances in kirigami. We conclude by comparing the different techniques in terms of their suitability to approximate curved surfaces and discussing the practical aspects as well as providing an outlook on future directions and applications.

## 6.2 Geometry of surfaces and origami

### 6.2.1 Creating intrinsic surface curvature

In Chapter 2 of this thesis, we discussed the fundamentals of surface curvature and introduced the concepts of principal, mean and Gaussian curvatures. We highlighted that the mean curvature is an extrinsic measure, requiring information about the embedding of the surface in 3D space. The Gaussian curvature, on the other hand, is an intrinsic measure, which means that it does not require information about the embedding. In other words, the mean curvature of the surface could only be determined by an observer outside of the surface that has knowledge of its surroundings, while the Gaussian curvature of the surface could be also determined by a 2D resident living on the surface that has no perception of the surrounding 3D space. The concept of intrinsic curvature was introduced in Gauss’ landmark paper on the *Theorema Egregium* (“remarkable theorem”), considered by some to be the most important theorem within differential geometry<sup>41</sup>.

The distinction between these two types of curvature is important, as some surfaces might be extrinsically curved, yet remain intrinsically flat. For example, rolling a flat sheet into a cylindrical shape endows the surface with a non-zero mean curvature.

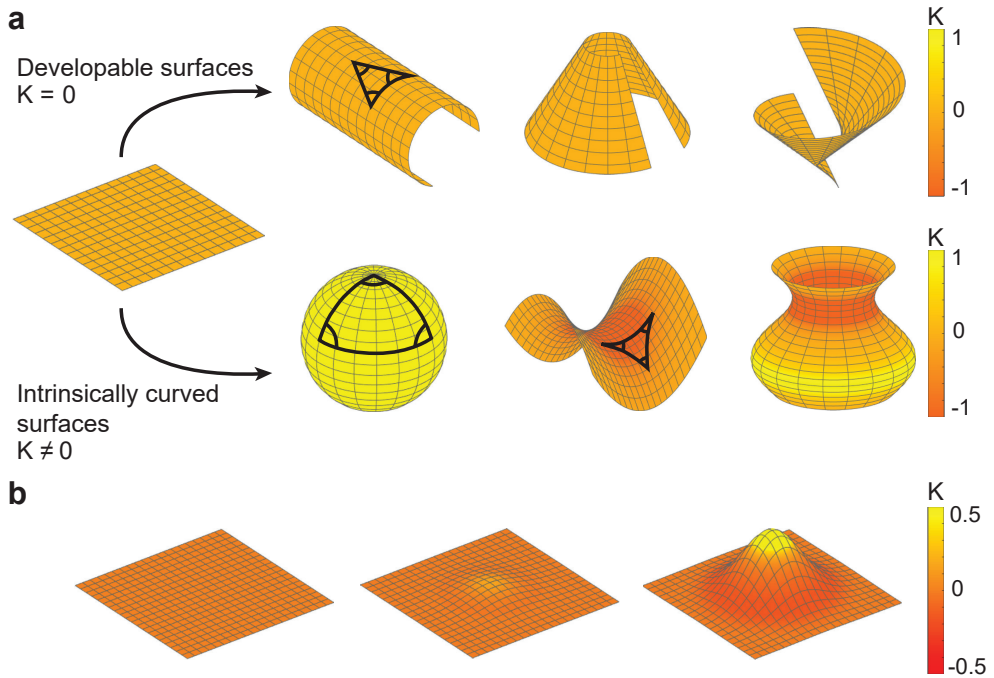


**Figure 6.2:** Intrinsic and extrinsic surface curvature. a) Transforming a planar surface (color bar indicates the Gaussian curvature). Top row: three types of developable surfaces, which could be flattened onto the plane through bending. From left to right: a cylindrical surface, a conical surface, the tangent developable surface to a space curve (a helix in this case). Bottom row: three types of intrinsically curved surfaces. From left to right: a sphere with  $K > 0$ , a saddle with  $K < 0$ , a vase surface with varying  $K$ . b) Interpretation of the relationship between the metric and the Gaussian curvature (color bar indicates Gaussian curvature). Creating the bell-shaped surface from an initially flat plane requires distortion of the grid on the plane, corresponding to a change in surface metric.

However, the Gaussian curvature of the surface remains zero, since one of the principal curvatures is zero (Figure 6.2a). Therefore, while the extrinsic curvature of the flat plane could be changed by bending it, its intrinsic curvature remains zero everywhere. Such a surface, having zero Gaussian curvature everywhere, is called a developable surface. In addition to the plane, three fundamental types of developable surfaces exist in 3D: the generalized cone, the generalized cylinder, and the tangent developable to a space curve (Figure 6.2a)<sup>41–43</sup>. The key feature of developable surfaces is that they could be constructed by bending a planar surface, without requiring extensional deformations. The observation that the Gaussian curvature of a flat plane does not change when bending the plane also holds more generally and forms the essence of Gauss' remarkable theorem: the Gaussian curvature is bending-invariant<sup>41,44</sup>. Consequently, a flat plane cannot be transformed into a spherical or saddle-shaped surface by bending deformations alone, since these surfaces have non-zero intrinsic curvature (Figure 6.2b).

We have stated that the Gaussian curvature is an intrinsic property of the surface, yet

the classical definition that we have been using throughout this work relies on extrinsic concepts, namely the principal curvatures. This is, in fact, the “remarkable” aspect in the Theorema Egregium of Gauss<sup>41;44</sup>. Gauss showed that the Gaussian curvature could also be defined on the basis of angle and distance measurements within the surface itself (*i.e.* intrinsically). A first indication of this intrinsic description is obtained when considering a triangle drawn on the various surfaces, as shown in Figure 6.2a. A triangle on the surface of the plane or any other developable surface ( $K = 0$ ) will always have the sum of its internal angles,  $\alpha_i$ , equal to  $\pi$ . However, on the surface of a sphere ( $K > 0$ ), the sum of the angles is larger than  $\pi$ , while on the surface of a saddle ( $K < 0$ ), the sum of the angles is smaller than  $\pi$ <sup>44;45</sup>. This angle measurement clearly relates to the intrinsic geometry of the surfaces, as a 2D resident of the surface that has no knowledge of the space in which the surface is situated could determine whether the surface has positive, negative, or zero Gaussian curvature, simply by measuring the angles of a triangle<sup>45</sup>. However, the resident would not be able to distinguish, for example, a flat plane from a cylinder surface since they both have the same (zero) intrinsic curvature.

A more formal intrinsic description of the Gaussian curvature requires the introduction of another important concept within differential geometry: the metric tensor, or simply metric. The metric of a surface describes the distances between the neighboring points on a surface which could be given as follows (in Einstein summation convention)<sup>46</sup>:

$$ds^2 = g_{ij}dx^i dx^j \quad (6.1)$$

Where  $ds$  represents the distance between points and  $g_{ij}$  represent the metric components. In the case of a flat plane, the metric tensor (which is called a “Euclidean metric” in this case) is simply represented in Cartesian coordinates as:

$$g = \begin{pmatrix} 1 & 0 \\ 0 & 1 \end{pmatrix} \quad (6.2)$$

In which case  $ds^2$  reduces to the standard expression:

$$ds^2 = dx^2 + dy^2 \quad (6.3)$$

Physically, the metric could be interpreted as a grid on the surface<sup>47;48</sup>. On a flat plane, this would be a regular grid consisting of equally spaced, perpendicular lines. When the flat plane is subjected to pure bending (see Figure 6.2a), the grid is not distorted and all distances and angles are preserved. For this reason, bending is called an isometric deformation, *i.e.* it leaves the metric unaffected. However, if the plane is deformed into, for example, a bell-shaped surface with regions of positive and negative Gaussian curvatures (Figure 6.2b), the grid becomes distorted, *i.e.* the metric changes

and becomes “non-Euclidean”. This simple interpretation of the metric as a grid on the surface, though not mathematically rigorous, does provide the important insight that we are aiming for: changing the Gaussian curvature requires a change in the surface metric (this leads to the inherent challenge that map-makers face: any map of the Earth will show some level of distortion<sup>49</sup>). Moreover, this change in metric (and thus in Gaussian curvature) cannot be achieved through bending alone but requires stretching or shrinking of the surface. Gauss showed that the Gaussian curvature could be defined entirely in terms of the components of the metric tensor and its derivatives, thereby proving the intrinsic character of this curvature measure<sup>44</sup>. As a simple example, consider a non-Euclidean metric defined in Cartesian coordinates of the form:

$$g = \begin{pmatrix} 1 & 0 \\ 0 & \gamma(x) \end{pmatrix} \quad (6.4)$$

The function  $\gamma(x)$  describes the distances between points in  $y$ -direction as a function of  $x$ -position ( $ds^2 = dx^2 + \gamma(x)dy^2$ ). In this case, the Gaussian curvature is indeed defined entirely in terms of the metric as<sup>44;46;47</sup>:

$$K = -\frac{1}{\sqrt{\gamma}} \frac{\partial^2 \sqrt{\gamma}}{\partial x^2} \quad (6.5)$$

Following the above definition, the Euclidean, “flat” metric introduced earlier would indeed result in  $K = 0$ , or zero intrinsic curvature. The direct relation between the surface metric and Gaussian curvature has been harnessed by several researchers to controllably transform flat sheets into intrinsically curved geometries<sup>19–21;50;51</sup>. As explained by Klein et al., this could be achieved by prescribing a non-Euclidean target metric in the flat sheets, which essentially means that a non-uniform expansion or contraction distribution is programmed into the sheets<sup>19</sup>. Upon activation by an external stimulus, differential swelling/shrinking occurs, which is accommodated by deforming into a curved, 3D geometry in accordance with the newly imposed metric. Hence, these “metric-driven”<sup>20</sup> approaches represent a successful application of Gauss’ results to the shape-shifting of advanced materials. However, an important remark is that these approaches deal with real sheet materials of a small but finite thickness, while our discussion thus far has only considered mathematical surfaces of zero thickness. The presence of this thickness forces researchers to consider the elastic energy of the curved sheets, consisting of a stretching component ( $E_s$ ) and a bending component ( $E_b$ ), both of which depend on the sheet thickness<sup>19;50;52</sup>:

$$E = E_s + E_b \quad (6.6)$$

When a non-Euclidean target metric is prescribed in the flat sheet with finite thickness, the sheet will adopt a shape that minimizes its elastic energy  $E$ . This leads to a competition between both components of the energy: the bending energy  $E_b$  is zero when

the sheet remains flat while the stretching energy  $E_s$  is zero when the sheet achieves the curved, 3D geometry with the prescribed target metric<sup>19;46;50</sup>. The final shape corresponds to a balance between both contributions, which is determined by the sheet thickness  $t$ . Since the stretching energy scales with  $t$  and the bending energy scales with  $t^3$ , there will be a certain thickness that marks a transition between bending energy domination and stretching energy domination<sup>46;53</sup>. Consequently, the thinner a sheet becomes, the more energetically favorable it becomes to bend than to stretch<sup>46;48;50</sup>. In other words, the bending energy decreases more rapidly with decreasing thickness than the stretching energy does, meaning that when given the choice between bending or stretching to accommodate local shrinking/swelling, it will “cost” much more energy for the thin sheets to stretch than to bend (which is why very thin sheets are often considered inextensible membranes<sup>52</sup>). The sheets will thus bend in 3D to adopt the target metric (if a suitable embedding of the target metric exists), although the exact target metric will not be achieved for finite thickness since there will always be some energetic cost to bending a sheet<sup>19;50</sup>.

In summary, the concept of surface curvature could be discussed from an extrinsic and an intrinsic perspective, using the mean and Gaussian curvature respectively. Some surfaces might be curved from an extrinsic view, yet intrinsically remain flat (a developable surface). When the aim is to achieve extrinsic curvature from a flat surface, this could be easily achieved by an inextensional bending deformation of the surface, which leaves the Gaussian curvature unaffected. However, achieving intrinsic curvature from a flat surface is more complicated, as it requires the distances between points on the surface to change. This cannot be achieved through bending alone, but requires in-plane stretching or shrinking of the surface. The geometrical aspects of origami introduced in the following section are better understood within the context of the ideas presented here.

### 6.2.2 Geometrical aspects of origami

Origami has inspired artists for hundreds of years to transform ordinary sheets of paper into intricate yet beautiful 2D or 3D geometries. Recently, engineers and scientists have also become attracted to origami and have studied the paper folding art from a more mathematical perspective, giving rise to the field of computational origami<sup>54</sup>. Origami offers many interesting mathematical challenges, such as the folding of an arbitrary polyhedron from a flat piece of paper<sup>55</sup> or the question of flat foldability, *i.e.* whether a crease pattern results in a folded state having all points lying in a plane<sup>56</sup>. Another aspect that has received broad attention and that is of greater relevance to the folding of 3D engineering structures is the question of rigid-foldability. An origami design is rigid-foldable, if the transition from the flat to the folded state occurs smoothly through bending at the creases only, thus, without bending or stretching of the faces in between the creases. In other words, a rigid origami design could be folded from rigid panels connected with hinges, which is desirable for deployable origami structures made from rigid materials, such as solar panels, medical stents or robots<sup>57;58</sup>.

Classical origami starts with a flat sheet of paper, which could be considered a developable surface and by definition has zero Gaussian curvature. Folding this flat sheet along predefined crease lines essentially means bending the sheet at a very high radius of curvature. Since bending does not change the metric of the sheet, the Gaussian curvature will remain zero at (nearly) all points on the folded sheet. In other words, no matter how a sheet is folded, it remains intrinsically flat. It must, however, be noted that some degree of stretching is involved in the folding of paper. More specifically, Witten<sup>52</sup> has explained that sharp folds must involve some stretching, as they would otherwise result in an infinitely high bending energy. Nevertheless, this stretching is only confined to the small fold lines and it is typically neglected, *i.e.* a non-stretchable sheet with idealized sharp folds is assumed<sup>59</sup>.

When discussing origami and polyhedral surfaces, it is useful to introduce yet another definition of the Gaussian curvature, known as Gauss' spherical representation. Gauss introduced this description in his original paper on the *Theorema Egregium*. This concept has been used, for example, by Miura<sup>60</sup> and Huffman<sup>61</sup> in the analysis of origami. Gauss' spherical representation could be obtained by first considering a closed, oriented contour  $\Gamma$  around a point  $P$  on an arbitrary surface (Figure 6.3a). The unit normals on  $\Gamma$  are collected and translated to the center of a unit sphere (the Gauss sphere), effectively tracing out a new oriented contour  $\Gamma'$  on the surface of the sphere, resulting in the "Gauss map" of the original contour. Both contours enclose a certain area on their respective surfaces:  $\Gamma$  encloses  $F$  and  $\Gamma'$  encloses  $G$ . The Gaussian curvature  $K$  is then defined as<sup>41;62</sup>:

$$K = \lim_{\Gamma \rightarrow P} \frac{G}{F} \quad (6.7)$$

While calculating the Gaussian curvature on an arbitrary surface might not be trivial using the above definition, Gauss' spherical representation does provide an additional interpretation of the intrinsic curvature. For example, the Gauss map of a closed contour on a developable surface encloses zero area on the Gauss sphere ( $G = 0$ ), indeed corresponding to zero Gaussian curvature following the above definition (Figure 6.3). On the other hand, the closed contours on spherical or saddle surfaces map into closed contours with non-zero enclosed areas on the Gauss sphere, indicating the non-zero Gaussian curvature of these surfaces. Note that  $G < 0$  when the orientation of  $\Gamma'$  is opposite to that of  $\Gamma$ , resulting in a negative Gaussian curvature (Figure 6.3a)<sup>62</sup>.

Applying Gauss' spherical representation to the simplest type of origami, a single straight crease crossing a flat sheet of paper, once again proves that folding has no intrinsic effect on the surface. The normals on each face map into a single point on Gauss' sphere, while the normals on the crease between the faces are not uniquely defined and map into an arc connecting both points, resulting in  $G = 0$  and, thus, no Gaussian curvature (Figure 6.3b)<sup>63</sup>. Miura<sup>60</sup> used Gauss' spherical representation to analyse different configurations of fold lines joining at a common vertex and showed that some combinations cannot be folded rigidly<sup>60</sup>. For example, a vertex of valency three (three

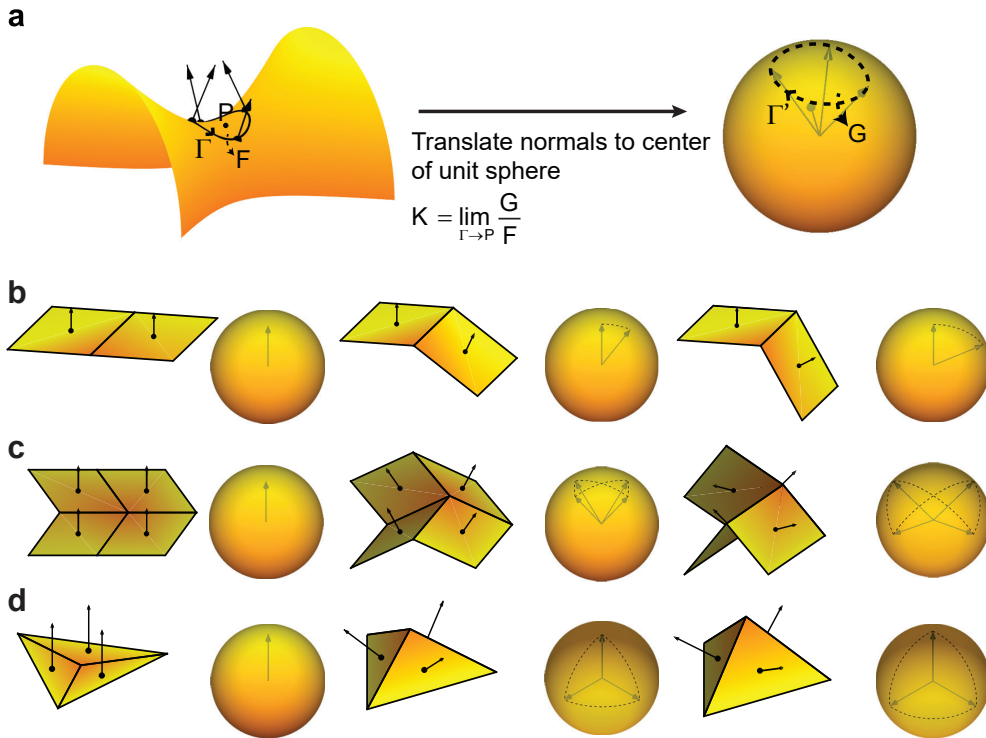


**Figure 6.3:** Gauss' spherical representation of the Gaussian curvature. a) Definition of the Gauss map using a closed, oriented contour on a point on an intrinsically curved surface. The unit normals on  $\Gamma$  are translated to the center of a unit sphere and trace out a new contour  $\Gamma'$ . b) Folding along a simple straight crease does not change the Gaussian curvature (c) The Gauss map applied to a unit cell of the rigid-foldable Miura-ori pattern. In the partially folded configurations (middle and right pane), the normals trace out a bowtie contour on the Gauss sphere, with one-half of the bowtie classifying as "positive" area (clockwise tracing) and the other half as "negative" area (counter-clockwise trace), resulting in zero net area. (d). The Gauss map applied to the three-valent vertex of a tetrahedron. The transformation of the flat state (left pane) to the folded state (middle and right pane) induces a change in the Gaussian curvature (non-zero area on the unit sphere), showing that a three-valent vertex cannot be achieved in rigid origami.

creases joining at the vertex) is never rigid-foldable: the three faces surrounding the vertex have normals in different directions, tracing out a spherical triangle on the Gauss sphere with non-zero area (Figure 6.3d). This would imply that  $K \neq 0$ , which is not possible when rigidly folding a flat surface. Similarly, Miura showed that a four-valent vertex with all mountain ("upwards") or valley ("downwards") folds cannot be folded rigidly, while a four-valent vertex with three mountain folds and one valley fold (and vice versa) could be rigidly folded<sup>62</sup>. It must be, however, emphasized that a three-valent vertex or a four-valent vertex with all mountain folds could be folded, when the rigid folding requirement is relaxed, *i.e.* when the faces are allowed to bend.

Based on the above insights, it might be argued that origami is not a suitable approach to create intrinsic curvature from flat sheets as origami deals with isometric

deformations. However, applying the right fold and cut patterns could alter the global or “apparent” Gaussian curvature, without the need for in-plane stretching or shrinking of the flat sheet. In essence, origami and kirigami techniques allow to approximate intrinsically curved surfaces through developable deformations of many small faces connected through fold lines. The specific origami and kirigami techniques that have been used by other researchers for this purpose are described in the next sections of this chapter.

## 6.3 Origami approaches

In this section, we will review different origami approaches that have been used to approximate intrinsically curved surfaces. The four different approaches discussed here, namely origami tessellations, tucking molecules, curved-crease origami, and periodic pleating, all start from a flat, uncut sheet that is folded along predefined creases.

### 6.3.1 Origami tessellations

Origami tessellations, characterized by a periodic crease pattern or “tiling” of a flat sheet, have inspired artists for many decades<sup>64</sup>, but have also found their way into scientific and engineering applications such as compliant shell mechanisms<sup>65</sup> and mechanical metamaterials<sup>37;66</sup>. Moreover, the rational design of the tessellation pattern allows for changing the apparent curvature of flat sheets without requiring local stretching of the faces.

#### Miura-ori

The most widely studied origami tessellation is the herringbone pattern known as Miura-ori, originally introduced as an efficient packing of solar sails<sup>34</sup> but also observed in spontaneous wrinkling of thin, stiff films on thick, soft substrates subjected to biaxial compression<sup>67</sup>. A Miura-ori unit cell consists of a four-valent vertex connecting four parallelograms using three mountain folds and one valley fold (Figure 6.4). An important property of this origami design is that it is rigid-foldable, as indicated by Gauss’ spherical representation<sup>60;62</sup> (Figure 6.3c). Schenk and Guest studied the geometry and kinematics of Miura-ori and showed that purely rigid Miura-ori has only a single degree of freedom, *i.e.* in-plane folding and unfolding<sup>36</sup>. Based on the analysis of a single unit cell, they concluded that a Miura-ori sheet is an auxetic material, characterized by a negative in-plane Poisson’s ratio. In a later study, however, Lv et al. showed that some specific configurations could exhibit a positive in-plane Poisson’s ratio as well<sup>68</sup>. While rigid-foldability of Miura-ori allows only in-plane deformations, experiments with simple paper models reveal that the folded sheets could also deform out-of-plane (Figure 6.4d-e). Indeed, Schenk and Guest identified saddle and twist deformation modes and showed that these are only possible in non-rigid Miura-ori, where the individual faces are allowed to bend<sup>36</sup>. This leads to an interesting property of Miura-ori (and origami tessellations in general): through developable deformations at unit cell level, the global Gaussian curvature of the sheet could be changed, making this origami tessellation an interesting candidate for compliant shell mechanisms<sup>65;69</sup>.

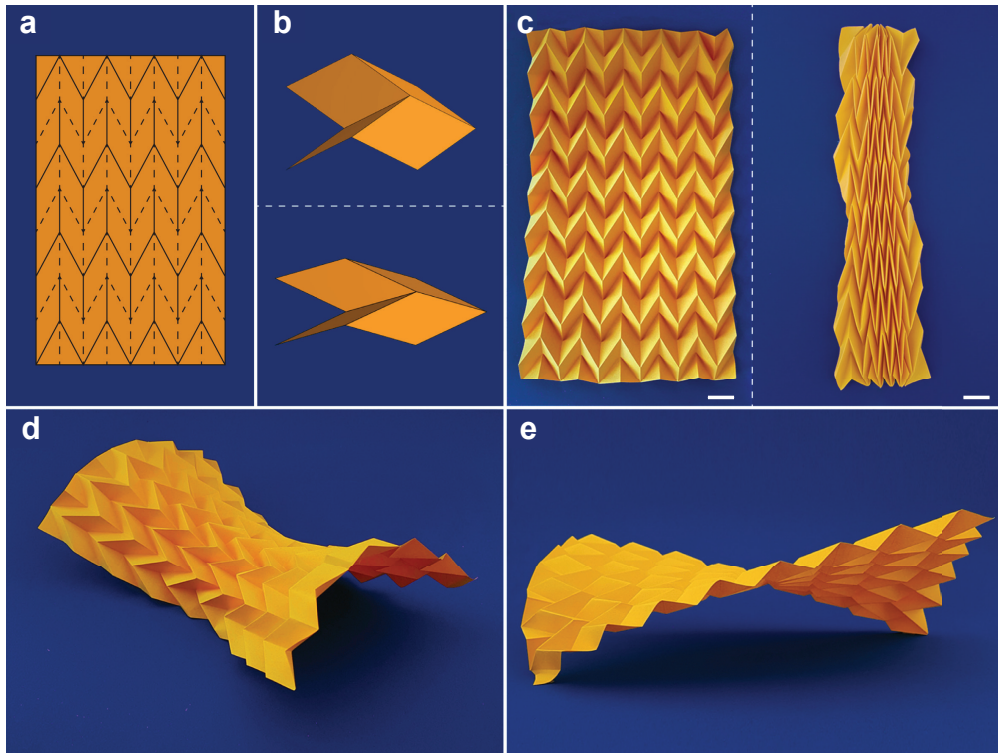


**Figure 6.4:** Miura-ori tessellation. a) A crease pattern of a Miura-ori tessellation. Solid lines are mountain folds and dashed lines are valley folds. b) two different unit cells for a Miura-ori tessellation, consisting of four parallelograms connected through three mountain folds and one valley fold. c) A paper model of the Miura-ori tessellation in a partially folded state (left) and collapsed state (right), showing the flat-foldability of this origami pattern (Scale bar is 2 cm). d) Saddle-shaped and e) twisted out-of-plane deformations of the (non-rigid) Miura-ori sheet.

Several researchers have sought for generalizations or variations of the Miura-ori pattern that approximate a curved surface when folded, without requiring out-of-plane deformations. Tachi investigated quadrilateral mesh origami consisting of quadrilateral faces joined at four-valent vertices and established rules for rigid-foldability. Starting from a regular Miura-ori pattern, he explored variations that could fit a freeform surface (*e.g.* a dome-shape), while remaining rigidly foldable<sup>70</sup>. Gattas et al. parameterized the Miura-ori to be able to systematically compare different pattern variations. They investigated five rigidly foldable “first-level derivatives” obtained by changing a single characteristic such as the crease orientation<sup>71</sup>. Depending on the derivative, geometries with an overall single- or double-curvature could be achieved, although the latter seemed to be limited to a non-developable crease pattern<sup>71</sup>. Sareh and Guest considered Miura-ori as one of the seventeen plane crystallographic or “wallpaper” groups (a pmg group) and provided a framework to obtain flat foldable symmetric generalizations of the Miura-ori, some of which could result in globally curved geometries when folded<sup>72</sup>. More recently, Wang et al. proposed a design method to obtain Miura-

ori generalizations that approximate cylindrical surfaces upon folding<sup>73</sup>. While their method takes into account rigid folding and the thickness of the faces, which is useful for practical applications, it is restricted to cylindrical geometries and hence single curvature<sup>73</sup>. Perhaps the most complete and successful approach to approximate arbitrarily curved surfaces with Miura-ori generalizations is the one recently proposed by Dudte et al. (Figure 6.5)<sup>74</sup>. Dudte et al. employed constrained optimization algorithms to solve the inverse problem of fitting an intrinsically curved surface with a generalized Miura-ori tessellation. They showed that the surfaces of generalized cylinders could be approximated using flat foldable and rigid-foldable tessellations, which could not be guaranteed for intrinsically curved surfaces. In the latter case, snapping transitions were required during the action of folding or unfolding, although the final configuration was strain-free<sup>74</sup>. The researchers also showed that a higher number of unit cells results in a more accurate fitting of the surface, but at the cost of a higher folding effort<sup>74</sup>.

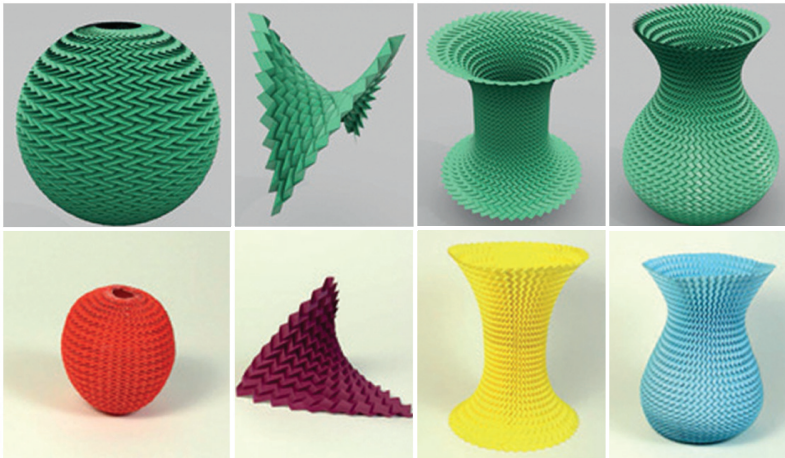


**Figure 6.5:** Generalized Miura-ori tessellations fitting curved surfaces. The top row depicts simulations, while the bottom row shows physical models. Adapted by permission from Macmillan Publishers Ltd: Nature Materials<sup>74</sup> copyright 2016.

### Other periodic tessellations

In addition to Miura-ori, several other tessellations are well known among origami artists and scientists. Examples are the tessellations obtained when tiling the plane with a six- or eight-crease waterbomb base, the former of which has been used to create an origami stent<sup>32;75</sup>. Other famous origami tessellations were developed by Ron Resch<sup>76;77</sup> and have inspired scientists to create origami-based mechanical metamaterials<sup>68</sup> or freeform surface approximations<sup>78</sup>. Origami tessellations that are rigid-foldable are of particular interest for engineering applications. Evans et al. used the method of fold angle multipliers to analyse the existing flat foldable tessellations and identify those that were rigid-foldable<sup>58</sup>. Furthermore, the researchers presented rigid-foldable origami “gadgets”, local modifications to a crease pattern, to develop new rigidly foldable tessellations<sup>58</sup>. Tachi studied the rigid foldability of “triangulated” origami tes-

sellations, in which the quadrangular faces are divided into triangles (essentially capturing the bending of faces of non-triangulated origami)<sup>79</sup>. Through numerical simulations (by means of a truss model), it was observed that most periodic triangulated origami tessellations exhibit two (rigid) degrees of freedom, a folding/unfolding motion and a twisting motion, with Miura-ori being an exception as it only shows the folding/unfolding motion<sup>79</sup>.

Applying a periodic tessellation such as Resch's triangular pattern to a flat sheet essentially means texturing the sheet with small-scale structures that give rise to unusual properties on a global scale<sup>69</sup>. Due to the strong interaction between the local kinematics and global shape, these tessellated sheets have earned the name "meta-surfaces", in analogy with 3D metamaterials<sup>65;69</sup>. An interesting property of the textured sheets is that folds may partially open or close locally, effectively simulating local stretching or shrinking. As a consequence, the sheets could undergo large deformations and change their global Gaussian curvature, without stretching of the actual sheet material<sup>65;69</sup> (Figure 6.6). However, the opportunities to approximate curved surfaces using this approach are limited, despite the ease with which small paper models could be manipulated. That is because approximating saddle shapes might involve some facet and crease bending that make it difficult, if not impossible, to achieve anticlastic geometries (negative Gaussian curvature) through rigid folding<sup>78</sup>. Moreover, for large tessellated sheets (with many unit cells), even synclastic geometries (positive Gaussian curvature) might not be rigid-foldable. Tachi showed that smooth rigid folding of (triangulated) periodic tessellations in dome shapes is obstructed once the tessellated sheet becomes too large, making only cylindrical surfaces feasible<sup>79</sup>. A similar conclusion was reached by Nassar et al.<sup>80</sup>. Indeed, the tessellation shown in Figure 6.6c naturally adopts a cylindrical shape in the partially folded configuration.

Although several standard origami tessellated sheets could conform to curved surfaces, the achievable geometries are limited. In order to obtain more complex 3D shapes, Tachi developed the Freeform Origami method to generalize existing tessellations, essentially building further on his work on quadrilateral mesh origami<sup>81</sup>. He provided mathematical descriptions of the conditions that apply to the traditional tessellations such as developability and flat-foldability, and numerically calculated perturbations of these tessellations while preserving those conditions. The algorithm was implemented in a software package that allows the user to actively disturb an existing folded origami tessellation and observe the corresponding changes to the crease pattern in real-time<sup>81</sup>. However, the software is not capable of solving the inverse problem of finding the crease pattern that belongs to a given 3D surface. Other researchers have also used mathematical methods to calculate new tessellations that could fold into 3D geometries. Zhou et al. proposed the "vertex method" to inversely calculate a developable crease pattern based on the Cartesian coordinates of a given 3D geometry<sup>82</sup>. While their method is versatile enough to develop the crease pattern for a structure that fits between two (single-) curved surfaces, a major limitation is that it is not applicable to intrinsically curved surfaces<sup>82</sup>. More recently, Song et al. built

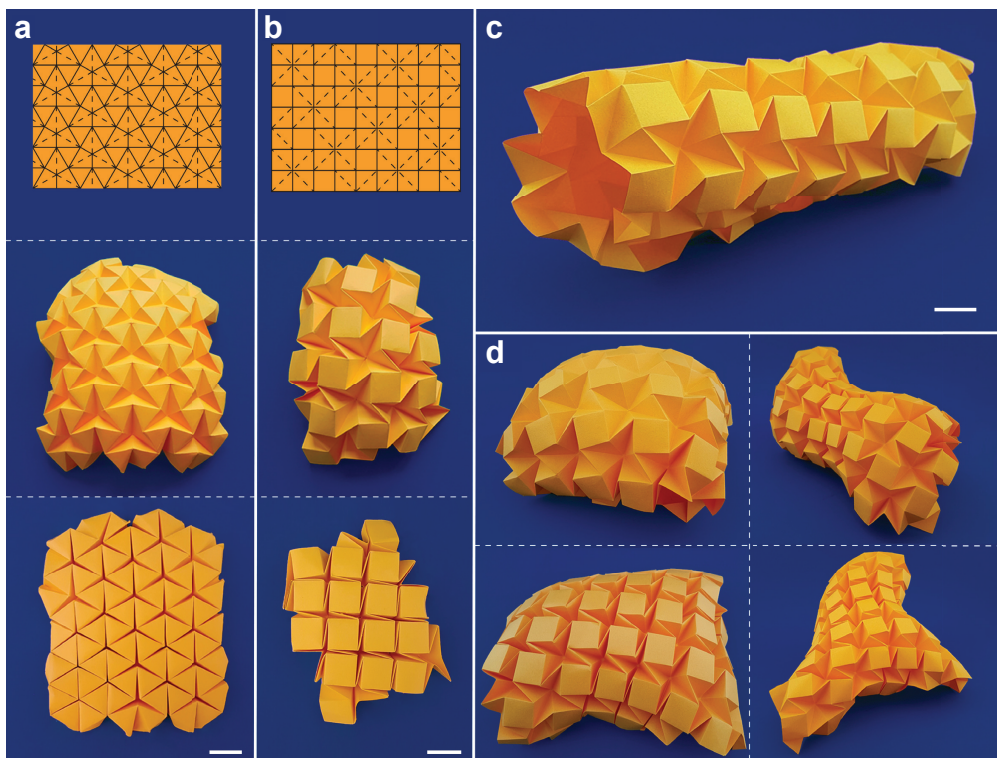


**Figure 6.6:** Origami tessellations. a-b) Triangular Ron Resch and square waterbomb tessellations, respectively. Top: crease pattern (solid lines are mountain folds, dashed lines are valley folds), middle: partially folded state, bottom: fully folded state (Scale bar is 2 cm). c) Natural resting state of the partially folded square waterbomb tessellation (for a large enough sheet), adopting a cylindrical shape (Scale bar is 2 cm). d) Various configurations with global intrinsic curvature of the same square waterbomb tessellated sheet, obtained through locally opening and closing the unit cells.

further on this work and developed a mathematical framework to create trapezoidal crease patterns that rigidly fold into axisymmetric double-curved geometries<sup>83</sup>. More specifically, their method calculates the crease pattern that fits both an inner and outer target surface with the same symmetry axis. While intrinsic curvatures could in this way be achieved, the proposed method is limited to very specific ring-like geometries, possessing rotational symmetry and having relatively small curvatures<sup>83</sup>.

### 6.3.2 Tucking molecules

Other approaches to approximate intrinsically curved surfaces could be obtained from the field of computational origami design, in which one searches for the crease pattern that belongs to a given shape, typically a 3D polyhedron. The first well-known computational tool facilitating origami design was proposed by Lang and is based on tree-like representations of the desired shapes (“stick-figures”)<sup>84</sup>. However, the method is restricted to calculating origami bases that need to be shaped afterwards into the de-

sired geometry. To enable the construction of crease patterns for arbitrary 3D polyhedrons, Tachi developed his well-known “origamizing” approach based on tucking molecules<sup>56,85</sup>. The starting point is a polyhedral representation of an arbitrary surface, which is made topologically equivalent to a disk (such that it is not a closed polyhedron but has a cut that allows it to open). The basic idea of the approach is to map all the surface polygons of the polyhedron onto a plane and to fill the gaps in between with tucking molecules, which are flat foldable segments, creating a 2D crease pattern in doing so<sup>85</sup>. The resulting crease pattern is not considered an origami tessellation in the context of this review, as it is highly non-periodic and comprises polygons of different shapes and sizes. The tucking molecules connect adjacent surface polygons and are tucked away behind the visible surface upon folding (Figure 6.7a). Tachi defined edge-tucking and vertex-tucking molecules, respectively bringing edges or vertices together in the folded configuration. In order to fit the desired 3D shape with the surface polygons, crimp folds are also employed to locally adjust the tucking angle<sup>85</sup>. The entire procedure was implemented in a software package for which the input is a polygon mesh and the output is a 2D crease pattern, allowing the creation of complex origami structures that were never folded before, such as the origami Stanford bunny (Figure 6.7c)<sup>56</sup>. Tachi attributed the increased practicality of this approach compared to earlier origami design methods to three reasons: multi-layer folds rarely occur, the crimp folds offer structural stiffness by keeping vertices closed, and the method has a relatively high efficiency, defined by the ratio of polyhedral surface area to required paper area<sup>56</sup>. Despite its versatility and generality, the origamizing method has the drawback that some 3D polyhedrons cannot be mapped into a 2D pattern, a problem that was recently addressed by Demaine and Tachi<sup>86</sup>, or that the proposed pattern is inefficient. Moreover, the flat folding requirement of the tucking molecules significantly reduces the applicability of this method to the folding of stiff, thicker materials<sup>78</sup> and the presence of crimp folds obstructs smooth folding<sup>56</sup>, making this method intractable for industrial applications.

Tachi also proposed a more practically applicable method to approximate curved surfaces, combining aspects from his earlier work on freeform origami<sup>81</sup> and the origamizing approach<sup>85</sup>. The basic idea is that generalizations of Resch's tessellations are calculated that fit a given polyhedral surface<sup>78</sup>. Contrary to the origamizing approach, the surface polygons do not have to be mapped onto the plane but a first approximation of the tessellation is directly obtained from the 3D structure, after which it is numerically optimized to become developable and to avoid collisions of faces. As such, the implementation of this method is related to the earlier work on Freeform Origami<sup>81</sup>, but it is still considered in this section since (simple) tucking molecules are used. Tachi defined a “star tuck” and variations thereof as building blocks to tessellate the given 3D surface<sup>78</sup>. The fundamental difference between conventional tucks and the star tucks is that the latter could also exist in a semi-folded state and do not have to be folded flat (Figure 6.7b). The surface polygons could be arranged to locally fit the desired shape through partial opening of the star tucks, while this required crimp folds

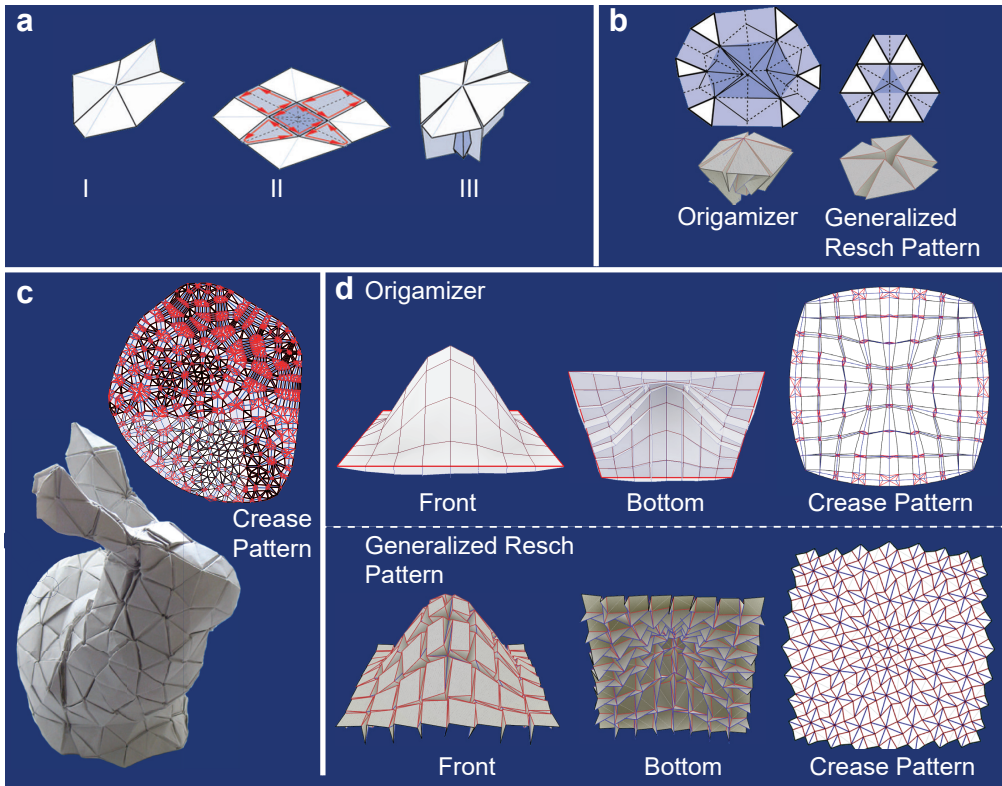


**Figure 6.7:** Origami involving tucking molecules. a) The definition of a tucking molecule used in the “Origamizer” approach. I) A section of a polyhedral surface, II) the flattened polyhedral surface, showing the surface polygons connected through edge- and vertex-tucking molecules. III) The folded configuration, showing the excess material being tucked away behind the outer surface. Reproduced with permission from IEEE from reference<sup>56</sup>. b) Comparison between tucking molecules in the “Origamizer” approach and the generalized Ron Resch tessellation approach. Reproduced from reference<sup>78</sup>. c) Origami Stanford bunny, folded from a single-sheet crease pattern created using the “Origamizer” software. Reproduced from Figure 1 from reference<sup>86</sup>. d) Comparison between the surface approximations of the “Origamizer” approach (top) and the generalized Ron Resch pattern approach (bottom) to an intrinsically curved bell-shaped surface. Note the partially opened tucking molecules in the latter approach. Figures and crease patterns were obtained using “Origamizer”<sup>56</sup> and “Freeform Origami”<sup>70</sup> (red lines are mountain folds, blue lines are valley folds).

in the origamizing approach. The algorithm was implemented in a software package, allowing users to interactively design generalized Resch tessellations corresponding to a given surface (Figure 6.7d). However, for highly complex surfaces, which would require significant stretching and shrinking to become developable, crease patterns cannot always be generated. Moreover, smooth rigid folding of the tessellations is not guaranteed for all cases. Nonetheless, the proposed method has significant potential for the practical folding of advanced materials into intrinsically curved surfaces.

### 6.3.3 Curved-crease origami

When discussing curvature and origami, it is natural to also consider curved-crease origami. While this variant of traditional origami has interested artists for several decades, the mathematics of curved-crease folding is underexplored and practical applications of origami have been primarily limited to straight creases<sup>87</sup>. Straight-crease and curved-crease origami are fundamentally different, since both faces adjacent to a curved crease always have to bend in order to accommodate the folding motion<sup>88;89</sup>. In other words, curved-crease origami is never rigid-foldable. As a consequence, curved-crease origami cannot be reduced to a matter of tracking vertex coordinates as in the case of rigid origami and the bending stiffness of the folded sheet becomes an important parameter<sup>87</sup>. Moreover, the bending induced in the faces necessitates simultaneous folding along multiple creases, complicating automated folding processes<sup>90</sup>.

One of the first and most influential analyses of curved creases was performed by Huffman, using Gauss' spherical representation to examine the local folding behaviour<sup>61</sup>. Indeed, the Gauss map of a closed contour crossing a straight crease maps into a zero-area arc while the map of a contour encompassing a curved crease has non-zero area due to the facet bending, which is indicative of its non-rigid-foldability. The geometry of curved-crease folding has been further explored by Duncan and Duncan<sup>88</sup> and Fuchs and Tabachnikov<sup>91</sup>. They presented several theorems relating the properties of the curved crease to those of the adjacent faces, which are outside the scope of this review. The most important take-away is that folding along a curved crease satisfies the developability of the sheet, meaning that a curved-folded origami consists of developable patches of either a generalized cylinder, a generalized cone, or a tangent developable to a space-curve<sup>88;92;93</sup>. Hence, folding along curved creases cannot alter the intrinsic curvature of the sheet, as no in-plane distortion of the faces occurs. However, curved-crease origami does provide means to alter the global intrinsic curvature of flat sheets, in a manner similar to straight-crease folding. More specifically, we identify two approaches to approximate non-zero Gaussian curvature: the use of curved-crease couplets and folding along concentric curved creases. In the current sub-section, only the first approach is discussed, as the latter fits within the broader concept of concentric pleating that is treated in the next sub-section.

Curved-crease couplets, a term introduced by Leong<sup>95</sup>, are pairs of curved and straight creases that have been employed by origami artists to create 3D origami with apparent positive and negative intrinsic curvature. Typically, axisymmetric structures are created from relatively simple crease patterns (Figure 6.8). A design method and software tool to generate crease patterns based on "rotational sweep" was proposed by Mitani<sup>94</sup> and a very similar tool was created by Lang<sup>84</sup>. The basic idea is that a flat sheet is "wrapped" around the desired cylindrical or conical geometry and that the excess material is folded into flaps, sections of material that are only connected at one edge<sup>96</sup>, on the outside surface. This is different from Tachi's origamizing approach<sup>56</sup> in which excess material is tucked away inside the geometry, resulting in more complicated crease

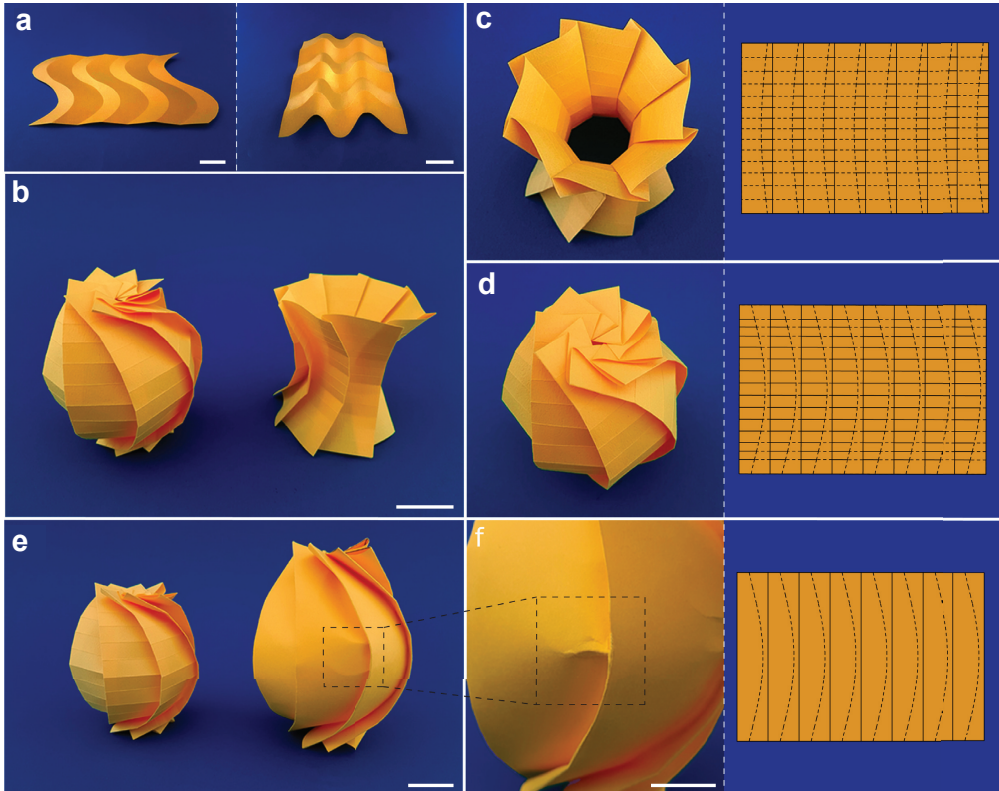


**Figure 6.8:** Curved-crease origami. a) Simple examples of curved-crease origami (Scale bar is 2 cm). b) An origami sphere (positive Gaussian curvature) and an origami hyperboloid (negative Gaussian curvature) created with the method described by Mitani<sup>94</sup> (Scale bar is 2 cm). c-d) Top views of the origami hyperboloid and sphere (left panes) and the associated crease patterns (right panes, solid lines are mountain folds and dashed lines are valley folds). e) Comparison between the standard origami sphere obtained with Mitani's method<sup>94</sup> and the “smooth” variant (Scale bar is 2 cm). f) Closer view of a wrinkle in the smooth origami sphere, indicative of the frustration between curved and straight creases (left) and the associated crease pattern without horizontal creases (right) (Scale bar is 1 cm).

patterns<sup>94</sup>. A flap in Mitani's method consists of a kind of curved-crease couplet, containing a straight mountain crease and a piecewise linear valley crease, approximating a curved line. The latter crease represents half of the vertical cross section of the desired shape and, when revolved around the vertical axis, traces out this shape<sup>94,95</sup>. To create the crease pattern, the curved-crease couplets are simply repeated  $N$  times and arranged on a rectangular sheet (for cylindrical geometries) or on an  $N$ -gon (for conical geometries), with higher values of  $N$  resulting in higher rotational symmetry. Using this method, double curved shapes could be approximated, as shown in Figure 6.8. More recently, Mitani also proposed a variant of this method in which the flaps are replaced by “triangular prism protrusions”<sup>97</sup>. Again, the excess material that results when wrapping the desired geometry is placed on the outside surface, this time in a slightly

different manner involving four creases instead of two.

Although recent efforts have been made to understand curved-crease origami from a more mathematical perspective<sup>98</sup>, it remains a field that is primarily reserved for artists. As such, only limited work has been done that explores the capabilities of curved-crease folding to approximate intrinsically curved surfaces. Nonetheless, it is expected that the use of curved-creases has a significant potential in practical origami, not only to achieve complex geometries but also for kinetic architectures<sup>93</sup> and shape-programmable structures<sup>99</sup>.

### 6.3.4 Concentric pleating

As a final category of folding strategies to approximate intrinsically curved surfaces, we consider origami based on concentric pleating, *i.e.* alternately folding concentric shapes into mountains and valleys. Geometries with apparent negative Gaussian curvature spontaneously result after folding the remarkably simple crease patterns (Figure 6.9). The original crease patterns for this origami consisted of equally spaced concentric squares or circles, although variants with ellipses or parabolas have also been folded<sup>87</sup>. One might classify the concentric pleating as a type of origami tessellation, however, we consider it separately due to its remarkable properties.

The classical model with the concentric squares is called the pleated hyperbolic paraboloid or simply *hypar*, after the negatively curved surface it seems to approximate. As explained by Demaine et al., the 3D shape naturally arises due to the paper's physics that balances the tendency of the uncreased paper to remain flat and that of the creased paper to remain folded<sup>100</sup>. Seffen explained the geometry by considering the pleating as a "corrugation strain" towards the center without causing an axial contraction of the hinge lines, thereby forcing the model to deform out-of-plane<sup>65</sup>. Thus, the pleating introduces a distortion of the flat sheet that is relieved by settling on an energy-minimizing 3D configuration. This principle of anisotropic strain (shrinking) has been recently used by van Manen et al. to program the transformation of flat shape memory polymer sheets into an approximation of a *hypar*, using thermal activation<sup>101</sup>.

Although paper models of the pleated *hypar* are ubiquitous and well-known among origamists, mathematicians have questioned whether the standard crease pattern of concentric squares could actually result in the pleated *hypar*. More specifically: does a proper folding (folding angles between 0 and  $\pi$ ) along exactly these creases exist? Demaine et al. proved the surprising fact that it does not, hence the folding along the standard crease pattern cannot result in the *hypar* without some stretching or additional creasing of the paper<sup>100;102</sup>. The problem lies in the twisting of the interior trapezoidal faces of the *hypar*. While a standard piece of paper could be effortlessly twisted and curled in space, Demaine et al. proved that this twisting should not occur for the interior faces of the *hypar*. Using aspects of differential geometry, such as the properties of torsal ruled surfaces, the researchers proved two theorems: straight creases must remain straight after folding and a section of the paper bounded by straight creases must remain planar and cannot bend or twist<sup>100</sup>. Demaine et al. conjecture that the actual

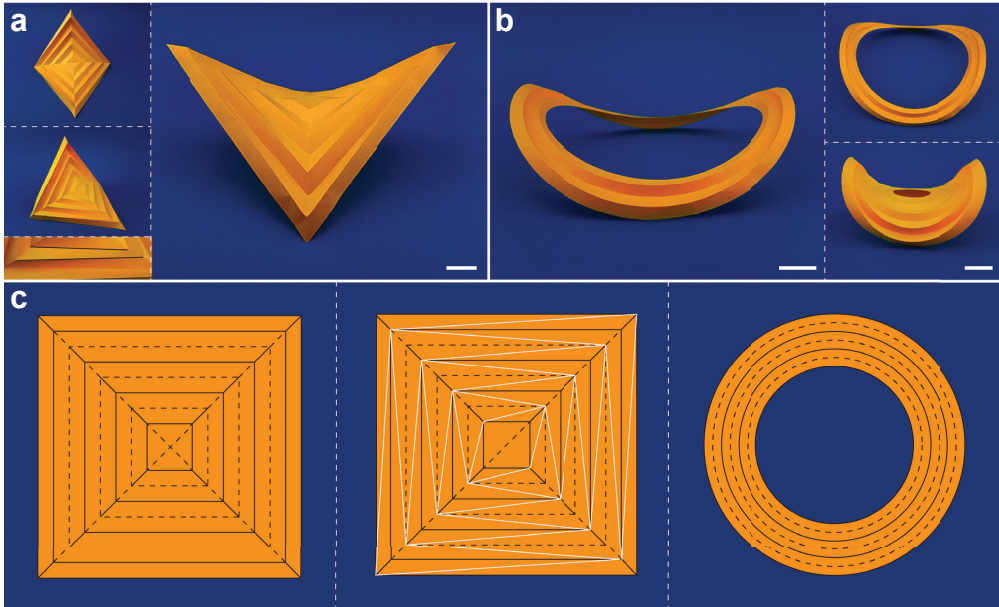


**Figure 6.9:** Concentric pleating origami. a) Origami hyperbolic paraboloid (“hypar”), obtained by pleating concentric squares. Top left: top view, middle left: side view, bottom left: Closer view of the twisted faces in the standard hypar model, right: side view showing the global saddle-shaped geometry of the hypar (Scale bar is 2 cm). b) Circular variant of the hypar, obtained by pleating concentric circles (with center hole). Left: side view of an annulus with three creases (Scale bar is 2 cm), top right: top view of an annulus with three creases, bottom right: side view of an annulus with eight creases (Scale bar is 1 cm). c) Different crease patterns. Left: standard crease pattern for the square hypar, middle: triangulated crease pattern for the square hypar, white lines represent the additional creases that enable proper folding of the hypar (adapted from reference<sup>100</sup>), right: crease pattern for the circular hypar (solid lines are mountain folds, dashed lines are valley folds).

folding of the hypar from the standard crease pattern is enabled through additional creases in the paper, potentially many small ones. Alternatively, some stretching at the material level might occur<sup>102</sup>. In any case, it is clear that the folding of the standard crease pattern into the pleated hypar is highly non-rigid, as could also be intuitively understood when drawing a closed curve in one of the square rings: the curve crosses four folds with the same mountain or valley assignment, which cannot fold rigidly according to Gauss’ spherical representation<sup>62</sup>.

The theorems of Demaine et al.<sup>100</sup> have implications for straight crease origami that exhibits non-rigid behaviour, such as the Miura-ori discussed above. It was explained that a (partially) folded Miura-ori could deform out-of-plane through facet bending, which should not be possible according to the above theorems. However, facet bending may be enabled by an additional spontaneous crease in the quadrangular facets, making the facet piecewise planar and satisfying the theorems in doing so. This “triangulation” of the facets has been employed by researchers to capture facet bending in mathematical

origami models<sup>66;69;74;103;104</sup>. Moreover, Demaine et al.<sup>100</sup> proved that a triangulation of the standard hyper crease pattern also renders the pattern rigid-foldable, making it possible to create hypars from more rigid materials such as sheet metal<sup>100</sup>. The insights on the hyper crease pattern are also relevant for the curved-crease couplets that were introduced in the previous section, consisting of alternating curved and straight creases. The curved creases require the adjacent faces to bend, while the straight creases do not allow bending. Furthermore, the straight creases do not remain straight in the folded 3D model. Following the theorems of Demaine et al.<sup>100</sup>, it thus seems that these curved-crease couplets cannot be folded. This problem is alleviated in Mitani's method<sup>94</sup> by including horizontal creases and representing the curved crease as a piecewise linear crease (Figure 6.8c-d), thereby ensuring that the model remains piecewise planar. It must also be noted that the theorems of Demaine et al.<sup>100</sup> are applicable to interior faces (not at the boundary) and fold angles between 0 and  $\pi$ , while the curved crease couplets end at the paper boundaries and the straight creases seem to be folded at an angle of  $\pi$ . Indeed, Mitani states that the horizontal creases can be omitted when the straight creases are folded close to  $\pi$ <sup>94</sup>, resulting in a smooth folded geometry (Figure 6.8e). However, closer inspection of such models still reveals the occurrence of small, spontaneous kinks or wrinkles, indicative of the frustration between the straight and curved crease (Figure 6.8f).

In addition to the pleated hyper, another classical model is obtained by pleating concentric circles with a hole in the middle (Figure 6.9b). Similar to the hyper, this pleated annulus deforms into a saddle, with the degree of curvature depending on the fold angles. Mouthuy et al. attributed this specific deformation to the "overcurvature" of the ring, which is a measure of how much the curvature of the ring exceeds that of a circle with the same circumference<sup>105</sup>. Indeed, the pleating causes the curvature of the concentric creases to increase while their length is preserved, resulting in overcurvature. While Demaine et al. proved that the standard hyper crease pattern cannot be folded without additional creases or stretching, it remains unknown whether this is also the case for the pleated annulus<sup>100</sup>. However, the researchers conjecture that the annulus could be folded from exactly the given crease pattern and that additional creases nor stretching are required. Dias et al. investigated the mechanics of the simplest type of pleated annulus: a paper strip with a single circular crease<sup>106</sup>. The researchers provided analytical expressions for the elastic energy of the annulus, to which both the faces and the crease contribute. While the incompatibility between the pleating and the resistance to in-plane stretching forces the model to buckle out-of-plane, the actual shape it settles on is determined by the minimization of this elastic energy<sup>106</sup>. Later, Dias and Santangelo extended the work to a pleated annulus with several concentric circles and investigated potential singularities that might arise when attempting to fold the model from the given crease pattern<sup>107</sup>. The researchers did not prove that the crease pattern is exactly foldable, but their results indicated that singularities do not occur for a sufficiently narrow crease spacing, supporting the conjecture of Demaine et al.<sup>100;107</sup>.

Concentric pleating is a captivating type of origami, as very simple crease patterns

result in geometries with apparent intrinsic curvature. Although the mechanisms of this technique are not yet fully understood, particularly for curved creases, concentric pleating could offer an interesting pathway to achieve intrinsic curvature. Especially when extreme values of overcurvature are induced or when different types of hypars or annuli are combined, complex geometries may arise, examples of which are the “hy-parhedra” proposed by Demaine et al.<sup>108</sup>.

## 6.4 Kirigami approaches

Kirigami is an artform that is closely related to origami but also involves cutting the paper at precise locations. Kirigami has not been explored to the same extent as origami, but has recently gained traction among scientists as a promising paradigm towards stretchable electronics<sup>39;40;109;110</sup> or advanced honeycomb structures<sup>111–113</sup>. In this section, we review two distinct kirigami approaches that could be employed to approximate intrinsically curved surfaces, namely lattice kirigami and kirigami-engineered elasticity.

### 6.4.1 Lattice kirigami

Lattice kirigami is a relatively novel and promising cutting and folding technique that was introduced by Castle et al.<sup>59</sup>. Its essence lies in removing some areas from the sheet through cutting, after which the resulting gaps are closed through folding along prescribed creases. Lattice kirigami has its roots in crystallography, particularly in the defects arising in crystal lattices. Understanding the essentials of this technique therefore requires some terms and concepts from crystallography.

The starting point is the honeycomb lattice, represented as a 2D tessellation of regular hexagons. An infinite flat plane (zero Gaussian curvature) could be tiled using only hexagons, but this is not possible for intrinsically curved surfaces such as spheres or saddles<sup>115</sup>. For example, a soccer ball cannot be tiled with hexagons entirely, but requires twelve pentagons to conform to the spherical shape. The insertion of a pentagon or a heptagon within a tiling of hexagons is known as a lattice disclination, which is a type of topological defect that disrupts the orientational order of the lattice<sup>115;116</sup>. These local lattice distortions cause the surfaces to deform out-of-plane to relieve in-plane strains, reminiscent of the metric-driven principles discussed before. The disclinations themselves form concentrated sources of Gaussian curvature: pentagons result in positive Gaussian curvature and heptagons in negative Gaussian curvature<sup>115</sup>. Figure 6.10 illustrates the effect of disclinations in a hexagonal weave when a single hexagon is replaced by a pentagon or a heptagon, a technique which has long been employed by basket weavers to create complex shapes<sup>114</sup>. Another type of topological defect is a dislocation, which disturbs the translational symmetry of the lattice and is formed by a dipole of disclinations (with opposite topological charge)<sup>115;116</sup>. While disclinations and dislocations are considered defects in a topological sense, they are often necessary distortions of the crystal lattice in natural processes. For example, Sadoc et al. showed that these defects are crucial elements in phyllotaxis, the efficient packing algorithm that nature uses in self-organizing growth processes, such as the spiral distribution of

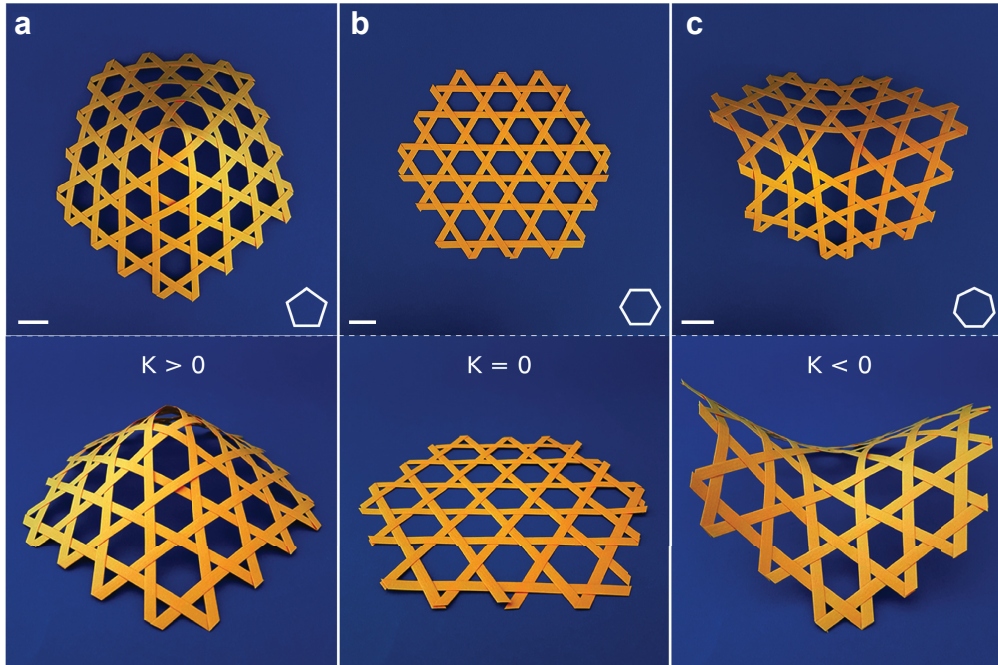


**Figure 6.10:** Lattice disclinations in a hexagonal lattice. a) Inserting a single pentagon in a hexagonal weave induces positive Gaussian curvature (Scale bars are 2 cm). b) A hexagonal weave without lattice disclinations remains flat. c) Inserting a single heptagon in the hexagonal weave induces negative Gaussian curvature (the physical models photographed were made based on the work presented in reference<sup>114</sup>).

florets in flowers<sup>116;117</sup>. The work of Sadoc et al.<sup>116</sup> was in fact a direct inspiration for Castle et al. to develop lattice kirigami<sup>59</sup>.

The basic idea behind lattice kirigami is to strategically remove areas from a honeycomb lattice, paste the newly formed edges together and fold along prescribed creases to create disclination dipoles, resulting in a stepped 3D surface with local concentrations of Gaussian curvature. Figure 6.11a provides a simple example showing two disclination dipoles at the ends of the cut<sup>59</sup>. Inspection of a single disclination dipole reveals that the cutting and pasting transforms one hexagon into a pentagon (by removing a wedge of  $\pi/3$ ) and combines two partial hexagons into a heptagon (*i.e.* adding a wedge of  $\pi/3$ ), see also Figure 6.11c. By systematically exploring cutting and pasting on the honeycomb and its dual lattice, Castle et al. established the basic rules for lattice kirigami that satisfy a no-stretching condition and preserve edge lengths on the lattices<sup>59</sup>. The researchers identified the basic units of lattice kirigami: *i.e.* a 5-7 disclination pair and a 2-4 disclination pair, with the values indicating the coordination number of the vertices (Figure 6.11c-d). The gaps that are left after cutting are closed through “climb” or “glide” moves, or a combination of both, in order to result in a 3D stepped surface (Figure 6.11a-d). Additionally, the researchers investigated the “sixon” (Figure 6.11e), which is obtained by removing an entire hexagon from the honeycomb and closing the

gap using appropriate mountain and valley folds in the adjacent hexagons. Through their basic rules, Castle et al.<sup>59</sup> constructed the foundations for an elegant and new approach towards stepped approximations of freeform surfaces.

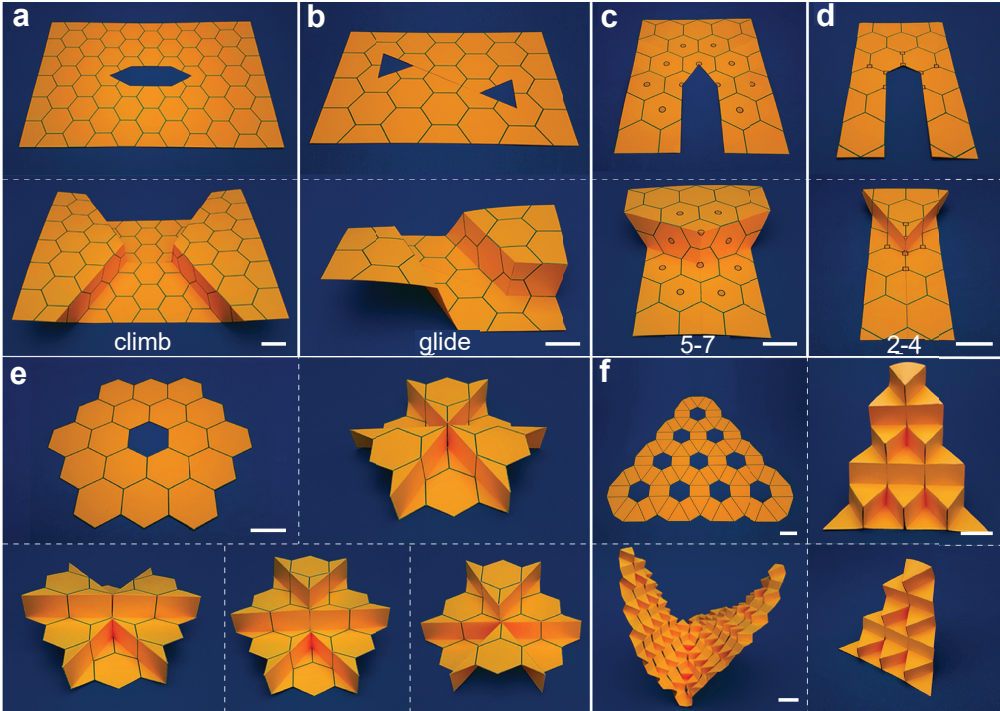


**Figure 6.11:** Lattice kirigami. a) The basic principle of lattice kirigami: a wedge is removed from a honeycomb lattice (top), the edges are brought together and the paper is folded along prescribed fold lines (known as a “climb” move). b) Another basic move, the “glide”, in which the gaps are closed through folding and sliding along the slit connecting the two excised triangles. c) A “5-7” disclination dipole, characterized by one vertex surrounded by five hexagon centers and one vertex surrounded by seven hexagon centers (represented with the solid circles). d) A “2-4” disclination dipole: one vertex has two neighbouring hexagon corners, the other vertex has four neighbouring corners (solid squares). e) Excising an entire hexagon results in a “sixon”, which could be folded into different configurations by popping the plateaus up or down. f) Folding a pluripotent “sixon sheet”, *i.e.* a tessellation of sixons on a triangular lattice, enables step-wise approximations of curved surfaces (*e.g.* left bottom pane). All scale bars are 2 cm.

Sussman et al. built upon these foundations and demonstrated that lattice kirigami is well-suited to obtain stepped approximations of arbitrarily curved surfaces, using a relatively simple inverse design algorithm<sup>118</sup>. Key to their approach is that the kirigami motifs presented by Castle et al.<sup>59</sup> could be folded into several configurations by “popping” the plateaus up or down (Figure 6.11e). By connecting many of these motifs together in admissible configurations and properly assigning the plateau heights, complex stepped structures could be obtained. Sussman et al. first considered the use of standard 5-7 climb pairs, but this approach has the important limitation that every target structure requires a new fold and cut pattern<sup>118</sup>. In order to obtain a truly pluripotent

kirigami pattern that could fit several target shapes, the researchers used sixon motifs. These sixons could be conveniently arranged on a triangular lattice with the centers of the excised hexagons on the lattice points (Figure 6.11f). The hexagonal gaps are then closed by folding the remaining hexagons in either one of their allowed configurations (*i.e.* popping the plateaus upwards or downwards). As a consequence, a myriad of stepped surfaces could be achieved from this basic kirigami tessellations, simply by varying the mountain/valley assignment of the fold lines while making sure that adjacent plateaus only differ by one sidewall height (*i.e.* one step at a time), as shown in Figure 6.11f for a saddle-like geometry<sup>118</sup>. The mountain/valley assignment for every fold line could be easily determined from a “height map” of the target surface. Sussman et al. showed that surfaces with arbitrary curvature could be approximated, provided that the gradient with which the surface rises or falls is not too steep (depending on the ratio of plateau width to plateau height). Their results showed that lattice kirigami constitutes a very versatile approach to approximate intrinsically curved surfaces, and has great potential for self-folding due to its simplicity as compared to conventional origami techniques<sup>118</sup>.

The most recent progress into lattice kirigami has been made by Castle et al.<sup>119</sup> who generalized their earlier work by relaxing some of the initially imposed rules and restrictions. Natural generalizations included the removal of larger wedges from the sheet and cutting and folding along different angles than in the original method. Additionally, the researchers demonstrated lattice kirigami on other Bravais lattices and arbitrarily complex lattices with a basis<sup>119</sup>. However, the most extensive generalizations came in the form of area-preserving kirigami, in which only slits are made and no material is removed, and additive kirigami, in which new material is actually inserted in the slits, reminiscent of natural growth of cells. Furthermore, Castle et al. showed that complex cuts could be decomposed into the general basic kirigami operations they presented<sup>119</sup>. The researchers envision that the generalized lattice kirigami framework provides more opportunities to create arbitrary shapes from initially flat sheets than the original method, due to the increased freedom in distributing local sources of Gaussian curvature along the sheet. However, a drawback is that the generalizations are not yet suitable with inverse design algorithms, which inhibits the use of such kirigami techniques in practical applications<sup>119</sup>.

Lattice kirigami has not received the same attention as traditional origami by the scientific community, the great steps undertaken by the abovementioned researchers notwithstanding. However, it is clear that lattice kirigami offers an exciting and promising paradigm towards 3D structures. By strategically removing material or creating incisions, this technique could alleviate some of the traditional origami issues such as interlocking folds or the cumbersome tucking of excess material (which is non-existent in kirigami), thereby offering higher design freedom and simplicity<sup>59;120</sup>.

### 6.4.2 Kirigami-engineered elasticity

The second kirigami technique we consider here involves cutting the paper at many locations without folding it afterwards. The basic idea is that specific cut patterns imbue flat sheets with a high “apparent” elasticity, or stretchability, which does not arise from stretching the actual material but rather from the geometric changes enabled by the cuts, which is why we term this technique kirigami-engineered elasticity<sup>40</sup>. Owing to the high stretchability and the scale-independent nature, this technique has recently been proposed as an interesting avenue towards stretchable electronic devices<sup>39;40</sup>, small-scale force sensors<sup>109</sup>, macro-scale sun-shading<sup>121</sup>, and solar-tracking photovoltaics<sup>110</sup>. However, the kirigami-engineered elasticity technique is also useful for wrapping flat sheets on intrinsically curved surfaces, since the cuts allow the sheet to locally stretch in-plane, thereby permitting the required metric distortions to conform to the curved surfaces.

We distinguish two approaches towards kirigami-engineering elasticity in the available literature, one involving out-of-plane buckling of cut struts and one involving in-plane rotation of polygonal units, as shown in Figure 6.12 for standard paper models. The former approach involving the out-of-plane buckling was first used by Shyu et al. to create highly stretchable nanocomposite sheets with predictable deformation mechanics<sup>40</sup>. The researchers enriched the nanocomposite sheets with a cut pattern consisting of straight slits in a rectangular arrangement such as the one shown in Figure 6.12a. Upon tensile loading perpendicular to the slits, the struts formed by the cutting operation buckle out-of-plane, allowing the overall sheet to reach an ultimate strain of almost two orders of magnitude higher than that of the pristine material (from 4% to 370%)<sup>40</sup>. Around the same time, Blees et al. demonstrated that the same technique is applicable to graphene, since this one-atom thick material behaves similarly to paper in terms of the Föppl-von Kármán number, a measure for the ratio of in-plane stiffness to out-of-plane bending stiffness<sup>109</sup>. Although Figure 6.12a shows the struts buckling all in the same direction, this is not necessarily the case and struts might randomly buckle upwards or downwards, resulting in unpredictable and non-uniform stretching behaviour. In order to control and program the tilting of the struts in the desired direction, Tang et al. recently introduced “kiri-kirigami” in which additional notches are etched into the material between the cuts<sup>121</sup>. Those notches are geometrical imperfections in the context of buckling and serve as cues to guide the tilting in the desired direction. By implementing the appropriate notch pattern, the tilting orientation of the struts could be programmed beforehand, and could be varied throughout the same kirigami sheet<sup>121</sup>. All of the abovementioned works used the kirigami technique solely for imparting greater elasticity to flat sheets. However, the out-of-plane buckling that this kirigami technique entails could also be used to efficiently create textured metamaterials from flat sheets, as was recently demonstrated by Rafsanjani and Bertoldi<sup>122</sup>. These researchers perforated thin sheets with a square tiling of orthogonal cuts with a varying orientation with respect to the loading direction. Uniaxial tensile loading results in out-of-plane buckling of the square units, and this could be made permanent

by increasing the load beyond the plastic limit of the hinges between the squares. The results are textured “metasheets” which are flat-foldable and could show similar deformation characteristics as miura-ori sheets, such as negative Gaussian curvature upon non-planar bending<sup>122</sup>.

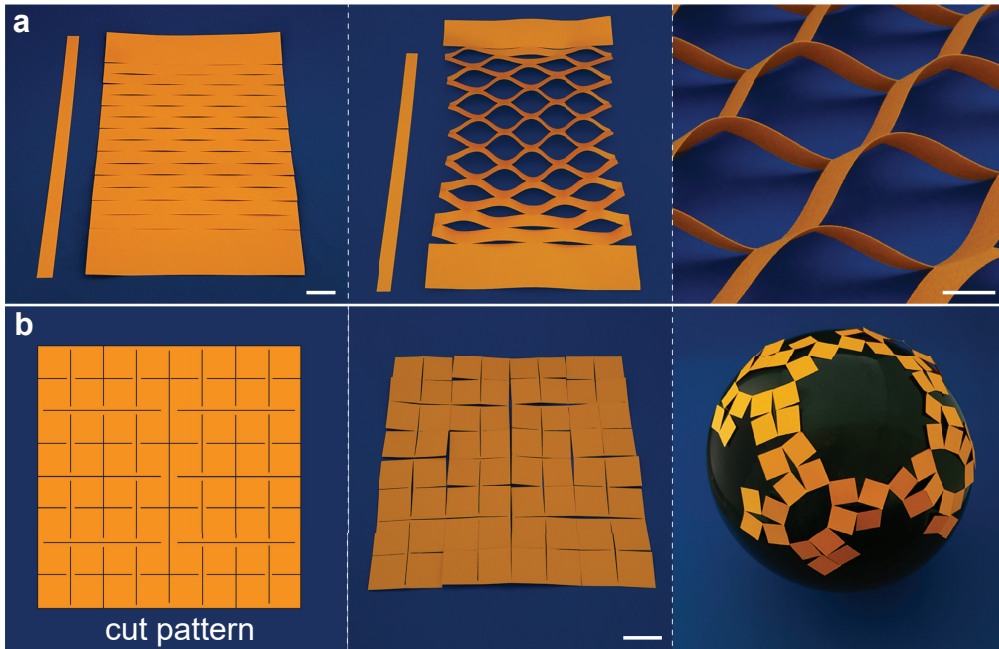


**Figure 6.12:** Kirigami-engineered elasticity. a) A parallel arrangement of slits (left) causes the small struts in between to buckle out of the plane upon tensile loading (middle), thereby providing the sheet with higher elasticity (Scale bar is 2 cm). Right: a closer view showing the struts buckling in the same direction (Scale bar is 1 cm). b) Fractal cut kirigami. Left: a three-level cut pattern with motif alternation, according to reference<sup>29</sup>. The small amount of material between adjacent cuts serves as hinge between the rigid square units. Middle: the cut pattern applied to a standard piece of paper (Scale bar is 2 cm). Right: the cut sheet of paper shows a high degree of expandability and could conform to a spherical geometry through rotation of the square units.

The second method to achieve kirigami-engineered elasticity involves in-plane rotation rather than out-of-plane buckling. In this approach, the imposed cut pattern divides the sheet into (typically square or triangular) units connected through small “hinges” (Figure 6.12b). Upon stretching the sheet, the units rotate (almost) freely around the hinges, resulting in a deformation that is driven mostly by the rigid unit rotation instead of stretching of the units themselves. Cho et al. used this principle and developed a fractal kirigami technique in which the sheet is hierarchically subdivided into ever smaller units that could rotate and contribute to the overall extension of the sheet (Figure 6.12b)<sup>29;123</sup>. While an increased level of hierarchy (*i.e.* more subdivisions) could increase the expandability, there is a limit which is dictated by the allowable rotations of the units. Cho et al. showed that the maximum expandability may be increased by alternating the cut motif between levels, allowing larger rotation angles for

the individual units<sup>29</sup>. The researchers demonstrated the fractal kirigami technique at different length scales and achieved an areal expandability of up to 800%. Furthermore, they showed that the kirigami sheets could conform to an object of non-zero Gaussian curvature (a sphere in this case) through non-uniform stretching of the pattern<sup>29</sup>, as also shown in Figure 6.12b. Further research into fractal kirigami was aimed at understanding the complex mechanics of the hinges, prone to stress concentrations, as well as the influence of material properties<sup>124</sup>. Based on experiments and numerical simulations, Tang et al. proposed dogbone-shaped cuts and hinge widths that vary with the hierarchy level in order to increase the strength and ultimate expandability of the fractal cut patterns (even when applied to brittle materials)<sup>124</sup>. Despite the impressive expandability that could be achieved with these standard cut patterns, a drawback impeding the adoption in real applications was the lack of compressibility. Therefore, Tang and Yin recently proposed to extend the standard cut pattern, consisting of only slits with actual cut-outs<sup>125</sup>. By introducing circular pores in the original square units, sheet compressibility could be obtained through buckling of the pore walls, while stretchability was still guaranteed by the straight cuts<sup>125</sup>.

Comparing the two kirigami-engineered elasticity approaches discussed above, it seems that the fractal cut method is currently more suitable to conform to intrinsically curved surfaces, as it allows biaxial stretching and compression. A drawback of both approaches is that a full coverage of the target surface cannot be achieved, as the stretching is enabled through significant “opening up” of the material. Nonetheless, both methods are expected to receive considerable attention in future research, not only in the field of stretchable electronics but also as a pathway towards mechanical metamaterials. For example, the fractal kirigami patterns are very similar to earlier work on rotation-based auxetic mechanical metamaterials<sup>126;127</sup>.

## 6.5 Discussion and conclusions

We reviewed current origami and kirigami techniques that could be used to approximate or conform to intrinsically curved surfaces. Starting off with some concepts from differential geometry, we highlighted the inherent difficulty of transforming flat sheets into intrinsically curved surfaces. Moreover, we explained the geometry of origami, which involves isometric deformations of developable surfaces and therefore retains the intrinsic flatness of the starting material. While scientific research into origami and kirigami is still in its infancy, we could nonetheless identify several promising techniques for the transformation of flat sheets into curved geometries.

### 6.5.1 Approximations of intrinsically curved surfaces

The origami and kirigami techniques that we have reviewed could essentially approximate intrinsically curved surfaces in two different ways. One approach is to use origami and kirigami to transform ordinary flat sheets into “metasheets” with significantly altered properties, which are then deformed into the desired geometry. In a second approach, the prescribed fold and cut patterns directly correspond to the final 3D

shape and no additional deformation is required after folding. The kirigami-engineered elasticity techniques<sup>29;40;109;121;124;125</sup> are examples of the first approach, while the techniques with tucking molecules<sup>56;78;85</sup> and curved-crease couplets<sup>94;95;97</sup> are examples of the second. Some techniques could be classified in both categories. For example, origami tessellations could be employed to texture sheets so that they may be deformed into an intrinsically curved geometry<sup>36;65;69;102</sup>, but (generalized) tessellations have also been calculated to fit a target surface once folded<sup>70-74</sup>. The lattice kirigami technique may be considered an example of the second approach, as the target shape is programmed into the flat sheet using appropriate cuts and folds. However, a pluriopotent version of lattice kirigami has been also proposed<sup>118</sup>, in which the same kirigami pattern could be folded to fit multiple curved surfaces.

Due to the developability constraint, no origami or kirigami technique can exactly fit a flat sheet onto an intrinsically curved smooth surface. Such surfaces could be approximated in a “global” sense, but locally the folded sheets remain intrinsically flat. Some techniques, such as lattice kirigami<sup>59;118;119</sup> or the origamizing technique<sup>56;85</sup> do imbue the sheets with Gaussian curvature, but this curvature remains concentrated in single points surrounded by developable patches, *i.e.* “non-Euclidean vertices”<sup>10</sup>. Even when a sheet of paper is crumpled, the majority of the paper remains developable and non-zero Gaussian curvature only arises at specific points due to local stretching of the paper<sup>52;128</sup>. However, owing to the different underlying mechanisms, some techniques will result in a “smoother” approximation of the target surface than others. This is an important factor to consider in applications where the surface topography plays a role, *e.g.* in fluid flow over an object. Surfaces approximated using origami tessellations or periodic pleating exhibit a textured surface topography. For the periodic pleating technique, this texture is in the form of sharp, parallel ridges. In the case of origami tessellations, the texture is determined by the specific unit cell geometry, with the square waterbomb or Ron Resch patterns resulting in a smoother surface than the Miura-ori pattern, for example. The axisymmetric geometries created by the curved-crease couplets could result in a relatively smooth surface due to the bent faces, although the frustration between the curved and straight creases might entail additional creases that disturb this smoothness. The smoothest approximation of the target surface is likely obtained with the origamizing technique, as the calculated crease pattern (almost) exactly folds into a polygon mesh of this surface. Naturally, a finer mesh results in a smoother representation, yet also entails a more complex folding process. The lattice kirigami technique results in a stepped surface approximation, consisting of many small units that simulate the convex and concave curvatures of the sheet. Interestingly, both the origamizing and lattice kirigami techniques bear strong similarities with computer graphics techniques used to represent 3D objects, either using polygonization of the surface or by means of a “voxel” (volume pixel) representation. Finally, the fractal kirigami technique allows conforming initially flat sheets, made from relatively rigid materials, to surfaces of non-zero Gaussian curvature through non-uniform opening of the cut pattern<sup>29</sup>. However, it was also mentioned that this opening of the perforations inhibits a full coverage of

the target surface, which might be a drawback in certain applications.

### 6.5.2 Practical considerations

There are several practical challenges that need to be overcome in order to accelerate the adoption of origami and kirigami as a shape-shifting technique for development of advanced materials. First and foremost is the challenge of the folding itself, which is a labour intensive manual process in traditional origami. Although all the macroscale paper models that we have presented in this review could be folded by hand, such manual folding becomes increasingly complex at much smaller or much larger scales and for more advanced materials<sup>14;129</sup>. As a consequence, self-folding (*i.e.* “hands-free”<sup>11</sup>) techniques are required. A wide range of such techniques have been developed during recent years, in particular aimed at smaller length scales<sup>9–11;13–15;16;101;130–137</sup>. While these techniques, for example, differ in terms of materials used, speed, actuation method, and suitable length scales, the underlying principle is typically the same: the self-folding behavior is programmed into the flat starting materials, most often in the form of “active hinges” which are triggered by an external stimulus to activate folding. In many cases, stimuli-responsive polymeric materials have been employed for this purpose. Examples are hydrogels that swell or de-swell upon a change in aqueous environment<sup>11;136;137</sup>, or shape memory polymers (SMP) that shrink when heated above the glass transition temperature<sup>9;101;132–135</sup>. Especially the use of thermally-responsive SMP for self-folding has attracted the interest of many researchers due to its simplicity and versatility in terms of actuation method<sup>133</sup>, for example via uniform oven heating<sup>118;132</sup>, localized joule heating<sup>9</sup> or localized heating by light or microwave absorption<sup>133;134</sup>. The shape memory effect is not exclusive to polymers but is also present in certain metallic alloys (giving rise to shape memory alloys (SMA)), making these materials also suitable for thermally activated self-folding origami<sup>130</sup>. In addition to these more common techniques, many other actuation methods for self-folding have been developed such as the folding of rigid panels driven by surface tension<sup>138–140</sup> or cell traction forces<sup>141</sup> to create nano- and microscale origami, and mechanically driven origami/kirigami<sup>142;143</sup> approaches in which folding is achieved through controlled buckling at specified locations. The reader interested in more detailed information on self-folding techniques and the associated materials is referred to other excellent reviews on these topics<sup>11;14;16;129;144;145</sup>.

Despite many recent developments, self-folding remains a challenging task, in part because of the need for sequential folding and control over the direction of folding and fold angles<sup>9;11;146</sup>. While many of these challenges have been addressed in recent years<sup>9;15;133;146–149</sup>, self-folding origami demonstrations have often been restricted to single folds or basic polyhedral shapes<sup>16;133–135;139</sup>, while demonstrations of more complicated patterns such as origami tessellations, are not yet so common<sup>132;148</sup>. Given these inherent complexities, it is not surprising that some of the reviewed origami and kirigami techniques are better suited for self-folding than others. Compared to straight creases, self-folding of curved crease origami is expected to be more challenging,

despite some recent demonstrations<sup>149</sup>. The facet bending, which is inherent in this type of non-rigid origami, would necessitate larger hinge actuation forces than for purely rigid origami with straight creases. Moreover, the possibility of arriving at a “locked” state during folding may further complicate the automated folding of curved crease origami<sup>90</sup>. Comparing the tucking molecules origami technique and the lattice kirigami technique, it has been argued that the latter is more applicable to self-folding<sup>59;118;119</sup>. The tucking molecules approach requires excessive material to be tucked away behind the outer surface, which is a cumbersome process involving many small (crimp) folds and high folding angles. This is in sharp contrast with the lattice kirigami technique, where no excessive material needs to be tucked away and a simple, repetitive folding pattern is used<sup>118</sup>. Indeed, self-folding of basic lattice kirigami units (millimeter and centimeter scale) has been recently demonstrated using localized heating<sup>149</sup> or controlled compressive buckling<sup>142;150</sup>, but more complex 3D geometries have not yet been reported. Regarding the techniques that employ the “metasheet” approach, such as the origami tessellations and the kirigami-engineered elasticity, one could argue that these are less suited for self-folding as the sheets need to be actively deformed into the desired shape. In order for these sheets to self-fold into the target geometry, local control over the fold angles or gap opening would be required. Preliminary results show that the standard kirigami cut pattern, consisting of parallel straight cuts, could be actuated using thermally activated local shrinkage<sup>121</sup>, but more investigations are needed for metasheets to automatically fit curved surfaces through remotely actuated opening or closing of folds and cuts.

In addition to the self-folding process, another practical consideration is related to locking the origami and kirigami structures in their curved folded geometries. This has, for example, been achieved by annealing titanium-rich origami structures at high temperatures<sup>151</sup>. Another approach is using sequential self-folding to include self-locking mechanisms<sup>145;152</sup>. Alternatively, the locking mechanisms might be inherent to the used origami or kirigami technique. For example, the origamizing technique with tucking molecules uses crimp folds to keep the tucks closed and maintain the desired shape on the outside surface<sup>56</sup>. On the contrary, the standard lattice kirigami cannot benefit from such excess material to lock the folds, although recent generalizations of lattice kirigami enable this to a certain extent by retaining some material for use as “fastening tabs”<sup>119</sup>.

In addition to aspects such as self-folding and locking, another prominent challenge is related to the medium to which origami and kirigami are applied. Origami and kirigami are often considered to be scale-independent processes on zero-thickness surfaces. The thin paper sheets that have traditionally been used in these art forms are not too far from zero-thickness surfaces<sup>153</sup>. However, in engineering and scientific applications, the thickness of the flat starting materials cannot be ignored, especially not for applications where the ratio of the sheet thickness to other sheet dimensions is substantial. A important consequence of finite sheet thickness is that appropriate hinge design is required to enable obstruction-free folding and flat-foldability<sup>154</sup>. In recent

years, several hinge design approaches to account for finite material thickness have been proposed for rigid-foldable origami<sup>154–156</sup>. In addition to hindering flat-foldability, the material thickness also affects the fold regions themselves, *i.e.* when the materials are actually folded and the folds are not replaced by hinges. Origami design methods typically assume perfectly sharp folds applied to the (zero-thickness) sheets, meaning that all folding is concentrated along a single line of infinitesimal width (such a sharp fold is considered to be “*G0* continuous”)<sup>129;157</sup>. While such idealized sharp folds could be approximated to some extent in a thin paper sheet, a fold in a finite thickness sheet will never be perfectly sharp but will rather be defined by some bent region with a certain radius of curvature, especially when thicker materials or materials that cannot withstand high bending strains are used<sup>129;157</sup>. Peraza et al., inspired by Tachi’s origamizing approach, recently developed an origami design method based on “smooth” folds<sup>157</sup>, which are bent surface regions of finite width. Such “smooth” folds form the connection between the rigid origami faces and are characterized by higher-order geometric continuity than the sharp folds. Smooth folds are not only relevant for folding of thicker materials but also for self-folding techniques based on “active hinges”<sup>157</sup>. Swelling or shrinking at these hinge locations also results in finite regions of bending rather than perfectly sharp folds<sup>158</sup>. This distinction between folds in idealized origami (zero thickness sheet) and folds in origami on real materials (non-zero thickness sheet) essentially revolves around the subtle difference between bending and folding<sup>11;153</sup>. Lauff et al. described bending (*i.e.* smooth fold) as “distributed curvature” while folding is “localized curvature”. However, Liu et al. correctly stated that an overlap between bending and folding exists, as it is difficult to draw a clear boundary between localized and distributed curvature<sup>11</sup>. Note that in this context, the term “curvature” refers to single or extrinsic curvature. Bending and folding both result in zero Gaussian (intrinsic) curvature, see Figure 6.3b<sup>153</sup>.

In light of the techniques reviewed in this chapter, origami with finite material thickness is expected to be particularly challenging in the tucking molecules approach, due to many small folds (which are considered to be sharp folds in the origamizer software) and the requirement for flat-folding to tuck away excess material. As mentioned before, improvements to the standard tucking molecules approach have been proposed to make the technique more apt to real applications with finite thickness materials<sup>78;86;157</sup>. The approach based on the curved-crease couplets is limited by the fact that very high folding angles (close to  $\pi$ ) are required, which could be difficult to realize with thicker materials. The techniques based on origami tessellations, concentric pleating and lattice kirigami are expected to be better suited for origami with finite thickness sheets, as they are generally characterized by simple fold patterns and have already been (self-)folded from materials other than paper<sup>118;148;149;154;158</sup>. Finally, the kirigami-engineered elasticity techniques do not require folding, hence they do not suffer from challenges with tight folds or flat-foldability. Nevertheless, the sheet thickness does influence the load at which out-of-plane buckling of the struts occurs (see Figure 6.12a), thereby making it also an important design parameter<sup>40;121</sup>.

Besides the thickness, another aspect that is often neglected in “idealized” origami is the mechanical properties of the material, which may also hinder practical application of the origami and kirigami techniques<sup>158</sup>. For example, permanently folding a finite thickness sheet entails a complex stress state involving plasticity and some degrees of stretching, aspects which are strongly linked to the mechanical properties of the sheet<sup>52;100</sup>. Furthermore, non-rigid origami also involves facet bending<sup>87</sup> which is strongly tied to the bending stiffness of the sheets that are used. As for the kirigami-engineered elasticity techniques, it has been already mentioned that these techniques are characterized by high stress concentrations, both for the out-of-plane buckling and in-plane rotation approaches<sup>29;40;121;124</sup>. Consequently, implementation of these techniques to real materials will require certain levels of understanding regarding the local material behavior under these high stress states<sup>124</sup>. Some techniques might therefore be more suitable than others for a given application depending on the chosen material.

As is clear from the preceding discussion, scientific and engineering origami/kirigami are not purely “scale-independent” processes that could be treated solely from a geometrical perspective. For example, self-folding techniques that are suitable for micro-scale origami are not necessarily suitable for architectural-scale origami (*e.g.* surface tension or cell traction forces). As a final remark, we note that traditional paper seems to remain an excellent medium for origami and kirigami, considering its balance of relative thickness, bending and tearing resistance, and the ability to withstand relatively sharp creases. However, this does not necessarily mean that other materials (on different scales) are less well suited, as these materials might behave very similarly to paper when used for origami or kirigami<sup>109</sup>.

### 6.5.3 Outlook

Approximating intrinsically curved surfaces using origami and kirigami is relevant for many applications that can benefit from the specific advantages offered by these techniques: the ability to obtain complex geometries from (nearly) non-stretchable flat sheets and the ability to apply this on virtually any length scale. As such, the folding-and-cutting paradigm could enable the development of flexible electronics<sup>29;39</sup>, shape-morphing materials<sup>118</sup>, nano- and microscale devices<sup>14;159</sup>, architectural structures<sup>81;155</sup>, or any other complex geometry involving intrinsic curvature. The applications of origami and kirigami are not limited to static designs, but could also be of a more dynamic nature. In fact, certain fold patterns involving facet bending or curved creases may form energetic barriers between different folding states, giving rise to bi-stability and fast snapping motions that could be leveraged for switchable or tunable devices<sup>99;160</sup>.

Interesting opportunities for origami and kirigami may be also found in the rapidly expanding field of biomedical engineering<sup>38</sup>, with such examples as patterned micro-containers for controlled drug delivery<sup>31</sup>, origami stent grafts<sup>32</sup>, or self-folding tetherless micro-grippers<sup>161</sup>. A particularly interesting bio-application is the folding of 3D tissue scaffolds from flat sheets enriched with cell-regulating surface topographies.

Self-folding of patterned scaffolds with simple geometries has already been demonstrated<sup>162</sup>, but more complex curved geometries would be needed in order to better stimulate and guide tissue regeneration<sup>163</sup>. For example, it has been hypothesized that promising bone-mimicking scaffolds could be based on triply periodic minimal surfaces (TPMS)<sup>164;165</sup>. These are area-minimizing 3D surfaces with zero mean curvature ( $H$ ) everywhere, corresponding to negative (or zero) Gaussian curvature everywhere ( $H = 1/2(\kappa_1 + \kappa_2) = 0$  and thus  $\kappa_1 = -\kappa_2$ )<sup>41</sup>. These intrinsically curved minimal surfaces are ubiquitous in biological systems<sup>166–169</sup> and are nature's best attempt at dealing with the frustration of embedding constant negatively curved surfaces in Euclidean 3-space (Hilbert's theorem)<sup>170;171</sup>. Current TPMS scaffolds are created with additive manufacturing<sup>4;165</sup>, meaning that the surface topographies needed to enhance tissue regeneration cannot be included. However, the origami and kirigami techniques we have reviewed here might enable just that: transforming patterned flat sheets into intrinsically curved scaffolds through appropriate cutting and folding.

In conclusion, we have reviewed recent work on origami and kirigami to identify the techniques that enable shape shifting of flat sheets into complex geometries. By introducing aspects from differential geometry, in particular the Gaussian curvature, we have illustrated the fundamental difference between flat sheets and intrinsically curved surfaces, which can explain gift-wrapping of spheres to wavy edges in plant leaves. While in-plane distortions could imbue the flat sheets with intrinsic curvature, we have shown that origami and kirigami offer alternative approaches to approximate curved surfaces with (almost) no stretching of the underlying material. Despite originating from centuries-old art forms, the techniques we have reviewed here are promising for many applications across a broad range of length scales. It could therefore be expected that the relatively recent interest in “scientific” origami and kirigami will only keep on growing in the near future.

## Bibliography

- [1] A. A. Zadpoor and J. Malda. Additive manufacturing of biomaterials, tissues, and organs. *Ann Biomed Eng*, 45(1):1–11, 2017.
- [2] M. Kadic, T. Bückmann, N. Stenger, M. Thiel, and M. Wegener. On the practicability of pentamode mechanical metamaterials. *Applied Physics Letters*, 100(19):191901, 2012.
- [3] R. Hedayati, A. M. Leeflang, and A. A. Zadpoor. Additively manufactured metallic pentamode meta-materials. *Applied Physics Letters*, 110(9):091905, 2017.
- [4] F. S. L. Bobbert, K. Lietaert, A. A. Eftekhari, B. Pouran, S. M. Ahmadi, H. Weinans, and A. A. Zadpoor. Additively manufactured metallic porous biomaterials based on minimal surfaces: A unique combination of topological, mechanical, and mass transport properties. *Acta Biomater*, 53:572–584, 2017.
- [5] E. B. Duoss, T. H. Weisgraber, K. Hearon, C. Zhu, W. Small, T. R. Metz, J. J. Vericella, H. D. Barth, J. D. Kuntz, R. S. Maxwell, C. M. Spadaccini, and T. S. Wilson. Three-dimensional printing of elastomeric, cellular architectures with negative stiffness. *Advanced Functional Materials*, 24(31):4905–4913, 2014.
- [6] T. Jiang, Z. Guo, and W. Liu. Biomimetic superoleophobic surfaces: focusing on their fabrication and applications. *J. Mater. Chem. A*, 3(5):1811–1827, 2015.
- [7] O. Y. Loh and H. D. Espinosa. Nanoelectromechanical contact switches. *Nature Nanotechnology*, 7(5):283–95, 2012.

- [8] S. Dobbenga, L. E. Fratila-Apachitei, and A. A. Zadpoor. Nanopattern-induced osteogenic differentiation of stem cells - a systematic review. *Acta Biomater*, 46:3–14, 2016.
- [9] S. M. Felton, M. T. Tolley, B. Shin, C. D. Onal, E. D. Demaine, D. Rus, and R. J. Wood. Self-folding with shape memory composites. *Soft Matter*, 9(32):7688–7694, 2013.
- [10] C. D. Santangelo. Extreme mechanics: Self-folding origami. *Annual Review of Condensed Matter Physics*, 8(1), 2016.
- [11] Y. Liu, J. Genzer, and M. D. Dickey. “2D or not 2D”: Shape-programming polymer sheets. *Progress in Polymer Science*, 52:79–106, 2016.
- [12] R. Guseinov, E. Miguel, and B. Bickel. Curveups: shaping objects from flat plates with tension-actuated curvature. *ACM Trans. Graph.*, 36(4):1–12, 2017.
- [13] A. M. Hubbard, R. W. Mailen, M. A. Zikry, M. D. Dickey, and J. Genzer. Controllable curvature from planar polymer sheets in response to light. *Soft Matter*, 13(12):2299–2308, 2017.
- [14] J. Rogers, Y. Huang, O. G. Schmidt, and D. H. Gracias. Origami mems and nems. *MRS Bulletin*, 41(02):123–129, 2016.
- [15] N. Bassik, G. M. Stern, and D. H. Gracias. Microassembly based on hands free origami with bidirectional curvature. *Appl Phys Lett*, 95(9):91901, 2009.
- [16] T. G. Leong, A. M. Zarafshar, and D. H. Gracias. Three-dimensional fabrication at small size scales. *Small*, 6(7):792–806, 2010.
- [17] M. Li, Z. Cai, Z. Sui, and Q. Yan. Multi-point forming technology for sheet metal. *Journal of Materials Processing Technology*, 129:333–338, 2002.
- [18] T. Gutowski, D. Hoult, G. Dillon, and J. Gonzalez-Zugasti. Differential geometry and the forming of aligned fibre composites. *Composites Manufacturing*, 2:147–152, 1991.
- [19] Y. Klein, E. Efrati, and E. Sharon. Shaping of elastic sheets by prescription of non-euclidean metrics. *Science*, 315(5815):1116–1120, 2007.
- [20] A. S. Gladman, E. A. Matsumoto, R. G. Nuzzo, L. Mahadevan, and J. A. Lewis. Biomimetic 4D printing. *Nat Mater*, 15(4):413–8, 2016.
- [21] J. Kim, J. A. Hanna, M. Byun, C. D. Santangelo, and R. C. Hayward. Designing responsive buckled surfaces by halftone gel lithography. *Science*, 335(6073):1201–1205, 2012.
- [22] E. Sharon, M. Marder, and H. L. Swinney. Leaves flowers and garbage bags making waves. *American Scientist*, 92:254–261, 2004.
- [23] E. Sharon, B. Roman, M. Marder, G.-S. Shin, and H. L. Swinney. Buckling cascades in free sheets. *Nature*, 419:579, 2002.
- [24] H. Liang and L. Mahadevan. Growth, geometry, and mechanics of a blooming lily. *Proc Natl Acad Sci U S A*, 108(14):5516–21, 2011.
- [25] S. A. Zirbel, R. J. Lang, M. W. Thomson, D. A. Sigel, P. E. Walkemeyer, B. P. Trease, S. P. Magleby, and L. L. Howell. Accommodating thickness in origami-based deployable arrays. *Journal of Mechanical Design*, 135(11):111005, 2013.
- [26] J. T. Overvelde, J. C. Weaver, C. Hoberman, and K. Bertoldi. Rational design of reconfigurable prismatic architected materials. *Nature*, 541(7637):347–352, 2017.
- [27] E. T. Filipov, T. Tachi, and G. H. Paulino. Origami tubes assembled into stiff, yet reconfigurable structures and metamaterials. *Proc Natl Acad Sci U S A*, 112(40):12321–6, 2015.
- [28] M. Eidini and G. H. Paulino. Unraveling metamaterial properties in zigzag-base folded sheets. *Science Advances*, 1(8), 2015.
- [29] Y. Cho, J.-H. Shin, A. Costa, T. A. Kim, V. Kunin, J. Li, S. Y. Lee, S. Yang, H. N. Han, I.-S. Choi, and D. J. Srolovitz. Engineering the shape and structure of materials by fractal cut. *Proceedings of the National Academy of Sciences of the United States of America*, 111(49):17390–17395, 2014.
- [30] S. Felton, M. Tolley, E. Demaine, D. Rus, and R. Wood. A method for building self-folding machines. *Science*, 345(6197):644–646, 2014.
- [31] C. L. Randall, T. G. Leong, N. Bassik, and D. H. Gracias. 3D lithographically fabricated nanoliter containers for drug delivery. *Adv Drug Deliv Rev*, 59(15):1547–61, 2007.
- [32] K. Kuribayashi, K. Tsuchiya, Z. You, D. Tomus, M. Umemoto, T. Ito, and M. Sasaki. Self-deployable origami stent grafts as a biomedical application of ni-rich tini shape memory alloy foil. *Materials*

- Science and Engineering A*, 419(1-2):131–137, 2006.
- [33] R. J. Lang. The science of origami. *Physics world*, 20(2):30, 2007.
- [34] K. Miura. Method of packaging and deployment of large membranes in space. *The Institute of Space and Astronautical Science Report*, 618:1–9, 1985.
- [35] S. D. Guest and S. Pellegrino. Inextensional wrapping of flat membranes. In R. Motro and T. Wester, editors, *First Int. Sem. on Struct. Morph.*, pages 203–215.
- [36] M. Schenk and S. D. Guest. Geometry of miura-folded metamaterials. *Proceedings of the National Academy of Sciences of the United States of America*, 110(9):3276–3281, 2013.
- [37] J. L. Silverberg, A. A. Evans, L. McLeod, R. C. Hayward, T. Hull, C. D. Santangelo, and I. Cohen. Using origami design principles to fold reprogrammable mechanical metamaterials. *Science*, 345(6197):647–650, 2014.
- [38] C. L. Randall, E. Gultepe, and D. H. Gracias. Self-folding devices and materials for biomedical applications. *Trends Biotechnol.*, 30(3):138–46, 2012.
- [39] Z. Song, X. Wang, C. Lv, Y. An, M. Liang, T. Ma, D. He, Y. J. Zheng, S. Q. Huang, H. Yu, and H. Jiang. Kirigami-based stretchable lithium-ion batteries. *Scientific Reports*, 5:10988, 2015.
- [40] T. C. Shyu, P. F. Damasceno, P. M. Dodd, A. Lamoureux, L. Xu, M. Shlian, M. Shtein, S. C. Glotzer, and N. A. Kotov. A kirigami approach to engineering elasticity in nanocomposites through patterned defects. *Nat Mater*, 14(8):785–9, 2015.
- [41] D. Hilbert and S. Cohn-Vossen. *Geometry and The Imagination*. Chelsea Publishing Company, New York, USA, 1990.
- [42] V. Toponogov and V. Rovenski. *Differential Geometry of Curves and Surfaces: A Concise Guide*. Birkhäuser Boston, New York, NY, USA, 2005.
- [43] V. Rovenski. *Modeling of Curves and Surfaces with MATLAB*. Springer Science & Business Media, New York, NY, USA, 2010.
- [44] M. Spivak. *A Comprehensive Introduction to Differential Geometry, Vol. II*. Publish or Perish, inc., Houston, Texas, USA, 1990.
- [45] J. R. Weeks. *The shape of space*. CRC press, Boca Raton, FL, USA, 2001.
- [46] E. Sharon and E. Efrati. The mechanics of non-euclidean plates. *Soft Matter*, 6(22):5693–5704, 2010.
- [47] M. Marder, R. D. Deegan, and E. Sharon. Crumpling, buckling, and cracking: Elasticity of thin sheets. *Physics Today*, 60(2):33–38, 2007.
- [48] R. D. Kamien. Better geometry through chemistry. *Science*, 315:1083–1084, 2007.
- [49] A. N. Pressley. *Elementary differential geometry*. Springer Science & Business Media, Dordrecht, The Netherlands, 2010.
- [50] E. Efrati, Y. Klein, H. Aharoni, and E. Sharon. Spontaneous buckling of elastic sheets with a prescribed non-euclidean metric. *Physica D: Nonlinear Phenomena*, 235(1-2):29–32, 2007.
- [51] H. Aharoni, E. Sharon, and R. Kupferman. Geometry of thin nematic elastomer sheets. *Phys Rev Lett*, 113(25):257801, 2014.
- [52] T. A. Witten. Stress focusing in elastic sheets. *Reviews of Modern Physics*, 79(2):643–675, 2007.
- [53] E. Efrati, E. Sharon, and R. Kupferman. Elastic theory of unconstrained non-euclidean plates. *Journal of the Mechanics and Physics of Solids*, 57(4):762–775, 2009.
- [54] E. Demaine and M. Demaine. *Recent Results in Computational Origami*, pages 3–16. A K Peters/CRC Press, Boca Raton, FL, USA, 2002.
- [55] E. D. Demaine, M. L. Demaine, and J. S. B. Mitchell. Folding flat silhouettes and wrapping polyhedral packages: New results in computational origami. *Computational Geometry: Theory and Applications*, 16(1):3–21, 2000.
- [56] T. Tachi. Origamizing polyhedral surfaces. *IEEE Transactions on Visualization and Computer Graphics*, 16(2):298–311, 2010.
- [57] Z. Abel, J. Cantarella, E. D. Demaine, D. Eppstein, T. Hull, J. Ku, R. J. Lang, and T. Tachi. Rigid origami vertices conditions and forcing sets. *Journal of Computational Geometry*, 7:171–184, 2016.
- [58] T. A. Evans, R. J. Lang, S. P. Magleby, and L. L. Howell. Rigidly foldable origami gadgets and tessellations. *Royal Society Open Science*, 2(9):150067, 2015.

- [59] T. Castle, Y. Cho, X. Gong, E. Jung, D. M. Sussman, S. Yang, and R. D. Kamien. Making the cut: lattice kirigami rules. *Phys Rev Lett*, 113(24):245502, 2014.
- [60] K. Miura. A note on intrinsic geometry of origami. In H. Huzita, editor, *First Int. Meeting of Origami Science and Technology*, pages 239–249.
- [61] D. A. Huffman. Curvature and creases: A primer on paper. *IEEE Transactions on Computers*, C-25(10):1010–1019, 1976.
- [62] T. Hull. *Project origami: activities for exploring mathematics*. CRC Press, Boca Raton, FL, USA, 2 edition, 2012.
- [63] C. R. Calladine. *Theory of Shell Structures*. Cambridge University Press, Cambridge, UK, 1983.
- [64] E. Gjerde. *Origami Tessellations: Awe-Inspiring Geometric Designs*. A K Peters/CRC Press, Boca Raton, FL, USA, 2008.
- [65] K. A. Seffen. Compliant shell mechanisms. *Philos Trans A Math Phys Eng Sci*, 370(1965):2010–26, 2012.
- [66] A. A. Evans, J. L. Silverberg, and C. D. Santangelo. Lattice mechanics of origami tessellations. *Physical Review E: Statistical, Nonlinear, Biological, and Soft Matter Physics*, 92(1):013205, 2015.
- [67] L. Mahadevan and S. Rica. Self-organized origami. *Science*, 307, 2005.
- [68] C. Lv, D. Krishnaraju, G. Konjevod, H. Yu, and H. Jiang. Origami based mechanical metamaterials. *Scientific Reports*, 4:5979, 2014.
- [69] M. Schenk and S. D. Guest. *Origami folding: A structural engineering approach*, pages 291–304. A K Peters/CRC Press, Boca Raton, FL, 2011.
- [70] T. Tachi. Generalization of rigid foldable quadrilateral mesh origami. *Journal of the International Association for Shell and Spatial Structures*, 50(3):173–179, 2009.
- [71] J. M. Gattas, W. Wu, and Z. You. Miura-base rigid origami: Parameterizations of first-level derivative and piecewise geometries. *Journal of Mechanical Design*, 135(11):1110111–11101111, 2013.
- [72] P. Sareh and S. D. Guest. A framework for the symmetric generalisation of the miura-ori. *International Journal of Space Structures*, 30(2):141–152, 2015.
- [73] F. Wang, H. Gong, X. Chen, and C. Q. Chen. Folding to curved surfaces: A generalized design method and mechanics of origami-based cylindrical structures. *Scientific Reports*, 6:33312, 2016.
- [74] L. H. Dudte, E. Vouga, T. Tachi, and L. Mahadevan. Programming curvature using origami tessellations. *Nat Mater*, 15(5):583–8, 2016.
- [75] Y. Chen, H. Feng, J. Ma, R. Peng, and Z. You. Symmetric waterbomb origami. *Proceedings of the Royal Society A: Mathematical, Physical and Engineering Science*, 472(2190):20150846, 2016.
- [76] R. Resch. The topological design of sculptural and architectural systems. In *Nat. Comp. Conf. and Exp.*, pages 643–650. ACM.
- [77] R. Resch and H. Christiansen. The design and analysis of kinematic folded plate systems. In *IASS Symp. on Folded Plates and Prism. Struct.*
- [78] T. Tachi. Designing freeform origami tessellations by generalizing reschs patterns. *Journal of Mechanical Design*, 135:111006, 2013.
- [79] T. Tachi. *Rigid folding of periodic origami tessellations*. American Mathematical Society, Providence, RI, USA, 2016.
- [80] H. Nassar, A. Lebee, and L. Monasse. Curvature, metric and parametrization of origami tessellations: theory and application to the eggbox pattern. *Proceedings of the Royal Society A: Mathematical, Physical and Engineering Science*, 473(2197):20160705, 2017.
- [81] T. Tachi. Freeform variations of origami. *Journal for Geometry and Graphics*, 14(2):203–215, 2010.
- [82] X. Zhou, H. Wang, and Z. You. Design of three-dimensional origami structures based on a vertex approach. *Proceedings of the Royal Society A: Mathematical, Physical and Engineering Science*, 471(2181):20150407, 2015.
- [83] K. Song, X. Zhou, S. Zang, H. Wang, and Z. You. Design of rigid-foldable doubly curved origami tessellations based on trapezoidal crease patterns. *Proceedings of the Royal Society A: Mathematical, Physical and Engineering Science*, 473(2200):20170016, 2017.
- [84] R. J. Lang. A computational algorithm for origami design. In *Twelfth Ann. Symp. on Comput. Geom.*
- [85] T. Tachi. *3D Origami Design Based on Tucking Molecules*, pages 259–272. A K Peters/CRC Press,

- Boca Raton, FL, USA, 2009.
- [86] E. Demaine and T. Tachi. Origamizer: A practical algorithm for folding any polyhedron. In B. Aronov and M. J. Katz, editors, *33rd Int. Symp. on Comput. Geom. (SoCG 2017)*. Schloss Dagstuhl–Leibniz-Zentrum fuer Informatik.
- [87] E. D. Demaine, M. L. Demaine, D. Koschitz, and T. Tachi. A review on curved creases in art design and mathematics. *Symmetry: Culture and Science*, 26(2):145–161, 2015.
- [88] J. P. Duncan and J. L. Duncan. Folded developables. *Proceedings of the Royal Society A: Mathematical, Physical and Engineering Science*, 383(1784):191–205, 1982.
- [89] R. Geretschläger. *Folding Curves*, pages 151–163. A K Peters/CRC Press, Boca Raton, FL, USA, 2009.
- [90] M. Kilian, A. Monszpart, and N. J. Mitra. String actuated curved folded surfaces. *ACM Transactions on Graphics*, 36(3):1–13, 2017.
- [91] D. Fuchs and S. Tabachnikov. More on paperfolding. *The American Mathematical Monthly*, 106:27–35, 1999.
- [92] M. Kilian, S. Floery, Z. Chen, N. Mitra, A. Scheffer, and H. Pottmann. Curved folding. *ACM Transactions on Graphics*, 27:75, 2008.
- [93] A. Vergauwen, L. D. Laet, and N. D. Temmerman. Computational modelling methods for pliable structures based on curved-line folding. *Computer-Aided Design*, 83:51–63, 2017.
- [94] J. Mitani. A design method for 3D origami based on rotational sweep. *Computer-Aided Design and Applications*, 6(1):69–79, 2009.
- [95] C. Leong. *Simulation of Nonzero Gaussian Curvature in Origami by Curved Crease Couplets*, pages 151–163. A.K. Peters/CRC Press, Boca Raton, FL, USA, 2009.
- [96] R. Lang. *Origami Design Secrets: Mathematical Methods for an Ancient Art*. A K Peters/CRC Press, Boca Raton, FL, USA, 2nd edition, 2011.
- [97] J. Mitani. *A Design Method for Axisymmetric Curved Origami with Triangular Prism Protrusions*, pages 437–447. A K Peters/CRC Press, Boca Raton, FL, 2011.
- [98] E. D. Demaine, M. L. Demaine, D. A. Huffman, D. Koschitz, and T. Tachi. *Characterization of curved creases and rulings design and analysis of lens tessellations*, pages 209–230. American Mathematical Society, Providence, RI, USA, 2016.
- [99] N. P. Bende, A. A. Evans, S. Innes-Gold, L. A. Marin, I. Cohen, R. C. Hayward, and C. D. Santangelo. Geometrically controlled snapping transitions in shells with curved creases. *Proc Natl Acad Sci U S A*, 112(36):11175–80, 2015.
- [100] E. D. Demaine, M. L. Demaine, V. Hart, G. N. Price, and T. Tachi. (non)existence of pleated folds: How paper folds between creases. *Graphs and Combinatorics*, 27(3):377–397, 2011.
- [101] T. van Manen, S. Janbaz, and A. A. Zadpoor. Programming 2D/3D shape-shifting with hobbyist 3D printers. *Materials Horizons*, 4(6), 2017.
- [102] M. Schenk. *Folded Shell Structures*. Phd thesis, 2011.
- [103] T. Tachi. *Simulation of rigid origami*. A K Peters/CRC Press, Boca Raton, FL, USA, 2009.
- [104] Z. Y. Wei, Z. V. Guo, L. Dudte, H. Y. Liang, and L. Mahadevan. Geometric mechanics of periodic pleated origami. *Phys Rev Lett*, 110(21):215501, 2013.
- [105] P. O. Mouthuy, M. Coulombier, T. Pardoën, J. P. Raskin, and A. M. Jonas. Overcurvature describes the buckling and folding of rings from curved origami to foldable tents. *Nature Communications*, 3:1290, 2012.
- [106] M. A. Dias, L. H. Dudte, L. Mahadevan, and C. D. Santangelo. Geometric mechanics of curved crease origami. *Phys Rev Lett*, 109(11):114301, 2012.
- [107] M. A. Dias and C. D. Santangelo. The shape and mechanics of curved-fold origami structures. *EPL (Europhysics Letters)*, 100(5):54005, 2012.
- [108] E. D. Demaine, M. L. Demaine, and A. Lubiw. Polyhedral sculptures with hyperbolic paraboloids. In *2nd Ann. Conf. of BRIDGES: Mathematical Connections in Art, Music, and Science*.
- [109] M. K. Bles, A. W. Barnard, P. A. Rose, S. P. Roberts, K. L. McGill, P. Y. Huang, A. R. Ruyack, J. W. Kevek, B. Kobrin, D. A. Muller, and P. L. McEuen. Graphene kirigami. *Nature*, 524(7564):204–207, 2015.

- [110] A. Lamoureux, K. Lee, M. Shlian, S. R. Forrest, and M. Shtein. Dynamic kirigami structures for integrated solar tracking. *Nat Commun*, 6:8092, 2015.
- [111] R. M. Neville, F. Scarpa, and A. Pirrera. Shape morphing kirigami mechanical metamaterials. *Scientific Reports*, 6:31067, 2016.
- [112] K. Saito, F. Agnese, and F. Scarpa. A cellular kirigami morphing wingbox concept. *Journal of Intelligent Material Systems and Structures*, 22(9):935–944, 2011.
- [113] S. Del Broccolo, S. Laurenzi, and F. Scarpa. Auxhex – a kirigami inspired zero poisson’s ratio cellular structure. *Composite Structures*, 176:433–441, 2017.
- [114] A. G. Martin. A basketmaker’s approach to structural morphology. In *Int. Assoc. Shell Spatial Struct. (IASS) Symp.*
- [115] W. T. Irvine, V. Vitelli, and P. M. Chaikin. Pleats in crystals on curved surfaces. *Nature*, 468(7326):947–51, 2010.
- [116] J. F. Sadoc, N. Rivier, and J. Charvolin. Phyllotaxis: a non-conventional crystalline solution to packing efficiency in situations with radial symmetry. *Acta Crystallographica Section A: Foundations of Crystallography*, 68(4):470–483, 2012.
- [117] J. Charvolin and J.-F. Sadoc. A phyllotactic approach to the structure of collagen fibrils. *Biophysical Reviews and Letters*, 06(01n02):13–27, 2011.
- [118] D. M. Sussman, Y. Cho, T. Castle, X. Gong, E. Jung, S. Yang, and R. D. Kamien. Algorithmic lattice kirigami: A route to pluripotent materials. *Proc Natl Acad Sci U S A*, 112(24):7449–53, 2015.
- [119] T. Castle, D. M. Sussman, M. Tanis, and R. D. Kamien. Additive lattice kirigami. *Science Advances*, 2(9):e1601258, 2016.
- [120] F. Wang, X. Guo, J. Xu, Y. Zhang, and C. Q. Chen. Patterning curved three-dimensional structures with programmable kirigami designs. *Journal of Applied Mechanics*, 84(6):061007, 2017.
- [121] Y. Tang, G. Lin, S. Yang, Y. K. Yi, R. D. Kamien, and J. Yin. Programmable kiri-kirigami metamaterials. *Advanced Materials*, 29(10):1604262, 2016.
- [122] A. Rafsanjani and K. Bertoldi. Buckling-induced kirigami. *Phys Rev Lett*, 118(8):084301, 2017.
- [123] S. Yang, I.-S. Choi, and R. D. Kamien. Design of super-conformable, foldable materials via fractal cuts and lattice kirigami. *MRS Bulletin*, 41(02):130–138, 2016.
- [124] Y. Tang, G. Lin, L. Han, S. Qiu, S. Yang, and J. Yin. Design of hierarchically cut hinges for highly stretchable and reconfigurable metamaterials with enhanced strength. *Adv Mater*, 27(44):7181–90, 2015.
- [125] Y. Tang and J. Yin. Design of cut unit geometry in hierarchical kirigami-based auxetic metamaterials for high stretchability and compressibility. *Extreme Mechanics Letters*, 12:77–85, 2017.
- [126] R. Gatt, L. Mizzi, J. I. Azzopardi, K. M. Azzopardi, D. Attard, A. Casha, J. Briffa, and J. N. Grima. Hierarchical auxetic mechanical metamaterials. *Sci Rep*, 5:8395, 2015.
- [127] H. M. A. Kolken and A. A. Zadpoor. Auxetic mechanical metamaterials. *RSC Advances*, 7(9):5111–5129, 2017.
- [128] M. Ben Amar and Y. Pomeau. Crumpled paper. *Proceedings of the Royal Society A: Mathematical, Physical and Engineering Science*, 453(1959):729–755, 1997.
- [129] E. A. Peraza-Hernandez, D. J. Hartl, R. J. Malak Jr., and D. C. Lagoudas. Origami-inspired active structures: a synthesis and review. *Smart Materials and Structures*, 23(9):094001, 2014.
- [130] E. Hawkes, B. An, N. M. Benbernou, H. Tanaka, S. Kim, E. D. Demaine, D. Rus, and R. J. Wood. Programmable matter by folding. *Proc Natl Acad Sci U S A*, 107(28):12441–5, 2010.
- [131] S. Janbaz, R. Hedayati, and A. A. Zadpoor. Programming the shape-shifting of flat soft matter: from self-rolling/self-twisting materials to self-folding origami. *Materials Horizons*, 3(6):536–547, 2016.
- [132] M. T. Tolley, S. M. Felton, S. Miyashita, D. Aukes, D. Rus, and R. J. Wood. Self-folding origami: shape memory composites activated by uniform heating. *Smart Materials and Structures*, 23(9):094006, 2014.
- [133] Y. Liu, J. K. Boyles, J. Genzer, and M. D. Dickey. Self-folding of polymer sheets using local light absorption. *Soft Matter*, 8(6):1764–1769, 2012.
- [134] D. Davis, R. Mailen, J. Genzer, and M. D. Dickey. Self-folding of polymer sheets using microwaves and graphene ink. *RSC Advances*, 5(108):89254–89261, 2015.

- [135] D. Davis, B. Chen, M. D. Dickey, and J. Genzer. Self-folding of thick polymer sheets using gradients of heat. *Journal of Mechanisms and Robotics*, 8(3):031014, 2016.
- [136] J. Guan, H. He, D. J. Hansford, and L. J. Lee. Self-folding of three-dimensional hydrogel microstructures. *The Journal of Physical Chemistry B*, 109(49):23134–23137, 2005.
- [137] G. Stoychev, N. Pureskiy, and L. Ionov. Self-folding all-polymer thermoresponsive microcapsules. *Soft Matter*, 7(7):3277–3279, 2011.
- [138] B. Gimi, T. Leong, Z. Gu, M. Yang, D. Artemov, Z. M. Bhujwalla, and D. H. Gracias. Self-assembled three dimensional radio frequency (rf) shielded containers for cell encapsulation. *Biomedical microdevices*, 7(4):341–345, 2005.
- [139] A. Azam, K. E. Laffin, M. Jamal, R. Fernandes, and D. H. Gracias. Self-folding micropatterned polymeric containers. *Biomed Microdevices*, 13(1):51–8, 2011.
- [140] D. H. Gracias, V. Kavthekar, J. C. Love, K. E. Paul, and G. M. Whitesides. Fabrication of micrometer-scale, patterned polyhedra by self-assembly. *Advanced Materials*, 14(3):235, 2002.
- [141] K. Kuribayashi-Shigetomi, H. Onoe, and S. Takeuchi. Cell origami: self-folding of three-dimensional cell-laden microstructures driven by cell traction force. *PLoS One*, 7(12):e51085, 2012.
- [142] Z. Yan, F. Zhang, J. Wang, F. Liu, X. Guo, K. Nan, Q. Lin, M. Gao, D. Xiao, Y. Shi, Y. Qiu, H. Luan, J. H. Kim, Y. Wang, H. Luo, M. Han, Y. Huang, Y. Zhang, and J. A. Rogers. Controlled mechanical buckling for origami-inspired construction of 3D microstructures in advanced materials. *Adv Funct Mater*, 26(16):2629–2639, 2016.
- [143] Y. Zhang, Z. Yan, K. Nan, D. Xiao, Y. Liu, H. Luan, H. Fu, X. Wang, Q. Yang, J. Wang, W. Ren, H. Si, F. Liu, L. Yang, H. Li, J. Wang, X. Guo, H. Luo, L. Wang, Y. Huang, and J. A. Rogers. A mechanically driven form of kirigami as a route to 3D mesostructures in micro/nanomembranes. *Proc Natl Acad Sci U S A*, 112(38):11757–64, 2015.
- [144] Y. Zhang, F. Zhang, Z. Yan, Q. Ma, X. Li, Y. Huang, and J. A. Rogers. Printing, folding and assembly methods for forming 3D mesostructures in advanced materials. *Nature Reviews Materials*, 2(4):17019, 2017.
- [145] T. Van Manen, S. Janbaz, and A. A. Zadpoor. Programming the shape-shifting of flat soft matter. *Materials Today*, DOI: 10.1016/j.mattod.2017.08.026, 2017.
- [146] T. Tachi and T. C. Hull. Self-foldability of rigid origami. *Journal of Mechanisms and Robotics*, 9(2):021008–021008–9, 2017.
- [147] Y. Liu, B. Shaw, M. D. Dickey, and J. Genzer. Sequential self-folding of polymer sheets. *Science Advances*, 3(3), 2017.
- [148] J.-H. Na, A. A. Evans, J. Bae, M. C. Chiappelli, C. D. Santangelo, R. J. Lang, T. C. Hull, and R. C. Hayward. Programming reversibly self-folding origami with micropatterned photo-crosslinkable polymer trilayers. *Advanced Materials*, 27(1):79–85, 2015.
- [149] Q. Zhang, J. Wommer, C. O’Rourke, J. Teitelman, Y. Tang, J. Robison, G. Lin, and J. Yin. Origami and kirigami inspired self-folding for programming three-dimensional shape shifting of polymer sheets with light. *Extreme Mechanics Letters*, 11:111–120, 2017.
- [150] Y. Shi, F. Zhang, K. Nan, X. Wang, J. Wang, Y. Zhang, Y. Zhang, H. Luan, K.-C. Hwang, Y. Huang, J. A. Rogers, and Y. Zhang. Plasticity-induced origami for assembly of three dimensional metallic structures guided by compressive buckling. *Extreme Mechanics Letters*, 11:105–110, 2017.
- [151] B. Y. Ahn, D. Shoji, C. J. Hansen, E. Hong, D. C. Dunand, and J. A. Lewis. Printed origami structures. *Adv Mater*, 22(20):2251–4, 2010.
- [152] Y. Mao, K. Yu, M. S. Isakov, J. Wu, M. L. Dunn, and H. Jerry Qi. Sequential self-folding structures by 3D printed digital shape memory polymers. *Scientific Reports*, 5:13616, 2015.
- [153] C. Lauff, T. W. Simpson, M. Frecker, Z. Ounaies, S. Ahmed, P. von Lockette, R. Strzelec, R. Sheridan, and J.-M. Lien. Differentiating bending from folding in origami engineering using active materials. In *Proceedings of the ASME 2014 International Design Engineering Technical Conferences & Computers and Information Engineering Conference*, page V05BT08A040.
- [154] Y. Chen, R. Peng, and Z. You. Origami of thick panels. *Science*, 349(6246):396–400, 2015.
- [155] T. Tachi. *Rigid-Foldable Thick Origami*, pages 253–263. A K Peters/CRC Press, Boca Raton, FL, 2011.

- [156] R. J. Lang, T. Nelson, S. Magleby, and L. Howell. Thick rigidly foldable origami mechanisms based on synchronized offset rolling contact elements. *Journal of Mechanisms and Robotics*, 9(2):021013, 2017.
- [157] E. A. Peraza Hernandez, D. J. Hartl, and D. C. Lagoudas. Design and simulation of origami structures with smooth folds. *Proceedings of the Royal Society A: Mathematical, Physical and Engineering Science*, 473(2200):20160716, 2017.
- [158] N. An, M. Li, and J. Zhou. Predicting origami-inspired programmable self-folding of hydrogel trilayers. *Smart Materials and Structures*, 25(11):11LT02, 2016.
- [159] L. Xu, T. C. Shyu, and N. A. Kotov. Origami and kirigami nanocomposites. *ACS Nano*, 11:7587–7599, 2017.
- [160] J. L. Silverberg, J. H. Na, A. A. Evans, B. Liu, T. C. Hull, C. D. Santangelo, R. J. Lang, R. C. Hayward, and I. Cohen. Origami structures with a critical transition to bistability arising from hidden degrees of freedom. *Nat Mater*, 14(4):389–93, 2015.
- [161] T. G. Leong, C. L. Randall, B. R. Benson, N. Bassik, G. M. Stern, and D. H. Gracias. Tetherless thermobiochemically actuated microgrippers. *Proceedings of the National Academy of Sciences of the United States of America*, 106(3):703–708, 2009.
- [162] M. Jamal, N. Bassik, J. H. Cho, C. L. Randall, and D. H. Gracias. Directed growth of fibroblasts into three dimensional micropatterned geometries via self-assembling scaffolds. *Biomaterials*, 31(7):1683–90, 2010.
- [163] A. A. Zadpoor. Bone tissue regeneration: the role of scaffold geometry. *Biomaterials Science*, 3(2):231–45, 2015.
- [164] S. C. Kapfer, S. T. Hyde, K. Mecke, C. H. Arns, and G. E. Schröder-Turk. Minimal surface scaffold designs for tissue engineering. *Biomaterials*, 32(29):6875–82, 2011.
- [165] S. B. Blanquer, M. Werner, M. Hannula, S. Sharifi, G. P. Lajoinie, D. Eglin, J. Hyttinen, A. A. Poot, and D. W. Grijpma. Surface curvature in triply-periodic minimal surface architectures as a distinct design parameter in preparing advanced tissue engineering scaffolds. *Biofabrication*, 9(2):025001, 2017.
- [166] S. Hyde, Z. Blum, T. Landh, S. Lidin, B. Ninham, S. Andersson, and K. Larsson. *The Language of Shape: The Role of Curvature in Condensed Matter: Physics, Chemistry and Biology*. Elsevier Science, Amsterdam, The Netherlands, 1996.
- [167] K. Michielsen and D. G. Stavenga. Gyroid cuticular structures in butterfly wing scales: biological photonic crystals. *Journal of the Royal Society Interface*, 5(18):85–94, 2008.
- [168] J. W. Galusha, L. R. Richey, J. S. Gardner, J. N. Cha, and M. H. Bartl. Discovery of a diamond-based photonic crystal structure in beetle scales. *Phys Rev E Stat Nonlin Soft Matter Phys*, 77(5 Pt 1):050904, 2008.
- [169] H. Jinnai, Y. Nishikawa, M. Ito, S. D. Smith, D. A. Agard, and R. J. Spontak. Topological similarity of sponge-like bicontinuous morphologies differing in length scale. *Advanced Materials*, 14(22):1615–1618, 2002.
- [170] M. E. Evans and G. E. Schröder-Turk. In a material world hyperbolic geometry in biological materials. *Asia Pacific Mathematics Newsletter*, 5(2):21–30, 2015.
- [171] S. T. Hyde and G. E. Schröder-Turk. Geometry of interfaces: topological complexity in biology and materials. *Interface Focus*, 2:529–538, 2012.

# 7

## HYPERBOLIC ORIGAMI OF MINIMAL SURFACES

Origami-inspired folding methods present novel pathways to fabricate three-dimensional (3D) structures from 2D sheets. A key advantage of this approach is that planar printing and patterning processes could be used prior to folding, affording enhanced surface functionality to the folded structures. This is particularly useful for 3D lattices, possessing very large internal surface areas. While folding polyhedral strut-based lattices has already been demonstrated, more complex, curved sheet-based lattices have not yet been folded due to inherent developability constraints of conventional origami. Here, a novel folding strategy is presented to fold flat sheets into topologically complex cellular materials based on triply periodic minimal surfaces (TPMS), which are attractive geometries for many applications. The approach differs from traditional origami by employing material stretching to accommodate non-developability. Our method leverages the inherent hyperbolic symmetries of TPMS to assemble complex 3D structures from a net of self-foldable patches. We also demonstrate that attaching 3D-printed foldable frames to pre-strained elastomer sheets enables self-folding and self-guided minimal surface shape adaption upon release of the pre-strain. This approach effectively bridges the Euclidean nature of origami with the hyperbolic nature of TPMS, offering novel avenues in the 2D-to-3D fabrication paradigm and the design of architected materials with enhanced functionality.

S. J. P. Callens, N. Tümer, A. A. Zadpoor, Hyperbolic origami-inspired folding of triply periodic minimal surface structures, *Applied Materials Today*, 15, 453-461, 2019

## 7.1 Introduction

Stochastic sheet-based micro-architectures are ubiquitous in engineering and natural materials and appear in the form of foams, sponges, bone tissue, or at the interface of phase-separated materials<sup>1</sup>. Their periodic counterparts, being more tractable to study, have received widespread attention too, especially geometries based on triply periodic minimal surfaces (TPMS). Minimal surfaces are surfaces that locally minimize area and are defined to have vanishing mean curvature everywhere ( $H = 0$ ), which gives rise to their saddle-shaped appearance (with Gaussian curvature  $K \leq 0$ ). Triply periodic minimal surfaces form a special class of minimal surfaces that are bicontinuous and periodic in three directions, hence they extend infinitely and divide space into two continuous, intertwined labyrinths<sup>1</sup>. While mathematicians were the first to study TPMS following the seminal work of Schwarz<sup>2</sup>, the frequent observations of TPMS morphologies in a wide range of natural systems<sup>3</sup>, ranging from self-assembled lipids<sup>4</sup> to butterfly wing scales<sup>5</sup>, has sparked the interest of other scientists as well. Indeed, the unique structure-property relationships offered by TPMS have contributed towards development of highly efficient cellular solids. For example, TPMS-based structures have been shown to combine high yield stress, low elastic modulus, exceptionally high fatigue resistance, and bone-mimicking transport properties, making them an ideal group of bone substitutes<sup>6-8</sup>. Other examples include photonic metamaterials<sup>9</sup>, architected materials<sup>10;11</sup>, or porous membrane structures<sup>12</sup>. The functionality of lattice structures in general, and TPMS-based solids in particular, could be vastly augmented with planar surface-functionalization processes. For instance, precisely controlled surface nanopatterns could enhance the optical<sup>13</sup>, wetting<sup>14</sup>, osteogenic<sup>15</sup>, and antimicrobial<sup>16</sup> properties of surfaces, while planar printing/imprinting techniques enable integration of embedded electronics into materials<sup>17</sup>. The incorporation of surface-related functionalities is particularly attractive for TPMS structures, given their very large surface-to-volume ratios. However, most 3D lattice structures, especially those based on TPMS, can currently only be manufactured using 3D printing techniques, which are incompatible with the planar functionality-inducing processes. To circumvent this incompatibility between 3D printing and planar processes, an origami approach has recently been proposed<sup>18</sup>, where periodic beam-based lattices were shown to be foldable from a flat starting state, thereby enabling surface functionalization prior to folding. However, given the hyperbolic, *i.e.* non-developable, nature of TPMS, such conventional origami techniques are inherently ill-equipped to tackle the problem of folding TPMS morphologies from a flat state<sup>19</sup>. Therefore, we introduce a fundamentally different approach that circumvents the developability constraint and enables the folding of hyperbolic minimal surface morphologies, by leveraging sheet stretching. Due to the requirement of sheet stretching, one could describe this folding method as “origomu”, signifying the folding of stretchable rubber-like sheets (“ori” means folding, “gomu” means rubber), as opposed to origami, signifying the folding of non-stretchable paper-like materials. While computational tools and differential growth-based fabrication methods for the generation of non-developable geometries from flat surfaces have been devel-

oped in recent years<sup>20–23</sup>, these approaches typically require complicated material programming and the resulting shapes are often restricted to topological disks. The folding method that we introduce in this chapter enables the folding of topologically complex porous structures with minimal surface morphologies, while requiring very limited material programming. The rationale behind our approach consists of realizing curved minimal surface patches from a flat state, by combining rigid foldable frames with pre-stained elastomer sheets. Multiple of these foldable patches could then be connected together in a net, while respecting the inherent hyperbolic symmetries of TPMS, and used as building blocks to fold a myriad of 3D TPMS-based architectures, ranging from single unit cells to larger assemblies consisting of multiple unit cells and 3D stackable minimal surface layers.

## 7.2 Materials and methods

### 7.2.1 Patch kinematics

Our approach relies on the use of straight-edged TPMS patches (with curved faces), that can be smoothly folded/unfolded through the presence of hinges at certain patch vertices. The folding kinematics of the straight-edged TPMS patches were implemented in MATLAB (Mathworks, USA) by calculating the Cartesian coordinates of the vertices as a function of the fold angle  $\theta$ , from zero until the final folded configuration. The vertex coordinates in the folded configurations were obtained from Fisher and Koch<sup>24</sup>. By calculating the difference between the internal angle sum in the folded,  $\sum_i \alpha_i^f$ , and flat,  $\sum_i \alpha_i^s$ , configurations, the required amount of angular change for unfolding was obtained for every hinge vertex. For  $n$  hinged vertices, the angular change that needs to be accommodated for every hinge by the folding/unfolding is therefore given as:

$$\Delta\alpha_n = \frac{\left(\sum_i \alpha_i^f - \sum_i \alpha_i^s\right)}{n} \quad (7.1)$$

### 7.2.2 Minimal surface generation

The widely-used (open-source) Surface Evolver software<sup>25</sup> was used to find the minimal surface spanning a given boundary frame. The software numerically finds the minimal surface by minimizing the surface energy using a gradient descent method. Using Matlab, the input files for every desired fold angle were generated, containing the vertex coordinates and the edge numbers of the boundary frame. The surface was then evolved using two consecutive gradient descent and mesh refinement steps, supplemented with equiangularization and vertex averaging, until area convergence was achieved. The resulting minimal surface morphologies were then exported as .obj files and were rendered in KeyShot 5 (Luxion, USA).

### 7.2.3 Folding kinematics tool

Our approach consists of connecting multiple foldable patches together, while respecting the hyperbolic symmetries of TPMS, to construct a 2D net that could fold into larger TPMS assemblies. A MATLAB tool was developed to explore the folding of user-defined 2D nets consisting of flat patches connected together using either vertex- or edge-connections. By employing the symmetry properties that both types of connections entail, the vertex coordinates of every patch in the net could be determined for every fold angle from the initial patch, by using appropriate rotation matrices and translation vectors. For example, copying the initial patch along one of its edges requires rotating the coordinates by angle  $\pi$  around that edge (Figure 7.1). Thus, for both edge-connected patches in Figure 7.1, the coordinates of a vertex in the copied patch  $\mathbf{q}_i$  are related to the coordinates of the corresponding vertex in the original patch  $\mathbf{p}_i$  by:

$$\mathbf{q}_i = \mathbf{R}(\pi) \cdot \mathbf{p}_i + \mathbf{t} \quad (7.2)$$

where  $R(\theta)$  is the rotation matrix for a rotation of angle  $\theta$  about the unit vector  $\hat{\mathbf{r}} = \frac{\mathbf{r}}{\|\mathbf{r}\|}$  and is given as (32):

$$\mathbf{R}(\theta) = \begin{pmatrix} \cos(\theta) + \hat{r}_x^2(1 - \cos(\theta)) & \hat{r}_x\hat{r}_y(1 - \cos(\theta)) - \hat{r}_z\sin(\theta) & \hat{r}_x\hat{r}_z(1 - \cos(\theta)) - \hat{r}_y\sin(\theta) \\ \hat{r}_x\hat{r}_y(1 - \cos(\theta)) + \hat{r}_z\sin(\theta) & \cos(\theta) + \hat{r}_y^2(1 - \cos(\theta)) & \hat{r}_y\hat{r}_z(1 - \cos(\theta)) - \hat{r}_x\sin(\theta) \\ \hat{r}_x\hat{r}_z(1 - \cos(\theta)) - \hat{r}_y\sin(\theta) & \hat{r}_y\hat{r}_z(1 - \cos(\theta)) + \hat{r}_x\sin(\theta) & \cos(\theta) + \hat{r}_z^2(1 - \cos(\theta)) \end{pmatrix} \quad (7.3)$$

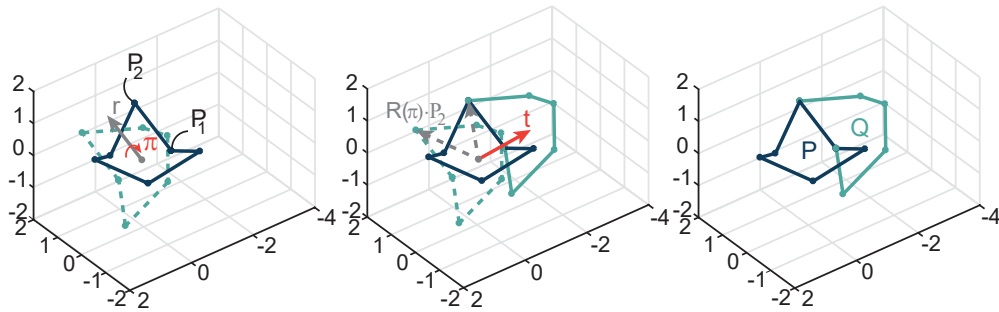


**Figure 7.1:** A schematic illustration of the implementation of the folding kinematics for two edge-connected P patches at 50% of their fold angle.

The vector  $\mathbf{t}$  represents a translation to ensure that the original patch and its rotated copy are connected at the desired vertex. For example, for an edge-connection about the edge defined by points  $\mathbf{p}_1$  and  $\mathbf{p}_2$  (Figure 7.1), the translation vector is given by:

$$\mathbf{t} = \mathbf{p}_2 - \mathbf{R}(\pi) \cdot \mathbf{p}_2 \quad (7.4)$$

We verified the absence of coinciding patches in the folded configurations by checking for duplicate coordinates in the total coordinate matrix. The folding sequences for multiple-unit assemblies were visually examined for patch collisions after the minimal surfaces were added to the boundary frames in Surface Evolver. To avoid collisions, sequential folding was implemented by using multiple fold angle variables  $\theta_i$  that increase at the same rate but are initiated at different time points. Figure 7.2 shows two edge-connected  $P$  unit cells that were folded according to different  $\theta$ , showing that one unit is essentially a “time-shifted” copy of the other, *i.e.*

$$\theta_a = \theta_b - \delta_t \quad (7.5)$$

where  $\delta_t$  represents the time shift and can be positive or negative.

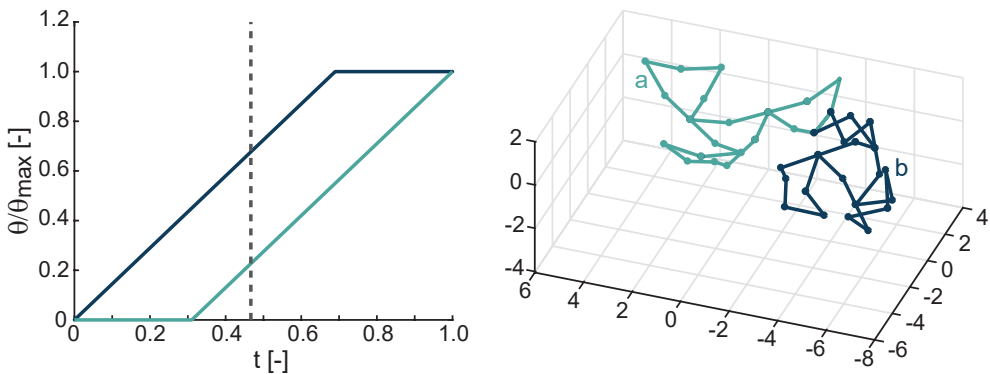


**Figure 7.2:** Sequential folding illustrated for two edge-connected  $P$  units. The left subfigure depicts the normalized fold angle *versus* time for both patches, while the right subfigure displays the state of the patches at the instance indicated by the dashed line in the left figure.

### 7.2.4 Design of foldable frames

Foldable patch and unit cell frames were designed in SolidWorks 2016 (Dassault Systèmes, France). The frame edges, which are supposed to behave rigidly, were given a square  $2 \times 2$  mm cross-section, while the hinges were designed as a 0.3 mm layer connecting the rigid edges and facilitating the folding motion through local bending. This hinge design enabled efficient folding yet simple fabrication. At the location of the hinges, the frame edges were given a chamfer such that the folding of the frame would be halted at the desired fold angle (Figure 7.3).

### 7.2.5 3D printing

The frames were 3D printed on an Ultimaker 2+ FDM printer (Ultimaker, The Netherlands) using poly-lactic acid (PLA) filaments with a 0.25 mm diameter nozzle and a layer thickness of 0.6 mm. In the case of the  $C(P)$  surface, a flat “star” patch (Section 7.5) was printed, which was manually deformed into the bow-tie configuration after printing to enable the in-plane sliding of the hinge vertices upon folding. Latex

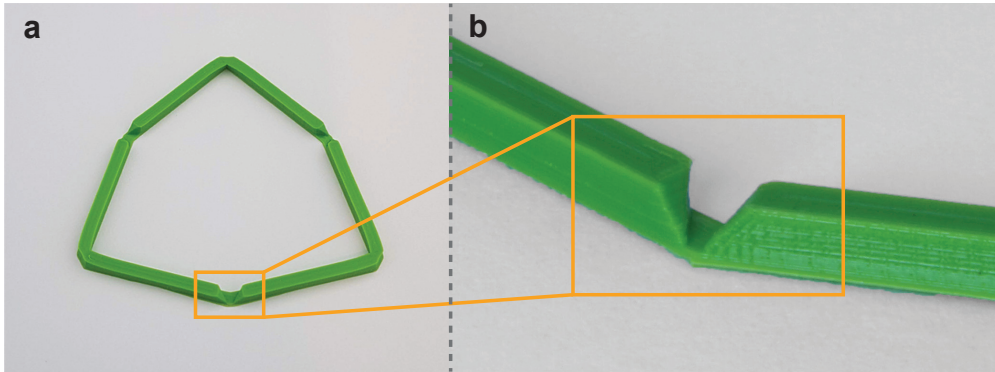


**Figure 7.3:** An example of a 3D printed frame. a) A printed hexagonal frame for the D surface. b) A close-up of a hinge, showing the thin hinge layer and the chamfer at the frame edges.

sheets (150  $\mu\text{m}$  thick, TheraBand, USA) were bi-axially stretched ( $\epsilon_1 = \epsilon_2 \approx 0.5$ ) and fixed to a cutting board. The flat frames were adhesively bonded to the stretched latex sheets using a cyanoacrylate adhesive (Bison, The Netherlands), which was cured at room temperature. Next, the excess of the latex sheet was cut along the outside boundary of the frame. The frame was then released from the cutting board and was allowed to self-fold into the final configuration.

### 7.2.6 Micro-computed tomography and curvature estimation

Micro-computed tomography ( $\mu\text{CT}$ ) images of four 3D-printed self-folded patches (one from each type of the minimal surfaces considered here) were acquired using a Phoenix Nanotom scanner (General Electric, USA). Tomographic reconstructions were made with a slice increment of 22.5  $\mu\text{m}$ , and a matrix of  $2284 \times 2284$  pixels. The voxel size of the volumetric data was  $22.5 \times 22.5 \times 22.5 \mu\text{m}$ . To enable subsequent processing on a desktop computer with Intel(R) Xen(R) E5-2687W (2 cores) at 3.40 GHz and 64.0 GB RAM, the volumetric data was resized by a factor of 0.4 using the function “imresize3” available in Matlab (Mathworks, USA). Subsequently, each volumetric dataset with a voxel size of  $56 \times 56 \times 56 \mu\text{m}$  was post-processed using Mimics (version 14.01, Materialise, Belgium). Using this software, all patches were segmented and 3D models were reconstructed based on the segmentation results. During the reconstruction, the smoothing function available in Mimics was applied with a smoothing factor of 1.0. To ensure proper definition of the contour of the patches, smoothing effects were visually examined. Using the same software, 3D models were exported as STL files. The mean curvature of each triangulated patch surface (.STL) was estimated using the “vtkCurvatures” class of The Visualisation Toolkit (VTK) in Python<sup>26</sup>.

## 7.3 Results

### 7.3.1 Hyperbolic geometry of TPMS

Triply periodic minimal surfaces belong to the realm of hyperbolic geometry and arise from symmetry operations on fundamental patches. This idea of constructing a TPMS structure as a 3D puzzle using a single, saddle-shaped puzzle piece that is repeated throughout the structure is central to our approach. As a demonstrative example, the translational unit cell of the well-known Schwarz P surface (Figure 7.4a), can be tiled by a fundamental asymmetric patch (Flächenstück) through two symmetry operations: mirror reflections about the plane lines of curvature, and two-fold ( $\pi$ ) rotations about the straight lines. The resulting triangular tiling, with angles  $\pi/2$ ,  $\pi/4$ , and  $\pi/6$ , is not compatible with the Euclidean plane  $\mathbb{E}^2$ , but is a tiling of the hyperbolic plane  $\mathbb{H}^2$  (it is the \*246 tiling in orbifold notation<sup>27</sup>), as seen in the conformal Poincaré disk model (Figure 7.4a). This illustrates the interesting feature that a portion of  $\mathbb{H}^2$  can be embedded in 3D Euclidean space  $\mathbb{E}^3$  by wrapping it onto the periodic minimal surface (albeit with some curvature distortion), analogous to embedding  $\mathbb{E}^2$  in  $\mathbb{E}^3$  by wrapping it onto a cylinder<sup>27;28</sup>. Within the context of this chapter, however, this intrinsic connection between  $\mathbb{H}^2$  and  $\mathbb{E}^3$  underpins the inherent complexity of trying to unwrap TPMS to a flat state, *i.e.*  $\mathbb{E}^2$ . The same minimal surface could be tiled with different patches (Figure 7.4b), all constructed from some symmetry operations on the elementary asymmetric patch. Within the wealth of known, intersection-free TPMS and their respective surface patches, our approach covers those surfaces that could be tiled by straight-edged skew polygonal patches (homeomorphic to a disk). A necessary (but not sufficient) condition therefore is the existence of embedded straight lines in the TPMS, which are axes of two-fold rotation and form the “linear skeletal net” of the surface<sup>29</sup>. TPMS with embedded straight lines were termed by Fisher and Koch as “spanning minimal surfaces”<sup>24</sup>, and they are necessarily also minimal balance surfaces (*i.e.* the two labyrinths on both sides of the surface are congruent)<sup>30</sup>. Our folding approach applies to those spanning minimal surfaces for which the generating patch is a surface spanning a skew polygon. This excludes certain TPMS such as the H surface, which does contain straight lines but cannot be tiled by skew polygonal patches<sup>24</sup>, and the well-known Gyroid surface, which does not contain embedded straight lines at all<sup>30</sup> (Section 7.5). The presented approach does, however, cover a range of other widely studied TPMS, four of which are included in this chapter as examples (see Figure 7.4c, tiled by skew polygon patches): The *P* surface, the *D* surface (adjoint to *P*), the *CLP* surface, and the *C(P)* surface (complementary to *P*).

### 7.3.2 Foldable minimal surface patches

The key to our origami approach is the rational design of skew polygonal patches that could be flattened. We achieve this by adding hinges at some of the vertices of the boundary frame while keeping the edge lengths constant, enabling a continuous folding of the frame from a skew polygon to a (simple) flat polygon. For a skew  $n$ -gon ( $n \geq 4$ ), this approach requires  $2 \leq k \leq n/2$  hinges at the vertices, while the other vertices are

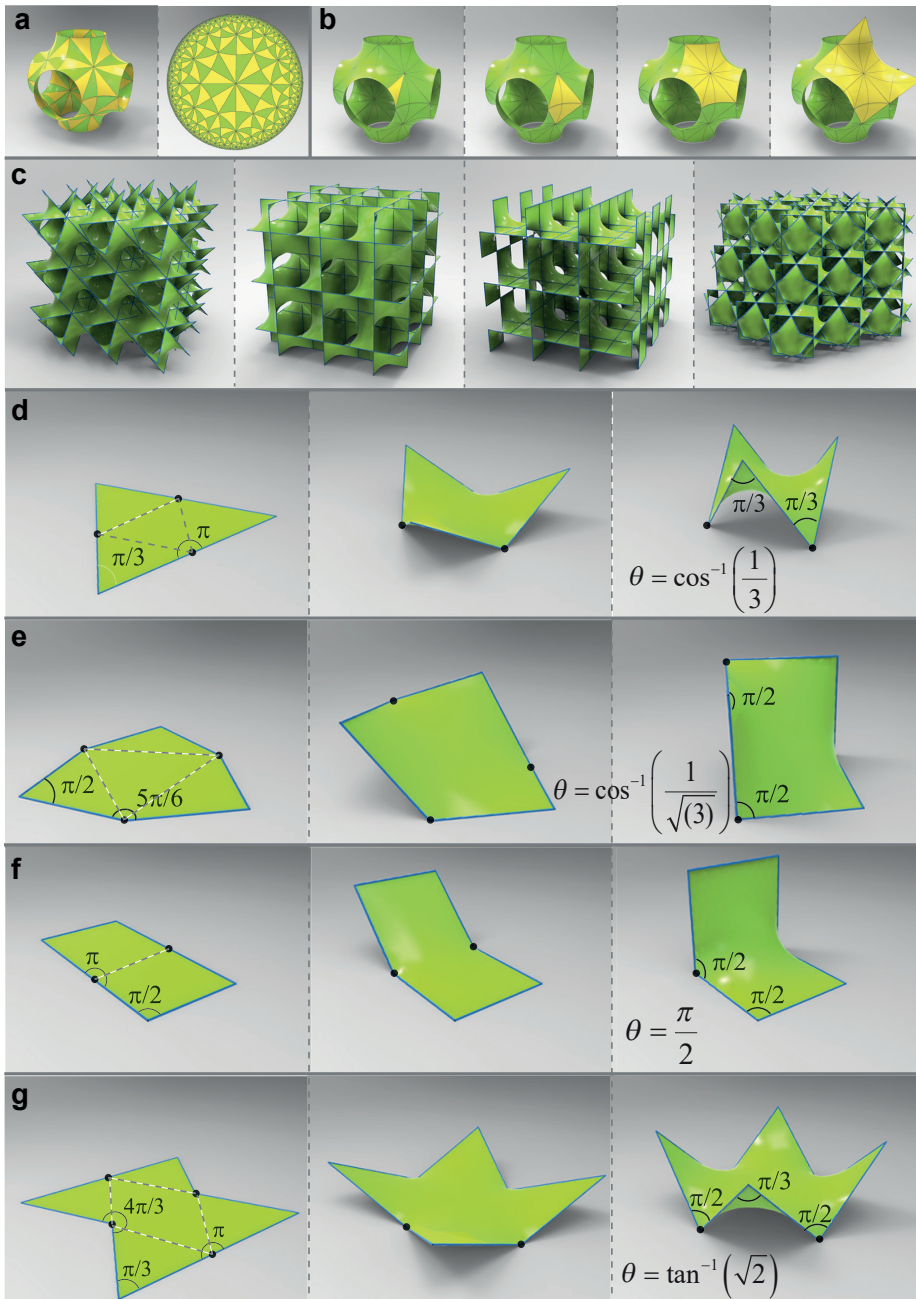


**Figure 7.4:** Geometry of TPMS and patch folding. a) A translational  $P$  unit cell decorated with the hyperbolic  $*246$  tiling of the fundamental asymmetrical patch. b) Alternative patches to tile the  $P$  surface, shown together with the conventional unit cell. c) The four TPMS considered here. From left to right:  $P$ ,  $D$ ,  $CLP$ , and  $C(P)$  surface. d) Folding kinematics for the straight-edged skew polygonal patches of the  $P$ ,  $D$ ,  $CLP$ , and  $C(P)$  surfaces, respectively.

kept fixed. Since the internal angle sum of the skew polygons is smaller than that of simple flat polygons, *i.e.*  $\sum_i \alpha_i \leq \pi(n-2)$ , the internal angles at the hinge vertices must increase during the unfolding motion (Figure 7.4d-g). Applying the Gauss-Bonnet theorem to the skew polygonal boundary frame indicates that the folded frame must enclose negative Gaussian curvature (see Section 7.5)<sup>31</sup>. Consequently, the folding/unfolding of the polygonal boundary frame necessitates a change in the Gaussian curvature of the surface spanning the frame that, according to Gauss' Theorema Egregium, can only be accommodated by an area distortion<sup>32</sup>. Indeed, flattening the saddle shaped patches requires the surface spanning the frame to stretch (see Methods). In other words, the metric of the surface has to transition between a Euclidean (flat) metric and a non-Euclidean (saddle-shaped) metric. With conventional origami folding, this would not be possible and the folded structures would remain intrinsically flat (except for some discrete points of non-zero Gaussian curvature in some techniques<sup>33</sup>). In our folding approach, the required area distortion during folding is achieved by attaching rigid, foldable frames to a bi-axially pre-strained elastomer sheet. The pre-strain in the flat sheet entails two key benefits: releasing the pre-strained sheet drives self-folding of the attached frame from the flat state to the folded state, and the remaining pre-strain in the sheet forces it to adopt a minimal surface shape, by the virtue of energy (or area) minimization. This is analogous to the famous demonstrations of minimal surface formation that are obtained when dipping 3D wireframes in a soap solution: the soap film adopts a minimum-energy minimal surface shape. The same principle has been employed to create physical models of minimal surfaces (before the advent of 3D printing) using stretched fabrics or polymer sheets<sup>34;35</sup>, and as a means to actuate certain origami tessellations<sup>36</sup>.

The four patches considered here and their folding kinematics are shown in Figure 7.4d-g. The skew hexagonal frames for the *P* and *D* surfaces (Figure 7.4d-e) are equilateral and equiangular, and are the Petrie polygons of the regular octahedron and the cube respectively. The *P*-patch is flattened to an equilateral triangle, and the *D*-patch to an equilateral hexagon with angles of  $\pi/2$  and  $5\pi/6$ . This simple folding/unfolding kinematics entails a rotation of angle  $\theta$  around three "creases" that connect the hinge vertices (the dotted lines). In the case of the hexagonal patch of the *CLP* surface (Figure 7.4f), only two hinges are required, and, thus, one "crease". The patch can then be flattened to a rectangle with sides  $l$  and  $2l$ . Finally, the patch for the *C(P)* surface is a skew octagon with alternating angles of  $\pi/2$  and  $\pi/3$ , which is flattened to a bow-tie shape with angles  $\pi$ ,  $\pi/3$ , and  $4\pi/3$ . Contrary to the three other patches where the location of the hinge points remains fixed, the flattening of the *C(P)* patch requires in-plane sliding of the hinge points during the folding motion (See Section 7.2). The *C(P)* skew octagonal patch could be flattened into different shapes that do not require sliding hinges, but these alternative shapes are unfit for building an "overlap-free" 2D net that could be folded into 3D TPMS morphologies (see Section 7.5).

### 7.3.3 Patch connections and unit cell folding

Now that a suitable folding/unfolding approach for the minimal surface patches, *i.e.* the pieces of the 3D TPMS puzzle, has been obtained, the next key step is to connect patches together to build larger portions of the minimal surfaces. As such, we develop a foldable 2D “net” that results in a 3D portion of the TPMS once all patches have been folded. We identify two possible attachment strategies, namely edge-connections and vertex-connections. In the first type (Figure 7.5a), two patches are connected by means of a  $\pi$ -rotation around their common edge  $\mathbf{u}$ , which is an inherent property of the straight lines embedded in minimal surfaces and justifies our focus on straight-edged skew polygonal patches. A consequence of this  $\pi$ -rotation is that the common edge remains coplanar with two adjacent edges  $\mathbf{v}_1$  and  $\mathbf{v}_2$ , *i.e.*  $\mathbf{u} \cdot (\mathbf{v}_1 \times \mathbf{v}_2) = 0$ , during the entire folding motion (Figure 7.5a). The connection between both patches is therefore “rigid” and there is no need to actuate the folding of one patch relative to the other. The vertex-connection type attaches two patches at a vertex that is not a hinge point (Figure 7.5b). A vertex-connection is established as a  $2\theta$  rotation about an axis  $\mathbf{n}$  that is normal to the edges  $\mathbf{u}_1$  and  $\mathbf{v}_1$  meeting at the vertex, where  $\theta = \cos^{-1} \left( \frac{\mathbf{u}_1 \cdot \mathbf{v}_1}{\|\mathbf{u}_1\| \|\mathbf{v}_1\|} \right)$ . In fact, this type of connection is the result of two consecutive edge-connections, *i.e.* a  $\pi$ -rotation over  $\mathbf{v}_1$  followed by a  $\pi$ -rotation over  $\mathbf{u}_2$  (Figure 7.5b). Similar to the case of edge-connections, the edges  $\mathbf{u}_1$ ,  $\mathbf{v}_1$ ,  $\mathbf{u}_2$ , and  $\mathbf{v}_2$  are coplanar, meaning that the vertex-connection is also rigid and can be physically realized without having to account for the relative motions between both patches at the connecting vertex. Experimenting with patch connections quickly reveals the most crucial challenge in our folding strategy: avoiding overlaps in the 2D net. This challenge arises as a consequence of trying to confine the hyperbolic tiling of TPMS patches to the Euclidean plane. For example, the tiling with skew hexagons of the  $D$  surface (Figure 7.5c), is a hyperbolic (6,4) tiling where four hexagons meet at every vertex. Attempting to achieve this with the flattened hexagonal patches leads to an overlapping 2D net, while the folded configuration is free of overlaps (Figure 7.5c). This shows that it is not trivial to unwrap TPMS morphologies into 2D overlap-free nets. Our rational approach to overcome this challenge consists of first creating foldable, overlap-free nets for the TPMS unit cells, and using those unit cell nets as prototiles in the construction of overlap-free nets for larger structures. Thus, instead of assembling larger morphologies patch by patch, we propose to first define the net for a single translational unit cell and consequently connect those unit cell nets together to build larger structures. As shown in Figure 7.5d-g, the translational unit cells for the  $P$ ,  $D$ ,  $CLP$  and  $C(P)$  surfaces respectively could all be folded from overlap-free 2D nets consisting entirely of vertex connections. In case of the  $P$ ,  $D$  and  $CLP$  surfaces, the unit cell consists of 4 patches while the  $C(P)$  unit cell is constructed using 6 patches. A consequence (and advantage during physical realization) of using vertex-connections is that all patches fold in the same direction, which is not the case for edge-connections, causing the unit cell net to close in on itself, analogous to the folding of a paper cube. Except for the  $CLP$  unit cell net, the vertex-connected unit cell nets presented in Figure 7.5 are not unique, *i.e.* different arrangements of vertex-connected patches could

be generated that fold into the same translational unit cell. Examples of different nets that fold into the same translational unit cell are shown in Figure 7.12 (see also Section 7.5). In general, the net for a unit cell consisting of  $n$  patches would need at most  $n - 1$  vertex-connections connecting two patches together. However, a net with fewer connections could be designed if more than two patches could be attached together at the same vertex (e.g. in the case of the  $P$  and  $C(P)$  surfaces, see also Section 7.5). The same rationale to design nets for larger TPMS structures applies, independent of the choice of unit cell net. However, certain unit cell nets might be preferable in order to construct larger assemblies, as explained in the next section.

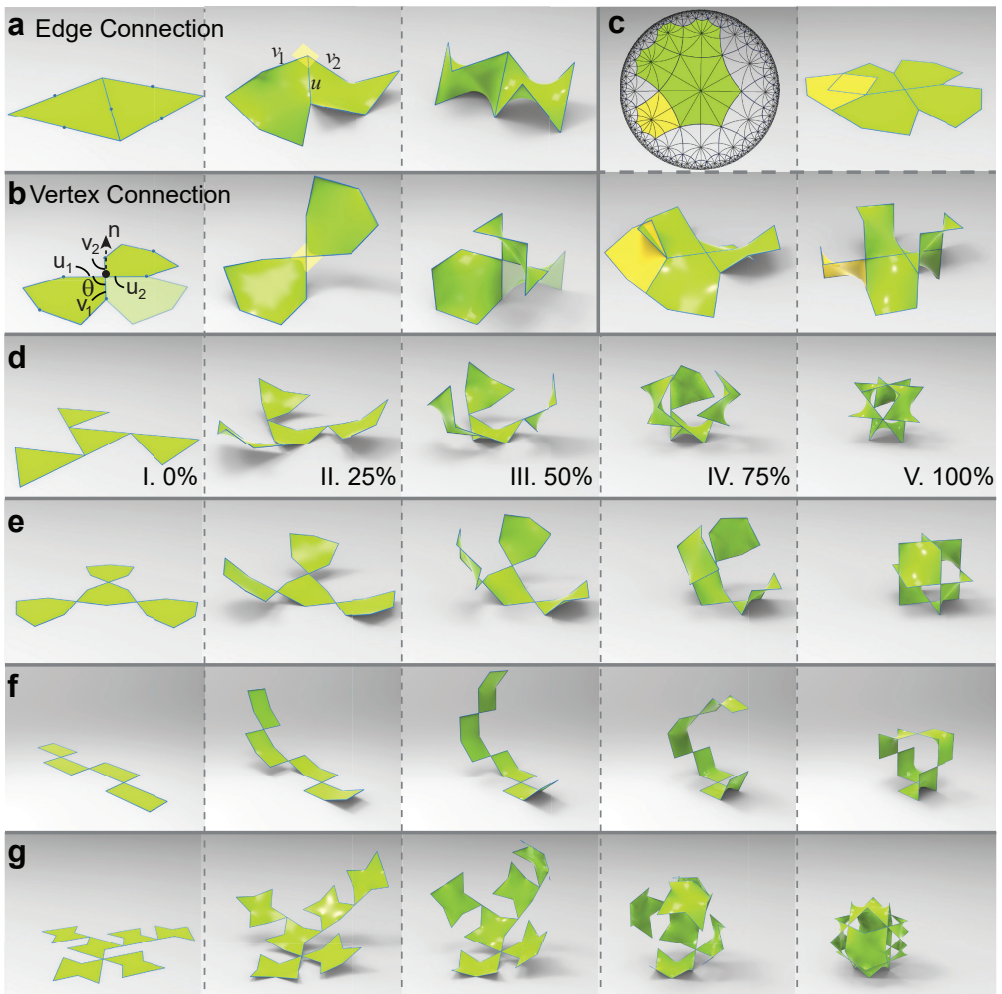


**Figure 7.5:** Connecting patches. a) The edge-connection of two  $P$  patches. b) The vertex-connection of two  $D$  patches. A transparent patch indicates a patch that fits in between two vertex-connected patches. c) When trying to conform the hyperbolic (6,4) tiling of the  $D$  surface to the flat plane, one frequently encounters overlaps in the 2D net. d-g) The folding of TPMS unit cells consisting of vertex-connected patches.

### 7.3.4 Multiple-unit cell assemblies

To establish folding of larger TPMS assemblies consisting of multiple unit cells, we connect the 2D nets of several unit cells together. This requires the use of edge-connections between the different unit cells, since further use of vertex connections would lead to overlaps in 3D, a consequence of the “closing” of the unit cells. To avoid overlaps in the 2D nets, however, not all edges are available for edge-connections. The admissible edges for the four unit cell nets considered here are highlighted in Figure 7.6a. Only along these admissible edges, two unit cells can be connected without causing overlaps in the 2D net. The admissible edges of a given unit cell net are those edges that lie on the edges of the convex polygon that defines the convex hull of the patch vertices (See Figure 7.12). Thus an edge whose end points are vertices of the convex hull would be an admissible edge for edge-connections. All edges that are contained entirely within the convex hull (and not on the boundary) are inadmissible for edge-connections. A simple example of two connected P unit cells is provided in Figure 7.6b, illustrating the opposite folding directions of both unit cells. Furthermore, Figure 7.6b shows how connecting two units along one edge, *e.g.*  $u_1$ , may prohibit a connection along another edge, *e.g.*  $v_1$ , as this would otherwise lead to overlaps in 2D. The number of admissible edges varies depending on the chosen unit cell net. For example, some unit cell nets of the  $C(P)$  surface allow for only a single edge-connection, making them unsuitable to extend the 2D net beyond two unit cells (see Figure 7.12 and Section 7.5). The net that is depicted in Figure 7.5g and Figure 7.6a, on the other hand, has six admissible edges (appearing in three pairs). Choosing the latter unit cell net as a prototile would thus offer more freedom to construct a larger net, since it could connect to three other unit cells.

To explore the folding of larger and more general TPMS morphologies, we constructed a computational tool that calculates the folding and the resulting 3D configuration of a user-defined input 2D net. Starting from a single unit cell, we extend the 2D net by adding more unit cells, without causing overlaps, and verify the resulting folding motion and the final 3D morphology. The underlying folding kinematics of our approach is surprisingly simple, since all folding information is captured in the kinematics of a single patch (assuming all patches fold simultaneously) and in the way the patches are connected together through vertex- and edge-connections. A large variety of 3D TPMS-based structures could be obtained without having to determine a separate folding strategy for each simply by varying the 2D arrangement of the patches (see Section 7.5). While still tractable for smaller structures, the relationship between a given 2D net and the resulting 3D structure becomes increasingly complex for larger structures with many patch connections, involving intricate folding motions and potentially overlapping patches in 3D that do not overlap in 2D, which are detected in the tool by checking for duplicate sets of vertex coordinates. Using this explorative tool, a multitude of 2D nets could be designed to fold a wide range of complex minimal surface structures, some of which are shown in Figure 7.6 and more can be found in Section 7.5 (*e.g.* minimal surface string-like morphologies or stackable layers). In Figure 7.6c-f, the

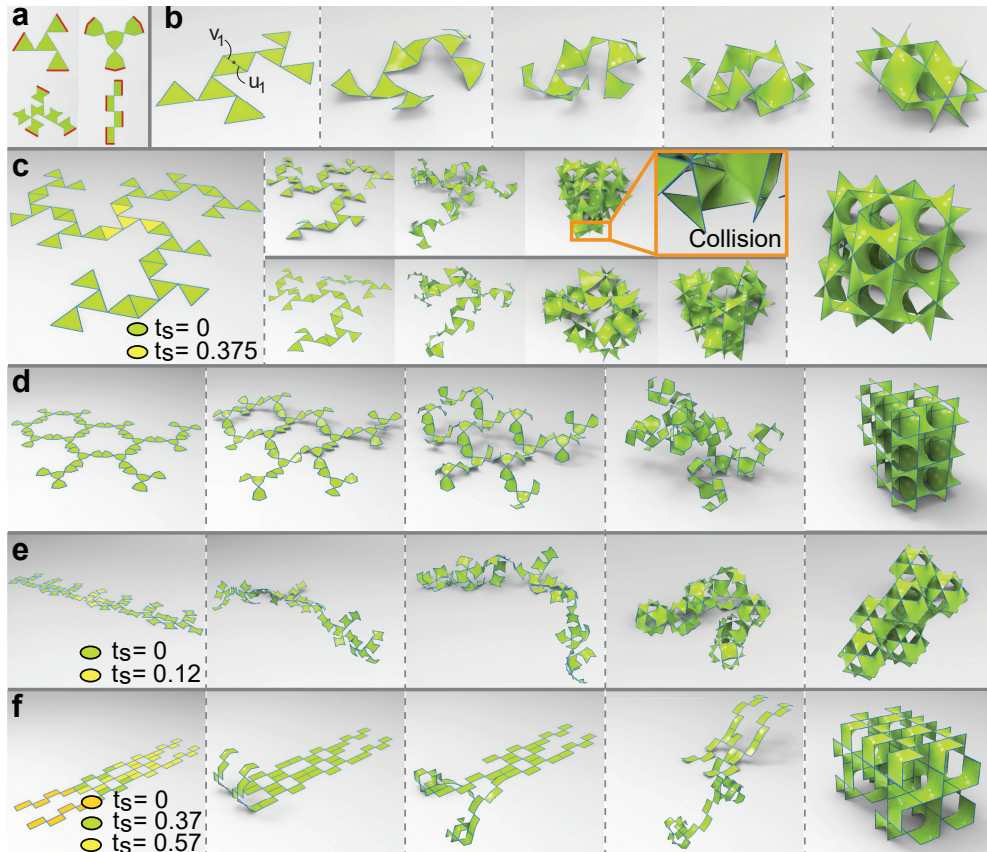


**Figure 7.6:** Folding multiple-unit assemblies. a) The unit cell edges that are available for edge-connections (highlighted in red) without causing overlaps in the 2D net. b) Folding of two edge-connected  $P$  unit cells. c) Folding of a 10-unit-cell net of the  $P$  surface without implementing sequential folding (top row), giving rise to collisions, and with sequential folding (bottom row), to avoid collisions. The yellow patch in the left pane starts folding with a delay relative to the other patches (fully folded configuration at  $t = 1$ ). d) Folding of a 14-unit-cell net of the  $D$  surface without requiring sequential folding. e) The sequential folding of a 7-unit-cell net of the  $C(P)$  surface, with a folding delay applied to the central patch (yellow in the left pane). f) Sequential folding of a 10-unit-cell assembly of the  $CLP$  surface, containing three separate folding starting times to avoid collisions. See Section 7.5 for additional morphologies and Supplementary Movies 1 through 6<sup>37</sup>

folding of multiple connected unit cells for the  $P$ ,  $D$ ,  $C(P)$ , and  $CLP$  surfaces is illustrated (see Supplementary Movies 1-6<sup>37</sup>). Due to the complex folding motions arising for such large structures, collisions during folding could occur, as shown in the top row of Figure 7.6c for the folding of ten  $P$  unit cells. We demonstrate that sequential folding, *i.e.* temporal control over the folding motion, could alleviate this problem. As a simple example, a slight delay in the folding initiation of a centrally located unit cell in the nets of the  $P$  (Figure 7.6c) and  $C(P)$  (Figure 7.6e) morphologies is sufficient to enable collision-free folding, by maintaining adequate separation between the outwards

extending arms. For the *CLP* example in Figure 7.6f, three different starting moments are implemented to avoid collisions, a consequence of the high aspect ratio of the unit cell net, while the assembly of 14 *D* unit cells (Figure 7.6d) did not require sequential folding. The folding sequences shown in Figure 7.6c-f are examples that demonstrate how small changes in the folding initiation of certain unit cells could prevent collisions. However, many different folding sequences could be employed to achieve the same result, *e.g.* sequences involving variations in the folding speed and the starting time of the unit cells, individual patches, or even individual hinges, thereby offering greater design freedom to ensure collision-free folding. Sequential folding could be physically realized in different ways, *e.g.* using localized external triggers<sup>38</sup> or built-in design features<sup>39</sup>.

### 7.3.5 Self-folding experiments

We physically realized our self-folding minimal surface structures by attaching stretched elastomer sheets to 3D printed foldable frames. Upon release, the strain energy in the sheets causes the flat polygonal frame to self-fold into the desired skew polygonal configuration, and the sheet spanning the frame adopts an energy-minimizing saddle-shaped geometry, approximating the minimal surface (Figure 7.7a). Being a combination of (semi-) rigid beams and flexible sheets, our structures represent a special case of Kirchhoff-Plateau surfaces<sup>40</sup>, in which virtually all frame deformation is concentrated at the hinges. The direction of folding of the frame is controlled by the eccentric position of the sheet with respect to the hinge location: the pre-stretched sheet is attached on one side of the frame, while the hinge layer (see Section 7.2 and Figure 7.3) is situated on the other side, ensuring preferential folding in the direction of the side to which the sheet is attached.

The level of pre-strain in the elastomer sheets should at least be high enough to accommodate the relative amount of area shrinkage that occurs in the sheet during the folding motion, which varies between approximately 10% and 30% depending on the patch type (Figure 7.8b). Moreover, the strain energy stored in the pre-stretched sheets should be high enough to drive the folding motion of the frame, *i.e.* to overcome the bending resistance at the hinges and the gravitational forces acting on the frame, and also to keep the frame in the folded configuration afterwards. During the experiments presented here, the sheets were bi-axially strained by 50% in both directions (see Section 7.2), which enabled the rapid self-folding of the frame and resulted in ample residual tension in the sheet to maintain the frame in its folded configuration. We assessed the mean ( $H$ ) curvature profile of the sheet surface on the basis of micro-computed tomography scans of the self-folded patches, finding that  $H$  is close to zero everywhere (Figure 7.7b). This demonstrates that the self-folded patches adopt a shape close to the ideal minimal surface, as minimal surfaces are mathematically defined as having  $H = 0$  everywhere. While deviations from the ideal minimal surface shape arise as a consequence of, *e.g.*, sheet wrinkling at the hinges, non-uniform sheet straining, and competition between the bending and stretching energies of the finite thickness sheet<sup>41</sup>, we demonstrate that a relatively simple combination of rigid and flexible components

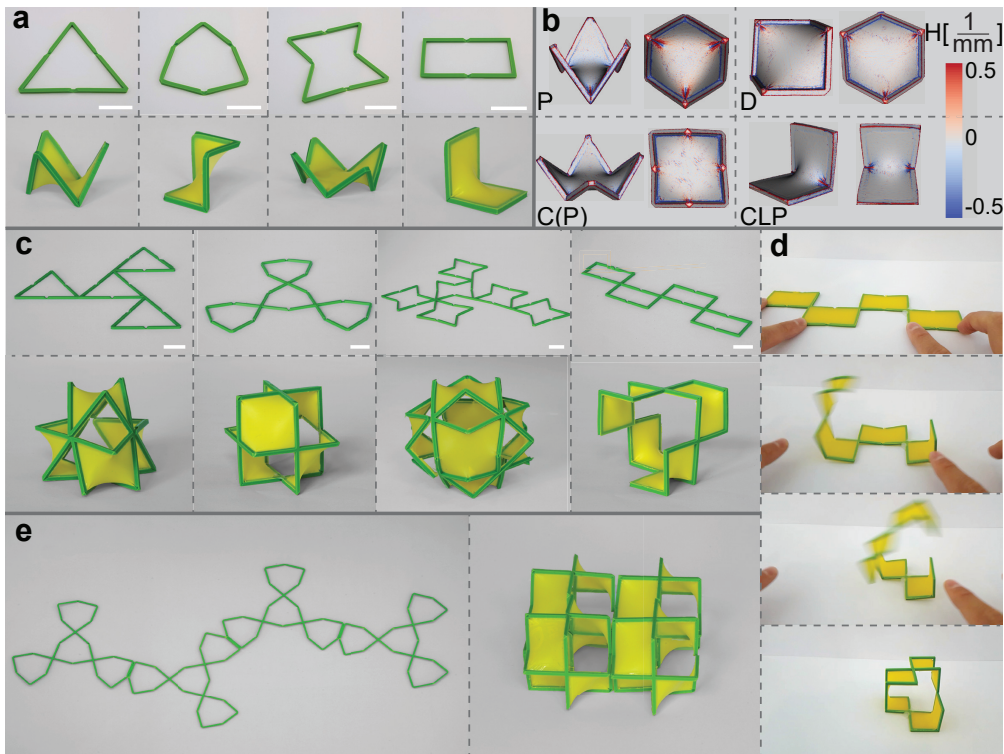


**Figure 7.7:** Self-folded physical models. a) 3D-printed foldable frames for the four patch types in flat (top row) and folded (bottom row) configurations after the stretched latex sheets have been attached (see Section 7.2). b) The mean curvature estimated using the 3D reconstructions of the four patch types obtained from micro-computed tomography data. c) 3D-printed foldable TPMS unit cells in the flat (top row) and folded (bottom row) configurations. d) The self-folding of the *CLP* unit cell through the pre-tension present in the latex sheet (See Supplementary Movie 7<sup>37</sup>). e) An assembly of four *D* unit cells in the flat (left) and folded (right) configurations. All scale bars are 20 mm.

enables the folding of complex, hyperbolic shapes that are incompatible with traditional origami methods. In addition to individual patches, we also 3D printed unit cell nets of the four TPMS, which were self-folded to the final configuration after attaching and releasing the pre-stretched sheet material (Figure 7.7c). Since all patches within the same unit cell fold in the same direction, a consequence of using vertex-connections, the sheet is attached to the same side for all patches within the unit cell, which is convenient during fabrication. To demonstrate the self-folding capability of this approach, a time sequence of the self-folding of the *CLP* unit cell is shown in Figure 7.7d (see also Supplementary Movie 7<sup>37</sup>). Upon release, the pre-stretched latex sheet rapidly causes the frame to self-fold, and the built-in stopping mechanisms cause it to stop at the desired configuration (See Section 7.2). Moreover, we show that attaching unit cell nets together using edge-connections enables the self-folding of larger assemblies (Figure 7.7e). As a demonstrative example, four connected unit cells for the *D*-surface are shown in Fig-

ure 7.7e, but this approach is also applicable to larger morphologies as long as collisions during folding are avoided.

## 7.4 Discussion

Whereas previous origami-based designs have been restricted to primarily developable geometries, such as polyhedral structures and classical origami tessellations, the presented approach realizes the self-folding of previously unfoldable, non-developable, TPMS structures through the rational design of foldable surface patches and their connections. While we focused here on four TPMS types, other spanning minimal surfaces could also be constructed, if a suitable flattening of the skew polygonal patch is found. By elucidating the folding kinematics of the four types of generating patches, and by connecting multiple patches using either vertex- or edge-connections, a large variety of foldable 3D morphologies could be generated that are all a portion of the infinite minimal surface. Our focus has been on generating 2D nets by first constructing unit cells, using vertex-connections, and connecting unit cells together using edge-connections. However, many different foldable 2D nets could be generated, *e.g.* to fold periodic layers of TPMS unit cells that could be stacked to assemble arbitrarily large portions of the TPMS (see Section 7.5). The relatively simple folding “rules” of our approach, capable of describing complex folding motions, could potentially benefit from efficient optimization algorithms to uncover foldable nets for specific TPMS morphologies. Due to the complexity of the TPMS morphologies, a key challenge in the further development of the presented origami approach is the ability to accurately control the folding motion, *i.e.* not only the temporal aspect but also the final configuration, as well as finding ways to lock the structure once folded. The presented approach offers new and exciting perspectives in the development of metamaterials, due to regained access to the flat starting surface. We envision not only origami biosystem applications<sup>42</sup>, *e.g.* biomimetic tissue engineering scaffolds with osteogenic and bactericidal surface nano-patterns, but also bi-continuous membranes for fluid transfer with tailored wettability (*e.g.*, self-cleaning membranes) or TPMS-based structures with embedded electronic components. In this work, we focused on sheet-based structures, but beam-based lattices derived from the boundary frames could also be folded. Finally, our approach is not strictly bound by a specific length scale, meaning that it could also inspire the self-folding of architectural-scale tensile structures, nor is it limited to specific constituent materials, as long as a sufficient area distortion of the sheet surfaces and the rigidity of the boundary frames can be obtained.

## 7.5 Supporting information

### 7.5.1 C(P) bowtie patch kinematics

As mentioned in the main text, the bowtie patch for the  $C(P)$  surface required the in-plane sliding of the hinge vertices. This is illustrated in the Figure 7.8a, where  $\delta_1$  and  $\delta_2$  represent the amount of in-plane sliding of the two pairs of opposite hinge vertices to accommodate the folding. These distances are given by:

$$\delta_1 = l \left( \cos\left(\frac{\pi}{6}\right) - \cos\left(\frac{\pi}{12}\right) + \sin\left(\frac{\pi}{12}\right) \right) = \frac{l}{2} (\sqrt{3} - \sqrt{2}) \quad (7.6)$$

$$\delta_2 = l \left( \cos\left(\frac{\pi}{12}\right) - \sin\left(\frac{\pi}{12}\right) + \sin\left(\frac{\pi}{6}\right) - 1 \right) = l \left( \frac{1}{\sqrt{2}} - \frac{1}{2} \right) \quad (7.7)$$

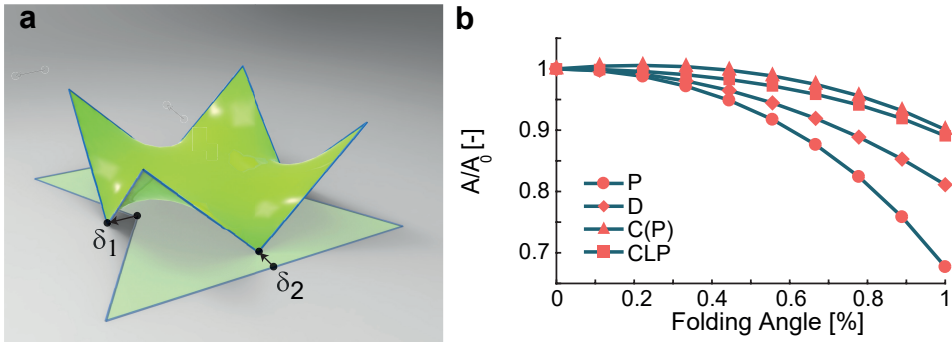


**Figure 7.8:** a) A schematic illustration showing the in-plane sliding of both pairs of the opposite hinge vertices for the  $C(P)$  bowtie patch. b) The normalized area of the minimal surface spanning the frames *versus* the relative fold angle, as calculated with Surface Evolver.

### 7.5.2 Surface area change during folding

As described in the main text, the folding motion of the frame entails an area distortion of the surface spanning the frame. This is illustrated in Figure 7.8b, showing the evolution of the normalized surface area  $A/A_0$  during folding, obtained by finding the minimal surface spanning the frames at every folding step using the Surface Evolver software.

### 7.5.3 H and Gyroid minimal surfaces

The  $H$  minimal surface, discovered by Schwarz, is a spanning minimal surface (*i.e.* it has embedded straight lines), but it does not have skew polygonal patches, and is, thus, excluded from our folding approach. It, however, has “catenoid-like” patches (following the naming of Fischer and Koch<sup>24</sup>) that consist of a surface spanning two vertically-spaced, concentric triangles (Figure 7.9a). The Gyroid minimal surface, first described by Schoen<sup>34</sup>, is a minimal balance surface (congruent labyrinths) that does not contain either embedded straight lines (axes of two-fold rotation), or the plane lines of curvature (mirror planes). Due to the absence of straight lines, however, the Gyroid minimal surface is not a suitable surface for the presented origami approach. Figure 7.9b shows a translational unit cell of the Gyroid TPMS.

### 7.5.4 Gauss-Bonnet theorem applied to skew polygonal patches

The Gauss-Bonnet theorem is one of the most important theorems in differential geometry, and relates the geometry of a surface to its global topology<sup>1</sup>. Following the

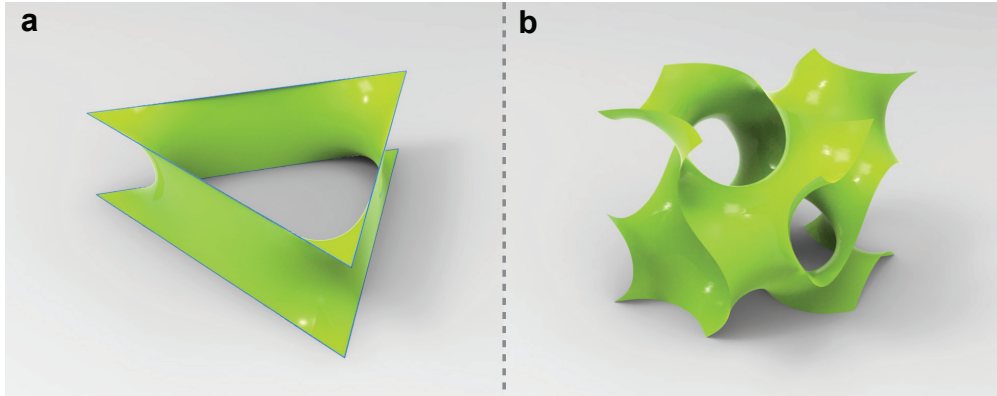


**Figure 7.9:** The unit cells for two TPMS that are excluded from the presented folding approach. a) The  $H$  surface, constructed from a catenoid-like patch. b) The Gyroid surface, which does not contain embedded straight lines.

formulation given by Demaine and O'Rourke<sup>31</sup>, it can be stated (for polygons or closed curves) as:

$$\tau + \gamma = 2\pi \quad (7.8)$$

where  $\tau$  is the total turn when traversing along the boundary of a curve or polygon and  $\gamma = \int K da$  is the area integral of the surface curvature inside the polygon. In the case of skew polygons, the total turn  $\tau$  is the sum of the turn at every vertex  $\tau_v$ , where  $\tau_v$  is the excess of the exterior angle over  $\pi$ . Applying this to, for example, the skew hexagonal patch of the Schwarz  $P$  surface, the turn at each of the 6 vertices is:

$$\tau_v = \frac{5\pi}{3} - \pi = \frac{2\pi}{3} \quad (7.9)$$

This gives a total turn of:

$$\tau = 6\tau_v = 4\pi \quad (7.10)$$

Applying the Gauss-Bonnet theorem gives:

$$\gamma = 2\pi - 4\pi = -2\pi \quad (7.11)$$

Thus, the skew hexagonal patch must enclose some negative Gaussian curvature, which is indeed true for minimal surfaces ( $K \leq 0$ ). In case the patch is flattened to the plane (and becomes an equilateral triangle), the total turn becomes:

$$\tau = 3 \cdot \frac{2\pi}{3} = 2\pi \quad (7.12)$$

In which case the integrated curvature term vanishes as expected, *i.e.*  $\gamma = 0$ .

### 7.5.5 Quadrilateral patches for the $P$ and $D$ surfaces

The  $P$  and  $D$  surfaces were constructed using skew hexagonal patches, as reported in the main text. However, these hexagonal patches could themselves be constructed from six smaller, straight-edged skew quadrilateral patches (Figure 7.10). In the case of the  $P$  surface (Figure 7.10a), the skew quadrilateral patch frame is equilateral and has two angles of  $\pi/3$  and two angles of  $\pi/2$ . By incorporating two hinge vertices, it can be flattened into a quadrilateral with two angles of  $\pi/3$  and two angles of  $2\pi/3$ . Connecting six of those patches using edge-connections results in the same folded hexagonal patch (Figure 7.10a bottom) as reported in the main text, though with a different flattened state (Figure 7.10a top).

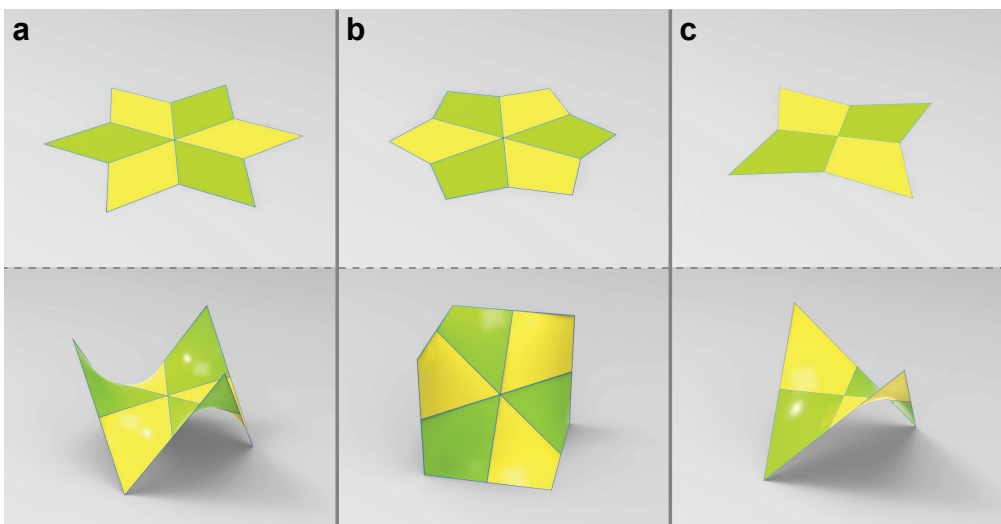


**Figure 7.10:** The quadrilateral patches for the  $P$  and  $D$  surfaces. a-b) Respectively six  $P$  and six  $D$  quadrilaterals can be connected to form the same hexagonal patches as reported in the main text. c) Four  $D$  quadrilaterals can also be connected along their short edge to form a different skew quadrilateral patch that can tile the  $D$  surface.

For the  $D$  surface, the skew quadrilateral has two sides of length  $l$ , two sides of length  $\sqrt{2}l$ , three angles of  $\pi/2$ , and one angle of  $\pi/3$ . It can be flattened to a quadrilateral with one angle of  $\pi/2$ , one angle of  $\pi/3$ , and two angles of  $7\pi/12$  (Figure 7.10b). Similar to the  $P$  quadrilaterals, connecting six  $D$  quadrilaterals using edge-connections along the  $\sqrt{2}l$  edges yields the same folded hexagonal patch as reported in the main text (Figure 7.10b, bottom), but with a different flattening (Figure 7.10b, top). However, four  $D$  quadrilaterals could also be edge-connected along the edges of the length  $l$  (Figure 7.10c). In the folded configuration, this gives an equilateral skew quadrilateral patch, with four angles of  $\pi/3$  (Figure 7.10c, bottom). This large quadrilateral patch was used in Schwarz' original work to describe the  $D$  surface<sup>2</sup>. Two additional points are noteworthy regarding Figure 7.10. First, the flat “star-like” tiles shown on the top row are all concave polygons. As a consequence of their concavity, they are not suitable for edge-connections, since this would lead to overlaps in the 2D net. The second remark

is made with regards to the points where the quadrilateral edges meet, *i.e.* the crossings of the embedded straight lines of the surface. These points are umbilical points, *i.e.* isolated flat points with zero Gaussian curvature. At these points, the minimal surface could be thought of as locally being “Euclidean”. Indeed, the sum of the internal angles at the points where the patches meet is equal to  $\pi$ , thus, abiding by the “Euclidean” rules. Therefore, while the surface spanning the patch frames is clearly hyperbolic, the points where the patches meet are not.

### 7.5.6 Alternative octagonal patches for the $C(P)$ surface

The skew octagonal patch for the  $C(P)$  surface, which has the alternating angles of  $\pi/2$  and  $\pi/3$ , could be folded from different flat polygons (Figure 7.11). As reported in the main text, the presented approach employs six bowtie patches attached to each other using vertex-connections at the  $\pi/3$  vertices, requiring the hinge vertices to slide in-plane.

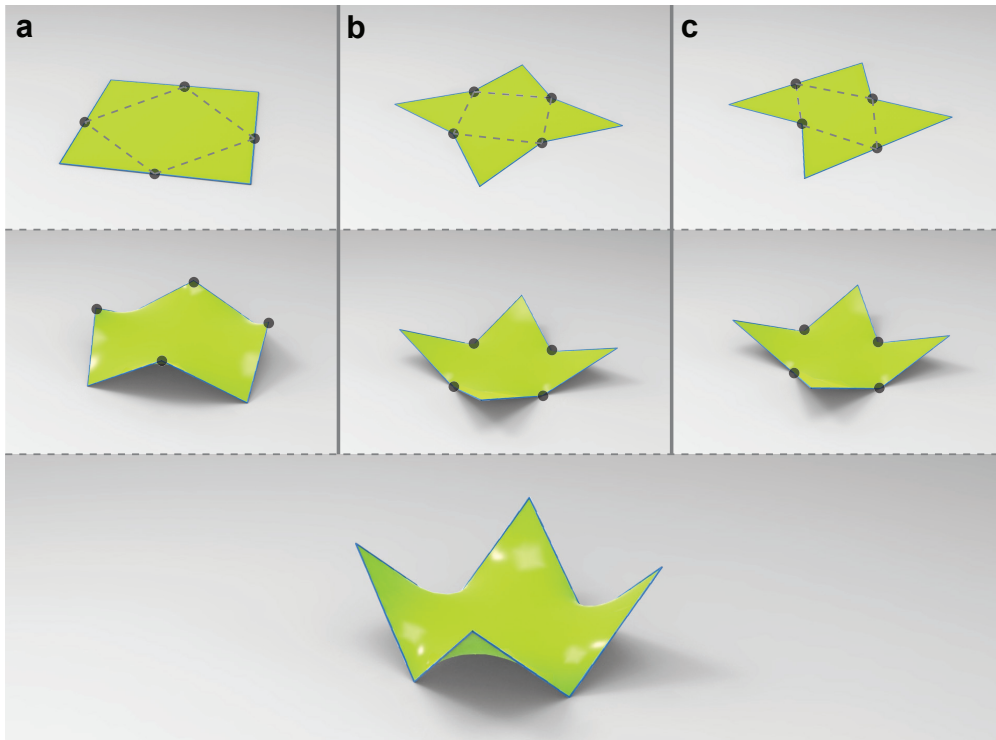


**Figure 7.11:** Three types of  $C(P)$  foldable patches. a) The square patch does allow for edge-connections but not for vertex-connections at the  $\pi/3$  vertices. b) The star patch allows for vertex-connections at the  $\pi/3$  vertices, but not for edge-connections. c) The bowtie patch allows for both vertex connections at the  $\pi/3$  vertices and edge-connections at some of its edges.

The patches illustrated in Figure 7.10a and Figure 7.10b do not require in-plane sliding during the folding motion, but are, however, not convenient for building larger  $C(P)$  morphologies. The patch in Figure 7.11a starts from a square configuration where

the hinge vertices change their angle from  $\pi$  to  $\pi/3$ . To construct a  $C(P)$  unit cell (Figure 7.6g) using these patches, however, the patches would need to be connected at the hinge vertices, which would inevitably lead to overlaps in the 2D net. The patch shown in Figure 7.11b, on the other hand, does allow vertex-connections at the fixed  $\pi/3$  vertices, but its flat configuration is a concave polygon that does not allow for any edge-connections without causing overlaps. This “star-like” patch could therefore be used to fold a  $C(P)$  unit cell using vertex-connections, but nothing more (as extensions beyond a single unit cell would require edge-connections). As compared to the two other patches, the bowtie patch shown in Figure 7.11c allows both vertex- and edge-connections, which is why this patch was used to build larger  $C(P)$  morphologies.

### 7.5.7 Alternative unit cell nets

Different unit cell nets could fold into the same translational unit cell. Figure 7.12a-d shows examples of unit cell net variations for the  $P$ ,  $D$ ,  $CLP$  and  $C(P)$  surfaces respectively, disregarding equivalent variations obtained through in-plane rotations and mirror reflections. Figure 7.12a shows four different unit cell nets for the  $P$  surface, all consisting of four vertex-connected patches. As explained in the main text, a unit cell net containing four patches would require at most three 2-coordinated vertex-connections. In case of the  $P$  surface, however, it is also possible to connect three patches at a single vertex, resulting in a net of one 3-coordinated vertex and one 2-coordinated vertex. In case of the  $D$  and  $CLP$  surfaces, all vertex-connections are two-coordinated. As such, the unit cell nets for the  $D$  and  $CLP$  surfaces contain three 2-coordinated vertex-connections. This leaves two distinct options for the  $D$  unit cell net (Figure 7.12b) and only a single option for  $CLP$  unit cell net (Figure 7.12c). Figure 7.12d displays four different nets for the  $C(P)$  unit cell, either containing five 2-coordinated vertex-connections, one 3-coordinated and three 2-coordinated vertex-connections, or two 3-coordinated and one 2-coordinated vertex-connection. The dashed (and red) lines in Figure 7.12 indicate the boundaries of the convex hull of the unit cell nets. Patch edges that lie on this boundary are admissible edges for the edge-connections in the construction of multiple-unit assemblies. It is clear from Figure 7.12 that some nets for a given unit cell have more admissible edges than other nets, making them more suitable for the expansion into larger nets. For example, the rightmost net of the  $C(P)$  surface in Figure 7.12d has only one admissible location for edge-connections (two adjacent admissible edges), while the leftmost net has three admissible locations (six admissible edges appearing in three pairs).

### 7.5.8 Alternative TPMS-based morphologies

As reported in the main text, the folding motion of larger structures is fully captured by the folding kinematics of the repeated patch and the specific connection pattern of the different patches. Figure 7.13 provides a simple example illustrating that the same apparent 2D net could give rise to very different 3D morphologies, depending on the specific connections between the individual patches. In Figure 7.13a, six flattened  $P$

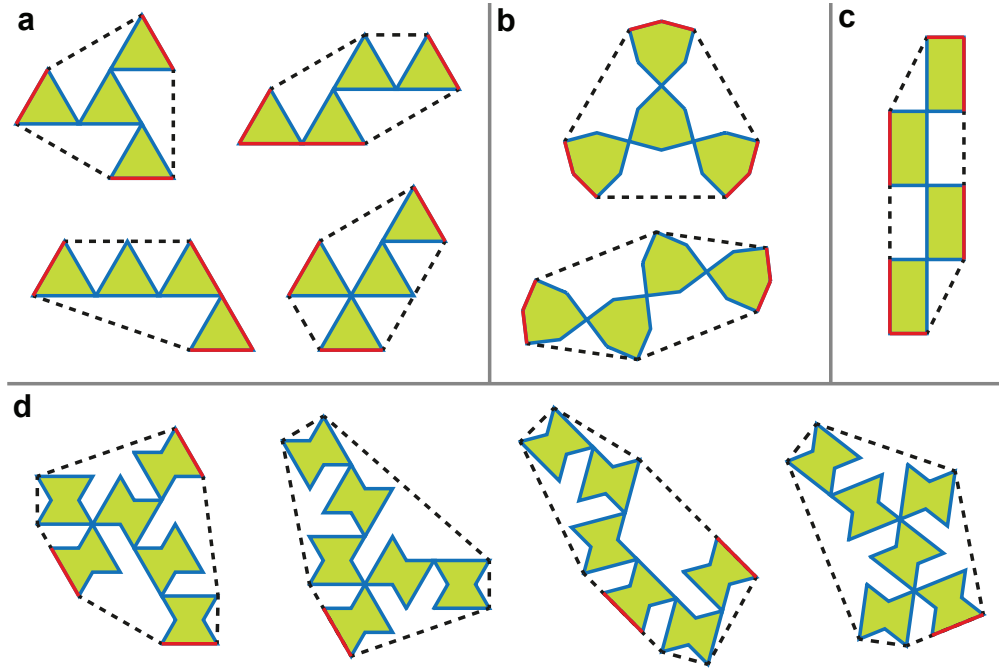


**Figure 7.12:** Variations of the unit cell net for the  $P$ ,  $D$ ,  $CLP$  and  $C(P)$  surface. The dashed (and red) lines indicate the boundaries of the convex hull, the red lines highlight the admissible edges for edge-connections a) Four different unit cell nets for the  $P$  surface, either containing three 2-coordinated connections or one 3-coordinated connection and one 2-coordinated connection. b) Two different unit cell nets for the  $D$  surface. Both unit cell nets have three 2-coordinated vertex connections. c) The only unit cell net for the translational unit cell of the  $CLP$  surface as shown in the main text. d) Four different unit cell nets for the  $C(P)$  surface, either consisting of five two-coordinated connections, one 3-coordinated connection and three 2-coordinated connections, or two 3-coordinated connections and one 2-coordinated connection.

patches are edge-connected to form a hexagonal pattern that folds into a string-like 3D configuration. The same hexagonal pattern is shown in Figure 7.13b, but now with the patches connected at different edges (highlighted by the crosses), thereby creating a very different 3D morphology. While the focus of this work has been on the folding of full, compact sections of the infinite minimal surfaces, the presented approach also enables the exploration of a richness of other 2D nets that could fold into alternative TPMS-based morphologies. An example is presented in Figure 7.13c, in which the hexagonal net of Figure 7.13b has been extended into a string-like configuration that folds into a compact periodic structure based on the  $P$  structure, although it is not complete due to the absence of some patches. An alternative approach to achieve large TPMS sections consists of folding relatively simple nets, without causing collisions, into structures that are periodic “building blocks” of the TPMS.

Figure 7.14 shows two examples for the  $CLP$  and  $D$  surfaces respectively (see also

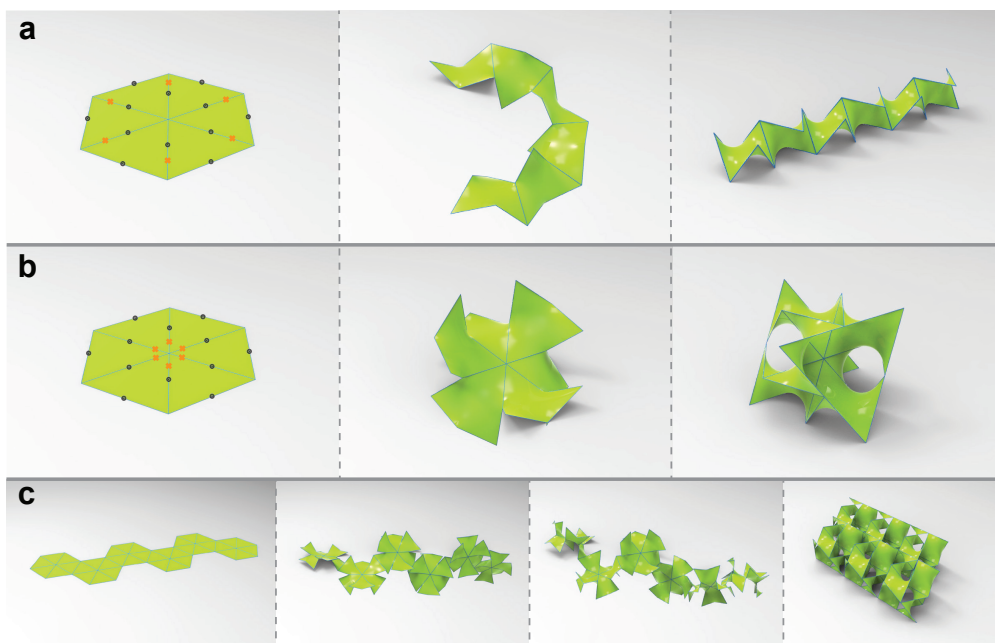


**Figure 7.13:** Alternative patch connections to build 3D morphologies. a) A hexagonal net that folds into a string-like morphology. b) The same apparent hexagonal net, but with different edge-connections, that folds into a compact 3D unit. c) Connecting the hexagonal nets of b) in a string-like connection folds into a compact (but not complete) TPMS-based structure.

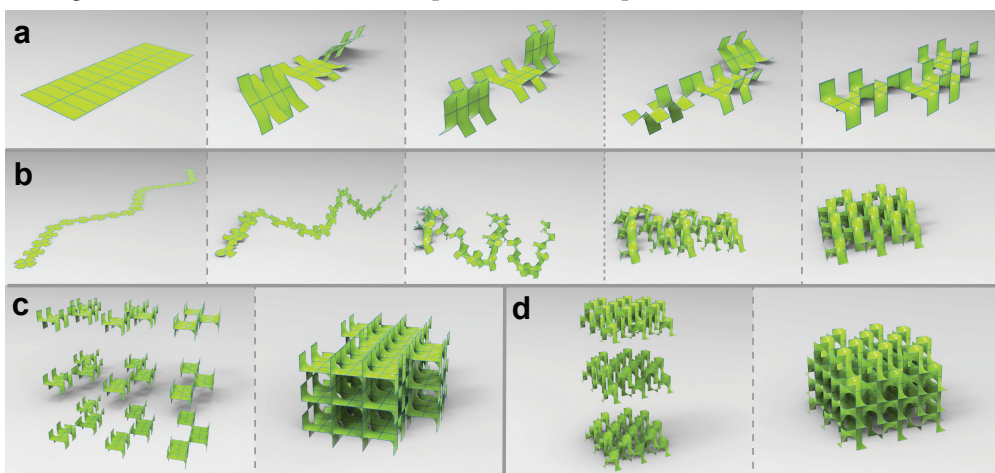


**Figure 7.14:** Constructing TPMS sections from stackable building blocks. a) A string-like *CLP* net, consisting of six unit cells. b) A string-like *D* net, consisting of 25 unit cells, that folds into a “zig-zag” layer. c-d) Stacking the *CLP* and *D* blocks, respectively, into larger TPMS sections.

Supplementary Movies 5-6<sup>37</sup>). In Figure 7.14a, a simple edge-connected net of the *CLP* surface is shown to fold into a structure containing six unit cells. The resulting structures could then be stacked together to form a larger portion of the *CLP* minimal surface

(Figure 7.14c). In Figure 7.14b, a string-like arrangement of edge-connected D patches is shown that folds into a “zig-zag” layer of  $D$  unit cells. While the current example shows  $5 \times 5$  unit cells, the foldable string could be generalized to  $n \times n$  unit cells. As shown in Figure 7.14d, the folded building blocks could then be vertically stacked into a larger TPMS portion, potentially in a manner similar to the stacking of polyhedral space-filling layers that has recently been described<sup>18</sup>.

## Bibliography

- [1] S. Hyde, Z. Blum, T. Landh, S. Lidin, B. Ninham, S. Andersson, and K. Larsson. *The Language of Shape: The Role of Curvature in Condensed Matter: Physics, Chemistry and Biology*. Elsevier Science, Amsterdam, The Netherlands, 1996.
- [2] H. A. Schwarz. *Gesammelte mathematische abhandlungen*, volume 1. Springer, Berlin, 1890.
- [3] L. Han and S. Che. An overview of materials with triply periodic minimal surfaces and related geometry: From biological structures to self-assembled systems. *Advanced Materials*, 30(17):1705708, 2018.
- [4] R. Lipowsky. The conformation of membranes. *Nature*, 349(6309):475–481, 1991.
- [5] V. Saranathan, C. O. Osuji, S. G. Mochrie, H. Noh, S. Narayanan, A. Sandy, E. R. Dufresne, and R. O. Prum. Structure, function, and self-assembly of single network gyroid (i4132) photonic crystals in butterfly wing scales. *Proceedings of the National Academy of Sciences*, 107(26):11676–11681, 2010.
- [6] S. C. Kapfer, S. T. Hyde, K. Mecke, C. H. Arns, and G. E. Schröder-Turk. Minimal surface scaffold designs for tissue engineering. *Biomaterials*, 32(29):6875–82, 2011.
- [7] F. S. L. Bobbert, K. Lietaert, A. A. Eftekhari, B. Pouran, S. M. Ahmadi, H. Weinans, and A. A. Zadpoor. Additively manufactured metallic porous biomaterials based on minimal surfaces: A unique combination of topological, mechanical, and mass transport properties. *Acta Biomater*, 53:572–584, 2017.
- [8] S. B. Blanquer, M. Werner, M. Hannula, S. Sharifi, G. P. Lajoinie, D. Eglin, J. Hyttinen, A. A. Poot, and D. W. Grijpma. Surface curvature in triply-periodic minimal surface architectures as a distinct design parameter in preparing advanced tissue engineering scaffolds. *Biofabrication*, 9(2):025001, 2017.
- [9] M. D. Turner, M. Saba, Q. Zhang, B. P. Cumming, G. E. Schröder-Turk, and M. Gu. Miniature chiral beamsplitter based on gyroid photonic crystals. *Nature Photonics*, 7(10):801–805, 2013.
- [10] O. Al-Ketan, K. A. Al-Rub Rashid, and R. Rowshan. Mechanical properties of a new type of architected interpenetrating phase composite materials. *Advanced Materials Technologies*, 2(2):1600235, 2016.
- [11] W. Lee, D. Y. Kang, J. Song, J. H. Moon, and D. Kim. Controlled unusual stiffness of mechanical metamaterials. *Sci Rep*, 6:20312, 2016.
- [12] N. Thomas, N. Sreedhar, O. Al-Ketan, R. Rowshan, R. K. A. Al-Rub, and H. Arafat. 3D printed triply periodic minimal surfaces as spacers for enhanced heat and mass transfer in membrane distillation. *Desalination*, 443:256–271, 2018.
- [13] M. L. Brongersma, Y. Cui, and S. Fan. Light management for photovoltaics using high-index nanostructures. *Nature materials*, 13(5):451–460, 2014.
- [14] T. L. Liu and C.-J. C. Kim. Turning a surface superrepellent even to completely wetting liquids. *Science*, 346(6213):1096–1100, 2014.
- [15] S. Dobbenga, L. E. Fratila-Apachitei, and A. A. Zadpoor. Nanopattern-induced osteogenic differentiation of stem cells - a systematic review. *Acta Biomater*, 46:3–14, 2016.
- [16] A. Elbourne, R. J. Crawford, and E. P. Ivanova. Nano-structured antimicrobial surfaces: From nature to synthetic analogues. *Journal of colloid and interface science*, 508:603–616, 2017.
- [17] X. Zang, C. Shen, Y. Chu, B. Li, M. Wei, J. Zhong, M. Sanghadasa, and L. Lin. Laser-induced molybdenum carbide–graphene composites for 3D foldable paper electronics. *Advanced Materials*, page 1800062, 2018.

- [18] S. Janbaz, N. Noordzij, D. S. Widyaratih, C. W. Hagen, L. E. Fratila-Apachitei, and A. A. Zadpoor. Origami lattices with free-form surface ornaments. *Science Advances*, 3(11), 2017.
- [19] S. J. P. Callens and A. A. Zadpoor. From flat sheets to curved geometries: Origami and kirigami approaches. *Materials Today*, 21(3):241–264, 2018.
- [20] R. Sawhney and K. Crane. Boundary first flattening. *ACM Transactions on Graphics (TOG)*, 37(1):5, 2017.
- [21] J. Kim, J. A. Hanna, M. Byun, C. D. Santangelo, and R. C. Hayward. Designing responsive buckled surfaces by halftone gel lithography. *Science*, 335(6073):1201–1205, 2012.
- [22] H. Aharoni, Y. Xia, X. Zhang, R. D. Kamien, and S. Yang. Universal inverse design of surfaces with thin nematic elastomer sheets. *Proceedings of the National Academy of Sciences*, page 201804702, 2018.
- [23] W. M. van Rees, E. Vouga, and L. Mahadevan. Growth patterns for shape-shifting elastic bilayers. *Proceedings of the National Academy of Sciences*, 2017.
- [24] W. Fischer and E. Koch. Spanning minimal surfaces. *Philosophical Transactions of the Royal Society of London A: Mathematical, Physical and Engineering Sciences*, 354(1715):2105–2142, 1996.
- [25] K. A. Brakke. The surface evolver. *Experimental mathematics*, 1(2):141–165, 1992.
- [26] vtk.org. vtkcurvatures class reference. <https://www.vtk.org/doc/nightly/html/classvtkCurvatures.html>, 2018.
- [27] T. Castle, M. E. Evans, S. T. Hyde, S. Ramsden, and V. Robins. Trading spaces: building three-dimensional nets from two-dimensional tilings. *Interface Focus*, 2(5):555–66, 2012.
- [28] J.-F. Sadoc and J. Charvolin. Infinite periodic minimal surfaces and their crystallography in the hyperbolic plane. *Acta Crystallographica Section A*, 45(1):10–20, 1989.
- [29] S. Hyde and S. Andersson. A systematic net description of saddle polyhedra and periodic minimal surfaces. *Zeitschrift für Kristallographie-Crystalline Materials*, 168(1-4):221–254, 1984.
- [30] E. A. Lord. Triply-periodic balance surfaces. *Colloids and Surfaces A: Physicochemical and Engineering Aspects*, 129:279–295, 1997.
- [31] E. D. Demaine and J. O’Rourke. *Geometric folding algorithms: linkages, origami, polyhedra*. Cambridge university press, 2008.
- [32] D. Hilbert and S. Cohn-Vossen. *Geometry and The Imagination*. Chelsea Publishing Company, New York, USA, 1990.
- [33] T. Castle, Y. Cho, X. Gong, E. Jung, D. M. Sussman, S. Yang, and R. D. Kamien. Making the cut: lattice kirigami rules. *Phys Rev Lett*, 113(24):245502, 2014.
- [34] A. H. Schoen. Reflections concerning triply-periodic minimal surfaces. *Interface focus*, 2(5):658–668, 2012.
- [35] E. Koch and W. Fischer. On 3-periodic minimal surfaces with non-cubic symmetry. *Zeitschrift für Kristallographie-Crystalline Materials*, 183(1-4):129–152, 1988.
- [36] J. Cui, F. R. Poblete, and Y. Zhu. Origami/kirigami-guided morphing of composite sheets. *Advanced Functional Materials*, page 1802768, 2018.
- [37] S. Callens. Chapter 7 - si movies. 4tu.researchdata online resource. <https://figshare.com/s/2c70fbc790f667d5f478>, 2021.
- [38] S. M. Felton, M. T. Tolley, B. Shin, C. D. Onal, E. D. Demaine, D. Rus, and R. J. Wood. Self-folding with shape memory composites. *Soft Matter*, 9(32):7688–7694, 2013.
- [39] X. Hu, J. Zhou, M. Vatankehah-Varnosfaderani, W. F. Daniel, Q. Li, A. P. Zhushma, A. V. Dobrynin, and S. S. Sheiko. Programming temporal shapeshifting. *Nature communications*, 7:12919, 2016.
- [40] L. Gomi and L. Mahadevan. Minimal surfaces bounded by elastic lines. *Proc. R. Soc. A*, 468(2143):1851–1864, 2012.
- [41] E. Sharon and E. Efrati. The mechanics of non-euclidean plates. *Soft Matter*, 6(22):5693–5704, 2010.
- [42] V. A. Bolaños Quiñones, H. Zhu, A. A. Solovev, Y. Mei, and D. H. Gracias. Origami biosystems: 3D assembly methods for biomedical applications. *Advanced Biosystems*, page 1800230, 2018.





# CONCLUSIONS

---

8	CONCLUDING REMARKS	247
8.1	Main findings of this thesis . . . . .	248
8.2	General discussion . . . . .	250
8.3	Future research opportunities . . . . .	252
8.4	Parting thoughts . . . . .	255
	Bibliography . . . . .	257

---



# 8

## CONCLUDING REMARKS

*“You can’t criticize geometry.  
It’s never wrong.”*  
- Paul Rand

## 8.1 Main findings of this thesis

In this thesis, we have adopted a geometric perspective in tackling mechanobiological and biomaterial challenges. The aim was to advance the understanding of the interactions between geometry and bone biology, and integrate geometry in the design of next-generation biomaterials for bone tissue engineering. Here, we summarize the main thesis findings pertaining to the three major research objectives that we identified:

### **To study the role of surface curvature on the spatiotemporal organization of cells and de novo tissue formation (Part II)**

By studying the available evidence on cell- and tissue-level curvature guidance within the framework of mean and Gaussian curvature, we found that tensile forces play a fundamental role on both the cell and tissue levels (Chapter 2). At the cell level, the interplay between actomyosin contractility and the surrounding geometry results in net forces on the nucleus, resulting in nuclear deformation and intracellular nuclear sliding, and endowing cells with a mesoscale curvature sensation ability. Moreover, cells with pronounced stress fibres have consistently been observed to avoid cell bending wherever possible. At the tissue level, surface tension emerges from cell-level contractility and causes a fluid-like behaviour in curved environments. Both individual cells and developing tissues were found to favour predominantly concave over predominantly convex regions.

To explore these phenomena more in depth, we set out to study the collective spatiotemporal organization of osteoblast precursor cells on mathematically defined, micro-engineered substrates, containing spherical, Euclidean and hyperbolic regions (Chapter 3). We found that the cells preferentially cover regions with negative minimum principal curvature ( $\kappa_2 < 0$ ). We also found that cells can collectively venture onto unfavourably curved regions, provided the distance to a region with  $\kappa_2 < 0$  is not too large. Moreover, we observed collective stress fibre alignment with the minimum principal direction on structures with sufficiently low curvature variations. At large concavities, such as the concave spherical wells, we found that the cells form multicellular bridges after several days, which eventually coalesce into detached cell sheets that span the concavity, yet remain anchored to the substrate through several cell bridges. Finally, our experiments also revealed that inhibiting cell contractility or ECM development results in weaker cell sheets and impairs the ability of cells to venture onto unfavourably curved regions.

### **To develop geometry-based tools for studying bone morphology and for designing architected materials that could serve as bone scaffolds (Part III)**

We established a framework to fundamentally quantify the local and global geometry of trabecular bone (Chapter 4). At the local level, we found that the mean, Gaussian and net curvature density maps of the trabecular interface are sensitive to morphological subtleties, such as more plate-like or rod-like morphologies, in bone from differ-

ent anatomical sites. We also found that trabecular bone does not closely approximate a minimal surface, contrary to what has often been assumed. At the global level, we observed that the scalar Minkowski functionals correlate with several traditional morphometric indices, and that the scalar  $W_3$  is more sensitive to differences in bone architecture than the equivalent traditional metric  $\chi$ . We also applied the relatively novel Minkowski tensors (rank 2 and higher) to quantify various types of bone anisotropy and ellipticity and detect differences between bone from different anatomical sites.

Next, we exploited the hyperbolic tiling theory and geometry of TPMS to establish a parametric design strategy for metabiomaterials with independently tunable properties, involving the spatial distribution of hard, soft and void phases (Chapter 5). We found that the same hyperbolic tiling projected onto the P or G surface, results in topologically different 3D networks. Computational analyses showed that our approach enables a substantial decoupling between the permeability and elastic mechanical properties of the structures, extending the property space beyond what can be achieved with uniphase structures. Moreover, our data showed that the elastic anisotropy can be tuned across a wide spectrum, by varying the stiffness or volumetric ratios of the hard and soft materials. Finally, we showed that our designs could successfully be fabricated using multi-material 3D printing of hard and soft polymers.

### **To uncover geometric rules and develop folding algorithms for the 2D-to-3D fabrication of architected porous biomaterials (Part IV)**

We explored the geometrical foundations of origami and kirigami, and the ability of both techniques to endow flat sheets with intrinsic (Gaussian) curvature (Chapter 6). By invoking concepts such as the surface metric and the Gauss map, we demonstrated that origami is inherently limited by its developability. Nevertheless, we identified several origami classifications that enable the generation of apparent intrinsic curvature. We furthermore demonstrated that the ability to cut (and glue) within kirigami affords slightly more possibilities to obtain intrinsic curvature, though only at isolated points.

To overcome these inherent limitations, we developed a novel folding strategy that employs controlled material stretching to enable the folding of non-developable 3D assemblies based on TPMS (Chapter 7). Our approach leveraged the fact that certain TPMS can be constructed from symmetric repetitions of skew polygonal patches with straight edges. Through kinematical analyses, we found that these patches could be flattened to planar polygons by adding hinges at certain vertices and allowing the faces to stretch, enabling smooth folding/unfolding. By attaching several patches along edges or vertices – while respecting the hyperbolic symmetries of TPMS – we could build 2D nets that smoothly and predictably transform from a planar configuration to the final TPMS structure. We found that delaying the folding of certain patches or unit cells enables one to avoid collisions during the folding sequence. Finally, we physically demonstrated self-folding TPMS structures by 3D printing a (semi-)rigid foldable frame and attaching this to a biaxially pre-strained elastomer sheet.

## 8.2 General discussion

This thesis covered a broad set of geometry-centred explorations, ranging from cell-material interactions to origami-based folding. Here, we reflect on the relevance of our findings, and identify challenges and outstanding questions.

### On the relevance of geometry in cell-environment interactions

While the effect of simple geometrical cues has long been observed (*e.g.* the term “contact guidance” is almost 80 years old<sup>1</sup>), a much more fundamental and widespread interest in geometry-guided cell response has emerged in recent years, fuelled by advances in microfabrication. When considering cells as mechanical agents that generate tensile forces, the shape of the extracellular environment could be seen as a boundary condition that controls the cellular force distributions and deformations. As such, it could be argued that geometry is not *per se* an independent mechanobiological cue, but instead regulates the effect of cell-generated forces. This is corroborated by ours and others’ evidence that up- or downregulating contractility affects cell and tissue organization in controlled-geometry environments. The interplay between shape and force has been studied across a wide spectrum of extracellular geometries, such as planar adhesive islands (2D) or curved substrates (2.5D). In these examples, cells are attached to the substrate on one side only, giving rise to an apicobasal polarity in their interaction with geometry. In truly 3D environments, such as inside macroporous hydrogels or fibrous scaffolds, cells might experience the shape of their environment along their entire membrane, establishing even more complex force-geometry interactions. Furthermore, the interplay between cells and geometry is highly dynamic, not only due to cell migration, but also due to aspects such as contractility-induced deformation, ECM deposition, or multi-cellular bridge formation. Another crucial aspect to consider is the scale of the extracellular shapes. In Chapters 2 and 3, we have considered mesoscale substrate curvatures, *i.e.* radii of curvature in the order of cell size and slightly larger. Landscapes with much larger radii of curvature would be perceived as flat by the cells, similarly to how humans do not “feel” the curvature of the Earth. At the other side of the spectrum are features with very small radii of curvature, *e.g.* subcellular-scale nanopillars, that interact with cells through highly localized membrane deformations, triggering much more specific mechanotransduction pathways. Moreover, cells might encounter hierarchically shaped environments, providing different, potentially conflicting, geometrical cues across multiple length scales<sup>2</sup>.

It is clear that geometry deserves a central position in mechanobiology. However, much of the underlying biological principles remain elusive. For example, it is still unclear to what extent complex geometrical features control stem cell fate, or how geometry-guidance at the cell level is translated to *de novo* tissue growth. Additionally, cells are exposed to many other biophysical and biochemical cues beyond geometry *in vivo*. It remains an open question how these other cues might alter, enhance, or counteract the effects of extracellular geometry, and which cues turn out to be most important, *e.g.* from a tissue engineering perspective.

## On suitable architectures for porous scaffolds

The advent of additive manufacturing has unlocked the ability to rationally design and reproducibly fabricate a vast range of scaffold architectures, offering much more design freedom than with conventional technologies such as solvent leaching, freeze drying, gas foaming, or phase separation<sup>3</sup>. Subsequently, the challenge has become to optimize the scaffold architecture to meet a desired performance within the triad of mechanical, mass transport and biological properties<sup>4,5</sup>.

From a geometric perspective, porous scaffolds are hyperbolic on average (Chapter 2). The Gauss-Bonnet theorem dictates that the high topological complexity of such porous structures must be accompanied by a sufficiently high amount of regions with negative Gaussian curvature. The distributions of such regions varies among the different types of scaffold architectures. In cylindrical strut-based scaffolds, all of the negative Gaussian curvature is concentrated at the strut intersections. In shell-based scaffolds, such as those based on TPMS, the negative Gaussian curvature is smoothly distributed along the entire scaffold surface. Our experiments (Chapter 3) indicated that preosteoblasts favour such saddle-shaped regions over cylindrically shaped regions. Moreover, recent *in vivo* results showed predominant tissue regeneration at the (negatively-curved) intersections of strut-based scaffolds<sup>5</sup>. While further research is required, these observations seem to imply that scaffolds with large regions of negative Gaussian curvature might be more attractive from a tissue regeneration perspective.

A commonly made claim in bone scaffold design studies is that the scaffold architecture should mimic that of trabecular bone. However, it remains unclear whether closely mimicking the healthy, homeostatic architecture of trabecular bone would enhance the tissue regeneration performance of the resulting scaffold, *e.g.* in the treatment of segmental defects. If the goal is to achieve as fast *in situ* tissue regeneration as possible, should the “starting scaffold” then replicate the healthy “end-state” of bone? During endogenous healing, bone formation occurs through a complex series of steps, involving dynamic tissue changes and remodelling, implying that the “final” architecture of bone is not yet present during initial tissue growth<sup>6</sup>. Moreover, there has recently been an increasing interest in shifting bone tissue engineering strategies from intramembranous ossification (IO) approaches, often lacking functional vascularity, towards “developmentally-inspired” endochondral ossification approaches (EO), involving a cartilaginous intermediary<sup>7</sup>. For such EO-based regeneration strategies, the biomaterial scaffolds tend to be softer, and would likely also have different geometric requirements than in IO-based approaches<sup>8</sup>. As such, the “ideal” geometric template from a tissue regeneration perspective remains elusive.

Finally, we note that most of the scaffold designs thus far are deterministic and periodic in nature. Well-known examples are the diamond strut-based scaffolds or the TPMS shell-based scaffolds. The latter types are interesting due to their high surface-to-volume ratio and efficient mechanical performance. However, stochastic shell-based structures might be even more attractive, as they offer a much larger design space and are not sensitivity to symmetry-breaking defects<sup>9</sup>. Following advances in data-driven

design and free-form fabrication, it is anticipated that such stochastic, yet highly tunable morphologies will adopt a more prominent position among tissue scaffold designs in the future<sup>10</sup>.

### On the geometric challenges of 4D printing

Since its inception, 4D printing has been considered a promising paradigm for a variety of biomedical applications, including digestible microrobots, controlled drug delivery devices, or smart implants<sup>11;12</sup>. Our interest has primarily been on the 2D-to-3D fabrication of surface-functionalized porous scaffolds. As mentioned above, such topologically complex structures belong to the realm of hyperbolic geometry, which conflicts with the Euclidean nature of the planar starting materials and origami-based folding techniques. Hence, there are “geometric barriers” that make 2D-to-3D fabrication of porous scaffolds inherently difficult. In the case of plate-based polyhedral structures, where hyperbolic curvature appears at discrete locations, these limitations have been overcome by rationally “cutting and gluing” the planar materials to distribute localized Gaussian curvature after folding. However, for smoothly-curved shell-based structures, such as those based on TPMS, 2D-to-3D fabrication is theoretically only possible when the planar materials are allowed to stretch (Chapter 7). The topological complexity of porous scaffolds not only has consequences for the average Gaussian curvature, but also implies that any folding strategy will entail kinematically complex folding motions, demand high control over the folding triggers, and require locking mechanisms at many locations. Thus, while we showed that the 2D-to-3D fabrication of such complex structures is feasible theoretically, there are still many challenges that need to be addressed before it becomes possible practically.

In this regard, an interesting avenue towards the 2D-to-3D fabrication of such topologically complex structures would be to combine folding with assembly. Specifically, smaller and simpler building blocks could be folded first, and consequently combined into a larger and more complex structure, for example using robotic pick-and-place approaches or magnetism-based self-assembly<sup>13;14</sup>. This could alleviate some of the complexities involved in trying to fold an entire scaffold structure from a single planar sheet.

## 8.3 Future research opportunities

While this thesis has contributed to novel geometric perspectives on cell-environment interactions and biomaterial design, many challenges are still outstanding. Here, we outline some general and more specific opportunities for future research. This list is not exhaustive, but rather proposes potential topics of investigation based upon the insights we have obtained in this thesis, as well as on ongoing developments in the field.

### Regarding the study of cell-environment interactions

From a tissue engineering perspective, there is a tremendous potential for using geometry to steer cell behaviour and tissue growth in engineered environments. However, leveraging this potential requires critical challenges to be addressed first:

- The biological mechanisms underlying mesoscale geometry sensation and response should be better understood. While specific mechanotransduction pathways have been identified for subcellular geometrical interactions, such insights are generally lacking at a larger scale. Specifically, the interplay between dynamic forces and the deformations of the cell membrane and nucleus should be investigated. Additionally, the role of 3D geometrical cues on stem cell fate should be studied more in depth.
- There is a need for micro-engineered, multi-cue environments, *i.e.* *in vitro* platforms that present controlled combinations of specific cues, such as stiffness gradients, mesoscale geometry, nanoscale topography, or chemical gradients. It is important to investigate how different cue combinations might have conflicting or synergistic effects on cells, and which biochemical and biophysical signals generally dominate in such multi-cue environments.
- More advanced *in vitro* platforms that facilitate studying dynamic cell-environment interactions should be developed (the *in vivo* cell-ECM interactions are also highly dynamic). Examples could be the dynamic control over the strain patterns, local shape variations, or stiffness distributions in the cell culture substrates. This will likely require the use of responsive materials with controlled external triggers, dedicated bioreactor systems, as well as high-resolution dynamic imaging modalities.
- The mechanisms through which cell-level geometry-guidance gives rise to tissue-level organization and maturation should be investigated. For example, how does curvotaxis (curvature-guided migration of individual cells) affect the patterning of larger cell collectives and ECM organization? What are the effects of complex geometric environments on ECM mineralization? How long do geometric cues remain relevant in the shaping of tissues? Answering these questions will involve dedicated experiments with time-lapsed imaging and quantitative longitudinal monitoring. Moreover, more in-depth investigations will be needed to uncover how well *in vitro* studies recapitulate *in vivo* geometric control of tissue growth.
- Research into cell-geometry interactions would benefit from more systematic, high-throughput investigations, using platforms that contain a wide variety of different mesoscale geometrical features. Such platforms have been developed for systematically screening the effect of a wide range of topographical features in a “materiomics” approach (*e.g.* topoChip), and these could likely be extended to study the effect of 3D mesoscale geometries<sup>15</sup>. These high-throughput platforms could also aid in elucidating the role of geometry across a wide range of cell types or co-cultures (*e.g.* epithelial cells *versus* fibroblastic-like cells). The high combinatorial complexity and large amounts of data inherent in such (au-

tomated) high-throughput screening studies would also interface well with machine learning techniques to expedite the discovery of “optimal” geometries<sup>16</sup>.

### Regarding high-resolution biofabrication

In recent years, new developments in biofabrication technologies have emerged in rapid succession, and this is expected to continue in the future. The increasing resolution and precision of these techniques is enabling unprecedented control over the geometry (and other characteristics) of the local cell environment. However, several challenges need to be addressed in future research to advance the success of these techniques in specific applications, such as on-chip disease models and tissue engineering:

- Light-based techniques, such as those relying on multiphoton polymerization, have attracted great interest for high-resolution fabrication of local cell environments<sup>17</sup>. However, more efforts are needed to extend the range of photosensitive polymers that are suitable for high-resolution fabrication and also exhibit good cytocompatibility<sup>18</sup>. In this regard, semi-synthetic hydrogel systems, designed to be permissive and promoting ECM-mimics<sup>19</sup>, present promising avenues.
- There is currently a wide spectrum of additive manufacturing techniques that could be applied in biomedical applications. For tissue engineering scaffolds, however, current techniques typically require a stringent trade-off between overall size and resolution. For example, selective laser melting (SLM) enables the printing of defect-size scaffolds (*e.g.* mm-cm range), yet does not offer sufficiently high resolution to tightly control the local geometries that cells will encounter. Two-photon polymerization (2PP), on the other hand, offers resolution at the (sub-)cellular scale, but is limited by its long processing time and small overall sizes. Future developments are necessary to combine the best of both worlds, and realize high-resolution tissue scaffolds in the mm-cm range.
- Future developments should aim at advancing multi-material printing capabilities in high-resolution biofabrication. The ability to combine widely different materials in complex spatial composites radically expands the design space and offers tunability beyond what can be achieved with single materials (see Chapter 5). Moreover, the different materials could be optimized for specific functions, *e.g.* by combining a stiff material to carry load with a soft cell-optimized hydrogel. Additionally, multi-material printing could be a powerful enabler for the development of shape-shifting bio-constructs, *e.g.* by combining different materials that shrink or swell by varying amounts in response to external triggers.

### Regarding computational modelling

*In silico* studies can complement experimental studies in developing a mechanistic understanding of cell and tissue behaviour, and can expedite the discovery of optimized biomaterials or scaffold architectures. However, such modelling efforts should be enhanced to more explicitly address the role of extracellular geometry:

- More detailed mechanics-based cell models should be developed, involving the

(dynamic) contributions of, for example, the contractile apparatus, membrane and nuclear deformability, and the presence of the cytosol, as well as the contribution of extracellular geometry, stiffness and adhesion<sup>20</sup>. Finite element modelling (FEM) would constitute a promising avenue in this endeavour. However, these types of models would require extensive validation with experimental data. Hence, dedicated experimental studies will be required to probe cell mechanics in controlled environments, for example using 3D traction force microscopy, high-resolution time-lapsed imaging, and atomic force microscopy (AFM).

- Future developments should aim at establishing more generalized tissue growth models, that can be used to simulate tissue growth on arbitrary scaffold geometries. Those tissue-level models should simultaneously take into account the mechanics of the developing tissue, the presence of external loading (*e.g.* through fluid flow) and the geometric boundary conditions<sup>21;22</sup>. Such models could be validated using experimental data obtained from longitudinal monitoring of *in vitro* tissue growth on additively manufactured micro-scaffolds.
- There is a need for more inverse-design algorithms in the quest for optimized tissue engineering scaffolds. In particular, it would be interesting to establish inverse tissue growth models, based on (“forward”) experimental data, that could be applied to compute scaffold geometries that enhance the growth rate and control the organization of the developing tissue.

## 8.4 Parting thoughts

Through advances in biofabrication and materials science, the available design space to biomaterial designers is rapidly expanding. In this work, we have approached a series of biomaterial-related challenges through the goggles of geometry, often by relying on the concept of surface curvature. We advocate that geometric considerations are important for biomaterial designers, not only because of their fundamental role in tissue morphogenesis, but especially because geometric cues can be precisely engineered in biomaterial systems to steer cell and tissue response. While many of the underlying mechanisms remain elusive, and several design and fabrication challenges ought to be addressed, we predict exciting opportunities for the ancient field of geometry in future biomaterials.

We end by revisiting Johannes Kepler’s 400 year-old statement that was highlighted in the introduction of this thesis. Here, we propose an adaption to this statement, reflecting the central perspective of our investigations:

*“Ubi biologia, ibi geometria”*

“Where there is biology, there is geometry.”

## Bibliography

- [1] P. Weiss. Experiments on cell and axon orientation in vitro: the role of colloidal exudates in tissue organization. *Journal of Experimental Zoology*, 100(3):353–386, 1945.
- [2] M. Werner, N. A. Kurniawan, G. Korus, C. V. Bouten, and A. Petersen. Mesoscale substrate curvature overrules nanoscale contact guidance to direct bone marrow stromal cell migration. *Journal of The Royal Society Interface*, 15(145):20180162, 2018.
- [3] D. W. Huttmacher. Scaffold design and fabrication technologies for engineering tissues—state of the art and future perspectives. *Journal of Biomaterials Science, Polymer Edition*, 12(1):107–124, 2001.
- [4] S. Ehrig, B. Schamberger, C. Bidan, A. West, C. Jacobi, K. Lam, P. Kollmannsberger, A. Petersen, P. Tomancak, and K. Kommareddy. Surface tension determines tissue shape and growth kinetics. *Science Advances*, 5(9):eaav9394, 2019.
- [5] M. Paris, A. Gotz, I. Hettrich, C. M. Bidan, J. W. C. Dunlop, H. Razi, I. Zizak, D. W. Huttmacher, P. Fratzl, G. N. Duda, W. Wagermaier, and A. Cipitria. Scaffold curvature-mediated novel biomineralization process originates a continuous soft tissue-to-bone interface. *Acta Biomaterialia*, 60:64–80, 2017.
- [6] B. M. Willie, A. Petersen, K. Schmidt-Bleek, A. Cipitria, M. Mehta, P. Strube, J. Lienau, B. Wildemann, P. Fratzl, and G. Duda. Designing biomimetic scaffolds for bone regeneration: why aim for a copy of mature tissue properties if nature uses a different approach? *Soft Matter*, 6(20), 2010.
- [7] E. J. Sheehy, D. J. Kelly, and F. J. O'Brien. Biomaterial-based endochondral bone regeneration: a shift from traditional tissue engineering paradigms to developmentally inspired strategies. *Materials Today Bio*, 3:100009, 2019.
- [8] A. Petersen, A. Princ, G. Korus, A. Ellinghaus, H. Leemhuis, A. Herrera, A. Klaumünzer, S. Schreivoegel, A. Woloszyk, and K. Schmidt-Bleek. A biomaterial with a channel-like pore architecture induces endochondral healing of bone defects. *Nature communications*, 9(1):1–16, 2018.
- [9] C. M. Portela, A. Vidyasagar, S. Krödel, T. Weissenbach, D. W. Yee, J. R. Greer, and D. M. Kochmann. Extreme mechanical resilience of self-assembled nanolabyrinthine materials. *Proceedings of the National Academy of Sciences*, 117(11):5686–5693, 2020.
- [10] S. Kumar, S. Tan, L. Zheng, and D. M. Kochmann. Inverse-designed spinodoid metamaterials. *npj Computational Materials*, 6(1):1–10, 2020.
- [11] C. L. Randall, E. Gultepe, and D. H. Gracias. Self-folding devices and materials for biomedical applications. *Trends Biotechnol*, 30(3):138–46, 2012.
- [12] B. Gao, Q. Yang, X. Zhao, G. Jin, Y. Ma, and F. Xu. 4D bioprinting for biomedical applications. *Trends in biotechnology*, 34(9):746–756, 2016.
- [13] D. H. Gracias, V. Kavthekar, J. C. Love, K. E. Paul, and G. M. Whitesides. Fabrication of micrometer-scale, patterned polyhedra by self-assembly. *Advanced Materials*, 14(3):235, 2002.
- [14] D. H. Gracias, J. Tien, T. L. Breen, C. Hsu, and G. M. Whitesides. Forming electrical networks in three dimensions by self-assembly. *science*, 289(5482):1170–1172, 2000.
- [15] H. V. Unadkat, M. Hulsman, K. Cornelissen, B. J. Papenburg, R. K. Truckenmüller, A. E. Carpenter, M. Wessling, G. F. Post, M. Uetz, and M. J. Reinders. An algorithm-based topographical biomaterials library to instruct cell fate. *Proceedings of the National Academy of Sciences*, 108(40):16565–16570, 2011.
- [16] A. Vasilevich, A. Carlier, D. A. Winkler, S. Singh, and J. de Boer. Evolutionary design of optimal surface topographies for biomaterials. *Scientific Reports*, 10(1):1–10, 2020.
- [17] M. Lee, R. Rizzo, F. Surman, and M. Zenobi-Wong. Guiding lights: tissue bioprinting using photoactivated materials. *Chemical Reviews*, 120(19):10950–11027, 2020.
- [18] J. Song, C. Michas, C. S. Chen, A. E. White, and M. W. Grinstaff. From simple to architecturally complex hydrogel scaffolds for cell and tissue engineering applications: Opportunities presented by two-photon polymerization. *Advanced healthcare materials*, 9(1):1901217, 2020.
- [19] M. W. Tibbitt and K. S. Anseth. Hydrogels as extracellular matrix mimics for 3D cell culture. *Biotechnology and bioengineering*, 103(4):655–663, 2009.
- [20] M. Vassaux, L. Pieuchot, K. Anselme, M. Bigerelle, and J.-L. Milan. A biophysical model for curvature-guided cell migration. *Biophysical journal*, 117(6):1136–1144, 2019.

- 
- [21] F. D. Fischer, G. A. Zickler, J. W. Dunlop, and P. Fratzl. Tissue growth controlled by geometric boundary conditions: a simple model recapitulating aspects of callus formation and bone healing. *Journal of The Royal Society Interface*, 12(107):20150108, 2015.
- [22] Y. Guyot, I. Papantoniou, F. P. Luyten, and L. Geris. Coupling curvature-dependent and shear stress-stimulated neotissue growth in dynamic bioreactor cultures: a 3D computational model of a complete scaffold. *Biomech Model Mechanobiol*, 15(1):169–80, 2016.



# VI

## EXTRA

---

ACKNOWLEDGEMENTS	261
LIST OF PUBLICATIONS	265
CURRICULUM VITAE	267

---



# ACKNOWLEDGEMENTS

Ever since I was a child, I have been a great fan of the trilogy *The Lord of the Rings*, in which a “fellowship of the ring” of very different characters undertakes an ambitious journey across Middle Earth to destroy a magical ring in the fires of Mordor. The central character along this quest is Frodo, a simple and ordinary hobbit who ends up being the chosen ring bearer. As a consequence, Frodo has to carry the main burden throughout the entire journey, which is riddled with obstacles, unexpected detours, stressful experiences, and seemingly insurmountable challenges. However, with the invaluable help of the other members of the fellowship, Frodo eventually manages to reach Mordor and destroy the ring, thereby defeating the enemy.

I cannot help but feel like the PhD journey exhibits some parallels to Frodo’s quest. Four years ago, I was a simple hobbit entering the world of science, accepting a serious commitment and embarking on a magical journey. Just like Frodo’s journey, mine was riddled with obstacles, unexpected detours, stressful experiences and major challenges. However, it was also a beautiful, passionate and rewarding period of growth that I will cherish forever. And just like Frodo, I had to carry most of the (sometimes heavy) load along this path myself, but I would have never succeeded without the help of the many people in my “fellowship of the PhD”, for which I will be forever grateful.

First of all, I am grateful to **Amir** for giving me so many opportunities and supporting me along the way. I still vividly remember being a bit overwhelmed after my first day (you know that I hardly slept that night). However, you provided a guiding light and helped me on my way. During the next four years, you always provided opportunities for growth and development, you helped me pursue a broad range of topics and you enabled me to acquire many different skills. I have always appreciated your approachability, down-to-earthness, blazing fast review speed, and openness to discuss whatever topic at any possible time. You were the “Gandalf” in my fellowship, introducing me to the ins-and-outs of Academia, sharing wisdom, and always seeing potential in me. **Lidy**, I am truly thankful for the way in which you have embraced me in the CCB-team. I came in with a very different background, unaware of many of the complexities of biological experiments. From the first moment that we worked together, you invested a lot of time in me and helped me wherever it was needed. You are a truly kind person, with an eye for detail and a great sense of commitment to improving the lab operations. I only regret not having worked with you sooner. **Iulian, Jie** and **Paul**, I want to thank you for our many enjoyable interactions about education, research, and life in general. We shared many nice moments in the hallway or at the coffee machine, and I appreciate how you always took the time to discuss, and showed interest in my personal life. I am

also thankful to **Nazli** and **Mohammad**, the two newest staff members in the group. **Nazli**, I will always remember how kindly you welcomed me in your office when I joined, and how honest, gentle and open you were throughout all our interactions. We shared many laughs over the years, but also had deep scientific discussions, and I truly enjoyed working with you on educational activities over the years. **Mohammad**, I have always appreciated your ability to help others with a smile, while being swamped with work yourself. Both of you are great examples that hard work pays off, and I am confident you will keep on doing great in the future. I am also grateful to **Duncan** and **Ralph**, for kindly hosting me at ETH during my research visit. While the physical visit was cut short due to the pandemic, I still felt like a proper member of your team. I learned a lot from working with both of you, and I am looking forward to our future interactions.

Working in a scientific laboratory is virtually impossible without the assistance of highly skilled staff members that are dedicated to maintaining safe, reliable and high-standard lab operations. I was lucky enough to be supported by two of those wonderful people, **Sander** and **Michelle**. **Sander**, I am very grateful for all of your help and insights throughout the years. Your knowledge and skills related to AM, mechanical testing and design have been extremely valuable. It has been a pleasure to work with you (your door was always open to me), and I have always enjoyed our chats about cycling, Tanthof, and funny Belgian customs. **Michelle**, I am truly thankful for your training in the CCB lab, and for your involvement in our work. I will always fondly remember our chats about planning a wedding, visiting Aruba, or life in general, while working in the lab. Without your help, I would not have been able to do many critical experiments in this dissertation. I also want to acknowledge the “silent heroes” of our department: **Mirjam**, **Angelique**, **Sabrina** and **Marjolijn**, for ensuring smooth operations in our department and always helping me with complicated administrative tasks or the ordering of new equipment.

While I have been mentored by several people, I have served as a mentor and supervisor to several students as well. In particular, I would like to thank **Alina** and **Rafael** for our pleasant weekly interactions during your MSc thesis project, and for giving me the opportunity to grow in a supervisory role. I am proud of what we achieved together, I enjoyed our many moments, and I am convinced you both have a bright career ahead.

PhD candidates at TU Delft are, in general, in a very privileged position, as we have access to great resources, knowledgeable staff members and high-quality facilities. However, I feel extra lucky due to all the amazing PhD/Postdoc/teacher colleagues I have had the pleasure to spend time with, many of whom I consider my friends now. **Bob**, **Eric**, **Fabian**, **Helda**, **Jiahui**, **Juan**, **Katerina**, **Kirsten**, **Mahdiyeh**, **Mahya**, **Marike**, **Maryam**, **Mauricio**, **Merle**, **Niko**, **Pedro**, **Pier**, **Shahram**, **Teunis**, **Yageng**, thank you for all the great moments we shared together. In particular, I want to express my gratitude to a few other people, who made my PhD journey so much more enjoyable. **Costanza**, we have shared many laughs and nice chats over the years, as well as some recipes, which I have always enjoyed. **Ingmar**, my scientific twin, I am grateful for all the great moments we shared, and I will particularly treasure our Sci-comm adventures. **Khashayar**,

---

thank you for selflessly helping me so often, and for your kindness and honesty in our discussions. **Françoise**, you are one of the kindest people I know, and I am thankful for getting to know you (and Thomas and Alex). I am indebted to you for making me feel at home in the beginning of the PhD, and for all the nice moments we enjoyed. While I am writing this, I am enjoying one of Ben's Cookies that you so kindly sent me to ease my self-isolation period. **Eline**, we shared many things over the past years: laughs, complaints, our office, Flemish language confusion, and our love for chocolate. I have always enjoyed the moments we spent together, both during and outside office hours, and I look forward to seeing all the adventures you will take on in the future.

Contrary to what is often believed and assumed, PhD candidates do have a social life as well. My life outside of Academia is filled with people that deserve special thanks for the way they have supported me throughout this journey. I am grateful to my best friends **Pieter-Jan** en **Michael**, for your unwavering support, your ability to put things in perspective, and your commitment to understand the obstacles I faced. I probably do not say this enough, but I am deeply grateful for our friendship, and I am impressed by the ways you approach the challenges of life. Both of you have shown extreme resilience in the pursuit of your passions, for which I have the utmost respect. The evenings, weekends and holidays we spent together have always taken my mind off my PhD, and I have always enjoyed our dinners, long discussions, and board games (means a lot coming from a sore loser). Our work often leads us to different places, but fate seems to always bring us back together, so I look forward to all the precious moments we will share in the future. I will be forever indebted to my **parents**, who have supported my journey at this university ever since I first mentioned it as a fifteen-year-old reading an article about the aircraft of the future. Having reached this point, I realize how much you have nurtured my passion for science, drive to learn, and ambition to constantly challenge myself. I am grateful for all the opportunities you have given me, such as enabling me to study in different countries in a carefree manner, and for all your love and support throughout the years. I hope to one day be as good a parent as you are. To my siblings **Thomas**, **Manon** and **Louis**, thank you for being the best brothers and sister I could wish for. I hope you all realize how much I look up to each of you, and how proud I am to be your older brother. You are all three stronger and more disciplined than I am, and I am sure you will shine bright in your future endeavors. I am also grateful to my in-laws, **Gilles**, **Anne**, and **Sophie** for their continuous support and interest in my work.

Every connoisseur of *The Lord of the Rings* knows that Frodo is not the real hero of the story, but that it his companion Sam. Sam was the only member of the fellowship who was truly next to Frodo's side for the entire journey, and who always fought on his behalf. At the end of the trilogy, when Frodo is totally exhausted and cannot continue, Sam speaks the famous words "*I can't carry it for you, but I can carry you*", after which he carries Frodo to the endpoint of their journey to complete their quest. Dear **Delphine**, my lovely wife, you are the "Sam" in my story. Without you, I would be nowhere near the end of this PhD. You have been by my side for almost ten years now, and I am

immensely grateful for your unwavering love and support. During the past four years, you have lifted my spirits when times were tough, helped me crack difficult problems, and carried me over challenging obstacles, all while completing your own PhD journey (and doing so marvelously). I look up to you, not only as a scientist, but also as a person, and I am so proud and happy that I am now able to call you my wife. You are my soulmate, the one person I can face the world with, and my biggest supporter. We do not know where the wind will take us, but it will take us there together. Thank you, all of you.

# LIST OF PUBLICATIONS

## A. Publications

- **Callens, S.J.P., Bergsma, O.K.,** Two-matrix composites: carbon fiber micropultrusions embedded in flexible epoxy matrices (2018), *Composites Part A: Applied Science and Manufacturing*, 114, 1-12.
- **Callens, S.J.P., Zadpoor, A.A.,** From flat sheets to curved geometries: origami and kirigami approaches (2018), *Materials Today*, 21, 241-264.
- **Callens, S.J.P., Tümer, N., Zadpoor, A.A.,** Hyperbolic origami-inspired folding of triply periodic minimal surface structures (2019), *Applied Materials Today*, 15, 453-461.
- **Callens, S.J.P., Uyttendaele, R.J.C., Fratila-Apachitei, L.E., Zadpoor, A.A.,** Substrate curvature as a cue to guide spatiotemporal cell and tissue organization (2020), *Biomaterials*, 232, 229739.
- **Callens, S.J.P., Tourolle, D.C.B., Müller, R. Zadpoor, A.A.,** The local and global geometry of trabecular bone (2020), in revision, preprint available on bioRxiv.
- **Callens, S.J.P., Fan, D., van Hengel, I.J., Minneboo, M., Fratila-Apachitei, L.E., Zadpoor, A.A.,** Emergent collective organization of bone cells in complex curvature fields (2020), in revision, preprint available on bioRxiv.
- **Callens, S.J.P., Arns, C., Kuliesh, A., Zadpoor, A.A.,** Decoupling minimal surface metamaterial properties through multi-material hyperbolic tilings (2021), *Advanced Functional Materials* (accepted).
- **Mirzaali, M.J., Ghorbani, A., Nakatani, K., Nouri-Goushki, M., Tümer, N., Callens, S.J.P., Janbaz, S., Accardo, A. Bico, J., Habibi, M., Zadpoor, A.A.,** Curvature induced by deflection in thick meta-plates (2021), *Advanced Materials* (accepted).

## B. Conference presentations

- **Callens, S.J.P., Bergsma, O.K.,** Two-matrix composites, Dutch Materials, Utrecht, The Netherlands (2017, poster presentation).

- **Callens, S.J.P., Zadpoor, A.A.,** Metabiomaterials based on minimal surface skeletal nets, International Mechanical Engineering Conference and Exhibition, Pittsburgh, USA (2018, oral presentation).
- **Callens, S.J.P., Zadpoor, A.A.,** Bridging the Euclidean with the hyperbolic: hyperbolic origami-inspired folding, Origami & Deployable Mechanisms, Okinawa, Japan (2019, invited oral presentation).
- **Callens, S.J.P., Zadpoor, A.A.,** Microscale substrate curvature regulates spatiotemporal organization of preosteoblasts, Dutch Biomaterials & Tissue Engineering (NBTE) Annual Meeting, Lunteren, The Netherlands (2019, oral presentation).
- **Callens, S.J.P., Zadpoor, A.A.,** How soap films inspire 3D-printed bone scaffolds, Meeting Materials M2i, Noordwijkerhout, The Netherlands (2019, invited oral presentation).
- **Callens, S.J.P., Zadpoor, A.A.,** Curvature-guided cell behaviour on mathematically defined, microfabricated substrates, Mechanics of Biomaterials & Tissues, Hawaii, USA (2019, oral presentation).
- **Callens, S.J.P., Zadpoor, A.A.,** Curvature as a regulator for preosteoblast organization on precisely microfabricated substrates, World Biomaterials Congress Glasgow (virtual), United Kingdom (2020, oral presentation).

# CURRICULUM VITAE

Sebastien Jacob Paul Callens was born on April, 15 1993 in Leuven, Belgium. He attended the *Sint-Albertuscollege* in Leuven and graduated from high school in 2011. His passion for aviation and space flight brought him to the Netherlands to pursue a BSc in Aerospace Engineering at Delft University of Technology. He continued his education with an MSc in Aerospace Structures and Materials and obtained his degree in 2017 (cum laude) with a thesis on the development and evaluation of two-matrix composites.

Afterwards, Sebastien redirected his interests and continued his research in the Biomechanical Engineering department at the faculty of Mechanical, Maritime and Materials Engineering of Delft University of Technology. He pursued a PhD under the supervision of Prof. Amir A. Zadpoor. His research focused on the geometric design of novel biomaterials for bone tissue engineering applications. Over the course of his PhD program, Sebastien also contributed to several BSc- and MSc-level courses and he performed a three-month exchange at the Laboratory for Bone Biomechanics at ETH Zurich where he worked in the research group of Prof. Ralph Müller. Furthermore, he developed a strong passion for science communication and engaged in several competitions and nation-wide events.

In 2020, Sebastien got married to Delphine De Tavernier who is an academic researcher in wind turbine aerodynamics.

